Universidade de Brasília
Instituto de Geociências
Programa de Pós-graduação em Geologia

Evolução geológica da estrutura de impacto de Araguainha: gênesis e colocação das brechas de impacto

Geological evolution of the Araguainha impact structure: genesis and emplacement of impact breccias

CAROLINNA DA SILVA MAIA DE SOUZA

Tese de Doutorado nº 209

Orientadora: Profa. Dra. Natalia Hauser
Co-orientador: Prof. Dr. Wolf Uwe Reimold

Brasília, 13 de setembro de 2024

Universidade de Brasília
Instituto de Geociências
Programa de Pós-graduação em Geologia

Evolução geológica da estrutura de impacto de Araguainha: gênesis e colocação das brechas de impacto

Geological evolution of the Araguainha impact structure: genesis and emplacement of impact breccias

CAROLINNA DA SILVA MAIA DE SOUZA

Tese apresentada ao Programa de Pós-Graduação em Geologia – Instituto de Geociências – IG da Universidade de Brasília – UnB como requisito parcial obrigatório para a obtenção do título de Doutor em Geologia.

Área de concentração: Geologia Regional

Orientadora: Profa. Dra. Natalia Hauser

Comissão Examinadora:

Prof. Dr. Elder Yokoyama (IG/UnB);
Profa. Dra. Claudia Regina Passarelli (USP);
Prof. Dr. Álvaro Penteado Crósta (Unicamp);
Prof. Dr. Elton Luiz Dantas (Suplente IG/UnB);
Prof. Dr. Renato Henrique Pinto (Suplente USP)

Ficha catalográfica elaborada automaticamente,
com os dados fornecidos pelo(a) autor(a)

da Silva Maia de Souza, Carolinna
dS729e Evolução geológica da estrutura de impacto de Araguainha: gênesis e colocação das brechas de impacto / Carolinna da Silva Maia de Souza; orientador Natalia Hauser; co-orientador Wolf Uwe Reimold. -- Brasília, 2024.
352 p.

Tese(Doutorado em Geologia) -- Universidade de Brasília, 2024.

1. Estrutura de impacto de Araguainha. 2. Brechas de impacto. 3. Faixa Paraguai. 4. Bacia do Paraná. I. Hauser, Natalia, orient. II. Reimold, Wolf Uwe, co-orient. III. Título.

AGRADECIMENTOS

O presente trabalho foi realizado com apoio da Coordenação de Aperfeiçoamento de Pessoal de Nível Superior – Brasil (CAPES) – Código de Financiamento 001. Agradeço ao suporte financeiro que me foi oferecido pela CAPES e à *Barringer Family Fund for Meteorite Impact Research*.

Aos meus familiares pelo apoio durante todo o período dedicado ao doutorado, aos meus pais por serem a minha base de inspiração e me apoiaram em todos os momentos dessa jornada.

Obrigada a todas as pessoas que contribuíram, de alguma forma, para o desenvolvimento desta pesquisa, com troca de conhecimento, da generosidade, da sabedoria ou do apoio incansável. Cada ajuda foi fundamental para a realização deste trabalho. Aos professores Natalia Hauser e Wolf Uwe Reimold pela dedicação e tempo destinado às correções e orientações. Agradeço também aos professores que passaram pelo meu caminho nas universidades federias que frequentei desde a graduação, por todo conhecimento fornecido. À equipe do Laboratório de Estudos Geodinâmicos e Ambientais e ao Instituto de Geociências da Universidade de Brasília pelo suporte fornecido.

E agradeço a Deus por estar sempre ao meu lado e me guiar em todos os momentos.

RESUMO

Crateramento por impacto é um processo geológico que desempenha um papel fundamental na formação do sistema solar e dos planetas terrestres. No Brasil, a estrutura de impacto de Araguainha, a maior da América do Sul (40 km de diâmetro), foi formada próximo ao limite Permiano-Triássico (~254 Ma) e atingiu a porção nordeste da Bacia do Paraná, escavando todo o pacote sedimentar até o embasamento. Trata-se de uma estrutura de impacto do tipo complexa, que possui o núcleo central soerguido relativamente preservado (16 km de diâmetro), onde rochas-alvo deformadas por choque e brechas de impacto são bem expostas. Esta tese busca entender a evolução geológica e as brechas de impacto no núcleo central, por meio de análises de campo, análises qualitativas e quantitativas, e analises isotópicas (U-Pb). O estudo revelou: 1) Maior heterogeneidade litológica das rochas do embasamento metassedimentar envolvendo rochas metamórficas e não metamorfizadas. 2) Brechas polimíticas de impacto em contato com essas rochas do embasamento metassedimentar por diferentes mecanismos. Os componentes das brechas são relacionados às unidades inferiores das rochas-alvo. 3) Três tipos de rochas fundidas por impacto com diferentes relações de campo e composição foram identificados, formados em diferentes fases do processo de impacto. Um modelo multiestágio é proposto para a origem e colocação dessas brechas em Araguainha, sugerindo uma profundidade máxima de penetração do bólido na interface entre a sequência inferior da Bacia do Paraná e o embasamento. Nossos dados ressaltam o nível de erosão sofrido pela estrutura após o impacto, em que a configuração das brechas polimíticas de impacto está relacionada à topografia do fundo da cratera, ou seja, as brechas são produtos de preenchimento de crateras bem preservadas e representam material que nunca deixou a cratera. Este estudo amplia o conhecimento sobre a estrutura de impacto de Araguainha e seus produtos (ex., brechas de impacto), contribuindo significativamente para a geologia regional e local, abrindo caminho para novas investigações.

Palavras-chave: Estrutura de impacto de Araguainha, Brechas de impacto, Faixa Paraguai, Bacia do Paraná.

ABSTRACT

Impact cratering is a geological process that plays a fundamental role in the formation of the solar system and terrestrial planets. In Brazil, the Araguainha impact structure, the largest in South America (40 km in diameter), was formed near the Permian-Triassic boundary (~254 Ma) and struck the northeastern portion of the Paraná Basin, excavating the entire sedimentary sequence down to the basement. It is a complex impact structure, with a relatively well-preserved central uplift (16 km in diameter), where shock-deformed target rocks and impact breccias are well exposed. This thesis aims to understand the geological evolution and the impact breccias in the central uplift through field analyses, qualitative and quantitative analyses, and isotopic (U-Pb) analyses. The study revealed: 1) Greater lithological heterogeneity of the basement metasedimentary rocks, involving both metamorphic and unmetamorphosed rocks. 2) Polymict impact breccias in contact with these metasedimentary basement rocks through different mechanisms. The breccia components are related to the lower units of the target rocks. 3) Three types of impact melt rocks with different field relations and compositions were identified, formed during different stages of the impact process. A multi-stage model is proposed for the origin and emplacement of these breccias in Araguainha, suggesting a maximum penetration depth of the bolide at the interface between the lower sequence of the Paraná Basin and the basement. Our data highlight the level of erosion the structure underwent after the impact, where the configuration of the polymict impact breccias is related to the crater floor topography, meaning the breccias are well-preserved crater fill products and represent material that never left the crater. This study expands the knowledge of the Araguainha impact structure and its products (e.g., impact breccias), significantly contributing to both regional and local geology and paving the way for future investigations.

Keywords: Araguainha impact structure, Impact breccias, Paraguay Belt, Paraná Basin.

LISTA DE ILUSTRAÇÕES

CAPÍTULO 1

Figura 1.1 Distribuição mundial das 210 estruturas de impacto confirmadas designando os diâmetros e as idades estimadas. Modificado de Schmieder e Kring (2020). 3
Figura 1.2 Imagem de satélite de radar TanDEM-X para a estrutura de impacto de Araguainha. Modelo de elevação digital codificado por cores e sombreado em colina (iluminação na elevação: 45º, azimute: 315º). MT: Mato Grosso, GO: Goiás. Fonte: Courtesy of Manfred Gottwald, German German Aerospace Center (DLR, Oberpfaffenhofen, Germany). Modificado de Hauser et al. (2019). 5
Figura 1.3 Mapa de localização da área de estudo e uma das vias de acesso à estrutura de impacto de Araguainha com partida desde Brasília. 7

CAPÍTULO 2

Figura 2.1 Contexto geotectônico esquemático da Província do Tocantins com suas faixas móveis. Mapa geológico da Faixa Paraguai norte e sul em relação aos crátons Amazônico e Rio Apa. Modificado de Leite et al. (2021). 11
Figura 2.2 Distribuição regional das seis supersequências estratigráficas sugeridas por Milani (1997) para a Bacia do Paraná, apresentando a coluna estratigráficas simplificada e a localização das quatro estruturas de impacto confirmadas nesta bacia. Modificado de Montibeller et al. (2020). 15
Figura 2.3 Processos envolvidos durante a formação de estruturas de impacto do tipo simples. a) Primeiro estágio – contato e compressão: penetração inicial do projétil e radiação externa de ondas de choque; b) Fim do primeiro estágio e início do segundo estágio – escavação: expansão contínua da onda de choque na rocha alvo com o desenvolvimento de onda tensional (rarefação ou onda de liberação); c) Durante o estágio de escavação: desenvolvimento de revestimento de melt na cavidade transitória em expansão; d) Fim do segundo estágio: cavidade transitória com a extensão máxima; e) Início do terceiro estágio – modificação: colapso da cratera transitória; f) Estrutura final de uma estrutura de impacto do tipo simples: depressão em forma de tigela, parcialmente preenchida com brechas complexas e corpos de derretimento de impacto. Modificado de French (1998). 20
Figura 2.4 Processos envolvidos durante a formação de estruturas de impacto do tipo complexa. a) Segundo estágio – escavação (o primeiro estágio é o mesmo ilustrado na figura anterior 2.3): formação de uma grande cratera transitória; b) Fim do segundo estágio e início do terceiro estágio – modificação: desenvolvimento inicial do soerguimento central; c) Durante o terceiro estágio: início do colapso da cratera transiente acompanhado pelo desenvolvimento contínuo da elevação central e o afinamento e a queda da camada de fusão original (em preto) sobre as rochas elevadas; d) Estrutura final de uma estrutura de impacto do tipo complexa: consiste de uma elevação central composta por rochas mais profundas, cercada por uma planície relativamente plana com (ou não) deposição de camadas de melt, e por uma borda em terraços produzida pelo movimento para dentro ao longo de falhas normais escalonadas. Modificado de French (1998). 21

Figura 2.5 Evidências do impacto. a) Feições de shatter cones (ca. 5-10 cm) observados em metarenitos. b) Observação de planar deformation features (PDFs) com duas direções no mineral de quartzo. c) Imagem de backscattered electron (BSE) de um grão de zircão arredondado. d) Zoom da figura (c) em que se observa a textura granular na superfície do grão de zircão. Tomada de Hauser (2021). 23
Figura 2.6 Diagrama dos regimes de pressão (GPa) e temperatura (°C) do metamorfismo de choque por impacto e do metamorfismo da crosta terrestre. Modificado de Stöffler et al. (2018). 24
Figura 2.7 Classificação dos impactitos definida por Stöffler e Grieve (2007). Modificado de Stöffler e Grieve (2007). 25
Figura 2.8 Suevitos da estrutura de impacto Ries (Alemanha). a) Imagem de campo mostrando o melt preservado com forma complexa. b) Amostra de mão mostrando a variedade de clastos líticos e a presença de melt. Modificado de Osinski e Grieve (2024). 28

CAPÍTULO 4

Figure 4.1 Geological map of the Araguainha impact structure based on available geological maps (von Engelhardt et al., 1992; Lana et al., 2007; Machado et al., 2009; UnB-IG, 2012; Yokoyama et al., 2012; Crósta et al., 2019) and referenced against the WGS84 UTM Zone 22S geodetic datum, updated based on TanDEM-X radar satellite image (~53 x 61 km wide area; courtesy of the German Aerospace Center – DLR, Oberpfaffenhofen, Germany) and surface reflectance (Landsat 8/OLI) imagery. The SRTM digital elevation model multidirectional shaded relief (NASA JPL, 2013) was used in the map to give a sense of topography. The Araguainha impact structure straddles the border between Goiás and Mato Grosso states and is centered at 16º48'45" S, 52º59'02" W. On the right, a simplified stratigraphic column is presented for the sequences of the Paraná Basin and the Precambrian basement that constituted the target rocks for the Araguainha impact event. The basement is composed of Neoproterozoic rocks of the Paraguay Belt, probably mainly derived from the Cuiabá Group, and a Cambrian, post-collisional porphyritic granite of the Brazilian Granitic Province, from the Serra Negra Suite. The thicknesses indicated are based on data from Lana et al. (2007). Modified after UnB-IG (2012). Tr – Triassic. 42
Figure 4.2 Geological map for the area of the Araguainha central uplift (zoom from Figure 4.1). Also indicated is that the northern sector is related in this paper with the description of these outcrops: CA-99, the classical shatter cone locality in metasedimentary basement that are overlain by polymict impact breccia; CA-09, the polymict breccias that crop out along the path to the communication tower; and GAR-15, the profile across the megablock zone that illustrates the relationships between the basal target rocks and overlying impact breccias. The southern sector is indicated by Profiles 1, 2, and 3. The narrow zone with Type-III impact melt rock is not indicated, but it is possible to see the distribution of this melt rock type in the map of Figure S2. 44
Figure 4.3 (a) Panoramic photo showing some major observations along the GAR-15 profile (at UTM 22K 288556.67 E, 8142283.08 S): impact melt rock Type-I, heterogeneous basement lithologies, units of the lower sequence of the Paraná Basin, and also some transcurrent faulting. The road section shown is

350 m long. (b) Schematic 3D representation of part of this section (240 m long), with transcurrent faulting. The apparent dip of layers is also indicated with cross-hatching. 56
Figure 4.4 (a) Intrusion of a dike of IMR Type-I into (meta)sedimentary basement (at UTM 22K 288562 E, 8142192 S) along the GAR-15 profile. The person, shown in part for scale, is approximately 1.5 m tall in this image. The continuous lines indicate the bedding and the dashed lines represent the probable contact between the rocks. (b, c) Hand specimens of IMR Type-I with lithophysae structures (see text for detail). (d) Clasts of lithic material (granite), quartz, and partially plasticized K-feldspar in an aphanitic matrix of IMR Type-I. Coin, for scale, is 2.5 cm in diameter. 57
Figure 4.5 (a) An outcrop of impact melt rock Type-I adjacent to the MT-100 road, in contact with (meta)sedimentary basement, in the GAR-15 profile (at 22K 288562 E, 8142192 S), that is locally melted and annealed. The continuous lines indicate the bedding and the dashed lines the probable contact between the rocks. Hammer in a and b, for scale, is 31 cm long. (b) Part of the same outcrop, showing the contact (white dotted line) between IMR Type-I and deformed (folded) pelitic basement rock. (c) Melting and plasticization of some of the highly siliceous and folded basement rock in contact with IMR Type-I. Pencil for scale is 11 cm long. The contact is marked by the white dotted line. 59
Figure 4.6 (a) Outcrop CA-73 (at 22K 288549.45 E, 8142116.97 S) where thin polymict impact breccia (PIB) dikes up to 10-cm thick are injected into (meta)sedimentary basement (this exposure in the then unpaved MT-100 road has since been tarred over). Pencil, for scale, is 12 cm long. (b) Contact relationship between a dark-brown, brittle-deformed metasandstone of the metasedimentary basement, in subvertical fault contact with PIB, at the CA-07 outcrop (at 22K 288523 E, 8141975 S). The thicker dashed line represents the contact between the rocks and the thin dashed lines indicate the open folds. (c) This image of the CA-99 outcrop (at 22K 285788 E, 8139861 S) shows PIB adjacent to a large block of metasedimentary basement, near the classic shatter cone outcrop in phyllite thought to represent Cuiabá Group material. The main image shows the contact relationship between the PIB and the phyllite, and the hammer, for scale, is 31 cm long. The inset shows shatter cones within an approximately 30 cm large phyllite clast in PIB. Pencil, for scale, is ca. 12 cm long. 61
Figure 4.7 (a) Field photo of the polymict impact breccia (PIB) at the CA-07 location at 22K 288523 E, 8141975 S, showing gray matrix with some clast types identified by numbers (1, grey metapelite with or without spots; 2, brown metapelite; 3, white, fine- to medium-grained sandstone; 4, red conglomeratic sandstone; 5, conglomerate). Magnifying lens, for scale, is approximately 5 cm long. (b) Example of IMR Type-II, a silicious and partly melted clast type in CA-09 polymict impact breccia (at 22K 287445 E, 8141433 S). This IMR type is characterized by whitish/greyish and mostly highly porous melt rock. Coin, for scale, is 2.5 cm wide. (c) The impressive CA-98 PIB outcrop (at 22K 288483 E, 8141862 S; the entire exposure down to the main road level is approximately 15 m high, whereas the bench shown here has a height of approximately 8 m) with extensive development of green veining. The breccia in the vein system is mainly composed of clay minerals. One X-ray diffraction analysis (not presented here) shows that the main component is kaolinite and quartz. People, for scale, up to 1.8 m tall. (d) A photo with an enlarged part of a green vein cutting through

(meta)sedimentary basement rock. Width of section shown in this inset is estimated to be 8 m..... 65
Figure 4.8 Schematic representation of the three profiles investigated in detail in the southern sector of the central uplift: (a) Profile 1, (b) Profile 2, and (c) Profile 3 (compare with Figure 4.2). These profiles have been constructed without vertical exaggeration; some local apparent dips of bedding or foliation are indicated. 68
Figure 4.9 (a) Outcrop of meter-sized blocks of IMR Type-IIIa, at a site a few meters from the occurrence of alkali granite. Hammer, for scale, is 31 cm long. (b) Hand specimen of IMR Type-IIIa showing the quartz pebbles (whitish-pinkish) of the primary conglomerate surrounded by fluidal textured silicious groundmass. Coin, for scale, is 2.5 cm wide..... 69
Figure 4.10 (a) Panoramic view across a section of the southern part of the central uplift showing the contact zone between alkali granite and an occurrence of transitional (part-melted) granite. The area shown is approximately 50 m wide in the foreground and the megablocks of Furnas sandstone in the background are up to hundreds of meters wide. View towards the north. (b) Hand specimen of transitional granite with schlieren of plasticized and, in part melted feldspar, as well as remnant quartz that occasionally has biotite rimming. Mineral abbreviations after Warr (2021): Fsp, feldspar; Qz, quartz. 72
Figure 4.11 Schematic, unscaled illustration of the distribution of target rocks and impact related rocks prior, during, and after the cratering process, as suggested here for the Araguainha impact structure. Stage 1: The stratigraphy of the target rocks before impact (1 - shock wave, 2 - excavated area as proposed by Lana et al., 2006, 3 - excavated area proposed by us, 4 - the displaced area related to the development of the transient cavity). Stage 2: Intermediate stage, the strata are uplifted and deformed during crater modification. Stage 3: The final representation of the central uplift in NE-SW direction, where the geological context observed during our field campaigns is illustrated, with the typical settings of the different impact breccia types at Araguainha and the contact of alkali granite with the (meta)sedimentary basement. 89

SUPPLEMENTARY MATERIAL

Figure S1. The map of the central uplift of Araguainha after von Engelhardt et al. (1992). 100
Figure S2. (a) Map of the study locations from our 2019-2022 field campaigns in the central uplift region. The (b) northern and (c) southern study regions are enlarged to better show the distribution of points. The contour lines were extracted from the TanDEM-X digital elevation model at 50 m intervals. Some points overlap in the image. For more detail and to relate the points to study profiles we have also added the study points of von Engelhardt et al. (1992); for geographic coordinates refer to Table S1.....101
Figure S3. Photomicrographs taken in cross-polarized light for different impact-related rocks. (a) An image of transitional granite showing a core of remnant quartz surrounded by a rim of small, neoformed biotite crystals. (b) Impact melt rock (IMR) Type-I showing clusters of sanidine crystals in circular to radial aggregates and recrystallized quartz clasts. (c, d) Polymict impact breccia (PIB) matrix with fragments of sandstone, metapelite, quartz minerals, and melt particles (IMR Type-II). (e) IMR Type-III showing fluidal texture around a rounded

and thermally abraded quartzitic clast. Part of the quartz in this clast shows toasting. The fine-grained matrix is silicious and completely annealed or recrystallized. The dark bands are interpreted to represent primary pelitic seams. (f) Photomicrograph taken in plane-polarized light of IMR Type-III showing the toasted and granular zircon grains concentrated in specific laminae within the fluidal structure. Mineral abbreviations after Warr (2021): Ab – albite, Bt – biotite, Fsp – undifferentiated feldspar, Qz – quartz; Sa – sanidine; Zrn – zircon.....103
Figure S4. (a) IMR Type-IIIa with well-preserved quartz pebbles of the original conglomeratic target rock (at 22K 287525 E, 8137986 S). Hammer, for scale, ca. 31 cm long. (b) IMR Type-IIIb with fluidal structure (at 22K 287124 E, 8137954 S) emphasized by weathering. The part of the hammer shown is approximately 20 cm long. (c) A contact between IMR Type-I against Type-IIIb (at 22K 287329 E, 8138048 S). (d) Metarhythmite of the (meta)sedimentary sequence at the same locality as (a). Hammer, for scale, is approximately 35 cm long.....104
Figure S5. (a, b) Simplified, schematic profiles based on the cross sections A and B of fig. 2 of von Engelhardt et al. (1992). Profiles (c) and (d) are based on our field work along the same traverses and emphasize the differences to the interpretations of von Engelhardt et al. (1992). Elevations along our profiles were extracted from the TanDEM-X digital elevation model, whereas von Engelhardt et al. (1992) obtained topographic information by extrapolating between GPS measurements at certain reference points.. 104

CAPÍTULO 5

Figure 5.1 (A) Location of the Tocantins Province in the Brazilian territory and simplified geological map of the Paraguay and Brasília mobile belts. The Araguainha impact structure is also indicated. Modified after Leite et al. (2021). (B) Geological map of the Araguainha impact structure georeferenced against the WGS84 UTM Zone 22S geodetic datum, overlain on at TanDEM-X radar satellite image (~53 x 61 km wide) courtesy of the German Aerospace Center – DLR, Oberpfaffenhofen, Germany and surface reflectance (Landsat 8/OLI) imagery. 116
Figure 5.2 Geological map of the Araguainha central uplift region of 16 km diameter, after Souza et al. (2024). The outcrops of polymict impact breccia profiles and basement exposures used in this work are indicated in the map.117
Figure 5.3 (A) Light-grey breccia matrix from the CA-07 outcrop (at UTM 22K 288523 m E; 8141975 m S) along the MT-100 road. Person, for scale, up to 1.6 m tall. (B) Occurrence of blocks of phyllite above the PIB from CA-07 outcrop. Hammer, for scale, is 31 cm long. (C) Contact relationship between the polymict impact breccia of the CA-84 breccia deposit and altered phyllite, separated by a whitish thrust plane oriented at 280/60. Hammer, for scale, is 31 cm long. 130
Figure 5.4 Micro-X-Ray fluorescence results for sample CA-07A from the CA-07 profile. Thin section microphotograph in (A) plane-polarized light and (B) cross-polarized light. (C) A qualitative Fe-Si-Al multi-element map, whereby the colors relate to enhanced Fe (red), Si (green), and Al (blue). Purplish color indicates enhanced abundances of Fe and Al. The following five semi-quantitative single-element heat maps show the relative abundances of (D) Si, (E) Al, (F) K, (G) Fe, and (H) Ti. Some micro-clasts are classified by numbers: 1 - slate with spots (pseudomorphs after cordierite), 2 - metasandstone, 3 - slate, 4 - sandstone, 5 - quartz, 6 - impact melt.....135

Figure 5.5 Mineral maps from QEMSCAN analysis of samples from for three thin section of breccia deposits from the northern sector. (A) Thin section of sample CA-07D from the CA-07 profile. (B) Thin section of sample CA-09B from the CA-09 profile. (C) Thin section of sample M-0 from the CA-84 profile. Some micro-clast types are indicated by numbers: 1 - sandstone, 2 - slate, 3 - quartz, 4 - impact melt rock. 136
Figure 5.6 Examples of field and microscopic appearances of impact melt clasts in polymict impact breccia. (A) An impact melt clast of meter size from the upper part of the CA-09 profile (at UTM 22K 288093 m E, 8141598 m S). Hammer, for scale, 31 cm long. (B) Photomicrograph of melt particles in sample CA-07D – melt with fluidal texture. (C) QEMSCAN mineral map for sample SF-28C from the CA-09 profile. (D) Qualitative Fe-Si-Al multi-element map for µXRF data of sample CA-07D, with melt particles indicated by white lines. 137
Figure 5.7 Representative cathodoluminescence (CL) images from samples of polymict impact breccias (A-D) and (meta)sedimentary rocks (E-I). Displayed spot ages are 206Pb/238U ages < 900 Ma and 207Pb/206Pb ages > 900 Ma. Small circles (20-32 µm) represent the locations of U-Pb analyses. When these circles are in yellow color, represents the concordant data, whereas in red color, discordant data. In (A) representative backscattered electron (BSE) imaging on exterior surface when was observed granular texture in sample P-03. 147
Figure 5.8 (A) Wetherill plot for the polymict impact breccia (sample P-03) of 43 analyzed concordant grains. (B) Histograms for the concordant analyzed grains of sample P-03 with the age peaks of the probability density plot. (C) Wetherill plot for the polymict impact breccia (sample SF-04) of 26 analyzed concordant grains. (D) Histograms for the concordant analyzed grains of sample SF-04 with the age peaks of the probability density plot. (E) Wetherill plot for the polymict impact breccia (sample CA-73) of 13 analyzed concordant grains. (F) Histograms for the concordant analyzed grains of sample CA-73 with the age peaks of the probability density plot. (G) Wetherill plot for the conglomerate from Alto Garças Formation (sample CA-49) of 28 analyzed concordant grains. (H) Histograms for the concordant analyzed grains of sample CA-49 with the age peaks of the probability density plot. 150
Figure 5.9 (A) Wetherill plot for the phyllite (sample CA-111) of 58 analyzed concordant grains. (B) Histograms for the concordant analyzed grains of sample CA-111 with the age peaks of the probability density plot. (C) Wetherill plot for the phyllite (sample GAR-15-0) of 20 analyzed concordant grains. (D) Histograms for the concordant analyzed grains of sample GAR-15-0 with the age peaks of the probability density plot. (E) Wetherill plot for metasandstone (sample GAR-15-G10) of 70 analyzed concordant grains. (F) Histograms for the concordant analyzed grains of sample P-03 with the age peaks of the probability density plot. (G) Wetherill plot for siltstone (sample CA-22) of 60 analyzed concordant grains. (H) Histograms for the concordant analyzed grains of sample CA-22 with the age peaks of the probability density plot. 152
Figure 5.10 An integrated 110 m long vertical profile through the Araguainha polymict impact breccia deposits of the northern central uplift. The relative matrix : clast ratios, the occurrence of clast types, the melt distribution (vol %), and the variation of shock metamorphism observed along this profile are shown. Shock metamorphism is expressed semiquantitatively due to the amount accounted for in the thin sections, being + low = < 10; ++ medium = 20-10; +++ strong = > 20). The occurrences of clast types are indicated by (*) along the profile. Legend: 1 -

quartz pebbles, 2 - conglomerate, 3 - green sandstone, 4 - red conglomeratic sandstone, 5 - grey conglomeratic sandstone, 6 - white sandstone, 7 - black shale, 8 - brown slate, 9 - grey slate, 10 – granite, 11 – impact melt rock clasts. 156
Figure 5.11 Multidimensional scaling plot displaying the varied relationships of detrital zircon from samples studied here against zircon age data from the literature [impact melt rock of Type III (Hauser et al., 2019); lower units of the Paraná Basin – Ponta Grossa Formation samples (from Henrique-Pinto et al., 2021; López, 2022), Furnas Formation samples (from Santos et al., 2015; Henrique-Pinto et al., 2021; López, 2022), Rio Ivaí Group samples (Gezatt, 2011; Henrique-Pinto et al., 2021); basement rocks from Paraguay Belt – alkali granite samples (Tohver et al., 2012), Cuiabá Group samples (Pelosi, 2017; Babinski et al., 2018; Frugis et al., 2024), Puga Formation (McGee et al., 2014), Alto Paraguay Group samples (McGee et al., 2014); and rocks from Brasilia Belt (from Pimentel et al., 1991; Pimentel et al., 2003; Matteine et al., 2010; Della Giustina et al., 2011; Marques et al., 2019; Piauilino et al., 2021; Carneiro et al., 2021)]. The continuous lines represent the most similar samples and the discontinuous lines the second most-similar ones. 161
Figure 5.12 Kernel density estimates (normalized y-axis; 0–4000 Ma) for detrital zircon of all analyzed samples together with data from bibliography with the probable sources, Goiás Magmatic Arc (0.90-0.60 Ga) and Amazon Craton (>2.50-0.95 Ga). The six geochronological provinces from Amazon Graton are (Tassinari and Macambira, 1999): Sunsás Province (1.20-1.00 Ga), Rondonian-San Ignacio (1.55-1.30 Ga), Rio Negro Juruena (1.80-1.55 Ga), Ventuari-Tapajós (1.95-1.80 Ga), Maroní-Itacaiúnas (2.20-1.95 Ga), Amazônia Central (>2.5 Ga). 163
Figure 5.13 Cumulative probability plots for convergent, collisional, and extensional settings (Cawood et al., 2012) for the samples analyzed to this study. 164

SUPPLEMENTARY MATERIAL

Figure S2A. Representative X-ray diffraction patterns of the studied samples. (A) Siltstone of the Furnas Formation from outcrop GAR-19 (at UTM 22K 288679 m E; 8142465 m S). (B) Polymict impact breccia matrix from outcrop CA-98 (at UTM 22K 288483 m E; 8141862 m S). (C) Impact melt rocks of Type II clast from outcrop CA-07 (at UTM 22K 288523 m E; 8141975 m S). (D) Impact melt rocks of Type II clast from outcrop CA-116 (at UTM 22K 287915 m E; 8141449 m S). (E) Impact melt rocks of Type II clast from outcrop CA-84 (at UTM 22K 286769 m E; 8141191 m S). (F) Impact melt rocks of Type II clast from outcrop CA-98 (at UTM 22K 288483 m E; 8141862 m S). 197
Figure S2B. Representative backscattered electron images produced from scanning electron microscopy analysis in the breccia matrix for (A) sample CA-07C from CA-07 profile and (B) sample M-0 from CA-84 profile. 198
Figure S2C. Modal analysis data from macroscopic analysis of samples from the CA-07 profile, with clast type distribution per analyzed area, the clast size distribution, melt clast occurrence, and shock metamorphic features. N denotes the total number of clasts analyzed. The samples collected for laboratory analysis (hand specimens and thin sections) are also indicated. Clast sizes > 1 m are not indicated in the clast size frequency distribution. 199
Figure S2D Modal analysis data from macroscopic analysis of samples from the CA-09 profile, with clast type distribution per analyzed area, the clast size

distribution, melt clast occurrence, and shock metamorphic features. N denotes the total number of clasts analyzed. The samples collected for laboratory analysis (hand specimens and thin sections) are also indicated. Clast sizes > 1 m are not indicated in the clast size frequency distribution. 203
Figure S2E. Modal analysis data from macroscopic analysis of samples from the CA-84 profile, with clast type distribution per analyzed area, the clast size distribution, melt clast occurrence, and shock metamorphic features. N denotes the total number of clasts analyzed. The samples collected for laboratory analysis (hand specimens and thin sections) are also indicated. Clast sizes > 1 m are not indicated in the clast size frequency distribution. 207

Figure S3A. (A) Outcrop CA-111 composed by phyllite in contact relationship with conglomerate matrix supported. (B) Dark brown phyllite from CA-111 outcrop (at UTM 22K 291650 m E; 8141529 m S), which contains some small quartz veins (~1 cm). 211
Figure S3B. (A) Location of the outcrop GAR-15 (at UTM 22K 288556 m E, 8142283 m S) in the megablock zone, next to the polymict impact breccia profile (CA-07). Also, the three samples collected are indicated (GAR-15-0, GAR-15-G10, and CA-73). (B) Outcrop where the basement is located in between two apophysis of granite and around the sedimentary strata from Rio Ivaí Group. The person, shown in part for scale, is approximately 1.7 m tall. (C) A zoom from figure (B) showing a detail of the black phyllite from GAR-15-0 sample. Hammer in b to d, for scale, 31 cm long. 212
Figure S3C. (A) Outcrop that contains the metasandstone in the GAR-15 profile without scale. (B) A metasandstone characterized by light grey color, friable, from GAR-15-G10 sample.....213
Figure S3D. Grey siltstone with quartz veins of approximately 35 cm from CA-22 outcrop (at UTM 22K 290608 m E, 8139763 m S). Coin, for scale, 2.5 cm in diameter. 213
Figure S3E. Conglomerate from CA-49 outcrop with quartz sheared (at UTM 22K 289856 m E, 8140950 m S). Coin, for scale, 2.5 cm in diameter. 214
Figure S3F. (A) Sample P-03 collected for U-Pb analysis. (B) Sample SF-04 collected for U-Pb analysis. (C) CA-73 breccia matrix that corresponds to the ejected PIB dikes into the white sandstone from the megablock zone. (D). Sample CA-116, highly enriched in of impact melt rocks of Type II. Coin, for scale, 2.5 cm in diameter. 215

LISTA DE TABELAS

CAPÍTULO 1

Tabela 1.1 Resumo das estruturas de impacto confirmadas na América do Sul (Osinski et al., 2022; Crósta, 2024). 4

CAPÍTULO 4

Table 4.1 Comparison of rock nomenclatures applied to Araguainha impactite lithologies as identified in the central uplift by various authors. Modified after Crósta et al. (2019). 45
Table 4.2 Main characteristics of the three types of impact melt rock discerned in this study. 58
Table 4.3 Summary of the main characteristics of the polymict impact breccia outcrops studied in the field in the northern and southern parts of the central uplift. 63

SUPPLEMENTARY MATERIAL

Table S1. Geological points with coordinates of the lithologies identified during our field campaigns on the central uplift of the Araguainha impact structure, as well as information from previous authors (Fischer, 2015; Hauser et al., 2019; Preuss, 2012; von Engelhardt et al., 1992). The elevations in italics were acquired with the use of Google Earth Pro. 105

CAPÍTULO 5

Table 5.1 Schematic stratigraphic relationship between northern and southern sectors of the Paraguay Belt. The Maximum depositional age is also indicated. Modified after Vasconcelos (2018) and Leite et al. (2024). 121
Table 5.2 Qualitative proportions of clast types across different scales from the detailed descriptions of breccia deposits studied (CA-07, CA-09, CA-84). The total number of clasts analyzed is given as well. 139
Table 5.3 Percentages of occurrence of different shock features in quartz micro-clasts, in quartz of the matrix, or quartz grains in sandstone micro-clasts. N = total number of quartz grains analyzed. 140

SUPPLEMENTARY MATERIAL

Table S1.A Samples analyzed for the instrumental techniques: micro-X-ray fluorescence spectrometry (μXRF), quantitative evaluation of minerals by scanning electron microscopy (QEMSCAN), X-ray diffraction data (DRX), scanning electron microscopy (SEM), and U-Pb isotopic analyses on zircon grains. 186
Table S2A. Qualitative description of profile CA-07 at macro- and mesoscopic scales (M: matrix, C: clast types). The maximum size of the clasts is given in centimeters (cm). 200

Table S2B. Qualitative description of profile CA-07 samples at the microscopic scale. 202

Table S2C. Qualitative description of profile CA-09 at macro- and mesoscopic scales (M: matrix, C: clast types). The maximum size of the clasts is given in centimeters (cm). 204
Table S2D. Qualitative description of profile CA-09 samples at the microscopic scale. 206
Table S2E. Qualitative description of profile CA-84 at macro- and mesoscopic scales (M: matrix, C: clast types). The maximum size of the clasts is given in centimeters (cm). 208
Table S2F. Qualitative description of the CA-84 samples at the microscopic scale. 210

LISTA DE ANEXOS

Anexo 1. Tabela com todos os pontos registrados durante as campanhas de campo. Lat.: latitude, Long.: longitude, Fm.: Formação, Gr.: Grupo, IMR: rocha fundida de impacto, BPI: brecha polimítica de impacto, cong.: conglomerado. 262
Anexo 2. Mapas composicionais semiquantitativos de elementos maiores e traços analisados por micro florescência de raio-X (µFRX) em amostras do perfil CA-07 e de três rochas fundidas por impacto (CA-04, CA-05, CA-15). 263
Anexo 3. Caracterização mineral de alta resolução em sete lâminas polidas analisadas pela Avaliação Quantitativa de Minerais por Microscopia Eletrônica de Varredura (QEMSCAN). 266

SUMÁRIO

1 INTRODUÇÃO 2

1.1 Apresentação do tema 2

1.2 Relevância e objetivos da tese 4

1.3 Localização e vias de acesso 6

1.4 Estrutura da tese 7

2 REFERENCIAL TEÓRICO E REVISÃO BIBLIOGRÁFICA 10

2.1 Embasamento Pré-Ordoviciano 10

2.2 Bacia do Paraná 14

2.3 Estruturas de impacto 18

2.3.1 Processos de formação 18

2.3.2 Estruturas de impacto: reconhecimento 22

2.3.3 Impactitos 24

2.3.4 Brechas polimíticas de impacto 26

3 MATERIAIS E MÉTODOS 30

3.1 Etapa pré-campo 30

3.2 Trabalho de campo: mapeamento geológico 30

3.3 Análises petrográficas 31

3.4 Escaneamento por micro Florescência de Raio-X (μFRX) 31

3.5 Avaliação Quantitativa de Minerais por Microscopia Eletrônica de Varredura (QEMSCAN) 32

3.6 Procedimentos Mecânicos e Analíticos 33

3.6.1 Preparação de amostras 33

3.6.2 Análise por difração de raio-x 33

3.7 Separação de zircão e análises no espectrômetro de massa (LA-ICP-MS) 34

3.7.1 Concentração e montagem 34

3.7.2 Análise isotópica de U-Pb 35

3.8 Tratamento e análise de dados 37

4 ARTIGO 1 39

4.1 Introduction 41

4.2 Background 47
4.2.1 Stratigraphy 47
4.2.2 Structural division of the Impact structure 48
4.2.3 Background about the impact-related rocks at Araguainha 50

4.3 Methodology 51

4.4 Results 53
4.4.1 Field relationships in the northern sector of the central uplift 53
4.4.2 Field relationships in the southern sector of the central uplift 67

4.5 Discussion 75
4.5.1 Updated geology of the central uplift of the Araguainha impact structure 75
4.5.2 New insights about the impact breccias 79
4.5.3 Cratering processes in sedimentary targets: the Araguainha case 87
4.5.4 Considerations about the depth of erosion at Araguainha 91

4.6 Conclusions 92

4.7 References 94

4.8 Supplementary Material 100

5 ARTIGO 2 113

5.1 Introduction 114

5.2 Geological Setting 119
5.2.1 Regional Stratigraphy 119
5.2.2 Local Geology at Araguainha impact structure 123

5.3 Sampling and Methodology 126
5.3.1 Geological mapping 126
5.3.2 Sampling 127
5.3.3 Profiles through breccia deposits 127
5.3.4 Petrography 128

5.4 Results 128
5.4.1 Polymict impact breccia 129
5.4.2 Pre-Ordovician basement rocks: Field descriptions 144
5.4.3 U-Pb isotopic analyses on zircon 146

5.5 Discussion 154
5.5.1 Classification of the polymict impact breccia 154
5.5.2 Provenance analysis 157
5.5.3 Integrated profile of the PIB: composition/size clast variation and shock conditions 165
5.5.4 Emplacement of polymict impact breccia at Araguainha impact structure 166

5.5.5 Geological constraint of the basement below the Paraná Basin in Araguainha area 168

5.6 Conclusions 170

5.7 References 172

5.8 Supplementary Material 186

6 CONSIDERAÇÕES FINAIS 241

REFERÊNCIAS 244

ANEXOS 262

ARTIGOS PUBLICADO EM COLABORAÇÃO 268

CAPÍTULO 1
INTRODUÇÃO

1 INTRODUÇÃO

1.1 Apresentação do tema

A formação de crateras de impacto de hipervelocidade é um processo geológico fundamental que tem sido de extrema importância na formação e evolução do sistema solar e dos planetas terrestres (ex., French, 1998; Melosh, 1989; Melosh e Ivanov, 1999). Projéteis cósmicos atravessam a atmosfera da Terra em hipervelocidades e atingem a superfície terrestre (> 11 km/s; French, 1998), transmitindo um forte estresse cinético nas rochas alvo. A formação de crateras de impacto é um processo complexo e altamente dinâmico que opera em uma variedade de escalas espaço-temporais, desde a deformação por choque em microescala de minerais até a ruptura e perturbação em megaescala de corpos planetários (ex., Collins et al., 2012; Melosh, 1989).

Em sua maioria, o registro das crateras de impacto é totalmente preservado por mais de 4,5 bilhões de anos (ex., Lua, Marte, Mercúrio). Devido ao planeta Terra possuir uma superfície terrestre extremamente dinâmica em que constantes transformações ocorrem (ex., processos tectônicos, intemperismo, erosão), os registros de impacto na Terra são parcialmente preservados ou completamente destruídos (Crósta et al., 2019). Apesar disso, atualmente aproximadamente 210 estruturas de impacto foram confirmadas em toda superfície terrestre (Figura 1.1, Gottwald et al., 2020; Schmieder e Kring, 2020; Kenkmann, 2021; Osinski et al., 2022), as quais fornecem informações essenciais sobre processos e produtos de impacto. As principais ocorrências estão concentradas nos continentes da América do Norte, Europa e Austrália.

A América do Sul, apesar de ser um continente com grande território, possui escassez de estruturas de impacto, com apenas 12 confirmadas (Tabela 1.1; ex., Osisnki et al., 2022; Crósta, 2024). A estrutura de impacto de Araguainha, também conhecida como Domo de Araguainha, foi a primeira reconhecida e ainda é a maior estrutura de impacto identificada neste continente, localizada entre os estados brasileiros do Mato Grosso e Goiás (Fig. 1.2). O domo possui 40 km de diâmetro e, aproximadamente, 1.300 km^2 de área (Dietz e French, 1973; Crósta et al., 1981, 2019; Theilen-Willige, 1981). Morfologicamente, Araguainha é considera uma estrutura de impacto do tipo complexa, composta por um núcleo central soerguido, uma bacia anelar e pelo

menos dois anéis concêntricos (Lana et al., 2007). O evento de impacto atingiu a parte nordeste da Bacia do Paraná, o qual ocorreu próximo ao limite Permiano-Triássico (~254 Ma; Tohver et al., 2012; Erickson et al., 2017; Hauser et al., 2019).

Durante a formação de estruturas de impacto, uma ampla variedade de rochas é produzida e/ou modificada. Estas rochas geradas por impacto são nomeadas de impactitos (Stöffler e Grieve, 2007), os quais são encontrados dentro e/ou ao redor das estruturas de impacto. Impactitos são representados pelas brechas polimíticas de impacto, brechas monomíticas, rochas derretidas por impacto e rochas alvo chocada/metamorfizadas devido as altas pressões e temperaturas alcançadas durante o impacto (French, 1998; Stöffler e Grieve, 2007).

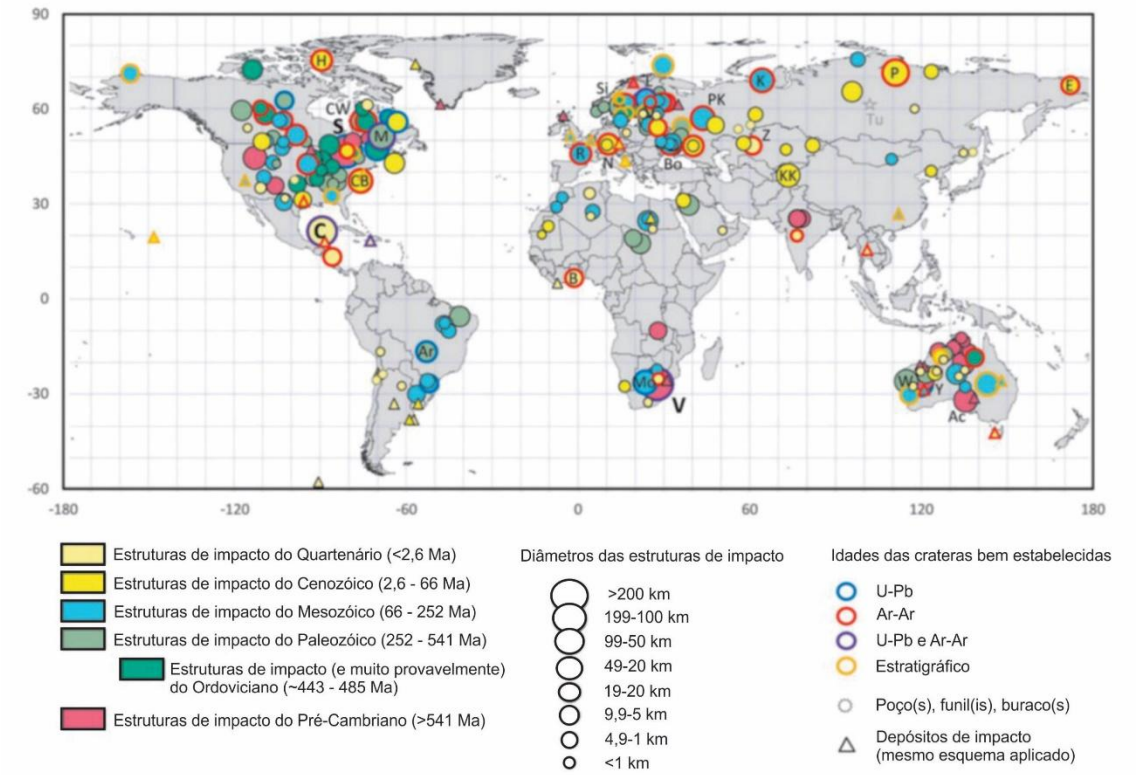

Figura 1.1 Distribuição mundial das 210 estruturas de impacto confirmadas designando os diâmetros e as idades estimadas. Modificado de Schmieder e Kring (2020).

Tabela 1.1 Resumo das estruturas de impacto confirmadas na América do Sul (Osinski et al., 2022; Crósta, 2024).

Nome da cratera	Localização	Latitude	Longitude	Diâmetro (km)	Idade (Ma)
Campo Del Cielo	Argentina	27°38' S	61°42' O	0.05	< 0,004
Araguainha	Brasil	16°47' S	52°59' O	40	254,7±2,5
Vargeão	Brasil	26°50' S	52°07' O	12	< 70
Cerro do Jarau	Brasil	30º12' S	56º32' O	13.5	<132
Serra da Cangalha	Brasil	08º05' S	46°12' O	12	< 300
Santa Marta	Brasil	10°10' S	45°15' O	10	66-100
Vista Alegre	Brasil	25°57' S	52°41' O	9.5	< 65
Riachão	Brasil	07°43' S	46°39' O	4.5	< 200
Nova Colinas	Brasil	07°09' S	46°06' O	7	200-250
São Miguel do Tapuio	Brasil	05º38' S	41º24' O	20	<150
Monturaqui	Chile	23°56' S	68º17' O	0.46	< 1
Carancas	Peru	16°40' S	69°03' O	0.0135	0.000007

1.2 Relevância e objetivos da tese

A estrutura de impacto de Araguainha vem sendo alvo de estudo desde os anos 70. As primeiras análises foram feitas a partir da identificação de uma anomalia circular na parte nordeste da Bacia do Paraná (Fig. 1.2; Northfleet et al., 1969). Dietz e French (1973) trouxeram os primeiros indícios para que Araguainha tenha sido originada por meio de um impacto meteorítico. A partir desse momento, pesquisas focadas nas evidências de impacto (ex., Theilen-Willige, 1981; Crósta et al., 1981; Crósta, 1982), nas rochas geradas pelo impacto (ex., von Engelhardt et al., 1992; Yokoyama, 2008; Machado et al., 2009; Preuss, 2012; Fischer, 2015; de Marchi et al., 2016; Hauser et al., 2019; Souza et al., 2024), nas análises estruturais (ex., Crósta, 1982; Lana et al., 2006, 2007, 2008), em dados geofísicos (ex., Masero et al., 1994; Fischer e Masero, 1994; Vasconcelos, 2007; Yokoyama et al., 2012; Miyazaki, 2018; Miyazaki et al., 2021), e geocronológicos (ex., Crósta, 1982; Hammerschmidt e von Engelhardt, 1995; Deutsch et al., 1992; Lacerda Filho et al., 2004; Jourdan et al., 2009; Tohver et al., 2012; Erickson et al., 2017; Hauser et al., 2019) foram realizadas.

O primeiro trabalho de mapeamento geológico na região em escala de detalhe (1:50.000) foi realizado em 2012 sob a coordenação da Profª. Drª. Edi Mendes Guimarães com a presença de alunos e professores da Universidade

de Brasília (UnB). O Trabalho de Mapeamento Final de Geologia do Instituto de Geociências (IG-UnB), foi denominado de “TF-2012 Projeto Astroblema de Araguainha/Ponte Branca – Mato Grosso”. O trabalho resultou na caracterização detalhada das litologias alvo afetadas pelo impacto (embasamento e unidades da Bacia do Paraná) e dos impactitos por meio das análises petrográficas, estruturais, estratigráficas, geoquímicas e geofísicas.

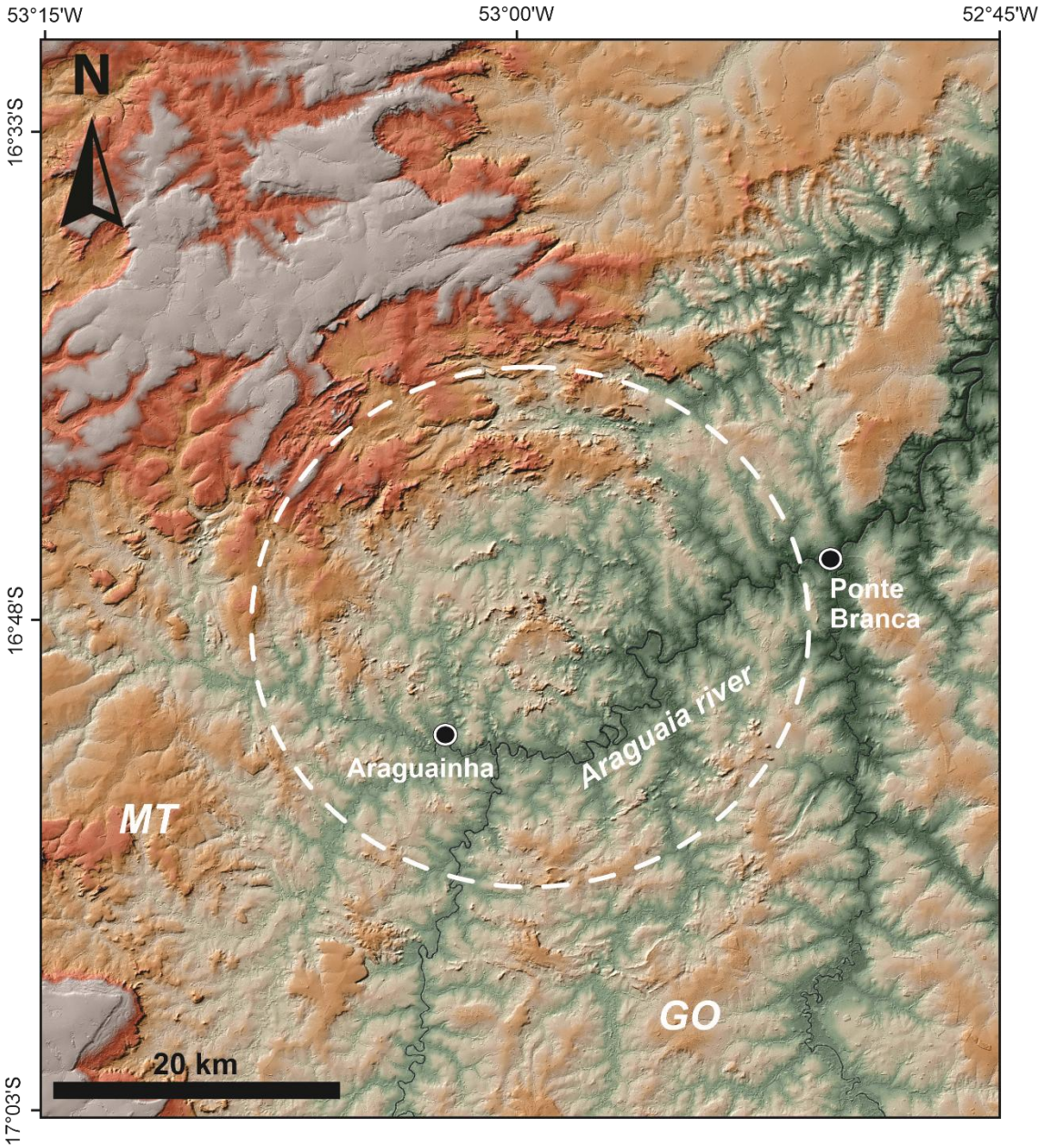

Figura 1.2 Imagem de satélite de radar TanDEM-X para a estrutura de impacto de Araguainha. Modelo de elevação digital codificado por cores e sombreado em colina (iluminação na elevação: 45º, azimute: 315º). MT: Mato Grosso, GO: Goiás. Fonte: Courtesy of Manfred Gottwald, German German Aerospace Center (DLR, Oberpfaffenhofen, Germany). Modificado de Hauser et al. (2019).

Os impactitos são bem expostos no núcleo central soerguido. No período de 2020 a 2022, foram realizadas obras de asfaltamento da rodovia MT-100 que liga as cidades Araguainha e Ponte Branca (MT), no qual engloba esta região. Novos e excelentes afloramentos foram expostos as quais possibilitaram enriquecidas informações nunca antes descobertas. Diante deste cenário, esta tese de doutorado busca contribuir na compreensão da evolução geológica do núcleo central soerguido a partir do entendimento da relação de contato geológico entre as rochas que afloram nesta região e a caracterização das brechas de impacto, bem como a compreensão da formação dessas brechas. Para isso, alguns objetivos específicos são propostos:

- Revisar e atualizar o mapa geológico do núcleo central soerguido da estrutura de impacto de Araguainha com os novos dados de campo adquiridos;
- Correlacionar a sequencia estratigráfica da Bacia do Paraná e seu embasamento na geração das brechas de impacto;
- Caracterizar detalhadamente as brechas polimíticas com respeito à sua composição, textura e proporção relativa entre matriz e arcabouço, bem como identificar a presença de material fundido e do metamorfismo de choque nos minerais para melhor classificá-las e agregá-las ao contexto de crateramento de impacto;
- Reconstruir os estágios de formação da estrutura de impacto de Araguainha e definir a colocação das brechas polimíticas na estrutura.

1.3 Localização e vias de acesso

A área em estudo está localizada entre os estados de Mato Grosso e Goiás, onde o rio Araguaia faz divisa entre os estados e corta a estrutura de impacto de Araguainha quase ao meio (Fig. 1.2).

O centro da estrutura está posicionado entre as coordenadas 16°48’S e 52°59’O e dista 710 km de Brasília/DF. O acesso, partindo de Brasília, se dá pelas rodovias federais BR-60 até Jataí/GO e BR-364 até Alto Araguaia/MT, a qual deve-se seguir pela rodovia estadual MT-100 que abrange os municípios de Araguainha e Ponte Branca (Fig. 1.3).

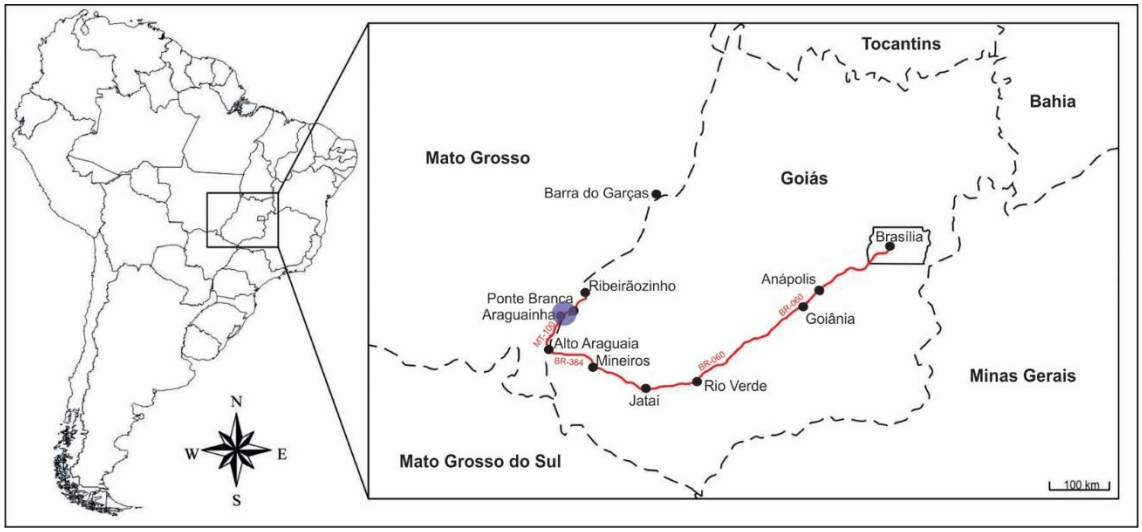

Figura 1.3 Mapa de localização da área de estudo e uma das vias de acesso à estrutura de impacto de Araguainha com partida desde Brasília.

1.4 Estrutura da tese

A tese de doutorado encontra-se organizada em 7 capítulos. Após este tópico introdutório do **Capítulo 1**, segue-se a revisão bibliográfica no **Capítulo 2** e os materiais e métodos utilizados para o desenvolvimento desta pesquisa no **Capítulo 3**.

Os capítulos 4, 5 e 6 concentram os resultados adquiridos. O **Capítulo 4** contém o artigo publicado no periódico *Meteoritics and Planetary Science* em 19 de junho de 2024, intitulado "*Araguainha impact structure, Brazil: new insights into the geology of the central uplift*." O principal objetivo deste artigo foi mostrar a geologia do núcleo central soerguido atualizado, o que inclui o novo mapa geológico, uma nova nomenclatura para as rochas relacionadas ao impacto em Araguainha, a distribuição e características dos três tipos de rochas fundidas por impacto agora distintos, e a natureza das brechas polimíticas de impacto.

O **Capítulo 5** contém o segundo artigo a ser submetido ao periódico *The Geological Society of America Bulletin*, intitulado "*Constrain on the provenance of polymict impact breccias from the Araguainha impact structure, Brazil: a petrographic and U-Pb zircon dating approach*." Para este artigo, fornecemos uma caracterização quantitativa detalhada dos clastos e da matriz das brechas polimíticas de impacto por meio de descrição composicional e textural em

diferentes escalas de trabalho. Adicionalmente, o estudo de proveniência tanto das brechas polimíticas de impacto como das rochas (meta)sedimentares relacionadas ao embasamento da Bacia do Paraná foram realizadas pelas análises isotópicas de U-Pb em grãos de zircão a fim de obter e entender as principais fontes dessas rochas.

As considerações finais e a síntese conclusiva desta pesquisa são expostas no **Capítulo 6** e a lista de referecias. Ao final do volume, concentra os anexos que incluem figuras e tabelas não apresentados no corpo do texto.

CAPÍTULO 2

REFERENCIAL TEÓRICO E REVISÃO BIBLIOGRÁFICA

2 REFERENCIAL TEÓRICO E REVISÃO BIBLIOGRÁFICA

2.1 Embasamento Pré-Ordoviciano

O embasamento da Bacia do Paraná é composto por terrenos granito-gnáissicos (Zalán et al., 1987) cercados por cinturões de dobras e empurrões (Cordani et al., 2009) formados no final da orogenia Brasiliana (Almeida e Hasui, 1984). Ele é pobremente conhecido e alvo de muitas pesquisas. Estudos prévios descreveram que o embasamento é constituído por um núcleo cratônico na região axial da bacia, circundado por faixas móveis brasilianas (Cordani et al., 1984; Zalán et al., 1990; Soares, 1991). Dados gravimétricos e magnéticos associado aos dados de reflexão sísmica revelaram uma orientação principal SW-NE da Bacia do Paraná, interpretada como rift central, relacionado a estruturação do embasamento (Marques et al., 1993; Milani, 1997).

Parte do embasamento pré-ordoviciano aflora na borda da Bacia do Paraná e possui relação com a Província Estrutural do Tocantins (Almeida et al., 1977), formada no Ciclo Brasiliano (810-530 Ma; Brito Neves e Fuck, 2013; Brito Neves et al., 2014). Localizada na parte central do Brasil, a Província Tocantins representa uma grande área orogênica. Sua formação resultou na convergência dos crátons Amazônico, São Francisco e Paranapanema, sendo composta pelas faixas móveis Brasília, Paraguai e Araguaia (Fig. 2.1a).

A Faixa Paraguai corresponde a um cinturão de dobramentos na região central no continente sul-americano (Almeida, 1965). Esta faixa encontra-se limitada a sudeste e leste, respectivamente, pelos crátons Amazônico e Rio Apa. As características gerais da Faixa Paraguai são a forma de um grande arco convexo, deformação linear intensa, presença de falhas inversas, dobramento isoclinais e recumbentes, escassez de vulcanismo e presença de plútons granitos (Fig. 2.1b; Almeida, 1984; Alvarenga, 1990; Alvarenga e Trompette, 1992).

Almeida (1984) subdividiu a Faixa Paraguai em três zonas estruturais (brasilides metamórfica, brasilides não-metamórfica e coberturas brasilianas), as quais foram posteriormente renomeados, respectivamente, de Zona Estrutural Interna, Zona Estrutural Externa e Cobertura Sedimentar plataformal (Alvarenga e Trompette, 1992). Um ramo da faixa estende-se de Corumbá até a Bolívia,

seguindo a direção WNW-ESSE, nomeada de Cinturão Tucavaca (Litherland et al., 1986).

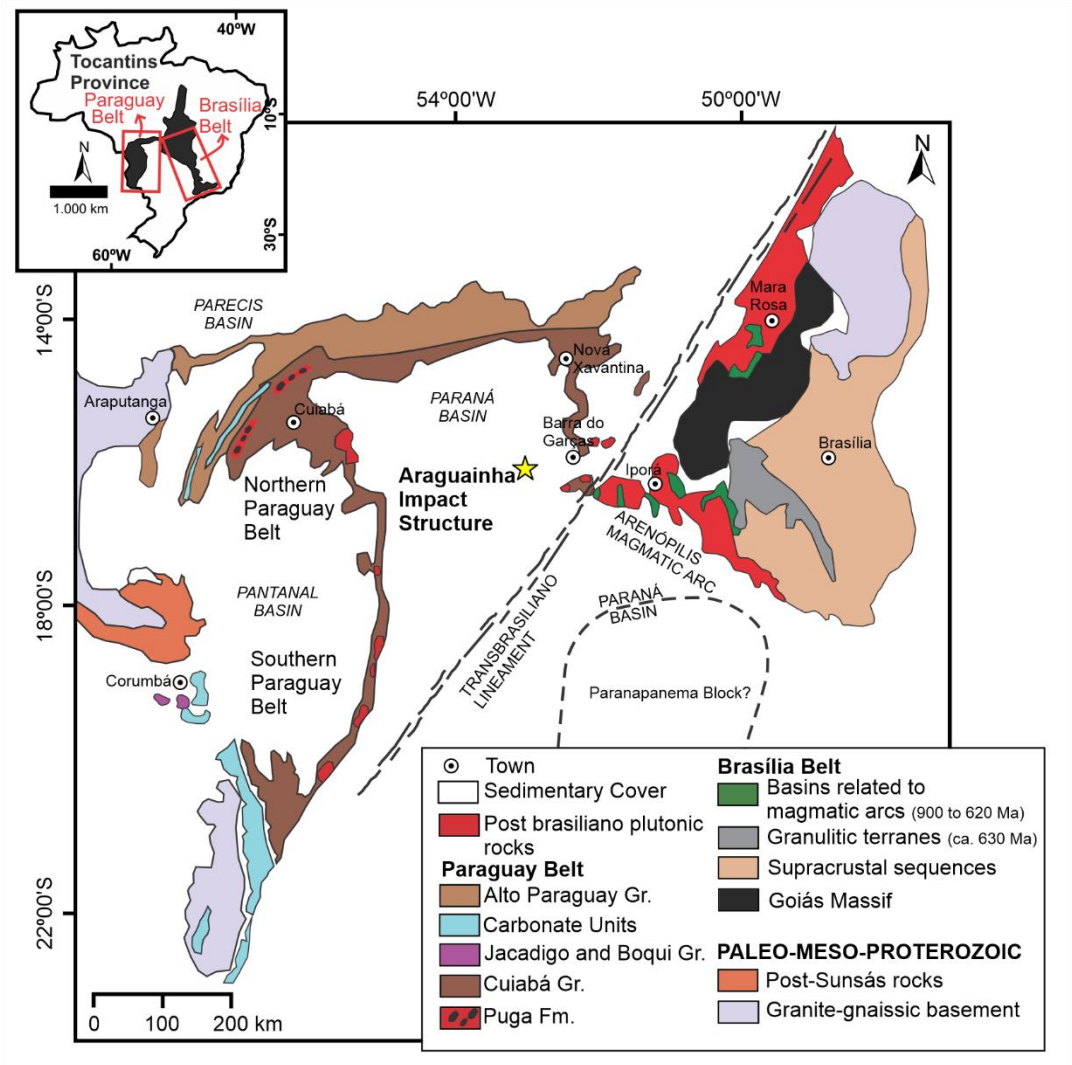

Figura 2.1 Contexto geotectônico esquemático da Província do Tocantins com suas faixas móveis. Mapa geológico da Faixa Paraguai norte e sul em relação aos crátons Amazônico e Rio Apa. Modificado de Leite et al. (2021).

A sucessão sedimentar da Faixa Paraguai é formada por uma espessa camada de rochas sedimentares glaciomarinho, turbidítico, carbonática e siliciclástica (Alvarenga e Saes, 1992; Alvarenga e Trompette, 1992, 1993; Alvarenga et al., 2000). Alvarenga et al. (2000) agruparam-na em três grandes grupos litoestratigráficos, denominados de unidade inferior (turbidítica-glaciogênica), unidade carbonática e unidade superior (cobertura cratônica detrítica). O setor norte da Faixa Paraguai é constituído por esses três grandes

grupos; unidade inferior, representado pelo Grupo Cuiabá e Formação Puga; unidade carbonática com o Grupo Araras; e unidade superior de rochas sedimentares do Grupo Alto Paraguai. Já o setor sul é composto pela unidade inferior, constituído pelos grupos Cuiabá e Jacadigo e pela Formação Puga; e pela unidade carbonática, com o Grupo Corumbá (Alvarenga, 1988; Alvarenga e Saes, 1992; Alvarenga e Trompette, 1992, 1993; Boggiani, 1997; Trompette et al., 1998; Alvarenga et al., 2000; Campanha et al., 2011).

O Grupo Cuiabá representa a unidade basal da Faixa Paraguai, sendo composto por rochas metassedimentares metamorfizadas sob fácie xisto verde, predominantemente metarenitos e filitos com intercalações de quartzitos, ambos cortados por veios de quartzo que são relacionados à intrusão dos granitos da Província Granitóide (Almeida, 1984). Nas proximidades do contato com esses corpos magmáticos, constatou-se a paragênese de metamorfismo de contato nas fácies albita a hornblenda hornfels, onde desenvolveram auréolas de metamorfismo termal (Godoy et al., 2007). Esta unidade é enquadrada no Neoproterozóico, em que a idade máxima de deposição foi definida, por meio de grãos de zircão detríticos, por Batalha (2017) em 923 Ma, por Pelosi (2017) em 601 Ma, por Babinski et al. (2018) em 652 Ma e por Frugis et al. (2024) em 900 Ma. A unidade superior desta faixa, Grupo Alto Paraguai, é composta de arenitos deltaicos, xisto vermelho, siltito, ardósia e argilito laminado (Dantas et al., 2009). Notavelmente, o Grupo Alto Paraguai carece de metamorfismo e a unidade superior, Formação Diamantino, tem idade máxima de deposição de 560 ± 13 Ma, interpretada como unidade mais jovem (McGee et al., 2014).

O último evento metamórfico e a fase final na Faixa Paraguai são evidenciados pela datação $^{40}Ar/^{39}Ar$ em minerais de baixo grau metamórfico que resultaram uma idade de aproximadamente 540 Ma para a Sequência Metavulcanosedimentar Nova Xavantina (Geraldes et al., 2003, 2008). O magmatismo Neoproterozóico é também relacionado à fase final e compreende distintas intrusões graníticas (Godoy et al., 2010). Além disso, McGee et al. (2014) através de análises em zircão detrítico da Formação Diamantino, sugere que a sedimentação final, deformação e metamorfismo na faixa Paraguai ocorreu entre 540 e 510 Ma.

A Sequência Metavulcanossedimentar Nova Xavantina foi considerada contemporânea a Sequencia Rio Bacuri por Pinho (1990) e interpretada como uma fase embrionária de expansão do fundo marinho da Faixa Paraguai ou uma bacia retroarco (Lacerda Filho et al., 2004). Silva et al. (2022) dataram essas rochas vulcânicas por meio das análises U-Pb em zircão que indicaram que essas rochas foram formadas em pelo menos três eventos magmáticos, começando com a formação de metabasaltos do fundo do mar de ~745 Ma e rochas vulcânicas félsicas datadas em ~735 Ma, e gabro intrusivo de ~714 Ma.

As intrusões graníticas formam a Província Granitóide Brasiliana, que incluem sete sin- a pós-tectônica corpos graníticos do sudeste matogrossense e, por meio das características genéticas e evolutivas, foram individualizados em dois eventos magmáticos, norte e sul (Godoy et al., 2004, 2007; Manzano, 2009): parte norte, composta por intrusões de batólitos dispostos na direção ENE-WSW no estado de Mato Grosso, gerados em ambiente de colisão e/ou descompressão pós-colisional e denominados de São Vicente, Araguaiana e Lajinha; e parte sul, aflorando como pequenas intrusões fissurais, alongadas e alinhadas na direção NNE-SSW no estado de Mato Grosso do Sul, gerados em ambientes sin-colisional de arco continental e são intitulados como Taboco, Rio Negro, Coxim e Sonora. Além dessa principal divisão, Lacerda Filho et al. (2004, 2006) propuseram duas suítes magmáticas em virtude do contexto evolutivo do magmatismo da Faixa Paraguai: Suíte São Vicente com os granitos Taboco, Rio Negro, Coxim, Sonora e São Vicente; e a Suíte Serra Negra, composta pelos corpos graníticos pós-tectônicos do Arco Magmático de Goiás (Pimentel et al., 1996) e os granitos Lajinha e Araguaiana, os quais constituem o Granito Serra Negra definito por Pimentel e Fuck (1987).

A Província Granitóide Brasiliana localiza-se na porção interna da Faixa Paraguaia, sendo intrusivas nas rochas do Grupo Cuiabá e relacionadas à evolução desta faixa (Godoy et al., 2007, 2010). Os granitos são classificados como do tipo-I, cálcio-alcalino potássico a alto potássio, peraluminosos a metaluminosos. Os eventos magmáticos foram gerados de fontes distintas, marcados por dois pulsos separados por cerca de 40 Ma com idade de cristalização Cambriana, sendo a parte sul mais antiga (~550 Ma) e a parte norte mais nova (500-510 Ma, Godoy et al., 2010).

2.2 Bacia do Paraná

A estrutura de impacto de Araguainha está localizada na parte nordeste da Bacia do Paraná (Fig. 2.2), uma típica bacia intracratônica em função do seu posicionamento geotectônico e suas características tectono-sedimentares (Milani e Ramos, 1998). A Bacia do Paraná mudou de retro-foreland colisional para sinéclise pericratônica durante o Neopaleozoico, seguida por quiescência tectônica no interior sudoeste do Supercontinente Gondwana (Henrique-Pinto et al., 2021). Durante o período de Oclóyica (Meso a Neo-Ordoviciano ~470-443 Ma) resltou-se da colisão do terreno alóctone Precordilheira com o Gondwana. Com grande parte territorial situada no Brasil e o restante no Uruguai, Paraguai e Argentina, esta é a maior bacia sedimentar totalmente inserida na Plataforma Sul-Americana e considerada uma das mais importantes sinéclises do continente. A Bacia do Paraná é caracterizada pela ampla área territorial (cerca de 1,5 milhões de km^2 de área; Almeida, 2004) e pela forma elíptica com tendência NNE-SSW (Fig. 2.2).

O máximo preenchimento sedimentar atinge 7.000 m de espessura na área central da Bacia do Paraná (Zalán et al., 1990; Peate, 1997; Milani et al., 2007). Associado a este preenchimento, ocorre o magmatismo básico com registro vulcânico da Formação Serra Geral de idade cretácea (Milani et al., 2007). Milani (1977) subdividiu as unidades estratigráficas da bacia em seis supersequências de natureza magmático-sedimentar depositadas entre o Ordoviciano ao Neo-Cretáceo (Fig. 2.2) detalhadas a seguir (Assine et al., 1994; Milani et al., 1994; Milani et al., 2007):

(1) Supersequência Rio Ivaí (Ordoviciano-Siluriano): Configura o início do preenchimento sedimentar da Bacia do Paraná. Esta é a unidade mais antiga da bacia composta por três formações, representando o ciclo de transgressão marinha: Formação Alto Garças (arenitos caoliníticos fluviais de ambiente transicional e costeiro e conglomerados), Formação Iapó (diamictitos glaciais) e Formação Vila Maria (pelitos micáceos vermelhos, xistos fossilíferos e siltitos);

(2) Supersequência Paraná (Devoniano): Unidade composta pelas formações Furnas (arenitos caoliníticos de ambiente fluvial transicional) e Ponta Grossa (folhelhos), representando um ciclo transgressivo-regressivo. Assine

(1996) caracterizou e subdividiu a Formação Furnas em três unidades: unidade I (inferior) representada por arenitos conglomeráticos com clastos do folhelho da Formação Vila Maria; unidade II apresenta arenitos intercalados com siltitos e argilitos contendo icnofósseis; e a unidade III (superior) possui um aumento brusco na granulometria e aporte sedimentar constituindo conjuntos com presença de depósitos residuais de cascalhos. A Formação Ponta Grossa é composta pelos folhelhos com lentes de arenito na base. Acima encontram-se folhelhos negros carbonáceos sucedidos por um pacote de arenito siltítico e, no topo, predominam os pelitos;

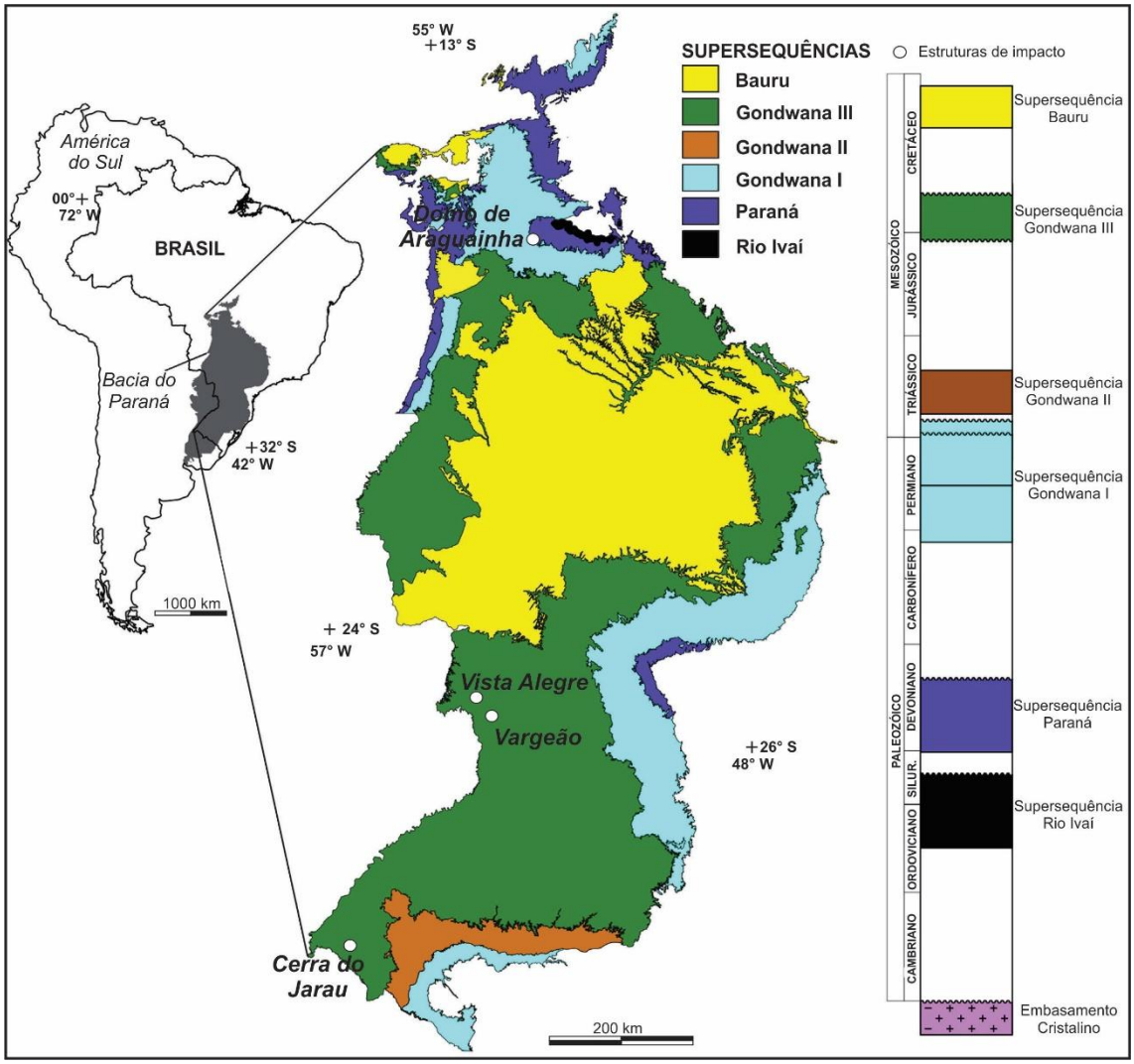

Figura 2.2 Distribuição regional das seis supersequências estratigráficas sugeridas por Milani (1997) para a Bacia do Paraná, apresentando a coluna estratigráficas simplificada e a localização das quatro estruturas de impacto confirmadas nesta bacia. Modificado de Montibeller et al. (2020).

(3) Supersequência Gondwana I (Carbonífero-Eotriássico): A supersequência é composta por três grupos que se enquadram em duas porções; a porção basal transgressiva com os grupos Itararé e Guatá e a porção superior regressiva com o Grupo Passa Dois. O Grupo Itararé é constituído por sedimentos de ambiente glacio-marinhos que compõem as formações Aquidauana (diamictito intercalando com arenito vermelho, siltito, ritmito, conglomerado e folhelho), Lagoa Azul (arenito sobreposto por diamictito e folhelho), Campo Mourão (diamictito intercalando com arenito) e Taciba (folhelho intercalando com arenito e diamictito). O Grupo Guatá contém sedimentos de ambiente deltaico, marinho e litorâneo das formações Rio Bonito (arenito, siltito e siltito carbonático intercalado com um nível de cravão) e Palermo (siltito, siltito arenoso cinza a amarelo, arenito com estratigrafia hummocky e folhelho cinza escuro). O Grupo Passa Dois é formado por depósitos sedimentares marinhos e transicionais que registram a instalação de clima desértico no final do ciclo. Este grupo é composto pelas formações Iratí (carbonato oolítico e contendo sulfeto, folhelho preto, folhelho betuminoso, siltito e chert), Serra Alta (folhelhos), Teresina (folhelho cinza e siltito), Corumbataí (parte inferior: argilito cinza escuro a preto, folhelhos e siltitos; argilito vermelho e folhelhos com lentes de calcário silicificado; parte superior: argilito verde, roxo e vermelho) e Rio do Rastro (arenito vermelho, siltito e folhelho);

(4) Supersequência Gondwana II (Meso a Neotriássico): Compreende o Grupo Rosário do Sul (formações Sanga do Cabral, Santa Maria, Caturrita e Guará) composto por arenitos e pelitos avermelhados de depósitos fluviais e lacustres. Esta supersequência ocorre restritamente na região Sul da bacia, nas regiões do Rio Grande do Sul (Brasil) e no Uruguai;

(5) Supersequência Gondwana III (Neojurássico-Eocretáceo): Esta supersequência compreende o Grupo São Bento (formações Botucatu e Serra Geral). A formação Botucatu é composta pelos depósitos de rios efêmeros e lençóis de areia, seguidos por arenitos eólicos que são intercalados por derrames basálticos da formação Serra Geral. O magmatismo básico com registro vulcânico da Formação Serra Geral, denominada de Grande Província Ígnea Paraná-Etendeka, é relacionada com a abertura do Oceano Atlântico Sul

durante o Cretáceo (Peate, 1997; Milani et al., 2007; Rocha-Campos et al., 2011);

(6) Supersequência Bauru (Neo-Cretáceo): A sexta e última supersequência é composta na base por depósitos vulcânicos da formação Serra Geral e no topo por rochas sedimentares das unidades cronocorrelatas aos grupos Caiuá e Bauru. Entretanto, Fernandes e Coimbra (1996) excluíram esta sequência do registro sedimentar da Bacia do Paraná por considerá-la acumulada em uma nova unidade tectônica, distinta, denominada Bacia Bauru.

A evolução da Bacia do Paraná foi controlada pela dinâmica das placas tectônicas durante a evolução do Supercontinente Gondwana, o que condicionou diferentes fatores climáticos (Zalán et al., 1990; Milani e Ramos, 1998; Milani e de Wit, 2008). Quatro estruturas de impacto foram confirmadas nesta bacia (Fig. 2.2): Araguainha (16º48'S/52º59'O; 40 km de diâmetro), Vargeão (26º49'S/52º10'O; 12,4 km de diâmetro), Vista Alegre (25º57'S/52º41'O; 9,5 km diâmetro) e Cerra do Jarau (30º12'S/56º32'O; 13 km diâmetro). Araguainha é a única formada sobre rochas sedimentares pertencentes aos grupos supersequências Rio Ivaí, Paraná e Gondwana I, enquanto que as outras três estruturas de impacto foram formadas nas rochas vulcânicas da Formação Serra Geral (Supersequência Gondwana III).

O evento de impacto que formou Araguainha escavou cerca de 2.000 m de estratos litológicos do Ordoviciano ao Permiano da bacia e elevou um núcleo com 5 km de largura de rochas do embasamento no centro da estrutura (von Engelhardt et al., 1992; Lana et al., 2006), representando uma janela estratigráfica da parte nordeste da Bacia do Paraná (Milani et al., 2007). Diversos furos de sondagem foram realizados na Bacia do Paraná, mas apenas um alcançou o embasamento (AG-1-MT, Petrobrás) o qual amostrou uma rocha metassedimentar que foi correlacionada ao Grupo Cuiabá (Cordani et al., 2009). Este poço dista cerca de 30 km a noroeste da estrutura de impacto de Araguainha. Da base para o topo, e com base nas informações obtidas no poço em conjunto com as correlações estratigráficas estabelecidas por Lana et al. (2007), as unidades atingidas pelo impacto e que estão presentes em Araguainha são: rochas do embasamento da Bacia do Paraná, representadas pelos granitos alcalinos e rochas metassedimentares do Grupo Cuiabá; Grupo

Rio Ivaí; Grupo Paraná, pelas formações Furnas e Ponta Grossa; Grupo Itararé com a Formação Aquidauana; e o Grupo Passa Dois, pelas formações Irati e Corumbataí.

2.3 Estruturas de impacto

2.3.1 Processos de formação

Os processos envolvidos durante a formação das estruturas de impacto são divididos em três estágios (ex., Gault et al., 1968; Melosh, 1989; French, 1998), que podem durar de 15-20 minutos (ex., Henkel e Reimold, 1998; Kenkmann et al., 2009).

O processo inicial, (1) estágio de contato e compressão, é o momento em que ocorre o contato do projétil com a rocha alvo e a transferência de energia cinética por meio das ondas de choque (Fig. 2.3a). No ponto do contato, a energia cinética pode atingir o pico de pressão em dezenas de gigapascal (GPa), o qual leva à vaporização da maior parte do projétil e uma parte da rocha alvo ao redor do ponto de impacto. A pressão de choque é liberada quando a onda de choque atinge a extremidade do projétil e reflete como onda de rarefação. Parte da energia cinética do projétil é transformada em energia térmica e depositada no material alvo. Grande parte do projétil evapora e pequenas porções podem ser incorporadas ao derretimento gerado pelo impacto (ex., melt sheet, suevito), acumulando-se no interior da estrutura de impacto. Este estágio é concluído quando o projétil é descarregado de alta pressão (Fig. 2.3b).

Em seguida acontece o (2) estágio de escavação (Fig. 2.3c e 2.4a). Este é o intervalo em que a onda de choque se expande em uma frente hemisférica viajando pela rocha alvo, enfraquecendo na sua transição radial para longe do ponto de impacto. A combinação da onda de choque com a onda de rarefação põe a rocha alvo em movimento (fluxo de escavação), causando a ejeção do material para fora da cratera e na forma de pluma cônica de vapor/ejeção na atmosfera. Esta pluma cresce e o material ejetado viaja lateralmente depositando tanto fora como acima da cratera ainda em desenvolvimento. O fluxo de escavação resulta em uma cratera transiente, caracterizada por uma depressão com bordas soerguidas de formato arredondado cujo diâmetro é de 10 a 20 vezes maior que o tamanho do projétil. Este estágio termina quando as

ondas de choque e de rarefação são dissipadas e o diâmetro máximo da cratera transiente foi atingido (Fig. 2.3d e 2.4b).

O terceiro e último estágio, (3) estágio de modificação e colapso, começa quando a cratera transiente entra em colapso sob o efeito da gravidade e produz a morfologia final da cratera (Fig. 2.3e e 2.4c). O material solto ao longo da borda da cratera transiente desliza para baixo na cavidade, resultando na formação de uma lente de brecha na base para as crateras simples, assumindo uma forma de tigela (Fig. 2.3f). Já para as crateras maiores, desenvolve-se uma estrutura de elevação central na transição entre os estágios de escavação e modificação (Fig. 2.4b). Isto é decorrente a partir da combinação dos efeitos de fluxo do material para dentro da cratera causado pelo colapso das bordas soerguidas e pelo ressalto do fundo da cratera, envolvendo regimes extensionais e compressionais e, no fim, caracterizando a geometria das crateras complexas (Fig. 2.4d).

O grau de alteração da cratera transiente, durante o terceiro estágio, depende do tamanho e das propriedades das rochas alvo. Com base na morfologia final adquirida e da extensão em que a cratera transiente é modificada, pode-se classificar as crateras como simples e complexas (ex., Osinski e Pierazzo, 2013; Melosh, 1989; French, 1998). Essa morfologia vai depender da dimensão, velocidade e ângulo de incidência do projétil como também da composição da rocha alvo e da gravidade do planeta (Pike, 1980).

As crateras com geometria simples (Fig. 2.3f) são as menores estruturas de impacto (<2-4 km de diâmetro). São caracterizadas por uma geometria uniformemente côncava, como depressões em formato de tigela, sugerindo pouco ou nenhum colapso gravitacional após o impacto (ex: Tswaing Crater, África do Sul; Melosh, 1989). Já as crateras com geometria complexa (Fig. 2.4d) são formadas com um levantamento central, anel de pico, bacia central e uma multi-morfologia de bacia de anel (Hargitai et al., 2015). Estruturas de impacto muito grandes podem exibir estruturas de anéis concêntricos (ex: Estrutura de impacto de Vredefort, África do Sul). O diâmetro dessas crateras varia de 20 a 150 km, sendo que o diâmetro final costuma ser 20 a 30 vezes maior que o diâmetro do projétil.

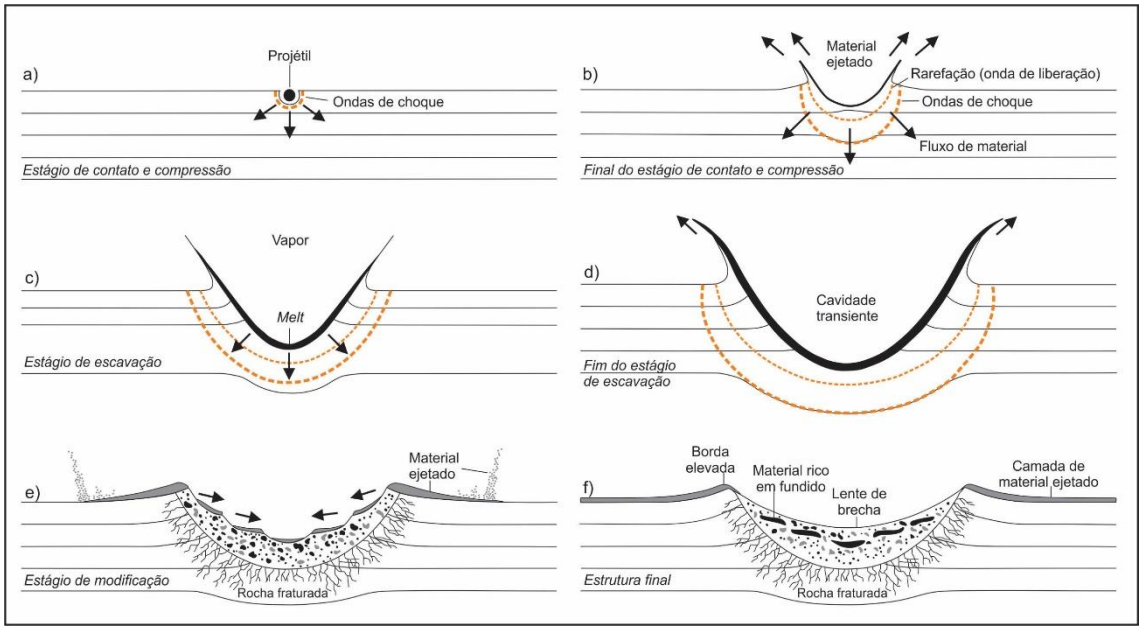

Figura 2.3 Processos envolvidos durante a formação de estruturas de impacto do tipo simples. a) Primeiro estágio – contato e compressão: penetração inicial do projétil e radiação externa de ondas de choque; b) Fim do primeiro estágio e início do segundo estágio – escavação: expansão contínua da onda de choque na rocha alvo com o desenvolvimento de onda tensional (rarefação ou onda de liberação); c) Durante o estágio de escavação: desenvolvimento de revestimento de melt na cavidade transitória em expansão; d) Fim do segundo estágio: cavidade transitória com a extensão máxima; e) Início do terceiro estágio – modificação: colapso da cratera transitória; f) Estrutura final de uma estrutura de impacto do tipo simples: depressão em forma de tigela, parcialmente preenchida com brechas complexas e corpos de derretimento de impacto. Modificado de French (1998).

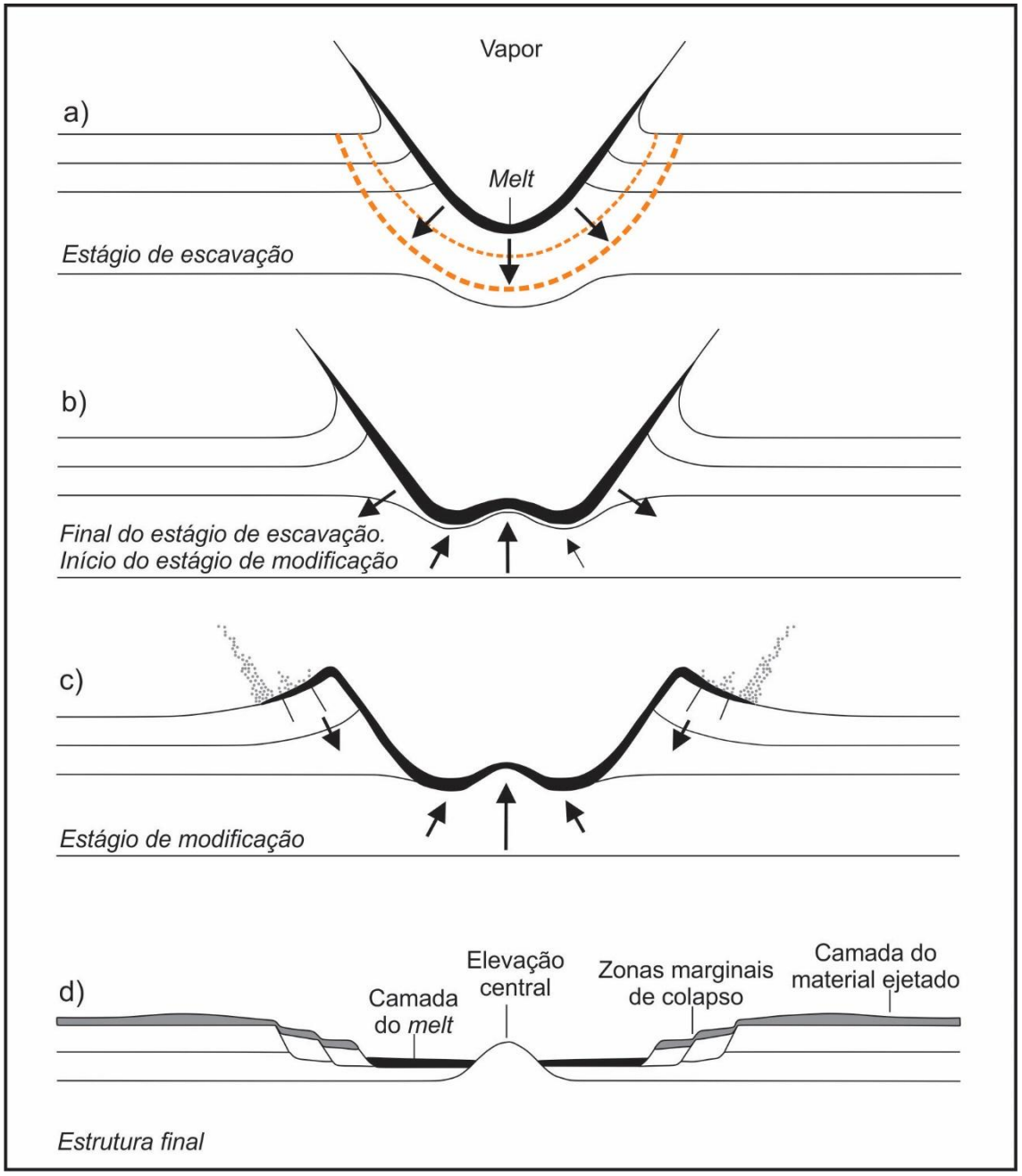

Figura 2.4 Processos envolvidos durante a formação de estruturas de impacto do tipo complexa. a) Segundo estágio – escavação (o primeiro estágio é o mesmo ilustrado na figura anterior 2.3): formação de uma grande cratera transitória; b) Fim do segundo estágio e início do terceiro estágio – modificação: desenvolvimento inicial do soerguimento central; c) Durante o terceiro estágio: início do colapso da cratera transiente acompanhado pelo desenvolvimento contínuo da elevação central e o afinamento e a queda da camada de fusão original (em preto) sobre as rochas elevadas; d) Estrutura final de uma estrutura de impacto do tipo complexa: consiste de uma elevação central composta por rochas mais profundas, cercada por uma planície relativamente plana com (ou não) deposição de camadas de melt, e por uma borda em terraços produzida pelo movimento para dentro ao longo de falhas normais escalonadas. Modificado de French (1998).

2.3.2 Estruturas de impacto: reconhecimento

Para o reconhecimento das estruturas de impacto, alguns critérios foram estabelecidos e, assim, poder distingui-las de outros fenômenos (ex., vulcânicos, tectônicos). Expressões morfológicas (formato circular), anomalias geofísicas ou contexto geológico fornecem sugestões preliminares na possível presença de uma estrutura de impacto (ex., Reimold e Koeberl, 2014; Crósta et al., 2019). A confirmação definitiva depende de uma análise detalhada nas rochas em que são observados metamorfismo de choque, efeitos de deformação e transformação causada pela onda de choque. A única feição de choque observada em escala de campo e/ou macroscópica são os shatter cones (cones de estilhaçamento, Fig. 2.5a). Esta feição são estruturas cônicas que ocorrem agregados e se caracterizam por estrias que iniciam no ápice e terminam na base de cada cone, atingindo tamanhos centimétricos a métricos (Crósta et al., 1981). Evidências químicas também são presentes e demonstram a presença de traços de um projétil extraterrestre nas rochas geradas durante o impacto (ex. Ni, Co, Cr e elementos do grupo platina; Reimold e Koeberl, 2014; Crósta et al., 2019).

Os efeitos observados em escala microscópica são, por exemplo, planar deformation features (PDFs), planar features (PFs), vidro diaplético e polimorfos de alta pressão. O desenvolvimento desses efeitos de choque é, principalmente, nos minerais de quartzo (Fig. 2.5b), sendo este um mineral abundante nas rochas da crosta terrestre e bastante resistente ao intemperismo. Minerais de zircão (Fig. 2.5c-d) também são bons registradores de efeitos de choque em sua superfície, pois possuem natureza muito refrativa e boa preservação no ambiente sedimentar. Neste são identificados, por exemplo, texturas granulares e vesicular por meio do microscópio eletrônico de varredura (ex., French, 1998; Reimold e Koeberl, 2014; Stöffler et al., 2018; Crósta et al., 2019; Hauser et al., 2019).

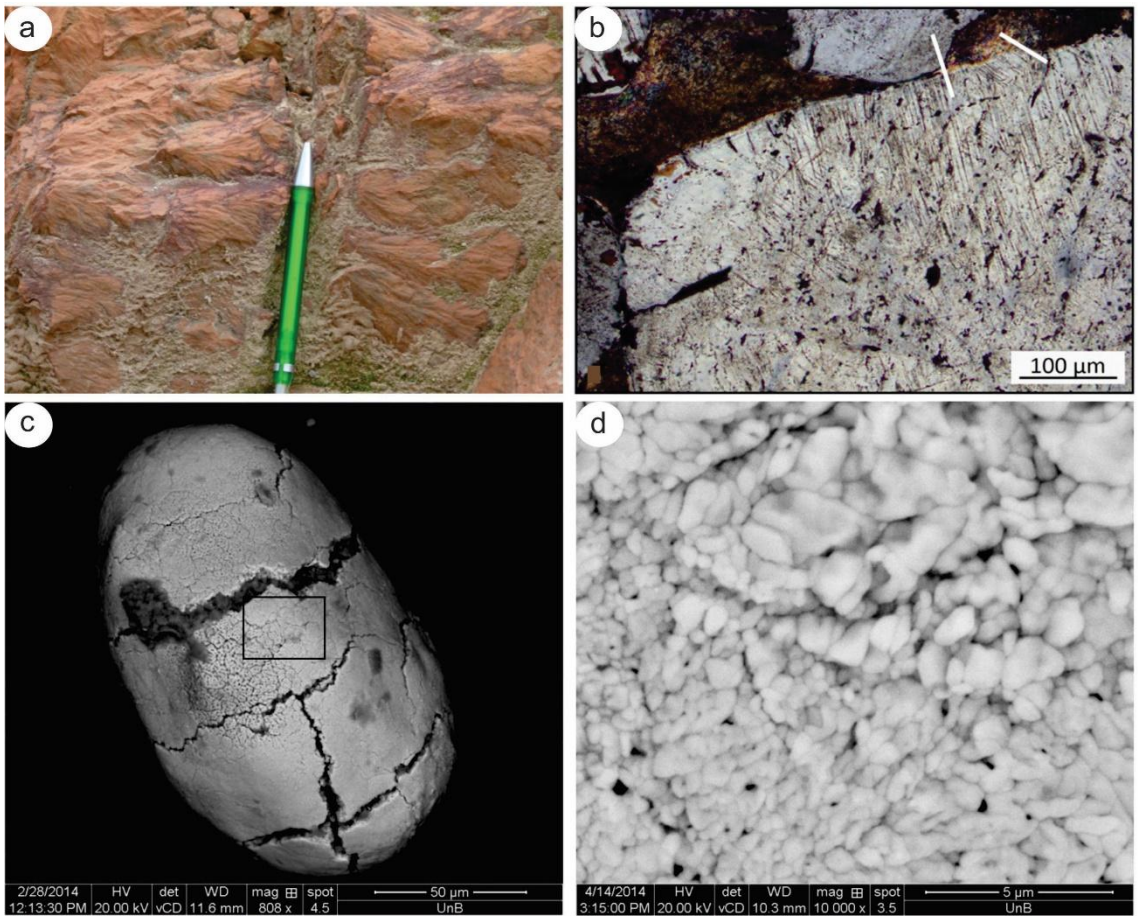

Figura 2.5 Evidências do impacto. a) Feições de shatter cones (ca. 5-10 cm) observados em metarenitos. b) Observação de planar deformation features (PDFs) com duas direções no mineral de quartzo. c) Imagem de backscattered electron (BSE) de um grão de zircão arredondado. d) Zoom da figura (c) em que se observa a textura granular na superfície do grão de zircão. Tomada de Hauser (2021).

As condições do regime pressão-temperatura (P-T) para o metamorfismo de choque possuem comportamento diferente com respeito ao metamorfismo da crosta terrestre, o qual ocorre limitado às temperaturas de 1.000° C e pressões < 1 GPa (Fig. 2.6). O metamorfismo de choque apresenta comportamento de caráter progressivo em direção ao ponto do impacto, em que as pressões se expandem a dezenas de GPa e as temperaturas atingem milhares de graus centígrados (ºC). Na zona inicial, o material atingido pelo impacto é vaporizado instantaneamente, assim como grande parte do projétil. Em outra zona, as pressões e temperaturas de choque resultam na fusão em massa da rocha alvo e de minerais. Após, tem-se a zona que há a formação de vidro diaplético (mineral precursor parcialmente preservado e essencialmente isotrópico),

deformações planares (PDF) e dos polimorfos de minerais a altas pressões (Fig. 2.6; ex., Reimold e Koeberl, 2014; Crósta et al., 2019).

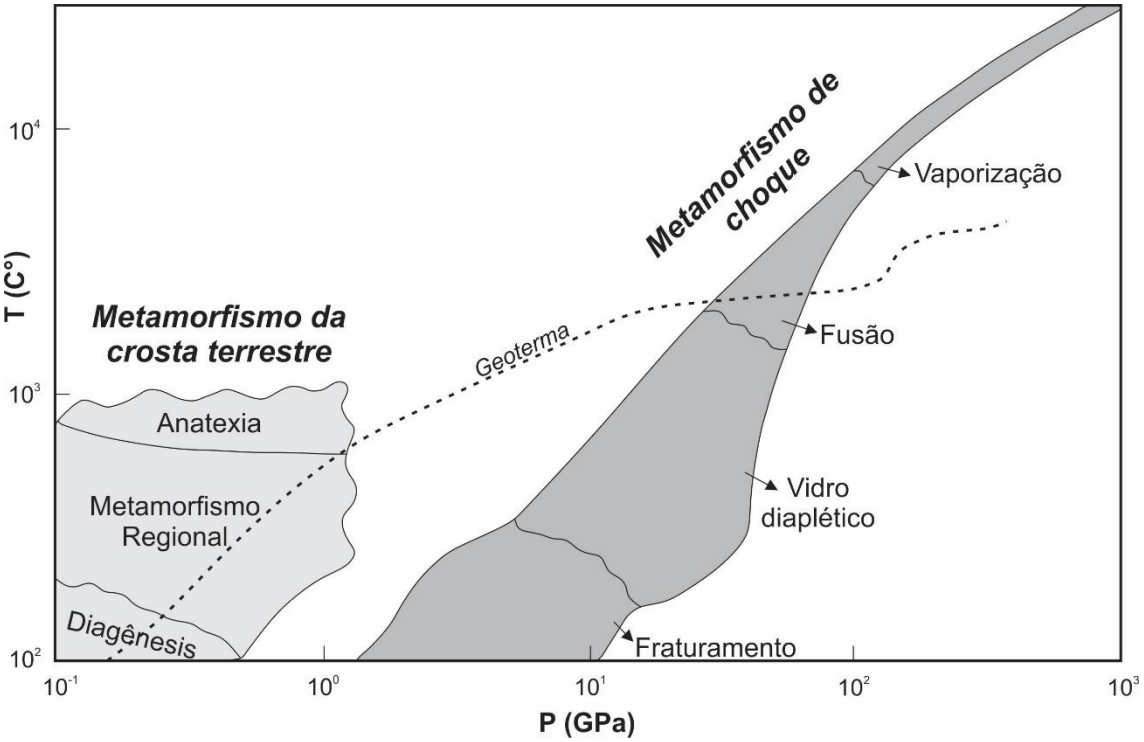

Figura 2.6 Diagrama dos regimes de pressão (GPa) e temperatura (°C) do metamorfismo de choque por impacto e do metamorfismo da crosta terrestre. Modificado de Stöffler et al. (2018).

2.3.3 Impactitos

O transporte e a mistura de rochas e minerais metamorfizados pelo choque, durante o estágio de escavação e formação da cratera transiente, produz ampla variedade de rochas que podem ser encontradas dentro, ao redor ou fora da cratera de impacto (Osinski e Pierazzo, 2013). Stöffler e Grieve (2007) atribuíram uma classificação detalhada para essas rochas, denominando-as de impactitos e as classificaram em dois grandes grupos, distais e proximais (Fig. 2.7). As evidências do metamorfismo de choque são observadas principalmente nos impactitos proximais e raramente identificadas nos impactitos distais (Stöffler et al., 2018).

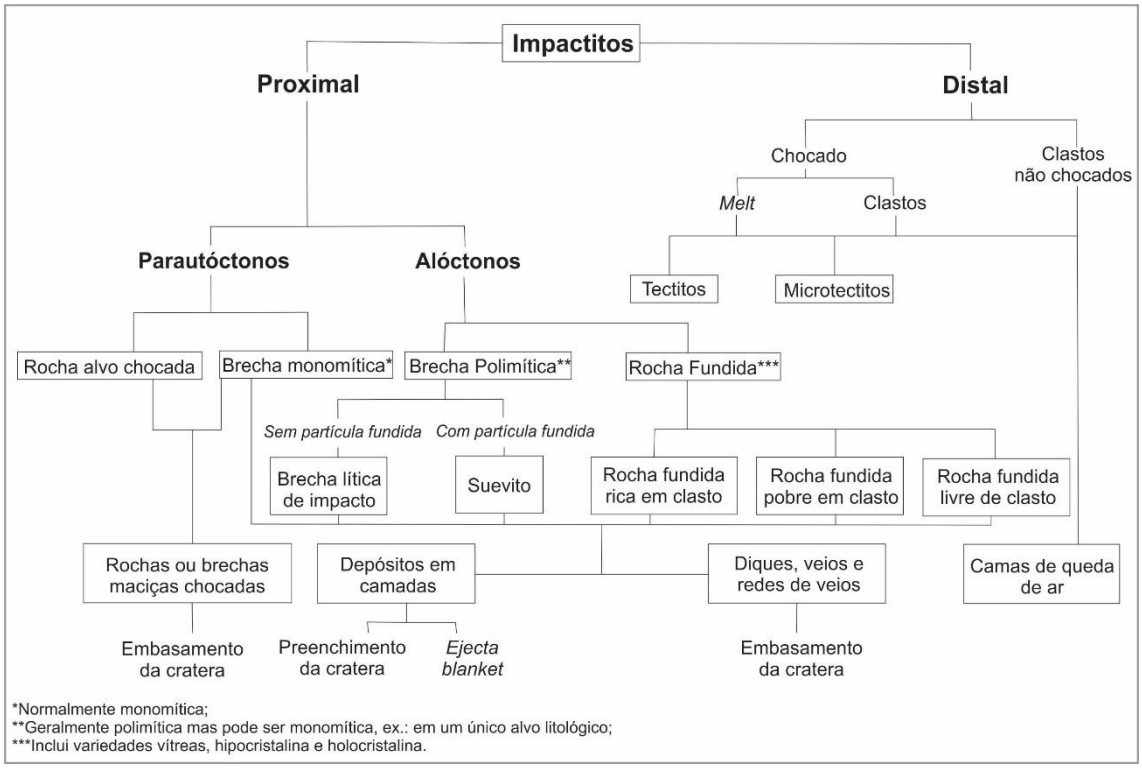

Figura 2.7 Classificação dos impactitos definida por Stöffler e Grieve (2007). Modificado de Stöffler e Grieve (2007).

Os impactitos distais contêm produtos distribuídos regionalmente ou em escalas continentais até globais, de acordo com a magnitude do evento de impacto. As principais ocorrências são as áreas com tectitos e microtectitos que atingiram centenas a milhares de quilômetros de extensão após o impacto. As ocorrências que estão espalhadas regionalmente são observadas em quatro campos: Centro-europeu (moldavitas), relacionado à estrutura de impacto Ries (Alemanha); Australasiano, que inclui as ocorrências na Austrália, Ásia e Antártica mas ainda não foram relacionados com uma estrutura de impacto; Costa do Marfim, relacionado com a estrutura de impacto Bosumtwi (Gana); e na América do Norte, relacionado com a estrutura de impacto Chesapeake Bay, litoral leste dos Estados Unidos (Glass e Simonson, 2012, 2013). Enquanto que as ocorrências globais são associadas, por exemplo, com o limite Cretáceo-Paleogênico (K-Pg); uma fina camada rica em elementos do grupo da platina, relacionada com uma possível colisão de um grande asteroide ou cometa na Terra que foi responsável pela extinção em massa e extinguiu grande parte dos dinossauros em, aproximadamente, 66 Ma (Alvarez et al., 1980).

Os impactitos proximais ocorrem dentro e ao redor da cratera. São as rochas depositadas perto de sua origem, representadas pelas rochas alvo chocadas, rochas fundidas de impacto, brechas monomíticas e brechas polimíticas de impacto. As rochas chocadas tem preservada a sua textura original e incorporado minerais metamorfoseados pelo choque em sua composição. As rochas fundidas de impacto são compostas por uma matriz fundida coerente com ampla variação de minerais, clastos líticos e de texturas. As brechas monomíticas de impacto são rochas alvo fragmentadas produzidas tectonicamente, equivalentes aos cataclasitos, contendo ou não minerais chocados. E as brechas polimíticas de impacto são diferenciadas pelo conteúdo de clastos e pela composição da matriz, sendo classificadas como brechas líticas e suevitos (ex., French, 1998; Stöffler e Grieve, 2007; Reimold e Koeberl, 2014; Crósta et al., 2019).

Todas essas brechas de impacto podem ocorrer como formações locais, injeções no fundo da cratera (ex: brechas de dique), ou desenvolvidas como brechas autigênicas locais no fundo da cratera e nas paredes de uma estrutura de impacto. As brechas de diques podem ser injeções de qualquer tipo de brecha de impacto de preenchimento de cratera (ex., Reimold e Koeberl, 2014; Crósta et al., 2019).

2.3.4 Brechas polimíticas de impacto

Estruturas de impactos são características geológicas com importância particular para entender a história e a evolução do planeta, possuindo uma alta relevância científica. Entre os depósitos expelidos durante o impacto, destacamos as brechas polimíticas de impacto, consideradas um dos registros mais importantes no processo de crateramento de impacto. Essas brechas possuem material provindo de todos os estágios de metamorfismo de choque (Stöffler e Grieve, 2007) e podem exibir texturas e composições químicas altamente variáveis, dependendo da rocha alvo envolvida (Siegert e Hecht, 2018). São rochas fundamentais para a compreensão da estratigrafia afetada pelo impacto e têm sido usadas para reconstruir a dinâmica de formação de estruturas de impacto (ex., Stöffler et al., 2004, 2013; Wittmann et al., 2004; Reimold et al., 2009; Osinski e Pierazzo, 2013; Siegert et al., 2017).

As brechas polimíticas de impacto são classificadas em dois tipos de acordo com seu arcabouço e composição da matriz (ex., Stöffler e Grieve, 2007; Stöffler et al., 2018): (1) brechas líticas de impacto, compostas apenas por componentes líticos (fragmentos de rochas e minerais) em uma matriz clástica de material semelhante à rocha alvo com granulometria fina; (2) suevitos, compostos por minerais e clastos líticos de diferentes graus metamórficos de choque com uma matriz particular, incluindo partículas fundidas cogenéticas que estão em um estado vítreo ou cristalizado. O termo “suevito” foi inicialmente usado para descrever as brechas polimíticas de impacto que ocorrem na estrutura de impacto Ries, Alemanha (ex., Sauer, 1920; Stöffler et al., 2013; Osinski e Grieve, 2024). O material fundido nesta estrutura é bem preservado e, ainda hoje, é usado como referência de comparação para descrever outras ocorrências de suevitos (Fig. 2.8; ex., Claeys et al., 2003; Coney et al., 2010; Stöffler et al., 2013; Artemieva et al., 2013; Osinski et al., 2016; Thompson e Spray, 2017; Siegert e Hecht, 2018; Mader e Osinski, 2018; Kaskes et al., 2022).

Apesar dos mecanismos da formação e distribuição dos suevitos ainda ser um assunto relativamente mal compreendido na ciência de crateramento, quatro modelos foram estabelecidos para a cratera de Ries: (1) deposição por precipitação de uma pluma de material ejetado (von Engelhardt e Graup, 1984; von Engelhardt, 1990); (2) deposição por fluxos superficiais ricos em melt aderentes ao solo (Osinski et al., 2004, 2011); (3) correntes de densidade aderentes ao solo semelhante às correntes de densidade piroclástica dos ignimbritos (Siegert et al., 2017); (4) resultado de erupções secundárias semelhantes a freatomagmática desencadeadas pela interação de fusão por impacto quente e material volátil, semelhante à molten-fuel-coolant interation – MFCI (Grieve et al., 2010), formando uma pluma secundária e a deposição do suevito como uma consequência do colapso dessa pluma (Stöffler et al., 2013; Artemieva et al., 2013). Recentemente, o (5) modelo de multiestágio foi propospo por Osinski e Grieve (2024) para a origem e colocação de suevita e outros impactitos alóctones, durante o evento de impacto de Ries. Este mesmo cenário já havia sido proposto para a origem e colocação dos impactitos da estrutura de impacto Mistastin Lake (Mader e Osinski, 2018). Além desses cenários, o modelo

de (6) ressurgimento do oceano dentro da cratera (Ormö et al., 2007; Gulick et al., 2019) foi proposto para a estrutura de impacto Chicxulub (México).

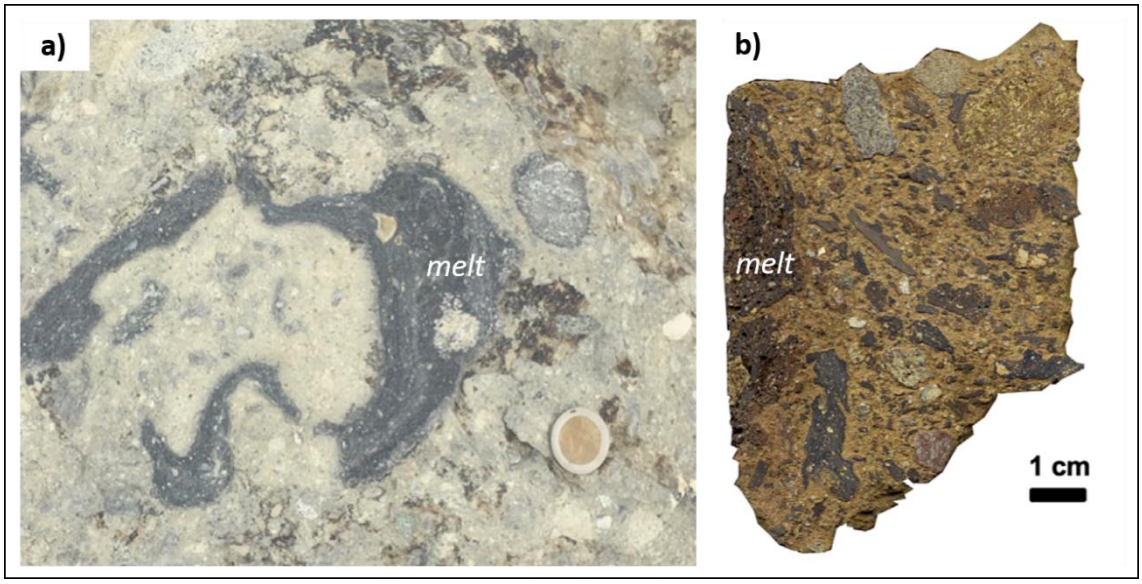

Figura 2.8 Suevitos da estrutura de impacto Ries (Alemanha). a) Imagem de campo mostrando o melt preservado com forma complexa. b) Amostra de mão mostrando a variedade de clastos líticos e a presença de melt. Modificado de Osinski e Grieve (2024).

Stöffler et al. (2013), baseados nas observações de campo, amostra de mão e microscopia, estabeleceram condições relevantes para discernir os mecanismos na determinação da deposição, formação e distribuição dos suevitos em qualquer estruturas de impacto: (1) configuração geológica e distribuição regional com relação à estrutura de impacto, (2) proveniência dos fragmentos líticos e minerais, (3) morfologia e tamanho das partículas fundidas, (4) composição modal quantitativa, (5) tamanho dos grãos e características texturais, (6) grau do metamorfismo de choque, e (7) parâmetros indicativos da história do resfriamento (ex., magnetização remanente, mineralização secundária). Essas observações podem ajudar a tirar algumas conclusões sobre a sequência de tempo para a colocação dos diferentes tipos de suevitos e outras rochas de impacto em uma estrutura de impacto, mas vale ressaltar que cada estrutura possui particularidades que não necessariamente devem ser incluídas a esses modelos preexistente.

CAPÍTULO 3
MATERIAIS E MÉTODOS

3 MATERIAIS E MÉTODOS

Os métodos utilizados para execução desta pesquisa são compostos basicamente por atividades pré-campo, amostragem, preparação de amostras, análises de amostras, tratamento de dados, apresentação e interpretação de dados.

3.1 Etapa pré-campo

Esta etapa de trabalho conta com um amplo levantamento bibliográfico contínuo sobre a geologia regional da Bacia do Paraná e Faixa Paraguai, da geologia local da estrutura de impacto de Araguainha, dos processos de crateramento por impacto com ênfases em trabalhos aplicados diretamente nas brechas de impacto. Artigos científicos, dissertações, teses, relatórios técnicos, mapas e resumos de eventos científicos em anais que abordam a área estudada e o tema da pesquisa foram compilados. Assim como foi feito o levantamento, compilação e interpretação de dados disponíveis que auxiliaram na definição dos alvos amostrais e técnicas a serem utilizadas, facilitando e direcionando a aquisição de dados e amostras que fornecessem respostas aos objetivos propostos.

3.2 Trabalho de campo: mapeamento geológico

Imagens de satélites foram analisadas previamente para o planejamento dos trabalhos de campo. O mapeamento geológico foi realizado a fim de entender as relações de contato entre as brechas de impacto com as rochas do embasamento pré-ordoviciano e da Bacia do Paraná. Durante esta etapa, as descrições dos afloramentos seguiram com a coleta de amostras litológicas para análises laboratoriais (ex., petrografia, geoquímica, isotópica), além do registro fotográfico, localização utilizando o Garmin Etrex 10 Global Positioning System (GPS) – WGS-84 UTM Zona 22S, e medidas estruturais, quando possível. Espessura, relações de campo, esboço de perfil e outras observações importantes foram documentadas. Ao todo, 116 pontos de exposições rochosas foram registrados (Anexo 1). Os trabalhos de campo foram realizados em sete etapas: CAMPO I (19-25/05/2019), CAMPO II (16-21/09/2019), CAMPO III (8-15/12/2020), CAMPO IV (11-21/01/2021), CAMPO V (13-24/06/2021), CAMPO VI (10-17/05/2022); CAMPO VII (5-11/11/2022), todas partindo de Brasília/DF.

3.3 Análises petrográficas

As análises petrográficas consistiram inicialmente em estudos macroscópicos que fundamentaram a seleção de amostras para confecção de lâminas delgadas. Ao total, foram feitas 92 sessões delgadas das brechas de impacto. Os principais aspectos considerados nas descrições microscópicas foram texturas, composição mineralógica, presença de material fundido, e metamorfismo de choque. As seções delgadas foram produzidas em diferentes laboratórios: Laboratório de Lâminas Delgadas do Museu de História Natural de Berlim, Alemanha; Laboratório de Preparação de Amostras e Laminação da Universidade Federal de Pernambuco; e no Laboratório de Laminação da Universidade de Salta, Argentina. As fotomicrografias das seções delgadas foram obtidas com polarizadores paralelos e cruzados com objetivas de aumento entre 2,5x e 40x, usando a câmera ZEISS acoplada ao microscópio ótico modelo Olympus nos Laboratório de Estudos Geodinâmicos, Geocronológicos e Ambientais e de Paleontologia do Instituto de Geociências da Universidade de Brasília (IG-UnB).

3.4 Escaneamento por micro Florescência de Raio-X (µFRX)

A microscopia óptica neste estudo foi combinada com as análises de escaneamento por micro florescência de raio-x (µFRX) usando o mapeamento de elementos maiores e menores em 43 lâminas (40 lâminas de brechas polimíticas de impacto e 3 lâminas de rochas derretidas por impacto). As análises foram realizadas com o instrumento Bruker (Bruker nano GmbH, Berlim, Alemanha) M4 Tornado µXRF disponível no grupo de pesquisa Archaeology, Environmental Changes & Geo-Chemistry da Vrije Universiteit Brussel, Bruxelas (Bélgica). Este instrumento usa um tubo de raios-X metalocerâmico com ânodo de ródio de 30 W e dois detectores de desvio de silício XFlash 430 de 30 mm^2 com resolução de 145 eV (Mn-Kα) a 300 kcps. As medições foram realizadas sob condições de quase vácuo (20 mbar), com configurações de energia Rh maximizadas da fonte de raios X (600 µA, 50 kV) e sem o uso de um filtro. O feixe de raios X foi focalizado por uma lente policapilar em um ponto com diâmetro de 25 µm (Mo-Kα) (de Winter et al., 2017). Um tempo de integração

padrão de 1 ms por pixel com um espaçamento de 25 µm foi empregado para todas as medições. No total, 18 seções finas podem ser montadas na câmara de vácuo de uma só vez.

Essa técnica produz mapas de distribuição química como mapas qualitativos de vários elementos, onde a cor de cada pixel é uma combinação de tons das cores selecionadas, e como mapas de calor semiquantitativos de elemento único. Estes últimos representam uma visualização semiquantitativa, pois as variações relativas de um único elemento são mostradas em uma escala de calor linear colorida RGB (0-255) em que o maior valor RGB (255) corresponde ao pixel no mapa com maior amplitude do pico principal (muitas vezes Kα ou Lα) desse elemento específico. Dessa forma, ao mapear várias amostras ao mesmo tempo, torna-se possível determinar variações químicas semiquantitativas entre amostras (Déhais et al., 2022). Todos os mapas composicionais semiquantitativos de elementos maiores e traços (Na, Mg, Al, Si, K, S, Cl, Ca, Ti, V, Cr, Mn, Fe, Ni, Cu, Zn, Sr, Rb, Zr) produzidos por este método estão em anexo (Anexo 2).

3.5 Avaliação Quantitativa de Minerais por Microscopia Eletrônica de Varredura (QEMSCAN)

A caracterização mineral de alta resolução em quinze lâminas polidas foi analisada pela Avaliação Quantitativa de Minerais por Microscopia Eletrônica de Varredura (QEMSCAN). As análises foram executadas no Laboratório de Caracterização Mineralógica Aplicada do IG-UnB. As seções finas foram revestidas com carbono e analisadas qualitativa e quantitativamente usando um analisador QEMSCAN, modelo Quanta FEI 650F, com espectroscopia de dispersão de raios X de duas energias (EDS) de Bruker. As análises foram operadas em alto vácuo, com feixe de corrente de 10 nA tensão de aceleração de 15 kV. Este procedimento resultou na geração de mapas composicionais de 15 µm de resolução lateral. Através das análises de QEMSCAN é possível identificar minerais de acordo com a proporção de elementos químicos. Como o método compara os dados obtidos com um banco de dados pré-existente, é imprescindível a previa caracterização mineral que, neste trabalho, foi dada pelo

método da petrografia óptica. Todos os mapas composicionais adquiridos estão em anexo (Anexo 3).

3.6 Procedimentos Mecânicos e Analíticos

3.6.1 Preparação de amostras

Amostras representativas das rochas alvo e brechas de impacto foram cuidadosamente separadas e preparadas para não ocorra contaminação. A primeira etapa consistiu na secagem delas em uma estufa por 24h em torno 60ºC. Em seguida, o tamanho das amostras foi reduzido para grãos por meio de uma marreta. Após esta etapa as amostras foram pulverizadas à granulometria de pó (~ 200 mesh) no moinho de panela de tungstênio e armazenadas em tubos plásticos. Todo esse processo foi realizado no Laboratório de Preparação de Amostras do Laboratório de Estudos Geodinâmicos, Geocronológicos e Ambientais (LEGGA) do Instituto de Geociências da Universidade de Brasília (IG-UnB).

3.6.2 Análise por difração de raio-x

Oito amostras foram analisadas pelo método de Difração de Raios-X (XRD) as quais incluem a matriz de brecha de impacto polimítico, rochas derretidas por impacto, a provável alteração encontrada ao redor de algumas populações de clastos e o siltito da Formação Furnas. As amostras foram trituradas na fração argila (< 2 μm) em uma tigela de ágata para serem analisadas no Raio-X usando o pó no método DRX. As análises foram realizadas no Laboratório de Difração de Raios-X do IG-UnB. O difratômetro é um instrumento Rigaku Ultima modelo IV com catodo de cobre e filtro de Ni, operado a 35 kV e 15 mA com ângulo de escaneamento variando ente 5º e 60º 2Θ. Os difratogramas foram analisados por meio do software JADE 9.0 (MDI – Material Data™), que possui busca automática de picos e busca de possíveis minerais no banco de dados mineralógicos do International Diffraction Data Center (IDDC).

3.7 Separação de zircão e análises no espectrômetro de massa (LA-ICP-MS)

A separação de zircão, imageamento do mesmo e análises isotópicas U-Pb tem, por objetivo, identificar evidências de metamorfismo de choque na superfície dos cristais de zircão e obtenção de idades de proveniência U-Pb. Foram feitas 4 análises na matriz das brechas de impacto e 4 amostras do embasamento pré-ordoviciano associado a sequencias metassedimentares.

3.7.1 Concentração e montagem

A preparação das amostras foi realizada de acordo com o procedimento convencional do Laboratório de Estudos Geodinâmicos, Geocronológicos e Ambientais (LEGGA, IG-UnB). A desintegração de 1-5 kg das rochas para obter um tamanho de material inferior a 300 µm constou com a britagem, pulverização em moinho de molas com posterior peneiramento das amostras em uma malha de 2 cm e o material menor a 2 cm foi levado para o moinho de panelas, no qual foi obtido um tamanho inferior a 500 µm. As amostras foram peneiradas em duas malhas, uma de 265 µm e outra de 120 µm. Os minerais pesados entre eles zircão, foram separados pelo método da bateia.

A fim de separar o excesso dos minerais pesados e magnéticos, primeiro foi passado um ímã de mão para depois utilizar o separador magnético isodinâmico Frantz. Este equipamento tem por objetivo fazer a separação dos minerais magnéticos daqueles não-magnéticos à uma corrente de 1.5 Å. Até essa amperagem, o mineral zircão se concentra no grupo dos não magnéticos. O mineral zircão foi separado manualmente por concentração em álcool com o auxílio de uma lupa binocular. Após a separação, os grãos de zircão foram selecionados e fixados em um molde de epóxi, polidos a aproximadamente meia espessura, limpos com ácido nítrico a 3 % antes da análise e caracterizados por imagens de elétrons retroespalhados (BSE) e catodoluminescência (CL) usando o Microscópio Eletrônico de Varredura FEI Quanta™ 450. As imagens obtidas forneceram a base para a categorização de grãos, caracterização de superfícies externas e para a seleção de locais para análise de ablação a laser.

3.7.2 Análise isotópica de U-Pb

Laboratório de Estudos Geodinâmicos, Geocronológicos e Ambientais (UnB)

Amostras SF-04 e P-03: Dados de U-Pb realizadas em grãos de zircão detríticos de 2 amostras de brechas de impacto foram obtidas no LEGGA (UnB), usando um Thermo-Fisher Neptune MC-ICP-MS acoplado a um sistema de ablação a laser Nd:YAG UP213 New Wave. As análises U-Pb em grãos de zircão foram realizadas pelo método de bracketing de amostra padrão (Albarède et al., 2004) usando o zircão padrão GJ-1 (Jackson et al., 2004) para quantificar a quantidade de fracionamento instrumental ICP-MS. As massas ajustadas foram 238, 204, 206, 207 e 202. O tempo de integração foi de 1 segundo e o tempo de ablação foi de 40 s para todos os isótopos. Foi usado um tamanho de ponto de 25 µm e a configuração do laser foi de 10 Hz e 2-3 J cm^{-2}. Dois a quatro grãos desconhecidos foram analisados entre as análises GJ-1. As proporções $^{206}Pb/^{207}Pb$ e $^{206}Pb/^{238}U$ foram corrigidas no tempo. Os dados brutos foram processados off-line em uma rotina de redução de dados baseada no Excel (Bühn et al., 2009). Durante as sessões analíticas, o padrão de zircão 91500 (Wiedenbeck et al., 1995, 2004) também foi analisado como um desconhecido. O ^{204}Pb comum foi monitorado usando as massas ^{202}Hg e ($^{204}Hg+^{204}Pb$). No entanto, as correções do Pb comum não foram necessárias devido aos sinais muito baixos para ^{204}Pb (<30 cps) e às altas proporções $^{206}Pb/^{204}Pb$. Erros relatados são propagados pela adição quadrática [(2DP^2+2SE^2)$^{1/2}$] (DP = desvio padrão; EP = erro padrão) da reprodutibilidade externa e precisão dentro da execução. A reprodutibilidade externa é representada pelo desvio padrão obtido de análises repetidas (n = 20, ∼1,1% para $^{207}Pb/^{206}Pb$ e até ∼2% para $^{206}Pb/^{238}U$) do padrão de zircão GJ-1 durante as sessões analíticas, e a precisão dentro da execução é o erro padrão calculado para cada análise. Diagramas de Concordia (elipses de erro 2σ) e idades médias ponderadas foram calculadas usando o software Isoplot-3/Ex (Ludwig, 2008).

Amostras CA-73 e CA-116: Dados de U-Pb foram obtidos no LEGGA para duas amostras de brechas polimíticas de impacto (CA-73 e CA-116), onde as massas de interesse foram medidas em um ICP-MS de campo setorial multicoletor de alta resolução Thermo Finningan Neptune XT acoplado a um sistema de ablação a laser Teledyne Analyte Excite de 193 nm. O sistema de

ablação a laser é equipado com uma câmara de volume duplo HelEx II. O espectrômetro de massa foi ajustado para melhorar a sensibilidade de U e Pb, minimizando a produção de óxido antes de cada sessão analítica. Cada análise consistiu em 10 s de medição de fundo, seguidos por 20 s de aquisição de dados da amostra. Todas as massas (202, 204, 206-208, 232, 238) foram medidas simultaneamente usando uma combinação de detectores Faraday, SEM e CDD. As condições do laser incluíram um diâmetro de ponto de 20 µm, 8 Hz e 4,0 J cm^{-2}. Os dados brutos foram processados com o software Iolite 4.0 (Paton et al., 2011), e a inspeção de sinal resolvido no tempo e sinal individual foi feita com VizualAge (Petrus e Kamber, 2012). A correção de dados incluiu subtração em branco e a correção LIEF usando um modelo exponencial mais linear e normalização para o zircão GJ-1 (Jackson et al., 2004). O zircão 91500 (Widenbeck et al., 1995) e o zircão Plešovice (Sláma et al., 2008) foram usados para controle de qualidade. O excesso de variância no calibrante primário foi propagado para cada ponto analítico. Uma incerteza sistemática de ca. 1% é propagada em cada idade final. Erros em idades são cotados em nível de confiança de 2s.

Centro de Pesquisas em Geocronologia e Geoquímica Isotópica (USP)

Amostras CA-111, CA-22, GAR-15-0, GAR-15-G10: Os estudos isotópicos realizados no Centro de Pesquisas em Geocronologia e Geoquímica Isotópica da Universidade de São Paulo (USP) foram feitos utilizando um espectrômetro de massa com plasma indutivamente acoplado multicoletor Thermo-Fisher Neptune (ICP-MS) conectado a um sistema de ablação a laser Excimer Excite ArF de 193 nm de comprimento de onda. A ablação foi realizada em spot de 32 µm e frequência de laser de 6 Hz, aplicando intensidade de 6 mJ e tempo de ablação de 40 segundos, com He como gás controlador MCF1 e MCF2 a uma taxa de fluxo de 0,3 L/min. A análise U-Pb segue a ordem de dois brancos, dois NIST, três padrões externos (padrão GJ1), seis amostras desconhecidas, um padrão secundário (Mud Tank), seis amostras desconhecidas e dois NIST, dois padrões externos (GJ1), e medição de dois espaços em branco. Uma interpolação das quatro sequências de medição em branco, duas antes e duas depois das amostras (método de bracketing), foi

subtraída de cada uma das 7 massas medidas (202, 204, 206, 207, 208, 232 e 238).

O isótopo ^{235}U não foi medido, mas calculado matematicamente usando a abundância relativa $^{238}U/^{235}U$ = 137,88. A interferência de ^{204}Hg para ^{204}Pb foi corrigida graças ao ^{202}Hg, assumindo $^{204}Hg/^{202}Hg$ = 4,350360. Utilizando a razão $^{207}Pb/^{206}Pb$ parcialmente corrigida como estimativa para a idade e as fórmulas de Stacey e Kramers (1975), foram calculadas as abundâncias relativas de $^{206}Pb/^{204}Pb$, $^{207}Pb/^{204}Pb$ e $^{208}Pb/^{204}Pb$ (variáveis com a idade geológica). A fração comum de Pb (não radiogênica) dos isótopos ^{206}Pb, ^{207}Pb e ^{208}Pb poderia então ser descontada, subtraindo de cada um o sinal de ^{204}Pb multiplicado, respectivamente, pelas três abundâncias relativas calculadas anteriormente. Outro agrupamento de medições (duas sequências antes e depois das amostras) dos padrões NIST-612 também foi usado para converter os três sinais totais (Pb=$^{204}Pb+^{206}Pb+^{207}Pb+^{208}Pb$; Th=$^{232}Th$; U=$^{235}U+^{238}U$) em ppm unidades.

Um bracketing final (três antes e dois depois das amostras) dos minerais padrão foi então usado para corrigir o efeito do fracionamento nas quatro proporções ($^{206}Pb/^{238}U$, $^{207}Pb/^{235}U$, $^{207}Pb/^{206}Pb$, $^{208}Pb/^{232}Th$), antes de serem ser extrapolado através dos melhores ajustes de linha para t = 0 e então usado para calcular as respectivas idades. Erros em todas as operações aritméticas simples foram propagados algebricamente, por exemplo, d(AB)=dA+dB e d(A/B)/(A/B)=dA/A+dB/B. O ajuste de mínimos quadrados foi a escolha para os melhores ajustes de linha e, em todos os resultados finais e gráficos, foi adotado o quadro de erro (no nível 2σ) já disponível no Isoplot 3.70 (Ludwig, 2008).

3.8 Tratamento e análise de dados

Os dados obtidos nas etapas descritas acima foram tratados e organizados em um banco de dado. Os dados de geoquímica e isotópicos foram organizados no Excel e processados nos softwares, IgPet 06, Isoplot-3, DetritalPyton. A confecção dos mapas e figuras foram realizados nos softwares Esri's ArcGIS PRO 3.X e CorelDRAW 2021.

CAPÍTULO 4
ARTIGO 1

4 ARTIGO 1

Artigo científico intitulado "**Araguainha impact structure, Brazil: new insights into the geology of the central uplift**" publicado no dia 19 de junho de 2024, na revista Meteoritics and Planetary Science com o seguinte DOI: 10.1111/MAPS.14236.

The Meteoritical Society

Meteoritics & Planetary Science 1–31 (2024)
doi: 10.1111/maps.14236

Araguainha impact structure, Brazil: New insights into the geology of the central uplift

Carolinna da Silva Maia de SOUZA[1]*, Natalia HAUSER[1], Wolf Uwe REIMOLD[1], Renato Borges BERNARDES[1], Lucieth Cruz VIEIRA[1], Edi Mendes GUIMARÃES[1], and Manfred GOTTWALD[2]

[1]Institute of Geosciences, University of Brasilia, Darcy Ribeiro Campus, Brasília, Brazil
[2]German Aerospace Center, Remote Sensing Technology Institute, Wessling, Germany

*Correspondence
Carolinna da Silva Maia de Souza, Postgraduate Program in Geology, Institute of Geosciences, University of Brasília, Darcy Ribeiro Campus, CEP 70910-900, Brasília, DF, Brazil.
Email: maia.carolinna@gmail.com

(Received 27 February 2024; revision accepted 19 June 2024)

ARAGUAINHA IMPACT STRUCTURE, BRAZIL: NEW INSIGHTS INTO THE GEOLOGY OF THE CENTRAL UPLIFT

Carolinna da Silva Maia de Souza[1]*, Natalia Hauser[1], Wolf Uwe Reimold[1], Renato Borges Bernardes[1], Lucieth Cruz Vieira[1], Edi Mendes Guimarães[1], and Manfred Gottwald[2]

[1]University of Brasilia, Institute of Geosciences, Postgraduate Program in Geology, Darcy Ribeiro Campus, CEP 70910-900, Brasília, DF, Brazil.

[2]German Aerospace Center, Remote Sensing Technology Institute, 82234 Wessling, Germany.

* Corresponding author: maia.carolinna@gmail.com

ABSTRACT

Extensive, new outcrops along the MT-100 state road in the northern part of the central uplift of the 40-km diameter, 252-259 Ma old Araguainha impact structure, Central Brazil, have become available for investigation. They offer new insight into the contact relationships between the different lithologies and the genesis of different types of impact-related rocks, as well as the current level of erosion of the structure. Three types of impact melt rock (IMR) with different field relationships and compositions can now be distinguished: (1) Type-I of granitic composition and occurring mainly as veins and dikes, besides a few larger pods, in the central alkali granite core of the central uplift; (2) Type-II in the form of plastically deformed clasts of mainly highly silicious compositions in polymict impact breccia; and (3) Type-III, derived from partially melted conglomerate or sandstone precursors, and that occurs at selected sites in (meta)sedimentary strata of the basement in the immediate environs of the alkali granite core. Both polymict lithic and melt-bearing (suevitic) impact breccias are recognized in the 110-m thick integrated section through impact breccia directly overlying the crater floor. This crater floor is composed of (meta)-sedimentary basement strata with granite injections and, locally, sandstones of the Devonian sedimentary Furnas Formation of the Paraná Basin. Main breccia components are (meta)-pelites and (meta)sandstones of the basement that is currently favored to be related to the regional Paraguay Belt and to the lower sequence of the Paraná Basin sedimentary strata. Locally, breccia contains clasts of IMR Type-II, and only very

rarely are granitic fragments observed. Clasts of IMR Type-I have never been observed in the breccia deposits. These new observations preclude significant involvement of alkali granite in the formation of the polymict breccia or in the production of shock melts. They also reveal the major role of the (meta)sedimentary precursors in the production of IMR by shock melting and provide essential information for better understanding the cratering processes involved in the formation of an impact structure in a sedimentary target, of the size of the Araguainha impact structure.

Keywords: Araguainha impact structure; Polymict impact breccia; Impact melt rock; Shock melting; Crater floor geology; (Meta)sedimentary target; Paraguay Belt; Paraná Basin.

4.1 Introduction

Hypervelocity impact cratering is a fundamental geological process that has been of utmost importance in the formation and evolution of the solar system and the terrestrial planets (e.g., Melosh, 1989; French, 1998; Melosh and Ivanov, 1999). Impact cratering is a complex and highly dynamic process that operates on a range of spatial-temporal scales, from micro-scale shock deformation of minerals to mega-scale disruption and perturbation of planetary bodies (e.g., Melosh, 1989; Collins et al., 2012). On Earth, some 210 impact structures have been confirmed (Gottwald et al., 2020; Kenkmann, 2021; Schmieder and Kring, 2020; Osinski et al., 2022), which provide essential ground truthing about impact processes and products. Comparison with meteorites, planetary bodies, and lunar impact breccias has provided further essential understanding (e.g., Stöffler et al., 2018 and references therein) about the cratering processes that have operated on Earth.

The 40-km diameter Araguainha impact structure of Central Brazil is the largest impact structure known in South America. It was formed in the northeasternmost part of the intracontinental Paraná Basin (see inset, Figure 4.1; also, Dietz and French, 1973; Theilen-Willige, 1981; Crósta et al., 1981, 2019; Lana et al., 2007, inter alia). The impact event occurred in the latest Permian,

between ca. 252 and 259 Ma (Tohver et al., 2012; Erickson et al., 2017; Hauser et al., 2019). The target for the Araguainha impact included a Cambrian alkali granite (von Engelhardt et al., 1992; Machado et al., 2009; Tohver et al., 2012) intruded into (meta)sedimentary basement that is currently assumed to be part of the Paraguay Belt of the Tocantins Province (Almeida, 1984; Sánchez, 2006; Yokoyama, 2008). The Paleozoic sedimentary units of the Paraná Basin (Milani et al., 2007), especially the Ordovician-Devonian sequences of the lower part of this succession, constituted the upper parts of the target sequence. It has been discussed that the Araguainha impact event could have contributed to the environmental catastrophe of global extent related with the end-Permian mass extinction at 251.6 Ma ago (e.g., Burgess et al., 2014). If the impact occurred at this time, cratering would have involved the carbon-rich Iratí Formation of the uppermost Paraná Basin sequence, which might have released a substantial amount of CO_2 into the atmosphere (Tohver et al., 2013).

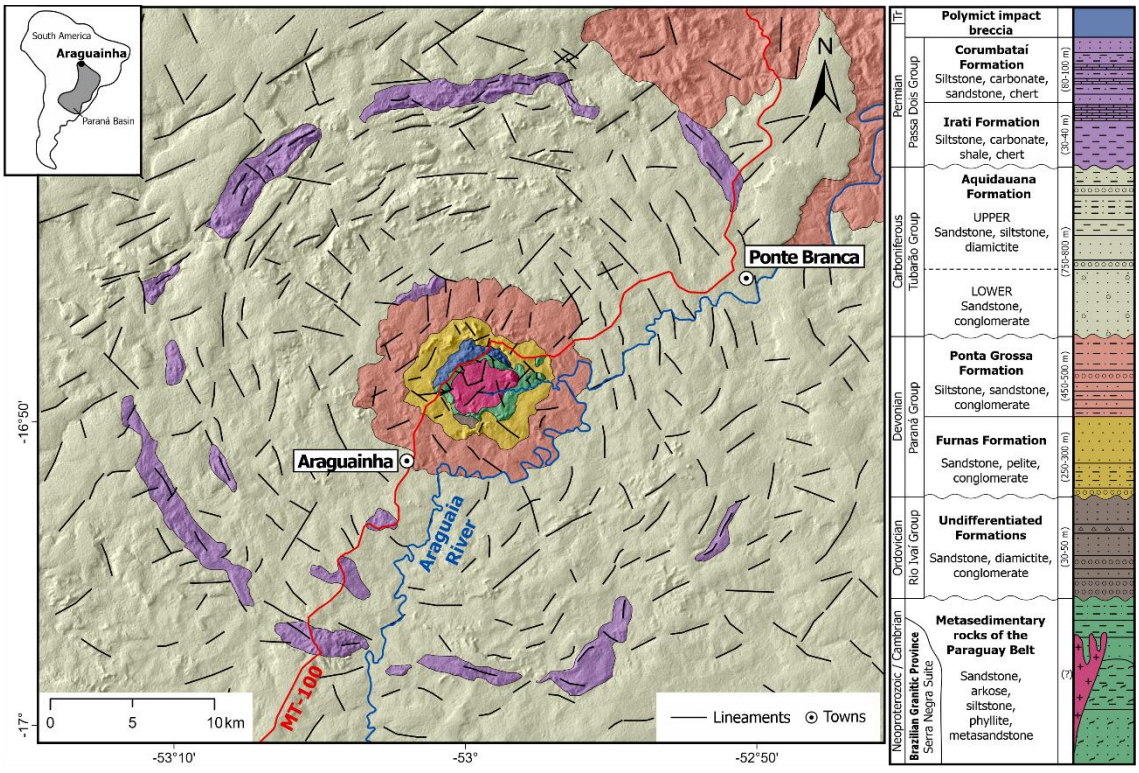

Figure 4.1 Geological map of the Araguainha impact structure based on available geological maps (von Engelhardt et al., 1992; Lana et al., 2007; Machado et al., 2009; UnB-IG, 2012; Yokoyama et al., 2012; Crósta et al., 2019) and referenced against the WGS84 UTM Zone 22S geodetic datum, updated based on TanDEM-X radar satellite image (~53 x 61 km wide area; courtesy of the German Aerospace Center – DLR, Oberpfaffenhofen, Germany) and surface reflectance (Landsat 8/OLI) imagery. The SRTM digital elevation model multidirectional shaded relief (NASA JPL, 2013) was used in the map to give a sense of topography. The Araguainha impact structure

straddles the border between Goiás and Mato Grosso states and is centered at 16º48'45" S, 52º59'02" W. On the right, a simplified stratigraphic column is presented for the sequences of the Paraná Basin and the Precambrian basement that constituted the target rocks for the Araguainha impact event. The basement is composed of Neoproterozoic rocks of the Paraguay Belt, probably mainly derived from the Cuiabá Group, and a Cambrian, post-collisional porphyritic granite of the Brazilian Granitic Province, from the Serra Negra Suite. The thicknesses indicated are based on data from Lana et al. (2007). Modified after UnB-IG (2012). Tr – Triassic.

The central uplift of this large impact structure is still reasonably well preserved with good exposures of impact-related rocks and basement lithologies of the crater floor. However, there is no consensus about the diameter of this central uplift region, which has been variably suggested to be between 8 and 16 km (Crósta et al., 1981; von Engelhardt et al., 1992; Lana et al., 2007, 2008; Miyazaki et al., 2021). Geological mapping of this area has evolved over nearly 50 years (e.g., Crósta et al., 1981; von Engelhardt et al., 1992; Yokoyama, 2008; UnB-IG, 2012; Yokoyama et al., 2012; Preuss, 2012; Fischer, 2015; Crósta et al., 2019) and different nomenclatures have been applied to the impact-related rocks at Araguainha. A summary of the different nomenclatures applied since 1981 is given in Table 4.1. Overall, the contact relationships between the different impact-related rocks, namely impact breccias (polymict breccias, suevite, and impact melt rocks [IMRs]) and shocked and unshocked target rocks, have not been addressed well in the past, and their nature and formation have not been studied in sufficient detail.

During 2021 and 2022, extensive new outcrops were exposed in the course of roadworks along the MT-100 state road that crosses the entire impact structure in a general SW-NE/E direction, and especially the northern part of the central uplift region. This has provided an excellent opportunity for renewed detailed geological mapping and especially to investigate the contact relationships of rocks in the central uplift.

After extensive field work followed by petrographic analysis, we can now present an updated geology for the central uplift (Figure 4.2). This includes the presentation of a new geological map and a new nomenclature for the impact-related rocks at Araguainha (Table 4.1). We discuss, inter alia, (i) the updated geological map for the central uplift, (ii) the distribution and characteristics of the now distinguished three types of IMR, as well as of part-melted and annealed basement materials, (iii) the nature of the polymict impact breccias (PIBs) mainly

found in contact with (meta)sedimentary lithologies of the basement, and (iv) a newly-proposed nomenclature for the Araguainha lithologies. These new observations provide improved knowledge about the cratering process that governed the formation of the Araguainha impact structure at the end of the Permian.

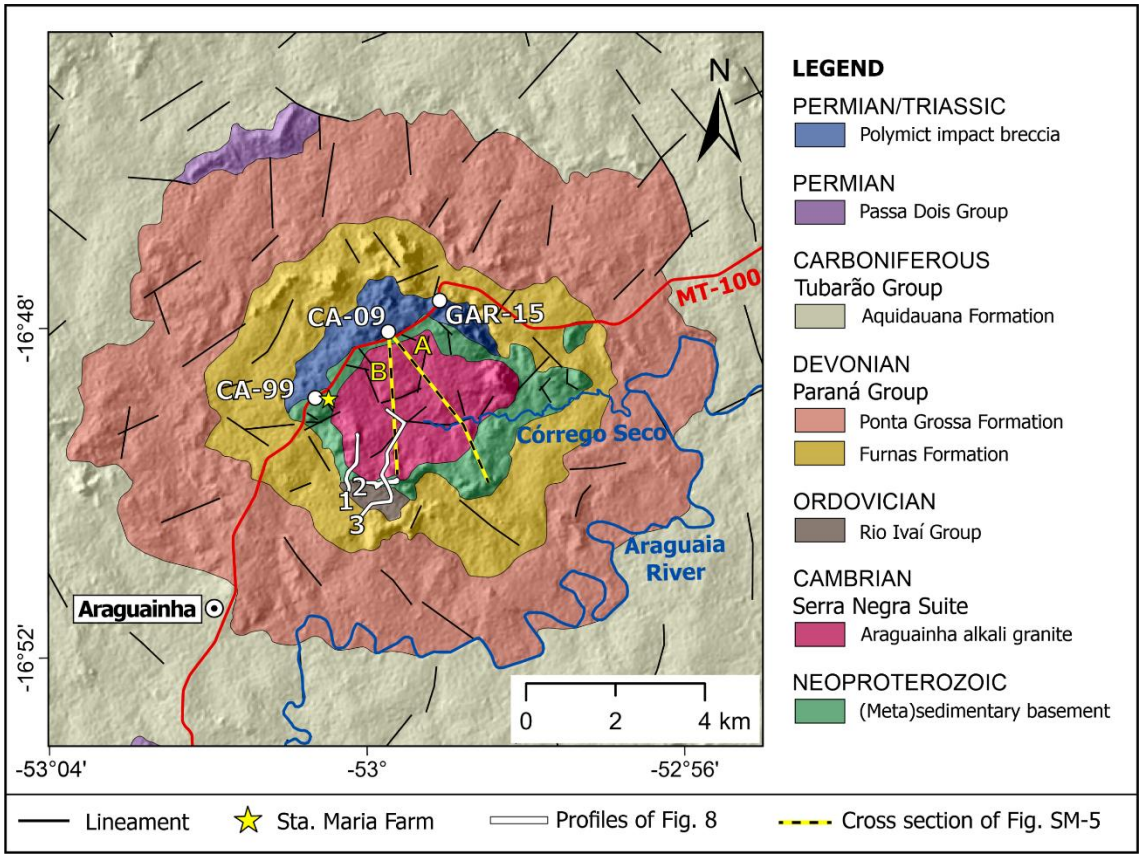

Figure 4.2 Geological map for the area of the Araguainha central uplift (zoom from Figure 4.1). Also indicated is that the northern sector is related in this paper with the description of these outcrops: CA-99, the classical shatter cone locality in metasedimentary basement that are overlain by polymict impact breccia; CA-09, the polymict breccias that crop out along the path to the communication tower; and GAR-15, the profile across the megablock zone that illustrates the relationships between the basal target rocks and overlying impact breccias. The southern sector is indicated by Profiles 1, 2, and 3. The narrow zone with Type-III impact melt rock is not indicated, but it is possible to see the distribution of this melt rock type in the map of Figure S2.

Table 4.1 Comparison of rock nomenclatures applied to Araguainha impactite lithologies as identified in the central uplift by various authors. Modified after Crósta et al. (2019).

Araguainha impact-related rocks	Souza et al. (this study)	Crósta et al. (1981)	von Engelhardt et al. (1992)	Machado et al. (2009)	Yokoyama (2008)	Preuss (2012)	Hippertt et al. (2014)	Fischer (2015)	Silva et al. (2016)
Impact melt rocks (IMR)	Type-I: Granitic precursor; mainly as red or gray dikes/veins or pods	Breccia rich in vitreous material	Red dikes/gray veins; impact breccia with melt matrix	Melt veins	Dikes and veins filled with molten material; rocks with little relict material	Impact melt rock: type 1 and 2	*	Impact melt rocks	Melt dikes; Melt sheet
	Type-II: sedimentary precursor (sandstone), found as melted clasts in PIB	Fragment of devitrified material with fluidal texture	Large, individual bodies of rocks with igneous textures	*	*	Melt bodies in suevite	*	Impact melt clasts after sedimentary precursors	*
	Type-III: sedimentary precursor: Conglomerate (sandstone)	*	*	*	*	*	Sandstone-derived melt rock	*	*
Polymict impact breccias (PIB)	PIB injected into the basement	*	*	*	*	*	*	*	*
	PIB covering or in contact with target rock	Polymict breccia	Polymict breccia	Polymict breccia	Polymict breccia	Suevite and polymict lithic breccia		Suevite	Polymict impact breccia
Monomict impact breccias	*	*	Monomict breccia after sandstone	Monomict impact breccia	*	Quartz breccia	*	*	Monomict impact breccia
Part-melted and annealed basement	Transitional granite	*	*	Melt sheet	Rocks with a lot of relict material	*	*	Transitional granite	Melt sheet
	Metasedimentary basement	*	*	*	*	*	*	*	*

Table 4.1. *(continued)*

		Souza et al. (this study)	Crósta et al. (1981)	von Engelhardt et al. (1992)	Machado et al. (2009)	Yokoyama (2008)	Preuss (2012)	Hippertt et al. (2014)	Fischer (2015)	Silva et al. (2016)
Target rocks	*Lower sequences of the Paraná Basin*	Ponta Grossa Formation, Furnas Formation, and Rio Ivaí Group	Furnas Formation	*	Furnas Formation	*	*	Furnas Formation	Furnas Formation	*
		Alkali granite (porphyritic)	Crystalline basement	Granite	Crystalline alkali granite	Porphyritic granite	Granite	Cambrian granitic basement	Porphyritic alkali granite	Shocked granite/Partially molten granite
	Basement	(Meta)sedimentary rocks of the Paraguay belt (mainly represented by Cuiabá Group)	*	Possibly identified as monomict breccia	*	Metamorphic basement (Cuiabá phyllite)	*	*	Metamorphic basement (Cuiabá Group)	*

** Not recognized by the authors*

4.2 Background

4.2.1 Stratigraphy

The Araguainha impact structure (Figure 4.1) centered at 16º48'45" S, 52º59'02" W in central Brazil represents a stratigraphic window into the Paraná Basin (for comprehensive stratigraphic background about the basin, see Milani et al., 2007) and underlying basement. According to Lana et al. (2007), the Araguainha impact structure has been eroded by some 250-350 m. This relatively shallow level of erosion has allowed the preservation of stratigraphy, crater morphology (Lana et al., 2007), and even remnants of polymict impact breccia and impact melt rocks in the central uplift of the impact structure.

From bottom to top, the stratigraphic section (Figure 4.1) affected by this impact event includes: Neoproterozoic (meta)sedimentary rocks thought to belong to the Paraguay Belt (Almeida, 1984; Alvarenga et al., 2004). This basement was intruded by a Cambrian post-collisional, porphyritic alkali granite that has been assigned to the Serra Negra Suite (e.g., Lacerda Filho et al., 2004, 2006; Godoy et al., 2007, 2010). The Serra Negra and the São Vicente suites (Lacerda Filho et al., 2004, 2006) represent postcollisional magmatism and were emplaced in the region between ca. 550 and 500 Ma (Godoy et al., 2007, 2010). The Araguainha granite was dated by Tohver et al. (2012) to 512 ± 11 Ma via U-Pb zircon geochronology.

The Paraguay Belt consists of metamorphosed sedimentary strata of Neoproterozoic and Cambrian age. The metasedimentary sequence has been divided into the older Cuiabá Group, which comprises metasandstones, phyllites, and schists (e.g., Yokoyama, 2008) in greenschist facies. On top of this group, diamictites of the Puga Formation and carbonates of the Araras Group were deposited (McGee et al., 2014). A maximum depositional age of 652 ± 5 Ma (Babinski et al., 2018) was obtained for the Cuiabá Group. The upper unit of the Paraguay Belt is known as the Alto Paraguay Group and is composed of deltaic sandstone, red shale, siltstone, arkose, and laminated mudstone (Dantas et al., 2009). Notably, the Alto Paraguay Group lacks metamorphism. The uppermost Diamantino Formation has a maximum depositional age of 560 ± 13 Ma, which has been interpreted as the youngest time of deposition of Paraguay Belt strata (McGee et al., 2014). Note that we prefer to use the expression

"(meta)sedimentary basement" when referring to both metamorphic and unmetamorphosed components of the basement (compare Figures. 4.1 and 4.2).

This basement sequence is followed by an erosive unconformity, which is - in turn - overlain by conglomerates, diamictites, sandstones, and pelites of the Ordovician to Silurian Rio Ivaí Group that defines the base of the sedimentary fill of the Paraná Basin (Assine et al., 1994). This unit is followed by sandstones and (mainly) pelites from the Furnas and Ponta Grossa formations of the Devonian Paraná Group; the Carboniferous sandstones and pelites of the Aquidauana Formation of the Tubarão Group; and siltstones, carbonates, and evaporites of the Corumbataí and Iratí formations of the Permian Passa Dois Group (Assine et al., 1994; Milani et al., 1994, 2007; compare stratigraphic column on Figure 4.1). At the top of the Permian stratigraphic sequence of the Paraná Basin follows the Araguainha unit (Lacerda Filho et al., 2004) that crops out in the central uplift of the impact structure and comprises the rocks related to the impact, that is, the polymict breccia deposits and impact melt rocks.

Comparative stratigraphic sections for this part of the Paraná Basin that are unaffected by the impact event are sparse. The AG-1-MT well (Cordani et al., 2009) drilled approximately 30 km WSW of the Araguainha impact structure near the town of Alto Garças encountered the metasedimentary basement at 1.9 km depth. The maximum depth of the borehole is about 2 km, in comparison with the maximum thickness of sedimentary and igneous fill in the central parts of the basin that extends to 7 km (Zalán et al., 1990; Milani et al., 2007). Based on this drilling information, both von Engelhardt et al. (1992) and Lana et al. (2007) estimated that the impact event could have excavated some 2,000 m of sedimentary strata concomitantly with the uplift of basement rocks.

4.2.2 Structural division of the Impact structure

Based on morphological and structural features (Theilen-Willige, 1981; Lana et al., 2006, 2007), the Araguainha impact structure was divided into four morphological domains: a central peak, an annular basin, and two concentric, so-called inner and outer, rings in the outer ring syncline of the structure.

Irrespective of the actual diameter of the central uplift area (8-16 km, as mentioned earlier), the central peak area comprises the innermost core that

consists of a somewhat circular basin, and a surrounding collar of (meta)-sedimentary strata (e.g., Lana et al., 2006, 2007, 2008; Yokoyama et al., 2012; Miyazaki et al., 2021; this work). The innermost core terrane is 4-5 km wide and shows numerous but mostly spatially limited exposures of porphyritic alkali granite. This core is surrounded by an annular belt of phyllites and metasandstones, which have been related to the Cuiabá Group.

This collar is surrounded in the north/northwest and south/southwest sectors by a ~1-km wide belt of PIBs and a 1- to 2-km wide zone of upright to overturned, and strongly deformed sedimentary rocks of the Devonian Furnas Formation (von Engelhardt et al., 1992; Lana et al., 2007, 2008; Hippertt et al., 2014). The inner part of this terrain comprises a ~500-m wide, structurally complex megablock zone of tens to hundreds of meter-sized blocks of basal sedimentary rock from the Furnas Formation (Lana et al., 2008). These blocks would relate to the “megalith size class” in sedimentological terminology, according to the classification scheme of Blair and McPherson (1999). However, in this article, we adhere to the “megablock” term introduced by Lana et al. (2008). IMRs have been described throughout the granitic core, mainly in the form of veins and dikes of up to 1 m width, besides a few larger, pod-like occurrences of up to several decameters extent.

Rare occurrences of Ordovician Rio Ivaí Group strata are also part of this collar. These latter strata were not recognized in the Araguainha area prior to the geological mapping of the 2012 Final Year students of the Universidade de Brasilia (UnB-IG, 2012).

The annular basin (“ring syncline”), located between the central uplift region and the outer rim, is a relatively flat depression, where yellow-ochre to brownish siltstone and sandstone of the Devonian Ponta Grossa Formation, and, further outward, reddish-pinkish sandstone and (minor) conglomerate of the Carboniferous Aquidauana Formation occur. Conglomerate forms the base of this formation.

The two ring structures proposed by Lana et al. (2007) are supposed to occur at 10-12 and 14-18 km from the center of the structure. The inner ring structure would mark the extent of deformation related to the outward movement of the target rocks during collapse of the central uplift, and the concentric ring

further out would record additional outward movement of the target rocks (Lana et al., 2008).

The crater rim area is composed of kilometer-scale blocks of variably deformed rocks from the upper Paleozoic units of the Paraná Basin – black shale and silicified limestones from the Irati Formation, and siltstone and sandstone from the Corumbataí Formation. There are also sandstone, siltstone, and diamictite from the upper part of the Aquidauana Formation. Associated with the Passa Dois Group, stromatolitic growths were identified in silicious rock (e.g., chert). This sequence in the outermost parts of the impact structure is well preserved as lenses in areas where normal faulting has resulted in graben or half-graben structures (see also Crósta et al., 2019).

4.2.3 Background about the impact-related rocks at Araguainha

Several authors have described the types of Araguainha impact breccias, that is, the IMRs and PIBs, including their petrographic characteristics and shock deformation within clasts. Lana et al. (2007), combining field-based and remote sensing information, presented a comprehensive stratigraphic analysis of the sedimentary target rocks. They reported contact relationships for the different structural domains. In the central peak, the granitic core and supracrustal strata of the Furnas Formation in the collar were separated by faulting, associated with fracturing and brecciation. In the annular basin and associated concentric ring regions, the Ponta Grossa and Aquidauana formations are linked through radial, vertical fault zones, separating large blocks of sedimentary rocks. The bedding in this area becomes more prominent near the annular ring zones and is arrayed concentrically around the basin, dipping shallowly to steeply inward. In the crater rim area, the contacts between the sedimentary rocks of the Aquidauana Formation and Passa Dois Group are complex and often defined by fault or breccia zones.

Not much has been written to date about the contact relationships between the different impact-related rocks in the central uplift, probably because there was a lack of extensive outcrop showing contact relationships in previous time. Nevertheless, von Engelhardt et al. (1992) proposed that the PIBs represent fallback material above a basal layer of IMRs of granitic composition

(corresponding to our IMR Type-I, see below and Table 4.1). Furthermore, Lana et al. (2007) suggested that both impact breccia types were deposited onto the crystalline basement and along the core-collar boundary of the central uplift. Tong et al. (2010) proposed, from results of electrical resistivity tomography (ERT) combined with surface geological constraint and gravity data, a model in which impact melt and other impact breccias resurged toward the crater center in the final stages of collapse of the impact structure.

The available geological maps of the last 50 years, especially for the central uplift, all show these major aspects: the PIB in direct contact with the alkali granite, three extensive outcrops of IMRs of granitic composition occurring over large areas of the core of the central uplift, and a wide swath of monomict breccia occurring in the south-southeast sector (von Engelhardt et al., 1992, see Figure S1 of the Supplementary Material). The main changes introduced to the maps through these decades are related to the differentiation of the basement from the lower part of the Paraná Basin (Sánchez, 2006; Yokoyama, 2008; UnB-IG 2012; Crósta et al., 2019) and the subclassification of IMRs of granitic composition. Several authors have called attention to a second type of IMR (Crósta et al., 1981; von Engelhardt et al., 1992; Tong et al., 2010; Preuss, 2012; Fischer, 2015) formed from sedimentary target, though detailed analyses and attempts to explain their formation have not been previously provided.

Different impactite nomenclatures have been used in the past, as we can see in Table 4.1. For example, for IMR of granitic composition, terms such as breccia rich in vitreous material (Crósta et al., 1981); impact breccia with melt matrix, red dikes, and gray veins (von Engelhardt et al., 1992); melt sheet and melt veins (Machado et al., 2009); impact melt sheet and impact melt dikes (Yokoyama et al., 2012; UnB-IG, 2012); impact melt rock, and even pseudotachylitic breccia (Preuss, 2012; Machado et al., 2009), or impact melt rock (Fischer, 2015) have been variably applied.

4.3 Methodology

We carried out geological mapping, mainly within the central uplift region (Figure 4.2), throughout seven field campaigns during different seasons between 2019 and 2022 (see Figure S2). Most of the field work was conducted in the

northern part of the central uplift, especially along the MT-100 state road, both prior to and after the generation of the new outcrops, especially where the road crosses the elevations of the central uplift. In addition, we mapped several profiles in the eastern, western, and southern areas (indicated in Figure 4.2, and also see Figure S3 for more detail). Contact zones between impact breccias and target rocks were investigated in detail. After compilation of previous information, we compared the rock nomenclatures used by previous workers (Table 4.1). The coordinates and lithoclassification for our 152 individual study points are presented in the Supplementary Material (Table S1). These locations are shown in Figure S2 in the Supplementary Material. We have also added the study points of von Engelhardt et al. (1992) to our analysis, thus arriving at a total of 211 locations.

The best exposures in the northern sector of the central uplift occur as tens to hundreds of meters long road cuts along the MT-100 road, besides some good exposures along, or on top of, hills throughout the central uplift. Our descriptions provide information on the geographic locations, including elevations, determined with a Garmin Etrex 10 Global Positioning System (GPS), lithology, stratigraphic thickness, and contact relationships where possible. In addition, we provide several schematic drawings of geological traverses (see Table S1 and Figure S3). We obtained structural data (e.g., bedding, fault, and foliation orientations) with a Brunton compass and a digital compass clinometer (FieldMove Clino); these data are presented in the “dip direction/dip notation” mode.

We used previous geological data and maps of the Araguainha impact structure (e.g., von Engelhardt et al., 1992; Machado et al., 2009; UnB-IG, 2012; Yokoyama et al., 2012; Crósta et al., 2019), together with our field observations, to derive the geological map of the central uplift region presented as our Figure 4.2. Remote-sensing data, that is, a TanDEM-X digital elevation model (see Rizzoli et al., 2017), Esri’s ArcGIS PRO 3.X high spatial resolution, World Imagery layer map service (Credits: Esri, Maxar, Earthstar Geographics, and the GIS User Community), and a Landsat 8 surface reflectance scene (product ID: LC08_L2SP_224072_20200806_20200916_02_T1; Collection 2 – Level 2 Science Products, courtesy of the U.S. Geological Survey) were complementarily used to help during the map production. This remote-sensing imagery aided the

interpretation of documented or inferred contacts, especially between the impact breccias and the different target rock sequences.

We collected impact breccia samples, that is, samples of IMRs and PIB, as well as samples from the (meta)-sedimentary basement and from the lower Paleozoic units of the Paraná Basin, for petrographic investigation. Some samples that had been collected by von Engelhardt et al. (1992) and that are now curated at the Museum für Naturkunde, Berlin, Germany, were studied by us as well. We examined a total of 103 thin sections using a polarizing microscope (Zeiss Axioscope 40) equipped with a digital camera system at the Geodynamic, Geochronological, and Environmental Studies Laboratory of the Geosciences Institute of the University of Brasilia (IG-UnB). The main characteristics of the samples, such as mineral content, textures, and the occurrence of melt particles and shock metamorphic features were recorded. We estimated shock levels based on the shock-stage scheme for quartzo-feldspathic rocks (Stöffler et al., 2018). The mineral abbreviations used herein are after Warr (2021).

4.4 Results

The impact-related rocks include impact breccias (IMRs plus PIBs), as well as shocked and unshocked target rocks from the (meta)sedimentary basement plus the lower part of the Paraná basin sequence. The four main lithologic groups identified by us are (i) target rocks, (ii) part-melted and annealed basement, (iii) IMRs, and (iv) PIBs. In this section, we describe the contact relationships between these four lithological packages in both the northern and southern sectors of the central uplift. Throughout, we will make multiple reference to the various profiles, types of outcrops, and their associated samples. For specific sample locations, consult Figure S2 and the corresponding details in Table S1 of the Supplementary Materials.

4.4.1 Field relationships in the northern sector of the central uplift

Newly exposed outcrops in the megablock zone of the northern sector of the central uplift (the GAR-15 and CA-99 profiles) illustrate the relationships between target rocks, IMRs, annealed basement, and PIBs. Two profiles, GAR-15 and CA-84 (see Table S1), are considered for the description of contact

relationships, whereas profiles CA-07, CA-09, CA-84 and CA-99 are excellent examples for PIB description.

Profile GAR-15 extends in NNE-SSW direction for about 3 km along the MT-100 road, straddling the Serra da Arnica Hill (Figure 4.2). This hill is the most prominent elevation within the megablock zone, being part of the inner collar, and composed of highly deformed Devonian Furnas Formation sandstone. At this location, the sedimentary package of white sandstone intercalated with red laminated sandstone, red pelite, and conglomeratic sandstone (at the Serra da Arnica roadcut: general bedding orientation 217º/58º) of the Furnas Formation is overthrust by a basement block of red and black metapelite, brown phyllite, and metarythmite, with intercalations of metasiltstone and metasandstone (Figure 4.3a), generally of subvertical bedding orientation (080º/69º; Figure 4.3b). This basement package is intruded by up to 2 m wide apophyses of leucocratic (< 5 % biotite), equigranular, and medium-grained granite. The rather rare granite clasts sometimes found in PIB throughout the collar around the inner part of the central uplift have similar textural characteristics. Notably, this granite does not resemble the porphyritic alkali granite of the core of the central uplift.

IMR Type-I (CA-04 dike) and Annealed basement

The largest dike of IMR of granitic composition (i.e., our Type-I, Table 4.2) that has been observed in the core of the central uplift is up to 2 m wide and exposed over 5 m at the CA-04 outcrop of the GAR-15 profile (Table S1). The dike intrudes the metasedimentary basement (Figure 4.4a) and along the contact caused local annealing over a several centimeter wide zone (compare Figure 4.5a-c).

The margin of this dike is characterized by spherulitic and lithophysae textures (Figure 4.4b,c). This spherulitic texture has been related to high-temperature devitrification of hot silicic glass (McPhie et al., 1993). Lithophysae are spherulites that form from gas-filled cavities where external pressure is low, so that dissolved gas present in a melt can expand at the time of devitrification (ibid). The spherulitic aggregates are intergrowths of fibroradial quartz, K-feldspar, and acicular oxide crystals of up to 5 mm size. The lithophysae are characterized by rounded, approximately 1-mm wide nodules of gray silica, which

are surrounded by up to 10-mm wide intergrowths of fibroradial quartz and K-feldspar. Boulders of IMR with lithophysae are found between the inner collar and the granitic core in the northeastern sector of the central uplift as well (CA-55; Table S1). The more common textural type of this rock is porphyroclastic, with varieties that range from clast rich to clast poor. Some aphanitic to very fine-grained domains are also common. Quartz and feldspar porphyroclasts, mostly quite strongly annealed, and millimeter- to centimeter-sized lithic clasts from the alkali granitic precursor are quite common. Schlieren of plasticized and partially melted feldspar minerals are also noted in the matrix of this melt rock (Figure 4.4d).

Porphyroclasts of quartz, orthoclase, albite, and biotite, all embedded in a fine-grained, crystalline matrix or in a hematite-rich, dark red, aphanitic matrix are observed in thin sections of IMR Type-I (see Figure S4b). Quartz clasts up to 1.5 mm size are recrystallized and composed of mosaics of finest grained, interlocking quartz microcrystals. Circular and radiating clusters of sanidine (0.5 mm) are also observed. Shock metamorphism is not common. In one small, not completely recrystallized, quartz clast planar fractures (PFs) and a single set of planar deformation features (PDFs) were noted.

The (meta)sedimentary basement is partially melted or annealed along the contacts with originally hot dikes of IMR of granitic composition (Type-I; Figure 4.5a). This was particularly observed at the contact with dike CA-04, where the annealed basement preserves the original stratification of alternating layers of quartz-rich (meta)sandstone and finer grained, pelitic sandstone (Figure 4.5b). It also displays small (< 30 cm) folds with locally occurring melted silicic material (Figure 4.5c). The composition of such local melt phases is always highly silicic. However, this phase is not abundantly found among the analyzed basement lithologies of the Araguainha impact structure.

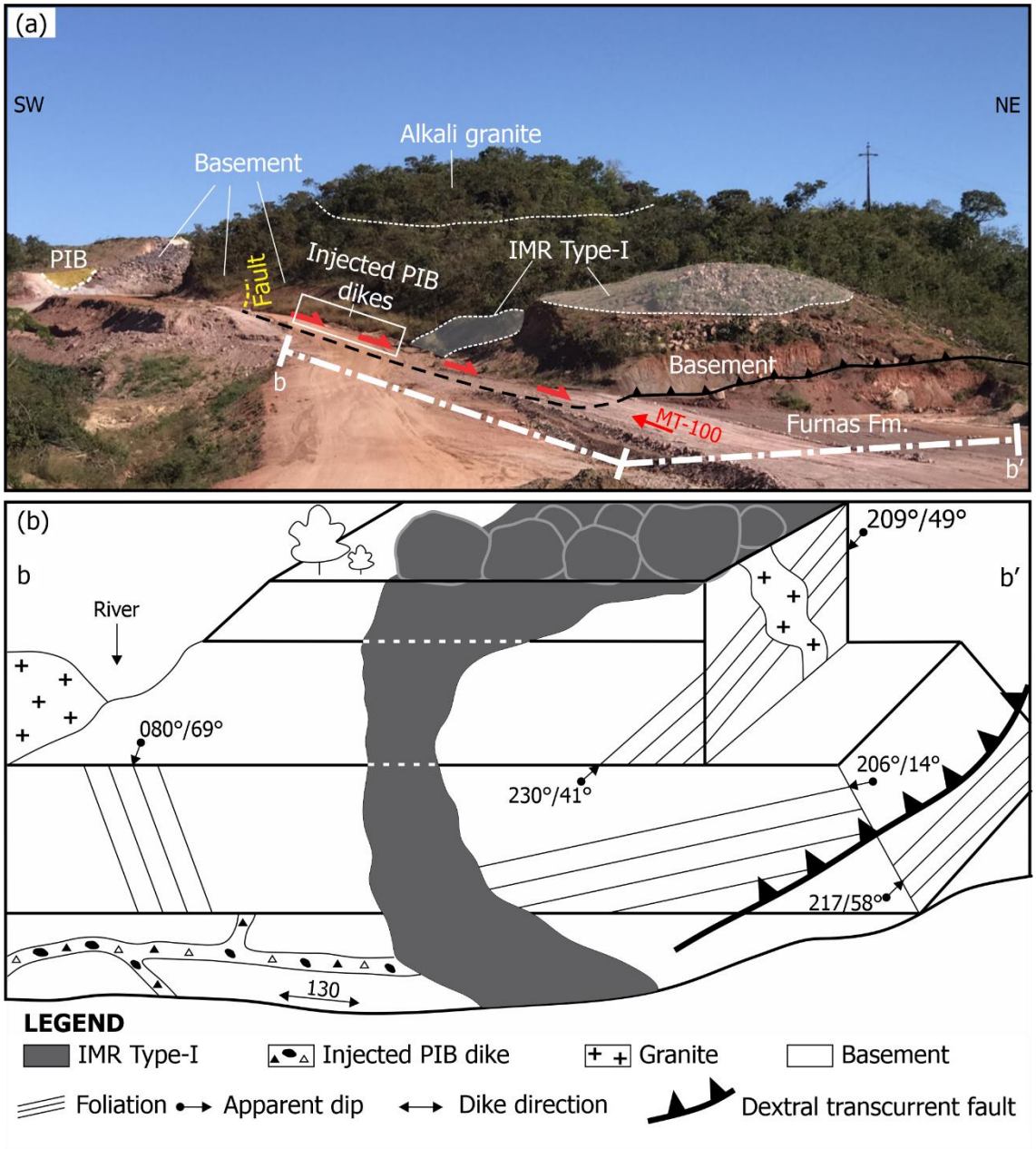

Figure 4.3 (a) Panoramic photo showing some major observations along the GAR-15 profile (at UTM 22K 288556.67 E, 8142283.08 S): impact melt rock Type-I, heterogeneous basement lithologies, units of the lower sequence of the Paraná Basin, and also some transcurrent faulting. The road section shown is 350 m long. (b) Schematic 3D representation of part of this section (240 m long), with transcurrent faulting. The apparent dip of layers is also indicated with cross-hatching.

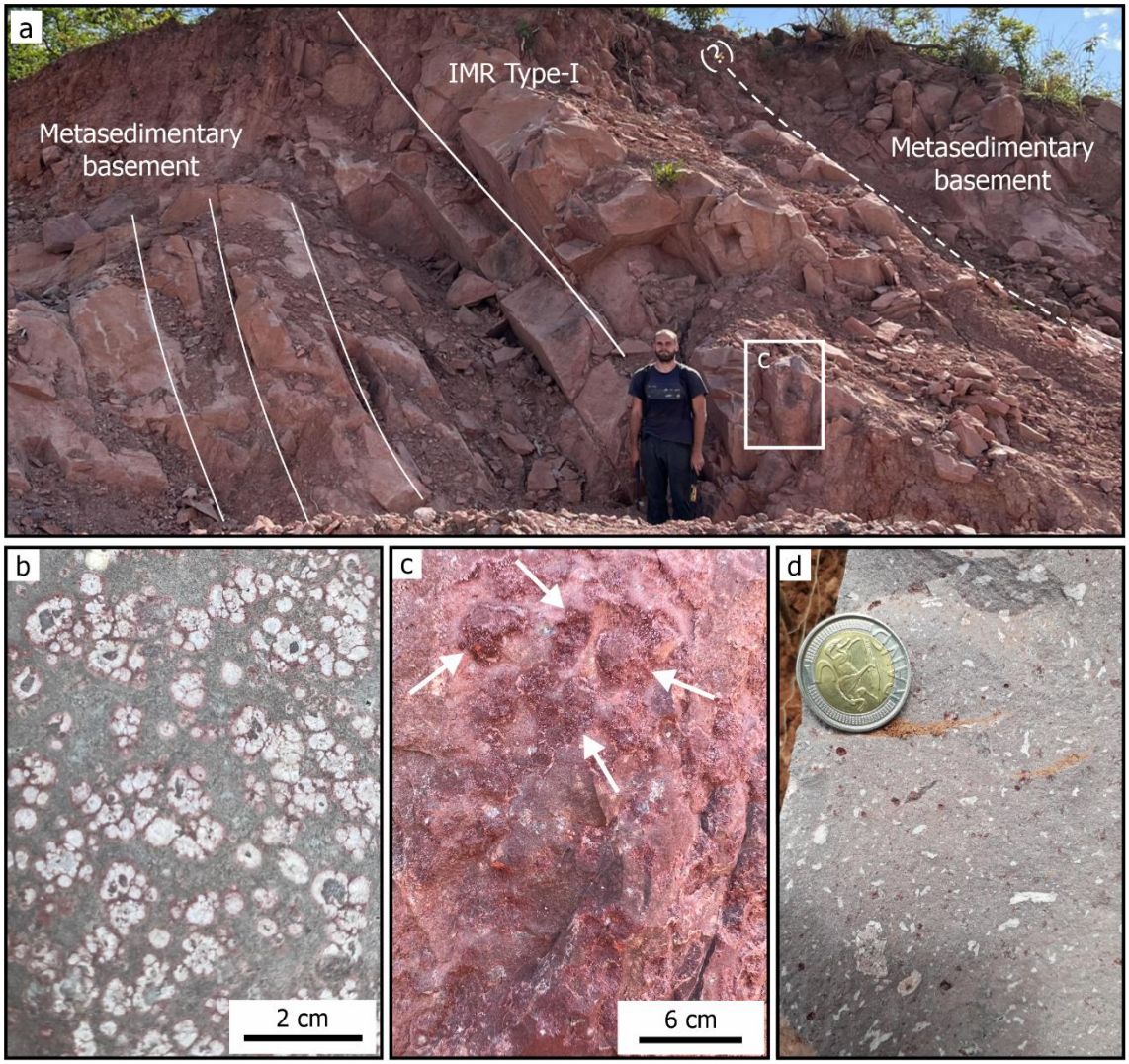

Figure 4.4 (a) Intrusion of a dike of IMR Type-I into (meta)sedimentary basement (at UTM 22K 288562 E, 8142192 S) along the GAR-15 profile. The person, shown in part for scale, is approximately 1.5 m tall in this image. The continuous lines indicate the bedding and the dashed lines represent the probable contact between the rocks. (b, c) Hand specimens of IMR Type-I with lithophysae structures (see text for detail). (d) Clasts of lithic material (granite), quartz, and partially plasticized K-feldspar in an aphanitic matrix of IMR Type-I. Coin, for scale, is 2.5 cm in diameter.

Table 4.2 Main characteristics of the three types of impact melt rock discerned in this study.

Main characteristics	**IMR Type-I**	**IMR Type-II**	**IMR Type-III**
Occurrences	Dikes, veins or pods	Clast components of polymict breccias	Blocks
Location	N, NE, S, SW	NW, N, NE, S, SW	N, NE, E, SE, S, SW
Form	Distinct dike	Stretched and strongly plastically deformed bodies	Irregular blocks in an annulus just inside of the (meta)sedimentary basement
Composition	Granitic	Sedimentary, after arenites	(Meta)sedimentary, from conglomerate and arenite
Texture	Porphyroclastic, aphanitic, spherulitic, with lithophysae	Fluidal structure, spherulitic textures in fan-like morphology	Fluidal structure, spherulitic texture, granular texture in zircon grains
Clast contents	Quartz and feldspar porphyroclasts and lithic clasts from the alkali granite	Quartz microclasts	Quartz microclasts
Contact to	Granitic core	Polymict lithic breccia	(Meta)sedimentary basement
Shock features	PFs, commonly 1 set of PDFs in quartz	PF, FF PDFs (1 set) in quartz, melt particles	PFs, FFs, PDFs (1 - > 5 sets) in quartz, FRIGN zircon
Interpretation	Decompression melt (akin to the massive Vredefort Pseudotachylitic breccias)	Shock melt – from shock compression/decompression, like shock veins in meteorites	Shock melt – formed in situ
Evidence	*Clasts from host rock (alkali granite); *Chemical composition quasi-identical to that of the host rock; *Sharp contacts to host rock without evidence for shear; *Apparent lack of a meteoritic component in the melt.	*Medium to high shock level (1 set of PDFs in quartz; granular zircon); *Glassy to microcrystalline texture; *Melt material with one composition; *Formed directly after shock compression in the (meta)sedimentary target.	*High shock level (up to 5 sets of PDFs, FRIGN zircon); *Glassy to microcrystalline texture; *Melt material of one composition akin to host rock.

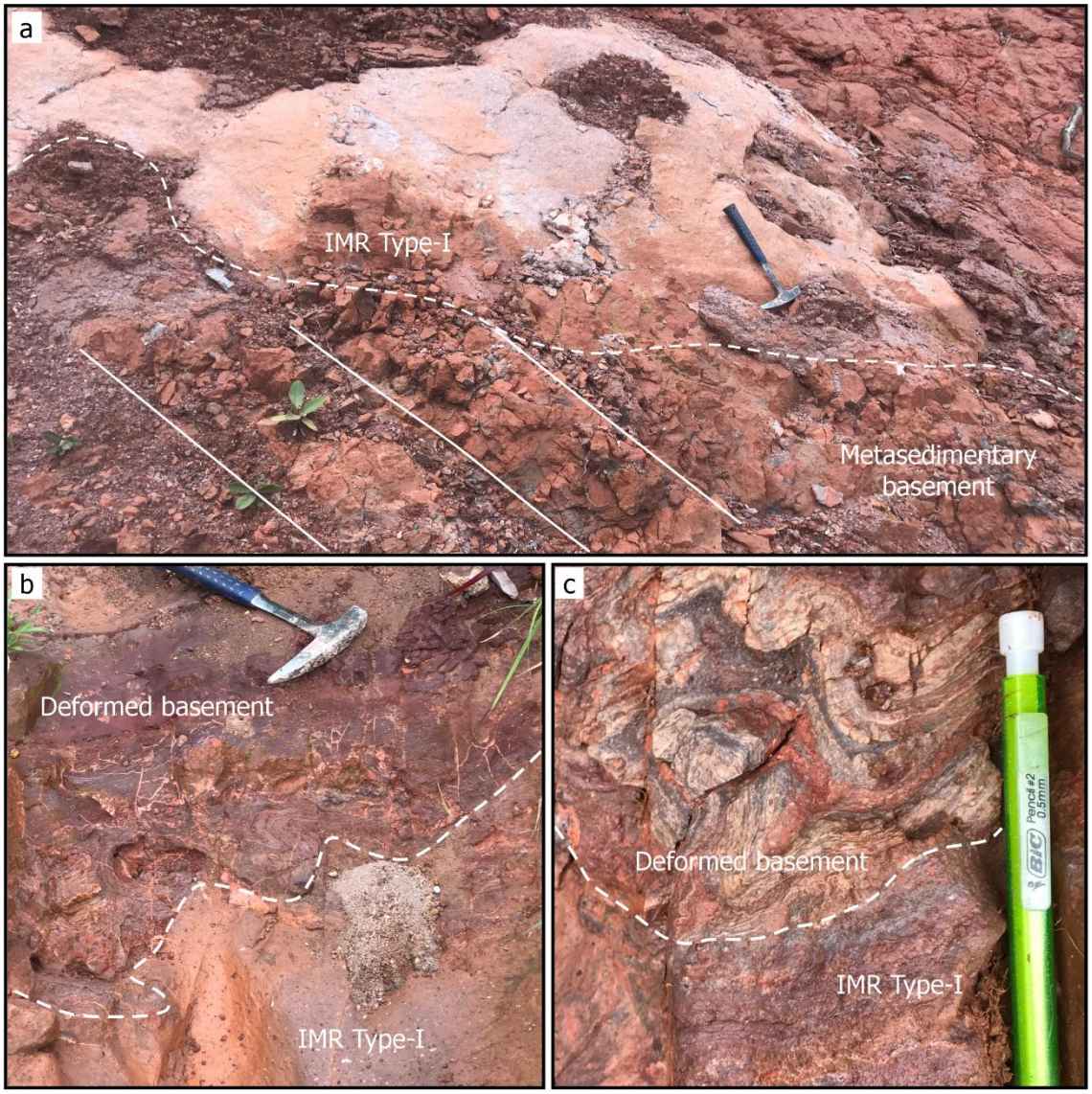

Figure 4.5 (a) An outcrop of impact melt rock Type-I adjacent to the MT-100 road, in contact with (meta)sedimentary basement, in the GAR-15 profile (at 22K 288562 E, 8142192 S), that is locally melted and annealed. The continuous lines indicate the bedding and the dashed lines the probable contact between the rocks. Hammer in a and b, for scale, is 31 cm long. (b) Part of the same outcrop, showing the contact (white dotted line) between IMR Type-I and deformed (folded) pelitic basement rock. (c) Melting and plasticization of some of the highly siliceous and folded basement rock in contact with IMR Type-I. Pencil for scale is 11 cm long. The contact is marked by the white dotted line.

Basement structure

In the mid-section of the GAR-15 profile (Figure 4.3a), a fault oriented at 275°/58° juxtaposes a 40-m wide granite block against a strongly fractured metapelite that also contains up to 20-cm wide sigmoidal lenses of metarhythmite composed of metasandstone and metapelite. The fault comprises an about 40-cm wide damage zone that contains greenish pelitic material that in some parts

is silicified. Next to the road, at the CA-73 outcrop (Table S1), occur up to 27-m long dikes of PIB injected into (meta)sedimentary basement (Figure 4.6a). The general structural trend of these dike injections is 234°/62°. In the tight curve where the MT-100 road crosses the Serra da Arnica (at the CA-06 outcrop, Table S1), a dark-brown, brittle metasandstone with subhorizontal open folds is in vertical fault contact with PIB (Figure 4.6b). The metasandstone is intruded by apophyses of granite with the same textural characteristics as described before (medium grained, not porphyritic). From here onward toward the west for some 4 km, discontinuous outcrops of PIB are observed along the road.

Description of PIB outcrops along the MT-100

The PIB is always in contact with basement rocks (phyllite or metasandstone). Four general types of contact relationships are noted: (1) PIB overlies the basement (Figure 4.6c); (2) PIB is in vertical fault contact with the basement (as at the end of the GAR-15 profile - Figure 4.6b); (3) PIB is injected as dikes into the basement, as described before (Figure 4.6a); and, less commonly, (4) PIB is overthrust along shear zones onto the metasedimentary basement, as seen along the CA-84 profile.

For ~4 km along the MT-100, and also along dirt roads branching off this state road, the PIB overlies or is in fault contact with the basement. PIB occurs here at 500 to 610 m elevation (Table 4.3). The PIB deposit (Figure 4.7a) is generally poorly to moderately sorted and matrix supported, and the groundmass is composed of fine-grained, mostly sandy to pelitic clastic material. The matrix color varies from red to light or dark grey (Figure 4.7a). The locally occurring reddish tones indicate secondary Fe staining (e.g., Figure 4.6a).

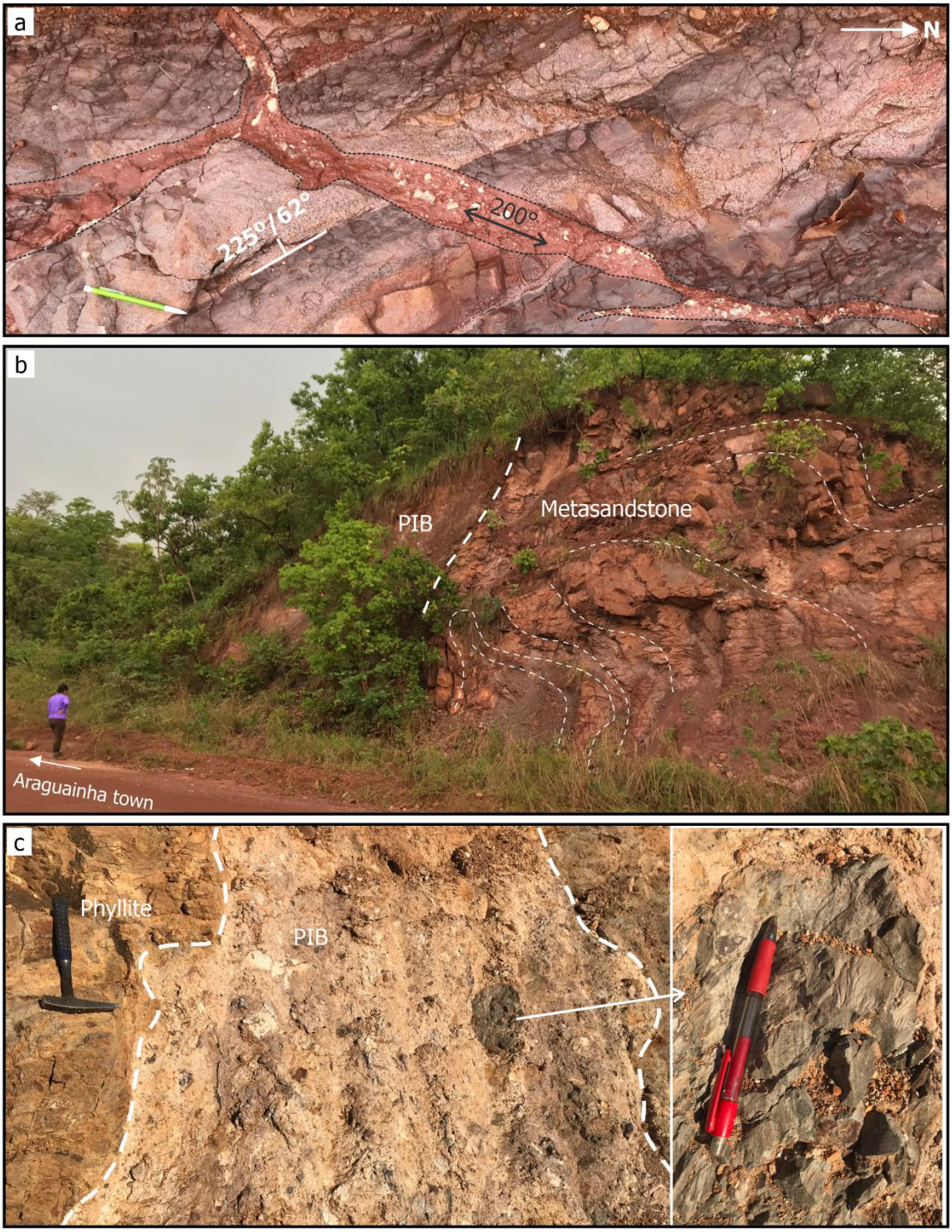

Figure 4.6 (a) Outcrop CA-73 (at 22K 288549.45 E, 8142116.97 S) where thin polymict impact breccia (PIB) dikes up to 10-cm thick are injected into (meta)sedimentary basement (this exposure in the then unpaved MT-100 road has since been tarred over). Pencil, for scale, is 12 cm long. (b) Contact relationship between a dark-brown, brittle-deformed metasandstone of the metasedimentary basement, in subvertical fault contact with PIB, at the CA-07 outcrop (at 22K 288523 E, 8141975 S). The thicker dashed line represents the contact between the rocks and the thin dashed lines indicate the open folds. (c) This image of the CA-99 outcrop (at 22K 285788 E, 8139861 S) shows PIB adjacent to a large block of metasedimentary basement, near the classic shatter cone outcrop in phyllite thought to represent Cuiabá Group material. The main image shows the contact relationship between the PIB and the phyllite, and the hammer, for scale, is 31

cm long. The inset shows shatter cones within an approximately 30 cm large phyllite clast in PIB. Pencil, for scale, is ca. 12 cm long.

The clastic components (> 1 cm) in the breccia (compare Figure 4.7a) are derived from (meta)sedimentary and sedimentary sources. They include metapelite, phyllite, and metasandstone and quartz pebbles, conglomerate, sandstone, and pelite. The metasandstone and phyllitic lithologies are predominant. Some of the relatively fine-grained clasts of metamorphosed lithologies (mostly phyllite) carry up to 10-cm-sized assemblages of shatter cones (an example is shown in the inset to Figure 4.6c). These phyllite and metasandstone clasts often show up to 1-cm long, lozenge-shaped pseudomorphs of cordierite crystals, which we relate to preimpact contact metamorphism at granite-basement contacts. Sandstone clasts are fine- to medium-grained, and many of them are rich in kaolinite. The fragments of conglomerate are mostly clast supported, composed of quartz grit and pebbles, and have a gray quartz-sand dominated matrix. They do not show any evidence of partial melting. Some quartz pebbles (<2 cm) have been observed to be multiply sheared (domino style).

Granite fragments are very scarce - at all scales - in the PIB. They occur rather frequently at the top of the CA-09 profile a few meters below the communication tower and at the beginnings of the CA-07 and CA-84 profiles (Table 4.3). None of these granitic clasts, however, show the typical appearance of the alkali granite exposed in the core of the central uplift. Rather, they have a fine-grained, equigranular, mosaic texture of K-feldspar and plagioclase (in part converted to kaolinite), and less abundant quartz, and <10 vol% biotite. These textures are similar to the textures of samples from apophyses of granite into metasedimentary basement, as observed along the state road (compare above). In the mid-section and near the base of the CA-84 profile, several up to 10-m-sized blocks of such granite are observed, with PIB deposited on top of them. These blocks seem to occur at the transition from the megablock zone to the massive basement below the crater floor.

Table 4.3 Summary of the main characteristics of the polymict impact breccia outcrops studied in the field in the northern and southern parts of the central uplift.

Outcrops		Location (UTM coord.)	Elevation (m)	Extent (m)	Nature of matrix	Main features of the Polymict Breccias
Northern sector	CA-07	288523 m E 8141975 m S	530-553	152	Up to 46 vol%. Sandy, grey to red, and fine-grained.	*Sorted:* moderately. *Rounding:* subangular to subrounded clasts *Main clast types:* brown metapelite, grey metapelite *Contact to:* phyllite and metasandstones (Figures 4.6b and 4.7a).
	CA-98	288483 m E 8141862 m S	546-558	67.8	Up to 68 vol%. Sandy, red, fine-grained.	*Sorted:* moderately. *Rounding:* subangular to subrounded. *Main clast types:* brown metapelite, red conglomeratic sandstone. No contact relationships (Figures 4.7c,d).
	CA-09	288122 m E 8141602 m S	567-610	952	Up to 38 vol%. Sandy, grey to red, fine-grained.	*Sorted:* poorly to moderately. *Rounding:* subangular. *Main clast types:* melt clast, grey conglomeratic sandstone. No contact relationships (Figure 4.7b).
	CA-116	287915 m E 8141449 m S	555-560	140	Up to 45 vol%. Sandy, grey, fine-grained.	*Sorted:* poorly. *Rounding:* subangular. *Main clast types:* melted clast, grey conglomeratic sandstone. *Contact to:* phyllite.
	CA-84	286769 m E 8141191 m S	500-575	535	Up to 65 vol%. Sandy, red, fine-grained.	*Sorted:* moderately to well. *Rounding:* subangular to subrounded. *Main clast types:* grey metapelite, red conglomeratic sandstone. *Contact to:* phyllite.
	CA-99	285788 m E 8139861 m S	512-549	480	Up to 40 vol%. Sandy, grey, fine-grained.	*Sorted:* moderately. *Rounding:* subangular to subrounded. *Main clast types:* brown metapelite, grey conglomeratic sandstone. *Contact to:* phyllite (Figure 4.6c).
Southern sector	CA-14	287403 m E 8137922 m S	517-525	96.8	Up to 30 vol%. Sandy, grey, fine-grained.	*Sorted:* poorly. *Rounding:* subangular. *Main clast types:* white sandstone, conglomerate. No contact relationships.

PIB can also be injected in the form of dikes into the (meta)sedimentary basement (e.g., at CA-73 or CA-84). At location CA-84, PIB is overthrust onto phyllite of the Cuiabá Group. The orientation of the thrust plane is 260°/60°. Injected PIB is poorly sorted, generally with a red, pelitic matrix and clast components dominated by whitish sandstone and red metapelite (e.g., Figure 4.6a). The clasts have the same characteristics as the host rocks, indicating that

they are likely of local provenance. In one of these injected breccia dikes (GAR-15 profile), a 5-cm large, black pelitic clast, rich in carbonate, was observed. The overthrust PIB is characterized by a relatively larger clast content. The phyllites locally exhibit up to 4-cm large shatter cones, as well as lozenge-shaped pseudomorphs after cordierite that are notably becoming larger close to a contact between phyllite and granite. The granite is exposed along the CA-84 profile on the southern side of the road. The rock is equigranular and has up to 3-cm large clods of tourmaline, which has never been described previously from the main alkali granite body. Also, mesoscopic K-feldspar phenocrysts, which are typical for many exposures of alkali granite in the core of the central uplift, do not occur in this road section.

The exceptional, approximately 15-m high CA-98 outcrop is characterized by an up to 1-m wide vein of greenish breccia, rich in quartz and kaolinite, that halfway up in the exposure branches into two thinner veins (Figure 4.7c). In total, the greenish vein system is some 10-m long (Figure 4.7d). Metapelite and sandstone clasts up to block size can be discerned where the breccia matrix is locally whitish. The greenish altered matrix and the whitish alteration rims around clasts suggest secondary alteration processes.

In thin section, the PIB is poorly to moderately sorted and supported by a fine-grained matrix. The matrix is composed essentially of quartz, sericite, biotite, muscovite, plagioclase, zircon, and Fe-Ti oxide minerals. The clast components at the microscale include unshocked and shocked quartz, minor unshocked plagioclase, and lithic microfragments including metasandstone, metapelite, and sandstone (see Figure S4c,d). Quartz with single sets of PFs, and rarely with a single set of PDFs, was occasionally observed in sandstone clasts. No mineral or lithic microclasts likely derived from granitic precursor could be identified. In plane-polarized light, some brownish metapelite clasts can be discerned, some of which contain spots of biotite/muscovite that might represent pseudomorphs after cordierite. The quartz microclasts are cataclastically deformed, sometimes toasted, and/or display wavy extinction. Mosaicism and, sometimes, intense recrystallization/annealing were also observed. Shock effects exhibited by some of these quartz microclasts are mainly PFs and sometimes PDFs. The PFs are well developed and often cut across entire grains. Occasionally, PFs occur in

conjunction with fine lamellae to form feather features (FFs). The PDFs mostly form single sets per host grain, but two sets of PDFs per grain have also been observed, though rather scarcely.

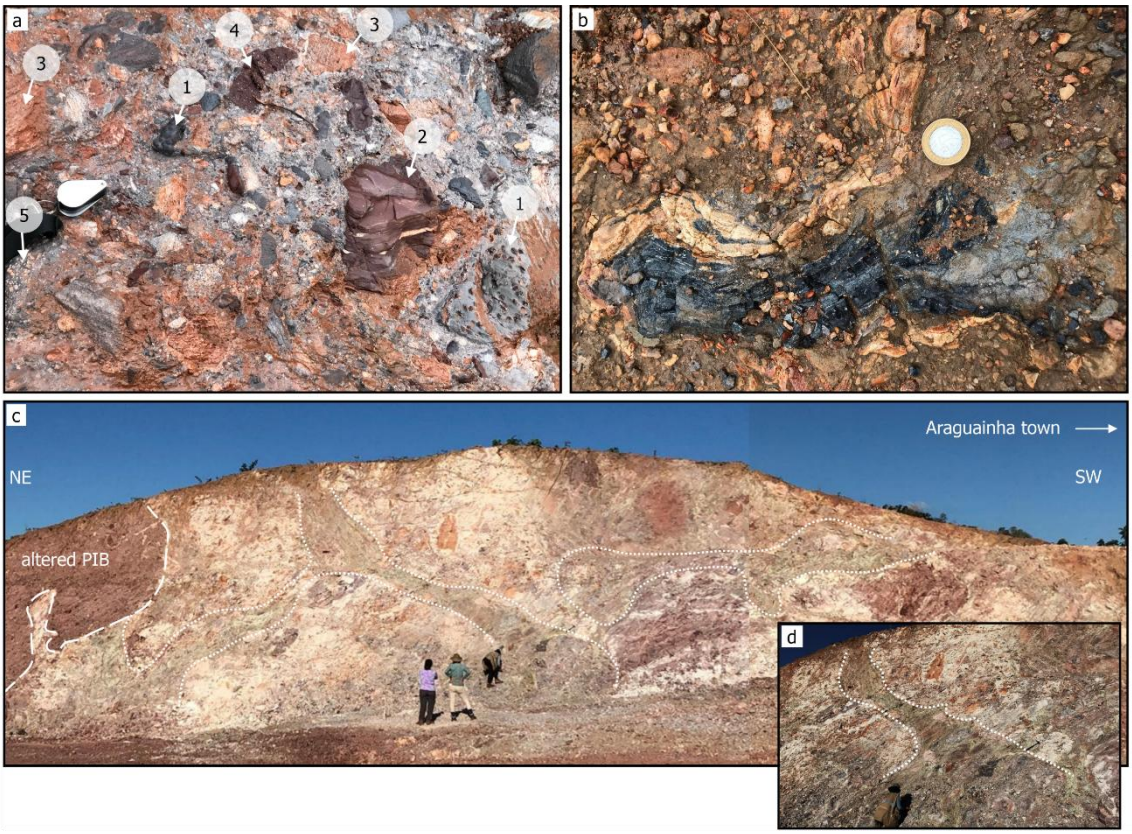

Figure 4.7 (a) Field photo of the polymict impact breccia (PIB) at the CA-07 location at 22K 288523 E, 8141975 S, showing gray matrix with some clast types identified by numbers (1, grey metapelite with or without spots; 2, brown metapelite; 3, white, fine- to medium-grained sandstone; 4, red conglomeratic sandstone; 5, conglomerate). Magnifying lens, for scale, is approximately 5 cm long. (b) Example of IMR Type-II, a silicious and partly melted clast type in CA-09 polymict impact breccia (at 22K 287445 E, 8141433 S). This IMR type is characterized by whitish/greyish and mostly highly porous melt rock. Coin, for scale, is 2.5 cm wide. (c) The impressive CA-98 PIB outcrop (at 22K 288483 E, 8141862 S; the entire exposure down to the main road level is approximately 15 m high, whereas the bench shown here has a height of approximately 8 m) with extensive development of green veining. The breccia in the vein system is mainly composed of clay minerals. One X-ray diffraction analysis (not presented here) shows that the main component is kaolinite and quartz. People, for scale, up to 1.8 m tall. (d) A photo with an enlarged part of a green vein cutting through (meta)sedimentary basement rock. Width of section shown in this inset is estimated to be 8 m.

Profile CA-99 contains the classical shatter cone outcrop of the Araguainha structure at its southwestern termination. This profile concludes the present description of the northern sector (Figure 4.2). Along this hundreds of meters long profile of mostly phyllite and metasandstone megablocks, PIB overlies this

metasedimentary basement with up to 50 m thickness (Figure 4.6c). An exemplary and already historically known shatter cone occurrence is located a few meters before the end of this exceptional roadcut exposure in a large block of strongly jointed phyllite. Shatter cones in this zone occur as up to >20 cm wide assemblages of mostly <15-cm-sized conical, striated fracture surfaces. In the course of the recent roadwork the level of the paved road was lowered by several meters in comparison to the bed of the original dirt road. Thus, many of the best shatter cones in this section are now found some 2-3 m above the level of the road. The majority of shatter cones can be observed on the northwestern side of the road.

IMR Type-II, the IMR component within the PIB

Highly siliceous (up to >90 wt% SiO_2), strongly plastically deformed clasts of impact melt, for which here the term IMR Type-II is introduced (Figure 4.7b, Table 4.2), are locally observed in the PIB. These subangular to ovoid, even roundish or entirely irregularly shaped clasts range in size from a few centimeters to over a meter. At specific locations, as at the base of the antenna hill in the CA-116 profile (between 555 and 560 m elevation, Table 4.3), the PIB is enriched in such strongly plastically deformed clasts of silicic impact melt. Petrographic analysis of this type of clasts reveals that these materials are indeed highly silicious, in part melted or annealed, and in all cases plastically deformed. This deformation may impart a strong fluidal texture on these materials. In some cases, preservation of original sedimentary lamination or stratification is observed despite extensive melting.

In the uppermost exposed part (~610 m of elevation, Table 4.3) of PIB in the Araguainha impact structure, at the end of the CA-09 profile (Figure 4.2) that also corresponds to the Tower profile of von Engelhardt et al. (1992), Type-II melt rock is abundant in the floor of the gravel road. Some tens of meters below the communication tower on the antenna hill, siliceous, melted, or partially melted, highly deformed clasts often with convoluted structures, and mostly stratified clasts of IMR Type-II of up to 4 m size can be observed. Some IMR-II bodies are strongly cohesive, though internally folded, others have locally porous schlieren or are strongly fractured by a postplasticization brittle deformation stage. The CA-

116 profile at the MT-100 at the base of the antenna hill, and nearly at the base of the CA-09 profile, represents an approximately 100-m wide exposure of PIB that exhibits the highest abundance of part-melted, highly porous, often in some parts kaolinitic clasts of this IMR Type-II, locally attaining 50 % of the exposed material.

Three main types of melt components can be distinguished at the hand specimen scale: (1) whitish/grayish and generally highly porous melt rock clasts; (2) part-melted clasts with remnant/adhering whitish/grayish sandstone that may grade into entirely unmelted, white, friable sandstone; and (3) yellowish, strongly silicified melt rock that still is remarkably dense even when a clast is severely altered. All of these materials occur in a light purplish-grayish breccia matrix, seemingly with a significant proportion of kaolinite. Sometimes, the porous sandstone facies is intercalated with banded/laminated (millimeter to a few centimeter wide), light gray or purplish pelitic material. Fluidal structure is a general feature at mesoscopic to microscopic scales (e.g., Figure S3c).

In thin sections of PIB matrix typically up to 15 vol% of clasts of this melt rock type are observed. The remnant stratification conserves the sedimentary structures of the protolith(s) to this IMR type at the microscopic scale as well. The IMR Type-II appears as elongated, angular to subrounded or even subangular microclasts, up to approximately 7 mm in size in thin sections (see Figure S3c). The clasts show aphanitic to very fine-grained groundmass textures with quench contacts towards the matrix. Sometimes the microclasts are recrystallized to finest grained micromosaics of silica. Spherulitic textures or fan/sheath-like devitrification textures of radiating quartz and feldspar microcrystals have also been observed.

4.4.2 Field relationships in the southern sector of the central uplift

The relationships between the target rocks and impact-generated rocks in the southern sector are described along three profiles (1-3, see Figure 4.2). They were chosen because they represent the best profiles to investigate the relationships between the different lithologies in this area. Even on these traverses, lithological contacts are often not well exposed in this sector but, at least, they can be inferred to be within a meter or two from the actual outcrop,

with the help of scattered rock debris. For each of these traverses, a schematic profile with simplified lithological sequences is shown in Figure 4.8.

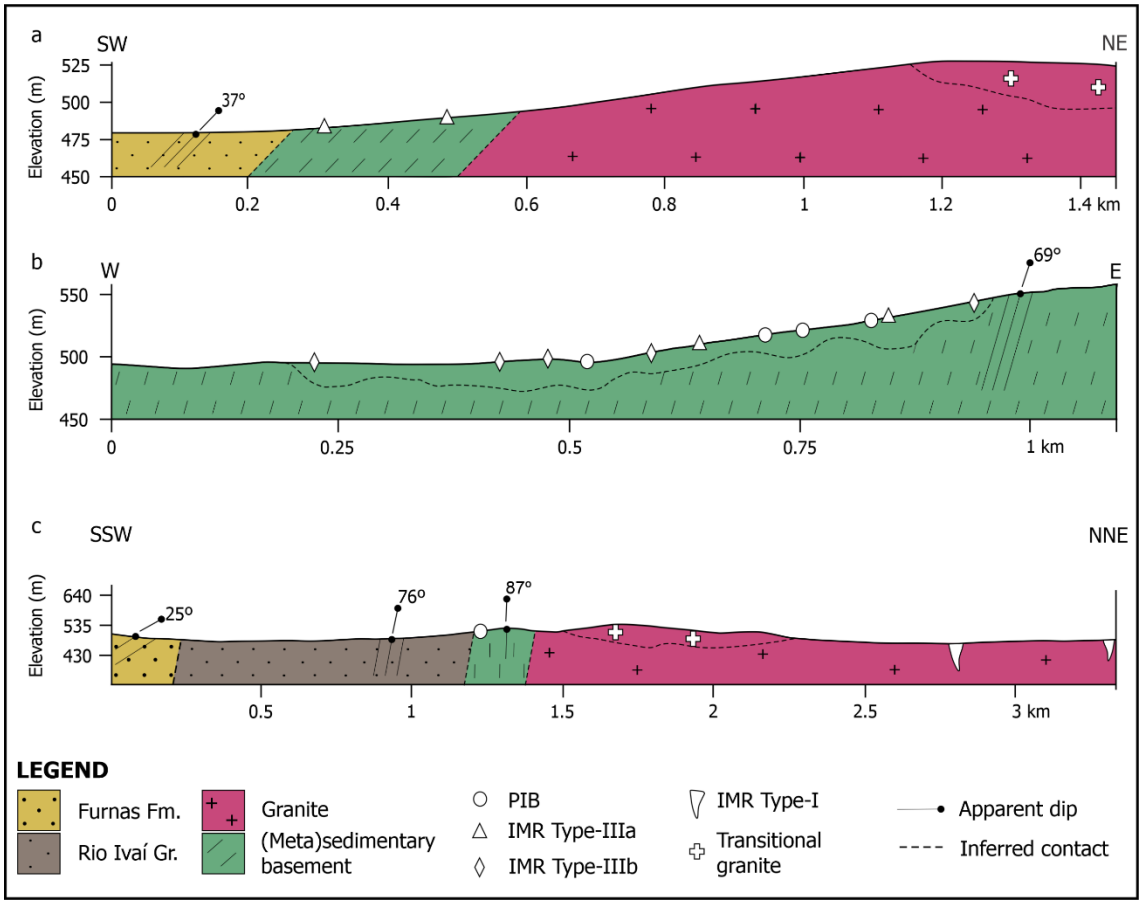

Figure 4.8 Schematic representation of the three profiles investigated in detail in the southern sector of the central uplift: (a) Profile 1, (b) Profile 2, and (c) Profile 3 (compare with Figure 4.2). These profiles have been constructed without vertical exaggeration; some local apparent dips of bedding or foliation are indicated.

Profile 1 starts at location CA-57 (Table S1 and Figure 4.8a), where a matrix-supported, greenish sedimentary breccia with subangular to angular clasts, interpreted as a diamictite, occurs over 85 m. Based on the stratigraphic setting at this site, between Furnas Formation to the south and alkali granite to the north, this sedimentary unit is assigned here to the Iapó Formation of the Rio Ivaí Group (in accordance with UnB-IG, 2012). Toward the NE, this diamictite is followed by 80 m of conglomerate that contains many polysynthetically (domino fashion) sheared quartz pebbles. Next follows a red conglomeratic sandstone that is thought to belong to the Alto Garças Formation of the Rio Ivaí Group. Some 170 m further in N/NW direction, and without any evident contact relationship,

blocks of partially melted conglomerate, here named IMR Type-IIIa, have been recorded. An example of such a location is shown in Figure 4.9a (see also Figure S4a). These blocks are clearly formed from a conglomerate precursor, which on surface is highly altered but has many well-preserved quartz pebbles, and is characterized by an overall fluidal structure (Figure 4.9b).

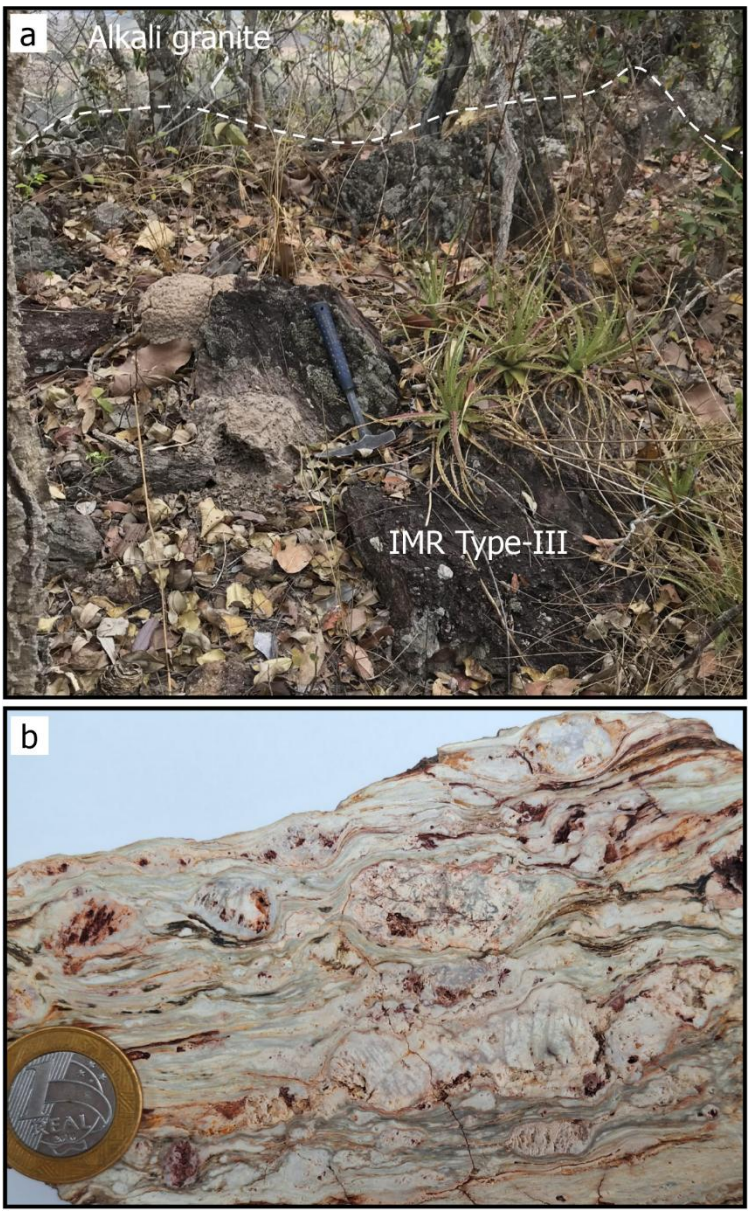

Figure 4.9 (a) Outcrop of meter-sized blocks of IMR Type-IIIa, at a site a few meters from the occurrence of alkali granite. Hammer, for scale, is 31 cm long. (b) Hand specimen of IMR Type-IIIa showing the quartz pebbles (whitish-pinkish) of the primary conglomerate surrounded by fluidal textured silicious groundmass. Coin, for scale, is 2.5 cm wide.

IMR Type-III

Like IMR Type-II, the IMR Type-III is silicious in composition (Table 4.2) and occurs stratigraphically between the alkali granite and the (meta)sedimentary basement. These outcrops are not continuous, extending for some 3-4 m only, but their positions in the eastern, southern, and southwestern sectors of the central uplift suggest that they may be part of a belt of at least partially melted basement. This melt rock phase is locally derived from either conglomerate (IMR Type-IIIa) or gritty sandstone (IMR Type-IIIb) precursors (Figure S4b). The melt phases are light to dark gray and have a well-marked fluidal structure. The IMR Type-IIIa is normally clast-supported and composed of up to 10-cm-sized quartz pebbles in a fluidal structured groundmass of thoroughly recrystallized, very fine-grained mosaic quartz. Sample AM-21b, previously described by Hauser et al. (2019), is also an example of IMR Type-IIIa. These authors interpreted this phase as possibly weathered out from decomposed PIB (see Discussion section). Their sample had been taken from a several meter wide strewn field of strongly deformed melt rock bodies formed from a sedimentary precursor in the eastern sector of the possible Type-III breccia belt. At the CA-15 outcrop (Figures 4.2 and S4c in the Supplementary Material), a 3-m wide, coherent IMR Type-IIIb occurrence has been identified in direct contact against PIB that seemingly overlies the Type-III breccia.

In thin section, IMR Type-III is characterized by aphanitic to microcrystalline silica matrix, sometimes with narrow (mm wide) bands of devitrified material. Whereas most of the material is annealed, there are some portions that are not completely transformed to masses of micromosaically textured silica. The matrix is commonly characterized by fluidal structure, which contains unannealed and locally recrystallized quartz microclasts up to 0.5 mm in size (see Figure S3e,f). Matrix wraps around these microclasts. Fine, pelitic laminations accentuate the fluidal texture. Primary, still unannealed quartz can sometimes be recognized because it shows mosaicism, wavy extinction, and toasting. The up to centimeter-sized quartz pebbles in thin section are also recrystallized. Shock metamorphism, including PFs, FFs, and, rare multiple sets of PDFs, was observed in unannealed quartz. Some levels resembling sedimentary foresets are rich in shocked zircon crystals with PFs and shock twins. Hauser et al. (2019) identified FRIGN zircon

in their sample Am-21b that indicates more than 30 GPa shock pressures (e.g., Cavosie et al., 2018).

Profile 1 continues with a 10- to 20-m long, “whale-back”-like outcrop of alkali granite with up to 5-cm large megacrysts of alkali feldspar and finishes in outcrops of transitional granite (part-melted granite) at location SF-02. In the southern part of the Santa Maria farm two exposures of relatively fresh, dark-grey IMR of Type-I occur in alkali granite (locations CA-69 and SF-01; not shown in the profile of Figure 4.8, as this location is 1.3 km further north from the northern profile termination). One of these IMR Type-I exposures is about 8-m long and of elongated pod shape, whereas the other represents a curvilinear, locally up to 0.5-m wide dike.

The transitional granite

The *transitional granite*, also known as part-melted granite, mostly crops out in hills that can reach several tens of meters above the normally low-lying, flattish granite plateaus of the central-southwestern parts of the central uplift (Figure 4.10a). There are also rare, scattered, a few meters wide outcrops of this lithology in the northeastern core (compare Figure S2). The part-melted granite phase was previously described by Machado et al. (2009) as remnants of a “melt sheet”. We prefer to use the terms “transitional granite” (after Fischer, 2015) or “part-melted granite”, as a “melt sheet” is definitely not in evidence. Such outcrops are invariably associated with primary porphyritic granite (Figure 4.10a), so that it has not been possible to evaluate volumes of this part-melted granite. These rocks are characterized by a light-gray to pink, aphanitic to microcrystalline matrix, with inclusions of feldspar minerals and quartz clasts derived from the parental granite. Sometimes quartz clasts are rimmed by biotite (Figure 4.10b). Three phases can be recognized: (1) melt phases, (2) remnants of the alkali granite, which may occur with linear contacts against the melt phase, or (3) as rounded to angular, often centimeter-sized relics encompassed by veining, or schlieren of melt (Figure 4.10b). There may be smaller relics of primary granite as constituents of the melt matrix, and there is distinct secondary crystallization of biotite within the melt matrix (compare with the descriptions of Machado et al., 2009). Locally, matrix may display linear or curvilinear flow structures.

In thin section, the transitional granite is characterized by a fine-grained matrix composed of albite, quartz, and phyllosilicate minerals (e.g., sericite, biotite; Figure S3a in the Supplementary Material). Quartz is extensively recrystallized, showing micromosaics that often display wavy extinction. Neoformed biotite around the mosaics of recrystallized quartz is common. Albite crystals are mostly some 0.2 mm in size and have euhedral shape. Schlieren of K-feldspar are nearly isotropic. Where not completely annealed, clasts in the melt phase are unshocked.

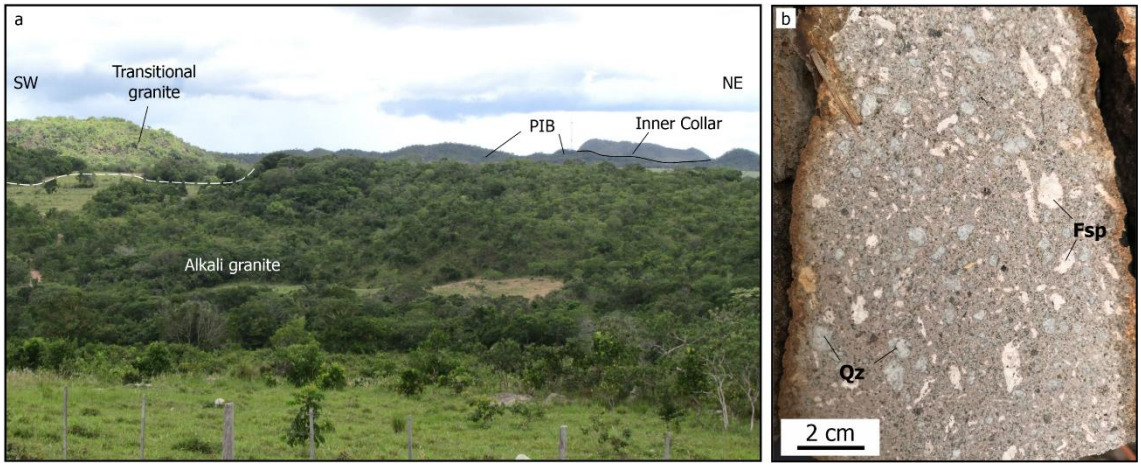

Figure 4.10 (a) Panoramic view across a section of the southern part of the central uplift showing the contact zone between alkali granite and an occurrence of transitional (part-melted) granite. The area shown is approximately 50 m wide in the foreground and the megablocks of Furnas sandstone in the background are up to hundreds of meters wide. View towards the north. (b) Hand specimen of transitional granite with schlieren of plasticized and, in part melted feldspar, as well as remnant quartz that occasionally has biotite rimming. Mineral abbreviations after Warr (2021): Fsp, feldspar; Qz, quartz.

Profile 2 represents a W-E profile that provides important information about the (meta)sedimentary basement in this southern sector (compare Figures 4.2 and 4.8b). Over the first 500 m of the profile from the west, loose blocks of impact-related rocks (IMR Type-III and PIB) without contact relationships were recorded. The IMR Type-IIIb is more prominent here than Type-IIIa, but the characteristics of the melted materials are the same: light to dark gray, with a well-marked fluidal structure. A 150-m wide occurrence of metarhythmite comprising alternating centimeter-wide layers of metasandstone and metapelite with lozenge-shaped micaceous pseudomorphs after cordierite follows further to the east toward the end of Profile 2 (Figure S4d of the Supplementary Material). This area is close to

the location where von Engelhardt et al. (1992) reported monomict impact breccia (compare in Supplementary Material Figures S1 and S2; see Discussion).

Profile 3 (SSW-NNE) starts at the base of the Morro Pelado hill (Lana et al., 2008) at location CA-10 (Table S1 and Figure 4.8c). This hill represents a prominent elevation within the megablock zone of the inner collar in the southern sector. Location CA-10 corresponds to an occurrence of whitish, kaolinitic sandstone of the Furnas Formation. This outcrop is followed in NE direction, and without clear contact relationship, by a zone rich in alluvium but with numerous sheared quartz pebbles of up to 30 cm length that are found scattered along the path over the next 550 m. These pebbles are probably derived from the conglomeratic units of the Alto Garças Formation at the base of the Rio Ivaí Group. This section is followed further east by PIB that is continuously exposed for 200 m along a winding, quite steeply upward sloping dirt road (location CA-14).

Description of PIB outcrops

The PIBs in the southern sector of the central uplift are exposed at elevations between 492 and 541 m (Table S1). PIB occurs along this winding, upward sloping dirt road over up to 100 m wide exposures, over a section of approximately 0.8 km length (Figure S2). Contact relationships with other lithologies are not readily observed due to erosion and dense vegetation along the track. The PIB deposits are generally poorly sorted, matrix-supported, with gray, fine-grained (mostly sandy), and coherent groundmass. The heterogeneous clast population gives a chaotic appearance, similar to the deposits in the northern region. However, here in the south, the components are mainly sedimentary clasts, that is, sandstone and conglomerate, with only few occurrences of clasts derived from the metamorphosed basement. No granite clasts have been observed in the PIB from this part of the central uplift, nor metapelites/metasandstone with shatter cones or lozenge-shaped pseudomorphs after cordierite crystals, which are quite common in the northern sector. Altered IMR Type-II clasts and, at the thin section scale, microclasts have been identified in groundmass but seem to be much less abundant than in such

breccia at some sites in the north (<5vol% in some thin sections from the southern PIB).

Generally, though, in thin section, the PIB from the northern and southern regions are more similar than they appear at the macro-scale. They are poorly to moderately sorted, and supported by a fine-grained matrix with similar constituents (quartz, sericite, biotite, muscovite, minor plagioclase, and accessory Fe-Ti oxides). The clast populations are also similar, though there is some variation in the respective proportions. As observed in the macro-/meso-clast population in the field, sedimentary clasts are also dominant at the thin section scale. No mineral or lithic microclasts derived from granitic precursor were identified in thin section either. The quartz microclasts have the same features as reported in the northern region (cataclastically deformed, toasted, wavy extinction, mosaicism, and sometimes intense recrystallization/annealing). Microparticles of IMR Type-II are small (approximately 1.7 mm in size) and often show aphanitic or finest grained spherulitic textures.

Shock features are identified in numerous quartz grains of PIB, with PFs being the most significant and PDFs occurring rarely and when, in one set per host grain and very rarely in two sets. The PFs are well developed and often cut across entire host grains. Occasionally, PFs occur in conjunction with fine lamellae branching off to form FFs.

Several meters after the PIB exposure on Profile 3, and without clear contact relationships, gray metasandstones from the metasedimentary basement occur until porphyritic granite crops out some tens of meters to the east of the track. The now quite narrow track passes the largest, approximately 65 x 70 m wide, outcrop of IMR Type-I (location SF-05) that we encountered in the entire central uplift structure. This IMR is on its northern side in contact with alkali granite, and to the northeast with a metasedimentary breccia zone that includes ductilely deformed metasandstone and locally IMR Type-IIIb (CA-15). In the further extension of the profile, and with intermittent granite exposures between grassy patches, one crosses into the porphyritic alkali granite, transitional granite, and again porphyritic alkali granite on the way into the interior of the central uplift (towards Santa Maria farm). Occasionally, centimeter-wide, red veins of IMR Type-I melt rock are crossed that do not exhibit a preferred orientation.

4.5 Discussion

Here, we discuss the updated geology of the central uplift of the Araguainha impact structure in terms of impact breccias and their relationship with the target rocks, as well as the genesis of these impact-related rocks. In the light of the new information obtained, we tentatively propose a simplified model for the Araguainha cratering process.

4.5.1 Updated geology of the central uplift of the Araguainha impact structure

Different maps, focused mainly on the geology of the central uplift, have been presented over time by Crósta (1982), von Engelhardt et al. (1992), Sánchez (2006), Yokoyama (2008), UnB-IG (2012), Yokoyama et al. (2012), and Crósta et al. (2019). Also, various nomenclatures have been applied to the lithologies identified in the central uplift region of the Araguainha impact structure (see Table 4.1), especially concerning the impact breccias.

Knowledge of the stratigraphy of the area, particularly with respect to the basement and the lower part of the Paraná Basin sequence, has been improved over time, and the main changes observed on our new map (Figure 4.2) are related to this. An important improvement on our geological map is the recognition of the regional importance of the (meta)sedimentary basement of the Paraguay Belt. Probably, the previous lack of outcrops contributed to the misunderstanding of the real stratigraphy in the central part of the structure. Indeed, outcrop CA-99 (Figure 4.6c), which has been widely known as the classical “shatter cone locality” at Araguainha, occurs in phyllites from the metasedimentary basement, but it had previously been described as part of the Furnas Formation by Crósta et al. (1981) and von Engelhardt et al. (1992).

We believe that there are at least two sequences of basement strata in the Araguainha impact structure: the typically metamorphosed rocks of the Cuiabá Group and, additionally, an unmetamorphosed sedimentary sequence of sandstones and pelites. It is still difficult to associate these unmetamorphosed basement rocks with a specific stratigraphic unit, as they could either represent the youngest (uppermost) part of the Paraguay Belt succession or the lowermost

strata of the Paraná Basin sequence, such as the Rio Ivaí Group. The ongoing analysis of this basement must include U-Pb isotope analysis on detrital zircon, geochemistry, and whole-rock Sm-Nd isotope analysis on representative samples from the newly exposed outcrops.

In the northern sector of the central uplift, the basement is exposed at elevations between 450 and 560 m. Here, the overlying remnant PIB has an integrated thickness of 110 m (between 500 and 610 m elevation) and exhibits the four types of contacts described earlier. In the southern region, the basement occurs between 506 and 558 m. In this area, the PIB exposure is more restricted; the maximum thickness is only 49 m (between 492 and 541 m elevation). A direct contact against the basement could not be observed. Due to the size and continuity of outcrops, and based on the scale of our work, only the PIB in the north can be represented as a nearly continuous body in the updated map (Figure 4.2). Several processes related to the impact and/or postimpact events, such as oblique impact from the south/southeast or postimpact tectonic activity or differential erosion (Lana et al., 2007), could have controlled the better exposure of basement and PIB in the northern than in the southern sector.

A large exposure of the metamorphic basement (plus IMR Type-IIIa) in the south was in part previously categorized as monomict breccia – essentially an impact-generated cataclasite (e.g., Stöffler and Grieve, 2007) – by von Engelhardt et al. (1992). These authors concluded that this monomict breccia was derived from a “quartz sandstone, and represented completely fused sandstone, poorly sorted, with angular quartz grains showing fluidal textures, curved schlieren, recrystallized to a mosaic of interlocking quartz grains with boundaries crossing the schlieren texture” (ibid, p. 453). Later, Yokoyama (2008) assigned this package to the Cuiabá Group of the Paraguay Belt. This author did not observe any macroscopic evidence of impact in this area, such as shatter cones.

Some samples from the “monomict breccia” area of von Engelhardt et al. (1992) were reanalyzed by us (the locations of their samples are also indicated in Figure S2 and Table S1 – both in the Supplementary Material). Indeed, there are cataclasites after quartzite that contain angular quartzitic fragments, but there are also metapelites with sericite and biotite and pseudomorphs after cordierite,

as well as several occurrences of IMR of our newly defined Type-IIIa or b. For that reason, we disagree with Yokoyama (2008) and von Engelhardt et al. (1992), as we observe far less occurrences of impact-related rock in the southern region than previously thought. Thus, the southeast area demarcated as monomict breccia by von Engelhardt et al. (1992) is now referred in the new geological map as (meta)-sedimentary basement (Figure 4.2, see also Yokoyama, 2008). The difference between Yokoyama's findings and ours is that we increased the local occurrence of IMR Type-III, mainly the partially melted conglomerate (IMR Type-IIIa), mostly found as patches in otherwise unaltered (meta)sedimentary basement. In thin sections, the Type-IIIa materials are characterized by different levels of shock metamorphism. Occasionally, a single set of PDFs has been observed. Much of the material is completely annealed. It varies from a totally melted conglomerate, where the matrix is fluidal, aphanitic with layers or spherulites, and pebbles that are also melted to partially melted conglomerate, where the matrix is also partially melted and the pebbles are sheared and partially dislocated. In the first case, toasted and granular zircon grains are observed concentrated in specific laminae of the fluidal texture in thin sections (Figure S3f).

Another important improvement on our geological map involves the differentiation of IMRs (Table 4.2). The annular string of occurrences of IMRs from conglomerates/sandstones, named IMR Type-IIIa and b, allows us to propose a belt of this type along the transition from alkali granite into (meta)-sedimentary basement. Further detailed field study is, however, needed to better understand this IMR Type-III and its possibly systematic occurrence. Additionally, the annealed granite, referred to as the transitional granite or part-melted granite, and annealed basement are now identified and distinguished.

Regarding the sedimentary units of the Paraná Basin, the distribution of the Furnas and Ponta Grossa formations remains consistent with previous maps. However, the Rio Ivaí Group is now restricted to the southern region (Figure 4.2). Previously, the unpublished map by UnB-IG (2012) mentioned this unit in both the northern and the southern sectors as a large belt along the outer margins of the PIB occurrences. During our field trips, we recognized a spatially limited occurrence of Rio Ivaí Group sedimentary rocks in the south, involving diamictite,

sandstone, and conglomerate. Contrary to UnB-IG (2012), we did not observe any conglomerate related to this unit in the northern part.

After the update of the geological map, we reanalyzed the two geological cross sections of von Engelhardt et al. (1992; shown in the Supplementary Material as Figure S5a,b). The cross sections of Figure S5c,d show the actual situation in terms of lithologies and contacts according to our findings. Von Engelhardt et al. (1992), as well as Machado et al. (2009), inferred a nearly continuous sheet of IMR of granitic composition, which they considered remnants of a melt sheet that was now partially eroded. While von Engelhardt et al. (1992) called these melt rock occurrences “impact breccias with melt matrix”, Machado et al. (2009) not only called them “melt sheet” but also distinguished these materials from “melt veins”. Our profiles show a more realistic situation in the sense that the areas of “melt sheet” are comparatively small portions of dikes within the granitic basement. In the cross section of Figure S5d that represents the updated version of von Engelhardt et al.’s cross section b, it is possible to observe that the impact breccia with melt matrix does represent transitional granite. Finally, our profiles show that PIB is always in contact with (meta)sedimentary basement and never with alkali granite as proposed in earlier works (e.g., von Engelhardt et al, 1992; Machado et al., 2009; Yokoyama et al., 2012; Crósta et al., 2019).

Lana et al. (2008) studied a SW-NE section along the collar-crystalline core contact, in the megablock zone of the collar. This section corresponds to our GAR-15 profile (Figure 4.3). These authors observed a repetition of sandstones and conglomerates from the Furnas Formation through NE-dipping reverse faults. Beyond that, siltstone assigned by these authors to the same Furnas Formation are in contact with the crystalline basement. Some veins of pegmatite intruded siltstones. An impact breccia layer (our IMR Type-I) covered the local contact between the crystalline basement and the supracrustal sequence.

Our profile GAR-15 illustrates the relationships between the basal target rocks – possibly some Furnas Formation, but mainly (meta)sedimentary basement, IMRs, annealed basement, and PIB. We found that the supracrustal strata are overthrust by basement (Figure 4.3b), the granite occurs in the form of apophyses reaching into (meta)sedimentary basement, red PIB crops out as a

dike into (meta)sedimentary basement (Figure 4.6a), and the largest outcrop of IMR Type-I along this profile causes local annealing at the contact with the basement (Figure 4.5). Having said that, the megablock zone is complex both structurally, as demonstrated by Lana et al. (2008), and stratigraphically, as presented in the present study (GAR-15 profile).

Two main improvements in our updated geological map (Figure 4.2) are related to the understanding of the basement. They include: (1) the identification of a belt of (meta)sedimentary basement around the granitic core, which involves phyllite, metasiltstone, metasandstone, metarhythmite, metaconglomerate, sandstone, and pelite; and (2) a direct contact between the PIB and the (meta)-sedimentary basement.

4.5.2 New insights about the impact breccias

Impact melt rock derived from alkali granite (IMR Type-I) and the transitional granite

IMR Type-I was classified previously as a breccia rich in vitreous material (Crósta et al., 1981) or impact breccia with melt matrix (von Engelhardt et al., 1992), or as melt vein and melt sheet characterized by aphanitic matrix with angular to rounded granite clasts (Machado et al., 2009). It has been debated but not resolved yet whether IMR Type-I could represent material intruded from a melt sheet into the granite (von Engelhardt et al., 1992; Machado et al., 2009), or whether it represents a product of local melt formation, that is, a pseudotachylitic breccia (for background on such breccias, see e.g., Reimold, 1998; Reimold et al., 2016, and as discussed in the Araguainha context by Machado et al., 2009, and also mentioned by Preuss, 2012).

According to von Engelhardt et al. (1992) and Machado et al. (2009), the maximum depth of crater excavation and melting in the Araguainha impact cratering event was ~ 2400 m. Thus, the chemical composition of the impact-generated melt sheet should represent a mixture of supracrustal and basement lithologies, including the alkali granite. However, this has not been demonstrated to date, because the chemical composition of IMR Type-I (e.g., von Engelhardt et al., 1992; Machado et al., 2009; Preuss, 2012; Fischer, 2015) is essentially

identical to that of the alkali granite. In addition, clasts derived from (meta)-sedimentary target lithologies are also essentially absent from IMR Type-I. Already von Engelhardt et al. (1992) emphasized the excellent fit between the compositions of their red and gray varieties of IMR, on the one hand, and the alkali granite, on the other. Further chemical and isotopic analysis are clearly required. The published data and our own unpublished chemical and isotopic (Sr-Nd) database do not support that the IMR Type-I, all of which is concentrated within and in the immediate proximity to the alkali granite complex, represent remnants of a coherent melt sheet of mixed (meta)sedimentary/granite composition.

The scarce presence of granite-derived clasts against the abundance of metasedimentary clasts in the Araguainha PIB indicates that the projectile excavated the nearly 2-km-thick sequence of Paraná sedimentary strata and even some (meta)sedimentary basement. This could indicate that IMR Type-I was not part of the high shock zone of impact melting of the growing transient cavity, but likely formed during the uplift of the central uplift.

The fact that these melt veins, dikes, and pods of IMR Type-I do not contain any evidence of high-pressure mineral polymorphs or other indications of exceptionally strong shock deformation (in comparison to the surrounding host rock) seemingly excludes the possibility that this material was formed during the initial shock compression/decompression phase of cratering (e.g., Spray and Biren, 2021 and references therein; Reimold et al., 2016, 2017). This would then favor the genesis of this material by rapid decompression and/or friction-related processes during central uplift formation and collapse. A problem that complicates genetic studies on these breccia veins and pods at Araguainha is the fact that only one type of host rock, the alkali granite, has ever been observed. This has effectively precluded investigations of kinematic indicators associated with such occurrences (material movement across lithological boundaries), as well as possible chemical mixing along veins across such boundaries. What is more, no such melt rock occurrence associated with a fault or shear deformation has to date been reported from such vein occurrences in the Araguainha alkali granite. Further field work is required to ascertain whether these veins were formed or emplaced under compressional or extensional conditions.

Anyway, a strong frictional strain component does not seem to have been involved in the formation of this phase. IMR Type-I resembles in many aspects the pseudotachylitic breccias of the Vredefort Dome in South Africa (e.g., Dressler and Reimold, 2004; Reimold and Gibson, 2006; Reimold et al., 2016, 2017). A pseudotachylitic breccia is defined as a clast-bearing melt vein or pod that occurs as cm- to km-sized bodies in crystalline target rocks of complex impact structures (e.g., Dressler and Reimold, 2004; Reimold et al., 2016). Characteristics of IMR Type-I like (1) a widespread occurrence in the eroded core of the central uplift; (2) clasts that are essentially derived from the host rock (alkali granite); (3) a composition that is quasi-identical to that of the host rock (Machado et al., 2009); (4) abundant sharp contacts to host rock without evidence for shear; and (5) apparent lack of a meteoritic component in the melt (unpublished data from N. Hauser) (Table 4.2) all constitute evidence in favor of this type of melt rock representing a pseudotachylitic breccia.

Besides the IMR Type-I, there is a second lithology of alkali granite composition – the so-called part-melted or transitional granite (Fischer, 2015). Yokoyama (2008) described this phase as “a rock with a lot of relict material” (ibid, p. 35). Fischer (2015) applied the transitional granite term to note rocks with some characteristics of the protolith, but that were, at the same time, melted in part. The obvious difference between this phase and IMR Type-I is the texture of the melt matrix. The transitional granite is characterized by quartz clasts with granoclastic texture surrounded by neoformed biotite crystals (Machado et al., 2009; Fischer, 2015; this work), which is embedded in a highly recrystallized melt matrix of quartz, feldspar, and biotite. In contrast, IMR Type-I textures vary from aphanitic to microporphyritic, and even spherulitic.

As we discussed before, the expected composition of a large impact melt volume at Araguainha – either in the form of a melt complex or large melt bodies in PIB – should have been that of a mixture of much (meta)-sedimentary material with alkali granite (if this lithology was included in the melt zone). The occurrences of the transitional granite do not account for a large volume of impact-generated melt, if we compare with the overall volume of IMR in the structure. The transitional granite crops out mainly in the hills of the SW sector of the central uplift (see map of Figure 4.2) and as Fischer (2015) and Machado et al. (2009)

demonstrated, the compositions of such occurrences are always very similar to the average composition of the alkali granite (e.g., von Engelhardt et al., 1992; Machado et al., 2009; Silva et al., 2016). These observations do not favor the possibility that part-melted granite could be a manifestation of material from a melt sheet. As this rock appears strongly annealed, originally present shock features have been obliterated.

Considering the overall lack of detailed mapping data regarding the setting and spatial distribution of this transitional granite phase, our understanding of the process that formed this transitional granite is still rather vague. One possibility is that the formation of this phase could be related to local decompression melting upon uplift of the central part of the impact structure, as it has also been proposed for the generation of IMR Type-I.

Impact melt rock types formed from (meta)sedimentary lithologies (Types-II and -III)

Two types of IMR derived from (meta)sedimentary target rocks are now recognized at Araguainha: (1) IMR Type-II, which represents partially or totally melted allochthonous fragments of (meta)sedimentary rock/melt in the PIB, and (2) IMR Type-III, partially or totally melted, possibly representing (par)autochthonous blocks of conglomerate or, less frequently, sandstone of the (meta)sedimentary basement or lowermost part of the Paraná basin sequence. Type-III always occurs near the contact of the basement and the granitic core of the central uplift.

IMR Type-II mainly represents fragments of (meta)-sandstones from the basement and sandstones from the lowermost part of the Paraná basin that have undergone partial or total melting and extensive plastic deformation. Von Engelhardt et al. (1992), based on textural evidence of rapid cooling (e.g., spherulitic textures), absence of fluidal arrangement of crystallites, and the presence of shocked quartz grains, also interpreted these bodies as IMR. A few examples show a typical “bomb shape” at the macroscale, which allowed some authors (von Engelhardt et al., 1992) to interpret them as ballistic ejecta of shocked sedimentary target rock. Under the microscope, this melt rock type normally shows microscopic particles of melt (generally smaller than 0.55 mm) of

aphanitic or devitrified texture, as well as spherulites that indicate high-T devitrification of silicic melt phases (e.g., Lofgren, 1971). It is highly doubtful that aerodynamically shaped ejecta would occur within this remnant of lowermost impact breccia crater fill, nearly at the contact with basement. With the new outcrops available in the northern sector of the Araguainha central uplift, we now know that the PIB accessible there represents the lowermost part of the crater fill just above the basement of the crater floor. This means that the clasts in PIB of the IMR Type-II represent material that probably never left the lower crater interior. The potential stratigraphic units that could have acted as protoliths for IMR Type-II probably are the same units that provide the main clast population of the accessible PIB – the lower units of the Paraná Basin sequence and/or the (meta)sedimentary basement. The largest, up to 4-m long, clasts of IMR Type-II were found at the top of profile CA-09, as described in the Results section. In the CA-116 profile, most melt clasts are reasonably fresh, and some of them contain unmelted layers of phyllosilicate minerals (e.g., kaolinite). Kaolinite is an important mineral of the arenitic Furnas Formation. Therefore, we tentatively regard this melt type as likely derived from Furnas Formation sandstone. Considering the stratigraphic information from borehole AG-1-MT (Cordani et al., 2009) only 30 km SW of the Araguainha Dome, this would indicate that the zone of impact melting would have extended to a depth of 1.9 km.

During the modification stage of impact cratering, the transient cavity collapses. A mixed crater fill is created, which includes turbulent movement of basement blocks. This results in the emplacement of complex mixtures of breccia, impact melt, and target rock blocks at the crater floor level (see also Melosh and Ivanov, 1999). This movement could also generate local friction melting and cataclastic brecciation on blocks. We did not find melts at the interfaces of displaced megablocks of target rocks and, thus, exclude friction melting as a likely process to generate IMR Type-II. The melts identified until now occur in a specific setting and with a distinct, silicic composition. The rounded shapes of some of these melt bodies could be the result of mechanical abrasion during the turbulent movement of the crater fill. In the absence of any evidence for ballistic emplacement of melt clasts into the currently exposed PIB at

Araguainha, we favor an interpretation that IMR Type-II represents hot (meta)sedimentary material generated by shock melting (Table 2).

At this point no high-pressure polymorphs have been found in the IMR Type-II. Nevertheless, zircon separated from a sample of this type in PIB matrix (e.g., sample P-03 from the CA-84), yielded some granular zircon, related with high shock pressure and temperature. Such melts could then have been mixed into the lowermost breccia fill (i.e., PIB) of the crater structure, through turbulent mixing with variably shocked and unshocked materials.

IMR Type-III occurs in the transition from the alkali granite into the surrounding (meta)sedimentary basement. IMR Type-III is silicic in composition, and the presence of multiple sets of PDFs (up to five in some quartz grains) and FRIGN zircon (Hauser et al., 2019) indicate relatively high shock pressure, at least in excess of 30 GPa. This seemingly excludes friction melting as a process of generation of this melt rock type. These melts seem to occur in situ, within their stratigraphic layering. Type-III was not described previously by other authors. Different from Type-II, melt rocks of Type-III predominantly originate from conglomeratic rocks (Type-IIIa), with minor amounts that were generated from sandstone (Type-IIIb). Hippertt et al. (2014) identified IMRs with similar characteristics on top of the Furnas Formation in the northeastern inner collar, not far from the location of the IMR Type-III site that yielded sample Am-21b studied by Hauser et al. (2019). Hippertt et al. (2014) described rare patches of black to varicolored fluidal and strongly silicic, fine-grained, polycrystalline IMR rich in schlieren and granular zircon. They associated this melt rock with the Furnas Formation, but they did not discuss the genesis of this melt.

Tong et al. (2010), using ERT, found that the granite, sedimentary strata, and IMRs occurring in the PIB (our IMR Type-II) have contrasting resistivity: the granite has low resistivity (~150-250 Ω m), which they linked to fracturing, whereas the sedimentary strata have resistivity >400 Ω m, and the IMRs in the PIB have still higher resistivity, due to their lower porosity when compared with the matrix of the polymict breccias. They measured five profiles to characterize the subsurface geometry of the Araguainha central uplift. It is important to highlight that these authors did not differentiate the (meta)-sedimentary basement from the Paraná Basin sedimentary strata.

The tomographic results show that the boundary between the granite and the (meta)sedimentary basement could be a well-defined structural interface that is characterized by blocks of high resistivity. They found that at the granite-basement contact (in their profile A1 that is equivalent to our Profile 3 in the southern part of the central uplift), a block of high resistivity occurred that had similar resistivity to the impact melts of silicic composition. Possibly, the blocks of high resistivity of Tong et al. (2010) could represent our IMR Type-III, located between the granite and the (meta)sedimentary basement. Further detailed ERT studies should be undertaken in the northern sector of the central uplift, as well, to better understand this transition zone between alkali granite and surrounding basement.

At this point, it is difficult to go deeper into a discussion of processes that could have been involved with the production of IMR Type-III. Our currently best hypothesis is that it could have been generated by shock melting. This hypothesis is supported by the presence of quartz with up to five sets of PDFs per host grain and FRIGN zircon that indicate a high level of shock metamorphism; the uniform composition of the melt material; and the occurrence of IMR Type-III as injected material within the crater floor (Table 4.2).

The polymict impact breccias

At the current exposure level, a 110-m integrated section of within-crater impact breccia is exposed – not in a single profile but as an integrated sequence based on observations from multiple traverses – in the northern sector of the central uplift at Araguainha. The exposed PIBs are intercalated with megablocks of up to hundreds of meters size, as well as smaller blocks of decameter size, of the collapsed crater floor and uppermost (meta)sedimentary basement.

The nature of clasts, mainly derived from the (meta)sedimentary basement as well as from the lower units of the Paraná Basin (likely mostly from the Furnas Formation and Rio Ivaí Group) and hardly any material sourced from granite, must be taken into account when the maximum level of excavation is discussed. Another important point is that the only IMRs found in the PIB, the IMR Type-II of this study, are derived from (meta)-sedimentary and sedimentary precursors. This demonstrates that the excavated and impact melting zone did not extend

beyond the uppermost basement. In this scenario, it appears impossible that a melt sheet could have had the composition of the alkali granite, and consequently, that any Type-I melt material could be derived from a melt sheet.

No occurrences of impact breccias at Araguainha have to date been described from outside of the central uplift. This suggests that the original impact breccia fill of the ring syncline has been completely eroded away. Lana et al. (2007) suggested a relatively shallow level of erosion (250-350 m) for Araguainha, which would explain the presence of remnant impact breccia and the good state of preservation of the stratigraphy and crater morphology. The new and extensive roadcuts along the MT-100 in the areas of the ring syncline do not show a single vein of polymict breccia injected into the exposed strata of the midsection of the Paraná Basin stratigraphy (Ponta Grossa and Aquidauana formations).

Considering the intercalation of PIB with blocks/megablocks of the crater floor and uppermost basement, and the predominance of a related clast population in the PIB, it must be concluded that the current PIB interval represents only material that never left the impact crater. These breccias represent the lowermost part of the breccia fill of the Araguainha impact structure. This is in agreement with the interpretation of Tong et al. (2010), who proposed that the gently inclined orientation of blocks of high resistivity and zones of low resistivity toward the granite reflect the topography of the crater floor. It means that the present architecture of the central uplift reflects the final stage of collapse of the structural uplift. According to von Engelhardt et al. (1992), the exposed PIB exhibits the comminuted material that was mixed and mobilized during the growth of the transient crater. There is, however, no evidence that would support any incorporation of material from the upper target sequence, the mid- to upper sequence of the Paraná Basin stratigraphy (like Aquidauana Formation and Passa Dois Group). Certainly, fallback breccia material is not part of the remaining PIB. If this is correct, any search for a projectile-derived meteoritic component in this PIB would likely be futile.

4.5.3 Cratering processes in sedimentary targets: the Araguainha case

Numerical modeling of the formation of large impact structures (e.g., Pierazzo and Melosh, 1999, 2000; Collins et al., 2012) has demonstrated that the projectile can enter the target to a depth of about half of its diameter and then become engulfed by shock waves that subsequently travel into the wider target realm and finally become decelerated. Recent results from hydrocode modeling (Miyazaki et al., 2021) applied to the Araguainha central uplift employed a 2 to 3 km diameter spherical impactor of granitic composition with an assumed impact velocity of 12 km/s^{-1} (it was not clarified by those authors how this velocity was constrained).

Considering that the formation of an approximately 40 km diameter impact structure, such as at Araguainha (Brazil) or other impact structures around the world (Chesapeake Bay and Manson [United States]; Montagnais, Lake Saint Martin, West Clearwater Lake, and Carswell [Canada]; Mjølnir [Norway]; Rochechouart [France]; or Saqqar [Saudi Arabia]; see Schmieder and Kring, 2020), likely required a 2- to 3-km diameter projectile (e.g., von Engelhardt et al., 1992; Lana et al., 2006; Miyazaki et al., 2021), it may be possible that the projectile would have entered to a depth of about 1-1.5 km. Miyazaki et al. (2021) proposed that this projectile penetrated through the entire supracrustal target sequence (nearly 2000 m) and reached the granitic basement, allowing the uplift of the entire target stratigraphy by some 2 km after some 280 s after initial contact.

Von Engelhardt et al. (1992) and Machado et al. (2009) alleged that the sedimentary target rock sequence should have been involved in the production of a coherent impact melt sheet, as well as the alkali granite. Von Engelhardt et al. (1992) identified two types of IMR, the fused granite as well as the fused quartz sandstones that they linked to the Furnas Formation. They explained that these two types of melts probably did not mix because of their difference in viscosity. In contrast, Machado et al. (2009) explained that the “melt sheet” of the Araguainha impact structure (based on their petrographic description equivalent to our transitional granite), was formed in isolation from the sediment-derived impact melts, most likely due to deeper penetration of the projectile into the target rocks or because the melt was formed below the main zone of impact melting. We must take into account that previous authors (e.g., Crósta et al., 1981; von Engelhardt

et al., 1992; Machado et al., 2009; Miyazaki et al., 2021) considered that the alkali granite was in direct contact with the strata of the Paraná Basin, possibly through an unconformity, and that the main impact melt volume produced was granitic in composition.

The newly available outcrops and the differentiation between IMR types of the Araguainha central uplift allows us to propose a different stratigraphic architecture. We observed that PIB is always in contact with the (meta)sedimentary basement. This is consistent with the nature of the majority of clasts in the PIB being derived from this (meta)sedimentary basement, besides a possible minor component of clasts from the lower sedimentary units of the Paraná Basin and essentially no porphyritic alkali granite clasts. The IMRs found in the PIB are all derived from the same precursors (IMR Type-II), with a clear absence of IMR Type-I (granitic in composition).

These observations allow to better constrain the impact event (Figure 4.11). First, the clast components of the PIB indicate that the main zone of excavation extended only to the (meta)sedimentary target rocks and not to a contact proper between the alkali granite and the supracrustal rocks, as had been assumed by von Engelhardt et al. (1992) and Machado et al. (2009). Second, shock melting could not extend into the alkali granite complex, probably because the granite was much deeper at the time of impact.

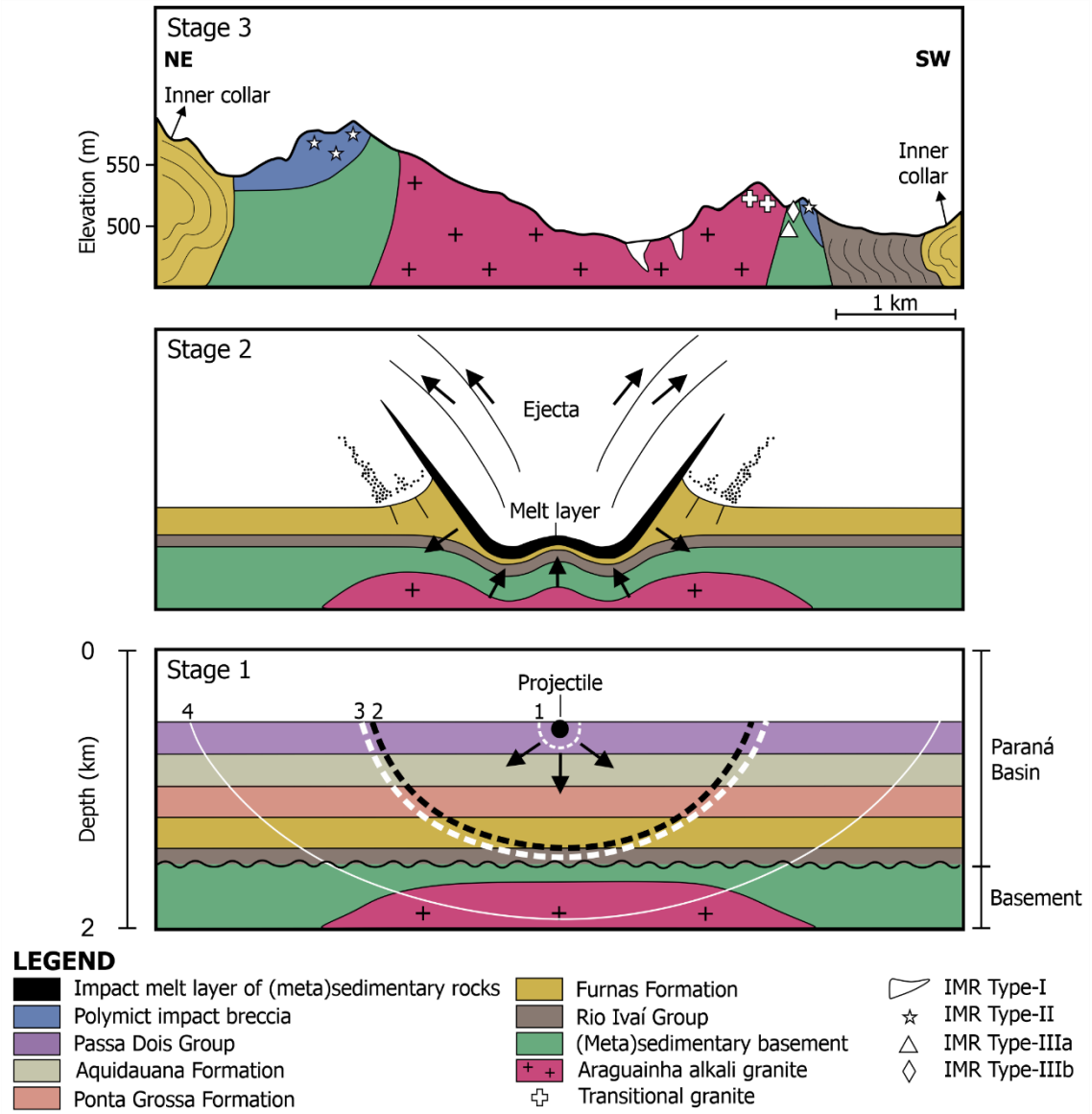

Figure 4.11 Schematic, unscaled illustration of the distribution of target rocks and impact related rocks prior, during, and after the cratering process, as suggested here for the Araguainha impact structure. Stage 1: The stratigraphy of the target rocks before impact (1 - shock wave, 2 - excavated area as proposed by Lana et al., 2006, 3 - excavated area proposed by us, 4 - the displaced area related to the development of the transient cavity). Stage 2: Intermediate stage, the strata are uplifted and deformed during crater modification. Stage 3: The final representation of the central uplift in NE-SW direction, where the geological context observed during our field campaigns is illustrated, with the typical settings of the different impact breccia types at Araguainha and the contact of alkali granite with the (meta)sedimentary basement.

Kieffer and Simonds (1980) demonstrated that the abundance of impact melt in impact structures formed on crystalline target rocks is approximately 2 orders of magnitude higher than the volume in structures formed in sedimentary target rocks. Wünnemann et al. (2008) observed that it is possible to form IMRs from sedimentary target rocks, but the quantity will depend on the porosity and

the work (i.e., impact energy) to be expanded to close pores (see also Güldemeister et al., 2013). We consider our Type-III melt rocks (meta)sedimentary strata-derived shock melt. For impact craters similar in size to the 40 km diameter Araguainha structure, transient crater sizes of ~24 km diameter were predicted (Wünnemann et al., 2008). A possible impact melt volume of ~100 km3 was derived from such modeling. If the Araguainha impact really occurred under the conditions suggested here, the only target rocks involved would have been the sedimentary units of the lower part of the Paraná Basin and/or the (meta)sedimentary basement (Figure 4.11), resulting in highly silicious melt compositions rather than in a granitic composition. This is in agreement with our observations on IMRs of Types II and III, as well as the observations by Tong et al. (2010) and Hippertt et al. (2014).

We have already taken issue with the previously published notion that there could have been an impact melt sheet overlying the basement. With erosion of some 250-350 m, as estimated by Lana et al. (2007), this impact melt sheet would have been significantly degraded as well, though on elevations of the collapsed central uplift, some remnants may have survived for some time. The authors infer two periods of erosion: the first period would have occurred in the Late Triassic-Early Jurassic, when 50-130 m of the original crater (Corumbataí sediments) would have been eroded; the second period was related to the recent removal of 200-220 m of target rocks and overlying impact-related material. While the currently exposed geology of the central uplift does not indicate large remnants of IMR, the limited occurrences of part-melted granite could perhaps be considered a remnant resulting from thermal overprint from hot, originally overlying IMR.

We tentatively propose a chronological scenario of formation for these three types of IMRs. Types II and III were probably formed during the early excavation stage by shock melting of (meta)sedimentary target rocks, in a zone close to the maximum penetration of the projectile. These melt rock types differ in occurrence, as discussed above. Type-II was formed by shock compression/decompression and was deposited in the PIB. Type-III could represent locally produced shock melt. Later, pseudotachylitic breccia represented by IMR Type-I was formed by decompression melting during uplift in the modification stage, analogous to the

massive pseudotachylitic breccias at Vredefort and the Sudbury Breccia in Canada.

4.5.4 Considerations about the depth of erosion at Araguainha

Lana et al. (2007) suggested a depth of erosion at the Araguainha site of as much as 250-350 m. This estimate was based on stratigraphic considerations – essentially information derived from the AG-1-MT borehole drilled some 30 km to the southwest of the Araguainha impact structure. Also, based on this information, Vasconcelos et al. (2016) used iSALE numerical modeling to simulate the formation of the Araguainha impact structure. The model showed that the currently exposed granitic basement would be ~4 to 6 km wide, in accordance with the actual ~5 km wide exposure. We would like to place this estimate into context. Current exposure across the Araguainha impact structure, especially outside of the complex central uplift terrane, reveals in a quasi-bull's eye pattern the stratigraphy of the lower to middle Paraná Basin sequence. Neither the available geological nor geophysical data allow us to estimate the remaining thickness of the stratigraphic packages between lowermost Furnas Formation and uppermost Passa Dois Group strata. It is, furthermore, entirely unconstrained how much erosional debris – from the topographic highs of the central uplift and the crater rim section has augmented the, also unknown, primary thickness of the crater fill over time, that is, how within-crater deposition may have retarded erosion. This kind of debris aggradation likely would have been strongest early after crater modification when the exposed strata were strongly deformed (brecciated, fractured, folded, and faulted) and slopes on central uplift blocks and crater rim the steepest.

It is also entirely unclear what the original topography of the central uplift section could have been. Heights of mountains, depths of valleys, and associated thicknesses of impact breccia deposits are obscure. Thus, it seems futile to apply breccia deposit thicknesses from other, better preserved impact structures to the remnants of impact breccia in the central uplift regime at Araguainha. This work has established that the difference between the topographically highest and the lowest occurrences of PIB presently exposed on the eroded central uplift amounts to a minimum interval of 110 m in the northern central uplift. But this does not

relate to a 110 m thickness of remaining impact breccia, as expected by Wünnemann et al.'s (2008) melt volume of ~100 km3. Instead, this likely mirrors the relief of crater floor and basement below a much thinner remaining breccia deposit. This would also account for the elevation difference between breccia occurrences in the northern and southern sectors. However, we must conclude that the current exposure provides an excellent perspective on the zone straddling the base of impact breccia deposits and strongly deformed, structurally highly complex crater floor and directly underlying basement.

4.6 Conclusions

The present detailed study of the geology and lithologies of the central uplift of the Araguainha impact structure provides a significant advance of the understanding of this central part of the largest impact structure currently known in South America. We have examined the interface between remnants of impact breccia and the crater floor as well as the basement below. Our results pertain to the emplacement of the impact-related rocks of the Araguainha impact structure. The main findings include:

- The recognition of wide exposures of metamorphosed basement rocks probably belonging to the Cuiabá Group of the Paraguay Belt, in the direct environs of the central alkali granite complex. There is clear evidence in the surrounding basement for fine-grained granitic apophyses into the older, in large part metamorphosed basement.
- The PIB along the new exposures at the MT-100 road occurs in close association with intercalated megablocks (tens to hundreds of meters) of sedimentary strata of the Furnas Formation and (meta)sedimentary strata of the Paraguay Belt. The breccias are exposed over a 110 m elevation gradient but certainly do not represent a package of such thickness. Instead, they seem to represent much thinner breccia deposits on top of a crater floor with complex relief.
- The PIB package has a consistent clast content that is dominated by micro- to macroclasts derived from sedimentary (lowermost part of the Paraná Basin sequence) and especially (meta)sedimentary protoliths. A granite component in the PIB is only of rudimentary significance, and it

appears likely that this component only represents granite apophyses that reached into the (meta)sedimentary basement.

- The three newly-proposed types of IMR have been characterized by distribution and mode of occurrence. They were not formed at the same stage of cratering and likely produced by different processes. We tentatively propose that the IMR Types II and III were probably formed during the early excavation stage as the first melt phases formed at Araguainha, by shock melting.
- IMR Type-I is interpreted here as an equivalent of the Vredefort pseudotachylitic breccia that would have been formed by decompression melting during uplift in the modification stage.
- Further field and petrographic studies must be conducted to better understand the formation and emplacement of the IMRs of Types II and III. Geochemical and isotopic analysis of these melt rocks and possible precursor lithologies should also be conducted.
- While the currently exposed geology of the central uplift does not indicate large remnants of impact melt, the restricted occurrences of part-melted granite could represent thermal overprint from hot, previously overlying impact melt breccia.
- The fact that the highly silicious IMR of Type-II are generally finest grained/annealed may be evidence that impact breccia exposed at the current erosion level must have been of high temperature. Why such a thermal overprint is not in evidence in the metasedimentary basement belt in the north and south remains unresolved at this stage.

Acknowledgements

This study was partially financed by the Brazilian Coordination for the Improvement of Higher Education Personnel (Coordenação de Aperfeiçoamento de Pessoal de Nível Superior – Brazil [CAPES] - Finance Code 001). The authors thank the University of Brasilia, Institute of Geosciences (IG/UnB), Postgraduate Program in Geology for providing the infrastructure required to conduct this research. CSMS is grateful to CAPES for a Ph.D. grant (process 88882.347189/2019-01). N. Hauser and W.U. Reimold have been supported by

the Brazilian National Council for Scientific and Technological Development (CNPq) through fellowship grants (Nos. 309878/2019-5 and 305761/2019-6, respectively). CSMS and RBB acknowledge financial support from research grants from the Barringer Family Fund for Meteorite Impact Research. We also acknowledge the support of the Museum für Naturkunde Berlin, which provided access to the sample collection of von Engelhardt et al. (1992) while NH was a postdoctoral research fellow there in 2017. Hans Knöfler provided a series of outstanding polished thin sections for the impact breccia types of this study. John Spray is thanked for editorial handling and constructive evaluation. Reviewers Sanna Alwmark and Axel Wittmann are also thanked for excellent reviews.

4.7 References

Almeida, F. F. M. 1984. Província Tocantins, setor sudoeste. In *O Pré-Cambriano do Brasil*, edited by F. F. M. Almeida, and Y. Hasui, 265-281. São Paulo: Edgard Blücher Publications.

Alvarenga, C. J. S., Santos, R. V., and Dantas, E. L. 2004. C–O–Sr isotopic stratigraphy of cap carbonates overlying Marinoan age glacial diamictites in the Paraguay Belt, Brazil. *Precambrian Research* 131: 1-21.

Assine, M. L., Soares, P. C., and Milani, E. J. 1994. Sequências tectono-sedimentares mesopaleozoicas da Bacia do Paraná, Sul do Brasil. *Revista Brasileira de Geociências* 24: 77-89.

Babinski, M., McGee, B., Tokashiki, C. C., Tassinari, C. C. G., Saes, G. S., and Pinho, F. E. C. 2018. Comparing two arms of an orogenic belt during Gondwana amalgamation: Age and provenance of the Cuiabá Group, northern Paraguay Belt, Brazil. *Journal of South American Earth Sciences* 85: 6-42. https://doi.org/10.1016/j.james.2018.04.009.

Blair, T. C., and McPherson, J. G. 1999. Grain-size and textural classification of coarse sedimentary particles. *Journal of Sedimentary Research* 69: 6–19.

Burgess, S. D., Bowring, S. A., and Shen S. Z. 2014. High-precision timeline for Earth's most severe extinction. *Proceedings of the National Academy of Sciences* 111: 3316-3321.

Cavosie, A. J., Timms, N. E., Ferriere, L., and Rochette, P. 2018. FRIGN zircon – The only terrestrial high-pressure and high-temperature mineral diagnostic of shock deformation. *Geology* 46: 891-894.

Collins, G. S., Melosh, H. J., and Osinski, G. R. 2012. The impact cratering process. *Elements* 8: 25-30. https://doi.org/10.2113/gselements.8.1.25.

Cordani, U. G., Brito Neves, B. B., Fuck, R. A., Porto, R., Thomaz Filho, A., and Cunha, F. M. B. 2009. Preliminary integration study of Precambrian with tectonic

events in Brazilian sedimentary basins (Republication). *Boletim de Geociências da Petrobrás* 17: 133-204.

Crósta, A. P. 1982. *Mapeamento geológico do Domo de Araguainha utilizando técnicas de sensoriamento remoto*. MSc thesis, São José dos Campos, São Paulo: Instituto Nacional de Pesquisas Espaciais.

Crósta, A. P., Gaspar, J. C., and Candia, M. A. F. 1981. Feições de metamorfismo de impacto no Domo de Araguainha. *Revista Brasileira de Geociências* 11: 139–146.

Crósta, A. P., Reimold, W. U., Vasconcelos, M. A. R., Hauser, N., Oliveira, G. J. G., Maziviero, M. V., and Góes, A. M. 2019. Impact cratering: The South American record – Part 1. *Chemie der Erde* 79: 1-61.

Dantas, E. L., Alvarenga, C. J. S., Santos, R. V., and Pimentel, M. M. 2009. Using Nd isotopes to understand the provenance of sedimentary rocks from a continental margin to a foreland basin in the Neoproterozoic Paraguay Belt, central Brazil. *Precambrian Research* 170: 1-12. https://doi.org/10.1016/j.precamres.2008.11.005.

Dietz, R. S., and French, B. M. 1973. Two probable astroblemes in Brazil. *Nature* 244: 561-562.

Dressler, B. O., and Reimold, W. U. 2004. Order or chaos? Origin and mode of emplacement of breccias in floors of large impact structures. *Earth-Science Reviews* 67: 1-54.

Erickson, T. M., Timms, N. E., Kirkland, C. L., Tohver, E., Cavosie, A. J., Pearce, M., and Reddy, S. M. 2017. Shocked monazite chronometry: Integrating microstructural and in situ isotopic age data for determining precise impact ages. *Contributions of Mineralogy and Petrology* 172(11): 1-19. https://doi.org/10.1007/s00410-017-1328-2.

Fischer, S. 2015. Ein Beitrag über die Impaktgesteine der Araguainha Impaktstruktur (Brasilien). MSc thesis, Berlin: Freie Universität.

French, B. M. 1998. *Traces of catastrophe: A Handbook of Shock-Metamorphic Effects in Terrestrial Meteorite Impact Structures*. Houston, TX: Lunar and Planetary Institute 130 p.

Godoy, A. M., Pinho, F. E. C., Manzano, J. C., Araújo, L. M. B., Silva, J. A., and Figueiredo, M. 2010. Estudos isotópicos das rochas granitoides Neoproterozóicas da Faixa de Dobramento Paraguai. *Revista Brasileira de Geociências* 40(3): 380-391.

Godoy, A. M., Ruiz, A. S., Manzano, J. C., and Araújo-Ruiz, L. M. B. 2007. Os Granitóides Brasilianos Pós-Tectônicos da Faixa de Dobramentos Paraguai, MS e MT. *Geologia USP Série Científica* 7: 29-44.

Gottwald, M., Kenkmann, T., and Reimold, W. U. 2020. *Terrestrial impact structures. The TanDEM-X atlas*. Munich: Verlag Dr. Friedrich Pfeil.

Güldemeister, N., Durr, N., Wuennemann, K., and Hiermeier, S. 2013. Propagation of Impact-Induced shock Waves in Porous Sandstone Using Mesoscale Modeling. *Meteoritics and Planetary Science* 48: 115–133.

Hauser, N., Reimold, W. U., Cavosie, A. J., Crósta, A. P., Schwarz, W. H., Trieloff, M., Souza, C. S. M., Rodrigues, E. N., and Brown, M. 2019. Linking shock textures revealed by BSE, CL, and EBSD with U-Pb data (LA-ICP-MS and SIMS) from zircon from Araguainha impact structure, Brazil. *Meteoritics and Planetary Science* 54: 2286-2311.

Hippertt, J. P., Lana, C., Weinberg, R. F., Tohver, E., Schmieder, M., Scholz, R., Gonçalves, L., and Hippertt, J. F. 2014. Liquefaction of sedimentary rocks during impact crater development. *Earth and Planetary Science Letters* 408: 285-295.

Kenkmann, T. 2021. The terrestrial impact crater record: A statistical analysis of morphologies, structures, ages, lithologies, and more. *Meteoritics and Planetary Science* 56: 1024-1070. https://doi.org/10.1111/maps.13657

Kieffer, S.W., and Simonds, C. H. 1980. The role of volatiles and lithology in the impact cratering process. *Reviews of Geophysics and Space Physics* 18: 143-181.

Lacerda Filho, J. V., Abreu Filho, W., Valente, C. R., Oliveira, C. C., and Albuquerque, M. C. 2004. *Geologia e recursos minerais do estado de Mato Grosso*. Mato Grosso: Programa Geologia do Brasil, CPRM/MME/SICME, 252 p.

Lacerda Filho, J. V., Brito, R. S. C., Silva, M. G., Oliveira, C. C., Moreton, L. C., Martins, E. G., Lopes, R. C., Lima, T. M., Larizzatti, J. H., and Valente, C. R. 2006. *Geologia e Recursos Minerais do Estado de Mato Grosso do Sul*. Mato Grosso do Sul: Programa Integração, atualização e difusão de dados de geologia do Brasil. Convênio CPRM/SICME-MS, MME, 121 p.

Lana, C., Romano, R., Reimold, W. U., and Hippertt, J. 2006. Collapse of large complex impact structures: Implications from the Araguainha impact structure. *Geology* 34: 9-12.

Lana, C., Souza-Filho, C. R., Marangoni, Y. R., Yokoyama, E., Trindade, R. I. F., Tohver, E., and Reimold, W. U. 2007. Insights into the morphology, geometry, and post-impact erosion of the Araguainha peak-ring structure, central Brazil. *Geological Society of America Bulletin* 119: 1135–1150.

Lana, C., Souza-Filho, C. R., Marangoni, Y. R., Yokoyama, E., Trindade, R. I. F., Thover, E., and Reimold, W. U. 2008. Structural evolution of the 40 km wide Araguainha impact structure, central Brazil. *Meteoritics and Planetary Science* 43: 701-716. https://doi:10.1111/j.1945-5100.2008.tb00679.x

Lofgren, G. 1971. Devitrified glass fragments from Apollo 11 and Apollo 12 lunar samples. *Proceedings of the Lunar Science Conference* 2: 949-955.

Machado, R., Lana, C., Stevens, G., Filho, C. R. S., Reimold, W. U., and McDonald, I. 2009. Generation, mobilization and crystallization of impact-induced alkali-rich melts in granitic target rocks. Evidence from the Araguainha impact structure, central Brazil. *Geochimica et Cosmochimica Acta* 73: 7183-7201.

McGee, B., Collins, A. S., Trindade, R. I. F., and Payne, J. 2014. Age and provenance of the Cryogenian to Cambrian passive margin to foreland basin sequence of the northern Paraguay Belt, Brazil. *Geological Society of America Bulletin* 127: 76-86. http://dx.doi.org/10.1130/B30842.1.

McPhie, J., Doyle, M., and Allen, R. 1993. *Volcanic Textures – A Guide to the Interpretation of Textures in Volcanic Rock*. Centre for Ore Deposit and Exploration Studies, University of Tasmania 196 pp.

Melosh, H. J. 1989. *Impact Cratering: A Geologic Process*. New York: Oxford University Press 258 pp.

Melosh, H. J., and Ivanov, B. A. 1999. Impact Crater Collapse. *Annual Review of Earth Planetary Sciences* 27: 385-415.

Milani, E. J., França, A. B., and Schneider, R. L. 1994. Bacia do Paraná. *Boletim de Geociências da Petrobrás* 8: 69-82.

Milani, E. J., Melo, J. H. G., Souza, P. A., Fernandes, L. A., and França, A. B. 2007. Bacia do Paraná. *Boletim de Geociências* 15: 265-287.

Miyazaki, M. R., Leite, E. P., Vasconcelos, M. A. R., Wünnemann, K., and Crósta, A. P. 2021. Bouguer anomaly inversion and hydrocode modeling of the central uplift of the Araguainha impact structure. *Annals of the Brazilian Academy of Sciences* 93: e20210081. https://doi.org/10.1590/0001-3765202120210081.

NASA JPL. 2013. NASA Shuttle Radar Topography Mission global 1 arc second [data set]. NASA EOSDIS Land Processes Distributed Active Archive Center https://doi.org/10.5067/MEaSUREs/SRTM/SRTMGL1.003.

Osinski, G. R., Grieve, R. A. F., Ferriere, L., Losiak, A., Pickersgill, A. E., Cavosie, A. J., and Hibbard, S. M. 2022. Impact Earth: A Review of the Terrestrial Impact Record. *Earth-Science Reviews* 232: 104112.

Pierazzo, E., and Melosh, H. J. 1999. Hydrocode modeling of Chicxulub as an oblique impact event. *Earth and Planetary Science Letters* 165: 163-176.

Pierazzo, E., and Melosh, H. J. 2000. Hydrocode modelling of oblique impacts: the fate of the projectile. *Meteoritics and Planetary Science* 35: 117-130.

Preuss, J. 2012. Characterization of impact-related melt breccias from the impact structure Araguainha (Brazil). MSc thesis, Potsdam: University of Potsdam 101 p.

Reimold, W. U. 1998. Exogenic and Endogenic Breccias: A Discussion of Major Problematics. *Earth Science Reviews* 43: 25–47.

Reimold, W. U., and Gibson, R. L. 2006. The melt rocks of the Vredefort Impact Structure: petrography, geochemistry, and implications for impact cratering and Witwatersrand evolution. *Chemier der Erde* 66: 1-35.

Reimold, W. U., Hauser, N., Hansen, B. T., Thirlwall, M., and Hoffmann, M. 2017. The impact pseudotachylitic breccia controversy: insights from first isotope analysis of Vredefort impact-generated melt rocks. *Geochimica et Cosmochimica Acta* 214: 266–81.

Reimold, W. U., Hoffmann, M., Hauser, N., Schmitt, R.-T., Zaag, P., and Mohr-Westheide, T. 2016. A geochemical contribution to the discussion about the genesis of impact-related pseudotachylitic breccias: studies of PTB in the Otavi and Kudu Quarries of the Vredefort Dome support the “in situ formation” hypothesis. *South African Journal of Geology* 119: 453–72.

Rizzoli, P., Martone, M., Gonzalez, C., Wecklich, C., Borla Tridon, D., Bräutigam, B., Bachmann, M., Schulze, D., Fritz, T., Huber, M., Wessel, B., Krieger, G., Zink, M., and Moreira, A. 2017. Generation and performance assessment of the global TanDEM-X digital elevation model. *ISPRS Journal of Photogrammetry and Remote Sensing* 132: 119-139.

Sánchez, J. P. 2006. Mapeamento 1:25.000 do núcleo do Astroblema Domo de Araguainha e aspectos geoturísticos da região. BSc thesis, Rio Claro, São Paulo: Universidade Estadual Paulista.

Schmieder, M., and Kring, D. A. 2020. Earth's impact events through geologic time: a list of recommended ages for terrestrial impact structures and deposits. *Astrobiology* 20(1): 91-141. https://doi.org/10.1089/ast.2019.2085.

Silva, D., Lana, C., and Souza-Filho, C. R. 2016. Petrographic and geochemical characterization of the granitic rocks of the Araguainha impact crater, Brazil. *Meteoritics and Planetary Science* 51: 443-467.

Spray, J. G., and Biren, M. B. 2021. Distinguishing friction- from shock-generated melt products in hypervelocity impact structures. In *Large Meteorite Impacts and Planetary Evolution VI*, edited by W.U. Reimold, and C. Koeberl, 147-170. Geological Society of America Special Paper 550.

Stöffler, D., and Grieve, R. A. F. 2007. Impactites. Recommendations by the IUGS Subcommission on the Systematics of Metamorphic Rocks. In *Metamorphic rocks: A classification and glossary of terms: Recommendations of the International Union of Geological Sciences Subcommission on the Systematics of Metamorphic Rocks*, edited by E. Fettes, and J. Desmons, Cambridge, U.K.: Cambridge University Press, 82-92, 111-125, and 126-242.

Stöffler, D., Artemieva, N. A., Wünnemann, K., Reimold, W. U., Jacob, J., Hansen, B. K., and Summerson, I. A. T. 2013. Ries crater and suevite revisited – Observations and modeling Part I: Observations. *Meteoritics and Planetary Science* 48: 515-589.

Stöffler, D., Hamann, C., and Metzler, K. 2018. Shock metamorphism of planetary silicate rocks and sediments: proposal for an updated classification system. *Meteoritics and Planetary Sciences* 53: 5-49. https://doi.org/10.1111/maps.12912.

Theilen-Willige, B. 1981. The Araguainha impact structure, Central Brazil. *Revista Brasileira de Geociências* 11: 91-97.

Tohver, E., Cawood, P. A., Riccomini, C., and Trindade, R. I. F. 2013. Shaking a methane fizz: seismicity from the Araguainha impact event and the Permian–Triassic global carbon isotope record. *Palaeogeography, Palaeoclimatology, Palaeoecology* 387: 66-75. https://doi.org/10.1016/j.palaeo.2013.07.010.

Tohver, E., Lana, C., Cawood, P. A., Fletcher, I. R., Jordan, F., Jourdan, F., Sherlock, S., Rasmussen, B., Trindade, R. I. F., Yokoyama, E., Souza Filho, C. R., and Marangoni, Y. 2012. Geochronological constraints on the age of a Permo–Triassic impact event: U–Pb and $^{40}Ar/^{39}Ar$ results for the 40 km Araguainha structure of central Brazil. *Geochimica et Cosmochimica Acta* 86: 214-227.

Tong, C. H., Lana, C., Marangoni, Y. R., and Elis, V. R. 2010. Geoelectric evidence for centripetal resurge of impact melt and breccias over central uplift of Araguainha impact structure. *Geology* 38(1): 91-94.

UnB-IG 2012. Final Mapping Project by the Graduate Class of 2012. Brasilia, Brasil: Institute of Geosciences, University of Brasilia, Unpubl. Report, Brasília DDF, Braszil 759 pp.

Vasconcelos, M. A. R., Crósta, A. P., Wünnemann, K., Collins, G. S., Reimold, W. U., and Köster, P. 2016. Numerical modelling of the Araguainha impact structure, Brazil (abstract #6013). *Meteoritics and Planetary Science* 51: A639.

von Engelhardt, W., Matthai, S., and Walzebuck, J. 1992. Araguainha impact crater, Brazil. I – The interior part of the uplift. *Meteoritics and Planetary Sciences* 27: 442-457.

Warr, L. N. 2021. IMA–CNMNC approved mineral symbols. *Mineralogical Magazine* 85(3): 291-320. https://doi.org/10.1180/mgm.2021.43

Wünnemann, K., Collins, G. S., and Osinski, G. R. 2008. Numerical modelling of impact melt production in porous rocks. *Earth and Planetary Science Letters* 269: 530–539.

Yokoyama, E. 2008. Trama magnética do núcleo soerguido da estrutura de impacto de Araguainha (MT/GO). MSc thesis, São Paulo: University of São Paulo 117 pp.

Yokoyama, E., Trindade, R. I. F., Lana, C. R., Souza-Filho, C. R., Baratoux, D., Marangoni, Y. R., and Tohver, E. 2012. Magnetic fabric of Araguainha complex impact structure (Central Brazil): Implications for deformation mechanisms and central uplift formation. *Earth and Planetary Science Letters* 331: 347-359.

Zalán, P. V., Wolff, S., Astolfi, M. A. M., Vieira, I. S., Conceição, J. C. J., Appi, V. T., Neto, E. V. S., Cerqueira, J. R., and Marques, A. 1990. The Paraná Basin, Brazil. In *Interior cratonic basins*, edited by M. W. Leighton, D. R. Kolata, D. F. Oltz, and J. J. Eidel, 51: 681-708. Rio de Janeiro: American Association of Petroleum Geologists Memoir.

4.8 Supplementary Material

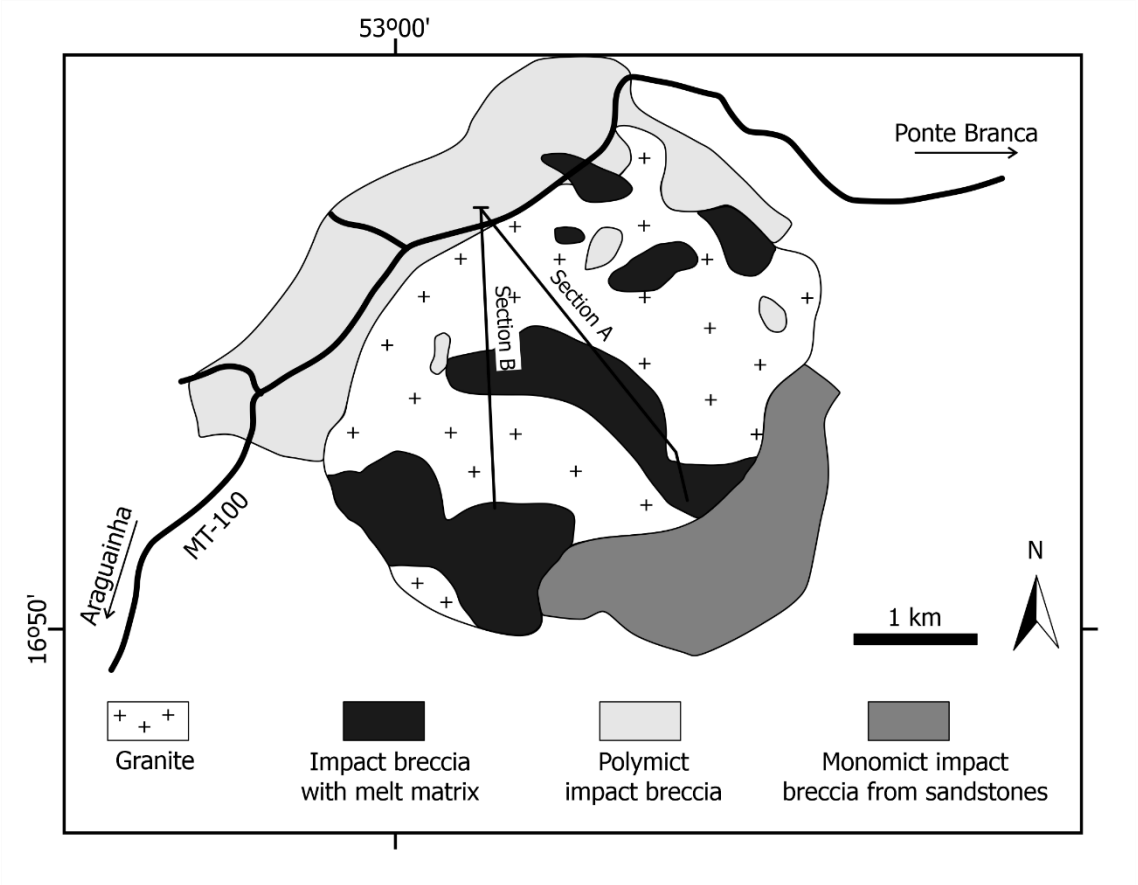

Figure S1. The map of the central uplift of Araguainha after von Engelhardt et al. (1992).

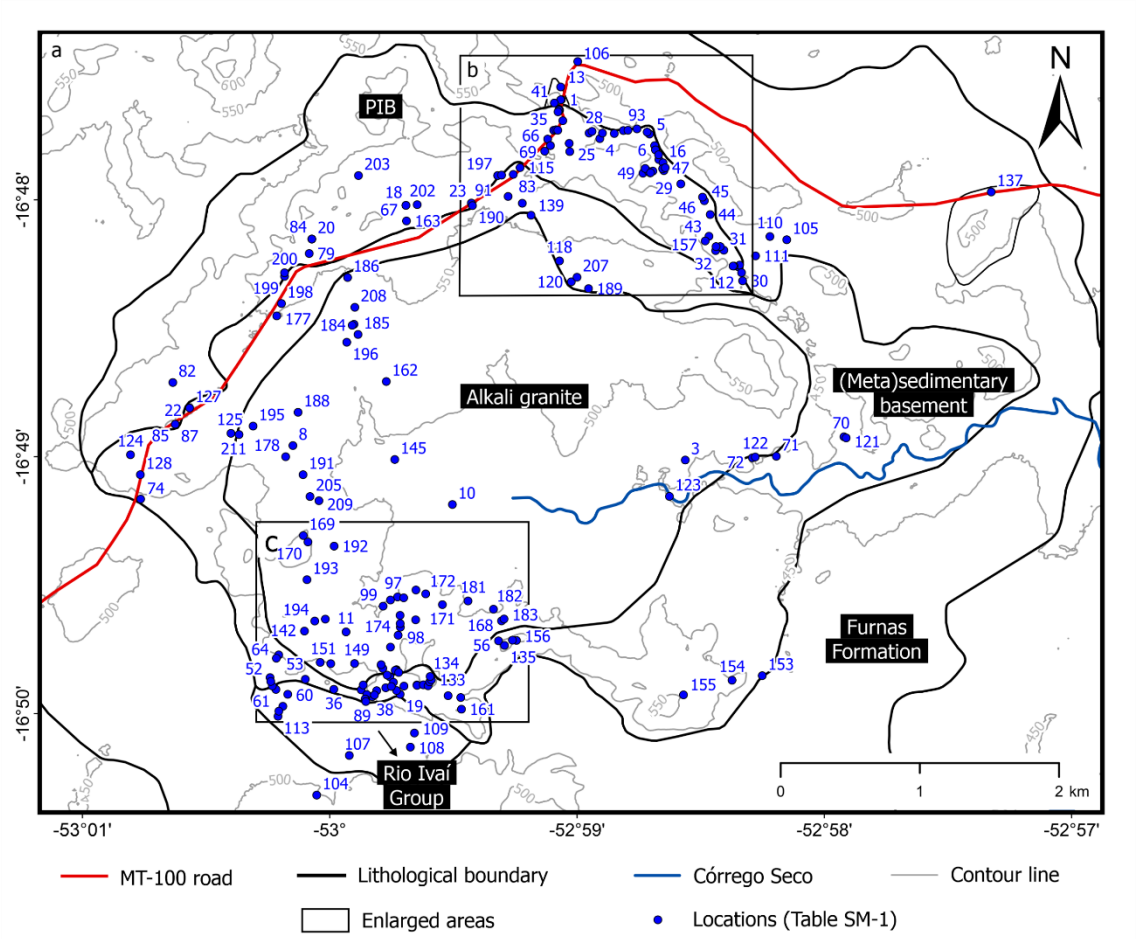

Figure S2. (a) Map of the study locations from our 2019-2022 field campaigns in the central uplift region. The (b) northern and (c) southern study regions are enlarged to better show the distribution of points. The contour lines were extracted from the TanDEM-X digital elevation model at 50 m intervals. Some points overlap in the image. For more detail and to relate the points to study profiles we have also added the study points of von Engelhardt et al. (1992); for geographic coordinates refer to Table S1.

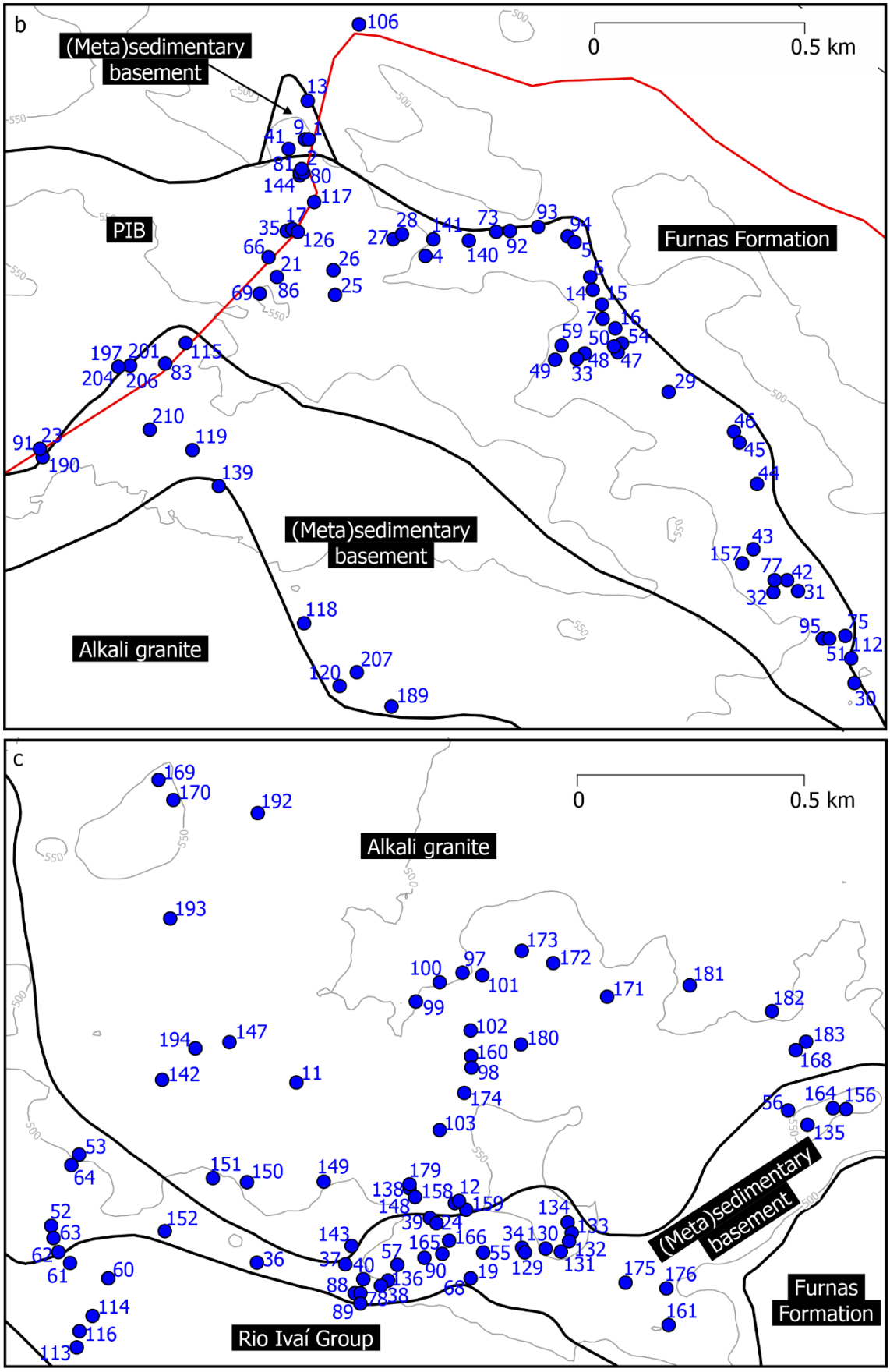

Figure S2. *(continued).*

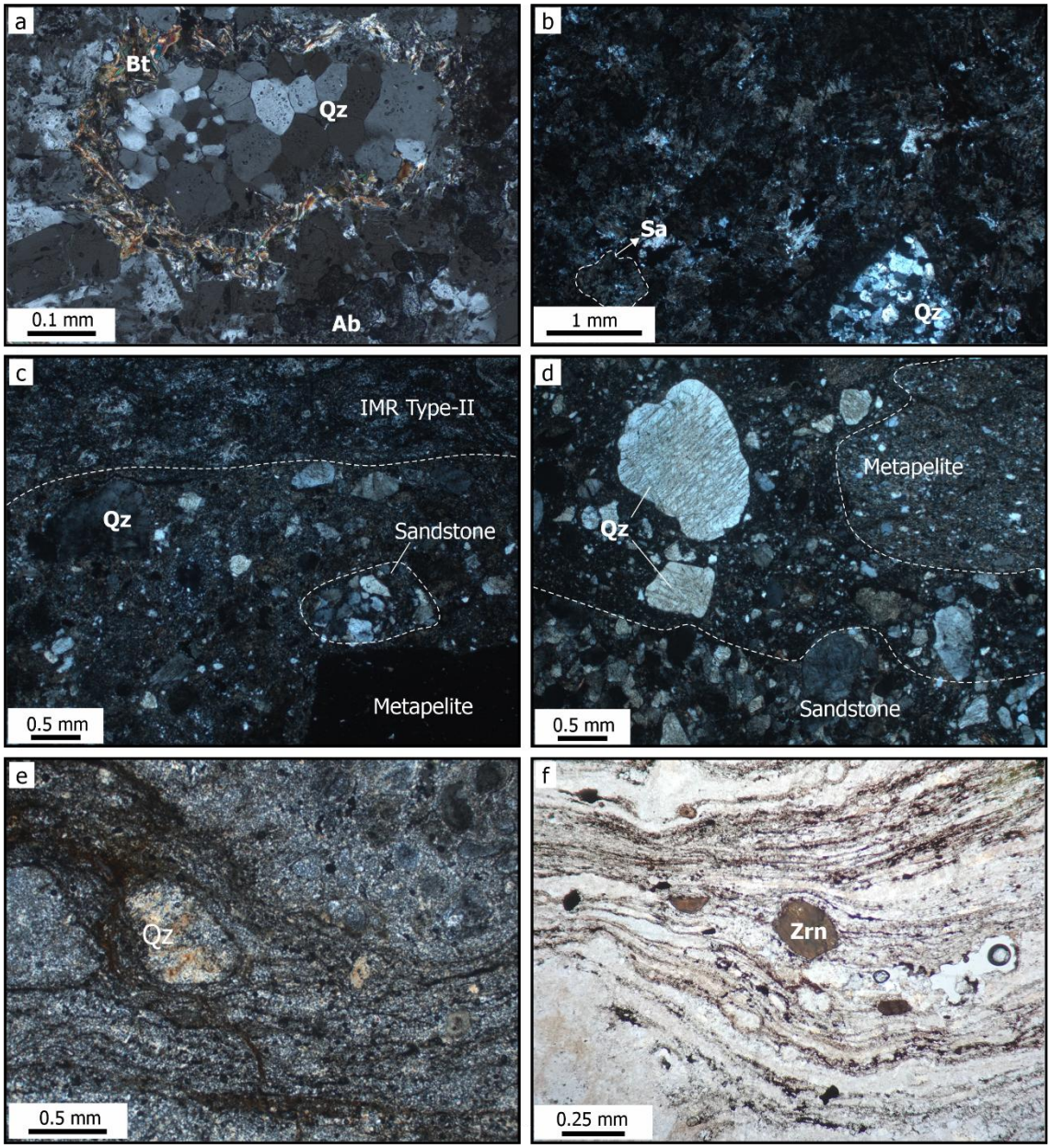

Figure S3. Photomicrographs taken in cross-polarized light for different impact-related rocks. (a) An image of transitional granite showing a core of remnant quartz surrounded by a rim of small, neoformed biotite crystals. (b) Impact melt rock (IMR) Type-I showing clusters of sanidine crystals in circular to radial aggregates and recrystallized quartz clasts. (c, d) Polymict impact breccia (PIB) matrix with fragments of sandstone, metapelite, quartz minerals, and melt particles (IMR Type-II). (e) IMR Type-III showing fluidal texture around a rounded and thermally abraded quartzitic clast. Part of the quartz in this clast shows toasting. The fine-grained matrix is silicious and completely annealed or recrystallized. The dark bands are interpreted to represent primary pelitic seams. (f) Photomicrograph taken in plane-polarized light of IMR Type-III showing the toasted and granular zircon grains concentrated in specific laminae within the fluidal structure. Mineral abbreviations after Warr (2021): Ab – albite, Bt – biotite, Fsp – undifferentiated feldspar, Qz – quartz; Sa – sanidine; Zrn – zircon.

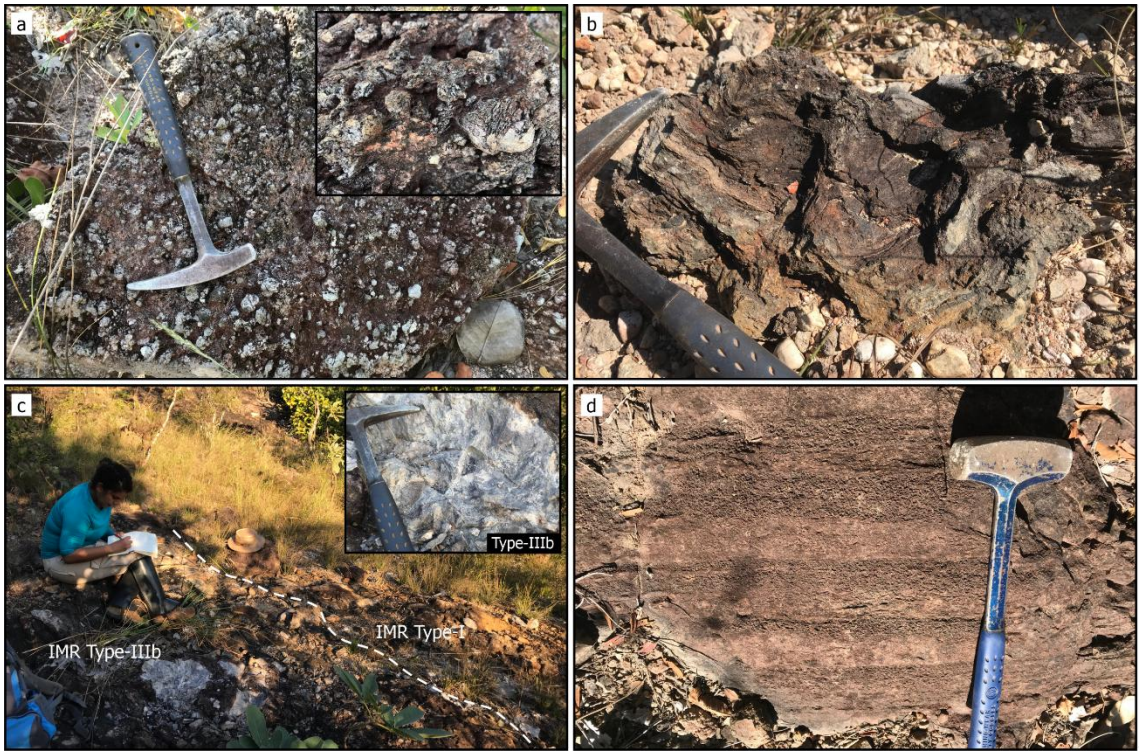

Figure S4. (a) IMR Type-IIIa with well-preserved quartz pebbles of the original conglomeratic target rock (at 22K 287525 E, 8137986 S). Hammer, for scale, ca. 31 cm long. (b) IMR Type-IIIb with fluidal structure (at 22K 287124 E, 8137954 S) emphasized by weathering. The part of the hammer shown is approximately 20 cm long. (c) A contact between IMR Type-I against Type-IIIb (at 22K 287329 E, 8138048 S). (d) Metarhythmite of the (meta)sedimentary sequence at the same locality as (a). Hammer, for scale, is approximately 35 cm long.

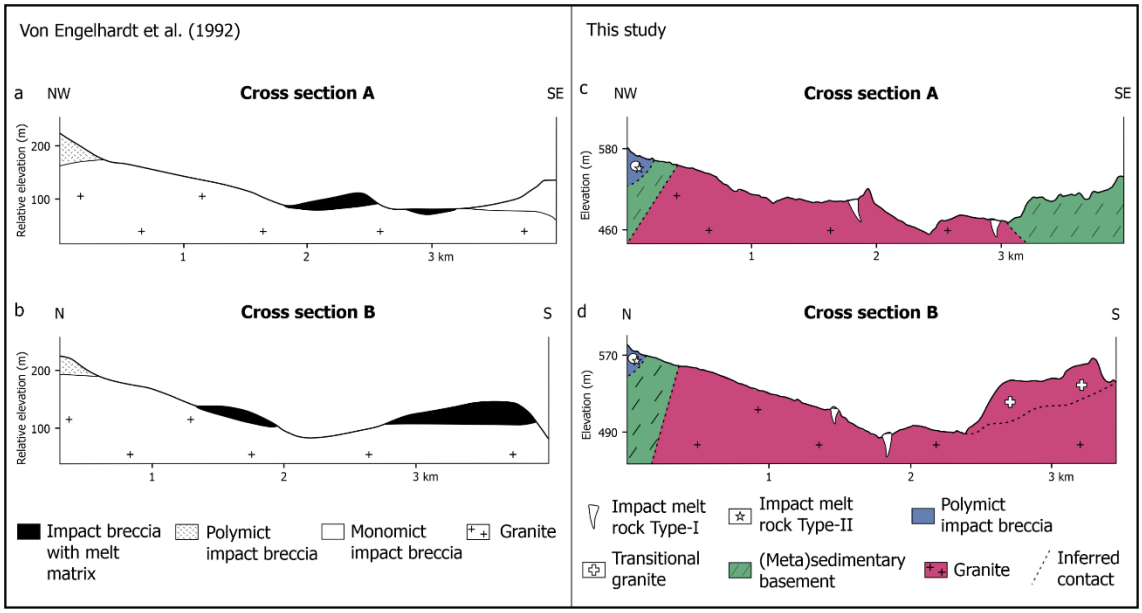

Figure S 5. (a, b) Simplified, schematic profiles based on the cross sections A and B of fig. 2 of von Engelhardt et al. (1992). Profiles (c) and (d) are based on our field work along the same traverses and emphasize the differences to the interpretations of von Engelhardt et al. (1992). Elevations along our profiles were extracted from the TanDEM-X digital elevation model, whereas von Engelhardt et al. (1992) obtained topographic information by extrapolating between GPS measurements at certain reference points..

Table S1. Geological points with coordinates of the lithologies identified during our field campaigns on the central uplift of the Araguainha impact structure, as well as information from previous authors (Fischer, 2015; Hauser et al., 2019; Preuss, 2012; von Engelhardt et al., 1992). The elevations in italics were acquired with the use of Google Earth Pro.

Point on the map	**Sample/Profile**	**Coordinates** Longitude (E)	Latitude (S)	**Elevation** (m)	**Unit**	**Outcrop**	**References and observations**
1	CA-04	288562	8142192	503	Impact melt rock Type-I	in situ	(This study)
2	CA-05	288546	8142122	515	Impact melt rock Type-I	in situ	(This study)
3	CA-27	289452	8139604	462	Impact melt rock Type-I	in situ	(This study)
4	CA-36	288838	8141912	488	Impact melt rock Type-I	in situ	Spherulitic texture (This study)
5	CA-38	289195	8141945	479	Impact melt rock Type-I	blocks	(This study)
6	CA-39	289232	8141862	472	Impact melt rock Type-I	in situ	Lithophysae texture (This study)
7	CA-40	289262	8141762	482	Impact melt rock Type-I	blocks	(This study)
8	CA-69	286633	8139708	*530*	Impact melt rock Type-I	in situ	Red dike (This study)
9	CA-76	288557	8142191	*509*	Impact melt rock Type-I	in situ	(This study)
10	CA-94	287779	8139285	487	Impact melt rock Type-I	in situ	Red dike (This study)
11	CA-95	287015	8138370	524	Impact melt rock Type-I	in situ	Red dike (This study)
12	CA-113	287377	8138099	537	Impact melt rock Type-I	blocks	(This study)
13	GAR-15	288557	8142283	492	Impact melt rock Type-I	in situ	Also is located Type-III (This study)
14	PC	289238	8141831	469	Impact melt rock Type-I	blocks	(This study)
15	PC	289260	8141796	475	Impact melt rock Type-I	blocks	(This study)
16	PC	289292	8141739	473	Impact melt rock Type-I	blocks	(This study)
17	CA-07	288523	8141975	519	Impact melt rock Type-II	in situ	(This study)
18	CA-09	287445	8141433	573	Impact melt rock Type-II	in situ	(This study)
19	CA-14	287403	8137922	512	Impact melt rock Type-II	in situ	(This study)
20	CA-84	286769	8141191	572	Impact melt rock Type-II	in situ	(This study)
21	CA-98	288483	8141862	546	Impact melt rock Type-II	in situ	(This study)
22	CA-99	285788	8139861	512	Impact melt rock Type-II	in situ	(This study)
23	CA-116	287915	8141449	555	Impact melt rock Type-II	in situ	(This study)
24	CA-15	287329	8138048	512	Impact melt rock Type-IIIb	in situ	(This study)
25	CA-30	288622	8141819	524	Impact melt rock Type-IIIb	blocks	(This study)
26	CA-31	288618	8141878	541	Impact melt rock Type-IIIb	blocks	(This study)
27	CA-32	288761	8141952	528	Impact melt rock Type-IIIb	blocks	(This study)

28	CA-33	288782	8141964	520	Impact melt rock Type-IIIb	blocks	(This study)
29	CA-42	289420	8141587	475	Impact melt rock Type-IIIb	blocks	(This study)
30	CA-48	289864	8140891	455	Impact melt rock Type-IIIb	blocks	(This study)
31	CA-53	289729	8141111	473	Impact melt rock Type-IIIb	blocks	(This study)
32	CA-55	289670	8141108	491	Impact melt rock Type-IIIb	blocks	(This study)
33	CA-56	289200	8141666	494	Impact melt rock Type-IIIb	blocks	(This study)
34	CA-64	287524	8137989	549	Impact melt rock Type-IIIb	in situ	(This study)
35	CA-78	288506	8141972	*541*	Impact melt rock Type-IIIb	in situ	(This study)
36	CA-101	286927	8137958	492	Impact melt rock Type-IIIb	in situ	(This study)
37	CA-102	287124	8137954	489	Impact melt rock Type-IIIb	blocks	(This study)
38	CA-105	287203	8137905	501	Impact melt rock Type-IIIb	blocks	(This study)
39	CA-109	287310	8138060	509	Impact melt rock Type-IIIb	in situ	(This study)
40	CA-112	287164	8137920	502	Impact melt rock Type-IIIb	blocks	(This study)
41	CA-115	288511	8142168	*513*	Impact melt rock Type-IIIb	blocks	(This study)
42	PC	289703	8141137	476	Impact melt rock Type-IIIb	blocks	(This study)
43	PC	289622	8141211	493	Impact melt rock Type-IIIb	blocks	(This study)
44	PC	289631	8141367	475	Impact melt rock Type-IIIb	blocks	(This study)
45	PC	289589	8141466	472	Impact melt rock Type-IIIb	blocks	(This study)
46	PC	289576	8141492	478	Impact melt rock Type-IIIb	blocks	(This study)
47	PC	289298	8141682	485	Impact melt rock Type-IIIb	blocks	(This study)
48	PC	289219	8141679	513	Impact melt rock Type-IIIb	blocks	(This study)
49	PC	289148	8141664	509	Impact melt rock Type-IIIb	blocks	(This study)
50	CA-41	289289	8141696	474	Impact melt rock Type-IIIa	blocks	(This study)
51	CA-51	289833	8140992	468	Impact melt rock Type-IIIa	blocks	(This study)
52	CA-59	286469	8138042	499	Impact melt rock Type-IIIa	in situ	(This study)
53	CA-60	286531	8138205	509	Impact melt rock Type-IIIa	in situ	(This study)
54	CA-67	289308	8141703	*498*	Impact melt rock Type-IIIa	blocks	(This study)
55	CA-86	287431	8137981	525	Impact melt rock Type-IIIa	in situ	(This study)
56	CA-96	288110	8138306	548	Impact melt rock Type-IIIa	in situ	(This study)
57	CA-107	287235	8137948	518	Impact melt rock Type-IIIa	blocks	(This study)
58	PC	289187	8141677	504	Impact melt rock Type-IIIa	blocks	(This study)
59	PC	289164	8141698	509	Impact melt rock Type-IIIa	blocks	(This study)
60	PC	286596	8137922	479	Impact melt rock Type-IIIa	blocks	(This study)

61	PC	286511	8137957	474	Impact melt rock Type-IIIa	blocks	(This study)
62	PC	286485	8137982	473	Impact melt rock Type-IIIa	blocks	(This study)
63	PC	286474	8138014	488	Impact melt rock Type-IIIa	blocks	(This study)
64	PC	286514	8138181	499	Impact melt rock Type-IIIa	blocks	(This study)
65	CA-07	288523	8141975	519	Polymict impact breccia	in situ	(This study)
66	CA-08	288463	8141909	542	Polymict impact breccia	in situ	(This study)
67	CA-09	287445	8141433	573	Polymict impact breccia	in situ	(This study)
68	CA-14	287403	8137922	512	Polymict impact breccia	in situ	(This study)
69	CA-17	288442	8141822	553	Polymict impact breccia	in situ	(This study)
70	CA-23	290592	8139771	437	Polymict impact breccia	blocks	(This study)
71	CA-24	290106	8139631	450	Polymict impact breccia	blocks	(This study)
72	CA-26	289934	8139620	460	Polymict impact breccia	in situ	(This study)
73	CA-37	289007	8141970	489	Polymict impact breccia	blocks	(This study)
74	CA-46	285539	8139324	496	Polymict impact breccia	in situ	(This study)
75	CA-50	289842	8141004	467	Polymict impact breccia	blocks	(This study)
76	CA-52	289803	8140997	469	Polymict impact breccia	in situ	(This study)
77	CA-54	289673	8141137	485	Polymict impact breccia	blocks	(This study)
78	CA-65	287155	8137887	496	Polymict impact breccia	in situ	(This study)
79	CA-70	286750	8141087	573	Polymict impact breccia	in situ	(This study)
80	CA-73	288549	8142117	516	Polymict impact breccia	in situ	(This study)
81	CA-74	288544	8142117	515	Polymict impact breccia	in situ	(This study)
82	CA-79	285770	8140161	*539*	Polymict impact breccia	in situ	(This study)
83	CA-83	288216	8141655	568	Polymict impact breccia	in situ	(This study)
84	CA-84	286769	8141191	528	Polymict impact breccia	in situ	(This study)
85	CA-85	285788	8139861	552	Polymict impact breccia	in situ	(This study)
86	CA-98	288483	8141862	546	Polymict impact breccia	in situ	(This study)
87	CA-99	285788	8139861	512	Polymict impact breccia	in situ	(This study)
88	CA-103	287152	8137888	492	Polymict impact breccia	in situ	(This study)
89	CA-104	287157	8137870	495	Polymict impact breccia	in situ	(This study)
90	CA-108	287300	8137969	541	Polymict impact breccia	in situ	(This study)
91	CA-116	287915	8141449	555	Polymict impact breccia	in situ	(This study)
92	PC	289040	8141972	492	Polymict impact breccia	blocks	(This study)
93	PC	289105	8141982	494	Polymict impact breccia	blocks	(This study)

94	PC	289178	8141959	481	Polymict impact breccia	blocks	(This study)
95	PC	289795	8140997	483	Polymict impact breccia	blocks	(This study)
96	PC	289202	8141667	519	Polymict impact breccia	blocks	(This study)
97	CA-62	287385	8138621	495	Transitional granite	in situ	(This study)
98	CA-63	287405	8138404	532	Transitional granite	in situ	(This study)
99	PC	287281	8138555	505	Transitional granite	in situ	(This study)
100	PC	287334	8138599	500	Transitional granite	in situ	(This study)
101	PC	287429	8138615	511	Transitional granite	in situ	(This study)
102	PC	287403	8138489	523	Transitional granite	in situ	(This study)
103	PC	287334	8138261	545	Transitional granite	in situ	(This study)
104	CA-10	286804	8137198	508	Furnas Formation	in situ	Sandstone (This study)
105	CA-47	290181	8141186	484	Furnas Formation	in situ	Sandstone (This study)
106	GAR-19	288679	8142466	*492*	Furnas Formation	in situ	Siltstone/Sandstone (This study)
107	CA-11	287038	8137483	494	Rio Ivaí Group	blocks	Sheared quartz (This study)
108	CA-12	287477	8137543	498	Rio Ivaí Group	in situ	Conglomerate (This study)
109	CA-13	287506	8137644	494	Rio Ivaí Group	in situ	Sandstone (This study)
110	CA-43	290060	8141209	494	Rio Ivaí Group	in situ	Sandstone (This study)
111	CA-44	289957	8141070	448	Rio Ivaí Group	in situ	Conglomerate (This study)
112	CA-49	289856	8140950	459	Rio Ivaí Group	in situ	Conglomerate (This study)
113	CA-57	286526	8137764	475	Rio Ivaí Group	in situ	Diamictite (This study)
114	CA-58	286561	8137836	485	Rio Ivaí Group	in situ	Sandstone (This study)
115	CA-82	288265	8141704	565	Rio Ivaí Group	in situ	Sandstone (This study)
116	CA-100	286532	8137801	472	Rio Ivaí Group	in situ	Sandstone (This study)
117	CA-06	288572	8142041	520	(Meta)sedimentary basement	in situ	Metasandstone (This study)
118	CA-18	288548	8141034	555	(Meta)sedimentary basement	blocks	Metasandstone with spots (This study)
119	CA-19	288281	8141448	559	(Meta)sedimentary basement	blocks	Metasandstone (This study)
120	CA-21	288633	8140884	540	(Meta)sedimentary basement	in situ	Black shale (This study)
121	CA-22	290608	8139763	430	(Meta)sedimentary basement	in situ	Siltstone with quartz vein (This study)
122	CA-25	289955	8139626	461	(Meta)sedimentary basement	in situ	Metasandstone with shatter cones (This study)
123	CA-28	289338	8139343	445	(Meta)sedimentary basement	in situ	Metasandstone (This study)
124	CA-45	285466	8139642	550	(Meta)sedimentary basement	in situ	Metasandstone (This study)
125	CA-68	286188	8139796	*542*	(Meta)sedimentary basement	in situ	Metasandstone with shatter cones (This study)
126	CA-77	288536	8141972	*539*	(Meta)sedimentary basement	in situ	Metasandstone with spots (This study)

127	CA-80	285891	8139978	*554*	(Meta)sedimentary basement	in situ	Metasandstone with spots (This study)
128	CA-81	285537	8139499	*531*	(Meta)sedimentary basement	in situ	Phyllite with shatter cones (This study)
129	CA-87	287525	8137986	534	(Meta)sedimentary basement	in situ	Metarythmite (This study)
130	CA-88	287570	8137990	559	(Meta)sedimentary basement	in situ	Metasandstone with spots (This study)
131	CA-89	287604	8137983	563	(Meta)sedimentary basement	in situ	Metasandstone (This study)
132	CA-90	287616	8138011	566	(Meta)sedimentary basement	in situ	Metasandstone (This study)
133	CA-91	287628	8138026	571	(Meta)sedimentary basement	in situ	Metasandstone (This study)
134	CA-92	287619	8138050	576	(Meta)sedimentary basement	in situ	Metasandstone (This study)
135	CA-97	288153	8138273	565	(Meta)sedimentary basement	in situ	Metasandstone with shatter cones and spot (This study)
136	CA-106	287219	8137917	507	(Meta)sedimentary basement	in situ	Metasandstone (This study)
137	CA-111	291650	8141529	485	(Meta)sedimentary basement	in situ	Slate (This study)
138	CA-16	287267	8138130	505	Granite	in situ	(This study)
139	CA-20	288344	8141362	556	Granite	in situ	(This study)
140	CA-34	288942	8141949	500	Granite	in situ	(This study)
141	CA-35	288857	8141952	499	Granite	in situ	(This study)
142	CA-61	286716	8138376	524	Granite	in situ	(This study)
143	CA-66	287138	8137989	484	Granite	in situ	(This study)
144	CA-75	288538	8142105	516	Granite	in situ	(This study)
145	CA-93	287365	8139608	475	Granite	in situ	(This study)
146	CA-114	287377	8138095	572	Granite	in situ	(This study)
147	PC	286866	8138462	520	Granite	in situ	(This study)
148	PC	287279	8138108	508	Granite	in situ	(This study)
149	PC	287076	8138143	503	Granite	in situ	(This study)
150	PC	286905	8138142	511	Granite	in situ	(This study)
151	PC	286829	8138151	497	Granite	in situ	(This study)
152	PC	286722	8138030	487	Granite	in situ	(This study)
153	66	290005	8138056	*470*	Impact melt rock Type-IIIa	in situ	Monomict breccia (von Engelhardt et al., 1992)
154	67	289788	8138023	*508*	Impact melt rock Type-IIIa	in situ	Monomict breccia (von Engelhardt et al., 1992)
155	68	289439	8137918	*544*	Impact melt rock Type-IIIa	in situ	Monomict breccia (von Engelhardt et al., 1992)
156	91	288239	8138309	*543*	Impact melt rock Type-IIIa	in situ	Monomict breccia (von Engelhardt et al., 1992)
157	AM21B	289595	8141177	*501*	Impact melt rock Type-IIIa	blocks	(Hauser et al., 2019)
158	SF-5	287368	8138094	532	Impact melt rock Type-I	in situ	(Fischer, 2015)
159	SF-6	287393	8138079	536	Impact melt rock Type-I	in situ	(Fischer, 2015)

160	SF-10	287404	8138430	533	Impact melt rock Type-I	in situ	(Fischer, 2015)
161	SF-23	287844	8137815	526	Impact melt rock Type-I	in situ	(Fischer, 2015)
162	SF-27	287304	8140168	527	Impact melt rock Type-I	in situ	(Fischer, 2015)
163	SF-28	287449	8141321	586	Impact melt rock Type-II	in situ	(Fischer, 2015)
164	SF-20	288210	8138311	545	Impact melt rock Type-IIIa	in situ	(Fischer, 2015)
165	SF-4	287378	8137949	520	Polymict impact breccia	in situ	(Fischer, 2015)
166	SF-7	287355	8138008	526	Polymict impact breccia	in situ	(Fischer, 2015)
167	SF-8	287340	8137978	523	Polymict impact breccia	in situ	(Fischer, 2015)
168	SF-19	288132	8138449	521	Polymict impact breccia	in situ	(Fischer, 2015)
169	SF-2	286708	8139062	566	Transitional granite	in situ	(Fischer, 2015)
170	SF-3	286741	8189016	575	Transitional granite	in situ	(Fischer, 2015)
171	SF-11	287707	8138566	518	Transitional granite	in situ	(Fischer, 2015)
172	SF-12	287587	8138643	522	Transitional granite	in situ	(Fischer, 2015)
173	SF-13	287517	8138671	529	Transitional granite	in situ	(Fischer, 2015)
174	SF-15	287389	8138346	535	Transitional granite	in situ	(Fischer, 2015)
175	SF-21	287748	8137912	*528*	Furnas Formation	in situ	(Fischer, 2015)
176	SF-22	287839	8137899	521	Furnas Formation	in situ	(Fischer, 2015)
177	SF-24	286517	8140639	553	(Meta)sedimentary basement	in situ	(Fischer, 2015)
178	SF-1	286581	8139628	530	Granite	in situ	(Fischer, 2015)
179	SF-9	287267	8138135	517	Granite	in situ	(Fischer, 2015)
180	SF-14	287515	8138457	*527*	Granite	in situ	(Fischer, 2015)
181	SF-16	287891	8138592	507	Granite	in situ	(Fischer, 2015)
182	SF-17	288074	8138533	509	Granite	in situ	(Fischer, 2015)
183	SF-18	288150	8138463	520	Granite	in situ	(Fischer, 2015)
184	SF-25	287072	8140579	533	Granite	in situ	(Fischer, 2015)
185	SF-26	287101	8140506	*534*	Granite	in situ	(Fischer, 2015)
186	JA-06	287026	8140915	*552*	Impact melt rock Type-I	in situ	(Preuss, 2012)
187	JA-08	287059	8140572	*533*	Impact melt rock Type-I	in situ	(Preuss, 2012)
188	JA-10	286670	8139947	*531*	Impact melt rock Type-I	in situ	Pseudotachylitic breccia (Preuss, 2012)
189	JA-15	288757	8140835	*540*	Impact melt rock Type-I	in situ	(Preuss, 2012)
190	JA-17	287923	8141431	*565*	Impact melt rock Type-I	in situ	(Preuss, 2012)
191	JA-19	286706	8139499	*524*	Impact melt rock Type-I	in situ	(Preuss, 2012)
192	JA-21	286929	8138986	*529*	Impact melt rock Type-I	in situ	(Preuss, 2012)

193	JA-22	286734	8138745	*535*	Impact melt rock Type-I	in situ	(Preuss, 2012)
194	JA-23	286790	8138448	*527*	Impact melt rock Type-I	in situ	Vein in granite (Preuss, 2012)
195	JA-24	286347	8139848	*545*	Impact melt rock Type-I	in situ	Vein in granite (Preuss, 2012)
196	JA-26	287020	8140450	*530*	Impact melt rock Type-I	in situ	Pseudotachylitic breccia (Preuss, 2012)
197	JA-03	288104	8141647	*571*	Impact melt rock Type-II	in situ	(Preuss, 2012)
198	JA-13	286551	8140728	*559*	Impact melt rock Type-II	in situ	(Preuss, 2012)
199	JA-18.A	286573	8140923	*568*	Impact melt rock Type-II	in situ	(Preuss, 2012)
200	JA-18.B	286573	8140949	*568*	Impact melt rock Type-II	in situ	(Preuss, 2012)
201	JA-27/28	288132	8141650	*571*	Impact melt rock Type-II	in situ	(Preuss, 2012)
202	JA-02.A	287526	8141438	*577*	Polymict impact breccia	in situ	(Preuss, 2012)
203	JA-02.B	287104	8141647	*593*	Polymict impact breccia	in situ	(Preuss, 2012)
204	JA-04	288104	8141647	*571*	Polymict impact breccia	in situ	(Preuss, 2012)
205	JA-20	286756	8139342	*525*	Polymict impact breccia	in situ	(Preuss, 2012)
206	JA-29	288132	8141650	*571*	Polymict impact breccia	in situ	(Preuss, 2012)
207	JA-14	288674	8140917	*544*	(Meta)sedimentary basement	in situ	(Preuss, 2012)
208	JA-07	287078	8140701	*542*	Granite	in situ	(Preuss, 2012)
209	JA-12	286820	8139312	*521*	Granite	in situ	(Preuss, 2012)
210	JA-16	288179	8141497	*567*	Granite	in situ	(Preuss, 2012)
211	JA-25	286246	8139787	*541*	Granite	in situ	(Preuss, 2012)

CAPÍTULO 5
ARTIGO 2

5 ARTIGO 2

CONSTRAINING ON THE PROVENANCE OF POLYMICT IMPACT BRECCIAS FROM THE ARAGUAINHA IMPACT STRUCTURE, BRAZIL: A PETROGRAPHIC AND U-PB ZIRCON DATING APPROACH.

Carolinna da S. M. de Souza[(1)]*, Natalia Hauser[(1)], Wolf U. Reimold[(1)], Pim Kaskes[(2,3)], Philippe Claeys[(2)], Steven Goderis[(2)], Paola F. Barbosa[(1)], and Miguel A. S. Basei[(4)]

[1]Institute of Geosciences, Postgraduate Program in Geoscience, University of Brasilia, Campus Darcy Ribeiro, 70910-900, Brasília, DF, Brazil (maia.carolinna@gmail.com).

[2]Archaeology, Environmental Changes & Geo-Chemistry (AMGC), Department of Chemistry, Vrije Universiteit Brussel, Pleinlaan 2, 1050 Brussels, Belgium (pim.kaskes@vub.be, phclaeys@vub.be, steven.goderis@vub.be).

[3]Laboratoire G-Time, Université Libre de Bruxelles, ULB, Av. F.D. Roosevelt 50, 1050 Brussels, Belgium.

[4]Univerdidade de São Paulo, Instituto de Geociências, Rua do Lago 562, 05508-080, São Paulo, SP, Brazil.

ABSTRACT

Polymict impact breccias (PIB) are important types of impactites that can provide information about various aspects of the dynamics of impact crater formation. This paper is focused on detailed characterization of clast populations and matrix composition, at different scales, of the 110 m long integrated profile through breccia deposits in the northern sector of the central uplift of the Araguainha impact structure in Brazil, and selected outcrops in the south. The clast populations at the macroscopic scale are dominated by slates, whereas at the meso- and microscopic scales sandstones are becoming more important. The breccias comprise heterogeneous metasedimentary components from the basement, sedimentary clasts from the overlying Paraná Basin sequence, and rare clasts from the Cambrian/Ordovician Araguainha granite intruded into the basement. The U-Pb provenance analyses on zircon from matrices of PIB and

from potential target rocks indicate that the main precursor rocks for the PIB were from the lowermost part of the Paraná Basin and the Neoproterozoic (meta)sedimentary sequences. Shock effects in PIB include shatter cones in slate and metasandstone clasts, single or multiple sets of planar deformation features in quartz grains, and some granular zircon grains. The presence of impact melt clasts/micro-clasts suggest a shock pressure range from <10 to ca. 50 GPa. The (meta)sedimentary basement of the Paraná Basin at Araguainha could be related with sedimentation in proximal basins to the Arenópolis Arc, to northeast of the Araguainha. The petrographic characterization and the provenance analyses suggest that the maximum penetration depth of the bolide was likely to the interface between the lowermost Paraná Basin strata and (meta)sedimentary sequences, i.e., a depth of 2000 m.

5.1 Introduction

Polymict impact breccias (PIB) are important types of impactites within and around many impact structures (e.g., Stöffler and Grieve, 2007; Stöffler et al., 2013; 2018). Such breccias may provide key information about various aspects of the dynamics of impact crater formation. This includes the composition of the now obliterated target rock volume, the generation of the breccia components within the transient crater cavity, the variation of shock-metamorphic degrees of breccia constituents, and the dynamics of melting. Furthermore, information about the mixing of target rock components within the crater, and the depositional mechanisms inside and outside of the crater may be provided (e.g., Stöffler et al., 2013; Osinski et al., 2016; Siegert and Hecht, 2018; Kaskes et al., 2022, and references therein).

Polymict impact breccias are classified into two basic types according to typical clast contents and matrix composition – (1) the framework of the polymict lithic breccia, composed entirely of lithic and mineral fragments and a matrix of the same terrigenous materials; and (2) suevite, which comprises mineral and lithic fragments, including cogenetic impact melt particles in a glassy or crystallized state (Stöffler and Grieve, 2007; Stöffler et al., 2018). The term “suevite” was originally coined for some of the polymict breccias from the Ries impact structure, Suevia, southern Germany (Sauer, 1920). Suevite is now

known from a large number of impact structures (e.g., Chicxulub – Claeys et al., 2003; Kaskes et al., 2022; Bosumtwi – Coney et al., 2010; Ferrière et al., 2010; Manicouagan – Thompson and Spray, 2017; Gardnos – Kalleson et al., 2010; inter alia). The genesis of suevite is still strongly debated (e.g., Grieve et al., 1977, 2015; Osinski et al., 2008, 2016; Artemieva et al., 2013; Stöffler et al., 2013) in terms of formation and emplacement.

Lithic fragments in polymict impact breccia may provide information about deeply buried lithologies of the target. Thus, the comparison of the populations of target rock-derived clasts and their distribution in the breccia packages can assist to reconstruct aspects of target stratigraphy and the dynamics of crater formation (e.g., Stöffler et al., 2004, 2013; Wittmann et al., 2004; Reimold et al., 2009, 2013; Osinski and Pierazzo, 2013; Siegert et al., 2017) and provide information about geological setting, regional distribution of impact breccia, the composition of clasts and melt particles, their relation with recognized target rocks, degree and distribution of shock metamorphism, contact relationships with other impactites, melt fragment abundance and morphology, and melt chemistry including, at times, analysis of traces of meteoritic components (e.g., Stöffler et al., 2013; Mader and Osinski, 2018; Feignon et al., 2022; and references therein).

The 40-km-diameter Araguainha impact structure is the largest complex impact structure known in South America. It is centered at 16º48'45" S / 52º59'02" W at the border between Goiás and Mato Grosso states in Central Brazil. The structure was formed between ca. 252 and 259 Ma ago (Tohver et al., 2012; Erickson et al., 2017; Hauser et al., 2019) in the northeasternmost part of the intracontinental Paraná Basin (Fig. 5.1A). In addition providing excellent opportunities to study cratering processes, the Araguainha impact structure allows detailed study of the not well-known basement of the Paraná Basin, because it represents a stratigraphic window into the underlying impact-uplifted basement. The basement includes a Cambrian/Ordovician alkali granite (von Engelhardt et al., 1992; Machado et al., 2009; Tohver et al., 2012) intruded into (meta)sedimentary basement that is currently assumed to be part of the Paraguay Belt of the Tocantins Province (Fig. 5.1; Almeida, 1984; Sánchez, 2006; Yokoyama, 2008; Souza et al., 2024; Frugis et al., 2024).

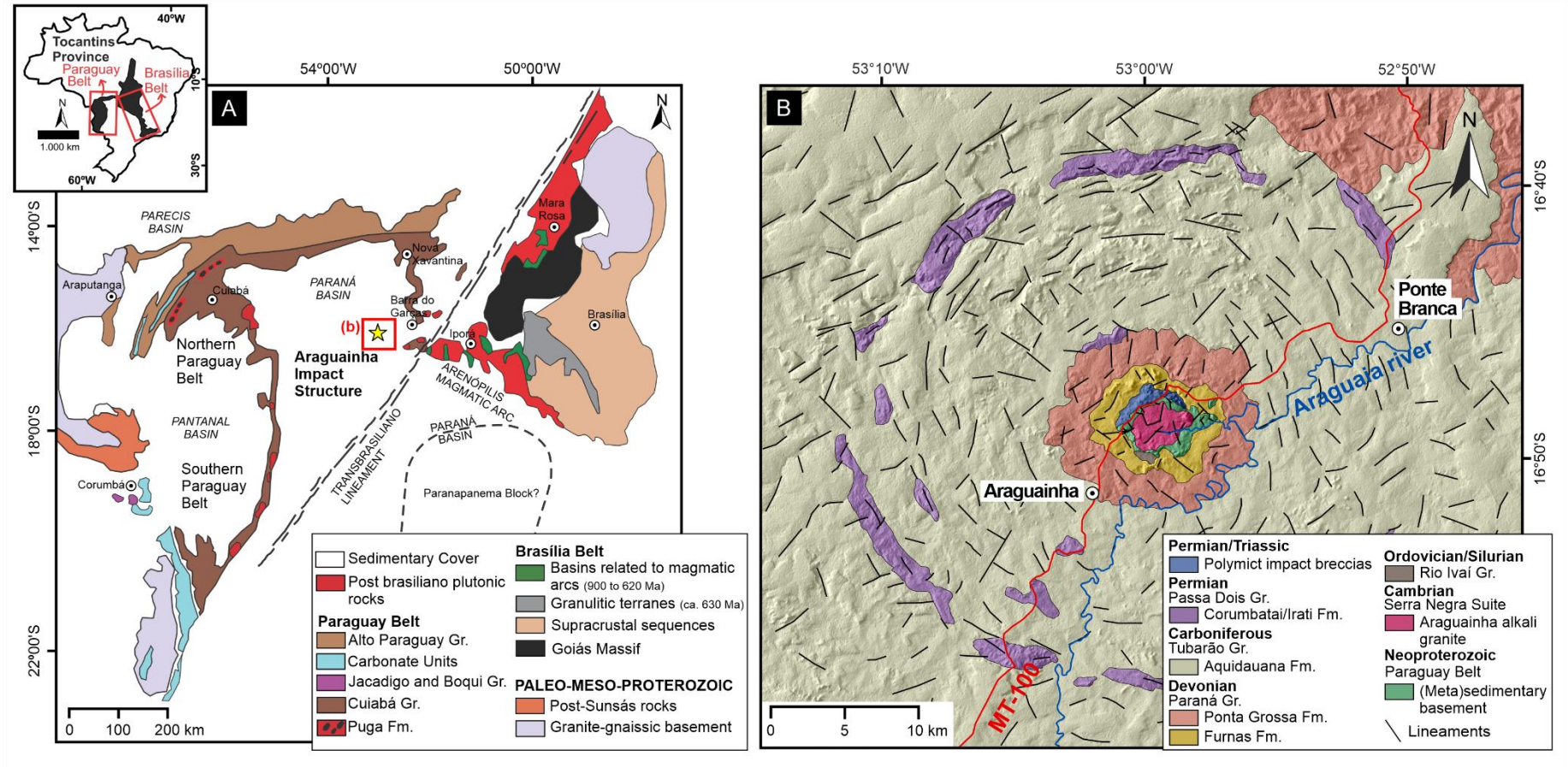

Figure 5.1 (A) Location of the Tocantins Province in the Brazilian territory and simplified geological map of the Paraguay and Brasília mobile belts. The Araguainha impact structure is also indicated. Modified after Leite et al. (2021). (B) Geological map of the Araguainha impact structure georeferenced against the WGS84 UTM Zone 22S geodetic datum, overlain on at TanDEM-X radar satellite image (~53 x 61 km wide) courtesy of the German Aerospace Center – DLR, Oberpfaffenhofen, Germany and surface reflectance (Landsat 8/OLI) imagery.

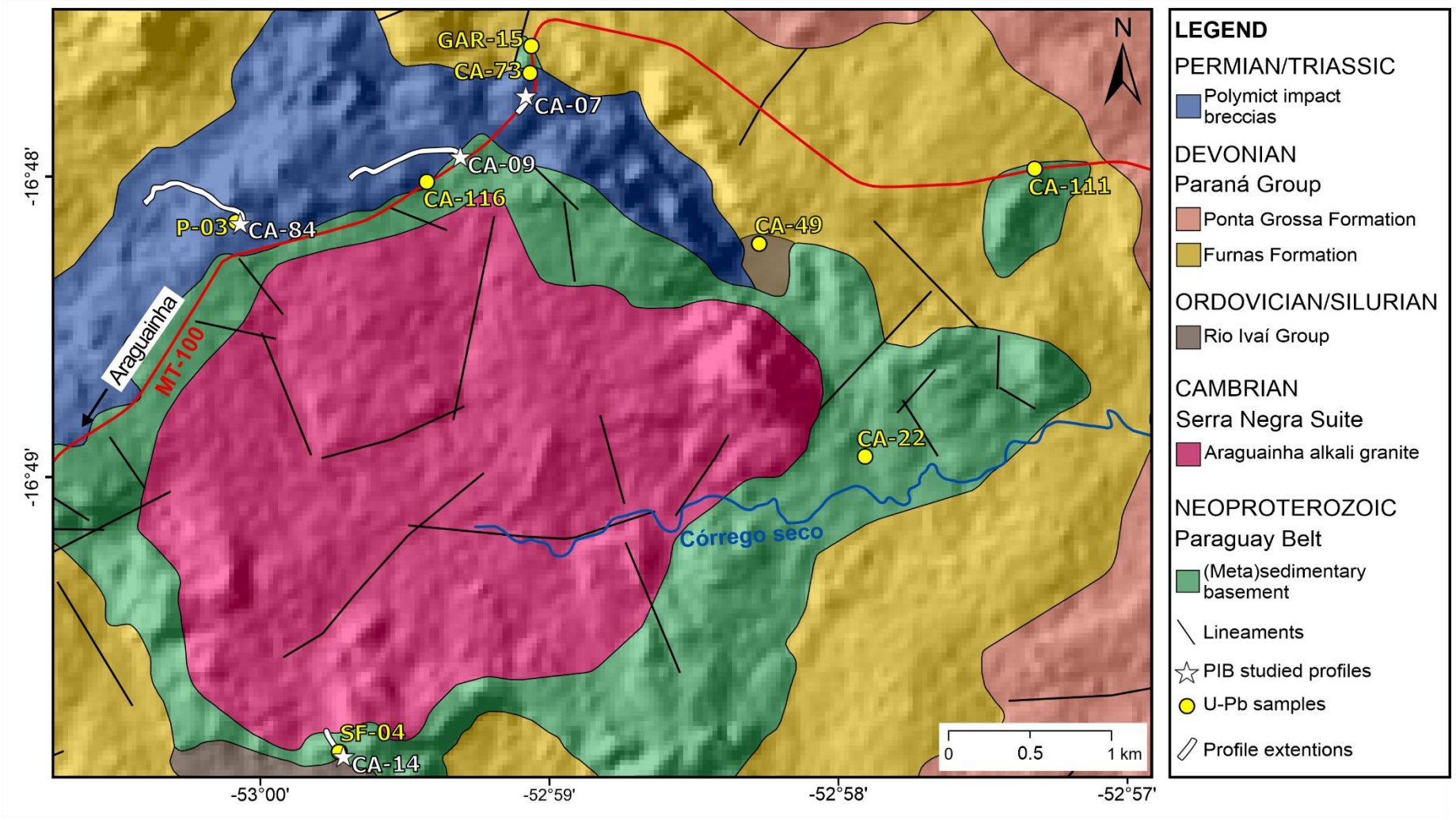

Figure 5.2 Geological map of the Araguainha central uplift region of 16 km diameter, after Souza et al. (2024). The outcrops of polymict impact breccia profiles and basement exposures used in this work are indicated in the map.

The entire structure was eroded, but the central uplift region is still reasonably well preserved (Fig. 5.2), with good exposures of impact-related rocks and especially basement of the crater floor. Excellent outcrops of polymict impact breccia are known from the northern and, to a lesser degree, from the southern parts of the central uplift. Field observations and some petrographic information have been reported in the past about the Araguainha polymict impact breccias occurrences (e.g., Crósta et al., 1981; von Engelhardt et al., 1992), but generally the breccias have not been subject to very detailed analysis yet. Besides this earlier work, only one quite limited study of a PIB deposit in the northern part was reported by de Marchi (2015; also de Marchi et al., 2016). Recently Souza et al. (2024) presented detailed information about these breccia deposits in the northern and southern parts of the central uplift and first observations about the contact relationships to underlying (meta)sedimentary pre-ordovician basement.

This paper is focused on the detailed characterization of clast populations and matrix composition, at different scales, including optical petrography of the polymict impact breccias. In addition, micro-X-Ray Fluorescence (μXRF), X-Ray Diffraction (XRD), Scanning Electron Microscopy (SEM), and Quantitative Evaluation of Minerals by Scanning Electron Microscopy (QEMSCAN) studies were conducted. To further characterize the main potential target rocks and to study the shock metamorphism, U-Pb provenance analysis on zircon grains has been carried out on the polymict impact breccias and on some of the potential target rocks from the basement. Questions like: what was the likely target stratigraphy and which part of it was implicated in breccia formation? what are the main features of the matrix and clast populations in terms of clast types, morphology, size, provenance, degree of shock metamorphism, and melt particles found? which material is part of the Araguainha basement in the megablock zone of the outer central uplift? will be approached here. The combined findings will contribute to understanding genesis of the polymict lithic and suevitic breccias, the geologic context of the basement, and infer the maximum depth of projectile penetration.

5.2 Geological Setting

5.2.1 Regional Stratigraphy

The target rocks exposed in the area of the Araguainha impact structure represent a good stratigraphic window into the northeasternmost part of the Paraná Basin (Milani et al., 2007) and its underlying basement. The Tocantins Structural Province (Fig. 5.1A; Almeida, 1984) constitutes a large orogenic belt that represents one of the most important tectonic features of the Precambrian basement of Brazil (Babinski et al., 2018). It is composed of the Paraguay, Brasília, and Araguaia mobile belts (Hasui, 2012), which result from the collision between the Amazonian, São Francisco, and Paranapanema cratonic blocks between ca. 540 and 520 Ma (Bandeira et al., 2012).

The Paraná Basin was developed between the Paleozoic and Mesosoic on this basement. Part of the basement of the Paraná Basin has been correlated with the Paraguay Belt by Yokoyama (2008) and Cordani et al. (2009). Tectonic models for the evolution of this belt (e.g., McGee et al., 2014; Frugis et al., 2024) suggest that the potential sources involve predominantly the Amazonian Craton and smaller contribution from the Goiás Magmatic Arc.

The Paraguay and Brasilia Belts

The Paraguay Belt comprises metamorphosed Neoproterozoic and Cambrian sedimentary strata from the Cuiabá Group, Puga Formation, Araras Group, and Alto Paraguay Group (Fig. 5.1A and Table 5.1). The Cuiabá Group, the basal unit of the belt, is composed of metasedimentary rocks in under greenschist facies, predominantly metarenites and phyllites. Neoproterozoic maximum depositional ages of 652 ± 5 Ma (Babinski et al., 2018) and 900 ± 10 Ma (Frugis et al., 2024) have been obtained through provenance studies on detrital zircon U-Pb ages. On top of the Cuiabá Group, diamictite of the Puga Formation and carbonates of the Araras Group were deposited (McGee et al., 2014). The maximum depositional age for the Puga Formation (706 ± 9 Ma; Babinski et al., 2013) and correlation of the $\delta^{13}C$ (–5.0‰) and $^{87}Sr/^{86}Sr$ (0.7080) ratios from carbonates of the Araras Group (Nogueira et al., 2003) with the global signature suggest that these units represent the ca. 635 Ma end-Cryogenian

glaciation (McGee et al., 2014). The upper unit of the belt, which lacks metamorphism, is known as the Alto Paraguay Group. It is composed of deltaic sandstone, shale, siltstone, arkose, conglomerate, and laminated mudstone (Dantas et al., 2009). The uppermost unit of this group, the Diamantino Formation, has a maximum depositional age of 560 ± 13 Ma, which has been interpreted as the youngest time of deposition of Paraguay Belt material (McGee et al., 2014).

The last metamorphic event in the Paraguay Belt was delimited by $^{40}Ar/^{39}Ar$ dating of low-grade metamorphic minerals to ca. 540 Ma for the Nova Xavantina Metavolcanosedimentary Sequence (Geraldes et al., 2003, 2008). Neoproterozoic magmatism is also related to the final phase of geological activity in the Paraguay Belt and involved distinct granitic intrusions (Godoy et al., 2010). McGee et al. (2014) suggested, based on U-Pb zircon isotope analyses for the Diamantino Formation, that final sedimentation, deformation, and metamorphism in the Paraguay Belt took place between 540 and 510 Ma.

The Nova Xavantina Metavolcanosedimentary Sequence was considered contemporaneous to the Rio Bacuri Sequence by Pinho (1990) and interpreted as an embryonic phase of seafloor spreading along the Paraguay Belt or as a retroarc basin (Lacerda Filho et al., 2004). Silva et al. (2022) dated these volcanic rocks through U-Pb on zircon analyses and indicated that they were formed in at least three magmatic events, starting with the formation of ca. 745 Ma seafloor basalts (now metamorphosed) and felsic volcanics dated at ca. 735 Ma, and ending with emplacement of gabbro at ca. 714 Ma.

The granitic intrusions in the region of the Paraguay Belt belong to the Brazilian Granitic Province, which includes seven syn- to post-tectonic granitic bodies grouped into two suites known as the São Vicente and Serra Negra suites (Lacerda Filho et al., 2004, 2006). They were emplaced between ca. 550 and 500 Ma (Godoy et al., 2007, 2010). Tohver et al. (2012) obtained an age of 512 ± 11 Ma for shocked zircons from a sample of the Araguainha granite, from the Serra Negra Suite. Emplacement of this granite may be related to the evolution of the Paraguay Belt (Godoy et al., 2007, 2010) and to other post-tectonic granites of the Brasilia and Paraguay orogenic belts (Pimentel et al., 1996).

Table 5.1 Schematic stratigraphic relationship between northern and southern sectors of the Paraguay Belt. The Maximum depositional age is also indicated. Modified after Vasconcelos (2018) and Leite et al. (2024).

<table>
<tr><th colspan="8">Southern sector of the Paraguay Belt</th><th colspan="5">Northern sector of the Paraguay Belt</th><th rowspan="2">Maximum Depositional Age</th></tr>
<tr><th colspan="2">Boggiani (1997)</th><th colspan="2">Lacerda Filho et al. (2004)</th><th colspan="2">Campanha et al. (2011)</th><th colspan="2">Alvarenga (1980); Alvarenga and Saes (1992)</th><th colspan="2">Tokashiki and Saes (2008)</th><th colspan="2">Alvarenga et al. (2007); Bandeira et al. (2012)</th></tr>
<tr><td rowspan="4">Corumbá Gr.</td><td>Guaicurus Fm.</td><td rowspan="4">Corumbá Gr.</td><td rowspan="2">Tamengo Fm.</td><td rowspan="4">Corumbá Gr.</td><td>Guaicurus Fm.</td><td rowspan="4">Detritic Upper Unit</td><td rowspan="4" colspan="2">Alto Paraguay Gr.</td><td rowspan="4">Alto Paraguay Gr.</td><td>Diamantino Fm.</td><td rowspan="4">560 ± 13 Ma (McGee et al., 2014)</td></tr>
<tr><td>Tamengo Fm.</td><td>Tamengo Fm.</td><td>Sepotuba Fm.</td></tr>
<tr><td>Bocaina Fm.</td><td>Bocaina Fm.</td><td>Bocaina Fm.</td><td>Raizama Fm.</td></tr>
<tr><td>Cerradinho Fm.</td><td>Cerradinho Fm.</td><td>Cerradinho Fm.</td><td>Serra Azul Fm.</td></tr>
<tr><td colspan="2">Cadieus Fm.</td><td rowspan="2">Jacadigo Gr.</td><td>Santa Cruz Fm.</td><td colspan="2" rowspan="2">Puga Fm.</td><td rowspan="2">Carbonatic Intermediate Unit</td><td rowspan="2">Cuiabá Gr.</td><td rowspan="2">Coxipó Fm.</td><td colspan="2">Araras Gr.</td><td rowspan="2">706 ± 9 Ma (Babinski et al., 2013)</td></tr>
<tr><td colspan="2">Puga Fm.</td><td>Urucum Fm.</td><td colspan="2">Puga Fm.</td><td colspan="2">Puga Fm.</td></tr>
<tr><td colspan="2" rowspan="4">Cuiabá Gr.</td><td rowspan="4">Cuiabá Gr.</td><td>Carbonatic Subunit</td><td rowspan="4">Cuiabá Gr.</td><td rowspan="4">Agachi Schists</td><td>Turbiditic-Glaciogenic Unit</td><td rowspan="4">Cuiabá Gr.</td><td>Acorizal Fm.</td><td rowspan="4" colspan="2">Cuiabá Gr.</td><td>652 ± 5 Ma (Babinski et al., 2018)
900 ± 10 Ma (Frugis et al., 2024)</td></tr>
<tr><td>Pelitic Subunit</td><td rowspan="3">Lower Unit</td><td rowspan="3">Campina de Pedra Fm.</td></tr>
<tr><td>Psamitic Subunit</td></tr>
<tr><td>Conglomeratic Subunit</td></tr>
<tr><td colspan="8">Rio Bacuri Sequence</td><td colspan="5">Nova Xavantina Metavolcanosedimentary Sequence</td><td></td></tr>
</table>

To the southeast of the Paraguay Belt, rocks of the southern Goiás Magmatic Arc of the Brasilia Belt – the Arenópolis Arc – are exposed (Fig. 5.1A; Pimentel et al., 2000). This arc consists of dioritic-tonalitic-granitic orthogneisses with calcic to calcalkaline composition, exposed between bands of volcano-sedimentary sequences (900-540 Ma; Pimentel and Fuck, 1987; Pimentel, 2016; Marques et al., 2019). The last major metamorphic event recorded in the Arenópolis Arc is represented by granite-gneisses that intruded the metavolcanic-sedimentary sequences at 630 Ma, compatible with the last regional metamorphic evidence in the Brasília Belt (Della Giustina et al., 2011; Pimentel, 2016; Pimentel and Fuck, 1987, and references therein).

The Paraná Basin

The Paraná Basin covers an area of around 1.5 million km² (Milani et al., 2007) that records a long period of sedimentary accumulation. Milani (1977) recognized six magmatic-sedimentary supersequences deposited from the Ordovician to the Late Cretaceous (Rio Ivaí, Paraná, Gondwana I, Gondwana II, Gondwana III, and Bauru). Fernandes and Coimbra (1996) separated the Upper Cretaceous sequence of the Paraná Basin, and considered this sequence to have been accumulated in the new Bauru Basin after the breakup of Gondwana (Milani et al., 2007). The Rio Ivaí and Paraná supersequences are the oldest sedimentary rocks (Ordovician-Devonian). The thickness of the lowermost package varies considerably with some elongated depocenters striking SW-NE direction (Henrique-Pinto et al., 2021).

The Rio Ivaí Group records deposition in fluvial to shallow marine environments. This unit marks the beginning of the sedimentary infill of the Paraná Basin controlled by the Transbrasiliano Lineation (Milani and Ramos, 1998). The Rio Ivaí Group is composed of conglomerates, diamictites, sandstones, and pelites that have been grouped into three formations that represent the marine transgression cycle. The minimum age of deposition of 436 ± 8 Ma was obtained through Rb-Sr dating on whole-rock siltstone from the Vila Maria Formation (Mizusaki et al., 2002). Gezatt (2011) recorded populations of detrital zircon with Neoproterozoic ages between 900-760 Ma. The maximum depositional age for Iapó (478 ± 8 Ma) and Alto Garças formations (466 ± 6 Ma)

have been obtained through provenance studies on detrital zircon U-Pb ages (Henrique-Pinto et al., 2021).

Assine (1996) characterized and subdivided the Furnas Formation into three units: Unit I (lower), composed of conglomeratic sandstones with clasts of shale; Unit II, consisting of sandstones interbedded with siltstones and claystones containing ichnofossils; and Unit III (upper) that shows a sharp increase in grain size and sediment supply, comprising assemblages with residual gravel deposits. The maximum depositional age of 485 ± 5 Ma (lower unit; Henrique-Pinto et al., 2021), 456 ± 4 Ma (middle unit; Henrique-Pinto et al., 2021), and 526 ± 23 Ma (Santos et al., 2015) have been obtained through provenance studies on detrital zircon U-Pb ages, which supports a dominant Neoproterozoic contribution from the Goiás Magmatic Arc. The Ponta Grossa Formation records a predominantly horizontal plane-parallel stratification and is composed mainly of rosy mudrocks and grayish siltstones with sparse sub-angular clasts of quartz (Henrique-Pinto et al., 2024). Based on geochemical characterization, Montibeller et al. (2017) suggested a mixture of provenance sources (arc and passive margin derived material).

Henrique-Pinto et al. (2021, 2024) reported a provenance study of samples from the lowermost part of the Paraná Basin sequence through U-Pb and Lu-Hf isotope analyses on detrital zircon. They observed a main age peak at ca. 610 Ma and a second subordinate peak at 2.1-2.2 Ga. This suggests that the main source(s) of detrital mass were from the Brasília, Don Feliciano, and Ribeira fold belts, and the supracrustal metasedimentary sequences of the Neoproterozoic Araçuaí, Ribeira, and Brasília fold belts. Additionally, the lowermost Paraná Basin strata document a recycled orogenic provenance with a mixing trend between mature polycyclic quartzose detritus and mafic/intermediate contributions (ibid).

5.2.2 Local Geology at Araguainha impact structure

From bottom to top, the stratigraphic section affected by the Araguainha impact event includes (Fig. 5.1B): Neoproterozoic (meta)sedimentary rocks thought to belong to the Cuiabá Group of the Paraguay Belt (Almeida, 1984; Alvarenga et al., 2004); the post-collisional Ordovician/Cambrian porphyritic alkali granite that was assigned to the Serra Negra Suite of the Brazilian Granitic

Province (Pimentel et al., 1996; Lacerda Filho et al., 2004, 2006; Godoy et al., 2007, 2010; Silva et al., 2016); and the nearly complete succession of sedimentary strata of the Paraná Basin (Milani et al., 2007), including the Ordovician-Silurian Rio Ivaí Group, the Devonian Paraná Group (Furnas and Ponta Grossa formations), the Carboniferous Tubarão Group (Aquidauana Formation), and the Passa Dois Group (Irati and Corumbataí formations). These target rocks are distributed into four distinct Araguainha morphological domains (Theilen-Willige, 1981; Lana et al., 2006, 2007), which include a central peak, an annular basin, and two concentric rings within the outer ring syncline of the crater.

The central peak area comprises the innermost core terrane (4-5 km wide) composed of porphyritic alkali granite, characterized as a magnesium-rich, post-collisional, A-type granite (Silva et al., 2016). This granitic core is surrounded by an annular belt of metasandstones and phyllites that has been assigned to the Cuiabá Group (e.g., Sánchez, 2006; Yokoyama, 2008; Souza et al., 2024). This basement is surrounded by a belt of polymict impact breccias (PIB), intercalated with impact melt rocks (IMR), and strata from the lowermost sequences of the Paraná Basin. The Rio Ivaí Group is rare occurrences limited to southern sector of the collar composed of conglomerates, diamictites, sandstones, and pelites (UnB-IG, 2012; Souza et al., 2024). Furnas Formation occurs in a zone of upright to overturned, and strongly deformed sedimentary rocks (von Engelhardt et al., 1992; Lana et al., 2007, 2008; Hippertt et al., 2014) – mainly kaolinitic white sandstone, with some conglomerate layers, and siltstone (Assine, 1996), which form the complexly folded and faulted megablock zone (Lana et al., 2008).

The annular basin is a relatively flat depression composed of yellow-ochre to brownish siltstone and sandstone of the Ponta Grossa Formation, and, further outward, reddish-pinkish sandstone and (minor) conglomerate of the Aquidauana Formation. The two ring structures proposed by Lana et al. (2007) are supposed to occur at 10-12 and 14-18 km from the center of the structure. The inner ring structure would mark the extent of deformation related to the outward movement of the target rocks during collapse of the central uplift, and the concentric ring further out would record additional outward movement of the target rocks (Lana et al., 2008). The crater rim area is composed of kilometer-scale blocks of variably deformed rocks from the upper Paleozoic units of the Paraná Basin – black shale

and silicified limestones from the Irati Formation, and siltstone and sandstone from the Corumbataí Formation. There is also sandstone, siltstone, and diamictite from the upper part of the Aquidauana Formation. Associated with the Passa Dois Group, stromatolitic growths were identified in silicious rock (e.g., chert).

Impact generated rocks: the polymict impact breccias

The impact-related rocks identified in the Araguainha impact structure include impact melt rocks and polymict impact breccias. Previously, von Engelhardt reported the presence of monomict impact breccias; however, this hypothesis was refuted by Souza et al. (2024) based on detailed field and petrographic analyses.

Impact melt rocks are distinguished in three types based on composition and type of occurrence (Souza et al., 2024): IMR Type-I, pods and dikes of granitic composition; IMR Type-II, in the form of deformed clasts of mainly highly silicious composition in polymict impact breccia; and IMR Type-III, part of the part-melted masses occurring in a belt along the contact with the granitic core. These Type-III breccias are highly silicic composition.

Limited U-Pb isotopic analyses were reported for Araguainha IMR. Tohver et al. (2012) analyzed zircon grains from IMR Type-I by the SHRIMP U-Pb method to obtain an age for the impact event. The sample yielded a few concordia ages of 247.8 ± 3.8 Ma for neoblastic zircon grains with granular texture, which was interpreted as a minimum age for the impact event. Hauser et al. (2019) observed different impact-induced microstructures on external surfaces of zircon grains of a IMR Type-III. Dating involved LA-ICP-MS and SIMS U-Pb methods. Their best age (251.5 ± 2.9 Ma) was obtained on a FRIGN zircon (Cavosie et al., 2018).

Two previous studies (von Engelhardt et al., 1992; de Marchi, 2015 - also see de Marchi et al., 2016) were carried out on the Araguainha polymict impact breccia, and they were essentially of a descriptive nature. Von Engelhardt et al. (1992) characterized the breccias as a mix of variously shaped, unsorted fragments of meter to centimeter size, embedded in a fine-grained clastic groundmass. They related that the breccia components were from granitic basement and the overlying sedimentary sequence. This interpretation was made

on the basis of knowledge at this time about the stratigraphy at the Araguainha Dome. They also divided the PIB into a lower and an upper unit based on the breccia clast components, presence or not of impact melt rocks.

De Marchi (2015; also de Marchi et al., 2016) described a 575 m long profile covering a 75 m vertical interval through polymict breccia. They characterized the clast population in terms of size, shape, provenance, and the ratios between clast and matrix proportions. Unlike von Engelhardt et al. (1992), de Marchi (2015) related the provenance of breccia components to all units possibly affected by the impact, including pre-ordovician basement strata from the Cuiabá Group and sedimentary rocks from the upper Paraná Basin sequence (Passa Dois Group). Several impact melt micro-clasts were identified in thin sections. These observations indicated that there was no general change of any of the studied parameters along this section through this breccia deposit (see also Crósta et al., 2019).

In summary, previous work provided brief descriptions of breccia deposits and attempted to relate the clast provenance to all possible target units. Recently, Souza et al. (2024) reported a more detailed characterization of the components in polymict breccias occurring over 4 km in the northern part of the central uplift, as well as in limited occurrences in the southern part. The PIB components are dominated by phyllite, slate, and (meta)sandstone clasts, with very rare granitic fragments (Souza et al., 2024).

5.3 Sampling and Methodology

5.3.1 Geological mapping

For the present work, we carried out geological mapping in the central uplift of the Araguainha impact structure over different field seasons between 2019 and 2021. Outcrops of both breccia deposits and (meta)sedimentary rocks were analyzed in detail. The polymict impact breccias occur mainly in meter to hundreds of meters long road cuts along the MT-100 state road with easy accessibility (Fig. 5.2). Our descriptions provide information on the geographic locations including elevations, which were determined with a Garmin Etrex 10 Global Positioning System (GPS). Lithologies, clast populations, detailed

descriptions of the profiles, and contact relationships between breccia and country rocks were recorded.

5.3.2 Sampling

In total, forty-nine samples of breccia groundmass, clasts of impact melt rock in the PIB (IMR Type-II, Souza et al., 2024), and (meta)sedimentary rocks, were collected. From these, forty-eight polished thin sections were prepared for petrographic analysis. Of these, forty thin sections were utilized for micro-X-ray fluorescence spectrometry (µXRF), eleven for quantitative mineral evaluation by scanning electron microscopy (QEMSCAN), and two for scanning electron microscopy (SEM); six samples were subjected to X-ray diffraction (XRD), and nine samples were prepared for detrital zircon U-Pb isotope analysis. A table of the analyzed samples and summarizing the methodologies for these instrumental techniques is given in Supplementary Material 1.

5.3.3 Profiles through breccia deposits

Four profiles of breccia deposits were selected as they present extensive and well exposed outcrops, and allow to integrate information from various elevation levels, covering the entire thickness of breccia deposits in this area (from elevation 500 to 610 m.a.s.l). Three profiles occur in the northern sector (CA-07, CA-09, CA-84) and one in the southern sector (CA-14) of the central uplift (Fig. 5.2). The exposures in the north were located along the MT-100 state road (CA-07) and another mainly along a winding, upward sloping dirt road (CA-09 and CA-84). The two previous profiles analyzed by von Engelhardt et al. (1992) and de Marchi (2015) were reanalyzed and correspond, respectively, to CA-09 and CA-84 profiles. Many outcrop areas that were studied in 2021-2022 have been modified during extensive roadworks along the MT-100 (e.g., the CA-07 profile was completely paved over). In the southern sector, the CA-14 exposure is limited and only occurs along a dirt track of 0.8 km length.

The detailed characterization of quantitative clast and matrix descriptions were made at different scales: a) macroscopic, in the field, where the clasts/particles of < 1 cm size was considered breccia matrix; b) mesoscopic, in hand specimen, where clasts/particles < 4 mm were considered matrix; and c)

microscopic, in thin section, where clasts/particles < 0.55 mm was considered matrix. We considered that when melt content is in excess of 15 % it denotes a suevite type, whereas breccias with melt content below 15% denotes polymict lithic breccia. The semiquantitative descriptions for breccia of the profiles in the northern sector, at macro-, meso-, and microscopic scales, are provided in the Supplementary Material 2.

Clast population analysis entailed determination of the main characteristics of clasts, such as type of lithology, sorting, size, and shape, as well as the relative proportions of different lithology types, and the proportions of total clast content and matrix. We analyzed the profiles by sections, normally of approximately 5 m length, except for profile CA-07 (northern area) where sections were distinguished due to changes in abundance of specific types of clasts and/or changes in matrix color.

5.3.4 Petrography

Forty-six polished thin sections from breccia matrix were studied with a polarizing microscope (Zeiss Axioscope 5) equipped with a digital camera system (ZEISS Zen 3.4 software) at the Micropaleontology Laboratory and with a polarizing microscope (Zeiss Axioscope 40) in the Geodynamic, Geochronological and Environmental Studies Laboratory (LEGGA), both of the Geosciences Institute of the University of Brasilia (IG-UnB). The main purpose was to generate modal data, abundances of different clast types and matrix by point-counting (600 points per sample). Clast morphology, abundance of melt particles, and shock metamorphic features in microclasts were recorded as well. Shock levels were estimated based on the shock stage scheme for quartzo-feldspathic rocks (Stöffler et al., 2018) and the mineral abbreviations used are from Warr (2021).

5.4 Results

We provide detailed descriptions of the polymict impact breccias, including their characterization in terms of matrix composition and clast types. These details are then placed in a geological context through the profile descriptions. For the XRD results, SEM images, and more information on the profile

descriptions, refer to Supplementary Material 2. Next, we describe the analyzed basement rocks, with outcrop photographs available in Supplementary Material 3. Finally, we present the provenance data for both the polymict impact breccias and the basement rocks studied. The U-Pb results can be found in Supplementary Material 4.

5.4.1 Polymict impact breccia

The polymict impact breccias from the Araguainha impact structure are exposed mainly in the northern part of the central uplift, besides occurrence of limited exposures in the southern part. For the current study, four breccia deposits covering the elevation interval of 500 to 610 m.a.s.l. were selected for investigation. These deposits designated as CA-07, CA-09, CA-84, and CA-14 (Fig. 5.2) were previously introduced by Souza et al. (2024). These breccia deposits can be generally characterized as poorly to moderately sorted and matrix-supported, with a matrix that is composed of fine-grained, mostly sandy to pelitic clastic material. The clastic components are mainly derived from metasedimentary and sedimentary sources, which includes slate, phyllite, metasandstone, quartz pebbles, conglomerate, sandstone, shale, as well rare granitic clasts (Souza et al., 2024).

Petrography of polymict breccia components

Matrix. The matrix of the breccias is mainly composed of light to dark grey color (Fig. 5.3A) – sometimes with reddish hues due to impregnation with Fe-bearing phases by alteration. The matrix of the breccia is fine-grained, sandy, and mostly composed of quartz and lithic fragments (e.g., slate and sandstone). The majority of samples have a rather friable matrix, but some of them have a dense, cohesive matrix.

In thin section, the breccia matrix is generally black to dark grey in cross-polarized light (Figs. 5.4A-5.4B), and composed of angular to subangular lithic and mineral micro-clasts of mostly quartz composition. Quartz micro-fragments are predominant. Sericite/muscovite, biotite, plagioclase, zircon, and Fe-Ti oxide

minerals are observed as well. In addition, albite, illite, kaolinite, and K-feldspar have been recognized by QEMSCAN analysis (Fig. 5.5).

Minerals like hematite and illite were identified on the polymict impact breccia matrix via XRD analysis (Fig. S2A). They are probably related with secondary overprint. At higher magnification by SEM analysis, the nature of the PIB matrix is revealed as purely terrigenous (Fig. S2B). Most of the micro-clasts have angular to subangular shapes. These micro-clasts are strongly cataclastic and fractured. Fe-Ti oxide grains of up to 37 µm size are disseminated in the matrix and has rounded to subangular shape. The compositional µXRF maps indicate high intensity in Si and relatively low intensity in Al in the PIB matrix (Figs. 5.4C-5.4E). For the rest of the elements (K, Fe, and Ti), the µXRF results gave only spurious concentrations (Figs. 5.4F-5.4H).

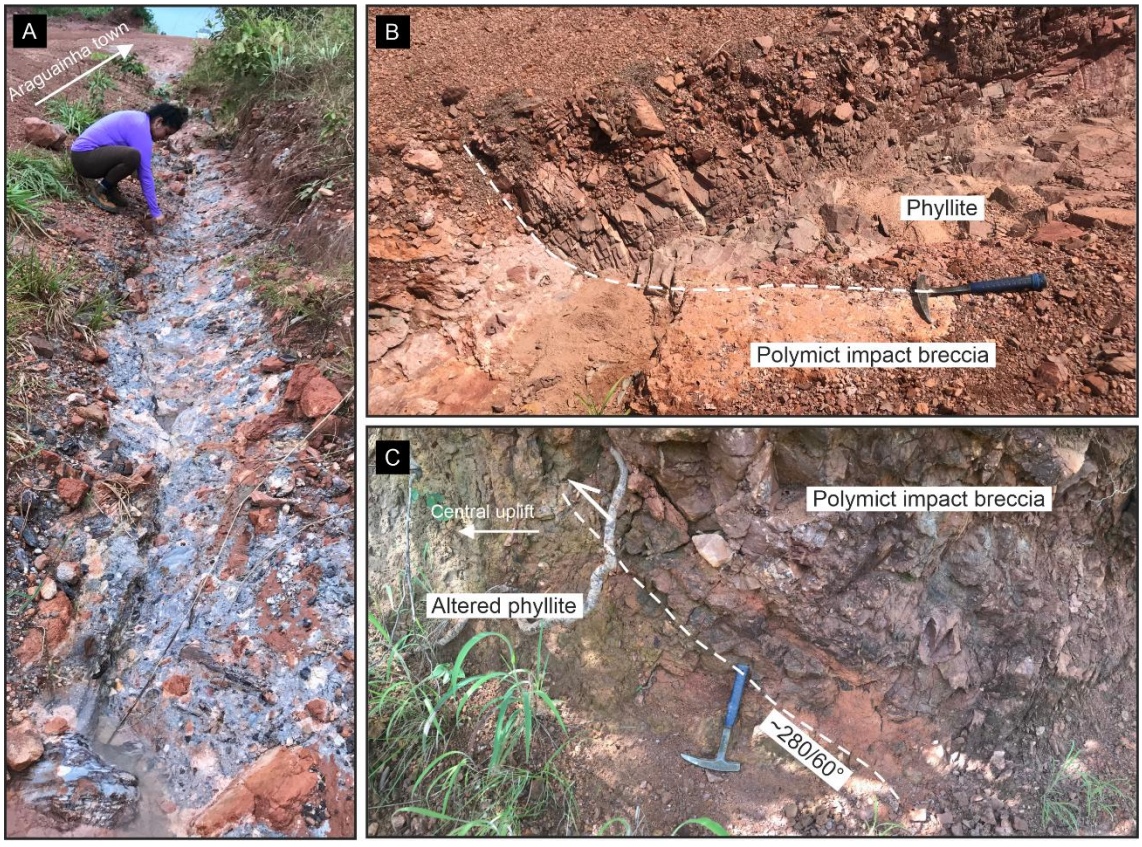

Figure 5.3 (A) Light-grey breccia matrix from the CA-07 outcrop (at UTM 22K 288523 m E; 8141975 m S) along the MT-100 road. Person, for scale, up to 1.6 m tall. (B) Occurrence of blocks of phyllite above the PIB from CA-07 outcrop. Hammer, for scale, is 31 cm long. (C) Contact relationship between the polymict impact breccia of the CA-84 breccia deposit and altered phyllite, separated by a whitish thrust plane oriented at 280/60. Hammer, for scale, is 31 cm long.

Macro- and mesoscopic descriptions of clast populations. In this part, we will describe clasts at macroscopic (> 1 cm) and at mesoscopic scale (> 4 mm). Characteristics like color, textures, and especially granulometry allow us to identify eleven litho-types of clasts (Table 5.2), like: (1) white, fine- to medium-grained sandstone; (2) grey conglomeratic sandstone; (3) red conglomeratic sandstone; (4) green sandstone; (5) coarse conglomerate; (6) black shale; (7) grey slate; (8) brown slate; (9) granite, (10) quartz pebbles, and (11) impact melt clasts (IMR Type-II).

Sandstones. Four varieties of sandstones were identified. They could represent the same lithology, but differ in color which could be a primary or secondary alteration feature. The *white, fine- to medium-grained sandstone* is a significant clast type of all breccia deposits (Table 5.2). It is moderately sorted, medium- to fine-grained, subangular to subrounded, and commonly the particles show low sphericity. This type of sandstone contains kaolinite. It is in part altered and has highly porous aspect. Most of these clasts are 20-90 cm in size, but up to 2 m size have been observed in the field. In hand specimens, the sizes are mainly between 1.1 and 3.5 cm, with a maximum size of 9.2 cm. The *grey conglomeratic sandstone* is another common clast type characterized by dark to light grey color, moderate sorting, low sphericity, subangular to subrounded, and fine grain size. Clasts subrounded of quartz with > 3 mm are significant. Some of these sandstones have whitish bands intercalated with darker ones carrying relatively more biotite. Clasts of this type attain sizes of up to 70 cm, but occur mostly between 10 and 50 cm in the field. In hand specimens, the sizes are mainly 1-3 cm, with a maximum size of 8 cm. *Red conglomeratic sandstone* clasts of low sphericity are present in all breccia deposits but are of minor abundance. This sandstone is dark to light red, moderately sorted, fine-grained, subangular to subrounded, dominated by quartz in the groundmass. Clasts of rounded to subrounded quartz (> 3 mm) rounded to subrounded were identified. The maximum size observed in the field for this sandstone is 74 cm, but occurs mainly between 20 and 40 cm. In hand specimens, the maximum size observed is 6.2 cm, but they occur mainly between 1.1 and 2.5 cm. *Green sandstone* is of light green color, well sorted, low sphericity, subrounded, very fine-grained, dominated

by quartz in the groundmass. This sandstone clast type is very rare (only three occurrences) and was observed only within the initial 30 meters of profile CA-07 in the field. Clasts are coherent and are between 8 and 14 cm in size.

Conglomerate. The *conglomerate* clasts are subrounded, of low sphericity, and up to 42 cm in size (long axis length) in the field. They occur mainly between 5 and 30 cm in size in the field, and are 1.5-30 cm in size in hand specimens. The conglomerate has sandy matrix, medium-grained, composed of subrounded quartz minerals. This lithic clast type has mostly quartz pebbles of less than 2 cm size, but pebbles up to 8 cm size have been noted. A small fraction of the quartz pebbles is fractured or polysynthetically sheared in domino-fashion. Also, the conglomerate is classified as either clast- or matrix-supported and seemingly not metamorphosed. They are present in all studied breccia deposits but relatively more prominent in profiles CA-84 and CA-14.

Shale. Only *black shale* clasts have been observed, and they frequently contain graphitic material. The black shale is quite friable and forms subangular clasts. They have low sphericity, occur mainly at 5-25 cm size, and the maximum size noted is 45 cm in the field. In hand specimens, they occur as 0.6 to 1.1 cm clasts. This clast type is rare (four occurrences observed in the field and three in hand specimens), and mainly present in profiles CA-07 and CA-84.

Slate. This lithic population comprises variegated slates, ranging from dark to light grey, dark red, brown, and purple. We observed abundant alteration fronts with changing colors, so that much of the color variance may be due to secondary alteration. The clasts are subangular to subrounded, and generally of low sphericity. They can be classified into two main types, *brown slate* and *grey slate*. Both these types display the same features, such as occurrence of circular-shaped spots considered pseudomorphs after cordierite (typical for lithologies of the metasedimentary basement in the direct environs of the alkali granite). Many clasts also contain shatter cones, quite frequently in aggregates of up to 10 cm wide cone fractures. Frequently a metamorphic fabric and foliation is recognizable in such clasts. Sizes of slate clasts vary from 5 to 95 cm, with larger blocks of up to 7 m size in the field. In hand specimens such clasts are mostly 1-3 cm in sizes, with a maximum size at 7 cm.

Granite. This lithotype is rare - overall. Normally, such clasts are subangular and have low sphericity. They are markedly altered – whereby especially the feldspar minerals are reduced to friable masses of secondary phyllosilicate. K-feldspar is strongly altered to kaolinite. These clasts are fine-grained and equigranular, and do not show any mafic minerals, like biotite. This feature differentinguishes this granite clast type from the Araguainha granite that normally is of medium grain size, porphyritic, and as a main mafic phase, has biotite. Granite clasts were found only in the northern profiles (CA-07, CA-84, and CA-09). The largest granite clasts were observed in the CA-09 polymict impact breccia, and measured 2.6 m in size in the field. However, the majority of such clasts has sizes between 7 and 40 cm. In hand specimens, the only occurrence observed is a clast of 0.7 cm size.

Quartz pebbles. The *quartz pebble clasts* are well distributed throughout the profiles. They are beige-yellowish, rounded to subrounded, of high sphericity, and generally fractured or even fragmented. In the latter case, parts of a parent pebble may be scattered in close proximity – attesting to limited lateral movement. Pebbles are abundantly multiply-sheared in domino fashion. The majority of quartz pebbles is 3-10 cm in size, but the maximum size observed is 30 cm in the field. In the hand specimens, the sizes are mainly between 1 to 2.3 cm in size.

Highly deformed/Impact melt clasts. Clasts of impact melt rock of Type-II (Souza et al., 2024) are plastically deformed (i.e., stretched, and folded) and often of convoluted shapes indicating plastic deformation. They are whitish/greyish and generally highly porous, or form part-melted clasts with adhering whitish/greyish sandstone. In addition, where such melt clasts are of significant abundance, there are usually also entirely unmelted but highly deformed intercalated white sandstone and red siltstone/mudstone clasts. All these partially impact-melted materials occur in a purplish-greyish breccia matrix that seemingly carries a significant proportion of kaolinite (e.g., in profile CA-09). These clasts are often altered to a yellowish color, as seen in profiles CA-84 and CA-14. Some clasts may be strongly silicified and then have a remarkably cohesive nature. These clasts are generally subangular to rounded/elliptical and up to 6.6 m in size, but also occur between 0.7 to 3 m in size in the field. In hand specimens, the IMR are rare, only three occurrences were observed and the sizes are between 1.1 to 2.1

cm. Strongly plasticized/deformed clasts often have a large aspect ratio (length/width) – see e.g., Figure 5.6A.

Microscopic descriptions of clast population. In In thin section, three litho-types have been identified: sandstone; metasandstone; and slate. Quartz, plagioclase, and melt particles were also identified (Table 5.2).

Sandstone. These micro-clasts are subangular, fine- to medium-grained, well or moderately sorted, clast-supported with little or no matrix. They occur mainly between 0.6 and 1.7 mm in size, but the maximum clast size is of 30 mm. The main mineral components of quartz (80-90 vol%), phyllosilicate minerals (e.g., muscovite, sericite; 5-20 vol%), and feldspar (plagioclase and K-feldspar, < 5 vol%). The matrix is composed by the same minerals, quartz, K-feldspar, and phyllosilicate (mostly muscovite). Biotite, K-feldspar, albite, zircon, and oxide minerals such as rutile or goethite were identified through QEMSCAN analysis (Fig. 5.5). Sandstone clasts in µXRF element maps show high intensity for Si, medium intensities for Al and K, and low intensities for Fe and Ti (Figs. 5.4C-5.4H).

Metasandstone. These micro-clasts are subangular, fine-grained, poorly sorted, and composed of quartz and layers of commonly oriented muscovite and/or biotite. Sandstones and metasandstones are distinguished by orientation of these phyllosilicate minerals that are more easily identified by QEMSCAN and µXRF than by optical microscopy (e.g., Fig. 5.4F, #1 and #2). These clasts are up to 11 mm in size, but occur mainly between 1.4 and 3.6 mm. In single-element heat maps (µXRF), the metasandstone micro-clasts are very similar to the sandstone clasts, with high intensity for Si, medium intensity for Al and K, and low intensity for Fe and Ti (Fig. 5.4).

Slate. The slate micro-clasts are also characterized by oriented phyllosilicates (muscovite/sericite, biotite). Some of these micro-clasts are brownish in both plane- and cross-polarized light (Figs. 5.4A-5.4B), others contain nearly circular pseudomorphs of cordierite, now replaced by biotite/muscovite, or are full of small quartz inclusions. Slate clasts are subangular to subrounded and up to 15 mm in size, but occur mainly between 0.55 and 2.5 mm. QEMSCAN analysis (Figs. 5.5A-5.5C) shows that such lithic fragments are essentially composed of muscovite, biotite, quartz, and K-feldspar.

Single-element heat maps from μXRF analysis show high intensities for Fe and Ti, medium to high intensity for Al, medium intensity for K, and relatively low intensity for Si (Figs. 5.4C-5.4H). Where slate clasts contain pseudomorphic spots after cordierite, there is a high concentration of K (e.g., Fig. 5.4F, #1).

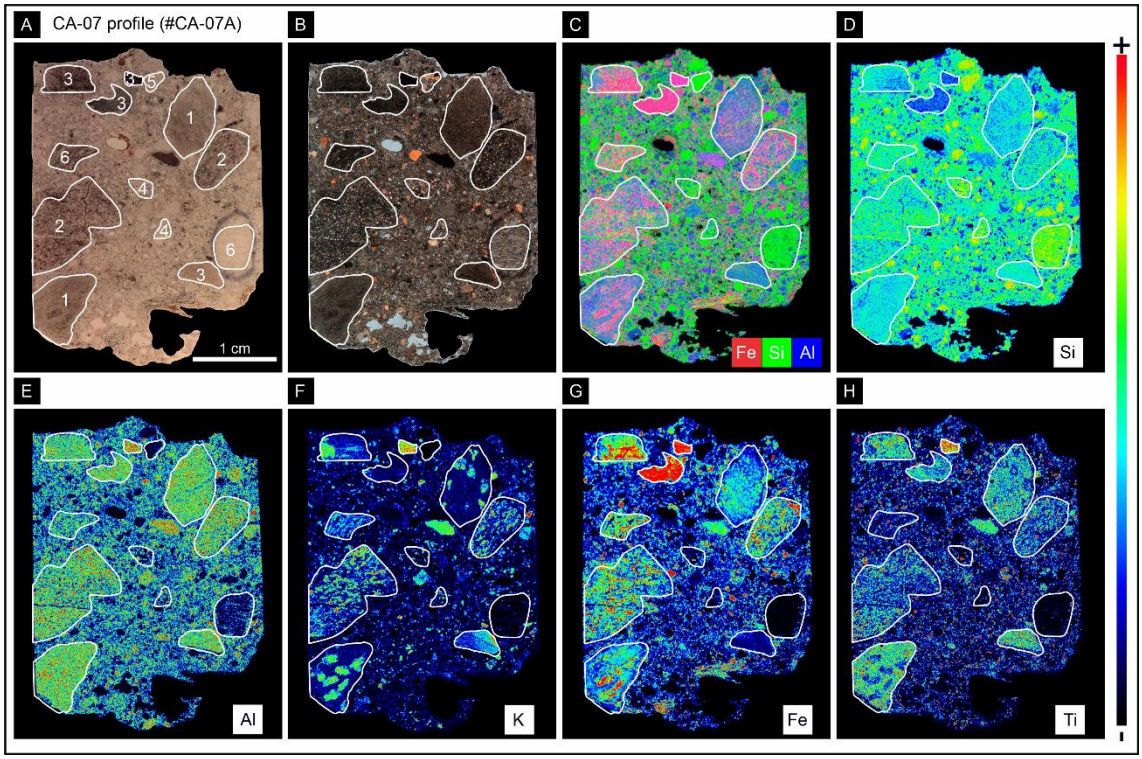

Figure 5.4 Micro-X-Ray fluorescence results for sample CA-07A from the CA-07 profile. Thin section microphotograph in (A) plane-polarized light and (B) cross-polarized light. (C) A qualitative Fe-Si-Al multi-element map, whereby the colors relate to enhanced Fe (red), Si (green), and Al (blue). Purplish color indicates enhanced abundances of Fe and Al. The following five semi-quantitative single-element heat maps show the relative abundances of (D) Si, (E) Al, (F) K, (G) Fe, and (H) Ti. Some micro-clasts are classified by numbers: 1 - slate with spots (pseudomorphs after cordierite), 2 - metasandstone, 3 - slate, 4 - sandstone, 5 - quartz, 6 - impact melt.

Quartz. The quartz micro-clasts are rounded to subrounded, up to 8.3 mm in size, but occur mainly between 0.55 and 0.9 mm. These micro-clasts frequently show strong wavy extinction, sometimes mosaicism, and abundantly recrystallization to finest-grained mosaics. Some crystals are toasted, many are fractured, and characteristic shock metamorphic effects (described in more detail in the next section) were recorded.

Plagioclase. These micro-clasts are scarce. They are subrounded, shows the polysynthetic mallets, and are between 0.55 and 0.8 mm in size. In

QEMSCAN and µXRF analysis, plagioclase was recognized as albite by the presence of Na.

Impact melt particles. The melt particles are sometimes aphanitic (Fig. 5.6B), others are composed of finest-grained (chert-like) quartz. Generally, these clasts have highly varied shapes, including elongated, subrounded, even droplet shapes, or have angular forms (akin to vitreous glass shards). These micro-clasts can be up to 31 mm in size, but are mainly between 0.7 and 4.3 mm. Some melt particles display fan-like and spherulitic textures of radiating quartz micro crystals, fluidal structure, or quench margins. Glassy melt clasts were not identified. In QEMSCAN analysis, these micro-clasts are composed essentially of quartz, with trace occurrences of Al-silicate and kaolinite in some fluidal-textured areas (Fig. 5.6C). The XRD data show that, in addition to quartz, small contributions from illite and rutile may be present (Fig. S2A). Single-element heat maps (µXRF) characterize such melt fragments with high intensity of Si (Fig. 5.6D), and low intensities of Al, K, Fe, and Ti (Figs. 5.4E-5.4H, #6).

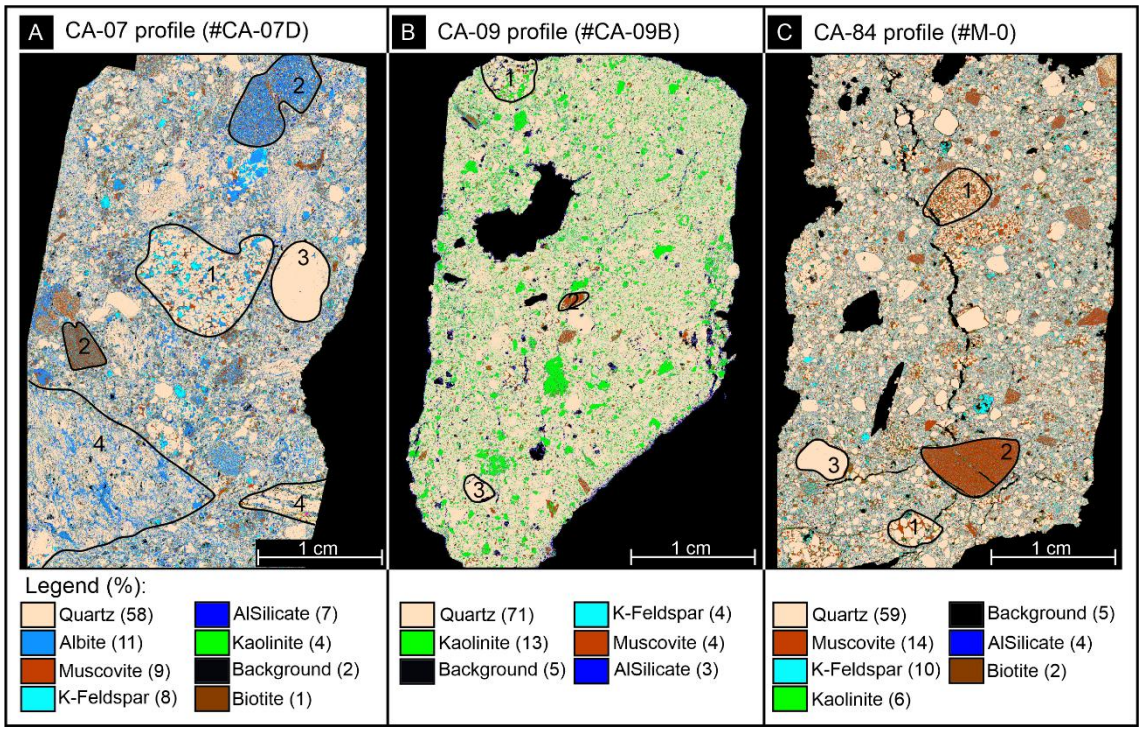

Figure 5.5 Mineral maps from QEMSCAN analysis of samples from for three thin section of breccia deposits from the northern sector. (A) Thin section of sample CA-07D from the CA-07 profile. (B) Thin section of sample CA-09B from the CA-09 profile. (C) Thin section of sample M-0 from the CA-84 profile. Some micro-clast types are indicated by numbers: 1 - sandstone, 2 - slate, 3 - quartz, 4 - impact melt rock.

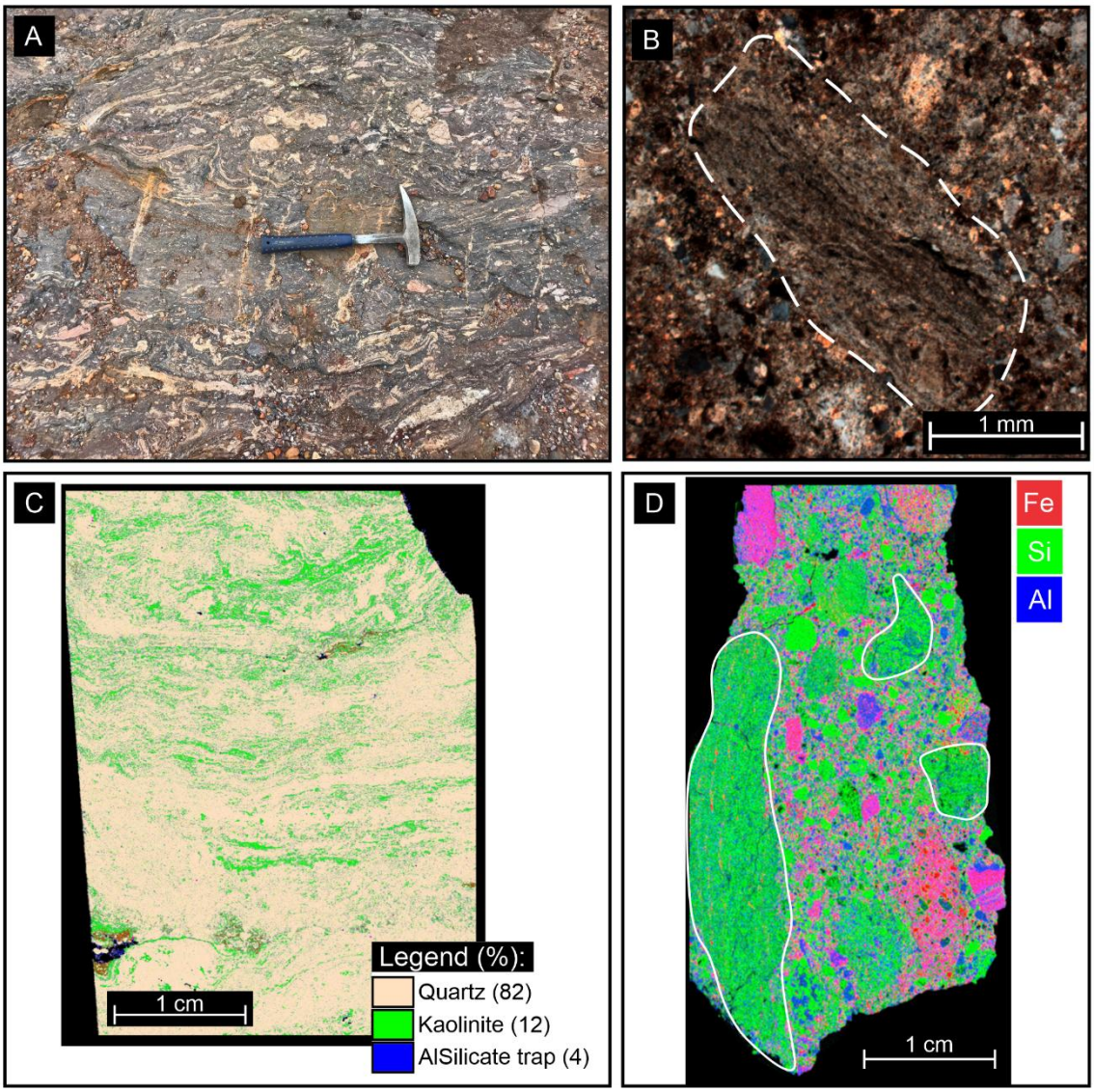

Figure 5.6 Examples of field and microscopic appearances of impact melt clasts in polymict impact breccia. (A) An impact melt clast of meter size from the upper part of the CA-09 profile (at UTM 22K 288093 m E, 8141598 m S). Hammer, for scale, 31 cm long. (B) Photomicrograph of melt particles in sample CA-07D – melt with fluidal texture. (C) QEMSCAN mineral map for sample SF-28C from the CA-09 profile. (D) Qualitative Fe-Si-Al multi-element map for µXRF data of sample CA-07D, with melt particles indicated by white lines.

(Semi)quantitative description of PIB profiles

Profile CA-07. The polymict impact breccia from profile CA-07 (Fig. 5.2; at UTM 22K 288523 m E, 8141975 m S; 530-553 m.a.s.l.) was studied along the – then still unpaved – MT-100 road on the north-northwestern side of the central uplift (Fig. 5.3A). To the east, the breccia is in a vertical fault contact with metasedimentary rocks assigned to the Cuiabá Group, specifically a dark-brown,

fractured metasandstone. Several 20 to 30 m wide blocks of phyllite occur above the PIB (e.g., Fig. 5.3B; Souza et al., 2024). The profile was divided into five sections (A to E) from NE to SW direction, based on changes in matrix color or the presence of distinct clast types (Fig. S2C). The transition between the fourth and fifth sections is covered by approximately 27 m of soil. The breccia matrix is predominantly light to dark grey in sections A to D and red in section E. Analysis of a sample from this profile (#CA-07D) through QEMSCAN revealed a matrix enriched with quartz and albite (Fig. 5.5A). Along this profile, a total of twelve hand specimens and fifteen polished thin sections was prepared. The majority of the samples were collected from section E, where there is a large exposure (77.3 m long; Fig. S2C and Table S2A).

Macroscopic analysis. Profile CA-07 extends over 152 m. A total of 896 clasts were classified according to lithology and grouped into the eleven litho-types (Table 5.2). This breccia deposit is classified as moderately sorted, with relative equal proportions of matrix and clasts of, on average, 50.3 and 49.7 %. The clast types, with their respective maximum sizes in brackets, make up 13.9 % brown slate (53 cm); 13 % grey slate (76 cm); 8.7 % white sandstone (2 m); 7 % quartz pebbles (22 cm); 3.3 % grey sandstone (56 cm); 2 % granite (36 cm); 0.6 % impact melt clasts (1.25 m); 0.5 % red sandstone (41 cm); 0.3 % green sandstone (14 cm); 0.3 % conglomerate (8 cm); and 0.1 % black shale (11 cm). Granitic fragments occur only over the first 40 m at the NE end of the profile, close to the contact against basement. Impact melt rock clasts (IMR Type-II) occur from the mid-section of the profile to its NW end.

Mesoscopic analysis. Twelve hand specimens were analyzed. A total of 429 clasts were classified by lithology and grouped into seven litho-types (Tables 2 and S2A). The samples are moderately sorted, with an average matrix to clast ratio of 53.3 to 46.7 %. The clast types, with their respective maximum sizes, make up 19.6 % white sandstone (9.2 cm); 14.5 % brown slate (7 cm); 7 % quartz pebbles (1.5 cm); 3.6 % grey sandstone (8.5 cm); 1.2 % grey slate (8.2 cm); 0.5 % red sandstone (2.1 cm); and 0.3 % black shale (0.8 cm). Clasts of granite, conglomerate, green sandstone, and IMR Type-II were not observed in hand specimen.

Table 5.2 Qualitative proportions of clast types across different scales from the detailed descriptions of breccia deposits studied (CA-07, CA-09, CA-84). The total number of clasts analyzed is given as well.

Macroscopic

	CA-07		CA-09		CA-84	
Clast types	N = 869	49.7%	N = 1068	59.8%	N = 191	34%
Quartz pebbles	122	7.0	109	6.1	44	7.9
Conglomerate	6	0.3	6	0.3	14	2.5
Red conglomeratic sandstone	9	0.5	87	4.9	28	5.0
Grey conglomeratic sandstone	58	3.3	150	8.4	11	2.0
White sandstone	152	8.7	214	12.0	27	4.8
Green sandstone	5	0.3	-	-	-	-
Black shale	1	0.1	-	-	9	1.6
Brown slate	243	13.9	247	13.8	29	5.2
Grey slate	228	13	103	5.8	23	4.1
Granite	35	2.0	45	2.5	6	1.1
Impact melt clast	10	0.6	107	6.0	-	-

Mesoscopic

	CA-07		CA-09		CA-84	
Clast types	N = 429	46.7%	N = 218	38.6%	N = 390	28.1%
Quartz pebbles	64	7.0	56	9.9	63	4.5
Conglomerate	-	-	5	0.9	4	0.3
Red conglomeratic sandstone	5	0.5	14	2.5	24	1.7
Grey conglomeratic sandstone	33	3.6	6	1.1	19	1.4
White sandstone	180	19.6	75	13.3	162	11.7
Green sandstone	-	-	-	-	-	-
Black shale	3	0.3	-	-	3	0.2
Brown slate	133	14.5	57	10.1	79	5.7
Grey slate	11	1.2	-	-	35	2.5
Granite	-	-	2	0.4	1	0.1
Impact melt clast	-	-	3	0.5	-	-

Microscopic

	CA-07		CA-09		CA-84	
Clast types	N = 4850	55.1%	N = 1310	46.3%	N = 4724	31.6%
Quartz	1158	13.2	450	15.9	1827	12.2
Plagioclase	1	0.0	0	0.0	4	0.0
Sandstone	1748	19.9	351	12.4	1420	9.5
Slate	1167	13.3	34	1.2	763	5.1
Metasandstone	169	1.9	0	0.0	170	1.1
Melt particles	607	6.9	475	16.8	540	3.6

Table 5.3 Percentages of occurrence of different shock features in quartz micro-clasts, in quartz of the matrix, or quartz grains in sandstone micro-clasts. N = total number of quartz grains analyzed.

	N	Unshocked	PFs	PFs+FFs	PDF (1set)	PDF (2set)	TOTAL
CA-07							
Quartz clast	**1158**	44.5	38.3	12.7	3.2	1.3	100
Sandstone fragment	**143**	-	74.8	16.8	2.8	5.6	100
Matrix (quartz grains)	**204**	90.2	6.4	2.0	1.5	0.0	100
CA-09							
Quartz clast	**450**	41.6	41.3	12.4	3.8	0.9	100
Sandstone fragment	**60**	-	85.0	11.7	3.3	0.0	100
Matrix (quartz grains)	**125**	92.0	8.0	0.0	0.0	0.0	100
CA-84							
Quartz clast	**1827**	38.3	36.5	18.4	6.6	0.2	100
Sandstone fragment	**375**	-	75.5	22.4	2.1	0.0	100
Matrix (quartz grains)	**964**	74.7	22.0	2.9	0.4	0.0	100

Note: PFs – Planar fractures; FFs – Feather features; PDFs - Planar deformation features.

Microscopic analysis. Fifteen polished thin sections were analyzed (Table S2B). Based on point counting, the proportions of matrix and clasts are 44.9 to 55.1 % (Table 5.2). The breccia is poorly to moderately sorted and matrix-supported. Abundances of recognized clast types with their respective maximum size are: 19.9 % sandstone (30 mm); 13.3 % slate (6 mm); 13.2 % quartz (8 mm); 6.9 % melt particles (31 mm); and 1.9 % metasandstone (11 mm).

Shock metamorphism. Fifty-five percent of the analyzed quartz micro-clasts are shocked (Table 5.3). Main shock effects are planar fractures (PFs), feather features (FFs), and planar deformation features (PDFs). The PFs are quite abundant in 38.3 % of the analyzed quartz grains, generally well developed, and mostly cut across the entire host grains. They frequently occur as parts of FFs, in 12.7 % of the analyzed quartz grains. A small proportion of quartz grains (4.5%) show PDFs, mostly as single sets (3.2 %) per host grain, but in 1.3 % of the clasts 2 sets of PDFs were observed. Among the analyzed quartz grains in sandstone fragments (N = 1748), only 143 exhibited shock features (Table 5.3), with prevalence of PFs (74.8 %). Then, FFs (16.8 %), crystals with PDFs with 2 sets (5.6 %), and with 1 set of PDFs (2.8 %) follow. Notably, 90 % of the quartz grains observed in the matrix are unshocked, but 6 % exhibit PFs, 2 % FFs, and only

1.5 % PDFs in single sets (Table 5.3). No micro-clasts with more than 1 set of PDFs were observed in the matrix.

Profile CA-09. The PIB from profile CA-09 (Fig. 5.2; at UTM 22K 288093 m E, 8141598 m S; 567-610 m.a.s.l.) is located 0.6 km SW of profile CA-07 in the middle and upper stretches of a winding dirt road that leads to the prominent Telecommunications Tower at 287426 m E, 8141338 m S. This section was studied previously by von Engelhardt et al. (1992) and represents the uppermost portion of the polymict impact breccia accessible in the Araguainha impact structure. Contacts against target rocks are obscured by soil or gravel cover. The entire profile is 952 m long but the first 810 m are widely covered by soil and loose road gravel that does not allow to study more than occasional small windows into the underlying breccia. Statistical evaluation of proportions of clasts and matrix, and nature of the breccia was carried out along the remaining 142 m (Fig. S2D). Profile CA-09 is characterized by breccia matrix of light grey color and, besides quartz, enriched in kaolinite minerals (#CA-09B, Fig. 5.6B). The profile was divided into four sections to observe the distribution of matrix and clast types across different areas. The sections range from approximately 20 to 40 meters, with the last section extending to around 70 meters. A total of seven hand specimens and six polished thin sections were prepared to this profile (Fig. S2D).

Macroscopic analysis. A total of 1068 clasts were classified according to lithology and grouped into nine litho-types (Tables 5.2 and S2C). The breccia is classified as moderately to poorly sorted, and the average matrix:clast ratio is 40.2:59.8. The clast types, with their respective maximum size, make up 13.8 % brown slate (77 cm); 12 % white sandstone (1.4 m); 8.4 % grey sandstone (70 cm); 6.1 % quartz pebbles (8 cm); 6 % impact melt clasts (6.6 m); 5.8 % grey slate (95 cm); 4.9 % red sandstone (42 cm); 2.5 % granite (2.6 m); and 0.3 % conglomerate (42 cm). Grey slate containing pseudomorphs after cordierite occurs along the entire profile. In the uppermost portion of the profile, granite clasts make up ca 4 % of the clasts and occur mostly in an assemblage what seems to be a probably a grey metasandstone. Considering the occurrences of impact melt clasts over the entire profile (952 m), the silicious IMR Type-II amounts to 19 %.

Mesoscopic analysis. Seven hand specimens were analyzed and a total of 218 mesoscopic clasts were classified by lithology and grouped into eight litho-types (Tables 5.2 and S2C). The samples are moderately sorted, and the average matrix:clast ratio is 61:39. The clast types, with their respective maximum sizes, are: 13.3 % white sandstone (3.4 cm); 10.1 % brown slate (3.1 cm); 9.9 % quartz pebbles (1.3 cm); 2.5 % red sandstone (2.4 cm); 1.1 % grey sandstone (1.2 cm); 0.9 % conglomerate (1.8 cm); 0.5 % impact melt clasts (2.1 cm); and 0.4 % granite (0.7 cm). Clasts of grey slate, green sandstone, and black shale were not observed.

Microscopic analysis. Six thin sections were analyzed (Tables 5.2 and S2D). The proportions of matrix and clasts are 53.7 and 46.3 %. The breccia is moderately to poorly sorted and matrix-supported. Abundances of recognized clast types with their respective maximum size are: 16.8 % melt particles (6.4 mm); 15.9 % quartz (4.3 mm); 12.4 % sandstone (18.3 mm); and 1.2 % slate (4 mm).

Shock metamorphism. 58.4 % of quartz clasts are shocked (Table 5.3). Shock effects include PFs (in 41.3 % of the total), FFs (12.4 %), PDFs in 1 set per host grain (3.8 %), and PDFs with 2 sets (0.9 %). Of the 351 sandstone fragments analyzed at the micro-scale, only 60 exhibit shock features in quartz (Table 5.3). Of these, 85 % contain PFs, 11.7 % FF, and 3.3 % 1 set of PDFs. Notably, 92 % of the 125 quartz grains studied in breccia matrix are unshocked, and 8 % exhibit PFs. No PDFs were noted in the very fine-grained matrix quartz (Table 5.3).

Profile CA-84. The PIB from profile CA-84 (Fig. 5.2; at UTM 22K 286281 m E, 8141329 m S; 500-575 m.a.s.l.) is located 1.3 km west of CA-07 and extends along a dirt road branching off at an acute angle from the MT-100. This outcrop had previously been studied by de Marchi (2015; also de Marchi et al., 2016) and reanalyzed here. It represents the lowermost part of the breccia deposit. This northwesternmost part of this profile also provides excellent exposure of the contact zone between PIB and underlying basement rocks. The polymict impact breccia is overthrust onto phyllite. The orientation of the thrust plane is 260/60 (Fig. 5.3C). 40 meters block of granite in contact with the phyllite is also observed. Profile CA-84 is characterized by breccia matrix of red color and, besides quartz,

enriched in muscovite and has minor contributions from other phyllosilicates and K-feldspar (#M-0, Fig. 5.5C). The profile was divided into five sections of 100 meters to observe the distribution of matrix and clast types across different areas; the last section is 135 m long (Fig. S2E). A total of fifteen hand specimens and twenty-five polished thin sections were prepared from samples for this profile (Fig. S2E).

Macroscopic analysis. Profile CA-84 is 535 m long. A total of 191 clasts were evaluated in the field and classified according to lithology into the nine litho-types (Tables 5.2 and S2E). This is a poorly sorted deposit, with relative proportions of matrix and clasts of 66 and 34 %. These clast types, with their respective maximum sizes, are: 7.9 % quartz pebbles (13 cm); 5.2 % brown slate (50 cm); 5 % red sandstone (74 cm); 4.8 % white sandstone (60 cm); 4.1 % grey slate (7 m); 2.5 % conglomerate (35 cm); 2 % grey sandstone (30 cm); 1.6 % black shale (45 cm); and 1.1 % granite (40 m). Impact melt clasts are at < 1 % exceedingly scarce, and only a single altered clast was positively identified towards the end of the profile. Matrix- or clast-supported conglomerate clasts are common in this breccia deposit. Black shale and granite clasts are the rarest clast types along the main part of the profile, but occur in very low proportion in the lowest part of the profile just above 500 m.a.s.l.

Mesoscopic analysis. Fifteen hand specimens of breccia matrix were analyzed. A total of 390 clasts were classified according to lithology into nine litho-types (Tables 5.2 and S2E). The samples are moderately to poorly sorted, and the average matrix to clast ratio is 71.9 to 28.1. The clast types, with their respective maximum sizes, make up 11.7 % white sandstone (3.5 cm); 5.7 % brown slate (3.1 cm); 4.5 % quartz pebbles (2.3 cm); 2.5 % grey slate (4.8 cm); 1.7 % red sandstone (6.2 cm); 1.4 % grey sandstone (1.8 cm); 0.3 % conglomerate (2.8 cm); 0.2 % black shale (1.1 cm); and 0.1 % granite (3 cm). Neither green sandstone nor impact melt clasts could be identified.

Microscopic analysis. Twenty-five thin sections were analyzed (Tables 5.2 and S2F). The proportions of matrix and clasts are 68.4 and 31.6 %. The breccia is moderately sorted and matrix-supported. Abundances of recognized clast types with their respective maximum sizes are: 12.2 % quartz clasts (11 mm); 9.5

% sandstone (14 mm); 5.1 % slate (15 mm); 3.6 % impact melt particles (15 mm); and 1.1 % metasandstone (12 mm). Plagioclase was not observed.

Shock metamorphism. Sixty-one percent of quartz micro-clasts are shocked (Table 5.3). The shock effects are PFs (36.5 %), FFs (18.4 %), PDFs in 1 set per host grain (6.6 %), and PDFs in 2 sets (0.2 %). Among 1420 analyzed sandstone fragments, 375 exhibit shock features (Table 5.3), with PFs occurring in the vast majority of quartz micro-clasts (75.5%), followed by FFs (22.4%), and PDFs in single sets (2.1 %). Notably, 74.7 % of the quartz grains observed in the matrix are unshocked, but 22 % exhibit PFs, 2.9 % FFs, and 0.4 % a single set of PDFs (Table 5.3).

Profile CA-14. The CA-14 profile (at UTM 22K 287403 m E, 8137922 m S; 512-520 m.a.s.l.), in the southern sector of the central uplift (Fig. 5.2), includes several hundred meters of breccia exposition, although the surface of this dirt-road is not very clean. The breccia crops out along the winding, upward sloping dirt road over a section of approximately 0.8 km length. Contact relationships with other lithologies are not readily observed due to erosion and dense vegetation along the track. No detailed descriptions were made along this profile due the relative low exposure. However, the main features and clast population were reported by Souza et al. (2024), such as: grey to red matrix color, heterogeneous clast population composed mainly by sedimentary clasts (sandstone and conglomerate), few occurrences of clasts derived from the metamorphosed basement but without shatter cones or circular-shaped pseudomorphs after cordierite crystals; no granitic clasts have been observed, and altered IMR Type-II clasts were identified.

5.4.2 Pre-Ordovician basement rocks: Field descriptions

In order to better understand the pre-ordovician basement that crops out in the Araguainha impact structure and for provenance comparison, three outcrops of (meta)sedimentary rocks of the basement and one of sedimentary strata of the Rio Ivaí Group were investigated and sampled for provenance analysis by U-Pb isotopic analysis on detrital zircon. These outcrops are designated as CA-111, GAR-15, CA-22, and CA-49 (Fig. 5.2). They were selected due to location in the central uplift region and as they are the more representative lithologies to the

(meta)sedimentary rocks from the Paraguay Belt and for the Alto Garças Formation for the Rio Ivaí Group.

At the boundary of the central uplift and the annular basin feature, along the MT-100 road, occurs the outcrop CA-111 (at UTM 22K 291650 m E, 8141529 m S). This outcrop represents one of the best exposures of the more common type of basement, a phyllite. The outcrop is 220 m in length and composed almost entirely of dark brown phyllite cut by 1 cm long quartz veins (Fig. S3A). The phyllite, with a dip direction of 108/88, is in contact relationship with a clast-supported conglomerate through an erosional unconformity, in which there are also some occurrences of sheared quartz pebbles. Along the profile, the clast-supported conglomerate changes to matrix-supported conglomerate and then conglomeratic sandstone (Fig. S3A). Further along this profile occur red sandstone, whitish sandstone, dark brown phyllite, and an altered, fine-grained granite occurs for a width of 1 meter. This granite is interpreted as a clast of alkali granite in the white sandstone.

Outcrop GAR-15 (at UTM 22K 288556 m E, 8142283 m S) is situated in the inner collar within the northern part of the central uplift, at locality that is known as Serra da Arnica, in part of the megablock zone (Fig. S3B; Lana et al., 2008), which is mainly formed by blocks of deformed sandstone from the Furnas Formation. This section involves a sedimentary package of the lower sequence of the Paraná Basin, overthrust by heterogeneous basement lithologies, and contains a significant exposure of impact melt rock of Type-I. Outcrop profile GAR-15 extends for 3 km in NNE-SSW direction (Figure 3 and description in Souza et al., 2024). From this profile, two samples, representing the other common type of basement at the area were collected: (1) a cohesive and friable black phyllite (sample GAR-15-0) situated between two apophysis of highly altered granite (Fig. 3SB), and (2) a light grey metasandstone (sample GAR-15-G10) that has sub-vertical bedding (69/80) took from the middle part of the profile (Fig. 3SC), where it was in contact with greywacke and altered impact melt rock of Type-I.

The third outcrop (CA-22; at UTM 22K 290608 m E, 8139763 m S) is situated in the “Córrego Seco” river, next to the center point of the impact structure. From this area, a dark grey siltstone, cut by quartz veins of

approximately 35 cm width, was sampled (Fig. S3D). Shatter cones were identified. The outcrop is about 100 m wide and occurs in the middle of a dense vegetation area. Contact relationships with other lithologies are not observed.

The outcrop related to the Alto Garças Formation from Rio Ivaí Group (CA-49, at UTM 22K 289856 m E, 8140950 m S) is situated near the inner collar. It is a conglomerate, clast supported of sand matrix (Fig. S3E). Contact relationship with other lithologies are not observed, but near red sandstones crops out.

5.4.3 U-Pb isotopic analyses on zircon

Representative samples from the polymict impact breccias and from the pre-ordovician basement were taken for U-Pb in zircon. Only data with concordance between 95 and 105 % and that pass the 5 % conventional discordance filter (Zimmermann et al., 2017) were considered for interpretation. The maximum depositional age was determined based on the youngest age detected on detrital zircon to constrain depositional age (e.g., Vermeesch, 2021) with concordance between 95 and 105 %.

Zircon textures

Polymict impact breccia samples. The zircon crystals from the polymict impact breccias are transparent. Most of the zircon grains are subrounded, elongated, ovoid, and some of them are fractured (Figs. 5.7A-5.7D). These zircon grains range in size up to 200 µm, but grains up to 270 µm are also present. The zircon textures observed in cathodoluminescence (CL) analysis are heterogeneous (Figs. 5.7A-5.7D), with the most common texture being oscillatory zoning represented by bands of different CL intensities (e.g., Fig. 5.7A, #29, #58, and Fig. 5.7C, #90). In additional to this texture, zircon crystals with sector zoning (e.g., Fig. 5.7B, #28, and Fig. 5.7D, #35), inherited cores (e.g., Fig. 5.7A, #35), metamorphic overgrowths (e.g., Fig. 5.7B, #39), homogeneous crystals (e.g., Fig. 5.7D, #8), and zones with local recrystallization (e.g., Fig. 5.7B, #38). According to backscattered electron (BSE) imaging on exterior surfaces, erosive features were observed in samples SF-04 and P-03. Granular texture (Fig. 5.7A, #45) and planar shock features of zircon grains are also observed only in sample P-03, but relatively rare (9 % of all grains studied). These shocked grains are rounded,

subhedral, and elongated. CL images record main textures in these shocked zircon grains as oscillatory zoning, homogeneous crystals, and inherited cores.

Figure 5.7 Representative cathodoluminescence (CL) images from samples of polymict impact breccias (A-D) and (meta)sedimentary rocks (E-I). Displayed spot ages are 206Pb/238U ages < 900 Ma and 207Pb/206Pb ages > 900 Ma. Small circles (20-32 µm) represent the locations of U-Pb analyses. When these circles are in yellow color, represents the concordant data, whereas in

red color, discordant data. In (A) representative backscattered electron (BSE) imaging on exterior surface when was observed granular texture in sample P-03.

(Meta)sedimentary basement samples. The zircon crystals from the basement samples are transparent to translucent. The grains are mostly subhedral, elongated, and prismatic, but a few are subrounded and ovoid (Figs. 5.7E-5.7I). These zircon grains range mainly 50 to 200 µm in size, and reaches up to 290 µm long. The zircon textures observed in CL images are heterogeneous (Figs. 5.7E-5.7I). In most samples the most common texture is oscillatory zoning with bands of different CL intensities that can be either broad or fine (e.g., Fig. 5.7E, #31.1, #42.1). Beyond that, zircon crystals with sector zoning (e.g., Fig. 5.7E, #49.1, Fig. 5.7G, #28.1), inherited core (e.g., Fig. 5.7E, #20.1, Fig. 5.7H, #1.1), metamorphic overgrowths (e.g., Fig. 5.7E, #30.1, Fig. 5.7G, #53.1), irregular zonation (e.g., Fig. 5.7G, #21.1), and zones with local recrystallization (e.g., Fig. 5.7F, #20.1) were found in these samples.

U-Pb age results for zircon from PIB

Sample P-03. The sample P-03 represents the red breccia matrix located at the beginning of PIB profile CA-84 (Figs. 5.2 and S3F). Of the 68 U-Pb analyses obtained on 66 zircon grains on cores and rims, 47 yielded concordant ages between 95 and 105 % concordance, and 43 pass the 5 % discordance filter (Fig. 5.8A and Table S4A). A bimodal age distribution was obtained: a main age population is Neoproterozoic, between 896 and 513 Ma, and a minor age population is Paleo- to Mesoproterozoic with ages at 2087-1021 Ma. The zircon of Neoproterozoic age has oscillatory zoning, homogeneous crystals, and sector zoning. Besides oscillatory zoning, the most common textures observed in the zircon grains of Paleo- to Mesoproterozoic ages also sector zoning and homogeneous crystals. The main age peaks are in the Neoproterozoic at 630 Ma and 880 Ma (Fig. 5.8B). The maximum depositional age interpreted for this sample is 233 ± 4 Ma.

Sample SF-04. The sample SF-04 is grey matrix of the polymict impact breccia that crops out in the southern part of the central uplift (Figs. 5.2 and S3F). Of the 48 U-Pb analyses obtained on rims of 48 zircon grains, 35 have concordant

ages within the 95-105 % range, and 26 grains pass the 5 % discordance filter (Fig. 5.8C and Table S4B). The data show a polymodal age distribution. A main zircon population is Neoproterozoic with ages between 969 and 519 Ma. Three minor zircon age distributions between 1297 and 1297 Ma, at 1886 Ma, and at 2879 Ma can be distinguished. According to CL images, these Neoproterozoic zircon grains record mainly sector zoning and the Proterozoic zircon grains have oscillatory zoning. The main age peaks are in the Neoproterozoic at 630 Ma and 850 Ma (Fig. 5.8D). The maximum depositional age interpreted for this sample is 519 ± 19 Ma.

Sample CA-73. The sample CA-73 is a red breccia matrix that corresponds to the PIB dikes injected into the white sandstone from the GAR-15 outcrop at megablock zone (Figs. 5.2 and S3F). Of the 114 analyses obtained on 114 zircon grains on cores and rims, 17 have concordance between 95 and 105 %, and 13 grains pass the 5 % discordance filter (Fig. 5.8E and Table S4C). A polymodal age distribution was obtained. Two main zircon populations have Paleo- to Mesoproterozoic ages between 2096 and 1430 Ma, and Meso- to Neoarchean ages between 2953 and 2693 Ma, and there is a minor zircon population with Neoproterozoic ages at 805-543 Ma. According to CL images, besides the oscillatory zoning, homogeneous crystals and sector zoning are observed in the zircon grains of Paleoproterozoic ages. For the Archean crystals, oscillatory zoning, sector zoning, metamorphic overgrowth, and inherited cores are identified. Oscillatory zoning is the most common texture of zircons of Neoproterozoic ages. The main zircon age peaks are in the Paleoproterozoic at 2000 Ma and in the Archean at 2700 and 2900 Ma (Fig. 5.8F). The maximum depositional age interpreted for this sample is 543 ± 19 Ma.

Sample CA-116. The breccia matrix of sample CA-116 (Figs. 5.2 and S3F) is sandy, cohesive, and light grey in color. Of the 111 analyses obtained on 106 zircon grains on cores and rims, only 4 grains have concordance between 95 and 105 %, and 1 grain passes the 5 % discordance filter (Table S4D). The zircon age obtained is in the Cambrian at 521 ± 18 Ma, recorded oscillatory zoning.

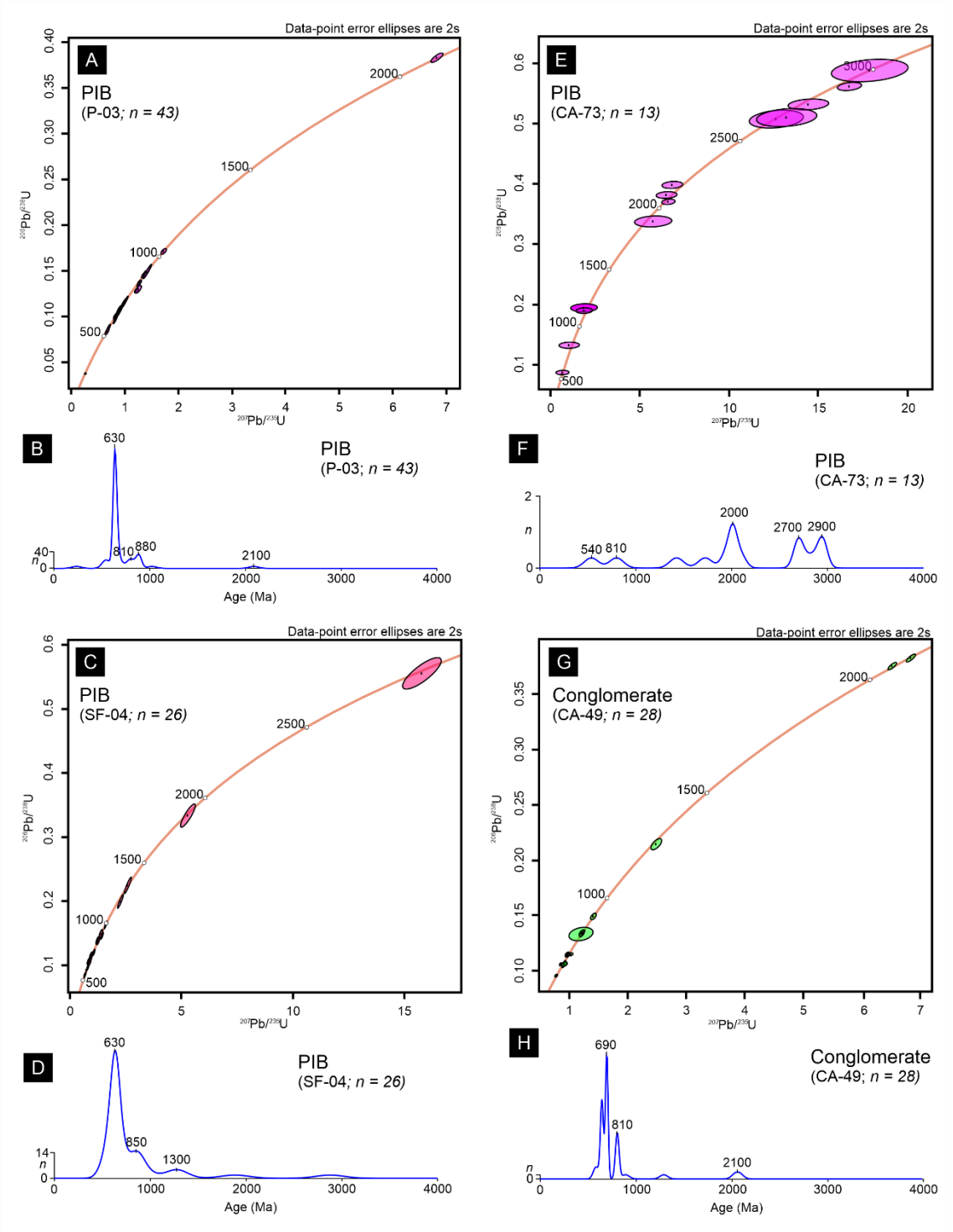

Figure 5.8 (A) Wetherill plot for the polymict impact breccia (sample P-03) of 43 analyzed concordant grains. (B) Histograms for the concordant analyzed grains of sample P-03 with the age peaks of the probability density plot. (C) Wetherill plot for the polymict impact breccia (sample SF-04) of 26 analyzed concordant grains. (D) Histograms for the concordant analyzed grains of sample SF-04 with the age peaks of the probability density plot. (E) Wetherill plot for the polymict impact breccia (sample CA-73) of 13 analyzed concordant grains. (F) Histograms for the concordant analyzed grains of sample CA-73 with the age peaks of the probability density plot. (G) Wetherill plot for the conglomerate from Alto Garças Formation (sample CA-49) of 28 analyzed concordant grains. (H) Histograms for the concordant analyzed grains of sample CA-49 with the age peaks of the probability density plot.

U-Pb age results for zircon from (meta)sedimentary basement samples

Sample CA-49. The conglomerate of sample CA-49 (Figs. 5.2 and S3E), in the northern part of the central uplift. Of the 45 analyses obtained on 45 zircon grains on cores and rims, 37 have concordance between 95 and 105 %, and 28 grains pass the 5 % discordance filter (Fig. 5.8G and Table S4E). A bimodal age distribution comprises a main zircon population with Neoproterozoic ages between 896 and 587 Ma and a minor zircon age population of Paleo- to Mesoproterozoic ages between 2094 and 1297 Ma. According to the CL images, besides oscillatory zoning to the Neoproterozoic zircon grains, homogeneous crystals are also quite common. Irregular zonation and inherited cores are also present. The most common features of Paleo- to Mesoproterozoic zircon crystals are oscillatory zonation and homogeneous crystal. The main age peaks are in the Neoproterozoic at 690 Ma and 810 Ma (Fig. 5.8H). The maximum depositional age interpreted for this sample is 587 ± 5 Ma.

Sample CA-111. The dark brown phyllite sample CA-111 is from the outcrop CA-111 (Figs. 5.2 and S3A), in the northern part of the central uplift, contain several small quartz veins. Of the 100 analyses obtained on 90 zircon grains on cores and rims, 60 have concordance between 95 and 105 %, and 58 grains pass the 5 % discordance filter (Fig. 5.9A and Table S4F). A bimodal age distribution comprises a main zircon population with Neoproterozoic ages between 818 and 587 Ma and a minor zircon age population of Paleo- to Mesoproterozoic ages between 2147 and 1138 Ma. According to the CL images, besides oscillatory zoning to the Neoproterozoic zircon grains, sector zoning and homogeneous crystals are also quite common. Metamorphic overgrowth, irregular zonation, and inherited cores are also present. Only irregular zonation was obtained in the rim of the zircon grains. The most common features of Paleo- to Mesoproterozoic zircon crystals are oscillatory zonation. In addition, homogeneous crystal and sector zoning were found in this group. The main age peaks are in the Neoproterozoic at 610 Ma and 780 Ma and in the Paleoproterozoic at 1800 Ma (Fig. 5.9B). The maximum depositional age interpreted for this sample is 587 ± 13 Ma.

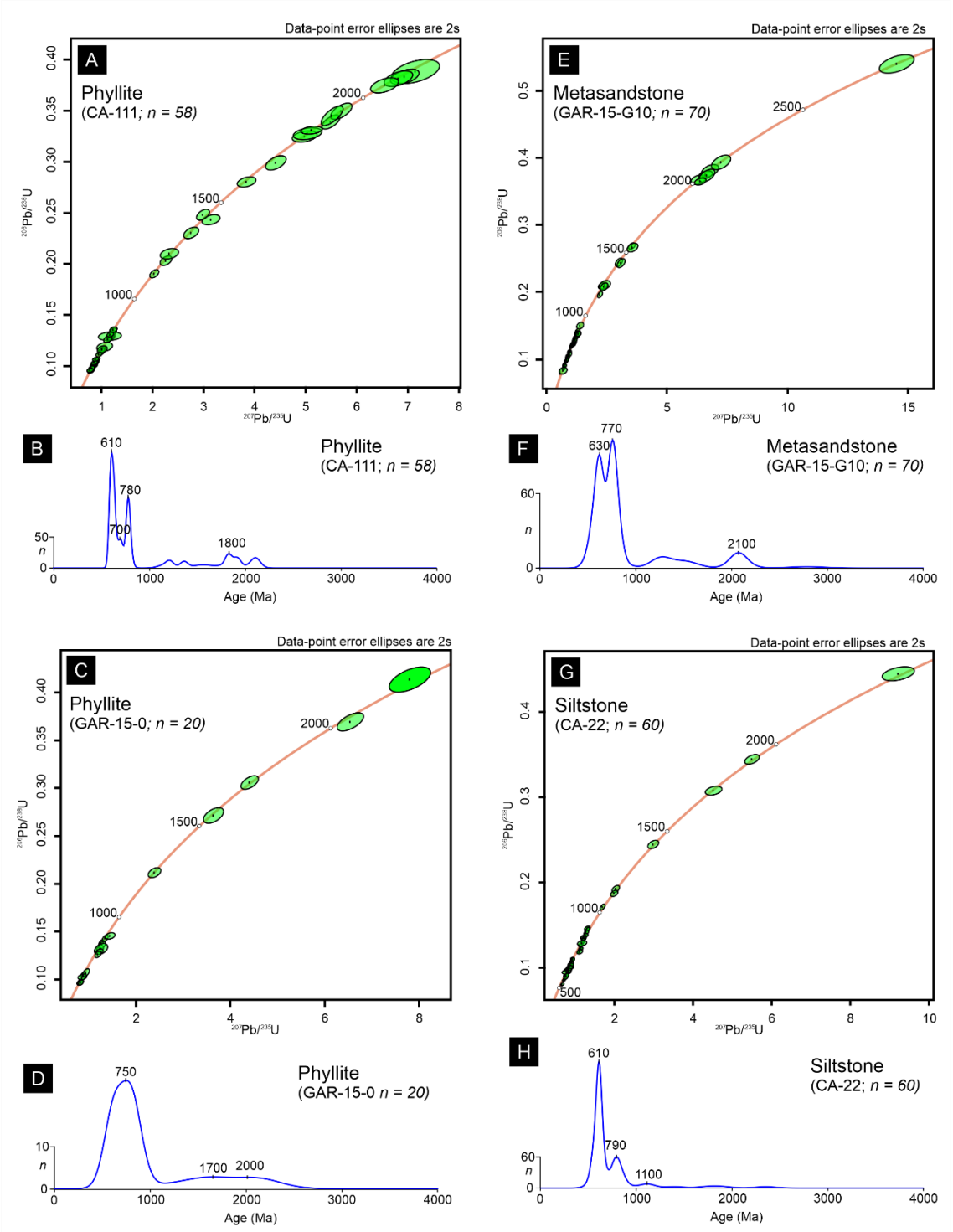

Figure 5.9 (A) Wetherill plot for the phyllite (sample CA-111) of 58 analyzed concordant grains. (B) Histograms for the concordant analyzed grains of sample CA-111 with the age peaks of the probability density plot. (C) Wetherill plot for the phyllite (sample GAR-15-0) of 20 analyzed concordant grains. (D) Histograms for the concordant analyzed grains of sample GAR-15-0 with the age peaks of the probability density plot. (E) Wetherill plot for metasandstone (sample GAR-15-G10) of 70 analyzed concordant grains. (F) Histograms for the concordant analyzed grains of sample P-03 with the age peaks of the probability density plot. (G) Wetherill plot for siltstone (sample CA-22) of 60 analyzed concordant grains. (H) Histograms for the concordant analyzed grains of sample CA-22 with the age peaks of the probability density plot.

Sample GAR-15-0. The black phyllite sample GAR-15-0 is from the outcrop GAR-15 in the northern part of the central uplift (Fig. 5.2). Of the 34 analyses obtained on 34 zircon grains on cores and rims, 24 ages gave concordance between 95 and 105 %, and 20 grains pass the 5 % discordance filter (Fig. 5.9C and Table S4G). A bimodal age distribution was obtained, with a main zircon population with Neoproterozoic ages between 876 and 595 Ma and minor age populations with Paleo- to Mesoproterozoic ages between 2190 and 1245 Ma. The Neoproterozoic zircon grains show oscillatory zoning, with homogeneous crystals and sector zoning also observed. The Paleo- to Mesoproterozoic age zircons are recorded on oscillatory zoned. Homogeneous crystals and sector zoning are the most common texture in the zircon grains with Paleoproterozoic ages. The main age peaks are in the Neoproterozoic at 750 Ma (Fig. 5.9D), recorded in oscillatory zoned and homogeneous crystals, and in the Proterozoic at 2000 Ma, recorded a core an oscillatory zoned zircon. The maximum depositional age interpreted for this sample is 595 ± 13 Ma.

Sample GAR-15-G10. The light grey metasandstone sample GAR-15-G10 is also from the outcrop GAR-15, in the megablock zone (Fig. 5.2). Of the 100 analyses obtained on 90 zircon grains on cores and rims, 79 have concordance between 95 and 105 %, and 70 data pass the 5 % discordance filter (Fig. 5.9E and Table S4H). A bimodal age distribution was obtained, with a main zircon population with Neoproterozoic ages between 899 and 511 Ma and a minor zircon population with Paleo- to Mesoproterozoic ages between 2788 and 1220 Ma. Besides oscillatory zoning, sector zoning is observed in the zircon grains of Neoproterozoic ages. This texture is quite common in the Paleo- to Mesoproterozoic zircons. The main age peaks are in the Neoproterozoic at 630 Ma and 770 Ma and in the Proterozoic at 2100 Ma (Fig. 5.9F). The maximum depositional age interpreted for this sample is 511 ± 24 Ma.

Sample CA-22. The metasedimentary siltstone sample from outcrop CA-22 (Fig. 5.2) is a foliated dark grey siltstone contain quartz veins. Of the 100 analyses obtained on 85 zircon grains on cores and rims, 66 have concordance between 95 and 105 %, and 60 results pass the 5 % discordance filter (Fig. 5.9G and Table S4I). A bimodal age distribution was obtained, with a main zircon population with Neoproterozoic age between 988 and 500 Ma, and a minor age

population is Paleo- to Mesoproterozoic with ages of 2350-1116 Ma. According to CL images, besides the oscillatory zoning for zircon grains of Neoproterozoic ages, sector zoning, metamorphic overgrowth, and inherited cores are quite common. In Paleo- to Mesoproterozoic zircons, oscillatory zoning and homogeneous crystals are observed. The main age peaks (Fig. 5.9H) are in the Neoproterozoic at 610 Ma and 790 Ma and in the Proterozoic at 1100 Ma. The maximum depositional age for this sample is 500 ± 8 Ma.

5.5 Discussion

5.5.1 Classification of the polymict impact breccia

The accepted classification for suevite is composed by a particulate matrix with lithic and mineral clasts, including cogenetic impact melt particles which are in a glassy or crystallized state (Stöffler and Grieve, 2007). However, this term is descriptive and very general. No percent of melt quantity is estimated as minimum or maximum to really named them as suevite. Indeed, some authors keeps the term descriptive suevite (e.g., Stöffler et al., 2013; Siegert et al., 2017; Siegert and Hecht, 2018; Kaskes et al., 2022; Hecht, 2022), or increase a prefix to indicate the presence estimated of the melt particles, such as, melt-poor to -rich suevite (e.g., McCall et al., 2023), (melt-free, -poor, and -bearing) polymict impact breccias, and impact melt-bearing breccia (e.g., Osinski et al., 2023). Despite these options, we preferred follow the stablished by French (1998), which adopt a minimum percentual of 3 % to indicate if the PIB is lithic (< 3 %) or a suevite (> 3 %). In this sense, it becomes easier to understand how much melt influences the formation of the breccia.

Silicious impact melt rock clasts occur from 530 m.a.s.l to the uppermost part of the integrated profile at 610 m.a.s.l, mainly in the profiles CA-07 and CA-09. The abundance of melt rock clasts seemingly increases in the mid-section of the profile, especially due to the overlap of data of the profiles and the microscopic data (Fig. 5.10). At this elevation, the melt volume reaches up to 35 %, indicating a richer composition, while at elevations of 500 to 530 m.a.s.l., the melt volume reaches up to 15 %. Both defines the Araguainha PIB as suevitic breccias. von Engelhardt et al. (1992) divided the polymict impact breccias into two units: the lower unit, composed of shocked granite, fused sandstones, and

impact melt rocks as coherent masses and distinct bodies; and the upper unit, composed of shocked granite and fused sandstones. Our study, however, reports the presence of impact melt rocks across all breccia deposits, which contradicts von Engelhardt et al. (1992) division. Additionally, we have more clearly defined the heterogeneous clast types.

In the lowermost 30 m of the studied section (500-530 m.a.s.l, profile CA-84; Fig. 5.10), hardly any silicious melt clasts are noted – however, there are a few injections of impact melt rock of Type-I of typical granitic composition into basement blocks at lower elevation (see also Souza et al., 2024). As these authors already stated, no melt particles of Type-I have ever been observed in the polymict impact breccia of this structure. The composition of melt particles found in the breccia deposits is invariably highly silicious (von Engelhardt et al., 1992; Preuss, 2012; Hauser et al., 2019; Souza et al., 2024; this study), which has been interpreted as indicating that this melt type was derived from melting of (meta)sedimentary target rocks (i.e., the (meta)sedimentary basement or the lower units of the Paraná Basin). Our µXRF and QEMSCAN investigations confirm this silicious nature of the melt rock clasts in breccia (see Figs. 5.6C-5.6D). The matrices of such clasts are invariably aphanitic to finest-grained (forming chert-like micro-mosaics of silica). In addition, presence of kaolinite, minor albite (QEMSCAN data), illite, and rutile have been observed in XRD data for some melt rock clasts (Fig. S2A). These results are similar to the composition identified on the siltstone from Furnas Formation (XRD data from Souza et al., 2024 and this work). Thus, it is plausible to interpret that the impact melt rock clasts are more likely derived from the sandstone of the Furnas Formation than from the metasedimentary target, which primarily consists of phyllosilicate and aluminosilicate compositions.

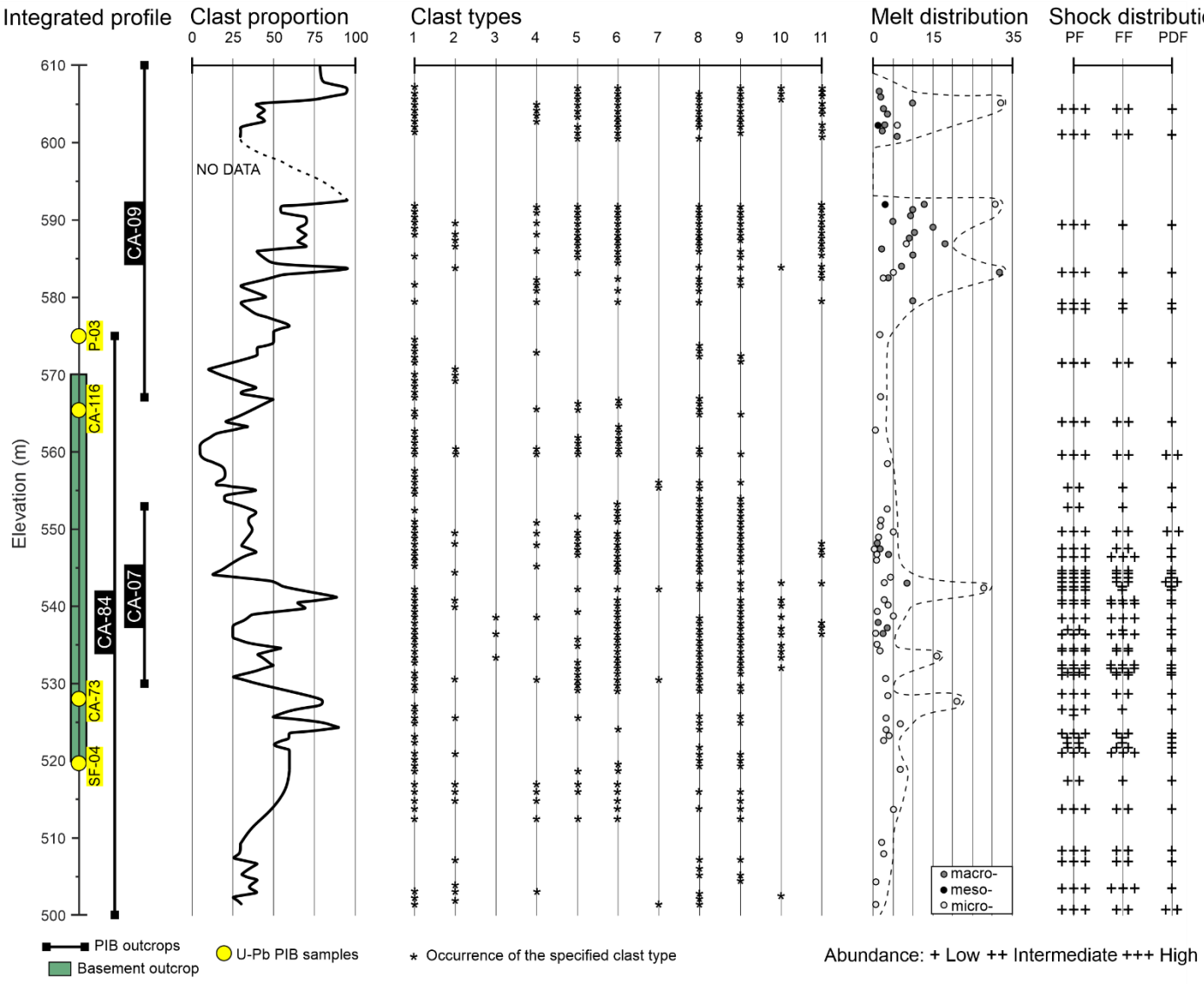

Figure 5.10 An integrated 110 m long vertical profile through the Araguainha polymict impact breccia deposits of the northern central uplift. The relative matrix : clast ratios, the occurrence of clast types, the melt distribution (vol %), and the variation of shock metamorphism observed along this profile are shown. Shock metamorphism is expressed semiquantitatively due to the amount accounted for in the thin sections, being + low = < 10; ++ medium = 20-10; +++ strong = > 20). The occurrences of clast types are indicated by (*) along the profile. Legend: 1 - quartz pebbles, 2 - conglomerate, 3 - green sandstone, 4 - red conglomeratic sandstone, 5 - grey conglomeratic sandstone, 6 - white sandstone, 7 - black shale, 8 - brown slate, 9 - grey slate, 10 – granite, 11 – impact melt rock clasts.

5.5.2 Provenance analysis

The provenance discussion is divided in two parts, taking account the comparison by compositional characterization of the breccia components and through the analyses of U-Pb ages.

Breccia components

The polymict impact breccias exposed on the central uplift of the impact structure represent the lowermost 110 m of impact breccia overlying the crater floor, where the bottommost occurrences intrude or structurally juxtapose basement blocks. As introduced in Results section, the target for the Araguainha impact involved (meta)sedimentary, sedimentary, and in scarce proportion plutonic lithologies. The polymict lithic and suevitic breccias are composed of lithic, impact melt rock, and mineral clasts derived from these rocks that were fragmented during the compression stage of cratering, and then mixed during the subsequent collapse of the transient cavity and into the modification stage. During final collapse of the central uplift, further mixing with basement-derived material occurred.

The breccias have been characterized in terms of their matrix character and clast population through macro- to microscopic scales. Grain size in the matrix is sand dominated, essentially of a quartzofeldspathic, or pelitic character. It does also contain a significant component of kaolinite. Kaolinite is a characteristic component of sandstones from the Furnas Formation. The micro-clasts of the matrix exhibit more pronounced sedimentary feature. This would support that Furnas Formation was one of the main contributors.

Slate and metasandstone macroscopic clasts of the (meta)sedimentary basement are recognized in the breccia primarily by foliation due to originated by the preferred orientation of minerals in the clast fabric, mainly accentuated by micaceous minerals and by pseudomorphs of cordierite due to thermal metamorphism.

We found different types of sandstones at the macroscopic scale. All sedimentary units of the Paraná Basin contain sandstone (Assine et al., 1994; Assine, 1996): (a) Passa Dois Group (Irati and Corumbataí Formation) – green, purple and grey, clay matrix with altered feldspar, very fine to fine-grained with

subrounded to rounded quartz grains; (b) Aquidauana Formation – red, iron-rich, coarse- to medium-grained, well sorted with rounded to rounded quartz grains; (c) Ponta Grossa Formation – yellow/ochre, laminated with iron oxide, very fine to fine-grained, very well sorted with angular minerals; (d) Furnas Formation – deformed, white-pink, containing kaolinite, medium- to fine-grained, poorly sorted with subrounded to angular quartz grains; (e) Rio Ivaí Group (Alto Garças Formation) – red, coarse-grained, poorly sorted. Except for the green sandstone clasts, our white, grey, and red sandstones are characterized as moderately sorted, medium- to fine-grained, and they may contain kaolinite (only in the white variety). The latter supports a correlation with Furnas Formation sandstone. The red and grey color be related to alteration. The green sandstone is a massive rock, cohesive, well sorted, and very fine-grained, which could be similar to the siltstone observed in the middle unit of the Furnas Formation (Assine, 1996).

Conglomerate lithologies occur, mainly in the lower units of the Paraná Basin. These macroscopic clasts are characterized as: (a) matrix-supported conglomerate, sandy with shale matrix from Furnas Formation (Assine, 1996); (b) clast-supported conglomerate, with quartz pebbles and feldspathic sandy matrix from Alto Garças Formation of the Rio Ivaí Group (Assine et al., 1994; Alvarenga et al., 1998). Also, (meta)conglomerate strata are part of the (meta)sedimentary units of the Paraguay Belt – for example, conglomerate in the Diamantino Formation (Alto Paraguay Group) and metaconglomerate in subunits 4 and 7 of the Cuiabá Group (Luz et al., 1980). Our conglomerate fragments are mainly clast-supported and seemingly not metamorphosed and, thus, could be derived from one of the Paraná Basin units, the Furnas or Alto Garças formations, or both.

The dominant mineral clast across the three working scales is quartz, derived from the comminution of target rocks. All units with a silicious base could have been suitable quartz sources. The abundance of quartz is certainly related to the fracture toughness of this mineral, and resistance to metamorphic and alteration overprint. Also, some quartz pebbles are sheared, they can be fractured and comminuted to small pieces. Our microscopic study shows a limited presence of plagioclase throughout the breccia (< 1 %), suitable sources for which could have been many sandstone strata of the target succession and even a very limited contribution from granite.

Black shale macroscopic clasts occasionally contain organic material and they are highly altered, which a feature identified in the rocks from Irati Formation. This unit is composed of black shale, silicified limestones, siltstone, and chert layers (Milani et al., 1994). However, the lack of stromatolites and chert clasts, typical from the Passa Dois Group, does not favor to support a correlation with the Irati Formation. We suggest that the black shale is more likely from the basement rather than from higher up in the stratigraphic column.

The rare granite clasts observed in the study profile must be related to the Araguainha granite exposed in the core of the central uplift. The texture of the granitic clasts observed in the breccia are similar with the injections of granite into metasedimentary basement strata recently described by Souza et al. (2024), however, they do not resemble the classical Araguainha granite. These clasts and dikes are generally finer-grained and lack the K-feldspar phenocrysts of the Araguainha granite, but contain less abundant quartz and < 10 vol% biotite. It was assumed by Souza et al. (2024) that this fine-grained granite facies represents a marginal phase of the Araguainha granite occurring at the interface between granite intrusion and relatively cold (meta)sedimentary basement, even involving apophyses into the basement. Certainly, the porphyritic Araguainha granite does not represent a direct constituent of the polymict lithic and suevitic breccias.

In conclusion, our findings suggest a provenance of breccia components involving only the lower target units of the Paraná Basin. Clasts predominantly originate from the (meta)sedimentary rocks of the basement, as well as the lower sedimentary units of the Paraná Basin (Furnas Formation and Rio Ivaí Group), with an exceeding low contribution from the granite of the basement. This is in contrast to both von Engelhardt et al. (1992) and de Marchi (2015, also de Marchi et al., 2016). Von Engelhardt et al. (1992) suggested that the components originate from both the granitic basement and the overlying sedimentary sequences, specially from the Passa Dois Group that had contributed silicic rock fragments such as chert, and from Furnas Formation sandstone. These authors did not acknowledge the widespread occurrence of lithologies of the metasedimentary basement. De Marchi (2015, and de Marchi et al., 2016) proposed a contribution to the breccia from all lithostratigraphic units of the target.

No chert was observed by us as a component in the polymict impact breccia, and it is not impossible that von Engelhardt et al. (1992) mistook some impact melt rock clasts of Type II with very fine-grained cherty micro-texture for a cherty sedimentary target component. There is also no evidence that would support a contribution from any of the upper unis of the Paraná Basin (maybe even from the Ponta Grossa Formation upward).

U-Pb zircon provenance

In the previous section we have laid out a tentative target provenance for the polymict impact breccias, based on the comparison of clast type statistics observed along the integrated profile and potential target rocks. Clasts were probably derived from the lithologies of the lower stratigraphic column – from the basement into the lower units of the Paraná Basin. With this in mind, we can compare the statistics of U-Pb isotopic data obtained on zircon from the matrices of the polymict impact breccias (samples P-03, SF-04, CA-73, CA-116) with the U-Pb isotope data for (meta)sedimentary rock samples (GAR-15-0, GAR-15-G10, CA-22, CA-111), conglomerate for Alto Garças Formation (CA-49), and published U-Pb on zircon provenance data for the basement strata. This includes the Araguainha alkali granite (Tohver et al., 2012), Cuiabá Group (Pelosi, 2017; Babinski et al., 2018; Frugis et al., 2024), Puga Formation (McGee et al., 2014), Alto Paraguay Group (McGee et al., 2014); rocks from the Arenópolis Arc from the Brasília Belt (Pimentel et al., 1991; Pimentel et al., 2003; Matteine et al., 2010; Della Giustina et al., 2011; Marques et al., 2019; Piauilino et al., 2021; Carneiro et al., 2021); the lower stratigraphic units of the Paraná Basin – Rio Ivaí Group (Gezatt, 2011; Henrique-Pinto et al., 2021), Furnas Formation (Santos et al., 2015; Henrique-Pinto et al., 2021; López, 2022), and Ponta Grossa Formation (Henrique-Pinto et al., 2021; López, 2022); and the impact mlet rock Type-III (Hauser et al., 2019). We apply both the kernel density estimation (KDE) and multidimensional scaling (MDS) methods, with age maxima, as calculated with the provenance package in R (Vermeesch et al., 2016; Figs. 5.11 and 5.12).

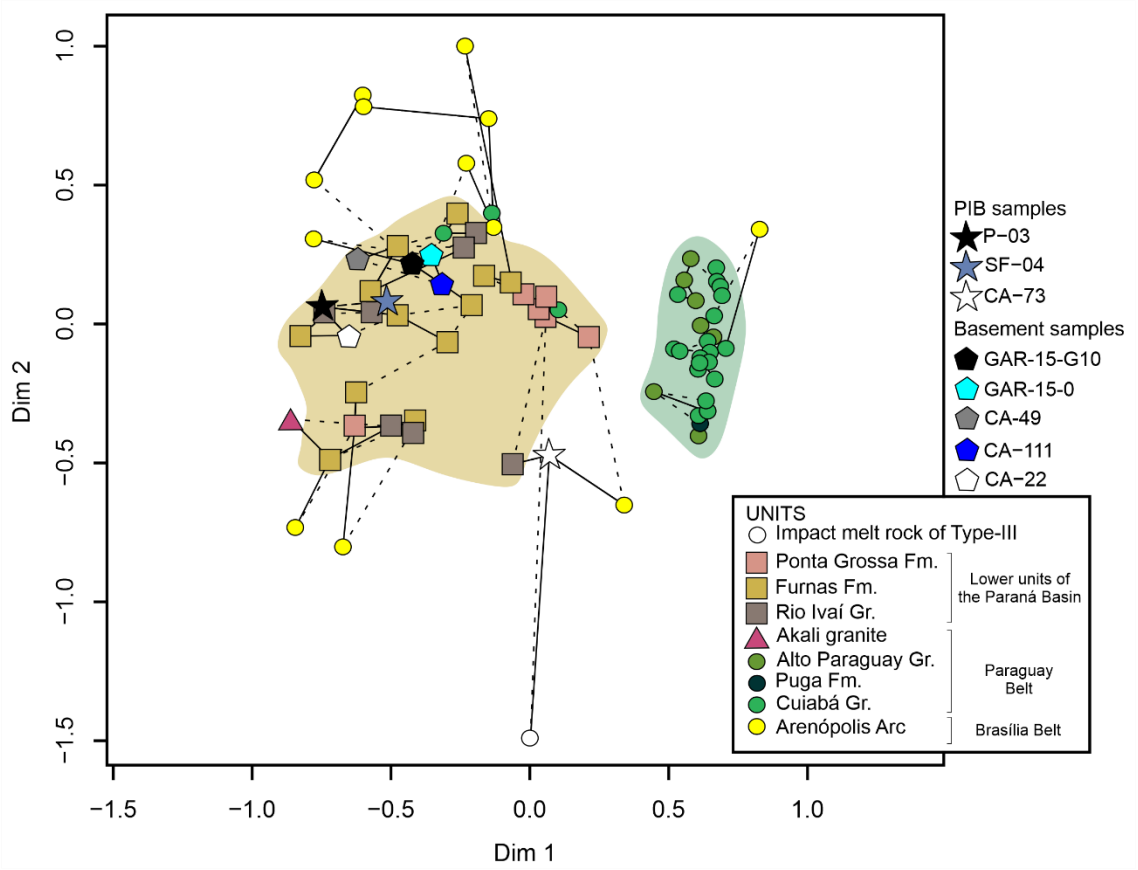

Figure 5.11 Multidimensional scaling plot displaying the varied relationships of detrital zircon from samples studied here against zircon age data from the literature [impact melt rock of Type III (Hauser et al., 2019); lower units of the Paraná Basin – Ponta Grossa Formation samples (from Henrique-Pinto et al., 2021; López, 2022), Furnas Formation samples (from Santos et al., 2015; Henrique-Pinto et al., 2021; López, 2022), Rio Ivaí Group samples (Gezatt, 2011; Henrique-Pinto et al., 2021); basement rocks from Paraguay Belt – alkali granite samples (Tohver et al., 2012), Cuiabá Group samples (Pelosi, 2017; Babinski et al., 2018; Frugis et al., 2024), Puga Formation (McGee et al., 2014), Alto Paraguay Group samples (McGee et al., 2014); and rocks from Brasilia Belt (from Pimentel et al., 1991; Pimentel et al., 2003; Matteine et al., 2010; Della Giustina et al., 2011; Marques et al., 2019; Piauilino et al., 2021; Carneiro et al., 2021)]. The continuous lines represent the most similar samples and the discontinuous lines the second most-similar ones.

The total KDE for our polymict impact breccia matrix samples (n = 82) yielded a polymodal age population distribution with a main peak at ~630 Ma, a second peak of age data at 1.9-2.2 Ga, a third age peak at 2.7-2.9 Ga (Fig. 5.12), with the maximum depositional age at 233 ± 4 Ma. This Archean age population is more significant in sample CA-73, whereas the zircon population with Neoproterozoic to Paleoproterozoic ages is significant in samples P-03 and SF-04. The CA-73 sample is different from the P-03, SF-04, and CA-116 samples. The CA-73 is a poorly sorted PIB, with red pelitic matrix, composed of whitish sandstone, red slate, and a few carbonate clasts (see also Souza et al., 2024). It

corresponds to the PIB dikes injected into the white sandstone from the Furnas Formation in the megablock zone, which probably could explain the wide concentration of older zircon population. The PIB from the northern and southern parts of the central uplift are more heterogeneous in composition, mainly composed of metasedimentary clasts and in contact relationship with the (meta)sedimentary basement rocks. Also, in the cumulative probability plot, the CA-73 is formed in the extensional settings while P-03 and SF-04 in the collisional settings (Fig. 5.13). Even so, the polymodal age population distribution for breccia deposits shows similarities with samples from the lower units of the Paraná Basin and are into the field of the Goiás Magmatic Arc (Fig. 5.12).

The provenance analyses of basement samples (n = 236) show a nearly bimodal zircon age distribution diagram with the main populations at the Neoproterozoic ages between ~600 and 810 Ma, and a second group of Proterozoic ages between ~1.6 and 2.1 Ga (Fig. 5.12), with the maximum depositional age at 500 ± 8 Ma. This pattern is different from that for the basement rocks typical from Paraguay Belt, which involves zircon population with Neo- to Mesoproterozoic ages between 970 and 1600 Ma, but reveals similarities with the lower units of the Paraná Basin (Fig. 5.11). In the cumulative probability plot (Fig. 5.13), all basement samples are related to the collisional settings.

According to the MDS and KDE plots (Figs. 5.11 and 5.12), our PIB and (meta)sedimentary samples indicate that provenance results are similar to the zircon age populations for the Furnas Formation and Rio Ivaí Group, especially with regard to the bimodal age distribution (at ~ 630 Ma and ~ 2.0 Ga), and rather similar with data for the Brasília Belt (between 594 and 800 Ma and at 2.0 Ga). In contrast, our samples differ significantly from those of the (meta)sedimentary strata (Cuiabá and Alto Paraguay groups and Puga Formation) and for the impact melt rock Type-III.

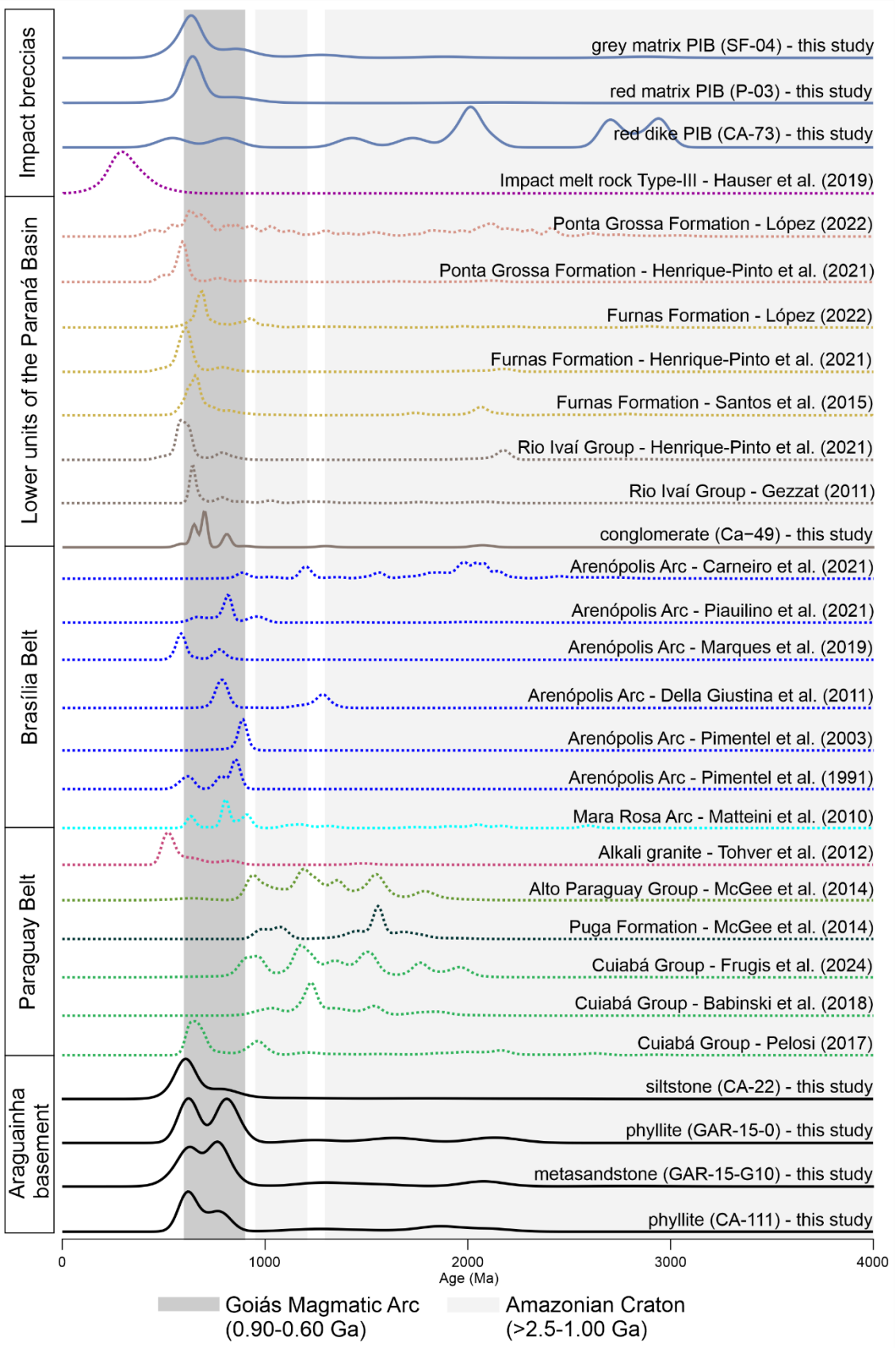

Figure 5.12 Kernel density estimates (normalized y-axis; 0–4000 Ma) for detrital zircon of all analyzed samples together with data from bibliography with the probable sources, Goiás Magmatic Arc (0.90-0.60 Ga) and Amazon Craton (>2.50-0.95 Ga). The six geochronological

provinces from Amazon Graton are (Tassinari and Macambira, 1999): Sunsás Province (1.20-1.00 Ga), Rondonian-San Ignacio (1.55-1.30 Ga), Rio Negro Juruena (1.80-1.55 Ga), Ventuari-Tapajós (1.95-1.80 Ga), Maroní-Itacaiúnas (2.20-1.95 Ga), Amazônia Central (>2.5 Ga).

Even so, an age peak around 600 Ma was recently identified by Frugis et al. (2024) identified as minor component of the provenance of the Cuiabá Group. This aligns with our field observations, that is in favor of strong contribution of clastic material from the metasedimentary basement, the provenance results favor that the analyzed samples are mainly derived from the sedimentary units. Especially samples CA-22 and CA-111 that are in the field similar to Cuiabá Group rocks, e.g., metamorphic and quartz veins involved. Thus, the MDS patterns against which we can compare our data relate to Cuiabá and other lithologies of the Paraguay Belt sampled at least 300 km further to the west.

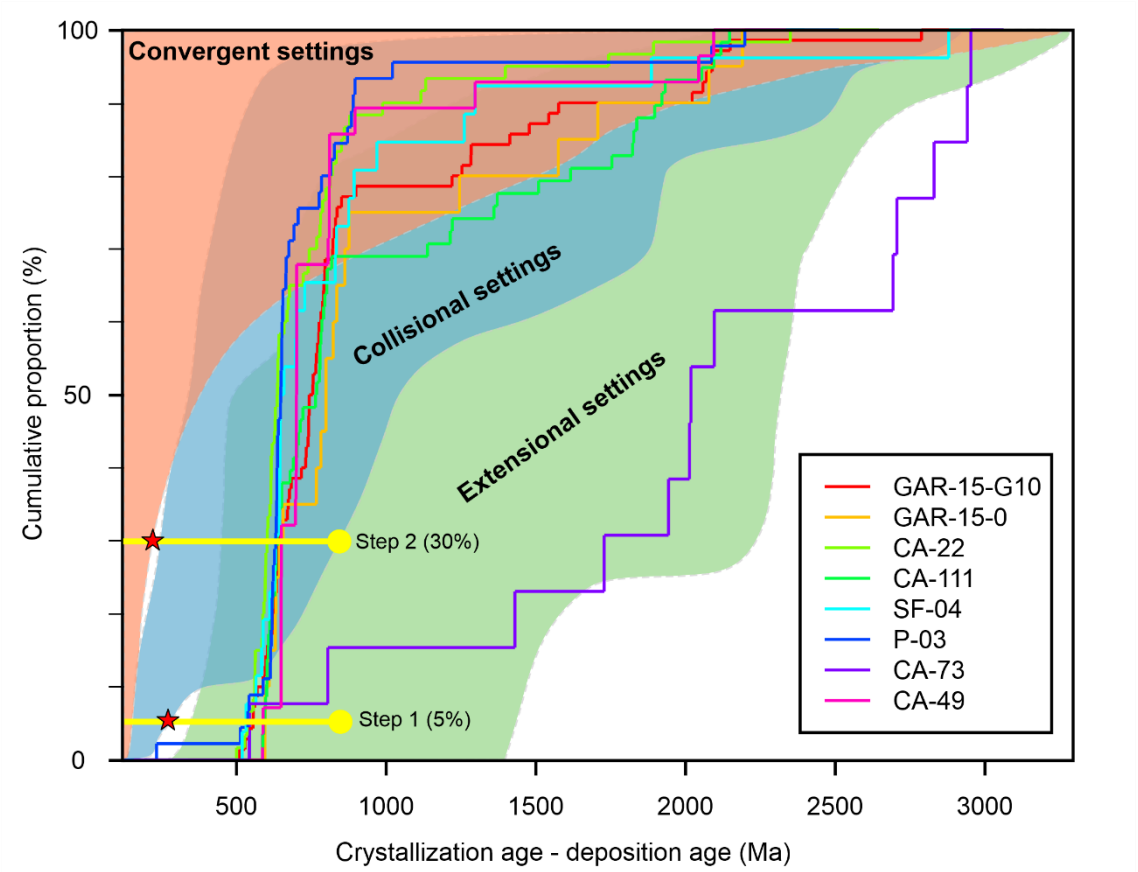

Figure 5.13 Cumulative probability plots for convergent, collisional, and extensional settings (Cawood et al., 2012) for the samples analyzed to this study.

5.5.3 Integrated profile of the PIB: composition/size clast variation and shock conditions

For the first time the polymict impact breccias from the Araguainha impact structure have been subjected to a focused textural and mineralogical analysis that combined field and laboratory analysis. This work provides a comprehensive characterization of the polymict impact breccia deposits along an integrated profile from the northern sector of the central uplift.

The breccia deposits are characterized along laterally extended profiles, where they can be described as having a chaotic, highly heterogeneous distribution of clast types. Grain size in the matrix is sand dominated, and at the microscopic scale the micro-clast size is mainly < 0.5 mm. The breccia contains brown slate and white sandstone clasts as the most frequently encountered clast types across all outcrops. Sizes of such clasts are most frequently up to 16 cm and 20 cm, respectively. Grain shapes are rounded to subrounded. However, no pattern could be discerned laterally or quasi-vertically.

The described profiles, CA-07, CA-09, and CA-84 representing in total 110 m thick breccia package, gave as main information (Fig. 5.10): (1) fragmented blocks of metasedimentary basement in contact with breccia deposits are preserved in the middle part of the profile (at 520-570 m.a.s.l.); (2) grey slate, brown slate, white sandstone, and quartz pebbles are abundant throughout the profile; (3) the clast size distribution along the profile are varied in macroscopic scale, from > 1 cm to meters; (4) granitic fragments are scarce and when observed, they only are in very small proportion at the bottom (500-505 m.a.s.l.), middle (530-545 m.a.s.l.), and in the uppermost (600-610 m.a.s.l) part of the integrated profile and associated with slate clasts; (5) impact melt clasts occur from 530 m.a.s.l to the uppermost part of the integrated profile, at 610 m.a.s.l, i.e., they are lacking in the lowermost section of the integrated profile; (6) planar fractures are stronger shock deformation occurrence along the outcrops, followed by feather features and planar deformation features.

Slates and white sandstone are the most important clast types. These lithologies can be related to the basement occurring directly below the breccia. Seemingly these lithologies have been added mechanically to the breccia, during turbulent scraping of the high-density breccia mass across the crater floor.

The clast size distribution varies from > 1 cm to meters at the macroscopic scale. The main size occurrences range from 5 to 23 cm, where is dominated by small clasts in the upper (5 cm), medium size clasts (8-14 cm) in the mid, and larger sizes in the bottom (16-23) parts of the integrated profile. Large clasts can be observed, for different clast types, at specific locations in the profile, such as: (a) impact melt clasts with 3 to 7 m sizes were observed at 575-610 m.a.s.l.; (b) white sandstone clasts with 1.3 to 2 m sizes at 545-580 m.a.s.l.; (c) grey slate with 7 m sizes at 575 m.a.s.l.; and (d) rare granitic clasts with up to 2.6 m sizes at 610 m.a.s.l. That is, the majority of the large clasts are concentrated at the bottom and towards the upper part of the integrated profile.

The silicious impact melt rock particles were formed in a regime of significant shock pressure of the order of 50 GPa or higher (Stöffler et al., 2018). The breccia deposits comprise a mixture of materials shocked within a wide range of shock pressures, ranging from less than 5 GPa (unshocked) to over 45 GPa. This involves (Stöffler et al., 2018): PF mostly < 10 GPa, FF up to 18 GPa (Poelchau, 2022; Tada et al., 2022) but mostly much lower; single sets of PDFs from ca. 8 to 15 GPa, and two sets of PDFs per host grain from ca. 15-25 GPa, as first order limits.

The variation in shock conditions for samples covering the entire extent of the 110 m integrated vertical profile is schematically represented in Figure 5.10. The PFs are distributed homogeneously along the profile, variably occurring between 60 and 80 % of PFs. They occur as part of feather features (FFs) in 15 to 30 % of PF+FFs in quartz minerals. On the other hand, occurrences of PDFs in quartz are seemingly riched in the middle and bottom parts of this profile, in up to 17 % of PDFs, but generally in significant numbers between 3 and 10 % of PDFs. That the amount of shocked micro-clasts is relatively diminished in the bottom part of the breccia profile is likely due to strong admixture of crater floor-derived clastic debris to the primary breccia mass of the fill.

5.5.4 Emplacement of polymict impact breccia at Araguainha impact structure

The Araguainha breccia deposits represent proximal impactites within the Araguainha impact structure, accessible only at the current erosion level on the

central uplift. Based on the combined field and petrographic observations of this work and of Souza et al. (2024), the components of the polymict lithic and suevitic breccias are derived from the lowermost target units – the lower units of the Paraná Basin (Furnas Formation and Rio Ivaí Group) and the basement rocks thought to be from the (meta)sedimentary rocks of the Paraguay Belt, with hardly any contribution from alkali granite. Also, the majority of PIB is in contact with the (meta)sedimentary basement. Thus, the breccia deposits are directly above the collapsed crater floor. This implies that the Araguainha polymict breccias are crater-fill deposits. No components of these breccias can be related to ballistic ejection, i.e., deposition of a fallback breccia (as also discussed by Souza et al., 2024).

The dominance of (meta)sedimentary target material in the breccia clast populations and occurring as intercalation/juxtaposition of blocks of basement rock and breccia may support that this intercalation results from central uplift collapse. This is in line with the heterogeneous nature of the clast population. Both Souza et al. (2024) and this study revealed that the PIB section accessible at Araguainha is the bottom-most impact breccia occurring just above the crater floor basement.

Previously several processes have been called upon regarding the emplacement of suevites, such as (e.g., Siegert et al., 2017): (a) fallback following the collapse of the ejecta plume (Wittmann et al., 2007; Stöffler et al., 2013, 2018; Artemieva et al., 2013); (b) ground-hugging density currents (Siegert et al., 2017); (c) ocean resurge into a crater (Ormö et al., 2007; Gulick et al., 2019); (d) phreatomagmatic (molten fuel coolant) interaction of hot melt and water – MFCI (Grieve et al., 2010; Stöffler et al., 2013, 2018; Artemieva et al., 2013; Osinski et al., 2016, 2020), and (e) multi-stage model (Mader and Osinski, 2018; Osinski and Grieve, 2024).

Scenario (a) – fallback following the collapse of the ejecta plume must be excluded for the Araguainha case. Our results prove that the breccia deposits superpose the crater floor of the structure and never left the crater. Hypothesis (c) – ocean resurge into the crater, is also disregarded. No evidence for a marine involvement in breccia emplacement has been observed in the Araguainha impact structure to date. Suevitic deposits resulting from process (d) –

phreatomagmatic (molten fuel coolant) interaction (MFCI), are characteristically multilayered, fine-grained, well sorted, and vitric clasts are a most abundant component (Büttner et al., 2002; Osinski et al., 2016). This is not in agreement with the features of the Araguainha polymict impact breccias. Thus, the most appropriate scenario would be (b) – ground-hugging density currents, or (e) – a multi-stage model.

Polymict impact breccia deposits with textural characteristics similar to those of our breccia at Araguainha are known from Ries crater. This includes evidence such as: "(1) topography-influenced thickness variations of the "suevite" sheet, (2) very poor sorting, (3) matrix support, (4) massive nature, (5) subtle coarse-tail grading, (6) abundant elutriation pipes, (7) abundance of broken and whole matrix-supported concentric-laminated accretionary lapilli in uppermost parts, and (8) an inverse-graded basal layer with low-angle cross-stratification" (Siegert et al., 2017, p. 855). Their items 1 to 4 are observed in the PIB studied here. Our breccia deposits are directly above paleotopographic surface of the crater floor, classified as poorly to moderately sorted, matrix supported, and of massive nature (sedimentary).

On the other hand, the multi-stage model has been proposed recently for impactite emplacement at the Mistastin Lake (Mader and Osinski, 2018) and Ries impact structures (Osinski and Grieve, 2024) based on a synthesis of the field and petrographic observations. This model could relate the Araguainha polymict impact breccias due to their particularity and pre-classification mentioned above, which are not adequately addressed by previous models.

5.5.5 Geological constraint of the basement below the Paraná Basin in Araguainha area

A borehole (AG-1-MT well) drilled ca. 30 km WSW of the Araguainha impact structure, near the town of Alto Garças, encountered metasedimentary rock associated with the Cuiabá Group, the basal unit of the Paraguay Belt, to 1.9 km depth (Cordani et al., 2009). This was the first evidence associated with the basement exposed at Araguainha. Souza et al. (2024) suggested that there are at least two sequences of basement strata in the Araguainha impact structure: the typically metamorphosed rocks (e.g., metasandstone and phyllites) correlated

with Cuiabá Group (previously reported by Sánchez, 2006 and Yokoyama, 2008) and an unmetamorphosed sedimentary sequence of sandstones and pelites. The provenance data of both PIB matrix and metasedimentary samples show similarity with lower units of the Paraná Basin and a few with Brasilia Belt, but differ significantly from the Cuiabá Group samples at the type locality (Fig. 5.12).

The maximum depositional age (500 Ma) and the zircon population of (meta)sedimentary rocks reveal ages of 2100 to ~600 Ma, involving the entire Proterozoic. Recently, Frugis et al. (2024) observed a similar pattern through analyses of metarenites and a schist from the Cuiabá Group, with age clusters of 1.2-0.9 Ga, 1.55-1.45 Ga, 1.80-1.75 Ga, and 2.0-1.9 Ga, whereas the depositional maximum age of 900 Ma. The authors interpreted this unit as passive margin deposits generated the erosion of depleted Mesoproterozoic and more evolved Paleoproterozoic rocks from the Amazonian Craton.

In the tectonic model for the evolution of the Paraguay Belt (e.g., McGee et al., 2014), the potential sources involve the Amazonian craton, Paranapanema block, and Goiás Magmatic Arc. The minor zircon age populations observed in our samples vary between 3.2 and 1.3 Ga and can be related to sources of the Amazonian craton that involve ages between 2.5 Ga and 1.0 Ga (Fig. 5.12; Tassinari and Macambira, 1999). The majority of our age data fall between ~ 600 and 900 Ma. Potential sources for these zircons include the 790-600 Ma Brasília Belt, the Neoproterozoic Goiás Magmatic Arc (Fig. 5.12; McGee et al., 2014). The Paranapanema Craton was developed during the Tonian tafrogenesis between 1000 and 850 Ma (Mantovani et al., 2005). The Nova Xavantina Sequence was formed around 745-714 Ma (Silva et al., 2022) and is considered contemporaneous with the Cuiabá Group (Pinho, 1990). The Goiás Magmatic Arc shows two zircon age provenance maxima related to the consumption of the Goiás-Pharusian Ocean at ca. 920-800 Ma and 660-630 Ma (Pimentel et al., 2000; Kroner and Cordani, 2003; Laux et al., 2005; Brito Neves et al., 2014).

The presence of zircon of specific ages reveals the proximity of the basin to its source area (Cawood et al., 2012). Today, the Araguainha metasedimentary basement is located ~500 km from the type section of the Cuiabá Group to the southwest and west, and ~200 km from the Brasilia Belt from the northeast. It is possible here to conclude that the high concentration of Neoproterozoic zircon

ages could be linked the Goiás Magmatic Arc located to the northeast of Araguainha impact structure (Fig. 5.12). This aligns in parts with the recent proposal of Frugis et al. (2024), who showed different sedimentary provenances for the eastern Paraguay Belt – the Amazonian Craton in the west and Goiás Magmatic Arc in the east. The authors suggested that the Cuiabá Group was deposited in an extensional tectonic regime through erosion, primarily from the Amazoian Craton and smaller contribution from the Brasília Orogen, while our samples were deposited in the extensional tectonic setting (Fig. 5.13). It is reasonable to assume that the Araguainha basement could represent the Cuiabá Group related to the proposed smaller component and zircon population from the Goiás Magmatic Arc.

5.6 Conclusions

Here, we present the integrated, detailed results of a clast and matrix investigation of the polymict lithic and suevitic breccias at Araguainha impact structure, as well as a first U-Pb zircon provenance study aimed at clarifying the provenance sources for the Araguainha breccias. The main new findings are:

- The polymict lithic and suevitic breccias are formed by angular to subrounded clast types derived from the basal units of the target stratigraphy, unsorted fragments of meter to centimenter size, embedded in a fine-grained sandy to pelitic matrix. The clast populations of the breccias are highly heterogeneous on a sample to sample basis. Along the quasi-vertical, integrated profile through the breccia deposits of the Araguainha central uplift (110 m thickness) a distribution pattern emerges.
- The polymict impact breccias and (meta)sedimentary basement samples have different zircon age populations. Breccia age population are similar to those of the Rio Ivaí Group, Furnas and Ponta Grossa formations of the lower part of the Paraná Basin, but they disagree with literature provenance data for the basement of the Paraguay Belt.
- The Araguainha basement were taken into the multilithological megablock zone of the collapsed central uplift and this geological context can complicate the interpretation of the real stratigraphy of the area. Nevertheless, samples CA-22 and CA-111 are clearly metasedimentary

and deposited, probably at the time when Cuiabá Group was deposited, but with provenance from proximal sources, like the Goiás Magmatic Arc.

- The clast populations of the breccia and the contact relationships between breccia and (meta)sedimentary basement exposed in the central uplift infer that the polymict impact breccias are deposited directly above the crater floor. There is no evidence for a contribution of ballistic ejecta. The lower units of the Paraná Basin suffered highly influence of shock waves, mainly Furnas Formation, and the metasedimentary clasts could be autochthone. This represents the material from within the central uplift that uplifted, fragmented, and after deposited in the matrix PIB.
- Our observations and the earlier work of Souza et al. (2024) suggest that the Araguainha polymict impact breccias were formed within the transient cavity and that this material never left the crater. The current configuration of breccia deposits juxtaposed with blocks and megablocks of the lowermost target stratigraphy confirms that these breccias represent the lowermost remnant of the original breccia deposit, directly above (and perhaps within) the crater floor.

Acknowledgements

This study was partially financed by the Brazilian Coordination for the Improvement of Higher Education Personnel (Coordenação de Aperfeiçoamento de Pessoal de Nível Superior – Brazil (CAPES) - Finance Code 001). The authors thank the University of Brasilia, Institute of Geosciences (IG/UnB), Postgraduate Program in Geology for providing the infrastructure for this research. CSMS is grateful to CAPES for a Ph.D. grant (process 88882.347189/2019-01). N. Hauser and W.U. Reimold have been supported by Brazilian National Council for Scientific and Technological Development (CNPq) fellowship grants (Nos. 309878/2019-5 and 305761/2019-6, respectively). CSMS also acknowledges financial support from a research grant from the Barringer Family Fund for Meteorite Impact Research.

5.7 References

Almeida, F.F.M., 1984, Província Tocantins, setor sudoeste, *in* Almeida, F.F.M., and Hasui, Y., eds., O Pré-Cambriano do Brasil: Edgard Blücher publishers, p. 265-281.

Alvarenga, C.J.S., Guimarães, E.M., Assine, M.L., Perinotto, J.A.J., and Laranjeira, N.P.F., 1998, Sequência Ordovício-Siluriana e Devoniana no flanco norte da Bacia do Paraná: Anais da Academia Brasileira de Ciências, v. 70, p. 587–606.

Alvarenga, C.J.S., Santos, R.V., and Dantas, E.L., 2004, C–O–Sr isotopic stratigraphy of cap carbonates overlying Marinoan age glacial diamictites in the Paraguay Belt, Brazil: Precambrian Research, v. 131, p. 1-21.

Artemieva, N.A., Wünnemann, K., Krien, F., Reimold, W.U., and Stöffler, D., 2013, Ries Crater and suevite revisited – Observations and modeling Part II – Modelling: Meteoritics and Planetary Science, v. 48, p. 590-627, https://doi.org/10.1111/maps.12085.

Assine, M.L., 1996, Aspectos da estratigrafia das sequências pré-carboníferas da Bacia do Paraná no Brasil [Ph.D thesis]: São Paulo, University of São Paulo, 207 p.

Assine, M.L., Soares, P.C., and Milani, E.J., 1994, Sequências tectono-sedimentares mesopaleozoicas da Bacia do Paraná, Sul do Brasil: Revista Brasileira de Geociências, v. 24, p. 77-89.

Babinski, M., Boggiani, P.C., Trindade, R.I.F., and Fanning, C.M., 2013, Detrital zircon ages and geochronological constraints on the Neoproterozoic Puga diamictites and associated BIFs in the southern Paraguay Belt, Brazil: Gondwana Research, v. 23, p. 988-997. https://doi.org/10.1016/j.gr.2012.06.011.

Babinski, M., McGee, B., Tokashiki, C.C., Tassinari, C.C.G., Saes, G.S., and Pinho, F.E.C., 2018, Comparing two arms of an orogenic belt during Gondwana amalgamation: Age and provenance of the Cuiabá Group, northern Paraguay Belt, Brazil: Journal of South American Earth Sciences, v. 85, p. 6-42, https://doi.org/10.1016/j.james.2018.04.009.

Bandeira, J., McGee, B., Nogueira, A.C.R., Collins, A.S., and Trindade, R.I.F., 2012, Closure of the Neoproterozoic Clymene Ocean: sedimentary and

detrital zircon geochronology evidence from the siliciclastic upper Alto Paraguai Group, northern Paraguay Belt, Brazil: Gondwana Research, v. 21, no. 2-3, p. 323-340. https://doi.org/10.1016/j.gr.2011.04.006.

Brito Neves, B.B., Fuck, R.A., and Pimentel, M.M., 2014, The Brasiliano collage in South America: a review: Brazilian Journal of Geology, v. 44, no. 3, p. 493-518. http://dx.doi.org/10.5327/Z2317-4889201400030010.

Büttner, R., Dellino, P., La Volpe, L., Lorenz, V., and Zimanowski, B., 2002, Thermohydraulic explosions in phreatomagmatic eruptions as evidenced by the comparison between pyroclasts and products from Molten Fuel Coolant Interaction experiments: Journal of Geophysical Research, v. 107, no. B11, p. 2277, https://doi.org/10.1029/2001JB000511.

Carneiro, J., Fuck, R.A., and Dantas, E.L, 2021, Arenópolis sequence, evolution of a marginal basin in the Neoproterozoic Goiás magmatic arc, central Brazil: Journal of South American Earth Sciences, v. 106, p. 103033. https://doi.org/10.1016/j.jsames.2020.103033

Cavosie, A.J., Timms, N.E., Ferriere, L., and Rochette, P., 2018, FRIGN zircon – The only terrestrial high-pressure and high-temperature mineral diagnostic of shock deformation: Geology, v. 46, p. 891-894.

Cawood, P.A., Hawkesworth, C.J., and Dhuime, B., 2012, Detrital zircon Record and tectonic setting: Geology, v. 40, no. 10, p. 875-878.

Claeys, P., Heuschkel, S., Lounejjeva-Baturina, E., Sanchez-Rubio, G., and Stöffler, D., 2003, The suevite of drill hole Yucatàn 6 in the Chicxulub impact crater: Meteoritics and Planetary Science, v. 38, p. 1299-1317.

Coney, L., Reimold, W.U., Gibson, R.L., Koeberl, C., and Ogilvie, P., 2010, Melt particle characteristics of the within- and out-of-crater suevites from the Bosumtwi impact structure, Ghana: Implications for crater formation: Geological Society of America Special Papers, v. 465, p. 411-442.

Cordani, U.G., Brito Neves, B.B., Fuck, R.A., Porto, R., Thomaz Filho, A., and Cunha, F.M.B., 2009, Preliminary integration study of Precambrian with tectonic events in Brazilian sedimentary basins (Republication): Boletim de Geociências da Petrobrás, v. 17, p. 133-204.

Crósta, A.P., Gaspar, J.C., and Candia, M.A.F., 1981, Feições de metamorfismo de impacto no Domo de Araguainha: Revista Brasileira de Geociências, v. 11, p. 139-146.

Crósta, A.P., Reimold, W.U., Vasconcelos, M.A.R., Hauser, N., Oliveira, G.J.G., Maziviero, M.V., and Góes, A.M., 2019, Impact cratering: The South American record – Part 1: Chemie der Erde, v. 79, p. 1-61.

Dantas, E.L., Alvarenga, C.J.S., Santos, R.V., and Pimentel, M.M., 2009, Using Nd isotopes to understand the provenance of sedimentary rocks from a continental margin to a foreland basin in the Neoproterozoic Paraguay Belt, central Brazil: Precambrian Research, v. 170, p. 1-12, https://doi.org/10.1016/j.precamres.2008.11.005.

de Marchi, L.P., 2015, Caracterização litológica da Brecha Polimítica de Impacto do Domo de Araguainha-MT [BSc thesis]: São Paulo, Universidade Estadual de Campinas, 68 p.

de Marchi, L.P., Hauser, N., Reimold, W.U., and Crósta, A.P., 2016, Geological and petrographical characterization of the polymict impact breccia of the Araguainha Dome, Brazil: Woodlands, Texas, Lunar and Planetary Institute, 47th Lunar and Planetary Science Conference, abstract 1903, p. 1120.

Della Giustina, M.E.S., Pimentel, M.M., Ferreira Filho, C.F., and Holanda, M.H.B.H., 2011, Dating coeval mafic magmatism and ultrahigh temperature metamorphism in the Anápolis Itaucú Complex, Central Brazil: Lithos, v. 124, p. 82-201.

Erickson, T.M., Timms, N.E., Kirkland, C.L., Tohver, E., Cavosie, A.J., Pearce, M., and Reddy, S.M., 2017, Shocked monazite chronometry: Integrating microstructural and in situ isotopic age data for determining precise impact ages: Contributions of Mineralogy and Petrology, v. 172, no. 11, p. 1-19, https://doi.org/10.1007/s00410-017-1328-2.

Feignon, J.G., Schulz, T., Ferrière, L., Goderis, S., de Graaff, S.J., Kaskes, P., Déhais, T., Claeys, P., and Koeberl, C., 2021, Search for a meteoritic component within the impact melt rocks of the Chicxulub impact structure peak ring, Mexico: Geochimica et Cosmochimica Acta, v. 323, p. 74-101. https://doi.org/10.1016/j.gca.2022.02.006.

Fernandes, L.A., and Coimbra, A.M., 1996, A Bacia Bauru (Cretáceo Superior, Brasil): Anais da Academia Brasileira de Ciências, v. 68, no. 2, p. 195-205.

Ferrière, L., Koeberl, C., Brandstätter, F., and Mader, D., 2010, Geochemistry of basement rocks and impact breccias from the central uplift of the Bosumtwi crater, Ghana – Comparison of proximal and distal impactites, *in* Gibson, R.L., and Reimold, W.U., eds., Large Meteorite Impacts and Planetary Evolution IV: Geological Society of America Special Paper, v. 465, p. 443–469, https://doi.org/10.1130/2010.2465(22).

French, B.M., 1998, Traces of catastrophe: A Handbook of Shock-Metamorphic Effects in Terrestrial Meteorite Impact Structures: Houston, Texas, Lunar and Planetary Institute, 130 p.

Frugis, G.L., Campos Neto, M.C., Westin, A., and Fanning, C.M., 2024, New perspectives on the tectonic evolution of the eastern Paraguay Belt revealed through zircon U-Pb-Hf-O systematics of the inner units: Precambrian Research, v. 411, p. 107529. https://doi.org/10.1016/j.precamres.2024.107529.

Geraldes, M.C., Tassinari, C.C.G., and Onoe, A.T., 2003, $^{40}Ar^{39}Ar$ metamorphic record of a collision related to the western Gondwana collage: the (541-531 Ma) Paraguay belt in the Nova Xavantina (MT) region. In *Simpósio Nacional de Estudos Tectônicos*, Búzios, Rio de Janeiro. Anais do IX SNET, pp. 54-57.

Geraldes, M.C., Tassinari, C.C.G., Babinski, M., Martinelli, C.D., Iyer, S.S., Barboza, E.S., Pinho, F.E.C., and Onoe, A.T., 2008, Isotopic evidence for the late Brasiliano (500-550 Ma) ore-forming mineralization of the Araés Gold Deposit, Brazil: International Geology Review, v. 50, p. 177-190. https://doi.org/10.2747/0020-6814.50.2.177.

Gezatt, J.N., 2011, Proveniência de rochas sedimentares detríticas do gráben de Piranhas e comparação com a Formação Vila Maria do Siluriano da Bacia do Paraná [BSc thesis]: Porto Alegre, Universidade Federal Do Rio Grande Do Sul, 64 p.

Godoy, A.M., Pinho, F.E.C., Manzano, J.C., Araújo, L.M.B., Silva, J.A., and Figueiredo, M., 2010, Estudos isotópicos das rochas granitoides

Neoproterozóicas da Faixa de Dobramento Paraguai: Revista Brasileira de Geociências, v. 40, no. 3, p. 380-391.

Godoy, A.M., Ruiz, A.S., Manzano, J.C., and Araújo-Ruiz, L.M.B., 2007, Os Granitóides Brasilianos Pós-Tectônicos da Faixa de Dobramentos Paraguai, MS e MT: Geologia USP Série Científica, v. 7, p. 29-44.

Grieve, R.A.F., Ames, D.E., Morgan, J.V., and Artemieva, N., 2010, The evolution of the Onaping Formation at the Sudbury impact structure: Meteoritics and Planetary Science, v. 45, p. 759-782.

Grieve, R.A.F., Dence, M.R., and Robertson, P.B., 1977, Cratering processes: as interpreted from the occurrences of impact melts, *in* Roddy, D.J., Pepin, R.O. and Merrill, R.B., eds., Impact and explosion cratering: New York, Pergamon Press, p. 791–814.

Grieve, R.A.F., Osinski, G.R., and Chanou, A., 2015, The suevite conundrum: A general perspective: Houston, Texas, Lunar and Planetary Institute, 46th Lunar and Planetary Science Conference, abstract 1861, p. 1036.

Gulick, S.P.S., Bralower, T.J., Ormö, J., Hall, B., Grice, K., Schaefer, B., Lyons, S., Freeman, K.H., Morgan, J.V., Artemieva, N., Kaskes, P., de Graaff, S.J., Whalen, M.T., Collins, G.S., Tikoo, S.M., Verhagen, C., Christeson, G.L., Claeys, P., Coolen, M.J.L., Goderis, S., Goto, K., Grieve, R.A.F., McCall, N., Osinski, G.R., Rae, A.S.P., Riller, U., Smit, J., Vajda, V., Wittmann, A., and The Expedition 364 Scientists, 2019, The first day of the Cenozoic: Proceedings of the National Academy of Sciences, v. 116, no 39, p. 19342–19351.

Hasui, Y., 2012, Sistema orogênico Tocantins. In *Geologia do Brasil*, edited by Hasui, Y., Carneiro, C. D. R., Almeida, F. F. M., and Bartorelli, A. Beca, Brazil, pp. 289-325.

Hauser, N., Reimold, W.U., Cavosie, A.J., Crósta, A.P., Schwarz, W.H., Trieloff, M., Souza, C.S.M., Rodrigues, E.N., and Brown, M., 2019, Linking shock textures revealed by BSE, CL, and EBSD with U-Pb data (LA-ICP-MS and SIMS) from zircon from Araguainha impact structure, Brazil: Meteoritics and Planetary Science, v. 54, p. 2286-2311.

Hecht L., 2022, The Formation and Emplacement of Suevite – A review of Genetic models and Unresolved issues: Glasgow, Scotland, Lunar and

Planetary Institute, 85th Annual Meeting of The Meteoritical Society, abstract. 2695, p. 6434.

Henrique-Pinto, R., Basei, M.A.S., Santos, P.R., Saad, A.R., Milani, E.J., Cingolani, C.A., and Frugis, G.L., 2021, Paleozoic Paraná Basin transition from collisional retro-foreland to pericratonic syneclise: Implications on the geodynamic model of Gondwana proto-Andean margin: Journal of South American Earth Sciences, v. 111, 103511, https://doi.org/10.1016/j.jsames.2021.103511.

Henrique-Pinto, R., Basei, M.A.S., Santos, P.R., Saad, A.R., Passarelli, C.R, Cingolani, C.A., and Milani, E.J., 2024, Tonian juvenile arc crust provenance recorded in the Paran´a Basin, Western Gondwana proto-Andean margin: Precambrian Research, v. 405, 107354, https://doi.org/10.1016/j.precamres.2024.107354.

Hippertt, J.P., Lana, C., Weinberg, R.F., Tohver, E., Schmieder, M., Scholz, R., Gonçalves, L., and Hippertt, J.F., 2014, Liquefaction of sedimentary rocks during impact crater development: Earth and Planetary Science Letters, v. 408, p. 285-295.

Kalleson, E., Dypvik H., and Nielsen, O., 2010, Melt-bearing impactites (suevite and impact melt rock) within the Gardnos structure, Norway: Meteoritics and Planetary Science, v. 45, no. 5, p. 798-827, https://doi:10.1111/j.1945-5100.2010.01055.x.

Kaskes, P., de Graaff, S.J., Feignon, J., Déhais, T., Goderis, S., Ferrière, L., Koeberl, C., Smit, J., Wittmann, A., Gulick, S.P.S., Debaille, V., Mattielli, N., and Claeys, P., 2022, Formation of the crater suevite sequence from Chicxulub peak ring: A petrographic, geochemical, and sedimentological characterization, Geological Society of America Bulletin, v. 134, no. 3-4, p. 895-927, https://doi.org/10.1130/B36020.1.

Kroner, A., and Cordani, U.G., 2003, African, southern Indian and South American Craton were not part of Rodinia continent: evidence from field relationship and geochronology: Tectonophysics, v. 375, no. 1-4, p. 325-352.

Lacerda Filho, J.V., Abreu Filho, W., Valente, C.R., Oliveira, C.C., and Albuquerque, M.C., 2004, Geologia e recursos minerais do estado de Mato Grosso: Programa Geologia do Brasil, CPRM/MME/SICME, 252 p.

Lacerda Filho, J.V., Brito, R.S.C., Silva, M.G., Oliveira, C.C., Moreton, L.C., Martins, E.G., Lopes, R.C., Lima, T.M., Larizzatti, J.H., and Valente, C.R., 2006, Geologia e Recursos Minerais do Estado de Mato Grosso do Sul: Programa Integração, atualização e difusão de dados de geologia do Brasil, CPRM/SICME-MS/MME, 121 p.

Lana, C., Romano, R., Reimold, W.U., and Hippertt, J., 2006, Collapse of large complex impact structures: Implications from the Araguainha impact structure: Geology, v. 34, p. 9-12.

Lana, C., Souza-Filho, C.R., Marangoni, Y.R., Yokoyama, E., Trindade, R.I.F., Tohver, E., and Reimold, W.U., 2007, Insights into the morphology, geometry, and post-impact erosion of the Araguainha peak-ring structure, central Brazil: Geological Society of America Bulletin, v. 119, p. 1135-1150.

Lana, C., Souza-Filho, C.R., Marangoni, Y.R., Yokoyama, E., Trindade, R.I.F., Thover, E., and Reimold, W.U., 2008, Structural evolution of the 40 km wide Araguainha impact structure, central Brazil: Meteoritics and Planetary Science, v. 43, p. 701-716, https://doi:10.1111/j.1945-5100.2008.tb00679.x.

Laux, J.H., Pimentel, M.M., Dantas, E.L. Armstrong, R., and Junges, S.L., 2005, Two Neoproterozoic crustal events in the Brasília Belt, central Brazil: Journal of South American Earth Sciences, v. 18, p. 183-198.

Leite, F.G.D.L., Fuck, R.A., Dantas, E.L., and Ruiz, A.S., 2021, Appinitic and high Ba-Sr magmatism in central Brazil: insights into the late accretion stage of West Gondwana: Lithos, v. 398–399, p. 106333. https://doi.org/10.1016/j.lithos.2021.106333.

Leite, F.G.D.L., Fuck, R.A., Dantas, E.L., Ruiz, A.S., Moniê, P., and Iemmolo, A., 2024, Tectonic significance of the late-Ediacaran syn-orogenic basin in the easternmost portion of the Paraguay Belt, Tocantins Province, central Brazil: Journal of South American Earth Sciences, v. 133, p. 104735. https://doi.org/10.1016/j.jsames.2023.104735.

López, W.H.A., 2022, Proveniência sedimentar das formações Ponta Grossa e São Domingos (Devoniano) do NW da Bacia do Paraná (Brasil): implicações regionais para os ventos T-R do SW de Gondwana [M.Sc thesis]: Brasilia, University of Brasilia.

Luz, J.S., Oliveira, A.M., Souza, J.O, Motta, J.F.M., Tanno, L.C., Carmo, L.S., and Souza, N.B., 1980, Projeto Coxipó – relatório final: Companhia de Pesquisa de Recursos Minerais, Superintendência Regional de Goiânia, DNPM/CPRM, v. 1, 136 p.

Machado, R., Lana, C., Stevens, G., Filho, C.R.S., Reimold, W.U., and McDonald, I., 2009, Generation, mobilization and crystallization of impact-induced alkali-rich melts in granitic target rocks. Evidence from the Araguainha impact structure, central Brazil: Geochimica et Cosmochimica Acta, v. 73, p. 7183-7201.

Mader, M.M., and Osinski, G.R., 2018, Impactites of the Mistastin Lake impact structure: Insights into impact ejecta emplacement: Meteoritics and Planetary Science, v. 53, p. 2492-2518, https://doi:10.1111/maps.13173.

Mantovani, M.S.M., Quintas, M.C.L., Shukowsky, W., and Brito Neves, B.B., 2005, Delimitation of the Paranapanema Proterozoic block: a geophysical contribution: Episodes, v. 28, p. 18-22.

Marques, G.C., Oliveira, C.G., Espada, E., and Dantas, E.L., 2019, The Fazenda Nova gold deposit, Goiás Magmatic Arc: late Neoproterozoic intrusion-related auriferous mineralization controlled by intracontinental strike-slip faulting: Ore Geology Reviews, v. 107, p. 546–572.

Matteini, M., Junges, S.L., Dantas, E.L., Pimentel, M.M., and Bühn, B., 2010, In situ zircon U–Pb and Lu–Hf isotope systematic on magmatic rocks: insights on the crustal evolution of the Neoproterozoic Goiás Magmatic Arc, Brasília belt, Central Brazil: Gondwana Research, v. 17, no. 1, p. 1–12. https://doi.org/10.1016/j.gr.2009.05.008.

McCall, N., Gulick, S.P.S., Karro, K., Jõeleht, A., Wilk, J., and Pösges, G., 2023, Understanding the Ries impact structure subsurface from high-resolution seismic data: Geology, v. 52, no. 1, p. 39–44. https://doi.org/10.1130/G51503.1.

McGee, B., Collins, A.S., Trindade, R.I.F., and Payne, J., 2014, Age and provenance of the Cryogenian to Cambrian passive margin to foreland basin sequence of the northern Paraguay Belt, Brazil: Geological Society of America Bulletin, v. 127, p. 76-86, http://dx.doi.org/10.1130/B30842.1.

Milani, E.J., 1997, Evolução tectono-estratigráfica da Bacia do Paraná e seu relacionamento com a geodinâmica fanerozóica do Gondwana sul-ocidental [PhD thesis]: Universidade Federal do Rio Grande do Sul, Porto Alegre, 255 p.

Milani, E.J., and Ramos, V.A., 1998, Orogenias Paleozóicas no Domínio Sul-ocidental do Gondwana e os ciclos de subsidência da Bacia do Paraná: Revista Brasileira de Geociências, v. 28, p. 473-484.

Milani, E.J., Melo, J.H.G., Souza, P.A., Fernandes, L.A., and França, A.B., 2007, Bacia do Paraná: Boletim de Geociências, v. 15, p. 265-287.

Mizusaki, A.M.P., Melo, J.H.G., Vignol-Lelarge, M.L., Steeman, P., 2002, Vila Maria Formation (Silurian, Paraná Basin, Brazil): integrated radiometric and palynological age determinations: Geological Magazine, v. 139, no. 4, p. 453-463.

Montibeller, C.C., Zanardo, A., and Navarro, G.R.B., 2017, Decifrando a proveniência dos folhelhos da formação Ponta Grossa na região de Rio Verde de Mato Grosso e Coxim (MS) através de métodos petrográfico e geoquímicos: Geologia USP Série Científica, v. 17, no. 1, p. 41-59.

Nogueira, A.C.R., Riccomini, C., Sial, A.N., Moura, C.A.V., and Fairchild, T.R., 2003, Soft-sediment deformation at the base of the Neoproterozoic Puga cap carbonate (southwestern Amazon craton, Brazil): confirmation of rapid icehouse to greenhouse transition in snowball Earth: Geology, v. 31, no. 7, p. 613-616. https://doi.org/10.1130/0091-7613(2003)031<0613:SDATBO>2.0.CO;2.

Ormö, J., Sturkell, E., and Lindström, M., 2007, Sedimentological analysis of resurge deposits at the Lockne and Tvären craters: Clues to flow dynamics: Meteoritics and Planetary Science, v. 42, p. 1929–1943, https://doi.org/10.1111/j.1945-5100.2007.tb00551.x.

Osinski, G.R., and Grieve, R.A., 2024, The “suevite” conundrum, Part 2: Re-examining the type locality at the Ries impact structure, Germany:

Meteoritics and Planetary Science, p. 1-29. https://doi.org/10.1111/maps.14241.

Osinski, G.R., and Pierazzo, E., 2013, Impact Cratering: processes and products: Oxford, Wiley-Blackwell, 316 p.

Osinski, G.R., Coulter, A.B., Flemming, R.L., Ozaruk, A., Pickersgill, A.E., and Singleton, A.C., 2023, Revisiting the Gow Lake impact structure, Saskatchewan, Canada: Meteoritic and Planetary Sciences, v. 58, p. 775-788. https://doi.org/10.1111/maps.13986.

Osinski, G.R., Grieve, R.A.F., Chanou, A., and Sapers, H.M., 2016, The “suevite” conundrum, Part 1: The Ries suevite and Sudbury Onaping Formation compared: Meteoritics and Planetary Science, v. 51, p. 2316-2333.

Osinski, G.R., Grieve, R.A.F., Collins, G.S., Marion, C., and Sylvester, P., 2008, The effect of target lithology on the products of impact melting: Meteoritics and Planetary Science, v. 43, p. 1939-1954.

Osinski, G.R., Grieve, R.A.F., Hill, P.J.A., Simpson, S.L., Cockell, C., Christeson, G.L., Ebert, M., Gulick, S., Melosh, H.J., Riller, U., Tikoo, S.M., Wittmann, A., 2020, Explosive interaction of impact melt and seawater following the Chicxulub impact event: Geology, v. 48, p. 108–112, https://doi.org/10.1130/G46783.1.

Pelosi, G.F.F., 2017. Age, Provenance and Tectonic Setting from Southern Portion of the Cuiabá Group: Implications for the Evolution of the Paraguay Belt [M.Sc thesis]: Cuiabá, University of Mato Grosso, 47 p.

Piauilino, P.F., Hauser, N., Dantas, E.L., 2021, From passive margin to continental collision: Geochemical and isotopic constraints for E-MORB and OIB-like magmatism during the Neoproterozoic evolution of the southeast Brasília Belt: Precambrian Research, v. 359, p. 105345. https://doi.org/10.1016/j.precamres.2019.105345.

Pimentel, M.M., 2016, The tectonic evolution of the Neoproterozoic Brasília Belt, Central Brazil: a geochronological and isotopic approach: Brazilian Journal of Geology, v. 46, p. 67–82.

Pimentel, M.M., and Fuck, R.A., 1987, Late proterozoic granitic magmatism in southwestern Goiás, Brazil: Revista Brasileira de Geociências, v. 17, no. 4, p. 415-425.

Pimentel, M.M., Fuck, R.A., and Alvarenga, C.J.S., 1996., Post-Brasiliano (Pan African) high-K granitic magmatism in central Brazil: the role of late Precambrian/early Paleozoic extension: Precambrian Research, v. 80, p. 217-238, https://doi:10.1016/S0301-9268(96)00016-2.

Pimentel, M.M., Fuck, R.A., and Dantas, E.L., 1991, Zircon and sphene U-Pb geochronology of Upper Proterozoic volcanic-arc rock units from southwestern Goiás, central Brazil: Journal of South American Earth Sciences, v. 4, no. 4, p. 295-305.

Pimentel, M.M., Fuck, R.A., Ferreira Filho, C.F., and Araújo, S.M., 2000, The basement of the Brasília Belt and the Goiás Magmatic Arc. In *31st International Geological Congress*, edited by Cordani, U. G., Milani, E. J., Thomaz Filho, A., and Campos, D. A. Tectonic Evolution of South America., Rio de Janeiro, 195-229.

Pimentel, M.M., Hollanda, M.H.B.M., and Armstrong, R., 2003, Shrimp U-Pb age and Sr-Nd isotopes of the Morro do Baú mafic intrusion: implications for the evolution of the Arenópolis volcano-sedimentary sequence, Goiás Magmatic Arc: Anais da Academia Brasileira de Ciências, v. 75, no. 3, p. 331-339.

Pinho, F.E., 1990, Geoquímica do depósito de ouro de Nova Xavantina - leste do Estado de Mato Grosso. *Congresso Brasileiro de Geologia*, 36. Anais SBG: pp. 3.1316-1330.

Poelchau, M.H., 2022, Constraints on the pressure range of feather features in shocked quartz: Glasgow, Scotland, Lunar and Planetary Institute, 85th Annual Meeting of The Meteoritical Society, abstract 2695, p. 6499.

Preuss, J. 2012. Characterization of impact-related melt breccias from the impact structure Araguainha (Brazil) [M.Sc thesis]: Germany, University of Potsdam, 92 p.

Reimold, W.U., Bartosova, K., Schmitt, R.T., Hansen, B., Crasselt, C., Koeberl, C., Wittmann, A., and Powars D.S., 2009, Petrographic observations on the Exmore breccia, ICDP-USGS drilling ar Eyreville, Chesapeake Bay impact structure, USA, *in* Gohn, G.S., Koeberl, C., Miller, K.G., and Reimold, W.U., eds., The ICDP-USGS deep drilling project in the

Chesapeake Bay impact structure: Results from the Eyreville core holes: Geological Society of America Special paper 458, p. 655-698.

Reimold, W.U., McDonald, I., Schmitt, R.T., Hansen, B., Jacob, J., and Koeberl, C., 2013, Geochemical studies of the SUBO 18 (Enkingen) drill core and other impact breccias from the Ries crater, Germany: Meteoritics and Planetary Science, v. 48, p. 1531–1571.

Sánchez, J.P., 2006, Mapeamento 1:25.000 do núcleo do Astroblema Domo de Araguainha e aspectos geoturísticos da região [B.Sc thesis]: São Paulo, Universidade Estadual Paulista, 57 p.

Santos, T.B., Mancini, F., Cury, L.F., and Ferreira, F.J.F., 2015, Proveniência de zircões detríticos e implicações para a paleogeografia da Formação Furnas no noroeste da Bacia do Paraná: Geologia USP Série Científica, v. 15, no. 2, p. 25-59, https://doi.org/10.11606/issn.2316-9095.v15i2p25-59.

Sauer, A., 1920, Erläuterugen zur geologischen: Karte Württemberg 1:50000, Blatt 20, Bopfingen 1.

Siegert, S., and Hecht, L., 2018, Heterogeneity of melts in impact deposits and implications for their origin (Ries suevite, Germany): Meteoritics and Planetary Science, v. 54, p. 2409-2447.

Siegert, S., Branney, M.J., and Hecht, L., 2017, Density current origin of a melt-bearing impact ejecta blanket (Ries suevite, Germany): Geology, v. 45, p. 855-858.

Silva, D., Lana, C., and Souza-Filho, C.R., 2016, Petrographic and geochemical characterization of the granitic rocks of the Araguainha impact crater, Brazil: Meteoritics and Planetary Science, v. 51, p. 443-467.

Silva, M.F., Dantas, E.L., Matteini, M., and Trindade, R.I.F., 2022, Late Tonian explosive volcanism and hyaloclastites in northern Paraguay Belt, Central Brazil: A record of Rodinia break-up in western Gondwana: Precambrian Research, v. 382, p. 106862. https://doi.org/10.1016/j.precamres.2022.106862.

Souza, C.S.S., Hauser, N., Reimold, W.U., Bernardes, R.B., Vieira, L.C., Guimarães, E.M., and Gottwald, M., 2024, Araguainha impact structure, Brazil: new insights into the geology of the central uplift: Meteoritics and

Planetary Science, v. 59, p. 2577-2607. https://doi.org/10.1111/maps.14236.

Stöffler, D., and Grieve, R.A.F., 2007, Impactites, *in* Fettes, D., and Desmons, J., eds., Metamorphic Rocks: A Classification and Glossary of Terms, Recommendations of the International Union of Geological Sciences: Cambridge, UK, Cambridge University Press, p. 82–92, p. 111–125, and p. 126–242.

Stöffler, D., Artemieva, N.A., Ivanov, B.A., Hecht, L., Kenkmann, T., Schmitt, R.T., Tagle, R.A., and Wittmann, A., 2004, Origin and emplacement of the impact formations at Chicxulub, Mexico, as revealed by ICDP deep drilling at axcopoil-1 and by numerical modeling: Meteoritics and Planetary Science, v. 39, p. 1035-1067.

Stöffler, D., Artemieva, N.A., Wünnemann, K., Reimold, W.U., Jacob, J., Hansen, B.K., and Summerson, I.A.T., 2013, Ries crater and suevite revisited – Observations and modeling Part I: Observations: Meteoritics and Planetary Science, v. 48, p. 515-589.

Stöffler, D., Hamann, C., and Metzler, K., 2018, Shock metamorphism of planetary silicate rocks and sediments: proposal for an updated classification system: Meteoritics and Planetary Sciences, v. 53, p. 5-49, https://doi.org/10.1111/maps.12912.

Tada, T., Kurosawa, K., Ono, H., Hamann, C., Okamoto, T., Niihara, T., Matsui, T., 2022, Shock recovery of granite with a decaying shock wave: feather features formation in quartz: Lunar and Planetary Institute, 53rd Lunar and Planetary Science Conference, abstract 2678, p. 1733.

Tassinari C.C.G., and Macambira M.J.B., 1999, Geochronological provinces of the Amazonian Craton: Episodes, v. 22, p. 174-182.

Theilen-Willige, B., 1981, The Araguainha impact structure, Central Brazil. Revista Brasileira de Geociências, v. 11, p. 91-97.

Thompson, L.M., and Spray, J.G., 2017, Dynamic interaction between impact melt and fragmented basement at Manicouagan: The suevite connection: Meteoritics and Planetary Science, v. 52, p. 1300-1329.

Tohver, E., Lana, C., Cawood, P.A., Fletcher, I.R., Jordan, F., Jourdan, F., Sherlock, S., Rasmussen, B., Trindade, R.I.F., Yokoyama, E., Souza

Filho, C.R., and Marangoni, Y., 2012, Geochronological constraints on the age of a Permo–Triassic impact event: U–Pb and $^{40}Ar/^{39}Ar$ results for the 40 km Araguainha structure of central Brazil: Geochimica et Cosmochimica Acta, v. 86, p. 214-227.

UnB-IG, 2012, Final Mapping Project by the Graduate Class of 2012: University of Brasilia, Institute of Geosciences, Unpublished Report, 759 pp.

Vasconcelos, B.R., 2018. Proveniência sedimentar do Grupo Cuiabá na Faixa Paraguai meridional [PhD thesis]: Brasília, University of Brasília, 173 p.

Vermeersch, P., 2021, Maximum depositional age estimation revisited: Geoscience Frontiers, v. 12, p. 843–850.

Vermeesch, P., Resentini, A., and Garzanti, E., 2016, An R package for statistical provenance analysis: Sedimentary Geology, v. 336, p. 14–25, https://doi.org/10.1016/j.sedgeo.2016.01.009.

von Engelhardt, W., Matthai, S., and Walzebuck, J., 1992, Araguainha impact crater, Brazil. I – The interior part of the uplift: Meteoritics and Planetary Sciences, v. 27, p. 442-457.

Warr, L.N., 2021, IMA–CNMNC approved mineral symbols: Mineralogical Magazine, v. 85, no. 3, p. 291-320, https://doi.org/10.1180/mgm.2021.43.

Wittmann, A., Kenkmann, T., Hecht, L., and Stöffler, D., 2007, Reconstruction of the Chicxulub ejecta plume from its deposits in drill core Yaxcopoil-1: Geological Society of America Bulletin, v. 119, p. 1151–1167, https://doi.org/10.1130/B26116.1.

Wittmann, A., Kenkmann, T., Schmitt, R.T., Hecht, L., and Stöffler, D., 2004, Impact-related dike breccia lithologies in the ICDP drill core Yaxcopoil-1, Chicxulub impact structure, Mexico: Meteoritics and Planetary Science, v. 39, p. 931-954.

Yokoyama, E., 2008. Trama magnética do núcleo soerguido da estrutura de impacto de Araguainha (MT/GO) [M.Sc thesis]: São Paulo, University of São Paulo, 173 p.

Zimmermann, S., Mark, C., Chew, D., and Voice, P.J., 2017, Maximising data and precision from detrital zircon U-Pb analysis by LA-ICPMS: the use of core-rim ages and the single-analysis concordia age: Sedimentary Geology, v. 375, p. 5-13.

5.8 Supplementary Material

Supplementary Material 1. Methodology

Table of the analyzed samples and the detailed methodologies for the instrumental techniques applied.

Table S1.A Samples analyzed for the instrumental techniques: micro-X-ray fluorescence spectrometry (μXRF), quantitative evaluation of minerals by scanning electron microscopy (QEMSCAN), X-ray diffraction data (DRX), scanning electron microscopy (SEM), and U-Pb isotopic analyses on zircon grains.

Sample	Rock type	Instrumental techniques				
		μFRX	QEMSCAN	DRX	SEM	U-Pb
CA-07A #1	Suevite	X	X			
CA-07A #2	Suevite	X				
CA-07B #3	Suevite	X				
CA-07C #4	Suevite	X	X		X	
CA-07C #5	Suevite	X				
CA-07D #6	Suevite	X	X			
CA-07D/ #7	Suevite	X	X			
CA-07D/1 #8	Suevite	X				
CA-07D/2 #9	Suevite	X				
CA-07D/3 #10	Suevite	X				
CA-07D/4 #11	Suevite	X				
CA-07D/5 #12	Suevite	X				
CA-07D/6 #13	Suevite	X				
CA-07D/7 #14	Suevite	X				
CA-17 #15	Suevite	X				
CA-07	IMR Type-II			X		
CA-09A	Suevite					
CA-09A	Suevite					
CA-09B	Suevite		X			
CA-09C	Suevite					
CA-09D	Suevite		X			
CA-09E	Suevite					
SF-28	IMR Type-II		X			
M-0	Suevite	X	X		X	
M-01	Suevite	X				
M-02	Suevite	X	X			
M-04	Suevite	X				
M-05	Suevite	X				
M-06	Suevite	X				
M-07	Suevite	X				
LL18	Suevite	X				

LL-33A	Suevite	X	X			
LL-33B	Suevite	X				
LL-33C	Suevite	X				
LL-33D	Suevite	X				
LL-33E	Suevite	X				
LL-44-10	Suevite	X				
LL-45	Suevite	X				
LL-49-48	Suevite	X				
LL-57-56	Suevite	X				
LL-57-56/2	Suevite	X				
LL-59-60	Suevite	X				
LL-61	Suevite	X				
LL-64-63A	Suevite	X				
LL-64-63B	Suevite	X				
LL-68-69	Suevite	X				
LL-80-81	Suevite	X				
CA-84	IMR Type-II			X		
P-03	Suevite					X
CA-73	Polymict lithic breccia					X
GAR-15-0	Basement					X
GAR-15-G10	Basement					X
CA-22	Basement					X
CA-111	Basement					X
CA-98	Polymict lithic breccia			X		
CA-98	IMR Type-II			X		
CA-116	IMR Type-II		X	X		X
SF-04	Suevite					X
GAR-19	Furnas Formation			X		
CA-49	Alto Garças Formation					X

Supplemental Text

Text S1A. Micro-X-ray fluorescence spectrometry

Forty thin sections of breccia groundmass were analyzed by micro-X-ray fluorescence spectrometry (μXRF) in order to create the chemical abundance distribution maps. It was produced as qualitative multi-element maps and as semi-quantitative single-element heat maps for 19 major and trace elements (Na, Mg, Al, Si, K, S, Cl, Ca, Ti, V, Cr, Mn, Fe, Ni, Cu, Zn, Sr, Rb and Zr), following procedures as outlined in Kaskes et al. (2021) and Wouters et al. (2020). The single-element heat maps of Al, Si, K, Fe, and Ti gave results with enough resolution and intensity that they could be used to identify matrix and clast

compositions. The remaining elements showed low signals, barely above background levels, since the X-ray attenuation depth for these elements exceed the 30 µm thickness of a regular thin section (Kaskes et al., 2021).

The µXRF analysis was performed with a Bruker M4 Tornado instrument at Archaeology, Environmental Changes & Geo-Chemistry (AMGC) research group at Vrije Universiteit Brussel (VUB), Belgium. This instrument uses a 30 W Rhodium anode metal-ceramic X-ray tube and two 30 mm² XFlash 430 Silicon Drift Detectors with a resolution of 145 eV (Mn-Kα) at 300 kcps. The measurements were carried out under near-vacuum conditions (20 mbar), with maximized Rh X-ray source energy settings (600 µA, 50 kV) and without the use of a filter. The X-ray beam (Mo-Kα) was focused by a poly-capillary lens onto a spot of 25 µm diameter (de Winter et al., 2017). A standard integration time of 1 ms per pixel with a spacing of 25 µm was employed for all measurements.

Text S1B. Quantitative Evaluation of Minerals by Scanning Electron Microscopy (QEMSCAN)

Eleven polished thin sections were analyzed at the Laboratory of Applied Mineralogical Characterization at the IG-UnB. Of these, nine samples represent breccia groundmass, and the other two samples are impact melt rock clasts (IMR Type-II). The thin sections were carbon-coated and studied qualitatively and quantitatively with a QEMSCAN analyzer, model Quanta FEI 650F, with two coupled Bruker energy dispersive X-ray spectrometers (EDS). The analyses were performed under high vacuum, with a beam current of 10 nA at 15 kV acceleration voltage. This resulted in the generation of compositional maps with a pixel resolution of 15 µm. QEMSCAN allows to identify minerals according to rapid EDS chemical analysis. As the method compares the data obtained with a pre-existing database, it is essential that optical microscopic sample characterization is available prior to analysis to assist with phase selection.

Text S1C. Scanning Electron Microscopy

The petrographic work also involved scanning electron microscopy (SEM). We analyzed two samples of breccia groundmass at the LEGGA lab. Backscattered electron (BSE) and secondary electron (SE) imaging were done

on a FEI QUANTA™ 450 instrument operated at 15 kV voltage and 100 μA current, at a working distance of 12.3 mm, and with a spot size of approximately 6 μm.

Text S1D. X-Ray Diffraction data

We complemented the characterization of groundmass mineralogy using X-Ray Diffraction (XRD). Samples of a breccia matrix, four impact melt rock clast (IMR Type-II), and a siltstone from the Furnas Formation were processed. The bulk samples were crushed to clay size fraction (< 2 μm) in an agate mortar and then analyzed at the X-Ray Diffraction Laboratory at the IG-UnB. The diffractometer is a Rigaku Ultima model IV instrument with a copper cathode and a Ni filter, operated at 35 kV and 15 mA with diffraction angles between 5° and 60° 2Θ. Bulk sample powder and clay diffractograms were evaluated using the JADE 9.0 software (MDI - Materials DataTM), which involves automatic peak search for possible minerals in the mineralogical database of the International Diffraction Data Center (IDDC).

Text S1E. U-Pb isotopic analyses on zircon

Nine samples were selected for U-Pb provenance analyses of detrital zircon grains: four samples of groundmass from polymict impact breccia, one sample of the conglomerate sample of the Alto Garças Formation (Rio Ivaí Group), and four metasedimentary rock samples of the basement. The preparation of the breccia samples, image capturing, and U-Pb analyses on zircon grains were performed at LEGGA (IG-UnB), whereas the image capture and U-Pb analyses of Alto Garças Formation and the metasedimentary basement samples were done at, respectively, the Applied Isotope Research Group at Federal University of Ouro Preto (UFOP), and the Geochronology and Isotopic Geochemistry Research Center at São Paulo University (USP). The Provenance R Package (Vermeesch et al., 2016) was used to produce kernel density plots (KDE) and perform multidimensional scaling (MDS) analysis with these data. These techniques are applied to visualize the detrital zircon signatures and compare large datasets (Bertolini et al., 2021) to discriminate zircon sources through geological context. The Concordia diagrams (2σ error ellipses),

probability density plots, weighted average ages, and the overall graph of concordant grains was drawn using the KDE and MDS were calculated via the IsoplotR online software.

Mineral separation and preparation procedures

Zircon concentrates for U-Pb analyses were extracted by 1-5 kg of rock samples, crushing, and panning at different grain sizes (100-400 µm). Then, the heavy minerals were concentrated by a magnetic separator Frantz isodynamic separator at 1.5 A. No further treatment was applied to the grains. The zircon grains were hand-picked (up to 115 zircon grains from each sample), placed into an epoxy mount, polished to approximately half thickness, and cleaned with 3 % nitric acid before analysis. Backscattered electron (BSE), Cathodoluminescence (CL), and secondary electron (SE) images of the zircon mounts from polymict impact breccia samples were obtained with a FEI QUANTA^{TM} 450 FEIJOL Scanning Electron Microscope (SEM) at LEGGA. The CL images of the zircon mounts from basement samples were obtained with FEI QUANTA^{TM} 450 SEM operated at 15 kV with a work distance of 5.5 µm spot at Geochronology and Isotopic Geochemistry Research Center (USP). The images provided the basis for grain categorization, characterization of exterior surfaces, and for selecting locations for laser-ablation analysis.

U-Pb ICP-MS analysis at UnB: samples SF-04 and P-03

The U-Pb isotopic analyses for polymict impact breccias samples SF-04 and P-03 were obtained at LEGGA, using a Thermo-Fisher Neptune MC-ICP-MS coupled with a Nd:YAG UP213 New Wave laser ablation system. The U-Pb analyses on zircon grains were carried out were carried out by the standard-sample bracketing method (Albarède et al., 2004) using the GJ-1 standard zircon (Jackson et al., 2004) in order to quantify the amount of ICP-MS instrumental fractionation. The tuned masses were 238, 204, 206, 207, and 202. Integration time was 1 second, and ablation time was 40 s for all isotopes. A 25 µm spot size was used and the laser setting was 10 Hz and 2-3 J cm^{-2}. Two to four unknown grains were analyzed between GJ-1 analyses. $^{206}Pb/^{207}Pb$ and $^{206}Pb/^{238}U$ ratios were time corrected. The raw data were processed off-line in an Excel-based

data reduction routine (Bühn et al., 2009). During analytical sessions, the zircon standard 91500 (Wiedenbeck et al., 1995, 2004) was also analyzed as an unknown. Common ^{204}Pb was monitored using the ^{202}Hg and (^{204}Hg+^{204}Pb) masses. Common Pb corrections were not required though due to very low signals for ^{204}Pb (<30 cps) and high ^{206}Pb/^{204}Pb ratios. Reported errors are propagated by quadratic addition [(2SD^2+2SE^2)$^{1/2}$] (SD = standard deviation; SE = standard error) of external reproducibility and within-run precision. External reproducibility is represented by the standard deviation obtained from repeated analyses (n = 20, ~1.1% for ^{207}Pb/^{206}Pb and up to ~2 % for ^{206}Pb/^{238}U) of the GJ-1 zircon standard during the analytical sessions, and the within-run precision is the standard error calculated for each analysis. Concordia diagrams (2σ error ellipses), and weighted average ages were calculated using the Isoplot-3/Ex software (Ludwig, 2008).

U-Pb ICP-MS analysis at UnB: samples CA-73 and CA-116

U-Pb data were obtained at LEGGA for two polymict impact breccias samples (CA-73 and CA-116), where masses of interest were measured on a Thermo Finningan Neptune XT high-resolution multi-collector sector field ICP-MS coupled to a 193 nm Teledyne Analyte Excite laser ablation system. *Table 1* provides the cup and ICP-MS configuration as well as the laser parameters used during the analysis. The laser ablation system is equipped with a HelEx II dual-volume chamber. The mass spectrometer was tuned to improve U and Pb sensitivity while minimizing oxide production prior to each analytical session. Each analysis consisted of 10 s of background measurement followed by 20 s of sample data acquisition. All masses (202, 204, 206-208, 232, 238) were measured simultaneously using a combination of Faraday, SEM and CDD detectors. Laser conditions included a spot diameter of 20 µm, 8 Hz, and 4.0 J cm^{-2}. Raw data were processed with the Iolite 4.0 software (Paton et al., 2011), and time-resolved signal and individual signal inspection was done with VizualAge (Petrus and Kamber, 2012). Data correction included blank subtraction and the LIEF correction using an exponential plus linear model and normalization to the GJ-1 zircon (Jackson et al., 2004). The 91500 zircon (Widenbeck et al., 1995) and Plešovice zircon (Sláma et al., 2008) were used for quality control.

Excess variance on the primary calibrant was propagated for each analytical point. A systematic uncertainty of ca. 1 % is propagated on each final age. Errors on ages are quoted at 2s confidence level.

Table 1. Cup configuration and instrument operating parameters for U-Pb LA-ICP-MS analyses at LEGGA.

Laboratory	Laboratório de Geocronologia e Geoquímica Isotópica, Instituto de Geociências, Universidade de Brasília (UnB)
Laser ablation system	
Make, Model and type	Teledyne Analyte Excite
Laser wavelength (nm)	193 nm
Fluence (J cm-2)	4.0 J cm^{-2}
Repetition rate (Hz)	8 Hz
Spot size	20 µm
ICP-MS Instrument	
Make, Model and type	Thermo-Fischer, NeptuneXT, MC-ICP-MS
Gas blank	10 s
Data processing package used / Correction for LIEF	Iolite v.4.0 (Paton et al., 2011) & VizualAge (Petrus and Kamber, 2012) using exponential plus linear modelling for LIEF correction. UComPbine DRS (Chew et al. 2014).
Quality control / Validation	GJ-1 zircon (601.7 ± 1.3 Ma; Jackson et al. 2004), and as quality control were used the 91500 (1062.4 ± 0.8 Ma; Wiedenbeck et al. 1995) and Plešovice (337.1 ± 0.37 Ma; Sláma et al. 2008).

U-Pb ICP-MS analysis at UFOP: sample CA-49

The U-Pb data for conglomerate sample (CA-49) from Alto Garças Formation (Rio Ivaí Group) were acquired in the Federal University of Ouro Preto (UFOP). The sample was crushed and undergo through a disk mill. The obtained material was then concentrated using a pan, dried between 50 and 70 degrees celsius and the magnetic fraction was separated using a neodymium magnet. The non magnetic fraction of the concentrated material was separated in a portion with density superior than 3.31 and other with density inferior than 3.31 using a decantation funnel and diiodomethane. The denser material undergo Frantz magnetic separator machine for the segregation in diamagnetic and paramagnetic portions. Diamagnetic material was mounted in acrylic resin and polished using alumina powder. Cathodoluminescence (CL) images were obtained in a Scanning Electron Microscope (SEM) JEOL 6510. U-Pb analysis were obtained using a Neptune Pluss Thermo Finnigan coupled with a Photon-Machines 193nm laser system. Data were acquired using peak jumping

mode with background measurement during 20 seconds, zircon ablation during 20 seconds and 30 micrometers spot size. Data reduction was done in Saturn Software.

MC-LA-ICP-MS U-Pb analyses at USP

The U-Pb isotopic analysis at USP were carried out using a Thermo-Fisher Neptune multicollector inductively coupled plasma mass spectrometer (ICP-MS) connected with an Excimer Excite ArF laser ablation system (LA) of 193 nm wavelength. Table 2 provides the cup and ICP-MS configuration as well as the laser parameters used during the analysis. Ablation was performed at a spot size of 32 µm and a laser frequency of 6 Hz, applying an intensity of 6 mJ and ablation time of 40 seconds, with He as controller gas MCF1 and MCF2 at 0,3 L/min flux rate. The U-Pb measurement protocol follows the order of: two blanks, two NIST standard glasses, three external standards (GJ-1 standard, Jackson et al., 2004), six unknown samples, one secondary standard (Mud Tank), six unknown samples, and two NIST, two external standards (GJ-1), and two blank measurements. An interpolation of the four blank measurement sequences, two at the beginner and two at the end of the samples analyses (bracketing method), was subtracted from each of the 7 measured masses (202, 204, 206, 207, 208, 232 and 238).

The ^{235}U isotope was not measured but mathematically calculated using the relative abundance of $^{238}U/^{235}U = 137.88$. The ^{204}Hg interference for ^{204}Pb was corrected based on ^{202}Hg intensity, assuming that $^{204}Hg/^{202}Hg = 4.350360$. Using the partially corrected $^{207}Pb/^{206}Pb$ ratio as an estimation for the age, and the formulas of Stacey and Kramers (1975), the $^{206}Pb/^{204}Pb$, $^{207}Pb/^{204}Pb$ and $^{208}Pb/^{204}Pb$ relative abundances (variable with geological age) were calculated. The common Pb (non-radiogenic) fraction of the isotopes ^{206}Pb, ^{207}Pb and ^{208}Pb could then be discounted, by subtracting from each mass the ^{204}Pb signal multiplied, respectively, by the three relative abundances calculated before. Another bracketing of measurements (two sequences before and after the samples) of the NIST-612 standard was also used to convert the three total signals (Pb = $^{204}Pb+^{206}Pb+^{207}Pb+^{208}Pb$; Th = ^{232}Th; U = $^{235}U+^{238}U$) to ppm units.

A final bracketing (three before and two after the samples analyses) of the standard minerals was then used to correct the effect of fractionation on the four ratios ($^{206}Pb/^{238}U$, $^{207}Pb/^{235}U$, $^{207}Pb/^{206}Pb$, $^{208}Pb/^{232}Th$), before they could finally be extrapolated through best fit lines to t = 0 and then used to calculate the respective ages. Errors in all simple arithmetic operations were algebraically propagated, e.g., d(A-B) = dA+dB and d(A/B)/(A/B) = dA/A+dB/B. Least-squares fitting was the choice for the best fit line determination and, on all final results and plots, the error framework (at the 2σ level) already available in Isoplot 3.70 (Ludwig, 2008).

Table 2. Cup configuration and instrument operating parameters for U-Pb LA-ICP-MS analyses at USP.

Cup configuration							
IC3	IC4	L4	IC6	L3	Axial	H2	H4
^{202}Hg	^{204}Pb	^{206}Pb	^{207}Pb	^{208}Pb	~219,59	^{232}Th	^{238}U

Instrument operating parameters					
MC–ICP–MS		Laser ablation			
Model	ThermoFinnigan Neptune	Type	193 nm Ar–F excimer laser		
Forward power	952 W	Model	Analyte G2 – Photon Machines		
Mass resolution	Low (400)	Repetition rate	6 Hz		
		Laser fluence	8.55 J/m^2		
		Spot size	32 µm		
Gas flows–laser ablation		Data reduction			
Cool/plasma (Ar)	16 L/min	Interference correction	$^{202}Hg/^{204}Hg$	4.350360	
Auxiliary (Ar)	0.80 L/min				
Sample cell gas (He)	~1 L/min				

Table 2. Cup configuration and instrument operating parameters for U-Pb LA-ICP-MS analyses.

References

Albarède, F., Telouk, S., Blichert-Toft, J., Boyet, M., Agranier, A., and Nelson, B., 2004. Precise and accurate isotopic measurements using multiple-collector ICPMS. Geochemica et Cosmochimica Acta, 68, 2725–2744.

Bertolini, G., Marques, J. C., Hartley, A. J., Basei, M. A. S., Frantz, J. C., and Santos, P. R. 2021. Determining sediment provenance history in a Gondwanan erg: Botucatu formation, Northern Paraná Basin, Brazil. *Sedimentary Geology* 417: 105883. https://doi.org/10.1016/j.sedgeo.2021.105883.

Bühn, B., Pimentel, M.M., Matteini, M., and Dantas, E.L., 2009. High spatial resolution analysis of Pb and U isotopes for geochronology by laser ablation

multi-collector inductively coupled plasma mass spectrometry (LA-MC-ICPMS). Annals of the Brazilian Academy of Sciences, 81, 99–114.

de Winter, N. J., Sinnesael, M., Makarona, C., Vansteenberge, S., and Claeys, P. 2017. Trace element analyses of carbonates using portable and micro-X-ray fluorescence: Performance and optimization of measurement parameters and strategies. *Journal of Analytical Atomic Spectrometry* 32: 1211-1223. https://doi:10.1039/c6ja00361c.

Jackson, S. E., Pearson, N. J., Griffin, W. L., and Belousova, E. A. 2004. The application of laser ablation-inductively coupled plasma-mass spectrometry to in situ U-Pb zircon geochronology. *Chemical Geology* 211: 47–69.

Kaskes, P., Déhais, T., de Graaff, S. J., Goderis, S., and Claeys, P. 2021. Micro–X-ray fluorescence (μXRF) analysis of proximal impactites: High-resolution element mapping, digital image analysis, and quantifications. In *Large Meteorite Impacts and Planetary Evolution VI*, edited by Reimold, W. U., and Koeberl, C. *Geological Society of America Special Paper* 550: 171-206 https://doi.org/10.1130/2021.2550(07).

Ludwig, K. R. 2008. User's manual for Isoplot 3.70: a geochronological toolkit for Microsoft Excel, 4. Geochronology Center Special Publication, Berkeley, California, 76 p.

Paton, C., Woodhead, J. D., Hellstrom, J. C., Hergt, J. M., Greig, A., and Mass, R. 2010. Improved laser ablation U-Pb zircon geochronology through robust downhole fractionation correction. *Geochemistry, Geophysics, Geosystems* 11: 1-36.

Petrus, J. A., and Kamber, B. S. 2012. VizualAge: a novel approach to laser ablation ICP-MS U-Pb 1157 geochronology data reduction. *Geostandards and Geoanalytical Research* 36(3): 247-270.

Sláma, J., Košler, J., Condon, D. J., Crowley, J. L., Gerdes, A., Hanchar, J. M., Horstwood, M. S.A., Morris, G. A., Nasdala, L., Norberg, N., Schaltegger, U., Schoene, B., Tubrett, M., Whitehouse, N. M. J. 2008. Plešovice zircon - a new natural reference material for U-Pb and Hf isotopic microanalysis. *Chemical Geology* 249(1-2): 1-35. https://doi.org/10.1016/j.chemgeo.2007.11.005.

Stacey, J. S., and Kramers, J. D. 1975. Approximation of terrestrial lead isotope evolution by a two-stage model. *Earth and Planetary Science Letters* 26: 207-221.

Vermeesch, P., Resentini, A., and Garzanti, E. 2016. An R package for statistical provenance analysis. *Sedimentary Geology* 336: 14-25, https://doi.org/10.1016/j.sedgeo.2016.01.009.

Widenbeck, M., Alle, P., Corfu, F., Griffin, W., Meier, M., Oberli, F., Quadt, A. V., Roddick, J., and Spiegel, W. 1995. Three natural zircon standards for U-Th-Pb, Lu-Hf, trace element and REE Analyses. *Geostandards Newsletter* 19: 1-23.

Wiedenbeck M. P., Hanchar J. M., Peck W. H., Sylvester P., Valley J., Whitehouse M., Kronz A., Morishita Y., Nasdala L., Fiebig J., Franchi I., Girard J.-P., Greenwood R. C., Hinton R., Kita N., Mason P. R. D., Norman M.,

Ogasawara M., Piccoli P. M., Rhede D., Satoh H., Schulz-Dobrick B., Sk_ar O., Spicuzza M. J., Terada K., Tindle A., Togashi S., Vennemann T., Xie Q., and Zheng Y.-F. 2004. Further characterisation of the 91500 zircon crystal. Geostandards and Geoanalytical Research 28:9–39.

Wouters, S., Hulsbosch, N., Kaskes, P., Claeys, P., Dewaele, S., Melcher, F., Onuk, P., and Muchez, P. 2020. Late orogenic gold mineralization in the western domain of the Karagwe-Ankole Belt (Central Africa): Auriferous quartz veins from the Byumba deposit (Rwanda). *Ore Geology Reviews* 125: 103666. https://doi.org/10.1016/j.oregeorev.2020.103666.

Supplementary Material 2. Semiquantitative descriptions

Figures of DRX and SEM as well as tables of the semiquantitative descriptions for polymict impact breccia of the profiles CA-07, CA-09, and CA-84 in the northern sector, at macro-, meso-, and microscopic scales.

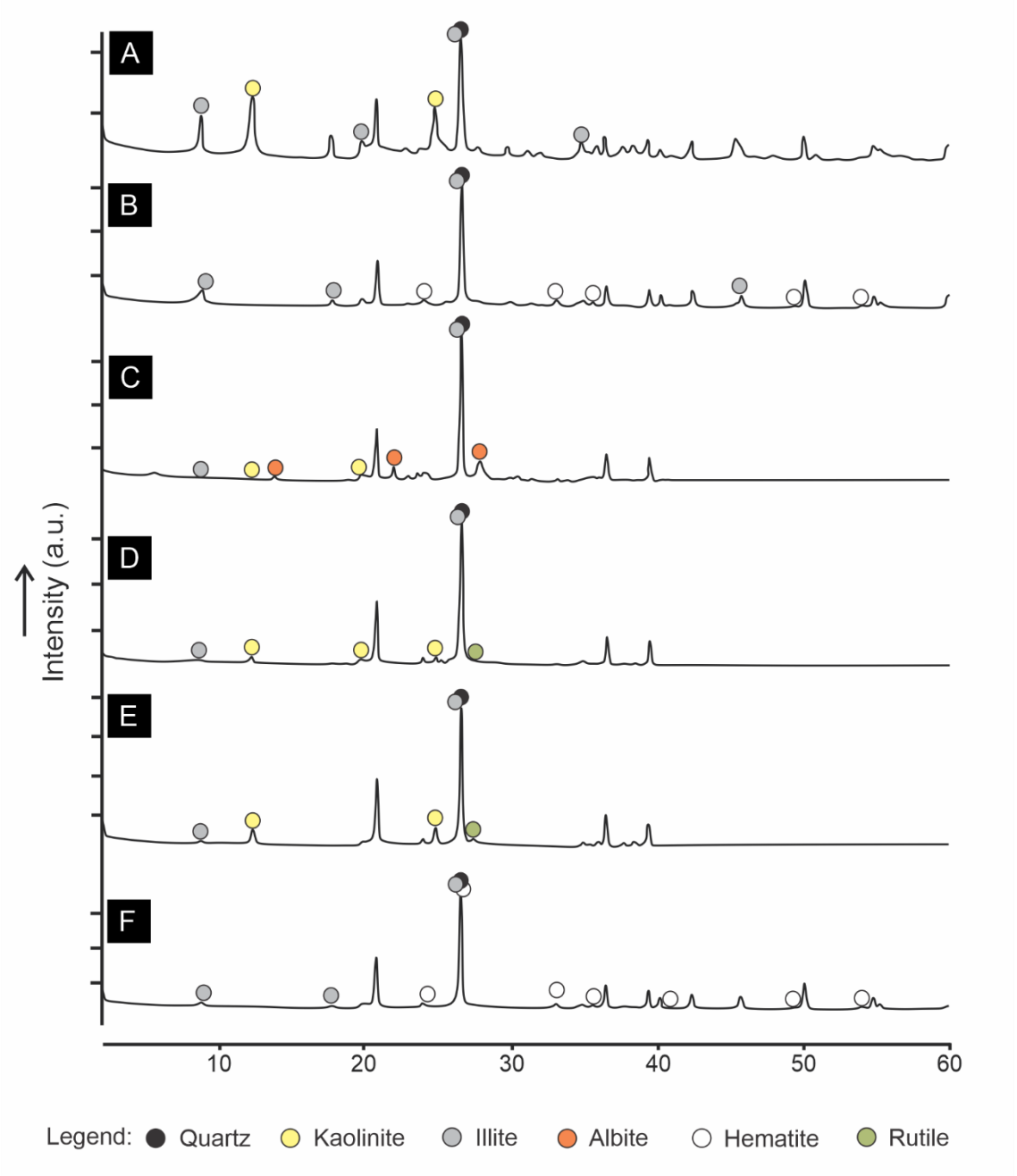

Figure S2A. Representative X-ray diffraction patterns of the studied samples. (A) Siltstone of the Furnas Formation from outcrop GAR-19 (at UTM 22K 288679 m E; 8142465 m S). (B) Polymict impact breccia matrix from outcrop CA-98 (at UTM 22K 288483 m E; 8141862 m S). (C) Impact melt rocks of Type II clast from outcrop CA-07 (at UTM 22K 288523 m E; 8141975 m S). (D) Impact melt rocks of Type II clast from outcrop CA-116 (at UTM 22K 287915 m E; 8141449 m S). (E) Impact melt rocks of Type II clast from outcrop CA-84 (at UTM 22K 286769 m E; 8141191 m

S). (F) Impact melt rocks of Type II clast from outcrop CA-98 (at UTM 22K 288483 m E; 8141862 m S).

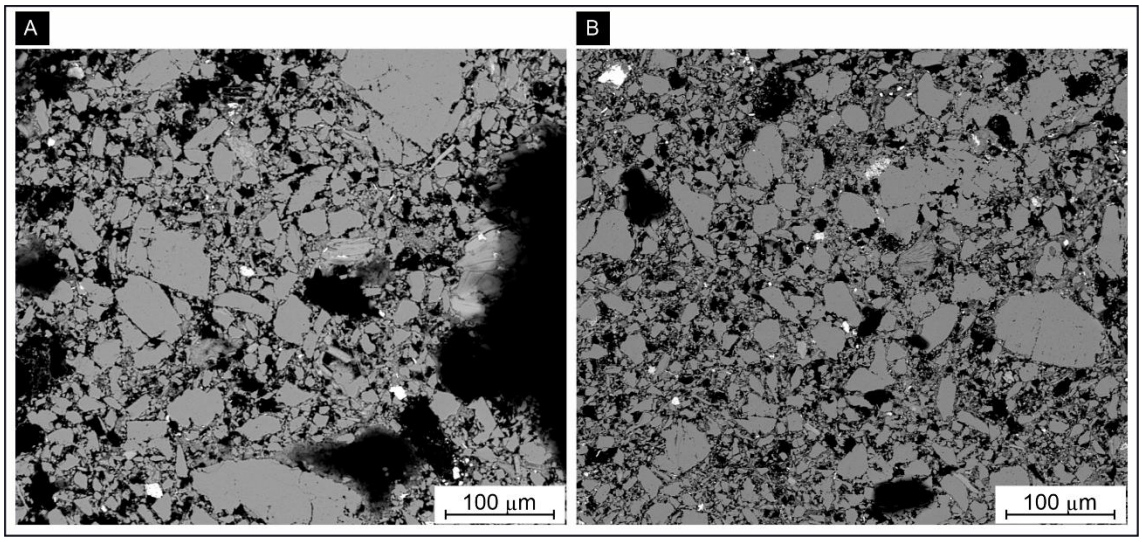

Figure S2B. Representative backscattered electron images produced from scanning electron microscopy analysis in the breccia matrix for (A) sample CA-07C from CA-07 profile and (B) sample M-0 from CA-84 profile.

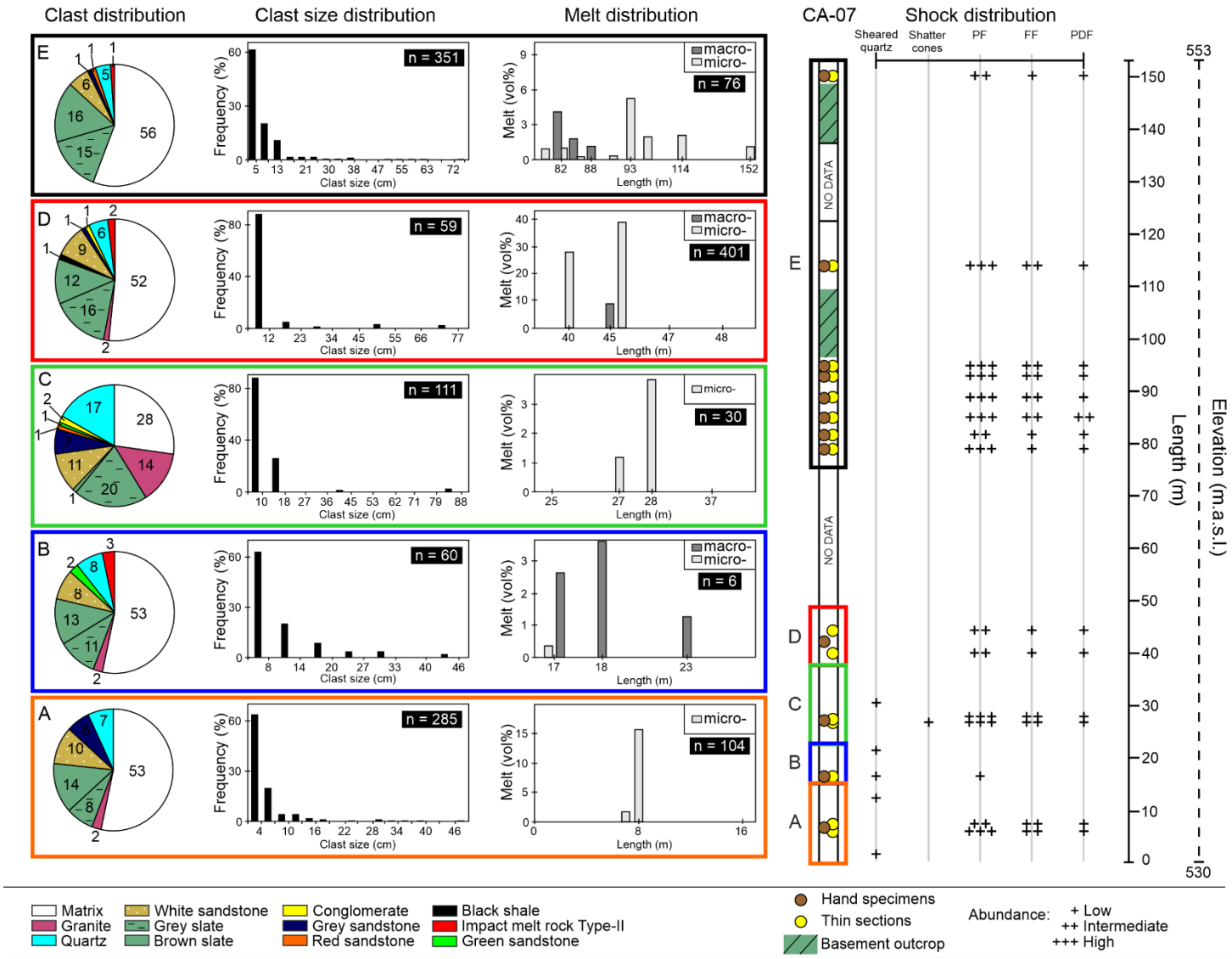

Figure S2C. Modal analysis data from macroscopic analysis of samples from the CA-07 profile, with clast type distribution per analyzed area, the clast size distribution, melt clast occurrence, and shock metamorphic features. N denotes the total number of clasts analyzed. The samples collected for laboratory analysis (hand specimens and thin sections) are also indicated. Clast sizes > 1 m are not indicated in the clast size frequency distribution.

Table S2A. Qualitative description of profile CA-07 at macro- and mesoscopic scales (M: matrix, C: clast types). The maximum size of the clasts is given in centimeters (cm).

Section	Clast population	Rounding	Sphericity	Field				Hand specimen			
				M x C	Max. Size	n	%	M x C	Max. Size	n	%
A	Quartz pebbles	subrounded to rounded	high		6.5	43	7		1.1	4	4.2
	Conglomerate	-	-		-	-	-		-	-	-
	Red conglomeratic sandstone	-	-		-	-	-		-	-	-
	Grey conglomeratic sandstone	subangular	low		30	38	6.4		1.8	1	1.1
	White sandstone	subangular	low	M: 53.3%	48	64	10.4	M: 60%	3	23	24.2
0 - 15.5 m	Green sandstone	subrounded	low	C: 46.7%	14	1	0.2	C: 40%	-	-	-
	Black shale	-	-		-	-	-		-	-	-
	Brown slate	subangular to subrounded	low		34	83	13.5		7	9	9.5
	Grey slate	subangular to subrounded	high		32	47	7.7		2	1	1.1
	Granite	subangular	low		38	10	1.6		-	-	-
	Impact melt rock clasts	-	-		-	-	-		-	-	-
B	Quartz pebbles	subrounded to rounded	high		22	10	7.7		-	-	-
	Conglomerate	-	-		-	-	-		-	-	-
	Red conglomeratic sandstone	-	-		-	-	-		-	-	-
	Grey conglomeratic sandstone	subrounded	low		-	-	-		3.5	4	8.8
	White sandstone	subangular	low	M: 53.3%	28	11	8.4	M: 45%	2	13	28.6
15.5 - 22.7 m	Green sandstone	subangular	low	C: 46.7%	11	3	2.3	C: 55%	-	-	-
	Black shale	-	-		-	-	-		-	-	-
	Brown slate	subangular	low		10.5	17	13		4.2	8	17.6
	Grey slate	subangular	high		32	14	10.7		-	-	-
	Granite	subrounded	high		14	2	1.5		-	-	-
	Impact melt rock clasts	angular	low		125	4	3.1		-	-	-
C	Quartz pebbles	rounded	high		4.5	26	17		1.4	13	14.9
	Conglomerate	subrounded	low		7	3	2		-	-	-
	Red conglomeratic sandstone	subrounded	low	M: 27.5%	41	1	0.7		-	-	-
	Grey conglomeratic sandstone	subangular to subrounded	low	C: 72.5%	11	11	7.2		8.2	5	5.7
	White sandstone	subangular	low		13	17	11.1	M: 45%	2.8	20	22.9
22.7 - 37.7 m	Green sandstone	subrounded	low		8	1	0.7	C: 55%	-	-	-

		Black shale	-	-		-	-	-		-	-	-
		Brown slate	subangular	low		5	1	0.7		3.2	8	9.2
		Grey slate	subrounded	high		88	30	19.6		2.1	2	2.3
		Granite	subangular to subrounded	high		15	21	13.7		-	-	-
		Impact melt rock clasts				-	-	-		-	-	-
D		Quartz pebbles	rounded	high		4.1	7	5.7		0.7	10	13.4
		Conglomerate	subrounded	low		5	1	0.8		-	-	-
		Red conglomeratic sandstone	-	-		-	-	-		-	-	-
		Grey conglomeratic sandstone	subrounded	low		32	1	0.8		2.2	5	6.7
	37.7 - 48.5 m	White sandstone	subangular	low	M: 51.7%	46	11	9	M: 45%	3.3	17	22.8
		Green sandstone	-	-	C: 48.3%	-	-	-	C: 55%	-	-	-
		Black shale	subangular	low		11	1	0.8		-	-	-
		Brown slate	subangular	low		8.1	15	12.3		2.7	9	12.1
		Grey slate	subrounded	high		11	19	15.6		-	-	-
		Granite	rounded	high		7.5	2	1.6		-	-	-
		Impact melt rock clasts	angular	low		77	2	1.6		-	-	-
NO DATA (48.5 - 75.5 m)												
E		Quartz pebbles	subrounded to rounded	high		5.5	36	4.6		1.5	37	5.9
		Conglomerate	subangular	low		8	2	0.3		-	-	-
		Red conglomeratic sandstone	subrounded	high		12	8	1		2.1	5	0.8
		Grey conglomeratic sandstone	subrounded	low		56	8	1		8	18	2.9
	75.5 - 152.8 m	White sandstone	subangular to subrounded	low	M: 55.5%	200	49	6.2	M: 56%	9.2	107	17
		Green sandstone	-	-	C: 44.5%	-	-	-	C: 44%	-	-	-
		Black shale	-	-		-	-	-		0.8	3	0.5
		Brown slate	subangular to subrounded	low		53	127	16.1		4	99	15.7
		Grey slate	subangular to subrounded	low		76	118	14.9		2.6	8	1.3
		Granite	-	-		-	-	-		-	-	-
		Impact melt rock clasts	angular	low		28	4	0.5		-	-	-

Table S2B. Qualitative description of profile CA-07 samples at the microscopic scale.

Section		Thin sections	M		C		Qz		Plg		Slate		Sandstone		Metasandstone		Melt		Sorted	Grain size	Fabric
			n	%	n	%	n	%	n	%	n	%	n	%	n	%	n	%			
A	0 - 15.5 m	CA-7A	357	59.5	243	40.5	86	14.3	0	0	50	8.3	98	16.3	0	0	9	1.5	moderately	fine- to medium-grained	matrix supported
		CA-7A	276	46	324	54	59	9.8	0	0	77	12.8	6	1	87	14.5	95	15.8	moderately	fine- to medium-grained	matrix supported
B	15.5 - 22.7 m	CA-7B	9	1.5	591	98.5	2	0.3	0	0	0	0	587	97.8	0	0	2	0.3	very poorly	fine-grained	clast supported
C	22.7 - 37.7 m	CA-7C	360	60	240	40	99	16.5	0	0	70	11.7	46	7.7	18	3	7	1.2	well	fine- to medium-grained	matrix supported
		CA-7C	341	56.8	359	43.2	132	22	1	0.2	82	13.7	19	3.2	2	0.3	23	3.8	moderately	fine- to medium-grained	matrix supported
D	37.7 - 48.5 m	CA-7D	326	54.3	274	45.7	59	9.8	0	0	16	2.7	33	5.5	0	0	166	27.7	poorly	fine- to medium-grained	matrix supported
		CA-7D	297	49.5	303	50.5	37	6.2	0	0.2	10	1.7	23	3.8	0	0	233	38.8	poorly	fine- to medium-grained	matrix supported
	48.5 - 75.5 m	NO DATA																			
E	75.5 - 152.8 m	CA-7D (3)	316	52.7	284	47.3	102	17	0	0	81	13.5	89	14.8	7	1.2	5	0.8	moderately	fine- to medium-grained	matrix supported
		CA-7D (4)	296	54.5	304	45.5	75	13.8	0	0	137	25.2	23	4.2	7	1.3	5	0.9	moderately	fine- to medium-grained	matrix supported
		CA-7D (5)	317	52.8	283	47.2	115	19.2	0	0	101	16.8	52	8.7	14	2.3	1	0.2	moderately	fine- to medium-grained	matrix supported
		CA-7D (1)	288	48	312	52	133	22.2	0	0	46	7.7	98	16.3	33	5.5	2	0.3	moderately	fine- to medium-grained	matrix supported
		CA-7D (2)	117	19.5	483	80.5	35	5.8	0	0	11	1.8	406	67.7	0	0	31	5.2	very poorly	fine-grained	clast supported
		CA-7D (6)	318	53	282	47	130	21.7	0	0	60	10	80	13.3	1	0.2	11	1.8	moderately	fine-grained	matrix supported
		CA-7D (7)	217	36.2	383	63.8	57	9.5	0	0	181	30.2	133	22.2	0	0	12	2	poorly	fine- to medium-grained	clast supported
		CA-17	143	29.5	457	70.5	37	7.6	0	0	245	50.5	55	11.3	0	0	5	1	poorly	fine-grained	clast supported

Note: M - matrix; C - clasts; Qz - quartz; Plg - plagioclase.

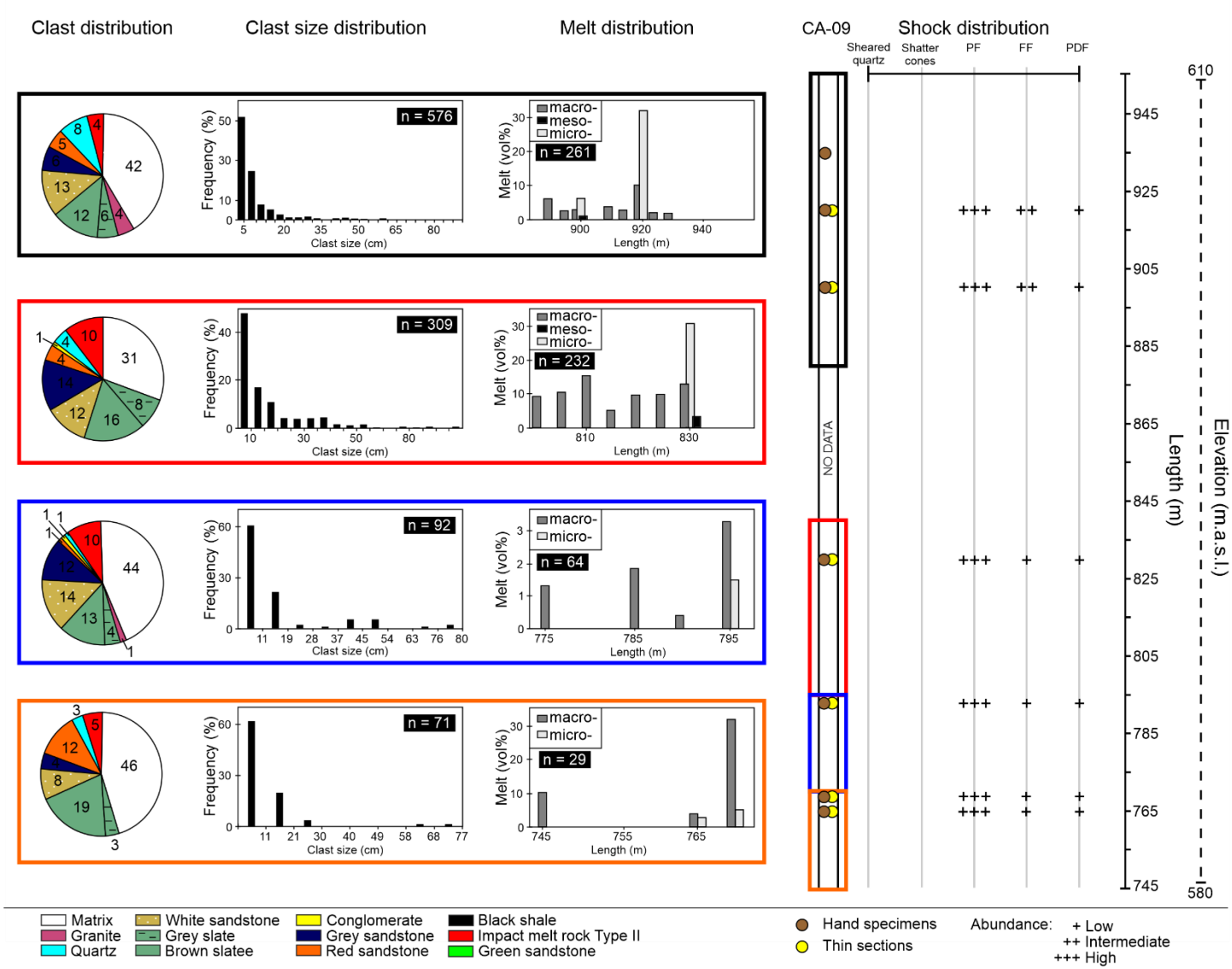

Figure S2D Modal analysis data from macroscopic analysis of samples from the CA-09 profile, with clast type distribution per analyzed area, the clast size distribution, melt clast occurrence, and shock metamorphic features. N denotes the total number of clasts analyzed. The samples collected for laboratory analysis (hand specimens and thin sections) are also indicated. Clast sizes > 1 m are not indicated in the clast size frequency distribution.

Table S2C. Qualitative description of profile CA-09 at macro- and mesoscopic scales (M: matrix, C: clast types). The maximum size of the clasts is given in centimeters (cm).

Section	Clast population	Rounding	Sphericity	Field				Hand specimen			
				M x C	Max. Size	n	%	M x C%	Max. Size	n	%
NO DATA (0 - 745 m)											
745 - 770 m	Quartz pebbles	rounded	high		3	4	2.9		0.8	20	19.5
	Conglomerate	-	-		-	-	-		-	-	0
	Red conglomeratic sandstone	subangular	low		24	16	11.5		2.4	1	1
	Grey conglomeratic sandstone	subrounded	high		8	6	4.3		-	-	-
	White sandstone	angular	low		15	11	7.9		3.4	14	13.7
	Green sandstone	-	-	M: 46%	-	-	-	M: 60%	-	-	-
	Black shale	-	-	C: 54%	-	-	-	C: 40%	-	-	-
	Brown slate	subangular	low		77	27	19.4		2.3	6	5.9
	Grey slate	subangular	low		66	4	2.9		-	-	-
	Granite	-	-		-	-	-		-	-	-
	Impact melt rock clasts	angular	low		210	7	5		-	-	-
770 - 795 m	Quartz pebbles	rounded	high		4	1	0.6		1.1	6	9.5
	Conglomerate	subangular	low		8	2	1.3		1.5	2	3.2
	Red conglomeratic sandstone	subangular	low		8	1	0.6		2.1	1	1.6
	Grey conglomeratic sandstone	sugangular	low		19	18	11.6		-	-	-
	White sandstone	subangular	low		40	22	14.2		3.1	12	19.1
	Green sandstone	-	-	M: 44%	-	-	-	M: 65%	-	-	-
	Black shale	-	-	C: 56%	-	-	-	C: 35%	-	-	-
	Brown slate	subrounded	low		23	20	12.9		1.4	1	1.6
	Grey slate	subrounded	high		14	6	3.9		-	-	-
	Granite	angular	low		10	2	1.3		-	-	-
	Impact melt rock clasts	angular	low		455	15	9.7		-	-	-
795 - 840 m	Quartz pebbles	rounded	high		5	20	4.4		1.3	5	7.8
	Conglomerate	subangular	low		42	3	0.7		-	-	-
	Red conglomeratic sandstone	subangular	low		20	20	4.4		1.1	4	6.2
	Grey conglomeratic sandstone	sugangular	low		70	62	13.6		-	-	-
	White sandstone	angular	low		130	53	11.6		1.1	13	20.2
	Green sandstone	-	-	M: 31%	-	-	-	M: 55%	-	-	-

	Black shale	-	-	C: 69%	-	-	-	C: 45%	-	-	-
	Brown slate	subangular	low		55	74	16.3		3.1	5	7.8
	Grey slate	subangular	low		95	36	7.9		-	-	-
	Granite	-	-		-	-	-		-	-	-
	Impact melt rock clasts	angular	low		246	46	10.1		1.5	2	3.1
NO DATA (840 - 880 m)											
880 - 952 m	Quartz pebbles	rounded	high		8	84	8.2		1.1	24	7.4
	Conglomerate	subangular	low		6	1	0.1		1.8	3	0.9
	Red conglomeratic sandstone	subangular	low		42	50	4.9		1.1	8	2.4
	Grey conglomeratic sandstone	subangular	low		50	64	6.3		1.2	6	1.8
	White sandstone	rounded	low		84	128	12.5		1.5	36	10.7
	Green sandstone	-	-	M: 42%	-	-	-	M: 62.5%	-	-	-
	Black shale	-	-	C: 58%	-	-	-	C: 37.5%	-	-	-
	Brown slate	subangular	low		30	126	12.3		0.8	45	13.4
	Grey slate	subangular	low		30	57	5.6		-	-	-
	Granite	angular	low		258	43	4.2		0.7	2	0.6
	Impact melt rock clasts	angular	low		660	39	3.8		1.1	1	0.3

Table S2D. Qualitative description of profile CA-09 samples at the microscopic scale.

Section	Thin sections	M		C		Qz		Plg		Slate		Sandstone		Metasandstone		Melt		Sorted	Grain size	Fabric
		n	%	n	%	n	%	n	%	n	%	n	%	n	%	n	%			
0 - 745 m	NO DATA																			
745 - 770 m	CA-09A	129	38.7	471	61.3	30	9	0	0	5	1.5	160	48	0	0	9	2.7	poorly	fine-grained	clast supported
	CA-09A	139	52.9	461	47.1	54	20.5	0	0	4	1.5	53	20.2	0	0	13	4.9	poorly	fine-grained	matrix supported
770 - 795 m	CA-09B	451	75.2	149	24.8	72	12	0	0	3	0.5	25	4.2	0	0	49	8.2	well	fine-grained	matrix supported
795 - 840 m	CA-09C	300	50	300	50	106	17.7	0	0	1	0.2	10	1.7	0	0	183	30.5	moderatelly	fine-grained	matrix supported
840 - 880 m	NO DATA																			
880 - 935 m	CA-09D	343	71.5	257	28.5	79	16.5	0	0	10	2.1	19	4	0	0	29	6	moderatelly	fine-grained	matrix supported
	CA-09E	204	34	396	66	109	18.2	0	0	11	1.8	84	14	0	0	192	32	poorly	fine-grained	clast supported
935 - 952 m	NO DATA																			

Note: M - matrix; C - clasts; Qz - quartz; Plg - plagioclase.

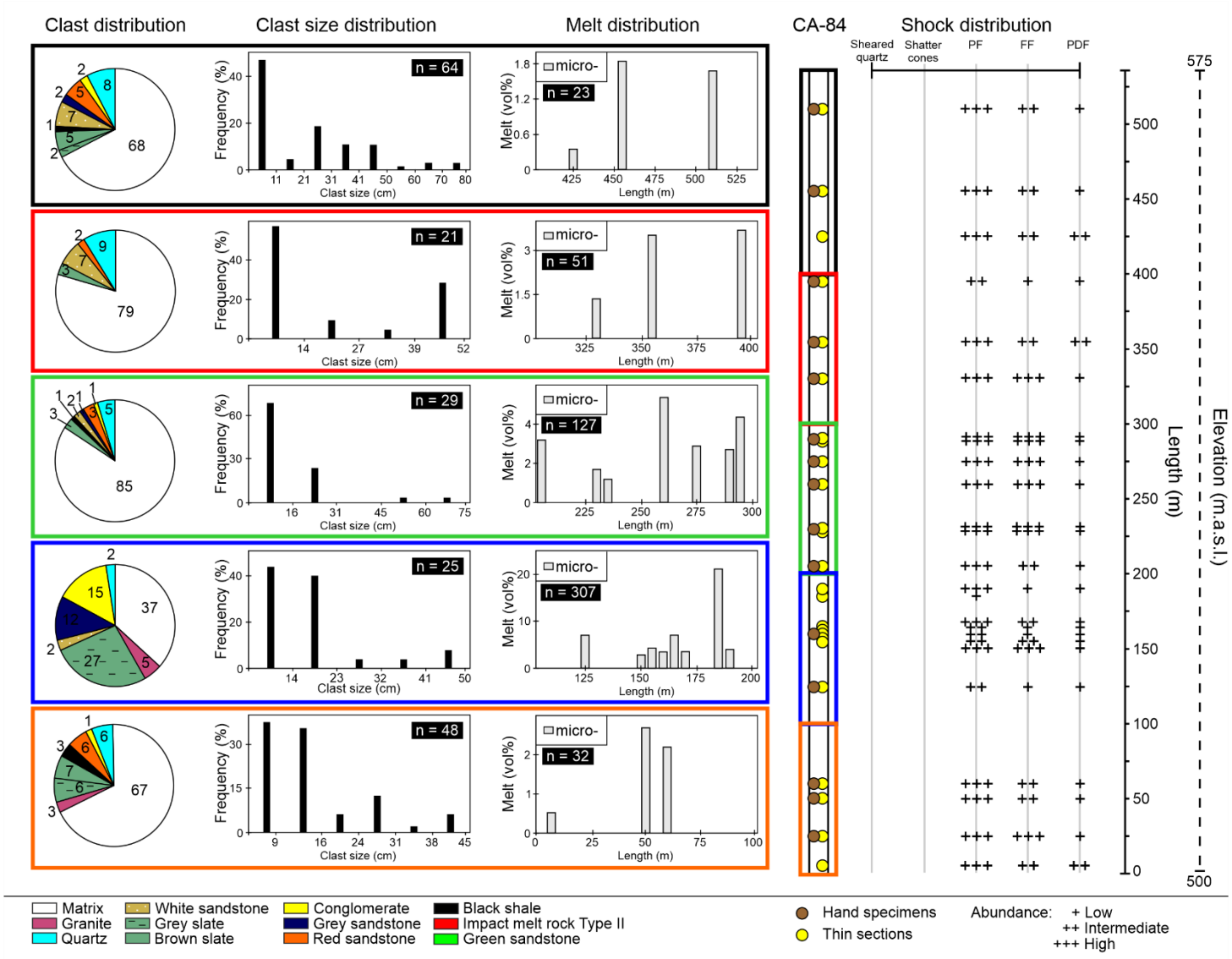

Figure S2E. Modal analysis data from macroscopic analysis of samples from the CA-84 profile, with clast type distribution per analyzed area, the clast size distribution, melt clast occurrence, and shock metamorphic features. N denotes the total number of clasts analyzed. The samples collected for laboratory analysis (hand specimens and thin sections) are also indicated. Clast sizes > 1 m are not indicated in the clast size frequency distribution.

Table S2E. Qualitative description of profile CA-84 at macro- and mesoscopic scales (M: matrix, C: clast types). The maximum size of the clasts is given in centimeters (cm).

Section	Clast population	Rounding	Sphericity	Field				Hand specimen			
				M x C	Max. Size	n	%	M x C	Max. Size	n	%
0 - 100 m	Quartz pebbles	rounded	high		13	9	6.1		1.3	24	7.2
	Conglomerate	subrounded to rounded	high		25	2	1.4		-	-	-
	Red conglomeratic sandstone	subangular	low		38	9	6.1		2.5	4	1.2
	Grey conglomeratic sandstone	subangular	low		-	-	-		1.3	8	2.4
	White sandstone	subrounded	low		-	-	-		3.5	25	7.5
	Green sandstone	-	-	M: 67%	-	-	-	M: 75%	-	-	-
	Black shale	subangular	low	C: 33%	45	5	3.4	C: 25%	-	-	-
	Brown slate	subangular	low		35	10	6.8		5	21	6.3
	Grey slate	subangular	low		15	9	6.1		1.4	1	0.3
	Granite	angular to rounded	low		150	4	2.7		-	-	-
	Impact melt rock clasts	-	-		-	-	-		-	-	-
100 - 200 m	Quartz pebbles	rounded	high		3	1	2.4		0.8	13	8.2
	Conglomerate	subangular to subrounded	low		20	6	14.5		-	-	-
	Red conglomeratic sandstone	subangular	low		-	-	-		0.5	1	0.6
	Grey conglomeratic sandstone	subangular	low		20	5	12.1		0.7	1	0.6
	White sandstone	subangular	low		20	1	2.4		2.4	19	12
	Green sandstone	-	-	M: 37%	-	-	-	M: 74%	-	-	-
	Black shale	subangular	low	C: 63%	-	-	-	C: 26%	1.1	2	1.3
	Brown slate	subangular	low		-	-	-		1.5	4	2.5
	Grey slate	subangular	low		5	11	26.6		1.7	1	0.6
	Granite	subrounded	low		4000	2	4.8		-	-	-
	Impact melt rock clasts	-	-		-	-	-		-	-	-
200 - 300 m	Quartz pebbles	rounded	high		4	9	4.7		1.5	9	2.3
	Conglomerate	subrounded	low		30	1	1		1.5	2	0.5
	Red conglomeratic sandstone	subangular to subrounded	low		35	6	3.1		3.5	8	2
	Grey conglomeratic sandstone	subrounded	low		30	2	1		1.2	4	1
	White sandstone	subangular	low		2.5	4	2.1		2.7	56	14.3
	Green sandstone	-	-	M: 85%	-	-	-	M: 67%	-	-	-
	Black shale	subangular	low	C: 15%	25	2	1	C: 33%	-	-	-
	Brown slate	angular to subangular	low		50	5	2.6		3.1	24	6.1

	Grey slate	subangular	low		-	-	-		4.8	26	6.7
	Granite	-	-		-	-	-		-	-	-
	Impact melt rock clasts	-	-		-	-	-		-	-	-
300 - 400 m	Quartz pebbles	rounded	high		4	9	9		1.3	16	4.2
	Conglomerate	subangular	low		-	-	-		2.8	2	0.5
	Red conglomeratic sandstone	subangular	low		25	2	2		6.2	10	2.6
	Grey conglomeratic sandstone	subangular	low		-	-	-		1.8	5	1.3
	White sandstone	subangular	low		60	7	7		2.5	42	10.9
	Green sandstone	-	-	M: 79%	-	-	-	M: 73%	-	-	-
	Black shale	-	-	C: 21%	-	-	-	C: 27%	-	-	-
	Brown slate	angular	low		35	3	3		3.1	24	6.2
	Grey slate	subrounded	low		-	-	-		0.8	4	1
	Granite	subangular	low		-	-	-		3	1	0.3
	Impact melt rock clasts	-	-		-	-	-		-	-	-
400 - 535 m	Quartz pebbles	rounded	high		4	16	7.6		2.3	1	0.8
	Conglomerate	subrounded	low		35	5	2.4		-	-	-
	Red conglomeratic sandstone	subangular	low		74	11	5.3		0.4	1	0.8
	Grey conglomeratic sandstone	angular to subrounded	low		30	4	1.9		0.5	1	0.8
	White sandstone	subangular	low		90	15	7.2		2.3	20	15.2
	Green sandstone	-	-	M: 67%	-	-	-	M: 75%	-	-	-
	Black shale	subangular	low	C: 32%	40	2	1	C: 25%	0.6	1	0.8
	Brown slate	subangular	low		80	11	5.3		1.2	6	4.5
	Grey slate	subangular	low		700	3	1.4		1.4	3	2.3
	Granite	-	-		-	-	-		-	-	-
	Impact melt rock clasts	-	-		-	-	-		-	-	-

Table S2F. Qualitative description of the CA-84 samples at the microscopic scale.

Section	Thin sections	M		C		Qz		Plg		Slate		Sandstone		Metasandstone		Melt		Sorted	Grain size	Fabric
		n	%	n	%	n	%	n	%	n	%	n	%	n	%	n	%			
0 - 100 m	M-01	331	55.2	269	44.8	194	32.3	3	0.5	7	1.2	63	10.5	2	0.3	0	0	moderately	fine- to medium-grained	matrix supported
	M-0	356	59.3	244	40.7	138	23	0	0	47	7.8	51	8.5	5	0.8	3	0.5	moderately	fine- to medium-grained	matrix supported
	LL18	413	68.8	187	31.2	57	9.5	0	0	15	2.5	11	1.8	88	14.7	16	2.7	poorly	fine- to medium-grained	matrix supported
	M-02	280	46.7	320	53.3	112	18.7	0	0	37	6.2	156	26	2	0.3	13	2.2	moderately	fine- to medium-grained	matrix supported
100 - 200 m	M-03	454	75.7	146	24.3	47	7.8	1	0.2	51	8.5	6	1	0	0	46	6.8	well	fine- to medium-grained	matrix supported
	LL33A	331	55.2	269	44.8	72	12	0	0	70	11.7	111	18.5	0	0	16	2.7	moderately	fine- to medium-grained	matrix supported
	LL33B	547	91.2	53	8.8	23	3.8	0	0	3	0.5	2	0.3	1	0.2	24	4	well	fine-grained	matrix supported
	LL33C	526	87.7	74	12.3	30	5	0	0	20	3.3	4	0.7	0	0	20	3.3	well	fine-grained	matrix supported
	LL33D	512	85.3	88	14.7	14	2.3	0	0	24	4	9	1.5	0	0	41	6.8	well	fine-grained	matrix supported
	LL33E	472	78.7	128	21.3	46	7.7	0	0	46	7.7	13	2.2	3	0.5	20	3.3	well	fine- to medium-grained	matrix supported
	LL45	383	63.8	217	36.2	91	15.2	0	0	0	0	0	0	0	0	126	21	well	fine- to medium-grained	matrix supported
	LL44-10	414	81.8	186	18.2	51	10.1	0	0	8	1.6	14	2.8	0	0	19	3.8	well	fine-grained	matrix supported
200 - 300 m	LL49-48	453	75.5	147	24.5	71	11.8	0	0	40	6.7	17	2.8	0	0	19	3.2	well	fine- to medium-grained	matrix supported
	LL57-56	320	53.3	280	46.7	44	7.3	0	0	15	2.5	195	32.5	16	2.7	10	1.7	moderately	fine- to medium-grained	matrix supported
	LL57-56/2	395	65.8	205	34.2	75	12.5	0	0	19	3.2	104	17.3	0	0	7	1.2	moderately	fine- to medium-grained	matrix supported
	LL59-60	473	78.8	127	21.2	42	7	0	0	46	7.7	7	1.2	0	0	32	5.3	moderately	fine- to medium-grained	matrix supported
	LL61	496	82.7	104	17.3	58	9.7	0	0	4	0.7	21	3.5	4	0.7	17	2.8	well	fine- to medium-grained	matrix supported
	LL64-63A	323	53.8	277	46.2	70	11.7	0	0	70	11.7	121	20.2	0	0	16	2.7	moderately	fine- to medium-grained	matrix supported
	LL64-63B	419	69.8	181	30.2	54	9	0	0	40	6.7	44	7.3	17	2.8	26	4.3	moderately	fine- to medium-grained	matrix supported
300 - 400 m	M-04	394	65.7	206	34.3	104	17.3	0	0	3	0.5	77	12.8	1	0.2	21	3.5	well	fine- to medium-grained	matrix supported
	M-05a	332	55.3	268	44.7	125	20.8	0	0	20	3.3	112	18.7	3	0.5	8	1.3	moderately	fine- to medium-grained	matrix supported
	LL80-81	539	89.8	61	10.2	24	4	0	0	9	1.5	4	0.7	2	0.3	22	3.7	well	fine-grained	matrix supported
400 - 535 m	M-06	358	59.7	242	40.3	147	24.5	0	0	13	2.2	59	9.8	21	3.5	2	0.3	poorly	fine- to medium-grained	matrix supported
	LL68-69	318	53	282	47	45	7.5	0	0	145	24.2	76	12.7	5	0.8	11	1.8	poorly	fine- to medium-grained	matrix supported
	M-07	343	57.2	257	42.8	93	15.5	0	0	11	1.8	143	23.8	0	0	10	1.7	moderately	fine- to medium-grained	matrix supported

Note: M - matrix; C - clasts; Qz - quartz; Plg - plagioclase.

Supplementary Material 3. Outcrops photographs

The outcrops photographs for the Araguainha basement rocks.

Figure S3A. (A) Outcrop CA-111 composed by phyllite in contact relationship with conglomerate matrix supported. (B) Dark brown phyllite from CA-111 outcrop (at UTM 22K 291650 m E; 8141529 m S), which contains some small quartz veins (~1 cm).

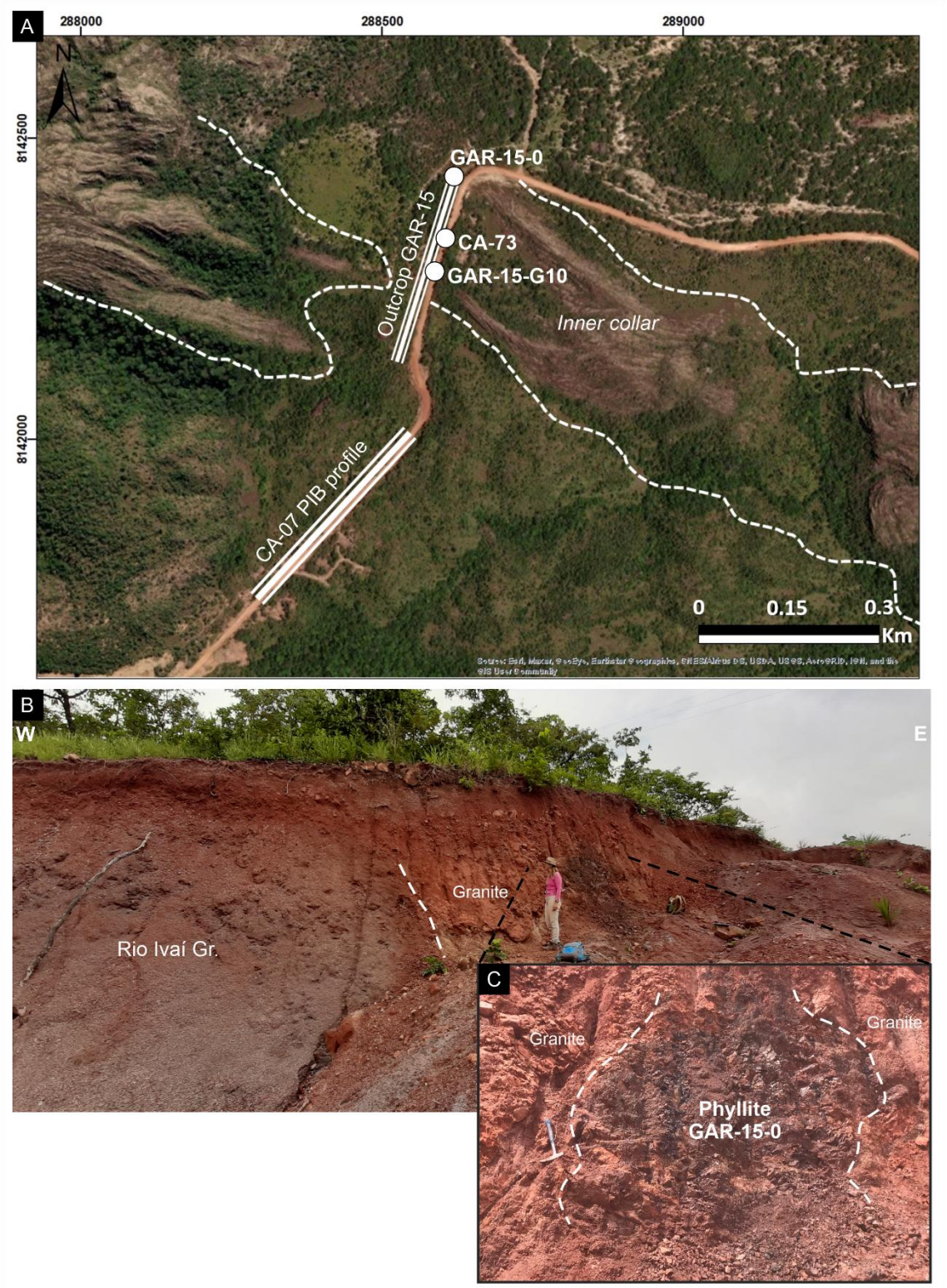

Figure S3B. (A) Location of the outcrop GAR-15 (at UTM 22K 288556 m E, 8142283 m S) in the megablock zone, next to the polymict impact breccia profile (CA-07). Also, the three samples collected are indicated (GAR-15-0, GAR-15-G10, and CA-73). (B) Outcrop where the basement is located in between two apophysis of granite and around the sedimentary strata from Rio Ivaí Group. The person, shown in part for scale, is approximately 1.7 m tall. (C) A zoom from figure

(B) showing a detail of the black phyllite from GAR-15-0 sample. Hammer in b to d, for scale, 31 cm long.

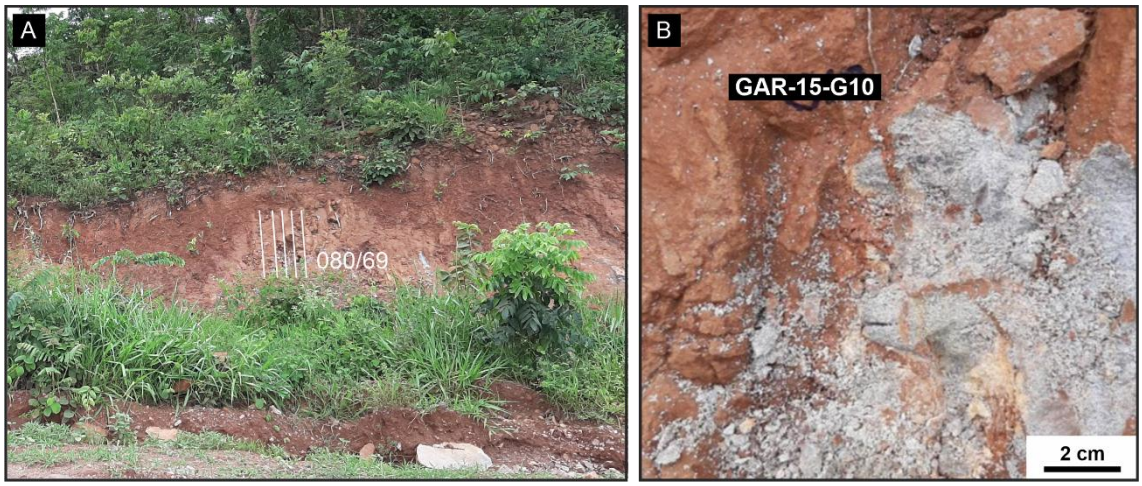

Figure S3C. (A) Outcrop that contains the metasandstone in the GAR-15 profile without scale. (B) A metasandstone characterized by light grey color, friable, from GAR-15-G10 sample.

Figure S3D. Grey siltstone with quartz veins of approximately 35 cm from CA-22 outcrop (at UTM 22K 290608 m E, 8139763 m S). Coin, for scale, 2.5 cm in diameter.

Figure S3E. Conglomerate from CA-49 outcrop with quartz sheared (at UTM 22K 289856 m E, 8140950 m S). Coin, for scale, 2.5 cm in diameter.

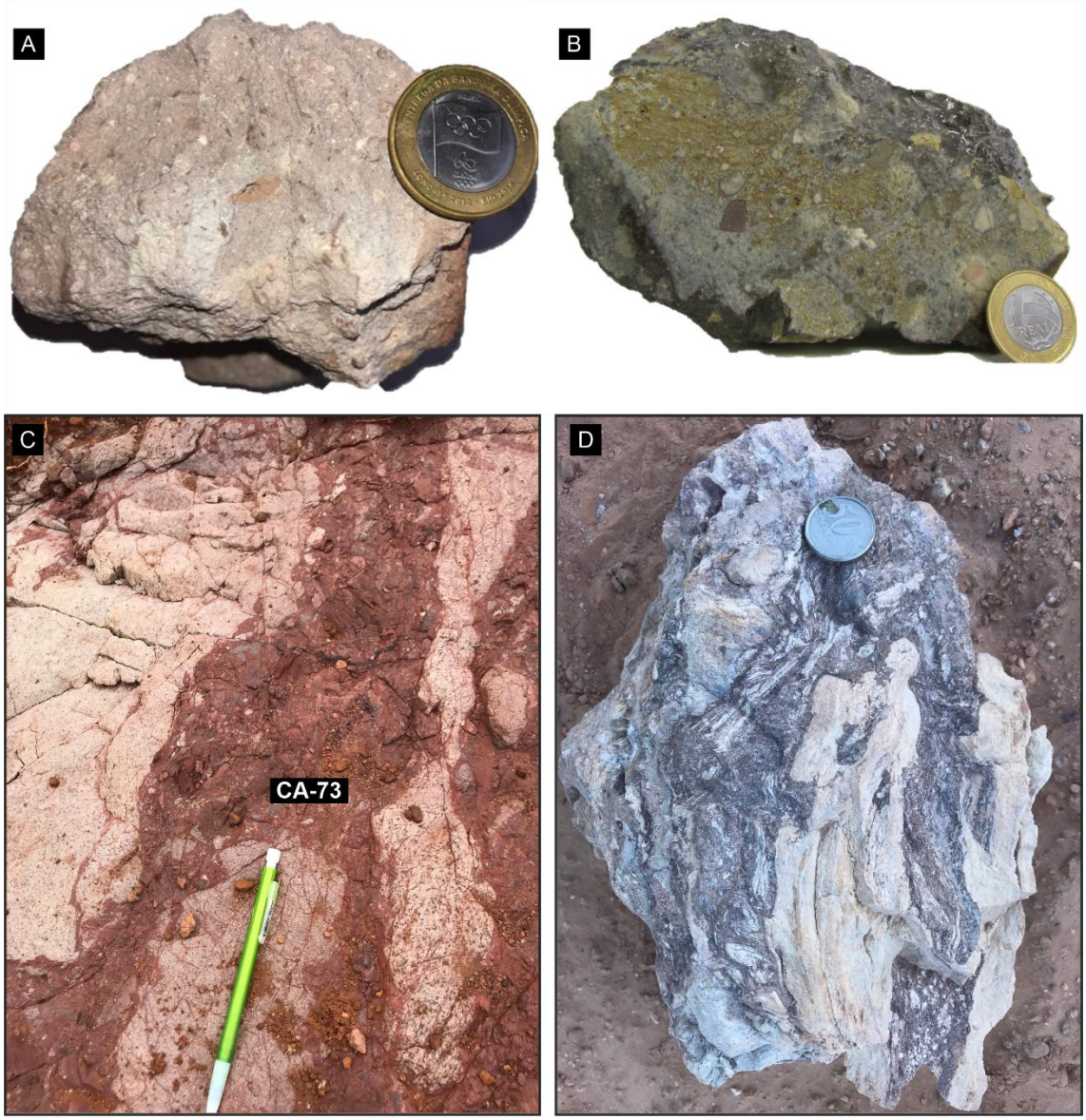

Figure S3F. (A) Sample P-03 collected for U-Pb analysis. (B) Sample SF-04 collected for U-Pb analysis. (C) CA-73 breccia matrix that corresponds to the ejected PIB dikes into the white sandstone from the megablock zone. (D). Sample CA-116, highly enriched in of impact melt rocks of Type II. Coin, for scale, 2.5 cm in diameter.

Supplementary Material 4. Analytical data

Tables with the U-PB isotope analysis results by LA-ICP-MS on zircon grains. Data in bold print were used in Provenance diagrams. Data in red were excluded, as concordance values were > 105 % and < 95%. (*) Data are grouped according to 206Pb/208U apparent ages. *% Conc: concordance.

Table S4A. Results of U-Pb isotope analysis by LA-ICP-MS on zircon from polymict impact breccia sample P-03. Data in bold print were used in provenance diagrams. Data in red were excluded, as concordance values were > 105 % or < 95%. (*) Data are grouped according to $^{206}Pb/^{208}U$ apparent ages. *% Conc: concordance.

Identifier	Spot number	f 206c (%)	Th/U	Ratio						rho	Apparent Ages (Ma)						*% Conc
				$^{207}Pb/^{206}Pb$	1σ (%)	$^{207}Pb/^{235}U$	1σ (%)	$^{206}Pb/^{238}U$	1σ (%)		$^{207}Pb/^{206}Pb$	2σ (abs)	$^{207}Pb/^{235}U$	2σ (abs)	$^{206}Pb/^{238}U$	2σ (abs)	
P-03 - Polymict impact breccia																	
ZR45	#65	6.8	0.9	0.0522	2.3812	0.2646	2.5444	0.0368	0.8351	0.33	294	105	238	11	**233**	4	102
ZR66	#90	0.3	0.5	0.0585	1.4898	0.6681	2.2894	0.0829	1.7326	0.76	547	64	520	18	**513**	17	101
ZR52	#74	0.1	0.2	0.0580	1.0324	0.6964	2.1570	0.0870	1.8927	0.88	532	45	537	18	**538**	20	100
ZR53	#75	0.1	0.4	0.0581	0.8333	0.7027	1.4319	0.0877	1.1645	0.81	535	36	540	12	**542**	12	100
ZR36	#53	0.1	0.3	0.0622	0.7401	0.8211	1.9487	0.0957	1.8015	0.92	682	31	609	18	**589**	20	103
ZR4	#8	0.2	0.7	0.0603	1.5136	0.8295	1.9537	0.0998	1.2352	0.63	613	65	613	18	**613**	14	100
ZR57	#79	0.1	0.1	0.0606	0.7845	0.8342	1.9538	0.0999	1.7884	0.92	624	33	616	18	**614**	21	100
ZR33	#48	0.2	0.5	0.0610	1.2438	0.8432	1.4392	0.1002	0.7225	0.50	640	53	621	13	**616**	8	101
ZR51	#73	0.0	0.3	0.0607	0.6157	0.8423	1.0504	0.1007	0.8508	0.81	627	26	620	10	**619**	10	100
ZR50	#70	0.1	0.4	0.0601	1.0015	0.8355	1.3464	0.1008	0.8991	0.67	607	43	617	12	**619**	11	100
ZR49	#69	0.0	1.1	0.0605	0.7242	0.8434	1.2044	0.1011	0.9622	0.80	621	31	621	11	**621**	11	100
ZR1	#4	0.1	0.3	0.0617	1.0047	0.8628	1.2103	0.1015	0.6742	0.56	662	42	632	11	**623**	8	101
ZR21	#33	0.1	0.6	0.0614	1.2490	0.8644	1.7437	0.1021	1.2167	0.70	652	54	632	16	**627**	15	101
ZR44	#64	0.0	0.4	0.0610	0.7954	0.8647	1.6520	0.1028	1.4476	0.88	640	34	633	15	**631**	17	100
ZR34	#49	0.0	0.2	0.0618	0.7080	0.8785	1.5510	0.1032	1.3796	0.89	666	30	640	15	**633**	17	101
ZR56	#78	0.1	0.3	0.0613	0.8991	0.8733	1.9212	0.1033	1.6979	0.88	651	39	637	18	**634**	20	101
ZR64	#88	0.1	0.3	0.0607	0.7348	0.8667	1.2011	0.1035	0.9496	0.79	630	31	634	11	**635**	11	100
ZR38	#55	0.1	0.4	0.0607	0.7174	0.8671	1.0498	0.1036	0.7660	0.73	629	31	634	10	**635**	9	100
ZR5 rim	#9	0.0	0.4	0.0605	0.6493	0.8652	0.9990	0.1038	0.7592	0.76	620	28	633	9	**637**	9	99
ZR22	#34	0.1	0.3	0.0614	0.7109	0.8797	1.0441	0.1039	0.7641	0.73	654	30	641	10	**637**	9	101
ZR15	#25	0.0	0.7	0.0610	0.5329	0.8764	2.0444	0.1043	1.9728	0.97	637	23	639	19	**640**	24	100
ZR24	#36	0.1	0.3	0.0613	0.9245	0.8922	1.2429	0.1056	0.8302	0.67	649	39	648	12	**647**	10	100
ZR65	#89	0.0	0.2	0.0610	0.6035	0.8888	2.1314	0.1057	2.0435	0.96	639	26	646	20	**648**	25	100
ZR13	#20	0.0	0.3	0.0612	0.6827	0.8939	2.9505	0.1060	2.8691	0.97	646	29	648	28	**649**	35	100
ZR10	#17	0.0	0.2	0.0604	0.8683	0.8841	2.1868	0.1062	2.0071	0.92	617	37	643	21	**651**	25	99
ZR6	#13	0.0	0.7	0.0615	0.6253	0.9011	1.3204	0.1062	1.1623	0.88	658	27	652	13	**651**	14	100
ZR17	#27	0.0	0.2	0.0616	0.5665	0.9038	2.0017	0.1064	1.9190	0.96	661	24	654	19	**652**	24	100
ZR55	#77	0.1	0.2	0.0610	1.1556	0.8974	1.5100	0.1067	0.9704	0.64	639	49	650	14	**654**	12	100
ZR12	#19	0.0	0.7	0.0625	0.6416	0.9205	2.4996	0.1069	2.4151	0.97	690	27	663	24	**655**	30	101
ZR37	#54	0.1	0.5	0.0613	0.8193	0.9198	1.0742	0.1087	0.6940	0.65	651	35	662	10	**665**	9	100
ZR23	#35	0.0	0.1	0.0615	0.6200	0.9228	0.9110	0.1089	0.6675	0.73	656	27	664	9	**666**	8	100
ZR14	#24	0.0	0.2	0.0620	0.7099	0.9427	2.3809	0.1104	2.2727	0.95	672	30	674	23	**675**	29	100

ZR11	#18	0.1	0.2	0.0623	0.8984	0.9733	2.2503	0.1133	2.0632	0.92	684	38	690	23	**692**	27	100
ZR8	#15	0.0	0.3	0.0631	0.6738	1.0069	2.2696	0.1157	2.1673	0.95	711	29	707	23	**706**	29	100
ZR47	#67	0.1	0.5	0.0692	1.0188	1.2211	1.3337	0.1280	0.8596	0.64	904	41	810	15	**776**	13	104
ZR41	#58	0.2	0.6	0.0702	1.3422	1.2516	1.9136	0.1292	1.3617	0.71	935	54	824	21	**784**	20	105
ZR39	#56	0.1	0.4	0.0678	0.6965	1.2592	1.0625	0.1347	0.8024	0.76	862	29	828	12	**815**	12	102
ZR48	#68	0.1	0.3	0.0677	0.8535	1.2771	1.1708	0.1369	0.8009	0.68	858	35	836	13	**827**	12	101
ZR54	#76	0.1	0.4	0.0676	0.7913	1.3497	1.1735	0.1447	0.8665	0.74	858	33	867	14	**871**	14	100
ZR20	#30	0.0	0.4	0.0678	0.5305	1.3733	0.9587	0.1469	0.7985	0.83	862	22	878	11	**884**	13	99
ZR19	#29	0.0	0.4	0.0693	0.6619	1.4139	2.0773	0.1480	1.9682	0.95	907	27	895	24	**890**	33	101
ZR18	#28	0.0	0.4	0.0693	0.6570	1.4239	2.2131	0.1490	2.1125	0.95	907	27	899	26	**896**	35	100
ZR35	#50	0.1	0.4	0.0733	0.9298	1.7259	1.2081	0.1708	0.7714	0.64	**1021**	38	1018	16	1017	15	100
ZR32	#47	0.0	0.2	0.1292	0.4139	6.8260	0.6974	0.3832	0.5613	0.80	**2087**	15	2089	12	2091	20	100
ZR7	#14	0.0	0.5	0.1376	0.3840	7.4714	5.2087	0.3937	5.1942	1.00	**2198**	13	2170	89	2140	186	101
ZR27	#39	1.8	0.4	0.0637	0.6378	0.3207	0.8582	0.0365	0.5639	0.66	731	27	282	4	231	3	122
ZR60	#84	4.3	0.6	0.0636	1.4795	0.3524	2.3150	0.0402	1.7031	0.75	729	62	307	12	254	9	121
ZR46	#66	0.6	1.3	0.0813	1.7359	0.5697	2.0122	0.0508	1.0114	0.50	1229	67	458	15	320	6	143
ZR59	#83	0.6	0.9	0.1000	0.6382	0.7199	1.4521	0.0522	1.2970	0.90	1623	24	551	12	328	8	168
ZR61	#85	8.0	1.5	0.0647	2.0288	0.5573	2.7273	0.0625	1.6767	0.64	763	83	450	20	391	14	115
ZR42	#59	3.1	0.4	0.0589	0.8148	0.5136	2.6815	0.0632	2.4763	0.95	565	35	421	18	395	20	107
ZR62	#86	4.5	0.6	0.0612	1.8047	0.5386	3.1700	0.0638	2.4882	0.81	648	76	437	22	399	20	110
ZR30	#45	0.1	1.1	0.0722	1.0295	0.6533	1.5311	0.0656	1.1317	0.74	992	41	511	12	410	9	125
ZR43	#60	0.2	1.8	0.0729	1.4688	0.6855	2.2020	0.0682	1.6369	0.74	1012	58	530	18	425	13	125
ZR2 rim	#6	0.2	0.7	0.0777	1.9473	0.8370	2.1650	0.0782	0.9439	0.44	1138	76	617	20	485	9	127
ZR28	#40	0.2	0.6	0.0682	0.7224	0.7771	1.2743	0.0826	1.0478	0.82	875	30	584	11	512	10	114
ZR40	#57	1.5	0.4	0.0708	0.7896	0.8422	1.6037	0.0862	1.3751	0.87	953	32	620	15	533	14	116
ZR5 core	#10	0.1	0.4	0.0663	0.8727	0.8521	1.0940	0.0932	0.6593	0.60	815	36	626	10	575	7	109
ZR2 core	#5	0.6	0.7	0.0701	2.8028	0.9286	3.4329	0.0961	1.9701	0.58	931	111	667	33	592	22	113
ZR16	#26	0.1	0.7	0.0677	1.0952	0.9400	2.0040	0.1008	1.6766	0.84	858	45	673	20	619	20	109
ZR63	#87	0.3	0.6	0.0731	2.5384	1.0163	2.8314	0.1008	1.2508	0.44	1017	100	712	29	619	15	115
ZR3	#7	0.1	0.5	0.0751	1.8713	1.1745	1.9786	0.1134	0.6421	0.32	1072	73	789	21	692	8	114
ZR31	#46	2.2	0.1	0.1081	0.4706	2.2824	1.2141	0.1532	1.0951	0.92	1767	17	1207	17	919	19	131
ZR9	#16	0.1	0.2	0.0993	1.1195	2.6926	2.9507	0.1966	2.7262	0.93	1611	41	1326	43	1157	58	115
ZR26	#38	0.0	0.5	0.1031	0.4122	2.9560	0.8366	0.2079	0.7278	0.87	1681	15	1396	13	1218	16	115
ZR29	#44	0.3	0.6	0.1940	0.4574	7.7721	2.2460	0.2905	2.1924	0.98	2777	15	2205	40	1644	64	134
ZR58	#80	0.0	0.8	0.1216	0.7168	5.3141	1.7083	0.3169	1.5501	0.91	1980	25	1871	29	1774	48	105
ZR25	#37	0.0	0.6	0.1229	0.5364	5.5822	1.4114	0.3294	1.3050	0.92	1999	19	1913	24	1836	42	104

Table S4B. Results of U-Pb isotope analysis by LA-ICP-MS on zircon from polymict impact breccia sample SF-04. Data in bold print were used in provenance diagrams. Data in red were excluded, as concordance values were > 105 % or < 95%. (*) Data are grouped according to $^{206}Pb/^{208}U$ apparent ages. *% Conc: concordance.

Identifier	Spot number	f 206c (%)	Th/U	Ratio						rho	Apparent Ages (Ma)						*% Conc
				$^{207}Pb/^{206}Pb$	1σ (%)	$^{207}Pb/^{235}U$	1σ (%)	$^{206}Pb/^{238}U$	1σ (%)		$^{207}Pb/^{206}Pb$	2σ (abs)	$^{207}Pb/^{235}U$	2σ (abs)	$^{206}Pb/^{238}U$	2σ (abs)	
SF-04 - Polymict impact breccia																	
ZR2	#4	0.0	0.8	0.0579	1.4330	0.6700	2.4470	0.0839	1.9486	0.80	527	62	521	20	**519**	19	100
ZR28	#36	0.0	0.5	0.0592	0.9796	0.7021	1.5342	0.0860	1.1211	0.73	574	42	540	13	**532**	11	102
ZR35	#45	0.0	0.2	0.0589	0.7516	0.7449	1.2346	0.0917	0.9067	0.73	565	33	565	11	**565**	10	100
ZR29	#37	0.0	0.3	0.0605	0.8779	0.7905	1.5570	0.0948	1.2314	0.79	622	38	591	14	**584**	14	101
ZR22	#28	0.0	0.6	0.0608	1.4004	0.8023	2.1509	0.0957	1.5900	0.74	632	60	598	19	**589**	18	102
ZR23	#29	0.0	0.5	0.0600	0.6508	0.8232	1.4167	0.0995	1.2025	0.85	603	28	610	13	**611**	14	100
ZR14	#18	0.0	0.0	0.0607	0.5816	0.8546	1.1041	0.1021	0.8623	0.78	629	25	627	10	**627**	10	100
ZR38	#48	0.0	0.3	0.0592	0.8387	0.8376	1.8524	0.1026	1.6095	0.87	575	36	618	17	**630**	19	98
ZR13	#17	0.0	0.3	0.0606	0.7560	0.8768	1.2416	0.1049	0.9125	0.73	626	32	639	12	**643**	11	99
ZR31	#39	0.0	0.7	0.0578	2.1768	0.8372	2.9170	0.1051	1.9060	0.65	521	94	618	27	**644**	23	96
ZR45	#57	0.0	0.4	0.0614	2.2232	0.8902	3.4439	0.1052	2.6040	0.76	652	94	646	33	**645**	32	100
ZR17	#23	0.0	0.9	0.0595	3.4397	0.8647	4.1270	0.1054	2.2501	0.55	585	146	633	38	**646**	28	98
ZR27	#35	0.0	0.6	0.0585	1.2929	0.8526	2.7612	0.1056	2.4116	0.87	550	56	626	26	**647**	30	97
ZR21	#27	0.0	0.7	0.0611	0.7578	0.9075	1.7668	0.1077	1.5524	0.88	644	32	656	17	**659**	19	99
ZR40	#50	0.0	0.5	0.0610	1.8533	0.9604	2.9088	0.1141	2.2111	0.76	640	79	683	29	**697**	29	98
ZR44	#56	0.0	0.8	0.0592	1.5215	0.9342	2.2560	0.1145	1.6240	0.72	573	66	670	22	**699**	21	96
ZR9	#13	0.0	0.1	0.0651	1.2645	1.0735	2.1655	0.1195	1.7184	0.79	779	53	740	23	**728**	24	102
ZR18	#24	0.0	0.4	0.0669	1.5550	1.2678	2.3634	0.1374	1.7407	0.74	835	64	831	27	**830**	27	100
ZR15	#19	0.0	0.5	0.0645	1.2280	1.2294	2.1220	0.1381	1.6904	0.80	759	51	814	24	**834**	26	98
ZR25	#31	0.0	0.4	0.0718	0.9638	1.4388	1.7859	0.1454	1.4572	0.82	979	39	905	21	**875**	24	103
ZR16	#20	0.0	0.4	0.0677	1.5577	1.3881	2.4396	0.1486	1.8406	0.75	860	64	884	29	**893**	31	99
ZR5	#7	0.0	0.3	0.0718	0.6377	1.6066	1.6679	0.1623	1.4960	0.90	980	26	973	21	**969**	27	100
ZR43	#55	0.0	0.6	0.0827	0.8634	2.2696	2.4133	0.1991	2.2230	0.92	**1261**	34	1203	34	1171	48	103
ZR19	#25	0.0	0.6	0.0842	0.9428	2.6053	2.5568	0.2245	2.3476	0.92	**1297**	36	1302	37	1305	55	100
ZR33	#41	0.0	0.3	0.1154	1.2605	5.3077	2.5896	0.3336	2.2315	0.86	**1886**	45	1870	44	1856	72	101
ZR11	#15	0.0	0.8	0.2065	1.3330	15.7777	2.2777	0.5540	1.8094	0.79	**2879**	43	2863	43	2842	83	101
ZR8	#10	0.0	1.0	0.0713	1.1988	0.8372	2.2654	0.0852	1.8862	0.83	966	49	618	21	527	19	117
ZR26	#34	0.0	1.6	0.0661	1.8519	0.8552	3.0714	0.0939	2.4221	0.79	808	77	628	29	578	27	108
ZR41	#51	0.0	0.4	0.0603	2.1010	0.8492	3.5230	0.1022	2.8036	0.80	613	90	624	33	627	33	100
ZR6	#8	0.0	1.3	0.0685	1.1044	0.9784	1.7212	0.1036	1.2671	0.74	883	45	693	17	636	15	109
ZR36	#46	0.0	0.4	0.0610	2.3154	0.8866	3.6989	0.1055	2.8606	0.77	638	98	645	35	646	35	100

ZR47	#59	0.0	1.0	0.0552	3.7334	0.8099	4.5957	0.1063	2.6542	0.58	422	162	602	41	651	33	92
ZR12	#16	0.0	1.2	0.0604	1.4418	0.8917	3.2346	0.1071	2.8716	0.89	618	62	647	31	656	36	99
ZR10	#14	0.0	0.4	0.0662	2.1898	0.9967	3.8384	0.1092	3.1306	0.82	812	90	702	39	668	40	105
ZR46	#58	0.0	0.4	0.0640	7.7344	0.9700	8.3622	0.1100	3.1572	0.38	741	311	688	82	673	40	102
ZR34	#44	0.0	0.3	0.0698	5.9557	1.1470	6.0570	0.1193	1.0389	0.17	921	236	776	65	726	14	107
ZR32	#40	0.0	2.4	0.0563	8.9346	0.9619	10.4814	0.1239	5.4677	0.52	464	373	684	102	753	77	91
ZR37	#47	0.0	2.1	0.0827	1.9406	1.7178	2.8291	0.1507	2.0251	0.72	1261	75	1015	36	905	34	112
ZR39	#49	0.0	0.6	0.0629	5.1906	1.3178	6.9425	0.1518	4.5956	0.66	706	213	854	79	911	78	94
ZR3	#5	0.0	0.6	0.0616	4.2043	1.3019	5.4789	0.1532	3.4935	0.64	662	175	847	62	919	60	92
ZR42	#54	0.0	0.1	0.0483	10.4851	1.0370	10.9959	0.1558	3.2917	0.30	112	461	722	111	934	57	77
ZR24	#30	0.0	0.3	0.1034	0.9083	4.2833	3.0184	0.3005	2.8545	0.95	1685	33	1690	49	1694	85	100
ZR4	#6	0.0	0.6	0.1378	1.9337	5.8897	2.7365	0.3100	1.9005	0.69	2199	66	1960	47	1741	58	113
ZR48	#60	0.0	0.5	0.1349	0.6911	6.3357	2.7516	0.3407	2.6375	0.96	2162	24	2023	48	1890	86	107
ZR20	#26	0.0	0.4	0.1231	2.0548	6.0760	4.3591	0.3578	3.8265	0.88	2002	72	1987	75	1972	129	101
ZR7	#9	0.0	0.3	0.1295	0.6745	6.4375	1.3229	0.3606	1.0760	0.81	2091	24	2037	23	1985	37	103
ZR30	#38	0.0	0.4	0.1426	2.1596	7.2949	3.2845	0.3711	2.4468	0.74	2259	74	2148	58	2034	85	106
ZR1	#3	0.0	0.3	0.1606	0.6127	9.6694	1.4123	0.4365	1.2173	0.86	2462	21	2404	26	2335	48	103

Table S4C. Results of U-Pb isotope analysis by LA-ICP-MS on zircon from polymict impact breccia sample CA-73. Data in bold print were used in provenance diagrams. Data in red were excluded, as concordance values were > 105 % or < 95%. (*) Data are grouped according to $^{206}Pb/^{208}U$ apparent ages. *% Conc: concordance.

Identifier	Spot number	f 206c (%)	Th/U	Ratio						rho	Apparent Ages (Ma)						*% Conc
				$^{207}Pb/^{206}Pb$	1σ (%)	$^{207}Pb/^{235}U$	1σ (%)	$^{206}Pb/^{238}U$	1σ (%)		$^{207}Pb/^{206}Pb$	2σ (abs)	$^{207}Pb/^{235}U$	2σ (abs)	$^{206}Pb/^{238}U$	2σ (abs)	
CA-73 - Polymict impact breccia																	
CA-73E	#27	1.1	0.0	0.0555	22.5370	0.8964	18.0812	0.0881	1.8310	0.04	1783	240	539	159	**543**	19	99
CA-73E	#47	1.4	0.0	0.0572	22.2850	0.8725	27.2919	0.1333	1.4970	0.24	1637	244	792	121	**805**	23	98
CA-73E	#86	0.7	0.0	0.0720	9.8855	1.8474	14.2298	0.1912	1.0660	0.45	**1430**	151	1154	88	1127	22	102
CA-73E	#12	1.4	0.0	0.0699	16.2610	2.7306	21.4165	0.1942	3.2260	0.31	**1728**	213	1130	137	1167	40	97
CA-73E	#37	0.7	0.0	0.1234	7.3430	5.8541	9.9304	0.3371	1.2100	0.04	**1943**	111	1926	88	1881	32	102
CA-73E	#35	0.2	0.0	0.1292	2.2700	6.6315	2.5792	0.3699	0.4473	0.17	**2096**	64	2054	42	2028	16	101
CA-73E	#69	0.2	0.0	0.1234	3.6400	6.1249	5.8869	0.3782	0.7111	0.15	**2013**	91	2027	58	2066	26	98
CA-73E	#75	0.8	0.0	0.1241	3.4400	6.8587	3.8439	0.4000	0.5455	0.21	**2018**	84	2112	56	2168	20	97
CA-73E	#1	0.5	-0.1	0.1879	5.0913	12.5005	5.3290	0.5051	1.6290	0.05	**2693**	72	2687	64	2652	54	101
CA-73E	#63	1.3	0.0	0.1806	4.7452	12.5707	4.9768	0.5137	1.0897	0.18	**2706**	110	2640	104	2667	48	99
CA-73E	#41	0.4	-0.1	0.1969	3.1403	14.7426	3.8157	0.5396	0.9491	0.12	**2830**	51	2806	36	2778	41	101
CA-73E	#99	0.2	0.0	0.2161	1.5820	16.6915	2.0297	0.5618	0.4610	0.18	**2941**	44	2922	30	2873	21	102
CA-73E	#93	-1.3	0.0	0.2203	4.7351	22.5521	20.9848	0.6807	8.1933	-0.06	**2953**	143	2965	112	3031	72	98
CA-73E	#43	6.6	0.0	-0.0364	-271.8890	-1.7075	-50.5711	0.0559	12.0040	-0.03	3451	313	460	264	264	37	174
CA-73E	#65	13.5	0.0	-0.0345	-234.9640	-0.3946	-62.6017	0.0430	9.2540	0.00	2987	320	543	207	266	52	204
CA-73E	#11	8.2	0.0	0.1619	53.2546	-0.5584	-316.8640	0.0201	160.9900	0.01	3828	194	913	331	281	122	325
CA-73E	#87	3.7	0.0	0.1353	65.6603	-0.3878	-166.5050	0.0674	28.6770	0.15	2939	333	479	262	310	55	155
CA-73E	#9	8.4	0.1	0.1731	44.3086	-0.3016	-353.7232	0.0467	37.7900	0.13	2815	325	728	234	331	75	220
CA-73E	#40	5.5	0.0	0.1746	43.4539	1.1447	43.4428	0.0527	6.1910	0.02	2529	348	692	205	338	36	204
CA-73E	#70	1.1	0.2	0.5773	29.0199	-9.2984	-81.8135	0.0866	55.9060	0.05	4414	47	3314	371	341	356	971
CA-73E	#13	-1.6	0.1	0.1064	31.5600	0.7966	30.0370	0.0558	4.0090	0.13	2391	304	591	149	348	27	170
CA-73E	#50	2.3	0.0	0.1091	64.5030	0.5572	122.3805	0.0422	40.2870	0.13	3249	239	791	222	351	71	225
CA-73E	#56	2.1	-0.1	0.7332	45.4494	13.1385	46.8324	0.0838	44.8000	-0.05	4395	45	2800	369	360	330	778
CA-73E	#51	18.1	-0.1	-0.3325	-60.3424	-1.0629	-52.7595	0.0930	42.5980	0.08	3797	286	845	411	380	240	222
CA-73E	#4	17.7	-0.2	0.3098	79.4601	-8.0829	-59.3453	0.0820	29.1570	0.09	4303	106	2443	549	442	245	552
CA-73E	#64	0.4	0.0	0.4125	41.0778	-0.9442	-262.0200	0.0790	14.5800	-0.02	4165	101	1871	416	483	154	387
CA-73E	#31	0.7	0.0	0.3986	75.1851	0.9627	38.8707	0.0839	5.0850	0.64	2474	344	696	180	512	40	136
CA-73E	#15	0.8	0.0	0.1047	53.9240	0.4846	73.4290	0.0835	4.1580	0.22	2393	347	456	176	513	40	89
CA-73E	#82	0.9	-0.1	-0.1258	-128.5760	2.3625	51.2301	0.0692	63.9180	0.02	3691	208	1946	272	519	143	375
CA-73E	#78	6.6	0.0	0.3243	20.3330	0.3606	403.6406	0.0954	11.2930	0.08	3551	213	1439	260	532	96	270
CA-73E	#39	0.9	0.1	0.0341	113.4900	1.5153	51.4230	0.0835	12.7970	-0.12	2665	345	992	264	548	81	181
CA-73E	#32	2.2	-0.2	0.0966	24.5690	1.2099	21.7534	0.0811	10.9360	0.25	2330	224	760	175	549	37	138
CA-73E	#67	21.1	0.0	0.3957	73.3937	-0.1626	-1215.0200	0.0788	20.9060	0.01	3706	229	1817	293	550	125	330
CA-73E	#108	2.2	0.1	-0.0895	-128.6300	-0.4431	-120.5396	0.0918	5.4542	-0.02	2536	334	806	241	558	62	145
CA-73E	#102	-1.1	0.0	-0.0596	-183.4040	1.1059	75.1247	0.0932	7.3635	-0.15	3048	264	1253	284	560	78	224
CA-73E	#22	1.1	-0.2	0.2057	32.8670	0.9614	64.5881	0.0920	4.6890	0.07	2711	246	1084	176	561	52	193

CA-73E	#107	3.6	0.0	0.0835	72.6065	-0.1954	-255.8360	0.0903	4.8650	0.29	2487	329	603	210	561	58	107
CA-73E	#5	4.3	0.0	0.6433	55.4781	-1.6345	-66.0829	0.0909	10.6010	0.19	3433	249	1068	325	564	143	189
CA-73E	#8	11.3	-0.1	0.3324	22.2849	3.0497	87.8910	0.0882	33.9100	-0.19	3703	224	1766	279	564	215	313
CA-73E	#59	-1.4	0.0	0.0675	40.8900	1.2707	55.5420	0.0927	4.5310	-0.06	2892	287	780	256	566	49	138
CA-73E	#79	1.7	0.0	0.0902	27.0800	1.6159	37.2603	0.0924	3.2810	-0.07	2308	265	984	160	566	36	174
CA-73E	#29	0.6	-0.1	0.0747	162.9000	-0.8364	-74.3812	0.0912	5.5386	0.07	2335	361	607	215	568	54	107
CA-73E	#38	2.4	0.0	0.0390	39.0740	0.4525	33.4710	0.0937	2.8350	0.06	1470	427	421	138	575	33	73
CA-73E	#57	0.2	0.0	0.0957	30.6970	1.3461	69.6124	0.0872	7.3691	0.00	2903	266	888	266	588	45	151
CA-73E	#7	2.3	0.0	0.0057	534.3100	0.4818	67.3423	0.0958	2.9350	0.02	2054	294	885	166	594	31	149
CA-73E	#101	-2.4	0.0	0.1686	91.5655	1.5379	53.3665	0.0985	6.0759	-0.02	2891	314	1096	247	595	68	184
CA-73E	#109	7.0	-0.1	0.1433	38.9489	2.2471	85.8039	0.0964	11.6660	0.19	3106	321	1337	291	595	115	225
CA-73E	#36	0.2	0.0	0.0637	19.0210	0.6836	27.2070	0.0948	3.9340	0.04	1442	244	713	83	600	26	119
CA-73E	#81	-3.7	0.0	0.0064	1476.1600	1.2175	45.4607	0.1028	6.2588	0.13	2535	262	1044	183	620	53	168
CA-73E	#85	-0.1	0.0	0.0369	110.1900	-0.9161	-71.4701	0.0782	27.1700	0.21	1915	344	814	151	621	43	131
CA-73E	#20	4.8	0.0	0.0321	66.8500	0.7492	47.4309	0.1022	2.8100	-0.01	2020	305	758	228	625	33	121
CA-73E	#34	6.5	-1.3	0.0535	132.5070	0.6290	180.4165	0.1037	5.7948	0.06	2522	365	860	248	625	69	138
CA-73E	#17	-1.1	-0.1	0.2877	66.7896	0.0299	4379.1340	0.0959	17.4910	0.04	3510	236	1985	226	625	154	318
CA-73E	#44	7.1	-0.1	0.1360	49.4783	1.7194	78.9723	0.1115	8.9395	-0.06	3162	259	1077	367	625	76	172
CA-73E	#98	7.2	0.1	0.1988	84.1852	0.1495	1558.7130	0.1075	19.1770	-0.09	3903	175	1994	444	641	199	311
CA-73E	#6	7.3	0.0	0.0558	58.5550	1.1366	57.9306	0.1023	3.7670	-0.01	1898	295	1010	181	648	69	156
CA-73E	#54	-4.1	0.0	0.2294	33.3361	0.9166	104.8604	0.1062	8.4774	-0.04	2898	308	1082	288	650	73	166
CA-73E	#89	3.1	0.0	0.1071	53.7183	-0.2607	-204.0220	0.1059	6.6303	0.01	3119	264	1157	247	651	75	178
CA-73E	#88	3.2	0.0	0.1143	33.7660	0.9726	39.3251	0.1052	4.1270	0.14	2419	300	835	194	653	44	128
CA-73E	#84	4.0	0.0	0.0318	90.8300	3.8502	58.8817	0.1028	10.6080	-0.10	2493	327	908	228	658	85	138
CA-73E	#68	-1.8	0.0	0.1116	43.4920	-0.1179	-537.9085	0.1259	13.3130	0.02	2909	283	1109	225	662	102	168
CA-73E	#115	2.0	0.0	0.0967	6.4200	1.5444	6.2753	0.1085	1.9150	0.93	1770	109	961	57	663	24	145
CA-73E	#74	-1.0	0.0	0.0684	138.3680	1.1592	57.8694	0.1120	5.5326	0.04	2602	313	1013	202	673	70	151
CA-73E	#46	0.7	0.0	0.1515	14.8830	2.6265	19.3937	0.1095	3.4740	-0.02	2768	196	1353	137	676	40	200
CA-73E	#24	-8.8	-0.3	0.1597	99.0350	-0.0581	-2137.1260	0.1181	11.9470	-0.14	2973	342	1481	270	681	151	217
CA-73E	#92	0.2	-0.1	0.0701	66.8760	0.5610	100.6674	0.1073	5.4945	-0.02	2161	295	765	190	686	49	112
CA-73E	#97	1.0	-0.1	0.0817	64.0810	1.1831	36.3073	0.1115	3.8600	0.09	2495	297	948	191	686	46	138
CA-73E	#28	-0.1	0.0	0.1225	15.8920	1.0239	37.1980	0.1133	2.5750	0.83	2101	171	973	98	689	33	141
CA-73E	#19	0.2	0.0	0.1298	27.3600	1.4584	48.2301	0.1339	14.2160	0.15	2362	347	962	247	699	68	138
CA-73E	#16	3.2	0.0	-0.0479	-397.3800	0.9389	110.1490	0.1174	8.9816	0.03	3177	292	1263	313	700	212	180
CA-73E	#55	-4.8	-0.1	0.2607	37.8095	3.8313	52.8467	0.1212	8.4588	0.11	3508	289	1279	357	708	97	181
CA-73E	#14	-1.9	0.1	0.1202	29.5460	1.2452	71.5010	0.1146	10.3150	-0.06	3117	272	1350	262	711	104	190
CA-73E	#66	0.7	0.2	0.1087	19.4210	0.9223	63.3181	0.1236	9.5605	0.69	2200	296	837	155	711	67	118
CA-73E	#48	0.9	0.0	0.1175	22.8890	3.0450	20.3642	0.1194	4.6308	0.01	2675	213	1479	157	718	62	206
CA-73E	#113	-1.1	0.0	0.0992	19.5690	1.2386	45.7934	0.1217	4.2990	0.13	2254	285	878	160	733	58	120
CA-73E	#71	2.8	0.0	0.0620	69.0270	-8.2216	-85.6492	0.0975	25.5060	0.03	2863	341	1156	252	746	151	155
CA-73E	#105	7.2	-0.2	0.0948	17.2000	1.7422	51.8805	0.1436	9.9872	0.28	2148	287	995	189	776	99	128
CA-73E	#100	0.6	0.0	0.2437	48.1680	1.4849	108.0875	0.1146	16.6400	0.11	3296	228	1371	268	797	106	172
CA-73E	#25	-0.3	0.0	0.0975	16.6560	2.0597	19.3270	0.1350	2.4220	0.12	1891	279	974	157	814	36	120
CA-73E	#2	-4.7	0.1	0.1612	25.9360	7.8317	48.1739	0.1372	6.7424	0.01	3304	239	1850	247	816	103	227
CA-73E	#103	5.0	0.0	0.0310	214.5750	2.1787	94.2952	0.1430	9.5009	0.04	2787	302	1458	282	822	101	177
CA-73E	#96	0.2	0.0	0.0998	51.8026	0.3973	501.0452	0.1403	11.3460	0.41	2542	337	1253	256	822	84	152

CA-73E	#33	1.0	-0.7	0.3851	29.5633	18.9482	83.2433	0.1329	24.9160	0.00	3634	299	2042	519	851	240	240
CA-73E	#94	0.4	0.0	0.0780	22.0780	1.5399	19.6321	0.1378	2.5130	0.17	1553	237	981	123	861	62	114
CA-73E	#112	2.9	0.6	0.0618	51.4420	1.2489	47.8332	0.1551	5.0251	-0.15	2375	313	1025	206	914	80	112
CA-73E	#62	15.4	0.0	0.2854	24.7174	-3.0207	-119.1840	0.1556	14.5000	-0.06	3652	207	2083	271	922	196	226
CA-73E	#53	-4.5	0.1	0.1020	70.6422	1.3368	180.0520	0.1001	45.5050	-0.01	3369	248	1833	268	930	102	197
CA-73E	#58	1.8	0.3	0.1110	25.7610	1.2869	62.7689	0.1604	3.6234	0.08	2318	233	1312	180	949	68	138
CA-73E	#114	-0.2	0.2	0.0747	36.0020	1.7671	92.4212	0.1573	4.9709	0.30	1847	300	1003	206	951	76	105
CA-73E	#72	0.5	0.0	0.3289	24.0022	-1.3543	-163.9947	0.2517	22.5428	-0.02	2870	261	1738	207	1100	160	158
CA-73E	#77	-1.4	0.0	0.2580	41.2414	-47.9746	-52.5200	0.1340	36.9920	0.03	3667	200	2659	304	1138	271	234
CA-73E	#91	-0.1	0.1	0.0528	44.8430	2.2129	35.3442	0.1977	4.8394	0.09	2351	325	1319	217	1185	83	111
CA-73E	#26	-0.1	0.0	0.0628	11.2190	1.1586	47.5703	0.2054	1.4520	0.54	1332	143	1113	92	1188	23	94
CA-73E	#10	0.0	0.0	0.0888	48.3200	2.9271	35.5363	0.1940	9.2627	-0.03	2815	237	1670	262	1240	91	135
CA-73E	#49	-1.1	0.0	0.0955	51.4100	4.7095	58.7116	0.2170	4.7401	-0.06	2620	277	1826	267	1264	100	144
CA-73E	#80	1.0	0.0	0.0722	64.4930	1.9768	42.8765	0.2254	4.5300	0.13	2287	262	1467	186	1312	89	112
CA-73E	#30	0.3	-0.3	0.1787	19.7290	5.6252	21.7423	0.2508	4.3786	0.20	2632	202	2046	149	1406	136	146
CA-73E	#18	0.5	0.0	0.1344	8.6151	4.0216	6.0040	0.2548	1.4230	0.29	1954	107	1654	61	1446	46	114
CA-73E	#60	-6.2	0.0	0.1384	20.5070	6.2626	25.0948	0.2734	11.1770	0.14	2738	282	1868	273	1569	194	119
CA-73E	#23	-1.0	0.0	0.1221	8.3660	5.4703	7.4176	0.2831	1.1220	0.38	2244	117	1882	91	1605	32	117
CA-73E	#110	2.1	0.0	0.1086	99.9374	3.6705	33.1382	0.2903	4.1825	0.37	2459	226	1881	162	1616	116	116
CA-73E	#73	-0.5	0.0	0.1215	3.7200	4.8872	6.4095	0.2878	0.6597	0.12	1947	107	1811	64	1630	19	111
CA-73E	#83	0.2	0.0	0.1405	1.9390	6.7145	2.0922	0.3369	0.4689	0.18	2240	56	2084	30	1875	13	111
CA-73E	#76	0.3	0.0	0.1456	5.8000	6.0734	9.6754	0.3411	1.2130	0.26	2199	146	2032	78	1888	39	108
CA-73E	#52	-0.1	0.0	0.1443	10.7960	5.6957	13.8015	0.3511	1.4975	0.06	2221	163	2040	95	1933	79	106
CA-73E	#106	0.0	0.0	0.1394	4.8077	6.3340	3.6687	0.3553	0.9210	0.40	2071	67	2011	36	1958	30	103
CA-73E	#111	1.0	0.0	0.0780	23.2000	5.0972	13.7242	0.3605	1.6809	0.10	2071	171	1960	128	1977	58	99
CA-73E	#61	2.1	0.0	0.1200	14.1000	6.1507	12.0389	0.3803	4.4189	0.20	2128	110	2110	73	1993	87	106
CA-73E	#21	1.0	0.1	0.1364	46.5975	9.7691	19.7020	0.4537	4.7184	0.86	2864	137	2634	105	2448	99	108
CA-73E	#95	0.0	0.0	0.1586	13.7700	12.4344	4.1576	0.5086	1.1158	0.41	2634	92	2645	56	2645	48	100
CA-73E	#42	1.1	0.0	0.2345	6.4199	13.9982	8.2143	0.5329	3.6668	0.24	3116	90	2852	68	2705	139	105
CA-73E	#3	-1.1	0.2	0.2188	17.0600	14.5964	15.1139	0.5155	3.6984	0.15	2922	162	2899	114	2731	123	106
CA-73E	#45	-0.6	-0.1	0.2258	9.1671	16.3742	19.6314	0.5385	5.2433	0.09	3011	147	2920	141	2810	69	104
CA-73E	#90	0.2	0.4	0.2549	0.8469	19.5761	1.1013	0.5537	0.4010	0.52	3219	28	3061	27	2840	18	108

Table S4D. Results of U-Pb isotope analysis by LA-ICP-MS on zircon from polymict impact breccia sample CA-116. Data in bold print were used in provenance diagrams. Data in red were excluded, as concordance values were > 105 % or < 95%. (*) Data are grouped according to $^{206}Pb/^{208}U$ apparent ages. *% Conc: concordance.

Identifier	Spot number	f 206c (%)	Th/U	Ratio						rho	Apparent Ages (Ma)						*% Conc
				$^{207}Pb/^{206}Pb$	1σ (%)	$^{207}Pb/^{235}U$	1σ (%)	$^{206}Pb/^{238}U$	1σ (%)		$^{207}Pb/^{206}Pb$	2σ (abs)	$^{207}Pb/^{235}U$	2σ (abs)	$^{206}Pb/^{238}U$	2σ (abs)	
CA-116 - Polymict impact breccia																	
CA-116B	#8	0.0	0.0	0.0615	19.0800	0.7329	19.0302	0.0843	1.7800	0.53	1501	255	561	160	**521**	18	108
CA-116B	#90	-18.4	0.1	0.4717	27.5159	1.4734	368.9890	0.0253	58.2000	-0.14	3818	158	1626	251	149	169	1088
CA-116B	#3	15.5	0.0	0.5955	78.6219	-0.9429	-187.6339	0.0270	38.0380	0.05	4158	141	1441	574	169	115	853
CA-116B	#67	1.2	-0.1	0.3462	65.9811	0.5146	130.6600	0.0268	23.1070	0.04	3466	299	916	281	184	94	498
CA-116B	#104	16.0	0.0	0.2322	48.8122	0.1301	585.9110	0.0340	14.5100	-0.05	3415	300	852	254	186	76	459
CA-116B	#48	7.5	0.3	-0.1444	-147.4260	-0.4038	-175.3960	0.0252	35.5900	-0.03	3894	199	1141	318	193	73	592
CA-116B	#106	19.2	0.0	0.5133	41.4146	8.8178	166.9314	0.0385	44.7270	-0.02	4349	92	1941	326	196	227	992
CA-116B	#42	91.4	0.6	0.0432	1285.0130	-4.0946	-52.4981	0.0323	41.4810	-0.03	4083	194	1646	505	211	186	780
CA-116B	#50	13.7	0.0	0.2823	31.1100	1.1736	82.0093	0.0379	18.3370	0.13	3596	208	906	285	221	95	411
CA-116B	#16	-25.0	0.0	0.4059	31.9142	0.7996	164.6367	0.0309	33.7500	-0.22	3925	190	1544	378	227	110	680
CA-116B	#21	-10.4	0.0	0.5832	14.8257	3.4623	36.8505	0.0394	25.5720	-0.02	4037	187	1551	325	233	130	667
CA-116B	#47	-10.7	0.0	0.1057	77.7940	0.3910	226.0140	0.0375	12.9900	0.04	3418	287	953	247	245	55	389
CA-116B	#40	3.5	0.1	0.0986	65.3476	0.7080	114.5633	0.0423	16.9810	0.10	3042	272	826	248	246	100	336
CA-116B	#102	29.8	0.0	-0.1959	-102.9460	-1.7409	-52.4655	0.0407	13.2470	0.04	3483	271	1154	203	247	67	468
CA-116B	#117	20.3	0.0	-0.0429	-448.1610	-0.9400	-75.0561	0.0403	11.5100	-0.07	3409	356	800	326	247	58	324
CA-116B	#45	-9.5	-0.1	0.3386	15.6142	1.2646	70.7960	0.0233	99.7080	0.29	3657	184	1174	223	253	194	465
CA-116B	#46	-0.7	0.0	0.0256	123.4100	0.4357	28.6334	0.0403	2.4710	0.30	1853	224	413	110	255	12	162
CA-116B	#114	42.4	0.1	-0.1027	-460.8030	-0.4878	-384.3740	0.0453	22.8470	-0.06	4129	164	1750	422	256	123	683
CA-116B	#14	-6.8	-0.1	-0.1603	-133.9240	0.9002	85.9729	0.0412	7.1160	0.12	2555	396	432	261	258	37	167
CA-116B	#43	3.0	-0.2	0.3121	37.4980	0.5949	237.5091	0.0369	33.7100	0.04	3573	283	982	339	258	110	380
CA-116B	#20	-5.4	-0.1	0.3701	20.3734	-1.9015	-179.3152	0.0354	41.1690	-0.01	3946	163	1386	313	263	144	526
CA-116B	#11	-3.5	0.0	0.1160	95.0486	0.2106	492.8973	0.0457	19.8080	0.08	3818	194	1074	257	265	117	406
CA-116B	#58	0.9	0.0	-0.0016	-3761.5300	-0.8299	-61.5637	0.0439	11.4140	-0.05	2992	358	382	234	269	59	142
CA-116B	#36	6.3	0.0	0.5333	28.3857	0.2381	228.3202	0.0372	23.2660	0.15	3356	239	1140	191	271	50	420
CA-116B	#95	16.4	0.0	0.6935	34.2937	1.4049	174.8884	0.0406	76.3680	0.23	3938	359	1877	709	281	338	669
CA-116B	#74	9.2	0.1	0.1229	100.1400	-1.0101	-59.1395	0.0078	314.0100	0.32	3310	336	461	306	285	63	161
CA-116B	#103	11.4	-0.9	0.8228	46.5977	5.2157	58.0476	0.0475	10.6340	-0.09	3523	214	1433	281	290	64	494
CA-116B	#54	3.3	-0.3	-0.0784	-113.2520	-0.5967	-78.6451	0.0433	9.6410	0.06	2838	241	468	171	290	34	161
CA-116B	#116	8.1	0.0	0.0572	208.3040	-0.9617	-117.0981	0.0441	52.2230	0.03	3551	239	1234	291	297	111	415
CA-116B	#2	4.2	0.0	0.0663	86.4800	-0.5847	-196.4155	0.0467	14.7260	0.12	2669	512	254	367	298	37	85
CA-116B	#27	9.7	0.0	0.3353	31.7170	-0.5405	-269.5600	0.0521	18.0200	0.39	3925	159	1402	353	300	115	467
CA-116B	#66	-3.1	0.0	0.3922	14.7448	0.5377	409.5410	0.0523	24.2010	0.30	3316	258	1129	236	302	81	374
CA-116B	#63	19.6	0.0	-0.6417	-77.2426	0.0894	2920.6800	0.0520	16.2200	0.17	3887	163	1305	365	302	103	431
CA-116B	#113	1.2	0.0	0.0358	184.9780	-0.1232	-298.0730	0.0487	4.7580	0.37	2374	355	442	155	305	28	145
CA-116B	#5	2.3	0.0	0.0632	58.3110	-0.0766	-380.5670	0.0495	7.7180	0.69	2487	662	190	316	310	45	61
CA-116B	#29	12.2	-0.1	-0.0661	-313.2640	-0.7835	-67.4287	0.0423	16.0010	0.02	3486	215	720	299	311	59	232

CA-116B	#32	7.7	0.0	0.1209	66.3986	0.2200	201.5500	0.0495	7.2310	0.09	2947	345	514	220	318	49	162
CA-116B	#73	10.6	0.0	0.0677	126.7820	-0.2696	-194.6272	0.0434	14.2960	0.08	3428	327	949	345	318	50	298
CA-116B	#71	7.7	0.0	0.1447	52.5450	0.3968	80.6200	0.0524	9.0800	0.31	2854	367	348	216	319	170	109
CA-116B	#69	9.1	0.1	-0.1019	-185.5530	0.5961	151.6338	0.0531	11.5410	0.29	3613	242	1329	307	321	73	414
CA-116B	#93	8.6	0.0	0.2145	62.9975	-1.8293	-48.6354	0.0594	17.9550	0.02	3598	221	843	281	321	79	263
CA-116B	#97	6.0	0.0	0.2660	28.1998	-2.6969	-98.6500	0.1023	69.9203	-0.15	3695	186	1257	241	323	226	389
CA-116B	#59	-7.3	-0.1	0.3360	22.1339	0.6934	116.2941	0.0542	12.2640	-0.08	3263	202	1205	151	324	85	372
CA-116B	#53	4.8	0.0	0.2002	44.2491	-0.1531	-1293.3760	0.0510	10.8640	0.17	3034	336	828	310	326	75	254
CA-116B	#51	-6.9	-0.2	0.2179	55.9971	1.0299	66.9980	0.0580	18.1000	-0.03	3608	211	1329	239	327	128	406
CA-116B	#24	6.1	0.0	0.0847	121.4860	0.1913	252.1590	0.0528	5.9160	0.04	3061	246	681	220	328	38	207
CA-116B	#31	-2.7	0.2	-0.0636	-265.0940	-0.1541	-385.0633	0.0536	9.2100	-0.10	3072	246	842	207	329	59	256
CA-116B	#41	-0.3	0.1	0.1561	38.8080	0.3078	203.8059	0.0505	9.8590	-0.08	3429	254	825	281	331	55	249
CA-116B	#94	-30.8	0.0	0.3384	17.8060	3.8602	36.3429	0.0626	20.4270	0.16	3801	189	1479	261	334	163	443
CA-116B	#65	-1.3	0.0	0.1372	35.2730	0.9061	61.1273	0.0542	7.4100	-0.06	3104	255	871	238	334	52	261
CA-116B	#15	-0.3	0.0	0.1024	25.4490	0.9141	36.7615	0.0546	8.0400	0.37	2323	342	523	186	338	55	155
CA-116B	#89	-2.5	-0.1	0.2756	22.6134	0.4088	307.9267	0.0550	26.0690	0.11	3466	245	1189	257	340	128	350
CA-116B	#4	-0.5	0.0	0.2815	54.1863	1.1124	77.0667	0.0534	10.6100	-0.10	2922	369	976	273	345	64	283
CA-116B	#61	-8.7	0.0	0.1173	44.3720	0.7681	69.6251	0.0554	4.8060	0.13	2977	241	836	200	345	32	242
CA-116B	#108	-1.4	0.0	0.1200	30.5620	1.9549	90.8297	0.0536	8.2890	0.27	2429	287	654	186	345	63	189
CA-116B	#92	1.3	0.0	0.0344	376.5960	0.5136	67.8283	0.0529	8.9000	0.55	2419	281	691	143	350	41	198
CA-116B	#68	5.5	0.0	0.2232	48.2430	1.4887	47.2009	0.0553	10.2510	0.20	3422	283	844	289	352	75	240
CA-116B	#115	4.3	0.0	0.2557	44.4040	0.8183	78.6758	0.0577	8.3160	0.10	2892	265	850	204	354	59	240
CA-116B	#10	-2.3	0.0	0.0614	46.7510	0.5824	27.1755	0.0566	4.3280	0.64	2207	325	461	172	354	29	130
CA-116B	#81	-0.6	0.0	0.0575	378.9680	-0.2398	-345.0290	0.0615	13.5460	0.18	3033	257	1083	204	355	121	305
CA-116B	#120	4.3	0.0	0.5573	16.7510	-0.7799	-228.3225	0.0554	22.1450	0.04	4028	158	1378	314	358	114	385
CA-116B	#84	15.1	-0.2	0.2009	62.9363	-3.1162	-35.6591	0.0698	26.7690	0.10	3547	236	774	237	360	165	215
CA-116B	#105	5.7	0.0	0.0061	491.3300	0.7595	50.6017	0.0571	4.2570	0.28	2515	349	433	263	363	26	119
CA-116B	#119	8.7	0.0	0.2099	75.6342	-2.0613	-54.2356	0.0549	22.0530	-0.06	3413	321	701	291	365	104	192
CA-116B	#85	5.9	-0.1	0.4059	40.9485	1.3875	70.3999	0.0683	14.7910	-0.08	2675	490	825	447	370	68	223
CA-116B	#7	-17.2	0.0	0.3095	51.7266	1.3602	98.7704	0.0615	18.7570	0.00	3251	368	1122	304	371	137	303
CA-116B	#37	0.4	0.1	0.0454	77.3410	0.8709	23.9408	0.0628	5.1360	0.09	2373	229	602	132	390	36	155
CA-116B	#57	2.6	-0.8	0.1146	43.3270	0.7582	38.7763	0.0606	4.9020	0.13	2477	268	660	152	393	50	168
CA-116B	#91	5.9	0.0	0.3159	42.5327	2.9059	45.7112	0.0677	13.5520	0.04	3881	164	1314	288	396	104	331
CA-116B	#96	-6.3	-0.1	0.5052	25.4565	4.6957	106.5685	0.0764	30.1550	-0.13	3966	124	1689	229	400	144	422
CA-116B	#30	3.6	0.0	0.1293	26.9090	0.0372	6077.1760	0.0666	7.9423	0.65	2627	285	730	187	406	63	180
CA-116B	#80	3.6	0.0	0.1035	42.8550	0.6253	61.5466	0.0669	4.8720	0.23	2543	302	957	178	414	40	231
CA-116B	#83	22.1	0.0	0.3105	40.5200	0.4189	355.2690	0.0620	17.7130	0.26	3548	240	1350	334	414	103	326
CA-116B	#75	1.5	0.1	0.2649	27.0943	3.0138	44.1830	0.0774	20.7110	0.07	3612	184	1524	206	421	74	362
CA-116B	#109	1.4	0.1	0.0866	46.5490	0.1748	263.1470	0.0689	4.5070	0.31	2242	271	647	150	438	46	148
CA-116B	#17	-28.5	-0.1	0.2776	51.4317	2.8620	30.6265	0.0846	17.3110	0.18	3676	179	1423	200	440	120	323
CA-116B	#64	-3.1	-0.1	0.3050	25.9688	1.4387	88.4324	0.0711	9.8772	0.47	3173	219	1399	192	444	78	315
CA-116B	#49	1.3	0.0	0.0853	92.8164	0.8603	46.3289	0.0731	6.5910	0.15	2723	275	864	211	447	60	193
CA-116B	#62	5.5	0.0	0.2032	18.3110	1.2551	47.3255	0.0719	14.2040	0.09	2699	259	898	177	448	74	201
CA-116B	#1	-3.7	0.0	0.1443	116.9110	1.7806	62.1414	0.0613	26.7820	0.10	3572	323	1601	288	448	128	357
CA-116B	#118	-1.4	0.0	0.4168	32.5182	1.2237	158.2354	0.0369	96.9990	-0.06	3954	131	1853	256	456	126	406
CA-116B	#98	5.2	0.0	0.1219	54.5035	-0.0824	-1202.8900	0.0727	12.5110	0.19	2996	230	1035	200	458	106	226

CA-116B	#82	7.3	0.1	0.0821	92.6150	0.3092	184.6662	0.0709	9.2000	0.48	3043	256	959	223	467	51	205
CA-116B	#39	3.0	0.0	0.1016	47.9010	1.3271	32.1864	0.0768	4.7690	0.63	2302	246	837	156	473	41	177
CA-116B	#100	3.6	0.0	-0.0041	-1103.0000	1.5956	72.0453	0.0836	17.1160	0.00	3022	329	618	285	478	116	129
CA-116B	#72	-10.7	0.0	0.4056	16.9015	5.8193	42.6536	0.0584	43.0610	0.09	4156	104	1545	345	480	166	322
CA-116B	#33	0.2	0.0	0.1325	25.6310	-0.1370	-904.2972	0.0800	7.4803	0.88	2201	304	672	204	484	72	139
CA-116B	#60	-4.7	0.0	0.3028	16.2140	1.3762	88.6285	0.0803	13.0720	0.47	3504	175	1601	189	520	107	308
CA-116B	#22	-6.1	0.0	0.1828	24.4130	0.7950	63.0203	0.0869	6.0463	0.03	2701	266	1004	198	528	65	190
CA-116B	#110	2.1	-0.6	-0.0606	-134.9740	1.7406	71.5791	0.0841	10.5610	0.01	2740	341	1094	292	549	65	199
CA-116B	#78	3.9	0.0	0.2313	40.4612	-0.0563	-1180.2580	0.0926	8.6291	-0.02	2496	284	808	188	553	86	146
CA-116B	#18	5.9	0.0	0.0394	97.3000	-1.8167	-92.8699	0.0891	5.1860	0.01	2262	344	687	187	559	48	123
CA-116B	#56	6.0	-0.1	0.0944	109.9320	0.2297	397.3126	0.0800	13.2580	0.53	3077	266	1231	209	563	83	219
CA-116B	#23	-1.8	-0.1	0.2571	26.3949	3.4988	20.6958	0.1120	16.5100	0.87	3205	233	1712	204	569	154	301
CA-116B	#9	-3.7	0.0	0.1136	68.1372	2.0639	75.9752	0.0956	7.4565	0.20	2729	419	1175	355	580	81	203
CA-116B	#26	2.7	-0.1	0.4498	58.2548	2.0048	93.0434	0.1009	8.9497	-0.07	2800	363	821	248	601	93	137
CA-116B	#44	-0.1	0.0	0.0589	29.6930	0.8371	27.8787	0.0988	1.9980	0.32	1562	248	686	123	606	23	113
CA-116B	#6	-2.0	-0.1	0.1744	48.2777	1.8095	37.1300	0.1123	11.1590	0.20	3271	332	776	303	614	67	127
CA-116B	#12	3.4	0.0	0.0631	23.6740	0.9652	37.1726	0.1062	3.4420	0.07	1815	282	719	149	617	22	116
CA-116B	#70	9.5	0.1	-0.1030	-287.0500	-2.9471	-131.3430	0.0935	19.9860	0.41	3387	309	1583	327	628	158	252
CA-116B	#55	-0.2	0.0	0.0824	73.2029	0.4210	249.6873	0.1149	8.2516	0.06	2628	379	1096	255	713	91	154
CA-116B	#52	0.5	20.8	0.0702	18.1900	1.4595	19.5635	0.1226	2.1610	0.09	1761	267	915	124	744	30	123
CA-116B	#99	2.5	0.0	0.0300	40.9370	0.5290	43.9025	0.1327	1.6940	0.60	1339	216	637	154	802	26	79
CA-116B	#19	0.8	0.0	0.1173	19.0750	2.6919	19.0829	0.1860	3.3344	0.96	2045	229	1325	155	1103	71	120
CA-116B	#87	-1.2	-0.1	0.1613	51.8830	9.0353	47.4721	0.1960	6.5328	0.41	3149	198	2027	215	1127	94	180
CA-116B	#101	-0.3	0.0	0.1103	69.3897	1.7968	134.2970	0.1939	5.1780	0.29	2273	246	1385	192	1150	90	120
CA-116B	#107	0.3	0.0	0.1329	8.2491	5.7990	14.1883	0.3543	1.6207	0.28	2062	155	1944	84	2018	109	96
CA-116B	#38	1.1	-0.1	0.2250	6.8236	10.4611	17.9340	0.3955	3.2493	0.97	2974	122	2559	94	2143	115	119
CA-116B	#34	0.8	-0.2	0.1406	19.0510	7.7826	21.1566	0.4234	3.9990	0.23	2584	169	2422	126	2169	93	112
CA-116B	#35	-0.3	0.1	-0.0344	-388.5500	2.4757	255.1861	0.4373	9.8206	0.36	2967	227	2403	249	2279	257	105
CA-116B	#13	0.2	-0.1	0.1868	35.7513	12.9555	38.6963	0.4440	6.6309	0.12	2881	213	2746	160	2399	190	114

Table S4E. Results of U-Pb isotope analysis by LA-ICP-MS on zircon from conglomerate sample CA-49. Data in bold print were used in provenance diagrams. Data in red were excluded, as concordance values were > 105 % or < 95%. (*) Data are grouped according to $^{206}Pb/^{208}U$ apparent ages. *% Conc: concordance.

Identifier	Spot number	f 206c	Th/U	Ratio						rho	Apparent Ages (Ma)						*% Conc
				$^{207}Pb/^{206}Pb$	1σ	$^{207}Pb/^{235}U$	1σ	$^{206}Pb/^{238}U$	1σ		$^{207}Pb/^{206}Pb$	2σ	$^{207}Pb/^{235}U$	2σ	$^{206}Pb/^{238}U$	2σ	
		(%)			(%)		(%)		(%)			(abs)		(abs)		(abs)	
CA-49 - conglomerate																	
1.sSMPABC054.TXT	#54	0.0	0.2	0.0588	0.6039	0.7725	0.7660	0.0953	0.4713	0.62	560	26	581	7	**587**	5	99
1.sSMPABC069.TXT	#69	0.1	0.6	0.0590	1.0779	0.7775	1.2009	0.0956	0.5294	0.44	567	47	584	11	**589**	6	99
1.sSMPABC011.TXT	#11	0.1	1.0	0.0584	0.7525	0.8514	0.9079	0.1058	0.5078	0.56	543	33	625	9	**649**	6	96
1.sSMPABC009.TXT	#9	0.0	0.7	0.0607	0.5268	0.8866	0.7217	0.1059	0.4933	0.68	630	23	645	7	**649**	6	99
1.sSMPABC012.TXT	#12	0.0	0.4	0.0622	1.1263	0.9090	1.6718	0.1060	1.2354	0.74	683	48	657	16	**649**	15	101
1.sSMPABC031.TXT	#31	0.0	0.4	0.0599	0.3933	0.8750	0.6131	0.1060	0.4704	0.77	600	17	638	6	**649**	6	98
1.sSMPABC033.TXT	#33	0.0	0.3	0.0603	0.4425	0.8802	0.6418	0.1060	0.4648	0.72	613	19	641	6	**649**	6	99
1.sSMPABC050.TXT	#50	0.0	1.0	0.0624	1.5720	0.9124	1.8260	0.1060	0.9291	0.51	690	67	658	18	**650**	11	101
1.sSMPABC019.TXT	#19	0.0	0.4	0.0628	2.0440	0.9182	2.1764	0.1060	0.7475	0.34	702	87	661	21	**650**	9	102
1.sSMPABC018.TXT	#18	0.0	0.3	0.0625	0.6582	0.9830	0.9600	0.1141	0.6988	0.73	692	28	695	10	**697**	9	100
1.sSMPABC030.TXT	#30	0.0	0.3	0.0614	0.6595	0.9687	0.8701	0.1145	0.5677	0.65	653	28	688	9	**699**	8	98
1.sSMPABC047.TXT	#47	0.0	0.8	0.0610	1.0622	0.9638	1.3279	0.1146	0.7969	0.60	639	46	685	13	**700**	11	98
1.sSMPABC032.TXT	#32	0.0	0.2	0.0626	0.5242	0.9901	0.8623	0.1147	0.6847	0.79	696	22	699	9	**700**	9	100
1.sSMPABC010.TXT	#10	0.0	1.1	0.0607	0.5652	0.9596	0.7323	0.1147	0.4657	0.64	628	24	683	7	**700**	6	98
1.sSMPABC040.TXT	#40	0.0	0.3	0.0601	0.6898	0.9515	0.8448	0.1148	0.4877	0.58	609	30	679	8	**701**	6	97
1.sSMPABC029.TXT	#29	0.0	0.5	0.0616	0.9113	0.9748	1.1343	0.1149	0.6754	0.60	659	39	691	11	**701**	9	99
1.sSMPABC008.TXT	#8	0.0	0.8	0.0652	1.1112	1.0327	1.2080	0.1149	0.4736	0.39	782	47	720	13	**701**	6	103
1.sSMPABC020.TXT	#20	0.0	0.5	0.0617	0.6043	0.9780	0.7604	0.1149	0.4615	0.61	665	26	693	8	**701**	6	99
1.sSMPABC058.TXT	#58	0.0	0.6	0.0620	0.5167	0.9829	0.7154	0.1149	0.4947	0.69	676	22	695	7	**701**	7	99
1.sSMPABC060.TXT	#60	0.0	0.0	0.0654	6.7554	1.2008	7.0093	0.1332	1.8696	0.27	788	284	801	81	**806**	28	99
1.sSMPABC028.TXT	#28	0.0	0.4	0.0642	0.4195	1.1841	0.5977	0.1338	0.4258	0.71	-	18	793	7	**810**	6	98
1.sSMPABC013.TXT	#13	0.0	0.2	0.0661	1.1019	1.2199	1.4917	0.1339	1.0056	0.67	810	46	810	17	**810**	15	100
1.sSMPABC057.TXT	#57	0.0	0.4	0.0668	0.5661	1.2334	0.7013	0.1340	0.4139	0.59	831	24	816	8	**811**	6	101
1.sSMPABC027.TXT	#27	0.0	0.7	0.0653	1.0774	1.2065	1.3523	0.1341	0.8173	0.60	783	45	804	15	**811**	12	99
1.sSMPABC051.TXT	#51	0.0	0.7	0.0688	1.1848	1.4136	1.4304	0.1491	0.8014	0.56	893	49	895	17	**896**	13	100
1.sSMPABC036.TXT	#36	0.0	0.7	0.0842	1.1756	2.4875	1.5179	0.2144	0.9603	0.63	**1297**	46	1268	22	1252	22	101
1.sSMPABC017.TXT	#17	0.0	0.5	0.1261	0.2759	6.5207	0.4587	0.3752	0.3665	0.80	**2044**	10	2049	8	2054	13	100
1.sSMPABC049.TXT	#49	0.0	0.3	0.1297	0.2728	6.8386	0.4692	0.3825	0.3817	0.81	**2094**	10	2091	8	2088	14	100
1.sSMPABC039.TXT	#39	0.0	0.6	0.0709	0.6835	0.7946	0.7956	0.0813	0.4072	0.51	954	28	594	7	504	4	118
1.sSMPABC015.TXT	#15	0.1	0.3	0.0679	2.2905	0.9906	2.4069	0.1059	0.7395	0.31	865	95	699	25	649	9	108
1.sSMPABC059.TXT	#59	0.0	0.0	0.0689	2.6862	1.0918	2.8692	0.1151	1.0083	0.35	894	111	749	31	702	13	107
1.sSMPABC067.TXT	#67	0.9	0.1	0.0625	135.1149	1.1318	135.4105	0.1314	8.9422	0.07	691	5763	769	-	796	135	97
1.sSMPABC070.TXT	#70	0.1	0.1	0.0767	11.0085	1.3969	11.3255	0.1322	2.6608	0.23	1113	440	888	144	800	40	111

1.sSMPABC072.TXT	#72	0.9	0.1	0.0624	179.3202	1.1427	179.3573	0.1329	3.6451	0.02	688	7653	774	-	804	55	96
1.sSMPABC007.TXT	#7	0.0	0.1	0.0712	0.4919	1.3084	0.6278	0.1333	0.3901	0.62	964	20	849	7	806	6	105
1.sSMPABC074.TXT	#74	0.6	0.1	0.0646	24.7525	1.1962	24.9122	0.1343	2.8159	0.11	763	1043	799	321	812	43	98
1.sSMPABC071.TXT	#71	0.8	0.3	0.0774	162.3416	1.6203	162.4030	0.1519	4.4636	0.03	1132	6465	978	-	911	76	107
1.sSMPABC056.TXT	#56	0.0	0.5	0.0868	0.6000	2.5865	0.8680	0.2161	0.6272	0.72	1357	23	1297	13	1261	14	103
1.sSMPABC016.TXT	#16	0.0	0.4	0.0801	0.5052	2.3884	0.6798	0.2163	0.4548	0.67	1200	20	1239	10	1263	10	98
1.sSMPABC035.TXT	#35	0.0	0.2	0.1211	0.3081	5.8195	0.5321	0.3487	0.4338	0.82	1973	11	1949	9	1928	14	101
1.sSMPABC037.TXT	#37	0.0	0.5	0.1177	0.2383	5.9562	0.4680	0.3671	0.4028	0.86	1922	9	1969	8	2016	14	98
1.sSMPABC052.TXT	#52	0.0	0.5	0.1315	0.2537	6.7917	0.4968	0.3748	0.4272	0.86	2118	9	2085	9	2052	15	102
1.sSMPABC034.TXT	#34	0.0	0.5	0.1253	0.2474	6.7262	0.4333	0.3896	0.3557	0.82	2033	9	2076	8	2121	13	98
1.sSMPABC048.TXT	#48	0.0	0.7	0.1341	0.2856	7.9734	0.5186	0.4316	0.4329	0.83	2152	10	2228	9	2313	17	96
1.sSMPABC055.TXT	#55	0.0	0.4	0.1291	0.2975	7.8982	0.5487	0.4439	0.4611	0.84	2086	10	2219	10	2368	18	94

Table S4F. Results of U-Pb isotope analysis by LA-ICP-MS on zircon from phyllite sample CA-111. Data in bold print were used in provenance diagrams. Data in red were excluded, as concordance values were > 105 % or < 95%. (*) Data are grouped according to $^{206}Pb/^{208}U$ apparent ages. *% Conc: concordance.

Identifier	Spot number	f 206c (%)	Th/U	Ratio						rho	Apparent Ages (Ma)						*% Conc
				$^{207}Pb/^{206}Pb$	1σ (%)	$^{207}Pb/^{235}U$	1σ (%)	$^{206}Pb/^{238}U$	1σ (%)		$^{207}Pb/^{206}Pb$	2σ (abs)	$^{207}Pb/^{235}U$	2σ (abs)	$^{206}Pb/^{238}U$	2σ (abs)	
CA-111 - phyllite																	
SPL 3935	97.1	0.2	0.3	0.0593	2.0236	0.7789	2.2082	0.0953	1.1756	0.78	578	87	585	19	**587**	13	101
SPL 3935	82.1	1.4	1.4	0.0592	3.2095	0.7798	3.2945	0.0955	0.8687	0.73	574	134	585	29	**588**	10	102
SPL 3935	96.1	0.0	0.6	0.0608	2.9605	0.8044	3.0446	0.0960	1.4058	0.83	630	130	599	27	**591**	16	95
SPL 3935	98.1	0.0	0.8	0.0602	2.8239	0.8020	3.5934	0.0967	1.3757	0.89	610	121	598	30	**595**	16	98
SPL 3935	44.1	1.2	1.1	0.0606	1.9802	0.8115	1.8140	0.0971	0.8447	0.90	626	87	603	16	**597**	10	96
SPL 3935	66.1	0.3	0.6	0.0599	2.6711	0.8061	2.6746	0.0977	0.8088	0.96	598	113	600	24	**601**	9	100
SPL 3935	99.1	0.3	0.6	0.0604	2.3179	0.8154	2.8502	0.0979	1.1541	0.93	618	104	606	25	**602**	13	98
SPL 3935	37.1	0.8	0.9	0.0611	2.4550	0.8256	2.5085	0.0980	0.5309	0.85	644	100	611	23	**602**	6	95
SPL 3935	58.1	0.2	1.0	0.061	1.6393	0.8277	1.6299	0.0985	0.8834	0.92	638	72	612	15	**606**	10	96
SPL 3935	57.1	1.3	0.5	0.061	2.2951	0.8305	2.4238	0.0987	1.0232	0.86	640	98	614	21	**607**	12	96
SPL 3935	100.1	0.0	1.1	0.0607	2.3064	0.8318	2.5078	0.0994	1.0364	0.83	629	97	615	23	**611**	12	98
SPL 3935	56.1	0.0	1.0	0.0616	3.2468	0.8521	3.0749	0.1003	0.9371	0.59	660	140	626	29	**616**	11	95
SPL 3935	68.1	14.9	0.5	0.0616	2.1104	0.8573	2.0566	0.1009	0.7432	0.99	661	91	629	19	**620**	9	95
SPL 3935	4.1	3.4	0.3	0.0614	1.6287	0.8663	2.0975	0.1024	0.8402	0.72	652	69	634	20	**628**	10	97
SPL 3935	84.1	0.0	0.5	0.0614	3.2573	0.8675	3.3716	0.1025	0.9370	0.81	654	140	634	32	**629**	11	97
SPL 3935	50.1	0.5	0.7	0.0607	2.4712	0.8624	2.2241	0.1030	0.8933	0.37	630	106	631	21	**632**	11	100
SPL 3935	93.1	3.0	0.5	0.0614	1.9544	0.8722	2.0568	0.1031	0.8734	0.90	653	84	637	20	**632**	11	98
SPL 3935	35.1	0.5	1.1	0.062	2.4194	0.8852	2.4130	0.1036	0.8492	0.73	673	107	644	23	**636**	10	96
SPL 3935	42.1	0.0	0.5	0.0623	2.7287	0.8916	2.6513	0.1038	0.5299	0.78	685	115	647	25	**637**	6	95
SPL 3935	81.1	1.3	0.3	0.0621	1.9324	0.8975	2.2829	0.1049	0.9345	0.99	677	81	650	21	**643**	11	96
SPL 3935	71.1	5.6	0.6	0.0605	2.6446	0.8854	2.7017	0.1062	0.7249	0.96	620	114	644	26	**651**	9	104
SPL 3935	70.1	0.0	0.6	0.0622	2.5723	0.9112	2.5978	0.1063	0.9500	0.72	679	113	658	25	**651**	12	97
SPL 3935	53.1	0.7	0.5	0.0622	2.4116	0.9527	2.4898	0.1110	0.8106	0.81	682	110	680	25	**679**	10	100
SPL 3935	30.1	0.0	1.3	0.0634	2.6814	0.9877	2.8499	0.1130	0.8232	0.54	722	108	698	29	**690**	11	97
SPL 3935	52.1	3.2	0.4	0.0636	2.2013	1.0083	2.1541	0.1150	0.8610	0.01	729	94	708	22	**702**	11	97
SPL 3935	54.1	0.0	1.1	0.0636	3.6164	1.0167	3.6629	0.1159	1.2859	0.83	730	156	712	36	**707**	17	98
SPL 3935	79.1	5.4	1.0	0.0641	1.5601	1.0333	1.7613	0.1170	0.7865	0.99	744	67	721	18	**713**	11	97
SPL 3935	60.1	0.0	0.8	0.0651	5.6836	1.0630	5.4282	0.1185	1.5616	0.41	777	209	735	55	**722**	21	95
SPL 3935	48.1	0.0	0.8	0.0649	2.7735	1.1261	2.5414	0.1259	1.0405	0.54	770	114	766	27	**764**	15	99
SPL 3935	31.1	0.0	0.4	0.0657	1.8265	1.1466	2.1037	0.1266	0.7664	0.99	797	78	776	23	**768**	11	97
SPL 3935	11.1	0.1	0.7	0.0669	2.6906	1.1816	2.9613	0.1281	0.9758	0.67	835	109	792	32	**777**	14	95

SPL 3935	39.1	0.0	0.9	0.0658	2.7356	1.1648	2.6907	0.1284	0.5842	0.75	800	117	784	30	**779**	9	98
SPL 3935	62.1	1.3	0.6	0.0671	2.0864	1.1874	2.0651	0.1284	0.6697	0.96	840	84	795	23	**779**	10	95
SPL 3935	91.1	0.0	0.5	0.0656	7.7744	1.1670	7.8850	0.1290	1.3416	0.36	795	297	785	81	**782**	20	99
SPL 3935	51.1	0.0	0.5	0.0664	1.9578	1.1869	1.9757	0.1296	0.9880	0.89	821	82	795	21	**785**	14	97
SPL 3935	69.1	0.2	0.9	0.0651	2.1505	1.1718	2.2956	0.1305	0.7508	0.91	778	86	788	25	**791**	11	101
SPL 3935	6.1	0.5	1.1	0.0665	1.2030	1.2029	1.4897	0.1312	0.8614	0.94	822	52	802	16	**795**	13	98
SPL 3935	29.1	0.0	0.2	0.0667	1.9490	1.2173	2.2666	0.1325	0.7247	0.94	827	79	809	25	**802**	11	98
SPL 3935	94.1	1.0	0.5	0.0666	2.4024	1.2167	2.5840	0.1326	1.2748	0.74	824	103	808	30	**803**	19	98
SPL 3935	63.1	0.3	0.4	0.0662	2.2659	1.2343	2.2905	0.1353	0.8651	0.94	812	91	816	26	**818**	13	100
SPL 3935	77.1	1.6	0.2	0.0777	1.5444	2.0354	1.5378	0.1901	0.8680	0.99	**1138**	60	1127	22	1122	18	99
SPL 3935	87.1	0.8	0.2	0.081	1.8519	2.2655	1.9740	0.2029	0.9513	0.99	**1221**	74	1202	27	1191	21	98
SPL 3935	86.1	0.9	0.6	0.0807	2.9740	2.3324	3.0175	0.2097	1.0063	0.49	**1214**	114	1222	42	1227	22	101
SPL 3935	85.1	0.0	0.3	0.087	1.9540	2.7598	1.9501	0.2301	0.9951	0.84	**1360**	78	1345	29	1335	24	99
SPL 3935	27.1	1.3	0.8	0.094	2.1277	3.1515	2.4620	0.2430	0.8394	0.89	**1509**	77	1445	37	1402	21	96
SPL 3935	14.1	0.0	0.5	0.0875	1.4857	2.9903	1.5125	0.2480	0.8873	0.95	**1371**	56	1405	23	1428	23	103
SPL 3935	61.1	3.4	1.3	0.0996	1.8072	3.8451	1.7703	0.2801	0.7284	0.94	**1616**	71	1602	32	1592	21	99
SPL 3935	20.1	0.0	0.8	0.1073	1.5843	4.4198	1.7302	0.2988	0.9607	0.35	**1754**	56	1716	28	1685	29	98
SPL 3935	75.1	0.0	0.4	0.1114	1.8851	4.9866	2.1091	0.3246	0.6840	0.97	**1823**	67	1817	33	1812	22	100
SPL 3935	73.1	0.0	0.5	0.1117	2.1486	5.0395	2.3665	0.3273	0.7241	0.90	**1827**	81	1826	41	1825	23	100
SPL 3935	40.1	0.7	1.3	0.1123	1.6028	5.1215	1.4683	0.3307	0.4747	0.99	**1837**	59	1840	26	1842	15	100
SPL 3935	8.1	0.3	0.8	0.1177	1.0195	5.4968	1.2114	0.3388	0.8353	0.99	**1921**	36	1900	21	1881	27	99
SPL 3935	24.1	0.0	1.0	0.1161	1.1197	5.5202	1.7046	0.3449	1.1394	0.95	**1897**	40	1904	30	1910	38	100
SPL 3935	10.1	0.0	0.8	0.1184	1.1824	5.7016	1.3802	0.3493	0.9333	0.99	**1932**	41	1932	24	1931	31	100
SPL 3935	5.1	0.0	0.8	0.1268	1.4984	6.5504	2.0345	0.3747	0.8114	0.92	**2054**	53	2053	36	2051	29	100
SPL 3935	17.1	0.3	0.7	0.1298	1.4638	6.8201	1.5401	0.3812	0.8237	0.83	**2095**	51	2088	28	2082	29	100
SPL 3935	16.1	0.5	0.8	0.1315	1.4449	6.9465	1.4222	0.3831	0.7987	0.99	**2118**	49	2105	26	2091	29	99
SPL 3935	89.1	0.0	1.6	0.1337	2.3934	7.1587	2.6436	0.3883	1.2363	0.77	**2147**	82	2131	46	2115	45	99
SPL 3935	21.1	28.0	0.3	0.0587	1.3629	0.3066	1.8136	0.0379	0.8712	0.98	556	61	272	8	240	4	49
SPL 3935	3.1	27.9	0.8	0.0585	1.7094	0.3098	2.2242	0.0384	0.8331	0.99	549	68	274	10	243	4	50
SPL 3935	9.1	18.5	0.1	0.0619	1.2924	0.3525	2.3289	0.0413	1.2579	0.99	669	56	307	11	261	6	46
SPL 3935	1.1	7.7	1.1	0.0633	1.7378	0.6729	2.3363	0.0772	0.8814	0.98	717	72	523	18	479	8	73
SPL 3935	64.1	0.0	1.2	0.0618	3.7217	0.7755	3.6662	0.0910	1.0215	0.86	666	160	583	33	562	11	87
SPL 3935	76.1	0.0	0.6	0.0624	2.0833	0.8049	2.2201	0.0936	0.5558	0.44	688	90	600	20	577	6	87
SPL 3935	95.1	0.1	3.7	0.062	2.7419	0.8018	2.8634	0.0939	1.2892	0.74	673	120	598	26	578	14	89
SPL 3935	47.1	0.0	0.4	0.0617	2.1070	0.8018	2.0330	0.0943	0.8697	0.96	663	89	598	18	581	10	90
SPL 3935	88.1	0.2	1.0	0.0618	6.3107	0.8081	6.1951	0.0948	1.4448	0.43	668	277	601	57	584	16	90
SPL 3935	33.1	0.0	0.5	0.0622	2.4116	0.8134	2.4034	0.0949	0.7061	0.83	680	102	604	22	584	8	89
SPL 3935	46.1	0.0	0.7	0.0643	4.5101	0.8452	4.1871	0.0954	1.4362	0.52	750	176	622	38	587	16	83
SPL 3935	41.1	1.3	0.9	0.0627	3.0303	0.8295	3.2850	0.0959	0.5421	0.48	699	123	613	28	591	6	88
SPL 3935	13.1	0.0	0.3	0.0645	2.4806	0.8558	2.6618	0.0962	0.9565	0.90	759	105	628	24	592	11	83
SPL 3935	74.1	0.0	0.5	0.0613	2.4470	0.8256	2.4952	0.0977	0.6554	0.98	651	102	611	23	601	8	94

SPL 3935	78.1	0.7	0.5	0.0623	2.0867	0.8396	2.2820	0.0978	1.0938	0.66	683	88	619	21	602	13	91
SPL 3935	72.1	15.7	0.6	0.0567	7.2310	0.7659	7.5310	0.0981	0.9689	0.80	478	274	577	66	603	11	121
SPL 3935	34.1	0.0	1.3	0.0655	3.2061	0.8876	2.7806	0.0982	0.9977	0.37	792	137	645	27	604	11	82
SPL 3935	2.1	0.0	1.4	0.0711	4.0788	0.9631	4.4616	0.0983	1.0885	0.56	959	171	685	44	605	12	71
SPL 3935	67.1	1.1	1.7	0.0618	2.7508	0.8431	2.7294	0.0990	0.8789	0.79	666	125	621	26	609	10	93
SPL 3935	19.1	2.1	0.6	0.0634	1.5773	0.8683	1.5940	0.0994	0.7548	0.99	721	65	635	16	611	9	88
SPL 3935	65.1	26.7	0.8	0.0656	2.8963	0.9014	2.7634	0.0997	0.8124	0.54	793	116	653	26	613	10	82
SPL 3935	83.1	0.0	1.4	0.0629	5.7234	0.8650	5.3329	0.0998	1.0923	0.34	704	242	633	52	613	13	90
SPL 3935	92.1	0.0	1.1	0.0645	13.0233	0.8931	12.2024	0.1004	2.3402	0.45	758	528	648	118	617	28	85
SPL 3935	43.1	0.0	0.9	0.0587	3.0664	0.8192	2.9163	0.1012	1.0967	0.60	556	128	608	26	622	13	109
SPL 3935	32.1	3.0	1.0	0.0626	2.2364	0.8765	2.2796	0.1015	0.6504	0.93	696	94	639	21	623	8	92
SPL 3935	36.1	0.0	0.5	0.0645	2.7907	0.9098	2.7281	0.1022	0.6162	0.61	759	114	657	26	628	7	87
SPL 3935	45.1	14.6	0.7	0.0649	4.1602	0.9180	3.9018	0.1025	1.6288	0.67	772	162	661	36	629	19	86
SPL 3935	26.1	0.0	0.6	0.0769	3.7711	1.1131	4.0473	0.1050	1.0763	0.56	1118	146	760	43	644	13	68
SPL 3935	12.1	0.0	0.8	0.0629	2.0668	0.9196	2.2683	0.1061	0.9614	0.93	704	90	662	22	650	12	94
SPL 3935	25.1	0.0	1.4	0.0646	1.5480	1.0017	2.0975	0.1125	1.2262	0.67	760	64	705	21	688	16	93
SPL 3935	55.1	0.0	0.7	0.0656	2.4390	1.0372	2.3042	0.1147	0.9769	0.77	794	103	723	23	700	13	91
SPL 3935	7.1	3.4	0.9	0.0743	6.5949	1.2340	6.5242	0.1205	1.5266	0.55	1048	259	816	72	734	21	78
SPL 3935	38.1	3.7	0.6	0.0669	2.2422	1.1492	2.3381	0.1245	0.5300	0.93	836	95	777	25	757	8	93
SPL 3935	80.1	0.0	0.5	0.0669	1.7937	1.1693	1.8516	0.1268	0.8360	0.87	834	73	786	20	770	12	94
SPL 3935	23.1	0.0	0.4	0.0672	2.2321	1.1887	2.8855	0.1284	1.3320	0.66	843	90	795	31	779	19	94
SPL 3935	49.1	0.0	1.1	0.0677	2.6588	1.2057	2.1307	0.1291	1.1308	0.45	860	103	803	24	783	17	93
SPL 3935	15.1	0.0	0.8	0.0737	4.4776	1.3262	4.1488	0.1305	1.2799	0.65	1034	169	857	48	791	19	83
SPL 3935	28.1	11.4	1.3	0.0953	1.6789	1.9089	2.0016	0.1453	0.7160	0.89	1534	59	1084	27	874	12	71
SPL 3935	59.1	3.7	1.2	0.1241	1.4504	3.7929	2.0673	0.2218	0.8568	0.99	2015	51	1591	27	1291	20	79
SPL 3935	90.1	3.2	0.5	0.1246	2.0064	5.0870	2.0116	0.2961	0.9557	0.99	2023	74	1834	35	1672	28	91
SPL 3935	18.1	0.0	1.5	0.1155	1.4719	5.1188	1.6750	0.3214	0.8774	0.97	1888	52	1839	29	1797	28	97
SPL 3935	22.1	0.4	1.3	0.1099	1.2739	5.1173	1.3685	0.3378	0.8674	0.97	1797	47	1839	25	1876	28	102

Table S4G. Results of U-Pb isotope analysis by LA-ICP-MS on zircon from phyllite sample GAR-15-0. Data in bold print were used in provenance diagrams. Data in red were excluded, as concordance values were > 105 % or < 95%. (*) Data are grouped according to $^{206}Pb/^{208}U$ apparent ages. *% Conc: concordance.

Identifier	Spot number	f 206c (%)	Th/U	Ratio						rho	Apparent Ages (Ma)						*% Conc
				$^{207}Pb/^{206}Pb$	1σ (%)	$^{207}Pb/^{235}U$	1σ (%)	$^{206}Pb/^{238}U$	1σ (%)		$^{207}Pb/^{206}Pb$	2σ (abs)	$^{207}Pb/^{235}U$	2σ (abs)	$^{206}Pb/^{238}U$	2σ (abs)	
GAR-15-0 - phyllite																	
SPL 3933	12.1	0.0	0.9	0.0605	2.8099	0.8068	3.0800	0.0968	1.1266	0.70	621	120	601	28	**595**	13	101
SPL 3933	3.1	0.3	0.9	0.0623	2.4077	0.8325	2.5033	0.0969	1.1766	0.86	685	101	615	23	**596**	13	103
SPL 3933	1.1	1.2	0.5	0.0597	1.5075	0.8144	1.5349	0.0990	0.8181	0.92	591	65	605	14	**609**	10	99
SPL 3933	11.1	3.3	0.7	0.0609	4.2693	0.8608	4.6540	0.1026	1.0722	0.31	634	180	631	44	**630**	13	100
SPL 3933	19.1	6.3	0.4	0.0631	1.7433	0.8953	1.9179	0.1030	1.2819	0.98	710	71	649	16	**632**	15	103
SPL 3933	10.1	0.0	0.0	0.0606	1.9802	0.8783	2.4025	0.1051	0.9422	0.94	626	85	640	23	**644**	11	99
SPL 3933	23.1	2.1	2.4	0.0636	2.6730	0.9397	3.0393	0.1072	1.5860	0.54	728	97	673	22	**656**	19	102
SPL 3933	14.1	0.1	0.7	0.0686	2.0408	1.1940	2.3651	0.1263	1.1084	0.98	886	84	798	26	**767**	16	104
SPL 3933	29.1	6.8	0.5	0.0689	2.4673	1.2250	2.1168	0.1290	0.9149	0.20	895	107	812	27	**782**	14	104
SPL 3933	7.1	0.0	1.0	0.0692	4.1908	1.2573	4.0888	0.1319	1.7896	0.82	903	167	827	44	**799**	27	104
SPL 3933	30.1	0.8	0.5	0.0680	2.3529	1.2366	3.0794	0.1320	1.0834	0.64	867	93	817	31	**799**	16	102
SPL 3933	24.1	2.4	0.9	0.0681	2.2026	1.2779	2.4188	0.1361	1.0654	0.96	872	94	836	28	**823**	16	102
SPL 3933	13.1	0.1	1.0	0.0661	1.3616	1.2605	1.9992	0.1382	1.0273	0.84	811	57	828	22	**835**	16	99
SPL 3933	20.1	2.0	0.2	0.0683	1.6105	1.3485	1.4935	0.1432	0.9920	0.06	878	70	867	17	**862**	16	101
SPL 3933	8.1	3.4	1.0	0.0723	2.7663	1.4503	3.1470	0.1456	0.9413	0.92	993	118	910	38	**876**	16	104
SPL 3933	31.1	0.0	0.9	0.0820	2.0732	2.3927	2.4847	0.2117	1.0017	0.90	**1245**	81	1240	36	1238	23	100
SPL 3933	26.1	0.0	0.4	0.0974	2.0534	3.6448	2.5176	0.2714	1.2308	0.96	**1575**	77	1559	37	1548	34	101
SPL 3933	18.1	6.9	1.0	0.1046	1.4340	4.4091	1.3123	0.3058	0.9451	0.99	**1707**	51	1714	22	1720	29	100
SPL 3933	15.1	0.0	1.2	0.1286	1.3997	6.5438	1.8454	0.3692	1.0537	0.94	**2078**	47	2052	32	2026	37	101
SPL 3933	5.1	0.0	0.5	0.1370	1.8978	7.8082	2.0788	0.4134	1.3015	0.94	**2190**	66	2209	38	2230	49	99
SPL 3933	17.1	15.4	1.9	0.0691	1.1577	0.3127	2.5487	0.0328	1.6453	0.99	902	51	276	11	208	7	133
SPL 3933	9.1	5.4	2.5	0.0650	5.2308	0.7166	5.5218	0.0800	1.0875	0.71	773	229	549	47	496	10	111
SPL 3933	34.1	0.0	0.7	0.0651	4.1475	0.8600	4.3594	0.0958	1.3886	0.41	778	186	630	41	590	16	107
SPL 3933	6.1	0.0	0.6	0.0644	2.7950	0.8659	2.9024	0.0975	1.2817	0.39	754	121	633	28	600	15	106
SPL 3933	25.1	0.5	0.8	0.0668	5.8383	0.9212	5.7824	0.1000	2.0504	0.55	832	246	663	55	614	24	108
SPL 3933	4.1	0.0	1.0	0.0671	3.8748	0.9645	3.9628	0.1043	1.4572	0.15	840	167	686	40	640	18	107
SPL 3933	32.1	2.8	0.1	0.0751	3.4621	1.2298	3.5704	0.1188	1.1537	0.86	1072	110	814	35	723	16	113
SPL 3933	2.1	0.5	0.5	0.0777	1.4157	2.3934	1.5380	0.2233	0.7925	0.96	1140	52	1241	21	1300	19	95
SPL 3933	16.1	0.9	0.4	0.0931	1.8260	2.9773	1.8856	0.2319	0.8884	0.99	1490	86	1402	31	1344	22	104
SPL 3933	27.1	2.2	0.9	0.1192	1.8456	4.4967	2.1178	0.2737	0.9427	0.98	1944	66	1730	36	1560	26	111
SPL 3933	22.1	8.7	0.8	0.1438	21.5577	5.9819	15.6126	0.3017	3.3147	0.69	2274	341	1973	284	1700	281	116

SPL 3933	21.1	0.0	0.3	0.2293	37.9852	9.7723	67.6075	0.3091	19.3699	0.22	3047	1177	2414	1662	1737	841	139
SPL 3933	28.1	0.2	0.8	0.1445	1.5917	7.6414	1.9082	0.3836	0.9412	0.98	2282	55	2190	34	2093	33	105
SPL 3933	33.1	0.0	1.8	0.1289	2.0946	7.3505	2.5370	0.4137	1.0563	0.99	2083	73	2155	46	2232	40	97

Table S4H. Results of U-Pb isotope analysis by LA-ICP-MS on zircon from metasandstone sample GAR-15-G10. Data in bold print were used in provenance diagrams. Data in red were excluded, as concordance values were > 105 % or < 95%. (*) Data are grouped according to $^{206}Pb/^{208}U$ apparent ages. *% Conc: concordance.

Identifier	Spot number	f 206c (%)	Th/U	Ratio						rho	Apparent Ages (Ma)						*% Conc
				$^{207}Pb/^{206}Pb$	1σ (%)	$^{207}Pb/^{235}U$	1σ (%)	$^{206}Pb/^{238}U$	1σ (%)		$^{207}Pb/^{206}Pb$	2σ (abs)	$^{207}Pb/^{235}U$	2σ (abs)	$^{206}Pb/^{238}U$	2σ (abs)	
GAR-15-G10 - metasandstone																	
SPL 3932	100.1	1.2	3.0	0.0610	9.1803	0.6946	8.7968	0.0826	2.5070	0.76	640	337	536	63	**511**	24	105
SPL 3932	38.1	0.5	0.4	0.0605	3.4711	0.7141	3.7265	0.0856	1.1103	0.46	623	149	547	31	**529**	11	103
SPL 3932	24.1	0.0	0.4	0.0605	2.8099	0.7322	2.9898	0.0877	0.8551	0.67	623	123	558	26	**542**	9	103
SPL 3932	72.1	0.0	0.7	0.0610	4.0984	0.7565	4.4639	0.0900	1.0224	0.68	639	175	572	38	**555**	11	103
SPL 3932	1.1	0.0	0.8	0.0605	2.6446	0.7521	3.0077	0.0901	1.0211	0.50	623	114	569	26	**556**	11	102
SPL 3932	85.1	2.6	0.7	0.0577	2.7730	0.7232	4.3461	0.0910	1.6163	0.99	517	96	553	28	**561**	17	98
SPL 3932	73.1	0.6	1.4	0.0591	2.3689	0.7521	2.4131	0.0923	1.1164	0.78	572	102	570	21	**569**	12	100
SPL 3932	30.1	0.6	0.7	0.0619	2.9079	0.8168	2.6113	0.0957	0.8880	0.80	670	125	606	24	**589**	10	103
SPL 3932	66.1	0.8	0.9	0.0607	2.1417	0.8102	2.3365	0.0968	0.8881	0.95	628	90	603	21	**596**	10	101
SPL 3932	78.1	1.2	1.1	0.0599	3.1720	0.8021	3.2476	0.0972	0.7308	0.76	599	139	598	29	**598**	8	100
SPL 3932	6.1	1.0	0.9	0.0633	2.8436	0.8572	3.4147	0.0982	1.0794	0.86	719	119	629	31	**604**	12	104
SPL 3932	28.1	0.0	1.1	0.0629	2.7027	0.8671	2.5614	0.1001	0.8195	0.78	703	116	634	24	**615**	10	103
SPL 3932	68.1	0.0	0.7	0.0638	2.8213	0.8855	2.8469	0.1007	0.9927	0.84	734	117	644	27	**619**	12	104
SPL 3932	51.1	0.0	1.2	0.0627	1.7544	0.8725	2.1846	0.1009	0.9114	0.98	698	74	637	20	**620**	11	103
SPL 3932	47.1	0.1	0.2	0.0627	1.9139	0.8774	1.7643	0.1015	0.8667	0.93	697	84	640	17	**623**	10	103
SPL 3932	69.1	5.5	1.4	0.0617	3.5656	0.8697	3.3207	0.1023	1.3591	0.87	663	147	635	31	**628**	16	101
SPL 3932	18.1	13.0	0.5	0.0619	3.3926	0.8823	3.4535	0.1034	1.0836	0.75	671	138	642	32	**634**	13	101
SPL 3932	20.1	1.2	0.6	0.0631	2.2187	0.8998	2.3595	0.1034	0.8125	0.62	712	97	652	23	**634**	10	103
SPL 3932	8.1	1.3	0.2	0.0619	3.0695	0.8883	3.2624	0.1040	1.2882	0.84	672	129	646	31	**638**	16	101
SPL 3932	16.1	1.0	0.6	0.0627	2.3923	0.8993	2.3662	0.1041	0.9031	0.55	697	99	651	23	**638**	11	102
SPL 3932	48.1	0.0	0.9	0.0633	3.0016	0.9090	2.7062	0.1041	1.0857	0.79	720	127	657	26	**638**	13	103
SPL 3932	59.1	0.9	2.1	0.0618	3.7217	0.8909	3.3526	0.1045	1.0523	0.85	668	148	647	33	**641**	13	101
SPL 3932	94.1	0.7	0.9	0.0660	2.7273	0.9730	2.6577	0.1070	1.4211	0.98	806	124	690	27	**655**	18	105
SPL 3932	96.1	0.5	0.1	0.0624	1.6026	0.9431	1.6764	0.1095	0.8581	0.99	689	72	675	17	**670**	11	101
SPL 3932	43.1	0.4	0.3	0.0609	2.2989	0.9242	2.1305	0.1101	0.8994	0.66	636	102	665	21	**673**	11	99
SPL 3932	82.1	0.8	1.0	0.0641	2.4961	0.9778	3.0631	0.1107	0.6777	0.99	744	101	693	28	**677**	9	102
SPL 3932	31.1	0.2	1.0	0.0620	2.7419	0.9555	2.5872	0.1118	0.7959	0.97	673	117	681	26	**683**	10	100
SPL 3932	83.1	0.2	1.0	0.0630	2.5397	1.0216	2.5950	0.1176	0.6547	0.95	708	103	715	26	**717**	9	100
SPL 3932	15.1	28.5	0.9	0.0627	2.3923	1.0378	2.1854	0.1200	0.8501	0.58	699	102	723	23	**731**	12	99
SPL 3932	65.1	0.0	0.4	0.0640	2.0313	1.0618	1.9345	0.1203	0.9141	0.97	741	84	735	21	**733**	13	100
SPL 3932	63.1	0.0	0.2	0.0665	2.2556	1.1143	2.2355	0.1215	0.9713	0.90	823	92	760	24	**739**	14	103
SPL 3932	14.1	0.0	0.3	0.0665	3.3083	1.1174	3.5082	0.1218	1.0428	0.81	824	145	762	37	**741**	15	103

SPL 3932	7.1	0.0	0.8	0.0638	2.6646	1.0721	2.6629	0.1218	1.2723	0.82	736	110	740	29	**741**	18	100
SPL 3932	12.1	0.2	0.8	0.0658	2.7356	1.1084	2.9693	0.1221	1.1628	0.89	801	113	757	32	**743**	16	102
SPL 3932	34.1	2.0	0.7	0.0673	1.6345	1.1334	1.6888	0.1221	0.9008	0.99	847	67	769	18	**743**	13	104
SPL 3932	54.1	0.0	0.3	0.0672	3.1250	1.1507	3.3726	0.1242	1.1190	0.48	844	130	778	37	**755**	16	103
SPL 3932	92.1	0.0	0.5	0.0662	2.5680	1.1361	2.3413	0.1245	1.4780	0.54	812	105	771	25	**756**	21	102
SPL 3932	17.1	0.2	0.7	0.0662	2.5680	1.1503	2.6063	0.1261	0.8647	0.80	812	108	777	28	**765**	12	102
SPL 3932	3.1	0.6	0.2	0.0664	2.8614	1.1557	3.2983	0.1263	0.9974	0.56	818	121	780	36	**767**	14	102
SPL 3932	5.1	0.4	0.6	0.0665	3.0075	1.1637	3.2302	0.1270	1.0788	0.95	821	130	784	35	**771**	16	102
SPL 3932	13.1	3.2	0.3	0.0652	2.6074	1.1482	2.9846	0.1277	1.1279	0.78	782	110	776	32	**775**	16	100
SPL 3932	37.1	0.0	0.1	0.0680	2.0588	1.1983	2.3400	0.1279	0.8601	0.98	867	86	800	26	**776**	13	103
SPL 3932	86.1	0.6	0.5	0.0660	2.1212	1.1738	2.4025	0.1290	1.0619	0.98	806	88	788	26	**782**	16	101
SPL 3932	91.1	3.2	0.5	0.0668	2.6946	1.1972	2.2226	0.1301	1.5378	0.63	830	105	799	24	**788**	23	101
SPL 3932	10.1	19.5	0.5	0.0667	2.5487	1.1999	2.7861	0.1305	1.1112	0.87	828	104	801	31	**791**	17	101
SPL 3932	70.1	0.5	0.3	0.0663	3.0166	1.1946	3.1191	0.1308	1.2082	0.66	814	129	798	35	**792**	18	101
SPL 3932	2.1	0.2	0.4	0.0662	2.7190	1.1982	3.2147	0.1312	1.0593	0.62	814	111	800	35	**795**	16	101
SPL 3932	9.1	0.0	0.3	0.0655	2.7481	1.1867	3.3235	0.1314	1.3095	0.99	791	105	794	34	**796**	19	100
SPL 3932	93.1	0.0	0.6	0.0673	2.2288	1.2601	2.0228	0.1358	1.3329	0.94	847	89	828	23	**821**	20	101
SPL 3932	40.1	2.7	1.0	0.0695	3.1655	1.3038	3.4508	0.1360	1.2280	0.61	915	131	847	39	**822**	19	103
SPL 3932	29.1	0.0	1.2	0.0687	4.2213	1.2966	4.0985	0.1369	0.8550	0.75	890	170	844	45	**827**	13	102
SPL 3932	58.1	0.0	0.6	0.0702	2.8490	1.3308	2.9081	0.1375	1.1564	0.95	934	114	859	34	**831**	18	103
SPL 3932	53.1	0.0	0.2	0.0669	2.8401	1.2775	2.8618	0.1384	1.0836	0.93	836	115	836	34	**836**	17	100
SPL 3932	49.1	0.5	1.2	0.0664	2.8614	1.2922	3.4112	0.1412	1.1050	0.78	819	119	842	36	**851**	17	99
SPL 3932	99.1	0.6	0.7	0.0678	3.9823	1.3985	3.1341	0.1496	1.3702	0.99	862	149	888	37	**899**	23	99
SPL 3932	97.1	0.2	0.3	0.0823	1.7011	2.2245	1.7802	0.1960	0.9644	0.99	**1253**	67	1189	26	1154	20	103
SPL 3932	55.1	0.6	0.5	0.0836	2.5120	2.3944	2.7164	0.2076	1.1511	0.93	**1284**	99	1241	39	1216	25	102
SPL 3932	79.1	0.0	0.5	0.0809	2.9666	2.3314	3.0646	0.2089	0.9381	0.59	**1220**	113	1222	43	1223	21	100
SPL 3932	74.1	26.6	0.9	0.0836	3.7081	2.4246	3.3973	0.2103	1.2932	0.86	**1283**	132	1250	43	1231	29	102
SPL 3932	62.1	0.0	0.2	0.0925	1.9459	3.0979	2.0772	0.2429	1.1156	0.99	**1478**	77	1432	33	1402	28	102
SPL 3932	89.1	0.0	0.3	0.0894	1.7897	3.0095	1.9903	0.2441	1.0568	0.96	**1413**	68	1410	30	1408	27	100
SPL 3932	4.1	0.0	0.6	0.0974	2.3614	3.5759	2.6978	0.2662	0.9993	0.99	**1576**	89	1544	44	1521	27	101
SPL 3932	52.1	0.1	0.4	0.0958	1.4614	3.5462	1.6353	0.2685	0.7113	0.99	**1543**	57	1538	29	1533	20	100
SPL 3932	80.1	0.0	0.7	0.1271	1.4162	6.3929	1.6287	0.3648	0.5949	0.98	**2058**	51	2031	29	2005	21	101
SPL 3932	39.1	0.1	0.7	0.1245	1.8474	6.3093	1.9614	0.3674	0.8001	0.99	**2022**	64	2020	37	2017	28	100
SPL 3932	50.1	0.0	0.8	0.1295	1.6988	6.6687	2.0626	0.3736	1.0439	0.89	**2091**	61	2069	37	2046	37	101
SPL 3932	81.1	0.0	0.7	0.1280	1.6406	6.6120	1.7657	0.3747	0.6565	0.99	**2070**	57	2061	31	2052	23	100
SPL 3932	41.1	0.0	0.6	0.1293	1.9335	6.7899	2.3569	0.3807	1.0034	0.99	**2089**	69	2084	41	2080	35	100
SPL 3932	11.1	0.0	1.2	0.1338	1.9432	7.2574	2.2795	0.3933	1.1162	0.85	**2149**	68	2144	41	2138	41	100
SPL 3932	71.1	0.0	0.8	0.1954	1.7400	14.5548	1.9059	0.5402	1.0403	0.97	**2788**	57	2787	36	2784	47	100
SPL 3932	26.1	3.3	2.1	0.0642	2.4922	0.7922	2.2458	0.0895	0.8153	0.99	747	103	592	20	553	9	107
SPL 3932	98.1	16.5	0.6	0.0649	10.6317	0.8365	8.4959	0.0935	2.8773	0.01	771	436	617	79	576	32	107
SPL 3932	90.1	3.4	0.9	0.0547	3.4735	0.7220	3.5650	0.0957	1.4422	0.97	401	123	552	27	589	16	94

SPL 3932	36.1	3.7	0.9	0.0651	1.5361	0.8706	1.8182	0.0970	0.9180	0.98	779	68	636	17	597	10	107
SPL 3932	88.1	1.7	0.8	0.0649	3.0817	0.8831	3.5510	0.0986	1.4194	0.98	773	124	643	31	606	16	106
SPL 3932	95.1	0.0	1.4	0.0655	7.0229	0.9033	7.0364	0.1001	1.4787	0.51	789	282	654	66	615	17	106
SPL 3932	67.1	0.0	0.1	0.0668	3.4431	0.9977	3.9370	0.1083	1.0616	0.94	832	143	703	37	663	13	106
SPL 3932	22.1	0.0	0.7	0.0700	2.4286	1.2113	2.4386	0.1255	0.9081	0.94	928	101	806	26	762	13	106
SPL 3932	57.1	2.0	0.7	0.0925	2.8108	1.7147	4.1645	0.1345	1.4797	0.99	1477	87	1014	39	813	22	125
SPL 3932	84.1	0.0	0.7	0.0958	2.2965	2.1781	5.6755	0.1648	2.3902	0.99	1545	61	1174	33	984	37	119
SPL 3932	23.1	0.0	0.6	0.0954	1.9916	2.4212	2.0668	0.1841	0.7332	0.98	1535	75	1249	30	1090	15	115
SPL 3932	75.1	0.0	0.4	0.1101	2.1798	3.3242	1.7607	0.2190	1.3286	0.99	1801	79	1487	28	1277	31	116
SPL 3932	32.1	38.4	0.9	0.1139	1.4925	3.5552	1.4649	0.2264	0.9320	0.58	1862	56	1540	26	1316	22	117
SPL 3932	42.1	2.4	0.2	0.1205	1.9087	4.3854	2.2479	0.2639	0.8601	0.99	1964	69	1710	38	1510	23	113
SPL 3932	56.1	0.4	0.5	0.1200	2.2500	4.4482	2.7085	0.2689	1.1531	0.99	1956	79	1721	42	1535	31	112
SPL 3932	87.1	0.7	0.4	0.1038	1.6378	3.9017	1.6859	0.2727	0.9168	0.99	1693	65	1614	28	1554	25	104
SPL 3932	35.1	0.0	0.6	0.1115	1.7040	4.4359	1.8497	0.2885	0.9013	0.99	1824	66	1719	32	1634	27	105
SPL 3932	25.1	0.2	0.9	0.1149	1.7406	4.9137	1.8100	0.3102	0.7834	0.99	1878	61	1805	30	1742	24	104
SPL 3932	27.1	0.8	0.8	0.1265	1.9763	5.5202	1.5829	0.3166	0.7170	0.99	2049	73	1904	30	1773	22	107
SPL 3932	46.1	0.0	0.8	0.1268	1.5773	5.5840	1.4396	0.3193	0.8863	0.93	2055	57	1914	25	1786	28	107
SPL 3932	76.1	0.2	0.7	0.1245	1.7671	5.5970	1.4040	0.3261	1.1499	0.97	2021	63	1916	25	1820	37	105
SPL 3932	19.1	0.2	0.4	0.1223	2.0442	5.6277	1.9642	0.3339	0.8327	0.97	1990	72	1920	36	1857	27	103
SPL 3932	64.1	1.3	0.6	0.1391	1.7973	6.4423	1.8928	0.3359	0.8931	0.99	2216	59	2038	31	1867	29	109
SPL 3932	44.1	0.6	0.8	0.1303	1.4582	6.2345	1.4500	0.3471	0.8325	0.99	2101	51	2009	24	1921	27	105
SPL 3932	21.1	0.2	1.0	0.1141	1.8405	5.9610	1.8593	0.3790	0.7335	0.99	1865	68	1970	34	2072	26	95
SPL 3932	33.1	3.8	0.6	0.1828	1.3676	10.4254	1.6666	0.4136	0.9840	0.99	2679	44	2473	29	2231	36	111
SPL 3932	77.1	21.3	1.1	0.2042	1.7630	11.6499	1.3556	0.4138	1.1381	0.86	2860	58	2577	27	2232	43	115
SPL 3932	61.1	0.0	0.3	0.1679	1.5485	10.2174	1.5843	0.4413	1.0470	0.99	2537	56	2455	32	2356	41	104
SPL 3932	60.1	0.0	0.4	0.1693	1.8311	10.5241	1.7987	0.4507	1.1004	0.99	2551	61	2482	34	2399	44	103
SPL 3932	45.1	0.1	1.3	0.1950	1.4872	12.5073	1.3908	0.4652	0.8427	0.98	2785	49	2643	26	2462	35	107

Table S4 I Results of U-Pb isotope analysis by LA-ICP-MS on zircon from siltstone sample CA-22. Data in bold print were used in provenance diagrams. Data in red were excluded, as concordance values were > 105 % or < 95%. (*) Data are grouped according to $^{206}Pb/^{208}U$ apparent ages. *% Conc: concordance.

Identifier	Spot number	f 206c (%)	Th/U	Ratio						rho	Apparent Ages (Ma)						*% Conc
				$^{207}Pb/^{206}Pb$	1σ (%)	$^{207}Pb/^{235}U$	1σ (%)	$^{206}Pb/^{238}U$	1σ (%)		$^{207}Pb/^{206}Pb$	2σ (abs)	$^{207}Pb/^{235}U$	2σ (abs)	$^{206}Pb/^{238}U$	2σ (abs)	
CA-22 - siltstone																	
SPL 3934	91.1	6.0	1.2	0.0608	2.4671	0.6754	2.7540	0.0806	0.8437	0.76	631	108	524	22	**500**	8	105
SPL 3934	43.1	3.8	1.1	0.0606	1.9802	0.7115	1.8552	0.0852	0.5755	0.99	625	78	546	16	**527**	6	104
SPL 3934	61.1	0.9	0.5	0.0614	1.9544	0.7326	2.2249	0.0866	0.7278	0.56	653	88	558	19	**535**	8	104
SPL 3934	73.1	28.8	1.2	0.0608	1.4803	0.7291	1.4552	0.0870	0.6899	0.49	632	66	556	13	**538**	7	103
SPL 3934	5.1	0.0	1.9	0.0629	2.7027	0.7802	3.3541	0.0900	1.6557	0.91	704	112	586	31	**556**	18	105
SPL 3934	49.1	0.9	0.5	0.0591	1.6920	0.7402	1.9899	0.0909	0.8472	0.95	570	76	563	17	**561**	9	100
SPL 3934	65.1	5.5	0.9	0.0612	1.9608	0.7672	2.3358	0.0910	0.8795	0.97	645	82	578	19	**561**	9	103
SPL 3934	47.1	1.7	1.1	0.0628	2.8662	0.7890	2.9063	0.0911	0.7575	0.87	702	121	591	26	**562**	8	105
SPL 3934	33.1	1.3	0.6	0.0622	1.9293	0.7822	2.1159	0.0912	0.7567	0.96	682	78	587	19	**563**	8	104
SPL 3934	74.1	5.4	1.2	0.0600	5.8333	0.7857	5.5312	0.0950	1.0950	0.02	604	251	589	50	**585**	12	101
SPL 3934	78.1	0.7	1.9	0.0612	1.3072	0.8055	1.6213	0.0955	0.8483	0.96	646	56	600	15	**588**	10	102
SPL 3934	32.1	0.0	0.6	0.0633	2.6856	0.8345	2.7549	0.0956	0.7953	0.82	720	113	616	25	**588**	9	105
SPL 3934	79.1	0.0	1.4	0.0616	1.9481	0.8158	2.3058	0.0961	0.9781	0.86	659	82	606	21	**592**	11	102
SPL 3934	45.1	1.6	0.3	0.0592	1.6892	0.7896	1.8097	0.0967	0.6207	0.96	576	75	591	16	**595**	7	99
SPL 3934	94.1	0.1	1.4	0.0633	2.6856	0.8457	3.1298	0.0969	1.0626	0.90	718	115	622	29	**596**	12	104
SPL 3934	42.1	0.0	1.0	0.0623	3.0498	0.8327	3.3133	0.0969	0.7427	0.60	684	131	615	30	**597**	8	103
SPL 3934	75.1	0.9	1.0	0.0588	3.5714	0.7880	3.5887	0.0972	0.8232	0.51	560	143	590	31	**598**	9	99
SPL 3934	38.1	1.1	0.3	0.0596	1.6779	0.8038	1.7915	0.0978	0.7872	0.99	589	73	599	16	**602**	9	100
SPL 3934	44.1	0.9	0.4	0.0606	1.8152	0.8192	2.0129	0.0981	0.6625	0.99	623	79	608	18	**603**	8	101
SPL 3934	85.1	1.3	0.5	0.0634	2.9968	0.8603	3.5662	0.0984	1.7988	0.99	722	126	630	30	**605**	20	104
SPL 3934	51.1	0.0	1.5	0.0635	2.2047	0.8726	2.5006	0.0997	0.8429	0.67	725	97	637	24	**612**	10	104
SPL 3934	76.1	1.3	0.5	0.0606	1.4851	0.8351	1.7626	0.1000	0.8999	0.98	624	61	616	16	**615**	11	100
SPL 3934	63.1	1.3	0.8	0.0610	1.9672	0.8417	2.0434	0.1000	0.6699	0.99	640	81	620	19	**615**	8	101
SPL 3934	67.1	0.2	1.7	0.0631	4.1204	0.8715	3.8223	0.1002	0.7285	0.97	711	173	636	37	**616**	9	103
SPL 3934	48.1	0.0	1.1	0.0627	4.1467	0.8662	4.4399	0.1002	0.8880	0.44	697	173	634	43	**616**	10	103
SPL 3934	100.1	0.7	1.2	0.0618	1.9417	0.8591	1.9928	0.1008	0.8137	0.88	668	87	630	18	**619**	10	102
SPL 3934	29.1	1.7	0.6	0.0604	1.4901	0.8500	1.8094	0.1021	0.7642	0.93	618	65	625	17	**627**	9	100
SPL 3934	70.1	7.2	1.9	0.0633	2.8436	0.8952	3.1857	0.1025	1.1707	0.90	720	112	649	28	**629**	14	103
SPL 3934	14.1	2.7	1.0	0.0629	1.7488	0.8901	2.0145	0.1027	0.7890	0.98	704	72	646	19	**630**	9	103
SPL 3934	99.1	0.0	0.7	0.0618	1.9417	0.8838	2.0253	0.1037	0.8394	0.88	669	82	643	19	**636**	10	101
SPL 3934	26.1	0.2	0.5	0.0607	1.8122	0.8692	2.0192	0.1039	0.6255	0.89	627	79	635	19	**637**	8	100
SPL 3934	25.1	3.1	0.3	0.0606	1.9802	0.8690	1.8171	0.1040	0.5192	0.99	625	85	635	18	**638**	6	100

SPL 3934	28.1	1.2	1.3	0.0599	1.6694	0.8589	1.9432	0.1041	0.8264	0.99	599	74	630	18	**638**	10	99
SPL 3934	57.1	0.5	1.1	0.0621	1.6103	0.8953	1.8017	0.1045	0.5454	0.97	679	70	649	18	**641**	7	101
SPL 3934	66.1	3.2	0.6	0.0634	2.2082	0.9153	2.1097	0.1047	0.8021	0.94	721	97	660	21	**642**	10	103
SPL 3934	86.1	0.9	0.6	0.0607	1.1532	0.8998	1.4348	0.1075	0.7346	0.98	628	52	652	14	**659**	9	99
SPL 3934	98.1	0.4	0.9	0.0625	1.9200	0.9422	2.3678	0.1094	0.9142	0.82	690	79	674	23	**669**	12	101
SPL 3934	50.1	0.6	0.6	0.0611	1.6367	0.9269	1.6690	0.1100	0.7640	0.92	644	68	666	17	**673**	10	99
SPL 3934	22.1	3.0	0.2	0.0609	1.8062	0.9295	1.8699	0.1108	0.5147	0.99	635	78	667	20	**677**	7	99
SPL 3934	54.1	0.4	0.7	0.0684	2.4854	1.1189	2.8645	0.1187	0.9014	0.94	880	105	762	30	**723**	12	105
SPL 3934	1.1	1.7	0.3	0.0671	1.3413	1.1247	2.0912	0.1215	1.3747	0.98	842	58	765	23	**739**	20	104
SPL 3934	36.1	3.4	0.5	0.0682	1.7595	1.1484	1.9706	0.1221	0.7862	0.96	875	75	777	22	**743**	11	105
SPL 3934	46.1	1.4	0.6	0.0650	1.6923	1.1342	1.6673	0.1266	0.6083	0.97	774	72	770	19	**768**	9	100
SPL 3934	31.1	0.5	0.1	0.0661	1.5129	1.1707	1.8801	0.1285	0.9181	0.97	809	62	787	19	**779**	13	101
SPL 3934	58.1	0.0	0.6	0.0664	3.9157	1.1800	3.6365	0.1288	1.0248	0.82	820	161	791	42	**781**	15	101
SPL 3934	11.1	1.6	0.4	0.0659	1.6692	1.1816	1.8679	0.1300	0.7230	0.96	804	70	792	21	**788**	11	101
SPL 3934	80.1	0.0	0.3	0.0658	1.3678	1.1974	1.8482	0.1319	0.9099	0.98	802	57	799	20	**799**	14	100
SPL 3934	52.1	0.6	0.8	0.0661	1.8154	1.2236	1.9615	0.1342	0.7599	0.96	810	73	811	22	**812**	12	100
SPL 3934	68.1	3.8	0.5	0.0648	2.1605	1.2121	1.8884	0.1357	0.7663	0.96	767	86	806	21	**820**	12	98
SPL 3934	23.1	2.2	0.9	0.0668	1.7964	1.2701	2.0141	0.1380	0.6814	0.95	831	76	832	23	**833**	11	100
SPL 3934	55.1	0.1	0.7	0.0661	1.6641	1.2858	1.9411	0.1411	0.8360	0.98	809	69	839	22	**851**	13	99
SPL 3934	84.1	0.0	0.4	0.0661	1.5129	1.2996	1.7067	0.1427	1.3457	0.93	808	62	846	19	**860**	22	98
SPL 3934	40.1	1.6	0.5	0.0653	2.1440	1.3125	2.2537	0.1458	0.8366	0.96	783	88	851	25	**878**	14	97
SPL 3934	92.1	1.5	0.3	0.0721	1.2483	1.7016	1.6320	0.1713	0.8292	0.99	**988**	54	1009	23	1019	16	99
SPL 3934	39.1	0.1	0.8	0.0774	1.6796	1.9982	1.8932	0.1872	0.7854	0.89	**1132**	68	1115	25	1106	16	101
SPL 3934	72.1	0.0	0.2	0.0768	1.6927	2.0373	1.7813	0.1924	0.8889	0.92	**1116**	70	1128	24	1134	18	99
SPL 3934	41.1	0.1	0.3	0.0887	1.6911	2.9916	1.8579	0.2446	0.8136	0.99	**1398**	64	1406	28	1411	21	100
SPL 3934	64.1	0.0	0.9	0.1067	1.7807	4.5254	1.8803	0.3077	0.6891	0.96	**1743**	64	1736	33	1729	21	100
SPL 3934	27.1	0.3	0.3	0.1159	1.2079	5.5016	1.2936	0.3444	0.6765	0.99	**1893**	45	1901	25	1908	23	100
SPL 3934	9.1	3.0	0.8	0.1504	1.6622	9.2238	1.9066	0.4448	0.7576	0.99	**2350**	56	2361	35	2372	30	100
SPL 3934	56.1	7.6	1.3	0.0611	1.8003	0.3333	2.6970	0.0396	0.7838	0.99	644	75	292	12	250	4	117
SPL 3934	13.1	5.8	1.8	0.0611	1.9640	0.3819	2.5164	0.0453	0.8387	0.96	644	85	328	14	286	5	115
SPL 3934	19.1	3.9	2.5	0.0604	1.4901	0.4869	1.3781	0.0584	0.7871	0.99	619	62	403	9	366	6	110
SPL 3934	4.1	2.9	1.2	0.0589	1.3582	0.4906	2.6091	0.0604	1.7384	0.99	564	57	405	17	378	13	107
SPL 3934	88.1	5.0	0.4	0.0628	1.1146	0.5296	1.3218	0.0611	0.7033	0.99	702	50	432	9	383	5	113
SPL 3934	37.1	5.7	0.2	0.0679	2.5037	0.7382	3.2877	0.0789	0.9632	0.95	864	122	561	27	490	9	115
SPL 3934	89.1	28.0	1.2	0.0664	1.5060	0.7599	1.6885	0.0830	0.7350	0.98	819	68	574	15	514	7	112
SPL 3934	53.1	5.6	0.9	0.0637	2.0408	0.7339	2.1108	0.0836	0.6340	0.95	731	90	559	18	518	6	108
SPL 3934	60.1	3.2	0.7	0.0631	3.3281	0.7395	3.6175	0.0850	0.7178	0.77	712	146	562	31	526	7	107
SPL 3934	10.1	6.5	0.7	0.0671	1.9374	0.7940	2.4282	0.0859	0.8966	0.99	839	90	593	21	531	9	112
SPL 3934	93.1	3.6	0.9	0.0639	4.2254	0.7709	4.4429	0.0876	1.3135	0.75	737	198	580	40	541	14	107
SPL 3934	96.1	6.0	0.4	0.0716	1.2570	0.8656	1.4822	0.0877	0.7870	0.99	975	55	633	14	542	8	117
SPL 3934	6.1	1.2	0.4	0.0635	2.0472	0.7939	2.9966	0.0907	1.5332	0.82	725	92	593	28	559	16	106

SPL 3934	15.1	2.7	1.1	0.0657	4.8706	0.8298	4.6230	0.0916	0.8846	0.56	798	193	614	43	565	10	109
SPL 3934	90.1	0.0	1.6	0.0676	3.8462	0.8551	3.9620	0.0917	0.9815	0.74	857	162	628	38	566	11	111
SPL 3934	8.1	1.9	0.7	0.0737	2.8494	0.9341	3.0146	0.0919	0.8490	0.92	1035	156	670	33	567	9	118
SPL 3934	83.1	40.4	1.7	0.0837	3.2258	1.0851	2.9518	0.0940	1.6165	0.94	1285	122	746	31	579	18	129
SPL 3934	82.1	1.2	1.3	0.0652	7.0552	0.8533	7.4583	0.0949	1.8973	0.70	782	254	626	65	584	21	107
SPL 3934	97.1	1.1	1.8	0.0680	6.0294	0.9195	5.8500	0.0981	1.7732	0.86	867	273	662	56	604	20	110
SPL 3934	12.1	2.1	1.2	0.0741	2.8340	1.0033	2.8425	0.0982	0.8557	0.92	1045	138	706	32	604	10	117
SPL 3934	59.1	12.7	1.7	0.0687	2.6201	0.9622	2.5711	0.1016	0.6398	0.58	890	111	685	26	624	8	110
SPL 3934	87.1	53.7	0.5	0.0686	1.4577	1.0526	1.4791	0.1113	0.7729	0.74	887	68	730	16	680	10	107
SPL 3934	7.1	41.9	0.7	0.0735	4.0816	1.1556	4.1928	0.1140	0.7634	0.96	1029	156	780	45	696	10	112
SPL 3934	17.1	12.0	2.4	0.1193	1.1735	2.0385	1.7277	0.1240	1.1051	0.99	1945	41	1129	17	753	15	150
SPL 3934	35.1	2.1	0.7	0.0829	2.0507	1.7581	2.2604	0.1537	0.8326	0.86	1268	78	1030	29	922	14	112
SPL 3934	2.1	1.8	0.5	0.0967	1.3444	2.0621	2.4969	0.1547	1.6417	0.99	1561	48	1136	32	927	28	123
SPL 3934	16.1	4.2	1.0	0.1470	1.2925	3.2503	2.4062	0.1604	1.0037	0.94	2311	40	1469	20	959	16	153
SPL 3934	71.1	1.4	0.2	0.0882	1.2472	2.1563	1.2419	0.1772	0.7053	0.99	1388	50	1167	18	1052	14	111
SPL 3934	3.1	2.3	0.4	0.1049	1.3346	2.7109	3.0293	0.1874	2.0176	0.99	1713	44	1331	35	1107	39	120
SPL 3934	30.1	3.0	0.3	0.0956	1.3598	2.9768	1.6592	0.2258	0.7839	0.99	1540	52	1402	25	1312	19	107
SPL 3934	69.1	4.6	0.5	0.0993	1.2085	3.3783	1.0482	0.2468	0.6726	0.99	1611	47	1499	17	1422	17	105
SPL 3934	20.1	2.7	1.7	0.1049	1.4299	3.7446	1.2159	0.2589	0.6797	0.99	1712	52	1581	21	1484	19	107
SPL 3934	34.1	0.4	1.0	0.1062	1.7891	3.8404	1.5405	0.2622	0.6369	0.99	1736	71	1601	31	1501	18	107
SPL 3934	24.1	0.4	1.0	0.1093	1.4639	4.5114	1.5999	0.2992	0.5815	0.97	1789	55	1733	28	1688	17	103
SPL 3934	21.1	1.8	0.8	0.1203	1.1638	5.2907	1.0764	0.3191	0.6739	0.92	1960	45	1867	19	1785	21	105
SPL 3934	18.1	0.4	2.1	0.1323	1.2094	6.2552	1.1475	0.3428	0.7001	0.99	2129	42	2012	21	1900	23	106
SPL 3934	81.1	0.0	0.4	0.1444	1.5235	7.0667	1.5768	0.3550	1.3014	0.99	2280	52	2120	29	1958	44	108
SPL 3934	77.1	0.0	0.4	0.1243	1.1263	6.8862	1.4289	0.4016	0.8191	0.99	2020	42	2097	27	2177	31	96
SPL 3934	62.1	0.2	0.3	0.1245	1.6064	7.1710	1.6543	0.4179	0.6437	0.99	2021	56	2133	32	2251	25	95
SPL 3934	95.1	0.7	0.3	0.1507	1.1281	8.8954	1.6326	0.4280	0.8832	0.99	2354	38	2327	31	2297	34	101

CAPÍTULO 6
CONSIDERAÇÕES FINAIS

6 CONSIDERAÇÕES FINAIS

A partir da compilação dos dados apresentados, o presente estudo detalha a geologia e as e as litologias aflorantes no núcleo central soerguido da maior estrutura de impacto conhecida na América do Sul. Estes dados fornecem um avanço significativo na compreensão geológica tanto desta parte central como das rochas que foram produzidas e ou modificadas durante o impacto. As principais descobertas incluem o detalhamento do embasamento, reconhecimento e diferenciação de três tipos de rochas fundidas de impacto (impact melt rocks - IMR), a caracterização detalhada e proveniência das brechas polimíticas de impacto, atualização do mapa geológico do núcleo central soerguido, e a gênesis e colocação das brechas de impacto na estrutura de impacto de Araguainha.

As rochas provenientes do embasamento estão hoje bem expostas ao longo do núcleo central soerguido, principalmente na zona de megablocos definida por Lana et al. (2008). O embasamento encontra-se nas imediações diretas com o granito alcalino e também com relação de contato com as brechas polimíticas de impacto. O conjunto de rochas é exemplificado por metapelito, filito, metaritimito, metasiltito, metarenito, arenitos e pelitos. Por meio do estudo de proveniência, elas são semelhantes à sequência inferior da Bacia do Paraná e podem estar relacionadas com a sedimentação em bacias proximais ao Arco de Arenópolis.

Os estudos de campo e petrográfico permitiram o reconhecimento e distinção de três tipos de rochas fundidas pelo impacto (impact melt rocks – IMR) devido as diferentes relações de campo e composições: (1) IMR Tipo-I, de composição granítica e ocorre principalmente como veios e diques no granito alcalino do núcleo central soerguido; (2) IMR Tipo-II, ocorre em forma de clastos plasticamente deformados de composição silicosa nas brechas polimíticas de impacto; e (3) IMR Tipo-III, rochas derivadas de conglomerados parcialmente fundidos ou precursores de arenito, e que ocorre nos estratos (meta)sedimentares do embasamento nas imediações do núcleo de granito alcalino.

As brechas polimíticas de impacto são compostas por clastos dominantemente derivados das unidades basais das rochas alvo imersos em

uma matriz composta por lama arenosa. Os clastos são predominantemente sedimentares, sendo estes derivados das unidades inferiores da Bacia do Paraná (ex., Formação Furnas), e metassedimentares, derivados do embasamento metamórfico. Raras ocorrências de clastos graníticos também são observados. As brechas polimíticas de impacto são essencialmente caóticas lateralmente, mas mostram um padrão vertical ao longo do perfil integrado por meio das ocorrências dos depósitos de brechas estudados no soerguimento central (110 m de espessura). Exemplos deste padrão vertical é identificado pela concentração de clastos graníticos no topo e na base do perfil e pelos clastos plasticamente deformados que persistem do meio ao topo do perfil. Os dados de proveniência também mostram similaridade com a parte inferior da Bacia do Paraná.

Sobre a gênese e a colocação das rochas fundidas por impacto (IMR), os três tipos reconhecidos não foram formados no mesmo estágio de Crateramento. Propomos pela primeira vez que os IMR Tipos II e III foram formados durante o estágio inicial de escavação, já que as primeiras fases de fusão se formaram em Araguainha por fusão de choque (shock melting). O IMR Tipo I é interpretado aqui como um equivalente às brechas pseudotaquilíticas da estrutura de impacto de Vredefort (África do Sul), que teria sido formada por fusão de descompressão durante a elevação no estágio de modificação.

Os componentes das brechas polimíticas de impacto e a relação de contato com o embasamento (meta)sedimentar indicam/sugerem que as PIB estão assentadas diretamente acima do fundo da cratera. Não há evidências de contribuição de ejetos balísticos. Mesmo assim, os componentes da brecha permitem sugerir que as unidades inferiores da Bacia do Paraná sofreram uma grande influência de ondas de choque, principalmente da Formação Furnas, e os clastos metassedimentares podem ser autóctones. Isso representa o material de dentro do soerguimento central que se elevou, fragmentou e depois se depositou na matriz das brechas polimíticas de impacto. Nossas observações sugerem também que as PIB de Araguainha foram formadas dentro da cavidade transitória e que esse material nunca deixou a cratera.

A configuração atual dos depósitos de brecha justapostos com blocos e megablocos da estratigrafia alvo mais baixa confirma que essas brechas

representam o remanescente mais baixo do depósito de brecha original, diretamente acima (e talvez dentro) do fundo da cratera. Nossos dados também sugerem que a profundidade máxima de penetração do bólido provavelmente se deu na interface entre a sequência mais baixa da Bacia do Paraná e o embasamento pré-ordoviciano (meta)sedimentar.

Apesar das contribuições significativas deste estudo, análises de geoquímicas e isotópicas das rochas que foram produzidas e ou modificadas durante o impacto são requeridas. Essese novos dados vão permitir corroborar os dados e interpretações apresentados nesta tese, bem como aprofundar o conhecimento sobre a gênesis e colocação dos impactitos na estrutura de impacto de Araguainha.

REFERÊNCIAS

Albarède, F., Telouk, S., Blichert-Toft, J., Boyet, M., Agranier, A., and Nelson, B., 2004. Precise and accurate isotopic measurements using multiple-collector ICPMS. Geochemica et Cosmochimica Acta, 68: 2725–2744.

Almeida F.F.M. 2004. Geologia do Continente Sul Americano: Evolução da Obra de Fernando Marques de Almeida. São Paulo: Ed. Beca. 673 p.

Almeida, F. F. M. 1965. Geossinclíneo Paraguai. In *Presented at the Semana de Debates Geológicos 1*, Porto Alegre, 87-101.

Almeida, F. F. M. 1984. Província Tocantins, setor sudoeste. In *O Pré-Cambriano do Brasil*, edited by F. F. M. Almeida, and Y. Hasui, 265-281. São Paulo: Edgard Blücher Publications.

Almeida, F. F. M., and Hasui, Y. 1984. In *O Pré-cambriano do Brasil*. São Paulo: Edgard Blücher Publications, pp. 378.

Almeida, F. F. M., Hasui, Y., and Brito Neves, B. B. 1977. Províncias Estruturais brasileiras. In *Atas do VII Simpósio de Geologia do Nordeste*, Campina Grande. Sociedade Brasileira de Geologia, Brazil, 363–391.

Alvarenga, C. J. S. 1988. Turbiditos e a glaciação do final do Proterozóico Superior no Cinturão Paraguai, Mato Grosso. *Revista Brasileira de Geociências* 18: 323-327.

Alvarenga, C. J. S. 1990. Phénomènes sédimentaires, estructuraux et circulation de fluides developpés à la transition chaine-craton: exemple de la chaine Paraguai d´age protérozoique supérieur, Mato Grosso, Brésil. Tese Doutorado – Faculté des Sciences et Techniques de St. Jérôme, Universithé d´Aix-Marseille II, Marseille.

Alvarenga, C. J. S., and Saes, G. S. 1992. Estratigrafia e Sedimentologia do Proterozóico Médio e Superior na região sudeste do Cráton Amazônico. *Revista Brasileira de Geociências* 22: 493-499.

Alvarenga, C. J. S., and Trompette, R. 1992. Glacial influenced sedimentation in the uppermost Proterozoic and lower Cambrian of the Paraguay Belt (Mato Grosso, Brazil). *Palaeogeography Palaeoclimatology Palaeoecology* 92: 85–105.

Alvarenga, C. J. S., and Trompette, R. 1993. Brasiliano tectonic of the Paraguay Belt: the structural development of the Cuiabá Region. *Revista Brasileira de Geociências* 23: 18–30.

Alvarenga, C. J. S., Guimarães, E. M., Assine, M. L., Perinotto, J. A. J., and Laranjeira, N. P. F. 1998. Sequência Ordovício-Siluriana e Devoniana no flanco norte da Bacia do Paraná. *Anais da Academia Brasileira de Ciências* 70: 587–606.

Alvarenga, C. J. S., Moura, C. A. V., Gorayeb, P. S. S., and Abreu, F. A. M. 2000. Paraguay and Araguaia belts. In *Tectonic Evolution of South America*. Sociedade Brasileira de Geologia, Rio de Janeiro, 183–194.

Alvarenga, C. J. S., Santos, R. V., and Dantas, E. L. 2004. C–O–Sr isotopic stratigraphy of cap carbonates overlying Marinoan age glacial diamictites in the Paraguay Belt, Brazil. *Precambrian Research* 131: 1-21.

Alvarez, L. W., Alvarez, W., Asaro, F., and Michel, H. V. 1980. Extraterrestrial cause for the Cretaceous-Tertiary extinction. *Science* 208: 1095-1108.

Artemieva, N. A., Wünnemann, K., Krien, F., Reimold, W. U., and Stöffler, D. 2013. Ries Crater and suevite revisited – Observations and modeling Part II – Modelling. *Meteoritics and Planetary Science* 48: 590-627. https://doi.org/10.1111/maps.12085.

Assine, M. L. 1996. Aspectos da estratigrafia das sequências pré-carboníferas da Bacia do Paraná no Brasil. Ph.D thesis, São Paulo, SP, University of São Paulo, 207 p.

Assine, M. L., Soares, P. C., and Milani, E. J. 1994. Sequências tectono-sedimentares mesopaleozoicas da Bacia do Paraná, Sul do Brasil. *Revista Brasileira de Geociências* 24: 77-89.

Babinski, M., Boggiani, P. C., Trindade, R. I. F., and Fanning, C. M. 2013. Detrital zircon ages and geochronological constraints on the Neoproterozoic Puga diamictites and associated BIFs in the southern Paraguay Belt, Brazil. Gondwana Research 23: 988-997. https://doi.org/10.1016 /j.gr.2012.06.011.

Babinski, M., McGee, B., Tokashiki, C. C., Tassinari, C. C. G., Saes, G. S., and Pinho, F. E. C. 2018. Comparing two arms of an orogenic belt during Gondwana amalgamation: Age and provenance of the Cuiabá Group, northern Paraguay Belt, Brazil. *Journal of South American Earth Sciences* 85: 6-42. https://doi.org/10.1016/j.james.2018.04.009.

Bandeira, J., McGee, B., Nogueira, A. C. R., Collins, A. S., and Trindade, R. I. F. 2012. Closure of the Neoproterozoic Clymene Ocean: sedimentary and detrital zircon geochronology evidence from the siliciclastic upper Alto Paraguai Group, northern Paraguay Belt, Brazil. Gondwana Research 21(2-3): 323-340. https://doi.org/10.1016/j.gr.2011.04.006.

Batalha, R. S. 2017. Estudo de Minerais Pesados, Análise Morfológica e Datação U-Pb por ICPMS-LA de Zircão Detrítico - Proveniência dos Metassedimentos do Grupo Cuiabá, Faixa Paraguai Norte-MT. Msc Thesis, University Federal of Mato Grosso, Cuiabá.

Bertolini, G., Marques, J. C., Hartley, A. J., Basei, M. A. S., Frantz, J. C., and Santos, P. R. 2021. Determining sediment provenance history in a Gondwanan erg: Botucatu formation, Northern Paraná Basin, Brazil. *Sedimentary Geology* 417: 105883. https://doi.org/10.1016/j.sedgeo.2021.105883.

Blair, T. C., and McPherson, J. G. 1999. Grain-size and textural classification of coarse sedimentary particles. *Journal of Sedimentary Research* 69: 6–19.

Boggiani, P. C. 1997. Análise Estratigráfica da Bacia Corumbá (Neoproterozóico) - Mato Grosso do Sul. PhD Thesis, University of São Paulo, São Paulo.

Brito Neves, B. B., and Fuck, R. A. 2013. Neoproterozoic evolution of the basement of the South-American Platform. *Journal of South American Earth Sciences* 47: 72-89. http://dx.doi.org/10.1016/j.jsames.2013.04.005.

Brito Neves, B. B., Fuck, R. A., and Pimentel, M. M. 2014. The Brasiliano collage in South America: a review. *Brazilian Journal of Geology* 44(3): 493-518. http://dx.doi.org/10.5327/Z2317-4889201400030010.

Bühn, B., Pimentel, M.M., Matteini, M., and Dantas, E.L., 2009. High spatial resolution analysis of Pb and U isotopes for geochronology by laser ablation multi-collector inductively coupled plasma mass spectrometry (LA-MC-ICPMS). Annals of the Brazilian Academy of Sciences, 81, 99–114.

Burgess, S. D., Bowring, S. A., and Shen S. Z. 2014. High-precision timeline for Earth's most severe extinction. *Proceedings of the National Academy of Sciences* 111: 3316-3321.

Büttner, R., Dellino, P., La Volpe, L., Lorenz, V., and Zimanowski, B. 2002. Thermohydraulic explosions in phreatomagmatic eruptions as evidenced by the comparison between pyroclasts and products from Molten Fuel Coolant Interaction experiments. *Journal of Geophysical Research* 107(B11): 2277, https://doi.org/10.1029/2001JB000511.

Campanha, G. A. C., Boggiani, P. C., Sallun Filho, W., Sá, F. S., Zuquim, M. P. S., and Piacentini, T. 2011. The Paraguay Fold Belt in the Serra da Bodoquena and Miranda River Depression, Mato Grosso do Sul. *Revista do Instituto de Geociências* 11: 79-96.

Carneiro, J., Fuck, R.A., and Dantas, E.L, 2021, Arenópolis sequence, evolution of a marginal basin in the Neoproterozoic Goiás magmatic arc, central Brazil: Journal of South American Earth Sciences, v. 106, p. 103033. https://doi.org/10.1016/j.jsames.2020.103033.

Cavosie, A. J., Timms, N. E., Ferriere, L., and Rochette, P. 2018. FRIGN zircon – The only terrestrial high-pressure and high-temperature mineral diagnostic of shock deformation. *Geology* 46: 891-894.

Cawood, P. A., Hawkesworth, C. J., and Dhuime, B. 2012. Detrital zircon Record and tectonic setting. *Geology* 40(10): 875-878.

Claeys, P., Heuschkel, S., Lounejjeva-Baturina, E., Sanchez-Rubio, G., and Stöffler, D. 2003. The suevite of drill hole Yucatàn 6 in the Chicxulub impact crater. *Meteoritics and Planetary Science* 38: 1299-1317.

Collins, G. S., Melosh, H. J., and Osinski, G. R. 2012. The impact cratering process. *Elements* 8: 25-30. https://doi.org/10.2113/gselements.8.1.25.

Coney, L., Reimold, W. U., Gibson, R. L., Koeberl, C., and Ogilvie, P. 2010. Melt particle characteristics of the within- and out-of-crater suevites from the Bosumtwi impact structure, Ghana: Implications for crater formation. *Geological Society of America Special Papers* 465: 411-442.

Cordani, U. G., Brito Neves, B. B., Fuck, R. A., Porto, R., Filho, A. T., and Cunha, F. M. 1984. Estudo preliminar de integração do Pré-Cambriano com os eventos

tectônicos das bacias sedimentares brasileiras. PETROBRÁS (Série Ciência-Técnica-Petróleo Seção Exploração de Petróleo), Rio de Janeiro, 15: 1-70.

Cordani, U. G., Brito Neves, B. B., Fuck, R. A., Porto, R., Thomaz Filho, A., and Cunha, F. M. B. 2009. Preliminary integration study of Precambrian with tectonic events in Brazilian sedimentary basins (Republication). *Boletim de Geociências da Petrobrás* 17: 133-204.

Crósta, A. P. 1982. *Mapeamento geológico do Domo de Araguainha utilizando técnicas de sensoriamento remoto*. MSc thesis, São José dos Campos, São Paulo: Instituto Nacional de Pesquisas Espaciais.

Crósta, A. P., Gaspar, J. C., and Candia, M. A. F. 1981. Feições de metamorfismo de impacto no Domo de Araguainha. *Revista Brasileira de Geociências* 11: 139–146.

Crósta, A. P., Reimold, W. U., Vasconcelos, M. A. R., Hauser, N., Oliveira, G. J. G., Maziviero, M. V., and Góes, A. M. 2019. Impact cratering: The South American record – Part 1. *Chemie der Erde* 79: 1-61.

Crósta, A.P., 2024. Geological records of meteoritic impacts in Brazil: evolution and current knowledge. Derbyana 45: e818. https://doi.org/10.14295/derb.v45.818

Dantas, E. L., Alvarenga, C. J. S., Santos, R. V., and Pimentel, M. M. 2009. Using Nd isotopes to understand the provenance of sedimentary rocks from a continental margin to a foreland basin in the Neoproterozoic Paraguay Belt, central Brazil. *Precambrian Research* 170: 1-12. https://doi.org/10.1016/j.precamres.2008.11.005.

de Marchi, L. P., Hauser, N., Reimold, W. U., and Crósta, A. P. 2016. Geological and petrographical characterization of the polymict impact breccia of the Araguainha Dome, Brazil. *47th Lunar and Planetary Science Conference*, abstract 1120, Woodlands, Texas, pp. 1-2.

de Marchi, L.P. 2015. Caracterização litológica da brecha polimítica de impacto do Domo de Araguainha-MT. BSc thesis, Campinas, SP, Universidade Estadual de Campinas, 68 p.

de Winter, N. J., Sinnesael, M., Makarona, C., Vansteenberge, S., and Claeys, P. 2017. Trace element analyses of carbonates using portable and micro-X-ray fluorescence: Performance and optimization of measurement parameters and strategies. *Journal of Analytical Atomic Spectrometry* 32: 1211-1223. https://doi:10.1039/c6ja00361c.

Déhais, T., Chernonozhkin, S. M., Kaskes, P., de Graaff, S. J., Debaille, V., Vanhaecke, F., Claeys, P., and Goderis, S. 2022. Resolving impact volatilization and condensation from target rock mixing and hydrothermal overprinting within the Chicxulub impact structure. *Geoscience Frontiers* 13:(5) 101410 https://doi.org/10.1016/j.gsf.2022.101410.

Della Giustina, M. E. S., Pimentel, M. M., Ferreira Filho, C. F., and Holanda, M. H. B. H. 2011. Dating coeval mafic magmatism and ultrahigh temperature

metamorphism in the Anápolis Itaucú Complex, Central Brazil. *Lithos* 124: 82–201.

Deutsch, A., Buhl, D., and Langenhorst, F. 1992. On the significance of crater ages: new ages for Dellen (Sweden) and Araguainha (Brazil). *Tectonophysics* 216:205-218.

Dietz, R. S., and French, B. M. 1973. Two probable astroblemes in Brazil. *Nature* 244: 561-562.

Dressler, B. O., and Reimold, W. U. 2004. Order or chaos? Origin and mode of emplacement of breccias in floors of large impact structures. *Earth-Science Reviews* 67: 1-54.

Erickson, T. M., Timms, N. E., Kirkland, C. L., Tohver, E., Cavosie, A. J., Pearce, M., and Reddy, S. M. 2017. Shocked monazite chronometry: Integrating microstructural and in situ isotopic age data for determining precise impact ages. *Contributions of Mineralogy and Petrology* 172(11): 1-19. https://doi.org/10.1007/s00410-017-1328-2.

Feignon, J. G., Schulz, T., Ferrière, L., Goderis, S., de Graaff, S. J., Kaskes, P., Déhais, T., Claeys, P., and Koeberl, C. 2021. Search for a meteoritic component within the impact melt rocks of the Chicxulub impact structure peak ring, Mexico. *Geochimica et Cosmochimica Acta* 323: 74-101. https://doi.org/10.1016/j.gca.2022.02.006.

Fernandes, L.A., and Coimbra, A.M., 1996, A Bacia Bauru (Cretáceo Superior, Brasil): Anais da Academia Brasileira de Ciências, v. 68, no. 2, p. 195-205.

Ferrière, L., Koeberl, C., Brandstätter, F., and Mader, D. 2010. Geochemistry of basement rocks and impact breccias from the central uplift of the Bosumtwi crater, Ghana – Comparison of proximal and distal impactites. In *Large Meteorite Impacts and Planetary Evolution IV,* Edited by Gibson, R. L., and Reimold, W. U. Geological Society of America 465: 645–51. https://doi.org/10.1130/2010.2465(22).

Fischer, G., and Masero, W. 1994. Rotational properties of the magnetotelluric impedance tensor − the example of the Araguainha impact crater, Brazil. *Geophysical Journal International* 119: 548–560.

Fischer, S. 2015. Ein Beitrag über die Impaktgesteine der Araguainha Impaktstruktur (Brasilien). MSc thesis, Berlin: Freie Universität.

French, B. M. 1998. *Traces of catastrophe: A Handbook of Shock-Metamorphic Effects in Terrestrial Meteorite Impact Structures*. Houston, TX: Lunar and Planetary Institute 130 p.

Frugis, G. L., Campos Neto, M. C., Westin, A., and Fanning, C. M. 2024. New perspectives on the tectonic evolution of the eastern Paraguay Belt revealed through zircon U-Pb-Hf-O systematics of the inner units. *Precambrian Research* 411: 107529. https://doi.org/10.1016/j.precamres.2024.107529.

Gault, D. E., Quaide, W. L., and Oberbeck, V. R. 1968. Impact cratering mechanics and structures. In *Shock Metamorphism of Natural Materials*, edited by French, B. M., and Short, N. M. Mono Book Corp., Baltimore 87-99.

Geraldes, M. C., Tassinari, C. C. G., and Onoe, A. T. 2003. $^{40}Ar^{39}Ar$ metamorphic record of a collision related to the western Gondwana collage: the (541-531 Ma) Paraguay belt in the Nova Xavantina (MT) region. In *Simpósio Nacional de Estudos Tectônicos*, Búzios, Rio de Janeiro. Anais do IX SNET, pp. 54-57.

Geraldes, M. C., Tassinari, C. C. G., Babinski, M., Martinelli, C. D., Iyer, S. S., Barboza, E. S., Pinho, F. E. C., and Onoe, A. T. 2008. Isotopic evidence for the late Brasiliano (500-550 Ma) ore-forming mineralization of the Araés Gold Deposit, Brazil. *International Geology Review* 50: 177–190. https://doi.org/10.2747/0020-6814.50.2.177.

Gezatt, J. N. 2011. Proveniência de rochas sedimentares detríticas do gráben de Piranhas e comparação com a Formação Vila Maria do Siluriano da Bacia do Paraná. BSc thesis, Porto Alegre, RS, Universidade Federal do Rio Grande do Sul, 64 p.

Glass, B. P., and Simonson, B. M. 2012. Distal impact ejecta layers: spherules and more. *Elements* 8: 15-60.

Glass, B. P., and Simonson, B. M. 2013. Distal Ejecta Layers: A Record of Large Impacts in Sedimentary Deposits. Springer, Heidelberg, 71, 6pp.

Godoy, A. M., Pinho, F. E. C., Manzano, J. C., Araújo, L. M. B., Silva, J. A., and Figueiredo, M. 2010. Estudos isotópicos das rochas granitoides Neoproterozóicas da Faixa de Dobramento Paraguai. *Revista Brasileira de Geociências* 40(3): 380-391.

Godoy, A. M., Ruiz, A. S., Araújo-Ruiz, L. M. B., Manzano, J. C., Souza, M. Z. A., and Matos, J. B. 2004. Caracterização Geológica dos Granitóides Brasilianos Póstectônico da Faixa de Dobramentos Paraguai do Sudeste Mato-Grossense. In: Congresso Brasileiro de Geologia, Araxá, 42.

Godoy, A. M., Ruiz, A. S., Manzano, J. C., and Araújo-Ruiz, L. M. B. 2007. Os Granitóides Brasilianos Pós-Tectônicos da Faixa de Dobramentos Paraguai, MS e MT. *Geologia USP Série Científica*, São Paulo 7: 29-44.

Gottwald, M., Kenkmann, T., and Reimold, W. U. 2020. *Terrestrial impact structures. The TanDEM-X atlas*. Munich: Verlag Dr. Friedrich Pfeil.

Grieve, R. A. F., Ames, D. E., Morgan, J. V., and Artemieva, N. 2010. The evolution of the Onaping Formation at the Sudbury impact structure. *Meteoritics and Planetary Science* 45: 759-782.

Grieve, R. A. F., Dence, M. R., and Robertson, P. B. 1977. Cratering processes: as interpreted from the occurrences of impact melts. In *Impact and explosion cratering*, edited by Roddy, D. J., Pepin, R. O., and Merrill, R. B. New York, Pergamon Press, p. 791–814.

Grieve, R. A. F., Osinski, G. R., and Chanou, A. 2015. The suevite conundrum: A general perspective. *46th Lunar and Planetary Science Conference*, abstract 1036, Houston, Texas, pp. 1861.

Güldemeister, N., Durr, N., Wuennemann, K., and Hiermeier, S. 2013. Propagation of Impact-Induced shock Waves in Porous Sandstone Using Mesoscale Modeling. *Meteoritics and Planetary Science* 48: 115–133.

Gulick, S. P. S., Bralower, T. J., Ormö, J., Hall, B., Grice, K., Schaefer, B., Lyons, S., Freeman, K. H., Morgan, J. V., Artemieva, N., Kaskes, P., de Graaff, S. J., Whalen, M. T., Collins, G. S., Tikoo, S. M., Verhagen, C., Christeson, G. L., Claeys, P., Coolen, M. J. L., Goderis, S., Goto, K., Grieve, R. A. F., McCall, N., Osinski, G. R., Rae, A. S. P., Riller, U., Smit, J., Vajda, V., Wittmann, A., and The Expedition 364 Scientists, 2019. The first day of the Cenozoic. *Proceedings of the National Academy of Sciences* 116(39): 19342–19351.

Hammerschmidt, K., and von Engelhardt, W., 1995. Ar/Ar dating of the Araguainha impact structure, Mato Grosso, Brazil. *Meteoritics and Planetary Science* 30:227-233.

Hargitai, H., Reimold, W. U., and Bray, V. J. 2015. Impact structure. In *Encyclopedia of Planetary Landforms*, edited by Hargitai H., and Kereszturi Á., Springer, New York, 2: 988-1023. https://doi.org/10.1007/978-1-4614-3134-3.

Hasui, Y. 2012. Sistema orogênico Tocantins. In *Geologia do Brasil*, edited by Hasui, Y., Carneiro, C. D. R., Almeida, F. F. M., and Bartorelli, A. Beca, Brazil, pp. 289-325.

Hauser, N., Reimold, W. U., Cavosie, A. J., Crósta, A. P., Schwarz, W. H., Trieloff, M., Souza, C. S. M., Rodrigues, E. N., and Brown, M. 2019. Linking shock textures revealed by BSE, CL, and EBSD with U-Pb data (LA-ICP-MS and SIMS) from zircon from Araguainha impact structure, Brazil. *Meteoritics and Planetary Science* 54: 2286-2311.

Hecht L., 2022. The Formation and Emplacement of Suevite – A review of Genetic models and Unresolved issues. In Program and Abstracts, 85th Annual Meeting of The Meteoritical Society 2022, Glasgow, Scotland. LPI contribution No. 2695, p. 6434.

Henkel, H., and Reimold, W. U. 1998. Integrated geophysical modelling of a giant complex impact structure: anatomy of the Vredefort structure, South Africa. *Tectonophysics* 287: 1-20.

Henrique-Pinto, R., Basei, M. A. S., Santos, P. R., Saad, A. R., Milani, E. J., Cingolani, C. A., and Frugis, G. L. 2021. Paleozoic Paraná Basin transition from collisional retro-foreland to pericratonic syneclise: Implications on the geodynamic model of Gondwana proto-Andean margin. *Journal of South American Earth Sciences* 111: 103511. https://doi.org/10.1016/j.jsames.2021.103511.

Henrique-Pinto, R., Basei, M. A. S., Santos, P. R., Saad, A. R., Passarelli, C. R., Cingolani, C. A., and Milani, E. J. 2024. Tonian juvenile arc crust provenance recorded in the Paraná Basin, Western Gondwana proto-Andean margin.

Precambrian Research 405: 107354. https://doi.org/10.1016/j.precamres.2024.107354.

Hippertt, J. P., Lana, C., Weinberg, R. F., Tohver, E., Schmieder, M., Scholz, R., Gonçalves, L., and Hippertt, J. F. 2014. Liquefaction of sedimentary rocks during impact crater development. *Earth and Planetary Science Letters* 408: 285-295.

Jackson, S. E., Pearson, N. J., Griffin, W. L., and Belousova, E. A. 2004. The application of laser ablation-inductively coupled plasma-mass spectrometry to in situ U-Pb zircon geochronology. *Chemical Geology* 211: 47–69.

Jourdan, F., Renne, P. R., and Reimold, W. U. 2009. An appraisal of the ages of terrestrial impact structures. *Earth and Planetary Science Letters* 286: 1–13.

Kalleson, E., Dypvik H., and Nielsen, O. 2010. Melt-bearing impactites (suevite and impact melt rock) within the Gardnos structure, Norway. *Meteoritics and Planetary Science* 45(5): 798-827. https://doi:10.1111/j.1945-5100.2010.01055.x.

Kaskes, P., Déhais, T., de Graaff, S. J., Goderis, S., and Claeys, P. 2021. Micro–X-ray fluorescence (μXRF) analysis of proximal impactites: High-resolution element mapping, digital image analysis, and quantifications. In *Large Meteorite Impacts and Planetary Evolution VI*, edited by Reimold, W. U., and Koeberl, C. *Geological Society of America Special Paper* 550: 171-206 https://doi.org/10.1130/2021.2550(07).

Kaskes, P., Graaff, S. J., Feignon, J., Déhais, T., Goderis, S., Ferrière, L., Koeberl, C., Smit, J., Wittmann, A., Gulick, S. P. S., Debaille, V., Mattielli, N., and Clayes, P. 2022. Formation of the crater suevite sequence from Chicxulub peak ring: A petrographic, geochemical, and sedimentological characterization. *Geological Society of America Bulletin* 134(3-4): 895-927.

Kenkmann, T. 2021. The terrestrial impact crater record: A statistical analysis of morphologies, structures, ages, lithologies, and more. *Meteoritics and Planetary Science* 56: 1024-1070. https://doi.org/10.1111/maps.13657

Kenkmann, T., Collins, G. S., Wittmann, A., Wünnemann, K., Reimold, W. U., and Melosh, H. J. 2009. A model for the formation of the Chesapeake Bay impact crater as revealed by drilling and numerical simulation. In *The ICDP-USGS Deep Drilling Project in the Chesapeake Bay Impact Structure: Results from the Eyreville Core Holes*, edited by Gohn, G. S., Koeberl, C., Miller, K. G., and Reimold, W. U. *Geological Society of America*, 571–585, Special Paper 458.

Kieffer, S.W., and Simonds, C. H. 1980. The role of volatiles and lithology in the impact cratering process. *Reviews of Geophysics and Space Physics* 18: 143-181.

Kroner, A., and Cordani, U. G. 2003. African, southern Indian and South American Craton were not part of Rodinia continent: evidence from field relationship and geochronology. *Tectonophysics* 375(1-4): 325-352.

Lacerda Filho, J. V., Abreu Filho, W., Valente, C. R., Oliveira, C. C., and Albuquerque, M. C. 2004. *Geologia e recursos minerais do estado de Mato Grosso*. Mato Grosso: Programa Geologia do Brasil, CPRM/MME/SICME, 252 p.

Lacerda Filho, J. V., Brito, R. S. C., Silva, M. G., Oliveira, C. C., Moreton, L. C., Martins, E. G., Lopes, R. C., Lima, T. M., Larizzatti, J. H., and Valente, C. R. 2006. *Geologia e Recursos Minerais do Estado de Mato Grosso do Sul*. Mato Grosso do Sul: Programa Integração, atualização e difusão de dados de geologia do Brasil. Convênio CPRM/SICME-MS, MME, 121 p.

Lana, C., Romano, R., Reimold, W. U., and Hippertt, J. 2006. Collapse of large complex impact structures: Implications from the Araguainha impact structure. *Geology* 34: 9-12.

Lana, C., Souza-Filho, C. R., Marangoni, Y. R., Yokoyama, E., Trindade, R. I. F., Tohver, E., and Reimold, W. U. 2007. Insights into the morphology, geometry, and post-impact erosion of the Araguainha peak-ring structure, central Brazil. *Geological Society of America Bulletin* 119: 1135–1150.

Lana, C., Souza-Filho, C. R., Marangoni, Y. R., Yokoyama, E., Trindade, R. I. F., Thover, E., and Reimold, W. U. 2008. Structural evolution of the 40 km wide Araguainha impact structure, central Brazil. *Meteoritics and Planetary Science* 43: 701-716. https://doi:10.1111/j.1945-5100.2008.tb00679.x

Laux, J. H., Pimentel, M. M., Dantas, E. L. Armstrong, R., and Junges, S. L. 2005. Two Neoproterozoic crustal events in the Brasília Belt, central Brazil. *Journal of South American Earth Sciences* 18: 183-198.

Leite, F.G.D.L., Fuck, R.A., Dantas, E.L., and Ruiz, A.S., 2021, Appinitic and high Ba-Sr magmatism in central Brazil: insights into the late accretion stage of West Gondwana: Lithos, v. 398–399, p. 106333. https://doi.org/10.1016/j.lithos.2021.106333.

Leite, F.G.D.L., Fuck, R.A., Dantas, E.L., Ruiz, A.S., Moniê, P., and Iemmolo, A., 2024, Tectonic significance of the late-Ediacaran syn-orogenic basin in the easternmost portion of the Paraguay Belt, Tocantins Province, central Brazil: Journal of South American Earth Sciences, v. 133, p. 104735. https://doi.org/10.1016/j.jsames.2023.104735.

Litherland, M., Annels, R. N., and Appleton, J. D. 1986. The Geology and Mineral Resources of the Bolivian Precambrian Shield, 9: 153.

Lofgren, G. 1971. Devitrified glass fragments from Apollo 11 and Apollo 12 lunar samples. *Proceedings of the Lunar Science Conference* 2: 949-955.

López, W. H. A. 2022. Proveniência sedimentar das formações Ponta Grossa e São Domingos (Devoniano) do NW da Bacia do Paraná (Brasil): implicações regionais para os ventos T-R do SW de Gondwana. MSc thesis, University of Brasilia, Brasilia, DF.

Ludwig, K. R. 2008. User's manual for Isoplot 3.70: a geochronological toolkit for Microsoft Excel, 4. Geochronology Center Special Publication, Berkeley, California, 76 p.

Luz, J. S., Oliveira, A. M., Souza, J. O, Motta, J. F. M., Tanno, L. C., Carmo, L. S., and Souza, N. B. 1980. Projeto Coxipó – relatório final. Companhia de pesquisa de recursos minerais, Superintendência Regional de Goiânia, DNPM/CPRM, Goiânia, Goiás, 136 p.

Machado, R., Lana, C., Stevens, G., Filho, C. R. S., Reimold, W. U., and McDonald, I. 2009. Generation, mobilization and crystallization of impact-induced alkali-rich melts in granitic target rocks. Evidence from the Araguainha impact structure, central Brazil. *Geochimica et Cosmochimica Acta* 73: 7183-7201.

Mader, M. M., and Osinski, G. R. 2018. Impactites of the Mistastin Lake impact structure: Insights into impact ejecta emplacement. *Meteoritics and Planetary Science* 53(12): 2492–2518. https://doi:10.1111/maps.13173.

Mantovani, M. S. M., Quintas, M. C. L., Shukowsky, W., and Brito Neves, B. B. 2005. Delimitation of the Paranapanema Proterozoic block: a geophysical contribution. *Episodes* 28: 18-22.

Manzano, J. C. 2009. Caracterização dos Granitóides Brasilianos da Faixa de Dobramento Paraguai, MT e MS. Dissertação de Mestrado, Instituto de Geociências e Ciências Exatas, Universidade Estadual Paulista, 99 p.

Marques, A., Zanotto, O. A., França, A. B., Astolfi, M. A. M., and Paula, O. B. 1993. Compartimentação tectônica da Bacia do Paraná. Curitiba: PETROBRÁS/ NEXPAR, (relatório interno), 87 p.

Marques, G. C., Oliveira, C. G., Espada, E., and Dantas, E. L. 2019. The Fazenda Nova gold deposit, Goiás Magmatic Arc: late Neoproterozoic intrusion-related auriferous mineralization controlled by intracontinental strike-slip faulting. *Ore Geology Reviews* 107: 546–572.

Masero, W., Schenegg, P. A., and Fontes, S. L. 1994. A magnetotelluric investigation of the Araguainha impact structure in Mato Grosso-Goiás, central Brazil. *Geophysical Journal International* 116: 366–376.

Matteini, M., Junges, S. L., Dantas, E. L., Pimentel, M. M., and Bühn, B. 2010. In situ zircon U–Pb and Lu–Hf isotope systematic on magmatic rocks: Insights on the crustal evolution of the Neoproterozoic Goiás Magmatic Arc, Brasília belt, Central Brazil. *Gondwana Research* 17: 1-12. doi:10.1016/j.gr.2009.05.008.

McCall, N., Gulick, S. P. S., Karro, K., Jõeleht, A., Wilk, J., and Pösges, G. 2023. Understanding the Ries impact structure subsurface from high-resolution seismic data. *Geology* 52(1): 39–44. https://doi.org/10.1130/G51503.1.

McGee, B., Collins, A. S., Trindade, R. I. F., and Payne, J. 2014. Age and provenance of the Cryogenian to Cambrian passive margin to foreland basin sequence of the northern Paraguay Belt, Brazil. *Geological Society of America Bulletin* 127:76-86. http://dx.doi.org/10.1130/B30842.1.

McPhie, J., Doyle, M., and Allen, R. 1993. *Volcanic Textures – A Guide to the Interpretation of Textures in Volcanic Rock*. Centre for Ore Deposit and Exploration Studies, University of Tasmania 196 pp.

Melosh, H. J. 1989. *Impact Cratering: A Geologic Process*. New York: Oxford University Press 258 pp.

Melosh, H. J., and Ivanov, B. A. 1999. Impact Crater Collapse. *Annual Review of Earth Planetary Sciences* 27: 385-415.

Milani, E. J. 1997. Evolução tectono-estratigráfica da Bacia do Paraná e seu relacionamento com a geodinâmica fanerozóica do Gondwana sul-ocidental. PhD thesis, Universidade Federal do Rio Grande do Sul, Porto Alegre, 255p.

Milani, E. J., and Ramos, V. A. 1998. Orogenias Paleozóicas no Domínio Sul-ocidental do Gondwana e os ciclos de subsidência da Bacia do Paraná. *Revista Brasileira de Geociências* 28: 473-484.

Milani, E. J., França, A. B., and Schneider, R. L. 1994. Bacia do Paraná. *Boletim de Geociências da Petrobrás* 8: 69-82.

Milani, E. J., Melo, J. H. G., Souza, P. A., Fernandes, L. A., and França, A. B. 2007. Bacia do Paraná. *Boletim de Geociências* 15: 265-287.

Milani, E.J., De Wit, M.J., 2008. Correlations between the classic Paraná and Cape-Karoo sequences of South America and southern Africa and their basin in fills flanking the Gondwanides: du Toit revisited. Geological Society London, Special Publications 294(1): 319–341. https://doi.org/10.1144/SP294.17.

Miyazaki, M. R. 2018. Modelagem Gravimétrica 3D da Estrutura de impacto de Araguainha. M.Sc. Thesis, Universidade Estadual de Campinas, São Paulo, 84 pp.

Miyazaki, M. R., Leite, E. P., Vasconcelos, M. A. R., Wünnemann, K., and Crósta, A. P. 2021. Bouguer anomaly inversion and hydrocode modeling of the central uplift of the Araguainha impact structure. *Annals of the Brazilian Academy of Sciences* 93: e20210081. https://doi.org/10.1590/0001-3765202120210081.

Mizusaki, A.M.P., Melo, J.H.G., Vignol-Lelarge, M.L., Steeman, P., 2002, Vila Maria Formation (Silurian, Paraná Basin, Brazil): integrated radiometric and palynological age determinations: Geological Magazine, v. 139, no. 4, p. 453-463.

Montibeller, C. C., Navarro, G. R. B., Zanardo, A., Rohn, R., Roveri, C. D., da Rocha, R. R., and Conceição, F. T. 2020. Geochemistry of siltstones from the Permian Corumbataí Formation from the Paraná Basin (State of São Paulo, Brazil): Insights of provenance, tectonic and climatic settings. *Journal of South American Earth Siciences* 102: 102582, https://doi.org/10.1016/j.jsames.2020.102582

Montibeller, C. C., Zanardo, A., and Navarro, G. R. B. 2017. Decifrando a proveniência dos folhelhos da formação Ponta Grossa na região de Rio Verde de Mato Grosso e Coxim (MS) através de métodos petrográfico e geoquímicos. *Geologia USP Série Científica*, 17(1): 41-59.

NASA JPL. 2013. NASA Shuttle Radar Topography Mission global 1 arc second [data set]. NASA EOSDIS Land Processes Distributed Active Archive Center https://doi.org/10.5067/MEaSUREs/SRTM/SRTMGL1.003.

Nogueira, A. C. R., Riccomini, C., Sial, A. N., Moura, C. A. V., and Fairchild, T. R. 2003. Soft-sediment deformation at the base of the Neoproterozoic Puga cap carbonate (southwestern Amazon craton, Brazil): confirmation of rapid icehouse to greenhouse transition in snowball Earth. *Geology* 31(7): 613-616. https://doi.org/10.1130/0091-7613(2003)031<0613:SDATBO>2.0.CO;2.

Northfleet, A. A., Medeiros, R. A., and Muhlmann, H. 1969. Reavaliação dos dados geológicos da Bacia do Paraná. *Boletim Técnico da Petrobrás* 12: 291–346.

Ormö, J., Sturkell, E., and Lindström, M. 2007. Sedimentological analysis of resurge deposits at the Lockne and Tvären craters: clues to flow dynamics. *Meteoritics and Planetary Science* 42: 1929–1943. https://doi.org/10.1111/j.1945-5100.2007.tb00551.x.

Osinski, G. R., and Grieve, R. A. 2024. The “suevite” conundrum, Part 2: Re-examining the type locality at the Ries impact structure, Germany. Meteoritics and Planetary Science 1-29. https://doi.org/10.1111/maps.14241.

Osinski, G. R., and Pierazzo, E. 2013. Impact cratering: processes and products. Oxford, Wiley-Blackwell, 316 p.

Osinski, G. R., Coulter, A. B., Flemming, R. L., Ozaruk, A., Pickersgill, A. E., and Singleton, A. C. 2023. Revisiting the Gow Lake impact structure, Saskatchewan, Canada. *Meteoritic and Planetary Sciences* 58: 775-788. https://doi.org/10.1111/maps.13986.

Osinski, G. R., Grieve, R. A. F., and Spray, J. G. 2004. The nature of the groundmass of surficial suevites from the Ries impact structure, Germany, and constraints on its origin. *Meteoritics and Planetary Science* 39: 1655–1684.

Osinski, G. R., Grieve, R. A. F., Chanou, A., and Sapers, H. M. 2016. The “suevite” conundrum, Part 1: The Ries suevite and Sudbury Onaping Formation compared. *Meteoritics and Planetary Science* 51: 2316-2333.

Osinski, G. R., Grieve, R. A. F., Collins, G. S., Marion, C., and Sylvester, P. 2008. The effect of target lithology on the products of impact melting. *Meteoritics and Planetary Science* 43: 1939-1954.

Osinski, G. R., Grieve, R. A. F., Ferriere, L., Losiak, A., Pickersgill, A. E., Cavosie, A. J., and Hibbard, S. M. 2022. Impact Earth: A Review of the Terrestrial Impact Record. *Earth-Science Reviews* 232: 104112.

Osinski, G. R., Grieve, R. A. F., Hill, P. J. A., Simpson, S. L., Cockell, C., Christeson, G. L., Ebert, M., Gulick, S., Melosh, H. J., Riller, U., Tikoo, S. M., and Wittmann, A. 2020. Explosive interaction of impact melt and seawater following the Chicxulub impact event. *Geology* 48: 108–112, https://doi.org/10.1130/G46783.1.

Osinski, G. R., Tornabene, L. L., and Grieve, R. A. F. 2011. Impact ejecta emplacement on terrestrial planets. *Earth and Planetary Science Letters* 310: 167–181.

Paton, C., Woodhead, J. D., Hellstrom, J. C., Hergt, J. M., Greig, A., and Mass, R. 2010. Improved laser ablation U-Pb zircon geochronology through robust downhole fractionation correction. *Geochemistry, Geophysics, Geosystems* 11: 1-36.

Peate, D. W. 1997. The Paraná-Etendeka Province. In *Large Igneous Provinces: Continental, Oceanic, and Planetary Flood Volcanism*, edited by Mahoney, J. J.,

and Coffin, M. F. Geophysical Monograph, American Geophysical Union, Washington, DC, 100: 217–245.

Pelosi, G. F. F. 2017. Age, provenance and tectonic setting from southern portion of the Cuiabá Group: implications for the evolution of the Paraguay Belt. MSc thesis, Cuiabá, MT, University of Mato Grosso, 47 p.

Petrus, J. A., and Kamber, B. S. 2012. VizualAge: a novel approach to laser ablation ICP-MS U-Pb 1157 geochronology data reduction. *Geostandards and Geoanalytical Research* 36(3): 247-270.

Piauilino, P. F., Hauser, N., and Dantas, E. L. 2021. From passive margin to continental collision: Geochemical and isotopic constraints for E-MORB and OIB-like magmatism during the Neoproterozoic evolution of the southeast Brasília Belt. *Precambrian Research* 359: 105345. https://doi.org/10.1016/j.precamres.2019.105345.

Pierazzo, E., and Melosh, H. J. 1999. Hydrocode modeling of Chicxulub as an oblique impact event. *Earth and Planetary Science Letters* 165: 163-176.

Pierazzo, E., and Melosh, H. J. 2000. Hydrocode modelling of oblique impacts: the fate of the projectile. *Meteoritics and Planetary Science* 35: 117-130.

Pike, R. J. 1980. Formation of complex impact crater: Evidence from Mars and other planets. *Icarus* 43: 1-19.

Pimentel, M. M. 2016. The tectonic evolution of the Neoproterozoic Brasília Belt, Central Brazil: a geochronological and isotopic approach. *Brazilian Journal of Geology* 46: 67–82.

Pimentel, M. M., and Fuck, R. A. 1987. Late proterozoic granitic magmatism in southwestern Goiás, Brazil. *Revista Brasileira de Geociências* 17: 4, 415-425.

Pimentel, M. M., Fuck, R. A., and Alvarenga, C. J. S. 1996. Post-Brasiliano (Pan African) high-K granitic magmatism in central Brazil: the role of late Precambrian/early Paleozoic extension. *Precambrian Research* 80: 217-238. https://doi:10.1016/S0301-9268(96)00016-2.

Pimentel, M. M., Fuck, R. A., Ferreira Filho, C. F., and Araújo, S. M. 2000. The basement of the Brasília Belt and the Goiás Magmatic Arc. In *31st International Geological Congress*, edited by Cordani, U. G., Milani, E. J., Thomaz Filho, A., and Campos, D. A. Tectonic Evolution of South America., Rio de Janeiro, 195-229.

Pimentel, M. M., Heaman, L., and Fuck, R. A. 1991. Zircon and sphene U-Pb geochronology of Upper Proterozoic volcanic-arc rock units from southwestern Goiás, central Brazil. *Journal of South American Earth Sciences* 4(4): 295-305.

Pimentel, M. M., Hollanda, M. H. B. M., and Armstrong, R. 2003. Shrimp U-Pb age and Sr-Nd isotopes of the Morro do Baú mafic intrusion: implications for the evolution of the Arenópolis volcano-sedimentary sequence, Goiás Magmatic Arc *Anais da Academia Brasileira de Ciências* 75(3): 331-339.

Pinho, F. E. 1990. Geoquímica do depósito de ouro de Nova Xavantina - leste do Estado de Mato Grosso. *Congresso Brasileiro de Geologia*, 36. Anais SBG: pp. 3.1316-1330.

Poelchau, M. H. 2022. Constraints on the pressure range of feather features in shocked quart. In *85th Annual Meeting of The Meteoritical Society*, abstract 2695, Glasgow, Scotland, pp. 6499.

Preuss, J. 2012. Characterization of impact-related melt breccias from the impact structure Araguainha (Brazil). MSc thesis, Potsdam: University of Potsdam 101 p.

Reimold, W. U. 1998. Exogenic and Endogenic Breccias: A Discussion of Major Problematics. *Earth Science Reviews* 43: 25–47.

Reimold, W. U., and Gibson, R. L. 2006. The melt rocks of the Vredefort Impact Structure: petrography, geochemistry, and implications for impact cratering and Witwatersrand evolution. *Chemier der Erde* 66: 1-35.

Reimold, W. U., and Koeberl, C. 2014. Impact structures in Africa: a review. *Journal of Earth Sciences* 93: 57-175.

Reimold, W. U., Bartosova, K., Schmitt, R. T., Hansen, B., Crasselt, C., Koeberl, C., Wittmann, A., and Powars D. S. 2009. Petrographic observations on the Exmore breccia, ICDP-USGS drilling ar Eyreville, Chesapeake Bay impact structure, USA. In *Geological Society of America Special Paper*, edited by Gohn, G. S., Koeberl, C., Miller, K. G., and Reimold, W. U. The ICDP-USGS deep drilling project in the Chesapeake Bay impact structure: results from the Eyreville core holes 458: 655-698.

Reimold, W. U., Hauser, N., Hansen, B. T., Thirlwall, M., and Hoffmann, M. 2017. The impact pseudotachylitic breccia controversy: insights from first isotope analysis of Vredefort impact-generated melt rocks. *Geochimica et Cosmochimica Acta* 214: 266–81.

Reimold, W. U., Hoffmann, M., Hauser, N., Schmitt, R.-T., Zaag, P., and Mohr-Westheide, T. 2016. A geochemical contribution to the discussion about the genesis of impact-related pseudotachylitic breccias: studies of PTB in the Otavi and Kudu Quarries of the Vredefort Dome support the “in situ formation” hypothesis. *South African Journal of Geology* 119: 453–72.

Reimold, W. U., McDonald, I., Schmitt, R. T., Hansen, B., Jacob, J., and Koeberl, C. 2013. Geochemical studies of the SUBO 18 (Enkingen) drill core and other impact breccias from the Ries crater, Germany. *Meteoritics and Planetary Science* 48: 1531–1571.

Rizzoli, P., Martone, M., Gonzalez, C., Wecklich, C., Borla Tridon, D., Bräutigam, B., Bachmann, M., Schulze, D., Fritz, T., Huber, M., Wessel, B., Krieger, G., Zink, M., and Moreira, A. 2017. Generation and performance assessment of the global TanDEM-X digital elevation model. *ISPRS Journal of Photogrammetry and Remote Sensing* 132: 119-139.

Rocha-Campos, A. C., Basei, M. A., Nutman, A. P., Keiman, L. E., Varela, R., Llambias, E., Canile, F. M., and Rosa, O. C. R. 2011. 30 million years of Permian

volcanism recorded in the Choiyoi igneous province (W Argentina) and their source for younger ash fall deposits in the Parana Basin: SHRIMP U–Pb zircon geochronology evidence. *Gondwana Research* 19: 509-523. https://doi.org/10.1016/j.gr.2010.07.003.

Sánchez, J. P. 2006. Mapeamento 1:25.000 do núcleo do Astroblema Domo de Araguainha e aspectos geoturísticos da região. BSc thesis, Universidade Estadual Paulista, Rio Claro, SP, Universidade Estadual Paulista, 57 p.

Santos, T. B., Mancini, F., Cury, L. F., and Ferreira, F. J. F. 2015. Proveniência de zircões detríticos e implicações para a paleogeografia da Formação Furnas no noroeste da Bacia do Paraná. *Geologia USP Série Científica*, São Paulo, 15(2): 25-59. https://doi.org/10.11606/issn.2316-9095.v15i2p25-59.

Sauer, A. 1920. Erläuterugen zur geologischen Karte Württemberg 1:50000, Blatt 20 Bopfingen 1.

Schmieder, M., and Kring, D. A. 2020. Earth's impact events through geologic time: a list of recommended ages for terrestrial impact structures and deposits. *Astrobiology* 20(1): 91-141. https://doi.org/10.1089/ast.2019.2085.

Siegert, S., and Hecht, L. 2018. Heterogeneity of melts in impact deposits and implications for their origin (Ries suevite, Germany). *Meteoritics and Planetary Science* 54: 2409-2447.

Siegert, S., Branney, M. J., and Hecht, L. 2017. Density current origin of a melt-bearing impact ejecta blanket (Ries suevite, Germany). *Geology* 45: 855-858.

Silva, D., Lana, C., and Souza-Filho, C. R. 2016. Petrographic and geochemical characterization of the granitic rocks of the Araguainha impact crater, Brazil. *Meteoritics and Planetary Science* 51: 443-467.

Silva, M. F., Dantas, E. L., Matteini, M., and Trindade, R. I. F. 2022. Late Tonian explosive volcanism and hyaloclastites in northern Paraguay Belt, Central Brazil: A record of Rodinia break-up in western Gondwana. *Precambrian Research* 382: 106862. https://doi.org/10.1016/j.precamres.2022.106862.

Sláma, J., Košler, J., Condon, D. J., Crowley, J. L., Gerdes, A., Hanchar, J. M., Horstwood, M. S.A., Morris, G. A., Nasdala, L., Norberg, N., Schaltegger, U., Schoene, B., Tubrett, M., Whitehouse, N. M. J. 2008. Plešovice zircon - a new natural reference material for U-Pb and Hf isotopic microanalysis. *Chemical Geology* 249(1-2): 1-35. https://doi.org/10.1016/j.chemgeo.2007.11.005.

Soares, P. C. 1991. Tectônica sinsedimentar cíclica na Bacia do Paraná - controles. Departamento de Geologia, Universidade Federal do Paraná, Monografia para concurso de Professor Titular, 131 p.

Souza, C. S. S., Hauser, N., Reimold, W. U., Bernardes, R. B., Vieira, L. C., Guimarães, E. M., and Gottwald, M. 2024. Araguainha impact structure, Brazil: new insights into the geology of the central uplift. *Meteoritics and Planetary Science* 59: 2577-2607. https://doi.org/10.1111/maps.14236.

Spray, J. G., and Biren, M. B. 2021. Distinguishing friction- from shock-generated melt products in hypervelocity impact structures. In *Large Meteorite Impacts and*

Planetary Evolution VI, edited by W.U. Reimold, and C. Koeberl, 147-170. Geological Society of America Special Paper 550.

Stacey, J. S., and Kramers, J. D. 1975. Approximation of terrestrial lead isotope evolution by a two-stage model. *Earth and Planetary Science Letters* 26: 207-221.

Stöffler, D., and Grieve, R. A. F. 2007. Impactites. Recommendations by the IUGS Subcommission on the Systematics of Metamorphic Rocks. In *Metamorphic rocks: A classification and glossary of terms: Recommendations of the International Union of Geological Sciences Subcommission on the Systematics of Metamorphic Rocks*, edited by E. Fettes, and J. Desmons, Cambridge, U.K.: Cambridge University Press, 82-92, 111-125, and 126-242.

Stöffler, D., Artemieva, N. A., Ivanov, B. A., Hecht, L., Kenkmann, T., Schmitt, R. T., Tagle, R. A., and Wittmann, A. 2004. Origin and emplacement of the impact formations at Chicxulub, Mexico, as revealed by ICDP deep drilling at axcopoil-1 and by numerical modeling. *Meteoritics and Planetary Science* 39: 1035-1067.

Stöffler, D., Artemieva, N. A., Wünnemann, K., Reimold, W. U., Jacob, J., Hansen, B. K., and Summerson, I. A. T. 2013. Ries crater and suevite revisited – Observations and modeling Part I: Observations. *Meteoritics and Planetary Science* 48: 515-589.

Stöffler, D., Hamann, C., and Metzler, K. 2018. Shock metamorphism of planetary silicate rocks and sediments: proposal for an updated classification system. *Meteoritics and Planetary Sciences* 53: 5-49. https://doi.org/10.1111/maps.12912.

Tada, T., Kurosawa, K., Ono, H., Hamann, C., Okamoto, T., Niihara, T., Matsui, T. 2022. Shock recovery of granite with a decaying shock wave: feather features formation in quartz. In *53rd Lunar and Planetary Science Conference*, abstract 2678, Lunar and Planetary Institute, pp. 1733.

Tassinari C. C. G., and Macambira M. J. B. 1999. Geochronological provinces of the Amazonian Craton. *Episodes* 22: 174-182.

Theilen-Willige, B. 1981. The Araguainha impact structure, Central Brazil. *Revista Brasileira de Geociências* 11: 91-97.

Thompson, L. M., and Spray, J. G. 2017. Dynamic interaction between impact melt and fragmented basement at Manicouagan: the suevite connection. *Meteoritics and Planetary Science* 52: 1300-1329.

Tohver, E., Cawood, P. A., Riccomini, C., and Trindade, R. I. F. 2013. Shaking a methane fizz: seismicity from the Araguainha impact event and the Permian–Triassic global carbon isotope record. *Palaeogeography, Palaeoclimatology, Palaeoecology* 387: 66-75. https://doi.org/10.1016/j.palaeo.2013.07.010.

Tohver, E., Lana, C., Cawood, P. A., Fletcher, I. R., Jordan, F., Jourdan, F., Sherlock, S., Rasmussen, B., Trindade, R. I. F., Yokoyama, E., Souza Filho, C. R., and Marangoni, Y. 2012. Geochronological constraints on the age of a Permo–Triassic impact event: U–Pb and $^{40}Ar/^{39}Ar$ results for the 40 km

Araguainha structure of central Brazil. *Geochimica et Cosmochimica Acta* 86: 214-227.

Tong, C. H., Lana, C., Marangoni, Y. R., and Elis, V. R. 2010. Geoelectric evidence for centripetal resurge of impact melt and breccias over central uplift of Araguainha impact structure. *Geology* 38(1): 91-94.

Trompette, R., Alvarenga, C. J. S., and Walde, D. H. -G. 1998. Geological evolution of the Neoproterozoic Corumbá graben system (Brazil). Depositional context of the stratified Fe and Mn ores of the Jacadigo Group. *Journal of South American Earth Science* 11: 587-597.

UnB-IG 2012. Final Mapping Project by the Graduate Class of 2012. Brasilia, Brasil: Institute of Geosciences, University of Brasilia, Unpubl. Report, Brasília DDF, Braszil 759 pp.

Vasconcelos, B.R., 2018. Proveniência sedimentar do Grupo Cuiabá na Faixa Paraguai meridional [PhD thesis]: Brasília, University of Brasília, 173 p.

Vasconcelos, M. A. R. 2007. Caracterização geofísica da estrutura de impacto de Araguainha. M.Sc. Thesis, Institute of astronomy, geophysics and atmospheric sciences, University of São Paulo, São Paulo, Brazil.

Vasconcelos, M. A. R., Crósta, A. P., Wünnemann, K., Collins, G. S., Reimold, W. U., and Köster, P. 2016. Numerical modelling of the Araguainha impact structure, Brazil (abstract #6013). *Meteoritics and Planetary Science* 51: A639.

Vermeesch, P. 2021. Maximum Depositional Age Estimation Revisited. *Geoscience Frontiers* 12: 843–850.

Vermeesch, P., Resentini, A., and Garzanti, E. 2016. An R package for statistical provenance analysis. *Sedimentary Geology* 336: 14–25, https://doi.org/10.1016/j.sedgeo.2016.01.009.

von Engelhardt, W. V. 1990. Distribution, petrography and shock metamorphism of the ejecta of the Ries crater in Germany – A review. *Tectonophysics* 171: 259-273.

von Engelhardt, W. V., and Graup, G. 1984. Suevite of the Ries crater, Germany: Source rocks and implications for cratering mechanics. *Geologische Rundschau* 73: 447-481.

von Engelhardt, W., Matthai, S., and Walzebuck, J. 1992. Araguainha impact crater, Brazil. I – The interior part of the uplift. *Meteoritics and Planetary Sciences* 27: 442-457.

Warr, L. N. 2021. IMA–CNMNC approved mineral symbols. *Mineralogical Magazine* 85(3): 291-320. https://doi.org/10.1180/mgm.2021.43.

Widenbeck, M., Alle, P., Corfu, F., Griffin, W., Meier, M., Oberli, F., Quadt, A. V., Roddick, J., and Spiegel, W. 1995. Three natural zircon standards for U-Th-Pb, Lu-Hf, trace element and REE Analyses. *Geostandards Newsletter* 19: 1-23.

Wiedenbeck M. P., Hanchar J. M., Peck W. H., Sylvester P., Valley J., Whitehouse M., Kronz A., Morishita Y., Nasdala L., Fiebig J., Franchi I., Girard

J.-P., Greenwood R. C., Hinton R., Kita N., Mason P. R. D., Norman M., Ogasawara M., Piccoli P. M., Rhede D., Satoh H., Schulz-Dobrick B., Sk_ar O., Spicuzza M. J., Terada K., Tindle A., Togashi S., Vennemann T., Xie Q., and Zheng Y.-F. 2004. Further characterisation of the 91500 zircon crystal. Geostandards and Geoanalytical Research 28:9–39.

Wittmann, A., Kenkmann, T., Hecht, L., and Stöffler, D. 2007. Reconstruction of the Chicxulub ejecta plume from its deposits in drill core Yaxcopoil-1. *Geological Society of America Bulletin* 119: 1151–1167. https://doi.org/10.1130/B26116.1.

Wittmann, A., Kenkmann, T., Schmitt, R. T., Hecht, L., and Stöffler, D. 2004. Impact-related dike breccia lithologies in the ICDP drill core Yaxcopoil-1, Chicxulub impact structure, Mexico. *Meteoritics and Planetary Science* 39: 931-954.

Wouters, S., Hulsbosch, N., Kaskes, P., Claeys, P., Dewaele, S., Melcher, F., Onuk, P., and Muchez, P. 2020. Late orogenic gold mineralization in the western domain of the Karagwe-Ankole Belt (Central Africa): Auriferous quartz veins from the Byumba deposit (Rwanda). *Ore Geology Reviews* 125: 103666. https://doi.org/10.1016/j.oregeorev.2020.103666.

Wünnemann, K., Collins, G. S., and Osinski, G. R. 2008. Numerical modelling of impact melt production in porous rocks. *Earth and Planetary Science Letters* 269: 530–539.

Yokoyama, E. 2008. Trama magnética do núcleo soerguido da estrutura de impacto de Araguainha (MT/GO). MSc thesis, São Paulo: University of São Paulo 117 pp.

Yokoyama, E., Trindade, R. I. F., Lana, C. R., Souza-Filho, C. R., Baratoux, D., Marangoni, Y. R., and Tohver, E. 2012. Magnetic fabric of Araguainha complex impact structure (Central Brazil): Implications for deformation mechanisms and central uplift formation. *Earth and Planetary Science Letters* 331: 347-359.

Zalán, P. V., Wolff, S., Astolfi, M. A. M., Vieira, I. S., Conceição, J. C. J., Appi, V. T., Neto, E. V. S., Cerqueira, J. R., and Marques, A. 1990. The Paraná Basin, Brazil. In *Interior cratonic basins*, edited by M. W. Leighton, D. R. Kolata, D. F. Oltz, and J. J. Eidel, 51: 681-708. Rio de Janeiro: American Association of Petroleum Geologists Memoir.

Zalán, P. V., Wolff, S., Conceicao, J. C., Astolfi, M. A. M., Vieira, I. S., Appi, C. T., and Zanotto, O. A. 1987. Tectônica e sedimentação da Bacia do Paraná. In *Atas do III Simposio Sul-Brasileiro de Geologia*, Curitiba, Brazil, 1: 441–477.

Zimmermann, S., Mark, C., Chew, D., and Voice, P. J.2017. Maximising data and precision from detrital zircon U-Pb analysis by LA-ICPMS: the use of core-rim ages and the single-analysis concordia age. *Sedimentary Geology* 375: 5-13.

ANEXOS

Anexo 1. Tabela com todos os pontos registrados durante as campanhas de campo. Lat.: latitude, Long.: longitude, Fm.: Formação, Gr.: Grupo, IMR: rocha fundida de impacto, BPI: brecha polimítica de impacto, cong.: conglomerado.

Ponto	COORDENADAS (UTM)		Unidade	Ponto	COORDENADAS (UTM)		Unidade
	Long. (E)	Lat. (S)			Long. (E)	Lat. (S)	
CA-01	272831	8110839	Fm. Serra Geral	CA-59	286469	8138042	IMR II: cong. fundido
CA-02	273052	8112278	Fm. Aquidauana	CA-60	286531	8138205	IMR II: cong. fundido
CA-03	278224	8123381	Gr. Passa Dois	CA-61	286716	8138376	Granito
CA-04	288562	8142192	IMR I	CA-62	287385	8138621	IMR I
CA-05	288546	8142122	IMR I	CA-63	287405	8138404	IMR I
CA-06	288572	8142041	Gr. Cuiabá	CA-64	287524	8137989	IMR II
CA-07	288523	8141975	BPI	CA-65	287155	8137887	BPI
CA-08	288463	8141909	BPI	CA-66	287138	8137989	Granito
CA-09	287445	8141433	BPI	CA-67	289308	8141703	IMR I
CA-10	286804	8137198	Fm. Furnas	CA-68	286188	8139796	Gr. Cuiabá
CA-11	287038	8137483	Gr. Rio Ivaí	CA-69	286633	8139708	IMR I
CA-12	287477	8137543	Gr. Rio Ivaí	CA-70	286750	8141087	BPI
CA-13	287506	8137644	Gr. Rio Ivaí	CA-71	285967	8160880	BPI
CA-14	287403	8137922	BPI	CA-72	284172	8137100	Fm. Ponta Grossa
CA-15	287329	8138048	IMR II	CA-73	288549	8142116	BPI
CA-16	287267	8138130	Granito	CA-74	288543	8142116	BPI
CA-17	288442	8141822	BPI	CA-75	288537	8142104	Granito
CA-18	288548	8141034	Gr. Cuiabá	CA-76	288557	8142191	IMR I+II
CA-19	288281	8141448	Gr. Cuiabá	CA-77	288536	8141972	Gr. Cuiabá
CA-20	288344	8141362	Granito	CA-78	288506	8141972	IMR II
CA-21	288633	8140884	Gr. Cuiabá	CA-79	285770	8140161	BPI
CA-22	290608	8139763	Gr. Cuiabá	CA-80	285890	8139977	Gr. Cuiabá
CA-23	290592	8139771	Gr. Rio Ivaí	CA-81	285537	8139499	Gr. Cuiabá
CA-24	290106	8139631	Gr. Rio Ivaí	CA-82	288265	8141704	Gr. Rio Ivaí
CA-25	289955	8139626	Gr. Cuiabá	CA-83	288216	8141655	BPI
CA-26	289934	8139620	BPI	CA-84	286769	8141191	BPI
CA-27	289452	8139604	IMR I	CA-85	285788	8139861	BPI
CA-28	289338	8139343	Gr. Cuiabá	CA-86	287431	8137981	IMR II: cong. fundido
CA-29	288521	8141803	*controle*	CA-87	287525	8137986	Gr. Cuiabá
CA-30	288622	8141819	IMR II	CA-88	287570	8137990	Gr. Cuiabá
CA-31	288618	8141878	IMR II	CA-89	287604	8137983	Gr. Cuiabá
CA-32	288761	8141952	IMR II	CA-90	287616	8138011	Gr. Cuiabá
CA-33	288782	8141964	IMR II	CA-91	287628	8138026	Gr. Cuiabá
CA-34	288942	8141949	IMR I	CA-92	287619	8138050	Granito+Gr. Cuiabá
CA-35	288857	8141952	IMR I	CA-93	287365	8139608	Granito
CA-36	288838	8141912	IMR I	CA-94	287779	8139285	Granito
CA-37	289007	8141970	BPI	CA-95	287015	8138370	Granito
CA-38	289195	8141945	IMR I	CA-96	288110	8138306	IMR II: cong. fundido
CA-39	289232	8141862	IMR I	CA-97	288153	8138273	Gr. Cuiabá
CA-40	289262	8141762	IMR I	CA-98	288483	8141862	BPI
CA-41	289289	8141696	IMR II: cong. fund	CA-99	285788	8139861	BPI
CA-42	289420	8141587	IMR II	CA-100	286532	8137801	Gr. Rio Ivaí
CA-43	290060	8141209	Gr. Rio Ivaí	CA-101	286927	8137958	IMR II
CA-44	289957	8141070	Gr. Rio Ivaí	CA-102	287124	8137954	IMR II
CA-45	285466	8139642	Gr. Cuiabá	CA-103	287152	8137888	BPI
CA-46	285539	8139324	BPI	CA-104	287157	8137870	BPI
CA-47	290181	8141186	Gr. Rio Ivaí	CA-105	287203	8137905	IMR II
CA-48	289864	8140891	IMR II	CA-106	287219	8137917	Gr. Cuiabá
CA-49	289856	8140950	Gr. Rio Ivaí	CA-107	287235	8137948	IMR II: cong. fundido
CA-50	289842	8141004	BPI	CA-108	287300	8137969	BPI
CA-51	289833	8140992	IMR II: cong. fund	CA-109	287310	8138060	IMR II
CA-52	289803	8140997	BPI	CA-110	293422	8142212	Fm. Ponta Grossa
CA-53	289729	8141111	IMR II	CA-111	291650	8141529	Gr. Cuiabá
CA-54	289673	8141137	BPI	CA-112	287164	8137920	IMR II
CA-55	289670	8141108	IMR II	CA-113	287377	8138099	IMR I
CA-56	289200	8141666	IMR II	CA-114	287377	8138095	Granito
CA-57	286526	8137764	Gr. Rio Ivaí	CA-115	288511	8142168	IMR I+II
CA-58	286561	8137836	Gr. Rio Ivaí	CA-116	287915	8141449	BPI

Anexo 2. Mapas composicionais semiquantitativos de elementos maiores e traços analisados por micro florescência de raio-X (μFRX) em amostras do perfil CA-07 e de três rochas fundidas por impacto (CA-04, CA-05, CA-15).

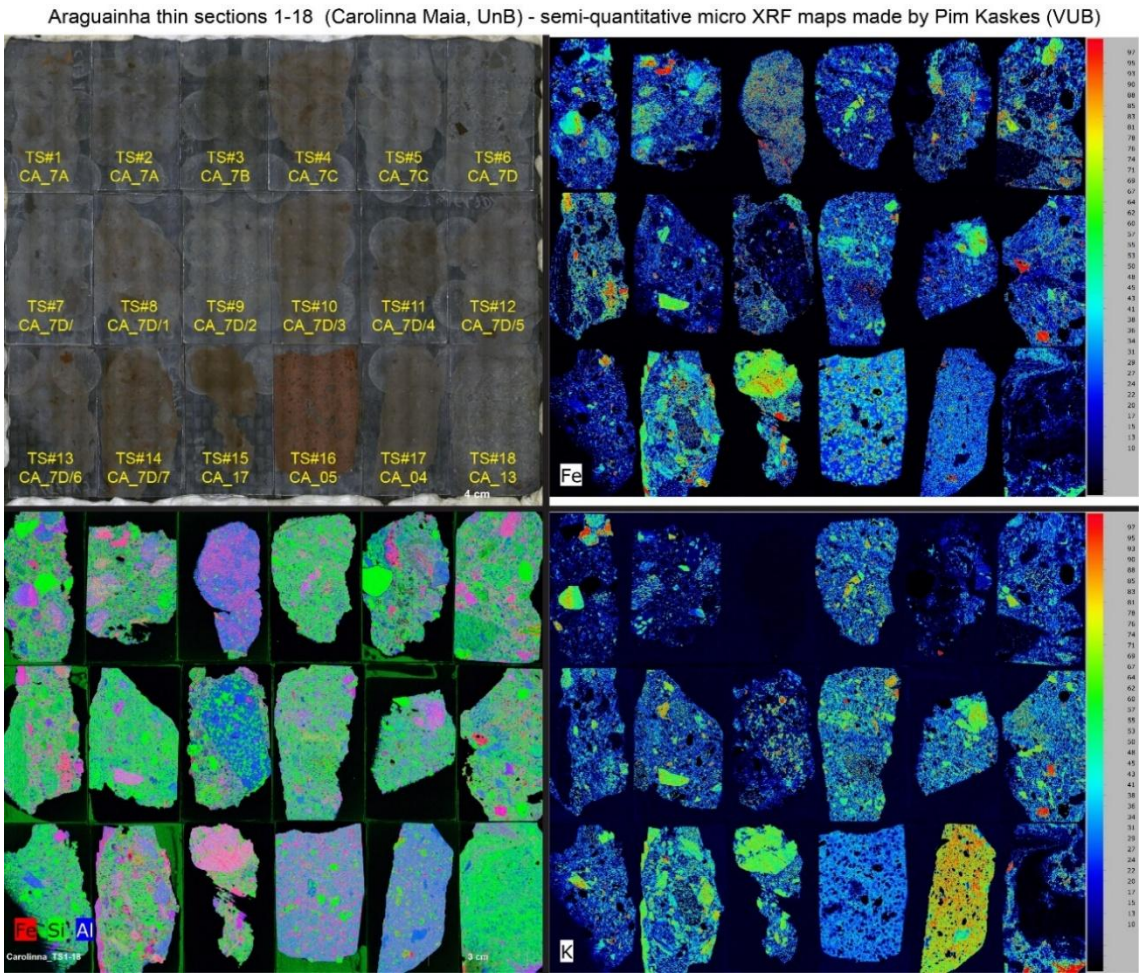

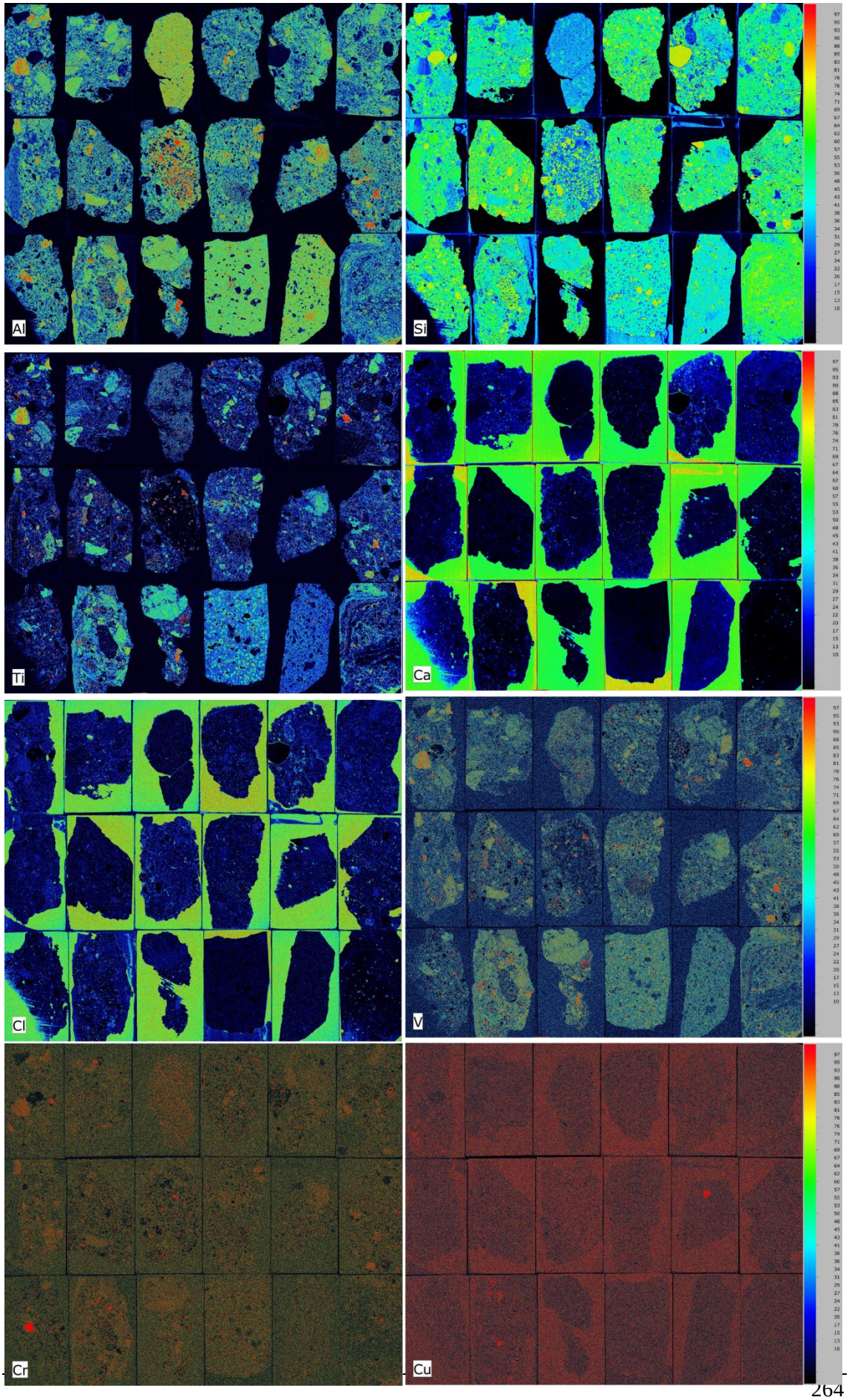
Al
Si
Ti
Ca
Cl
V
Cr
Cu

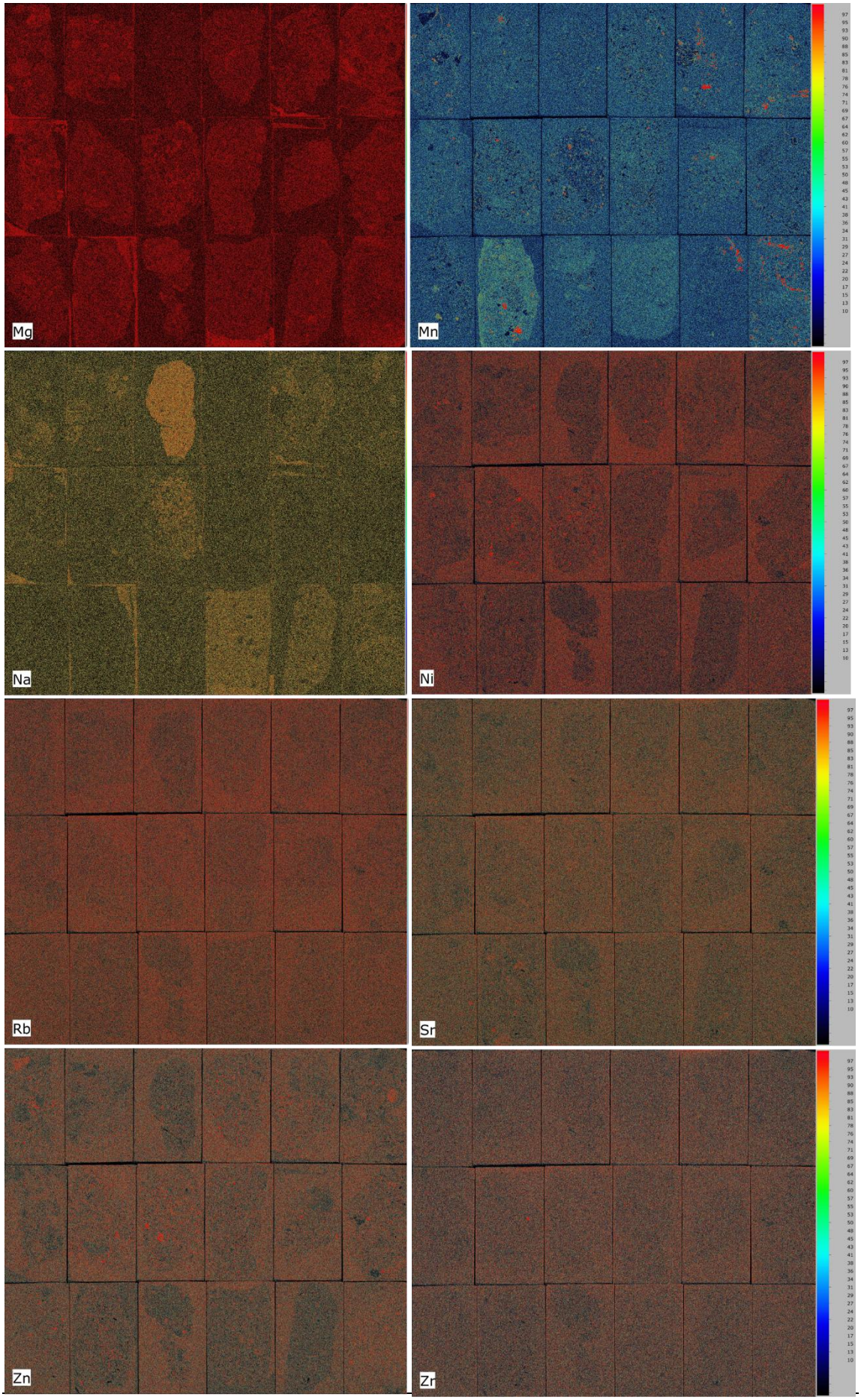
Mg
Mn
Na
Ni
Rb
Sr
Zn
Zr

Anexo 3. Caracterização mineral de alta resolução em sete lâminas polidas analisadas pela Avaliação Quantitativa de Minerais por Microscopia Eletrônica de Varredura (QEMSCAN).

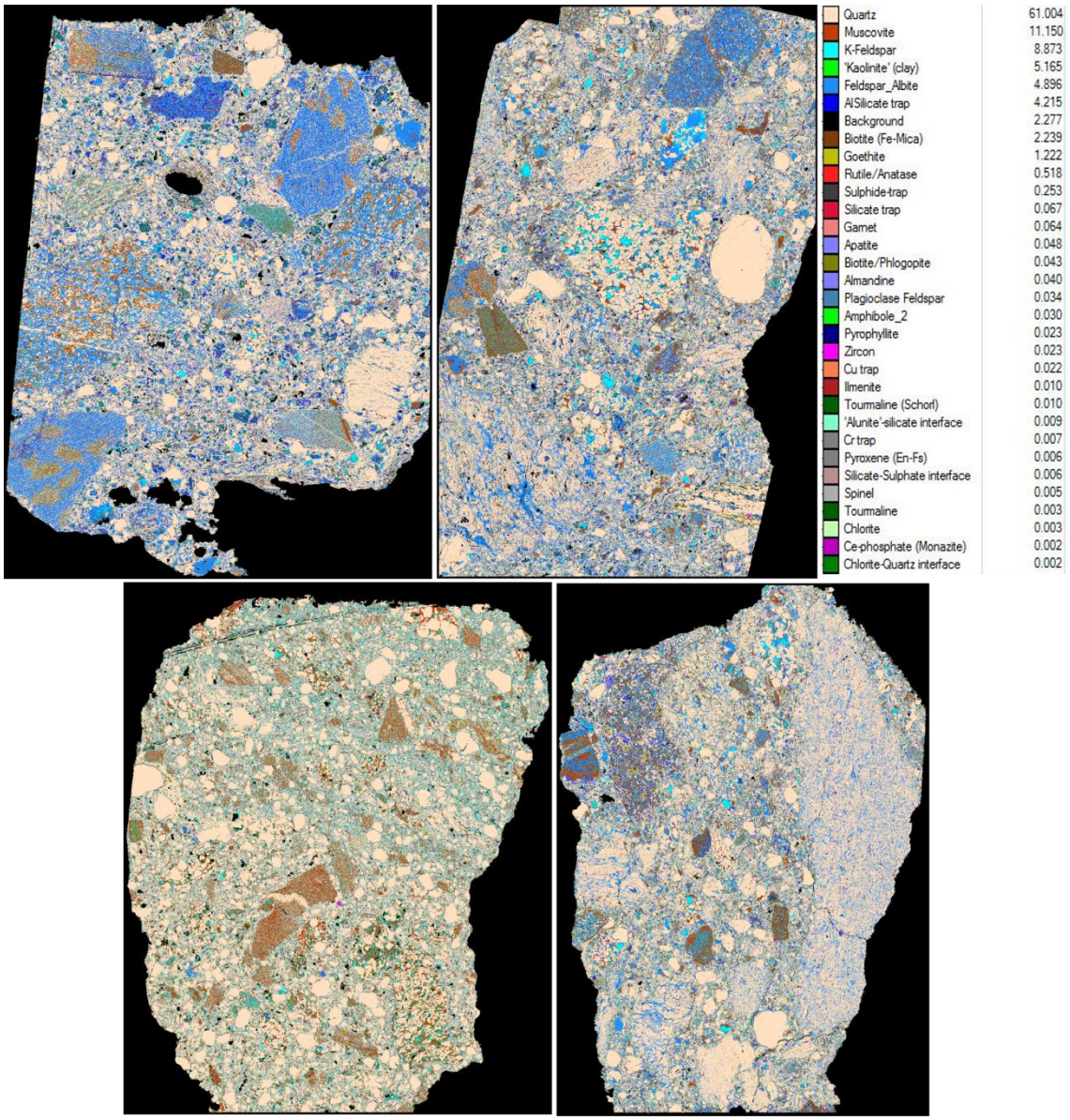

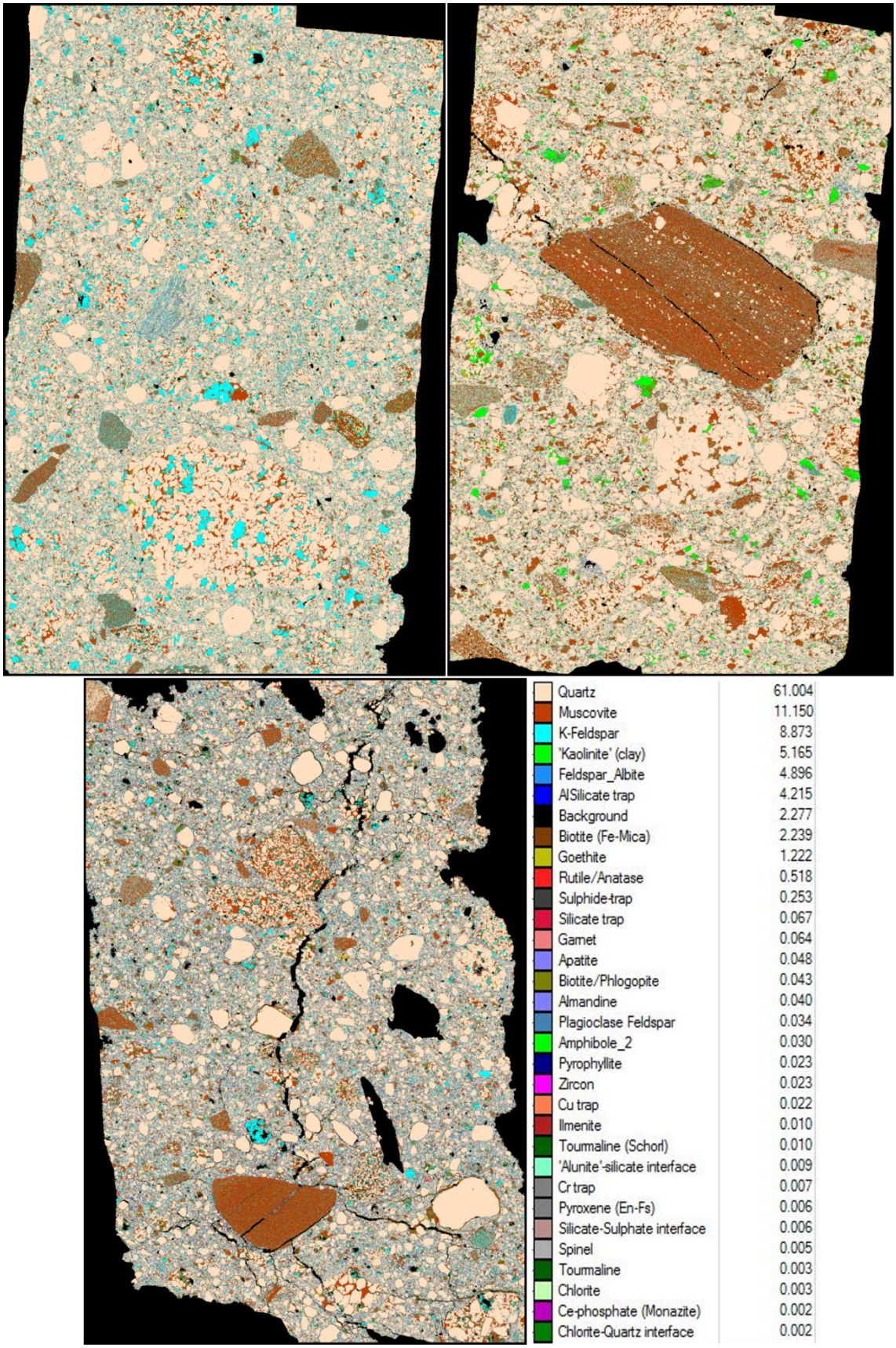
Quartz 61.004
Muscovite 11.150
K-Feldspar 8.873
'Kaolinite' (clay) 5.165
Feldspar_Albite 4.896
AlSilicate trap 4.215
Background 2.277
Biotite (Fe-Mica) 2.239
Goethite 1.222
Rutile/Anatase 0.518
Sulphide-trap 0.253
Silicate trap 0.067
Garnet 0.064
Apatite 0.048
Biotite/Phlogopite 0.043
Almandine 0.040
Plagioclase Feldspar 0.034
Amphibole_2 0.030
Pyrophyllite 0.023
Zircon 0.023
Cu trap 0.022
Ilmenite 0.010
Tourmaline (Schorl) 0.010
'Alunite'-silicate interface 0.009
Cr trap 0.007
Pyroxene (En-Fs) 0.006
Silicate-Sulphate interface 0.006
Spinel 0.005
Tourmaline 0.003
Chlorite 0.003
Ce-phosphate (Monazite) 0.002
Chlorite-Quartz interface 0.002

ARTIGOS PUBLICADO EM COLABORAÇÃO

The Meteoritical Society

Meteoritics & Planetary Science 58, Nr 7, 907–944 (2023)
doi: 10.1111/maps.14027

Genesis of the mafic impact melt rock in the northwest sector of the Vredefort Dome, South Africa

Wolf Uwe REIMOLD[1]*, Natalia HAUSER[1], Alisson Lopes OLIVEIRA[1], Ana Rita Pereira MACIEL[1], Steven GODERIS[2], Lidia PITTARELLO[3,4], Wencke WEGNER[3], Mario FISCHER-GOEDDE[5], Christian KOEBERL[4], Vinciane DEBAILLE[6], and Carolinna SILVA MAIA DE SOUZA[1]

[1]Laboratory of Geochronology and Isotope Geochemistry, Institute of Geosciences, Universidade de Brasília, Brasília, Brazil
[2]Research Unit: Analytical, Environmental, and Geo-Chemistry (AMGC), Vrije Universiteit Brussel, Brussels, Belgium
[3]Naturhistorisches Museum Wien, Wien, Austria
[4]Department of Lithospheric Research, University of Vienna, Vienna, Austria
[5]Institut für Geologie und Mineralogie, Universität zu Köln, Köln, Germany
[6]Laboratoire G-Time, Université Libre de Bruxelles, Brussels, Belgium
***Correspondence**
Wolf Uwe Reimold, Laboratory of Geochronology and Isotope Geochemistry, Institute of Geosciences, Universidade de Brasília, Campus Darcy Ribeiro, CEP 70910-900, Brasília, DF, Brazil.
Email: wolf.uwer@gmail.com

(Received 19 November 2022; revision accepted 09 May 2023)

Abstract–Genesis and emplacement of Vredefort Granophyre, the impact melt rock exposed on the Vredefort Dome, the erosional remnant of the central uplift of the Vredefort impact structure, South Africa, have long been debated. This debate was recently reinvigorated by the discovery that besides the previously known felsic variety of >66 wt% SiO_2, a second, somewhat more mafic phase of <66 wt% SiO_2 occurs along a Granophyre dike on farms Kopjeskraal and Eldorado in the northwest sector of the dome. Two hypotheses have been put forward to explain the genesis and emplacement of this second phase: (1) successive injections of impact melt into extensional fractures opened in the course of central uplift formation/crater modification, with melts of distinct compositions derived from a differentiating impact melt body in the crater, and (2) generation of the more mafic phase as a product of admixture/assimilation of a mafic country rock component, either the so-called epidiorite of possible Ventersdorp Supergroup affiliation or the Dominion Group meta-lava (DGL), to Felsic Granophyre. In the latter model, contamination with mafic country rock would have occurred during downward intrusion and stoping into and below the crater floor. The so-called Mafic Granophyre has previously only ever been sampled on a single site (Farm Kopjeskraal). In this study, samples of Granophyre occurring along the southerly extension of this dike on farm Rensburgdrif, and from a second dike on the Rietkuil property further southwest were investigated by field work, and petrographic, geochemical, and isotopic analysis. The mafic phase indeed occurs in the interior of the dike at Rensburgdrif, and also on Rietkuil. New geochemical and Sr-Nd isotope data support the hypothesis that the Mafic Granophyre composition represents a mixture between Felsic Granophyre and a mafic country rock. A 20% admixture of epidiorite or DGL to Felsic Granophyre provides an excellent match for the chemical composition of the Mafic Granophyre. The Sr-Nd isotope data indicate that this admixture likely involved the epidiorite component rather than DGL. Together with earlier Sr-Nd-Os-Se isotopic data, and other geochemical data, these results further support formation of the Mafic Granophyre by local assimilation/admixture of epidiorite to Felsic Granophyre.

© 2023 The Meteoritical Society.

INTRODUCTION

The Vredefort impact structure (VIS) in north-central South Africa is centered roughly 130 km southwest of Johannesburg on the Vredefort Dome, an extensive window into Archean and Paleoproterozoic crust of the central Kaapvaal Craton. The VIS represents the remnant of the largest known impact structure on Earth, with an estimated original diameter of 250–300 km (e.g., Allen et al., 2022; Gibson, 2019; Gibson & Reimold, 2008; Henkel & Reimold, 1998). This large structure encompasses the entire region of the erosional remnant of the Witwatersrand Basin between Johannesburg in the northeast and the Welkom gold mining district in the southwest. With an age of 2,023 ± 4 Ma (Kamo et al., 1996; see also Gibson et al., 1997; Spray et al., 1995), the VIS is also one of the oldest impact structures known on Earth. The structure involves the Vredefort Dome (Figure 1) and the surrounding Witwatersrand basin that, respectively, represent the deeply eroded central uplift structure of this large, complex impact structure, and the ring basin around the central uplift (e.g., Gibson & Reimold, 2008). The Vredefort Dome comprises a *core* of about 40 km width that exposes Archean granitoids, and a surrounding, about 20–25 km wide *collar* of Archean to Paleoproterozoic supracrustal strata. Overall, an about 25 km section through upper and middle crust is exposed in the Vredefort Dome, made accessible through post-impact exhumation by as much as 5–10 km.

The presence of impact-diagnostic features, such as shatter cones, high-pressure polymorphs of quartz (coesite and stishovite) and zircon (reidite), decorated planar deformation features (PDFs) in quartz, and unambiguous shock microdeformation in zircon in rocks of the dome, as well as chemical traces of the meteoritic projectile in impact melt rock, leaves no doubt that the Vredefort Dome is the eroded remnant of an originally even larger impact structure (e.g., Gibson & Reimold, 2008; Reimold & Koeberl, 2014).

Melt rocks in confirmed or possible impact structures have an important role: The possible presence of a meteoritic component mixed into impact melt (e.g., Koeberl, 2014) or the presence of shock metamorphosed clasts (e.g., French & Koeberl, 2010) can provide diagnostic evidence for genesis by impact. Impact melt rocks may contain clast populations that comprise material derived from all parts of the transient crater cavity, and thus, characteristically include clasts with diagnostic shock metamorphic effects. The petrology/petrography of impact melt rock can, furthermore, provide a wealth of data regarding the impact process itself, such as physicochemical processes at formation of impact melt, target composition, or dissemination and possible fractionation of the projectile component. The best option to radiometrically date an impact structure is to apply geochronological techniques to impact melt rock and its authigenic minerals (e.g., zircon).

There are abundant occurrences of two types of impact generated melt rock on the Vredefort Dome. First, the Vredefort Dome is the type locality for *pseudotachylyte/pseudotachylite/pseudotachylitic breccia* (PTB; e.g., Hopkins & Spray, 2022; Reimold, 1998; Shand, 1916; recent discussion and bibliography: Reimold et al., 2016, 2017). Recent chemical and isotopic work has made a strong case that the massive occurrences of PTB in the Vredefort and Sudbury structures could result from target rock melting during rapid decompression of the compressed crust in the center of the impact structure, although in the community an origin by friction melting is also favored (e.g., Reimold et al., 2021; see also Spray & Biren, 2021). In addition, thin veinlets with high-pressure polymorphs of coesite and stishovite at Vredefort are widely considered a terrestrial equivalent to the shock veins known from many meteorites.

The second type of impact-generated melt rock occurring at Vredefort—in fact, the *impact melt rock* of the VIS—is the so-called *Vredefort Granophyre*. Historically, this lithology has been known also as Enstatite Granophyre (Hall & Molengraaff, 1925), Basic Granophyre (e.g., Bisschoff, 1988; French et al., 1989; Willemse, 1937), or Bronzite Granophyre (e.g., Reimold et al., 1990). The latter authors established that most of the orthopyroxene in Granophyre is actually of hypersthene composition. The formation and emplacement of this lithology has long been debated (e.g., Bisschoff, 1988; French et al., 1989; French & Nielsen, 1990; Gibson & Reimold, 2008; Hall & Molengraaff, 1925; Lieger, 2011; Reimold et al., 1990, 2017, 2021; Reimold & Gibson, 2006; Therriault et al., 1996, 1997; Wannek, 2015). For example, Hall and Molengraaff (1925) regarded the Granophyre as "a glorified version of pseudotachylyte" (traditional spelling after Shand, 1916). Others, such as Willemse (1937) or Bisschoff (1972), interpreted the formation of this lithology via a basic mantle-derived magma that had assimilated a significant proportion of crustal and supracrustal material. Dietz (1961) proposed that the Granophyre represented impact melt rock, which became in subsequent decades widely—but not universally—accepted.

Vredefort Granophyre occurs in the form of 9 dikes of up to 9 km length and about 50 m width (Therriault et al., 1996; see also our Figure 1). Some of these dikes occur along the boundary between the basement core and the supracrustal rocks of the collar of the Vredefort Dome (see below, section Geological Setting). Four other dikes are exposed within the basement core. The Granophyre dikes are the only remnants of impact melt rock at Vredefort—the original crater, crater fill, and upper part of the crater floor have been eroded (Gibson & Reimold, 2008). The melt

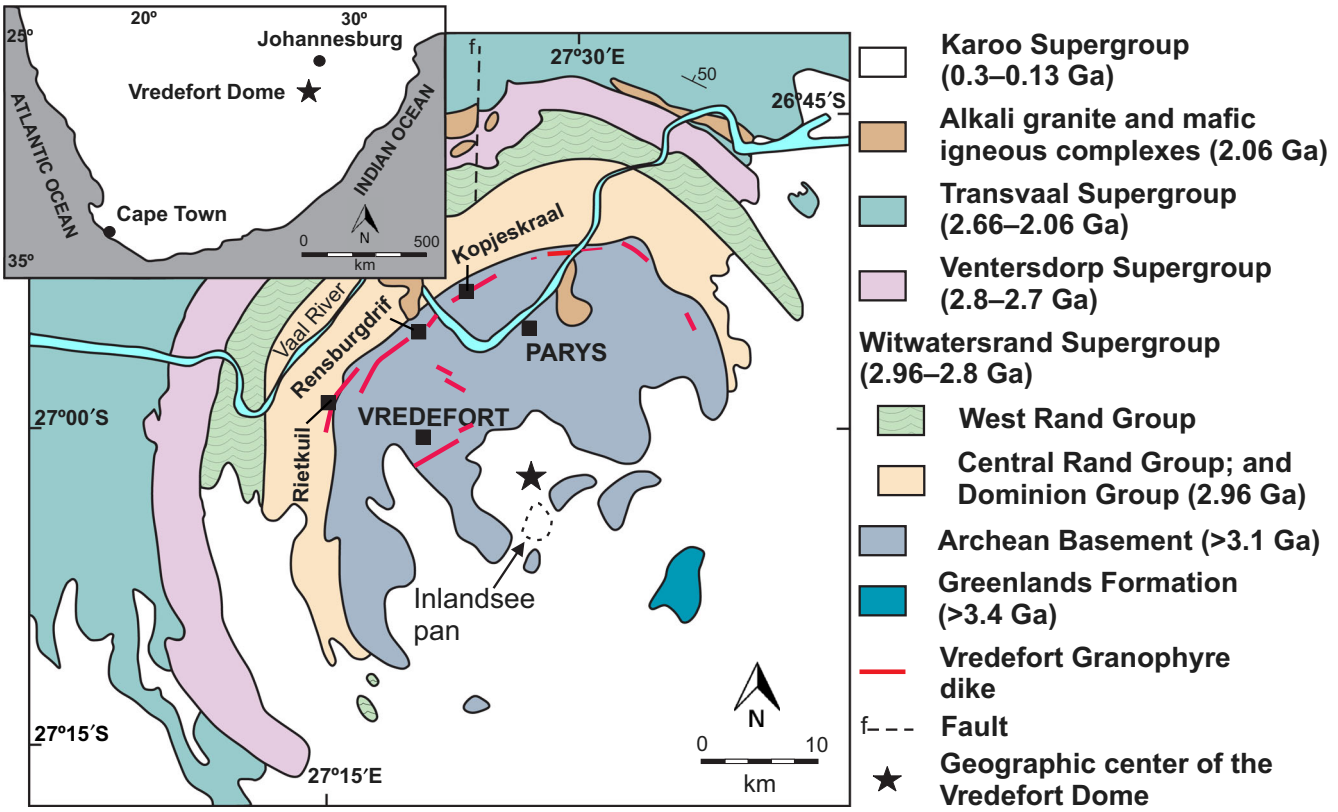

FIGURE 1. Schematic geology of the Vredefort Dome (inset shows the location of the Vredefort impact structure within the Southern African subcontinent). The study areas for this investigation of Vredefort Granophyre—the dikes on the Rensburgdrif, Kopjeskraal, and Rietkuil farms—are indicated with black squares. Modified after Reimold et al. (2017). (Color figure can be viewed at wileyonlinelibrary.com)

rock has a granophyric, micropegmatitic texture of the groundmass, from which the name Granophyre was derived. The clast population within the impact melt rock is dominated by fragments of granitoid of the Archean Basement Complex, with lesser contributions of quartzite and metapelite derived from supracrustal Witwatersrand strata (see next section). In the past, comparatively rare mafic inclusions were only observed in samples from where a dike cuts across the so-called epidiorite (i.e., metamorphosed diorite) (e.g., Reimold & Gibson, 2006; Therriault et al., 1996, 1997). This lithology occurs widespread within the collar of the Vredefort Dome and has been related to the regionally occurring, about 2.7 Ga old, Ventersdorp Supergroup (VS; e.g., Gumsley et al., 2020). Whether or not the Granophyre contains a component from the Transvaal and Ventersdorp supergroups has remained a topic of ongoing discussion (French & Nielsen, 1990; Reimold et al., 1990; Reimold & Gibson, 2006).

Geochemically, the Granophyre was long considered to be regionally of a homogeneous, chemically unique, felsic composition (with >66 wt% SiO_2, e.g., Reimold & Gibson, 2006). Rare analyses of comparatively more mafic character had been obtained ever since the pioneering work by Hall and Molengraaff (1925) but were explained by local assimilation of mafic country rock that had occurred only at sites where a Granophyre dike cuts across, or at current erosion level comes close to, an epidiorite occurrence (e.g., Therriault et al., 1996).

A new stage of Granophyre study was initiated when Lieger (2011) and Lieger and Riller (2012) discussed a comparatively more mafic Granophyre phase apparently occurring along the margins of an impact melt rock dike of otherwise "normal" felsic composition on Farm Kopjeskraal in the northwestern sector of the Vredefort Dome (Figure 1). These authors, and more recently Huber et al. (2020, 2022), proposed that two successive intrusions of melt from a differentiating impact melt sheet or generated by assimilation of a mafic lithology at the base of the melt sheet, above the original impact crater floor, had generated a composite felsic/mafic Granophyre dike. The idea was taken from the Offset Dikes of the Sudbury impact structure, which are widely considered to have been produced by multiple intrusions of impact melt (e.g., Hecht et al., 2008; Lightfoot, 2016).

Wannek (2015) reinvestigated the Granophyre dike on Kopjeskraal and its extension onto the neighboring farm Eldorado, and recognized that the mafic phase occurred in fact in the inner part of the dike, in direct contrast to

Lieger (2011) and Lieger and Riller (2012). The work of Wannek and the geochemical studies by Reimold et al. (2016, 2017, 2021) provided support for the hypothesis that the more mafic impact melt rock could have been generated by admixture/assimilation of a mafic country rock, such as epidiorite, component to Felsic Granophyre ("hybridization hypothesis" of Wannek, 2015), instead of resulting from a separate melt injection phase.

Here, we study the extension of this Granophyre dike on Kopjeskraal/Eldorado north of the Vaal River onto farm Rensburgdrif to the south of the Vaal River (Figure 1). Field analysis, together with petrographic and geochemical investigations, indicates that the mafic impact melt rock phase is also present in this section of the dike. Furthermore, an occurrence of Mafic Granophyre in a second impact melt rock dike on the Rietkuil property—already indicated by Therriault et al. (1996)—is confirmed. We contribute additional major and trace element, and Sr-Nd isotopic results with the aim to better understand the generation process for the Mafic Granophyre variety. We are applying the nomenclature of Felsic Granophyre and Mafic Granophyre for impact melt rock samples of > and < 66 wt% SiO_2, respectively, in keeping with Reimold et al. (2021). Wannek (2015) and Reimold et al. (2017) had previously referred to the Mafic Granophyre as "Hybrid Granophyre."

GEOLOGICAL SETTING

The about 90 km wide Vredefort Dome (Figure 1) is the deeply eroded central uplift of the VIS. The dome is located roughly in the center of the erosional remnant of the Witwatersrand basin. The 50 km wide Potchefstroom Synclinorium is located along the northern margin of the dome and is considered part of the ring syncline around the central uplift structure. The dome is well exposed in its northern and western sectors but widely covered by Mesozoic sedimentary strata and volcanics of the Karoo Supergroup in the eastern and southern sectors. The Vredefort Dome comprises an about 40-km-wide *core* composed of crystalline rocks of the Archean Basement Complex (>3.1 Ga; see, e.g., Lana et al., 2003, 2004), as well as a 20–25 km wide *collar* of younger (3.07 to ~2.10 Ga), meta-sedimentary and -volcanic rocks of the Dominion Group and the Witwatersrand, Ventersdorp, and Transvaal supergroups (e.g., Johnson et al., 2006). Both core and collar contain mafic intrusions that have been attributed to the 2.71 Ga Ventersdorp, 2.06 Ga Bushveld, and 1.1 Ga Kibaran-Umkondo events (Beaton et al., 2022; Gibson & Reimold, 2008; Pybus, 1995; Reimold et al., 2000). In addition, several ultramafic or peralkaline granite intrusions occur in the collar region, which have been correlated with the Bushveld magmatic event (Figure 1; Gibson, 2019; Reimold & Koeberl, 2014).

The Archean Basement Complex of the core of the dome is dominated by trondhjemitic and granodioritic to granitic gneisses, granodiorites, and granites. Tonalitic gneisses are relatively rare and appear to be confined to the innermost zone at granulite metamorphic grade, where subsidiary mafic, ultramafic, metapelitic, and meta-ironstone xenoliths, possibly as old as 3.5–3.4 Ga, occur as well (Armstrong et al., 2006; Gibson, 2019; Gibson & Reimold, 2008; Hart et al., 1981; Lana et al., 2004). The collar rocks include meta-lavas (in the literature also referred as meta-dolerite) of the Dominion Group; quartzite, conglomerate, metapelites, and banded iron formation of the Witwatersrand Supergroup; hypabyssal volcanics of the VS; and carbonate and arenites of the Transvaal Supergroup (Gibson & Reimold, 2008). The Dominion Group is a volcano-sedimentary sequence of 3.07 Ga age, which is stratigraphically positioned directly above the Archean Basement and below the Witwatersrand Supergroup (Gibson, 2019). Dominion Group is best exposed at the western margin of the Witwatersrand Basin, but also along the inner collar of the northwestern/western sectors of the Vredefort Dome (Jackson, 1992, 1994). The collar strata are intruded by sills of dioritic composition, which have been referred as *epi*diorite for their metamorphic overprint (e.g., Pybus, 1995). They have been repeatedly related to the 2.71 Ga Ventersdorp Supergroup (Pybus, 1995; Reimold et al., 2000). Mafic sills of likely Bushveld age also occur in the collar sequence and in the Transvaal Supergroup sedimentary strata of the outer collar and in the ring syncline around the Dome (Gibson, 2019). A larger mafic complex in this outer zone is the Losberg Complex, which Coetzee and Kruger (1989) considered a former part of the Rustenburg Layered Suite of the Bushveld Complex. All the so far referred strata and complexes in the collar and outer parts of the Vredefort Dome predate the impact event and are affected by shock metamorphism and, in many cases, macro- to mesoscopic occurrences of impact-generated pseudotachylitic breccia, or by shatter cones.

The Vredefort Dome experienced post-impact temperatures that increase from the collar toward the center of the structure, with metamorphic conditions progressing inward from greenschist to granulite facies. They are interpreted to reflect a combination of the centripetally increasing effects of shock heating and uplift of progressively deeper crustal levels as a consequence of impact (Allen et al., 2022; Gibson, 2019; Gibson & Reimold, 2005; Ivanov, 2005). Numerical modeling (Allen et al., 2022; Ivanov, 2005) showed that the rocks increase in post-shock temperature overprint radially inward from ~300°C in the collar rocks to >1000°C in the lithologies at the center of the dome, in good agreement with the shock petrographic findings of Gibson and Reimold (2005). Beaton et al. (2022) recently provided a detailed analysis

of metamorphic overprints in the collar of the Vredefort Dome and concluded that the regional Ventersdorp volcanism on the central Kaapvaal craton at about 2.7 Ga was likely responsible for lower amphibolite to upper greenschist facies metamorphism that affected the collar strata prior to the impact event.

METHODOLOGY

Field Work and Petrography

Field work (Figure 2a–e) was supported by previous geological maps (mainly Bisschoff, 1999), as well as satellite imagery (Landsat 8; GoogleEarth). Granophyre samples were collected along the dike on Rensburgdrif and neighboring farms at the dike margins and in the inner part, and from a second dike on Farm Rietkuil. Target rocks (epidiorite, Dominion Group meta-lava [DGL], and granite gneiss from the Archean basement) were collected from outcrops near the dike on Rensburgdrif (Figure 3).

In all, 26 polished thin sections of the Granophyre varieties and host rock types (epidiorite and DGL) were investigated using a Zeiss Axiophot polarizing microscope. Three samples (one each of Mafic Granophyre, Felsic Granophyre, and epidiorite) were selected for electron probe microanalysis of the main minerals, that is, plagioclase, pyroxene, and amphibole. These analyses were performed at the Naturhistorisches Museum Wien with a field-emission electron micro-analyzer of the type JEOL JXA 8530-F, equipped with five wavelength-dispersive spectrometers and two energy-dispersive spectrometers. Operating conditions were 15 kV acceleration voltage, 20 nA beam current, and a variably focused electron beam, depending on the nature of the investigated phase, from fully focused with a nominal spot size of <1 μm up to 6 μm (defocused mode) for glass and alkali-rich feldspar. Detection limits for major elements are as follows: 136 ppm for Na, 115 ppm for Mg, 124 ppm for Al, 151 ppm for Si, 83 ppm for K, 169 ppm for Ca, 261 ppm for Mn, 297 ppm for Ti, and 294 ppm for Fe. Instrument calibration was achieved with natural and synthetic in-house reference materials (NaCl, olivine, Al_2O_3, KCl, wollastonite, tephroite, TiO_2, and troilite), and ZAF corrections were applied. The instrument was also used to collect high-resolution back-scattered electron (BSE) images. The electron microprobe results can be obtained from the corresponding author upon request.

Sample Processing and Major and Trace Element Geochemistry

In all, 27 samples were crushed and pulverized using tungsten carbide ware at the Geochronology Laboratory of the Institute of Geosciences of the University of Brasília (UnB). Quantitative major and trace element concentrations were determined on sample powders at the Laboratoire G-Time of the Université Libre de Bruxelles (ULB), using inductively coupled plasma optical emission spectrometry (ICP-OES) and mass spectrometry (ICP-MS). Around 50 mg of powdered samples was weighed and mixed with ~1 g of a 4:1 ultrapure lithium metaborate (Li_2O)-tetraborate ($Li_2B_4O_7$) mixture by hand shaking. The mixtures were fused in graphite crucibles in a muffle furnace at 1000°C for 10 min. After cooling down, the resulting glass beads were dissolved in 50 mL of 2N HNO_3 using stirring magnets for 5 h. In all, 24 of these samples were analyzed at Brussels, the remaining three samples (denominated NWU) were analyzed commercially at SGS GEOSOL (see Supplementary Material).

At Brussels, following aliquoting, appropriate dilution, and the addition of yttrium (Y) as internal standard, all major element concentrations were determined by quantification versus external calibration curves constructed using multi-element standard solutions of Si, Mg, Fe, Al, Ca, Na, Ti, K, P, Mn, and Cr on the Thermo Scientific iCAP Series ICP-OES at the ULB. Trace element concentrations were determined in a similar way on the same digested sample solutions using an Agilent Technologies 7700 Series ICP-MS at the ULB, after aliquoting, adequate dilution, and the addition of an indium (In) internal standard. Oxide production was evaluated and corrected using standard element solutions of Pr and Nd, as well as of Ba and Ce. Besides samples and replicates, international reference basalt BHVO-2 and andesite AGV-2 of the U.S. Geological Survey with certified chemical compositions were used to evaluate the accuracy and precision of the applied procedures. Based on the measurement of BHVO-2 replicates, the external reproducibility expressed as relative standard deviation (RSD) is better than 5% for most major and trace elements, except for K, Rb, and Lu, for which they are better than 10%, 7%, and 10%, respectively. Loss on ignition (LOI) was determined by weighing 0.5 g of sample into a ceramic crucible that was heated to 1000°C in a muffle furnace for 1 h. After cooling down to room temperature, the samples were weighed again to determine the weight percent (wt%) of lost volatiles.

Strontium and Neodymium Isotopic Analysis

As indicated in Tables 2 and 3, isotopic analyses were obtained at the University of Brasília (UnB), as well as at the University of Cologne and the University of Vienna. Whenever a sample was analyzed in duplicate, the results were in all cases highly comparable (see Tables 2 and 3).

(a)
(b)
(c)
(d)
(e)

FIGURE 2. Field impressions from the Granophyre dike on farm Rensburgdrif. (a) A general view of typical, discontinuous outcrop of Granophyre near the Rensburgdrif homestead. Hammer, for scale, 35 cm long. (b) Flat outcrop of the clast-poor lithology with mostly sub-cm sized clasts that, at this location, are mostly felsic. Coin for scale about 2 cm in diameter. (c) A quartzite clast with fluidal texture and irregular shape, both indicating that this clast was strongly plasticized upon entry into the superheated impact melt. South African 50-cent coin, for scale, 2.2 cm in diameter. (d) Clast-poor Granophyre with a several centimeter-sized mafic clast (dashed outline). Hammer tip for scale about 9 cm long. (e) Clast-poor Granophyre with two sets of joints parallel (the E-W trend in this photo) to and oblique to dike extension. Note the sizable mafic clast just NE of the coin, the large quartzitic clast in the lower right corner, and the somewhat elongated granitic clast in the northwest corner. For scale, a South African One-Rand coin of 2.2 cm diameter. (Color figure can be viewed at wileyonlinelibrary.com)

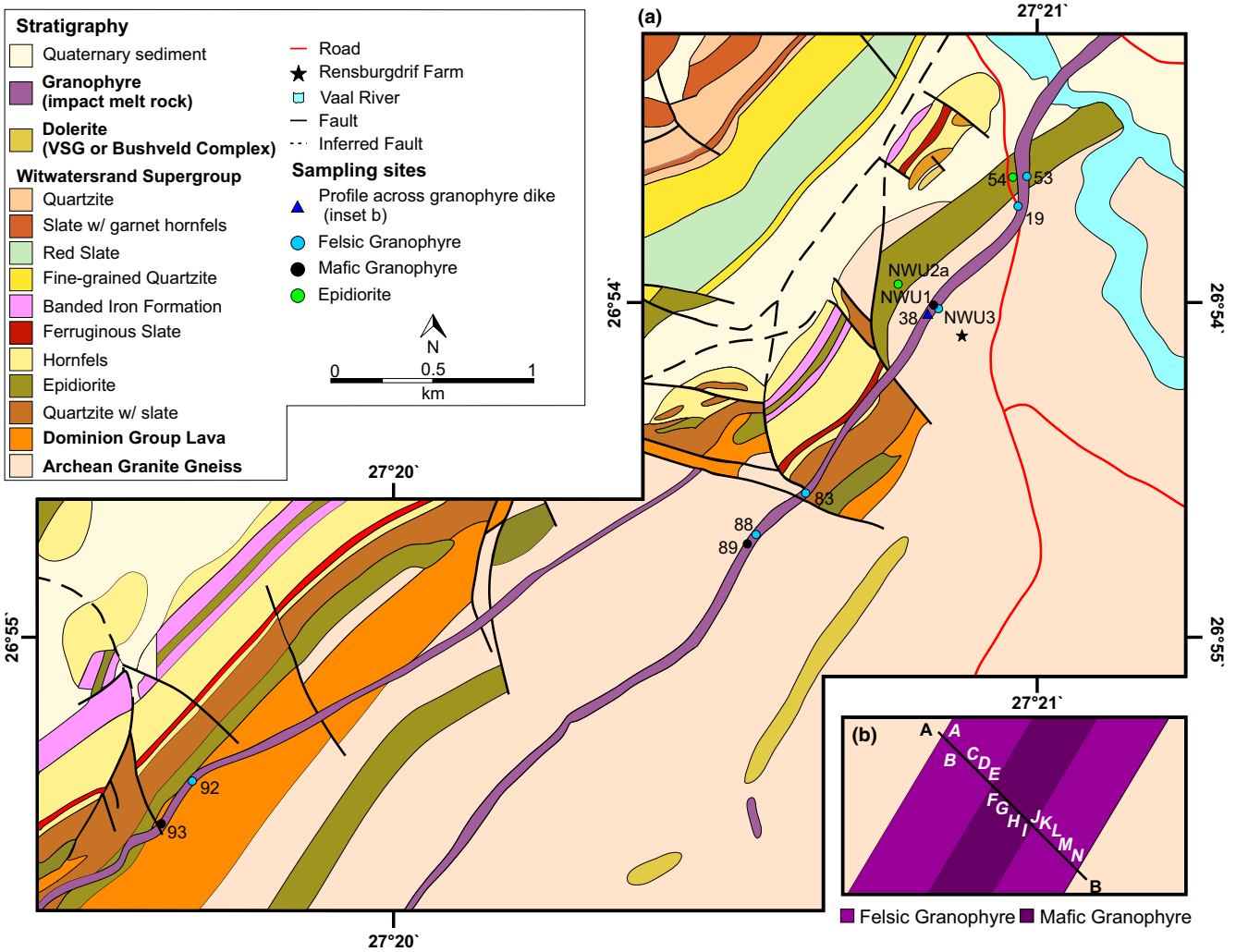

FIGURE 3. (a) Geological map (based on the 1: 50,000 geological map of Bisschoff, 1999) of the study area on Rensburgdrif Farm and neighboring properties, southwest of the Vaal River. A second Granophyre dike was visited on the Rietkuil property of the Johannesburg Zoo (in the lower left part of the map area). The sampling sites from this investigation are shown, whereby location numbers also represent the respective sample numbers. VSG (in legend) refers to Ventersdorp Supergroup, and the referred dolerite has not been correlated with the VSG or the Bushveld Complex intrusion phases. (b) Inset with a schematic representation of the profile samples across the dike on Rensburgdrif (Location 38). The section is not to scale. Sample numbers given below the black profile line are of the Mafic Granophyre phase (compare chemical abundance patterns in Figure 6). (Color figure can be viewed at wileyonlinelibrary.com)

Analyses at the University of Brasília

The samples were washed, and weathered parts were removed. Then remaining sample material was crushed and pulverized to a fine powder. After sample digestion, an aliquot of solution was directly loaded onto Teflon® columns containing approximately 83 mg of Eichrom®

Sr-Spec resin (50–100 μm) to separate the Sr fraction from the matrix. Rubidium concentration was not determined during this work. Strontium and Sm-Nd isotopic compositions of selected samples were determined using a Thermo Scientific TRITON™ Plus Thermal Ionization Mass Spectrometer (TIMS). The average $^{87}Sr/^{86}Sr$ obtained for the NBS-987 standard was 0.71029 ± 0.00001 and 0.71028 ± 0.00002 (2SD within run). This value agrees well, within uncertainty, with the most typically recommended value of 0.71034 ± 0.00026 (2s) of the National Institute of Standard and Technology. Mass bias was corrected by normalizing to $^{88}Sr/^{86}Sr = 8.3705209$. Rubidium interference was corrected using exponential law and the natural ratios of $^{85}Rb/^{87}Rb = 2.592310$.

The isotope dilution method for Sm-Nd isotopic analysis, separation procedures and analytical method applied at UnB were reported by Gioia and Pimentel (2000). Approximately 50 mg of rock powder was mixed with $^{149}Sm/^{150}Nd$ rapid solution and dissolved in Savillex capsules. All whole rock samples used for Sm-Nd extraction were subjected to conventional cation exchange techniques based on Teflon® columns containing LN-Spec resin (liquid resin HDEHP—Di-[2-ethylhexyl] phosphoric acid supported by polytetrafluoroethylene powder). The Sm and Nd fractions of 13 samples were extracted on Teflon columns and then loaded onto double evaporation filaments on the TRITON instrument. The average $^{143}Nd/^{144}Nd$ ratio obtained for the USGS BHVO-2 standard was 0.512970 ± 0.000002 (2s), which is consistent with recently published values (0.512979 ± 0.000028; 2SD; Jochum et al., 2016). Laboratory blanks were ~0.25 ng for Nd and ~0.04 ng for Sm. The uncertainties on Sm/Nd ratios and $^{143}Nd/^{144}Nd$ ratios were better than ±0.5% (2s) and ±0.005% (2s), respectively, based on repeated analyses of the BHVO-2 and BCR-1 rock standards.

Four samples (ARp-38A, ARp-38G, ARp-38I, and ARp-38L) were also analyzed in solution using a Thermo-Fisher Neptune MC-ICP-MS instrument at the University of Brasília. The samples were introduced into the spectrometer using a nebulizer with a flux of 100 μL min^{-1}. For Sm, the tuned masses were ^{146}Nd, ^{147}Sm, ^{148}Sm, ^{149}Sm, ^{150}Sm, ^{152}Sm, and ^{154}Sm. Five blocks of 10 cycles each with an integration time of 4.194 s were considered for each analysis. For mass bias correction, data were normalized to $^{147}Sm/^{152}Sm = 0.556083$. For Nd, the tuned masses were ^{142}Nd, ^{143}Nd, ^{144}Nd, ^{145}Nd, ^{146}Nd, ^{147}Sm, ^{148}Nd, and ^{150}Nd. Five blocks of 10 cycles each with an integration time of 4.194 second were considered for each analysis. After subtracting any (rare) ^{144}Sm interference, $^{143}Nd/^{144}Nd$ ratios were corrected for instrumental mass fractionation using the exponential law and assuming $^{146}Nd/^{144}Nd = 0.7219$.

The average $^{143}Nd/^{144}Nd$ ratio obtained for the Neptune solution standard (50 ppb Nd) was 0.512391 ± 0.00005 (2s; $n = 10$), which is consistent with accepted values (0.51239 ± 0.00003; 2s). Neodymium blanks were <100 pg.

Analysis at the University of Cologne

Two samples were analyzed for Rb-Sr (AR-53 and AR-54) and three samples (ARp-38G, ARp-38I, and Arp-38L) for Sm-Nd isotope systematics at Institut für Geologie und Mineralogie, Universität zu Köln (Cologne). Powder aliquots of 100 mg were weighed into Savillex vials and appropriate amounts of ^{87}Rb–^{84}Sr and ^{149}Sm–^{150}Nd mixed isotope tracers were added. Subsequently, the samples were digested using the high-pressure acid digestion procedure for felsic samples described by Hoffmann et al. (2011). In the first step, the samples were digested in 6 mL 14 M HNO_3/24 M HF (1:1) for 24 h on a hotplate at 120°C. Subsequently, the sample solutions were dried down and redigested in a (1:1) 14 M HNO_3/24 M HF mixture at 180°C using Parr pressure vessels for 2 days. Following this, the digestion solutions were dried down, redissolved, and dried down again in concentrated HNO_3 (3 times), and then redissolved in 6 M HCl. For the chemical separation of Rb, Sr, Sm, and Nd, well-established analytical procedures as described in Nebel et al. (2005) for Rb-Sr and Pin and Zalduegui (1997) for Sm-Nd were used. Total procedural blanks were <200 pg for Sr, <70 pg for Rb, <39 pg for Nd, and <19 pg for Sm.

Neodymium and Sr isotope compositions and isotope dilution measurements for Sm, Nd, Rb, and Sr concentrations were conducted on a Thermo Fischer Neptune© MC-ICP MS. Using the exponential law, measured ratios of $^{87}Sr/^{86}Sr$ and $^{87}Rb/^{85}Rb$ were normalized to $^{86}Sr/^{88}Sr = 0.1194$ and $^{91}Zr/^{90}Zr = 0.21795$ of doped Zr, respectively (Nebel et al., 2005). Strontium isotope results are given relative to an $^{87}Sr/^{86}Sr$ ratio of 0.710240 for NBS 987. Rubidium was measured relative to NBS 984 ($^{87}Rb/^{85}Rb = 0.38554$). Measured Nd isotope ratios were normalized to $^{146}Nd/^{144}Nd = 0.7219$ using the exponential law, and results are given relative to a $^{143}Nd/^{144}Nd$ of La Jolla of 0.511859. The long-term reproducibility of Nd isotope measurements is 40 ppm (2 RSD). The external reproducibility for $^{147}Sm/^{144}Nd$ is ≤0.2% (2 RSD).

Analysis at the University of Vienna

Three samples (Mafic Granophyre NWU-1, epidiorite NWU-2a, and Felsic Granophyre NWU-3) were analyzed at the Department of Lithospheric Research (University of Vienna, Austria). Rock powders (approximately 50–100 mg) were digested in tightly screwed Savillex beakers using an ultra-pure mixture of HF:HNO_3 at a 4:1 ratio for 2–4 weeks at 100–120°C on a hot plate, to make sure the

insoluble phases, such as zircon, were fully digested. After acid evaporation, repeated treatment of the residue using 6 M HCl resulted in clear solutions. Element isolation for Sr and rare earth elements (REE) was performed using AG 50W-X8 (200–400 mesh, BioRad) resin and 2.5 and 4.0 M HCl as eluants. Neodymium was separated from the REE group using Teflon-coated HDEHP and 0.22 M HCl as eluant. Maximum total procedural blanks were <1 ng for Sr and 40 pg for Nd, which can be considered negligible for the purpose of this work. The isolated element fractions were loaded onto a Re double filament assembly and run in static mode on a Thermo-Finnigan Triton TIMS instrument. Mass fractionation was corrected for $^{88}Sr/^{86}Sr = 8.3752$ and $^{146}Nd/^{144}Nd = 0.7219$, respectively. Samples were measured in two successive batches. Mean $^{87}Sr/^{86}Sr$ of 0.710260 ± 0.000004 (batch 1, $n = 5$) and 0.710257 ± 0.000006 (batch 2, $n = 5$) were determined for the NBS 987 (Sr) and mean $^{143}Nd/^{144}Nd$ ratios of 0.511846 ± 0.000003 (batch 1, $n = 5$) and 0.511841 ± 0.000002 (batch 2, $n = 5$) for the La Jolla (Nd) international standards during the period of investigation. Uncertainties quoted represent 2σ errors of the mean. The isotopic ratios $^{87}Rb/^{86}Sr$ and $^{147}Sm/^{144}Nd$ were derived from Rb/Sr and Sm/Nd ratios obtained following Rb–Sr and Sm–Nd concentration measurements performed by XRF and INAA, respectively. The assigned uncertainties to $^{87}Rb/^{86}Sr$ and $^{147}Sm/^{144}Nd$ are 1 and 7%, respectively, with an uncertainty on Rb, Sr, Sm, and Nd determinations of 1, 0.4, 2, and 5%, respectively (Mader & Koeberl, 2009; Nagl & Mader, 2019; Son & Koeberl, 2005).

A General Comment

Rb-Sr and Sm-Nd isotopic ratios for all Felsic and Mafic Granophyre samples and potential precursor rocks (i.e., epidiorite, granite, and DGL) were recalculated to the age of the impact event at 2.02 Ga (Kamo et al., 1996) (compare Tables 2 and 3). T_{DM} values were calculated based on the model by De Paolo (1981). The measured $^{143}Nd/^{144}Nd$ sample ratios are expressed in epsilon notation (ε_{Nd}) as the fractional deviation in part per 10^4 (units) from the $^{143}Nd/^{144}Nd$ value of the Chondritic Uniform Reservoir. All quoted errors on isotope data are 2 sigma standard deviations.

RESULTS

Field Observations

A map of the general study area, including the Rensburgdrif and the Rietkuil properties, is shown in Figure 3. This map is based on the Geological Map of the Vredefort Dome by Bisschoff (1999). The map section illustrates the two Granophyre dikes along the core-collar boundary in the northwestern sector of the Vredefort Dome. Note that at Location 38 a profile of 14 samples was collected across the, at that locality, about 20 m wide dike (see inset, Figure 3b).

The northeast trending Granophyre dike on Rensburgdrif and neighboring farms straddles the boundary between the granitoid core (on the eastern side) and the metasedimentary collar of the Vredefort Dome (toward the northwest)—see Figure 1. The dike extends from Rensburgdrif toward the north-northeast across a portion of Farm Kommandonek and then across the Vaal River onto the Eldorado and Kopjeskraal properties. This dike was investigated over a length of 2.3 km on Farm Rensburgdrif from coordinates (UTM 35S) 536304E/7025546S to coordinates 535127E/7023569S. In addition, an about 500 m section further north on farm Kommandonek was visited.

On Rensburgdrif, the dike trends in a sinusoidal way in the general direction of ~N50E. Its width is variable but mostly the dike is 20–30 m wide in the study section. Exposures are either in the form of semi-continuous, more massive sections, or more discontinuous (Figure 2a). Some of the dike segments are more curved and/or delineated on surface by up to meter-sized boulders (Figure 2b–e). Outcrops occur at different topographic levels, with an overall slope gradient of about 50 m.

Further observations were made near the southwestern end of a second dike (compare Figures 1 and 3) that crosses farm Rietkuil to the southwest of Rensburgdrif, in the general area around 531646E/7021491S. The reason for this, as yet, cursory visit to this site was that according to the geological map of Bisschoff (1999), a Granophyre dike was supposed to cut epidiorite in that area of the western collar of the Vredefort Dome. It was realized later that Therriault et al. (1996) had presented a chemical analysis for a sample (their number VAT-156) from the southern end of that dike, which indicated a rather unusual, more mafic composition with only 64.3 wt% SiO_2. At the time, Mafic Granophyre was not known yet. On Rietkuil, field access was severely limited due to the game-based operations of the landowner, the Johannesburg Zoo. Granophyre was observed in a series of blocky outcrops in an area of about 400 × 400 m. Contrary to the base map, only quartzite could be identified as country rock at this site. However, further dedicated mapping of this second dike is required—also because during our work we identified one of our samples from that dike as Mafic Granophyre (see below, "Geochemistry" Section). The impact melt rock observed at this location in the field is generally very fine-grained, with mostly small (<2 cm) clasts. No indication was noted in the field that a second variety of Granophyre could occur in this area. Two samples (AR-92 and -93; Figure 3) were collected for laboratory analysis.

On Rensburgdrif, the dike is of variable width but mostly 20–30 wide in the study section. Exposures are in the form of semi-continuous, more massive sections, or more discontinuous (Figure 2a), and some of the dike segments are more curved, and/or delineated on surface by up to meter-sized boulders (Figure 2b–e). The main country rocks in the study area are Archean granite–gneiss, epidiorite, and more locally, meta-lava of the Dominion Group. Granite–gneiss is the most common host rock to Granophyre along the studied extent of the dike. The granite–gneiss is mostly medium grained and has a typical granitic composition of hypidiomorphic alkali-feldspar, plagioclase, quartz, and biotite. The rock presents a gneissic texture with leucosome-rich stromatic migmatite in places, containing granitic leucosome and trondhjemitic melanosome. Contacts between host rock and dike are generally not exposed but can be traced locally to occur as close as <1 m from the exposed margin of the dike.

The studied Granophyre dike only transects epidiorite directly close to the southern bank of the Vaal River (536213E/7025581S) in the northeastern-most part of the study area on Farm Kommandonek (Figure 1). Here, outcrops of epidiorite are scarce and on surface strongly weathered, and they are often located in dense bush. Epidiorite has a medium-grained granoblastic texture of mainly amphibole and plagioclase and shows fractures perpendicular to the regional NE–SW strike trend of the dike. DGL is not well exposed in the study area, with only a few outcrops or boulders south of a fault (534995E/7023458S). The fine-grained, dark-gray rock consists of pyroxene, amphibole, quartz, and feldspar. Locally, a slight foliation is noted. This lithology has been described from the Vredefort Dome in detail by Jackson (1992, 1994) and in wider regional occurrence by Marsh (2006). Granite–gneiss and epidiorite contain veinlets of pseudotachylitic breccia (PTB) of up to 10 cm width, and network PTB occurrences of up to meter extent, with well-rounded clasts, occur in epidiorite and DGL. Excellent exposures of the latter type are also found near the homestead on Farm Kopjeskraal in DGL.

The contact between the Granophyre dike and epidiorite on Farm Rensburgdrif is not exposed. The closest epidiorite occurrence is about 80 m from the dike at 536144E/7025150S. These extensive epidiorite exposures feature also meter-sized occurrences of pseudotachylitic breccia with well-rounded, decimeter sized clasts of the country rock set into aphanitic PTB. Where the Granophyre dike cuts granite–gneiss, the contact is frequently irregular. Fractures, joints, and color changes are observed in the host rocks closest to the contact with the dike, which could indicate that the Granophyre intrusion affected the wall rocks both mechanically and thermally.

The Granophyre occurs as two distinct textural phases. The first one, occurring generally along the dike margins, is medium grained (0.5–0.8 mm grain size) and hosts abundant clasts primarily derived from granite (85%), with minor contributions from quartzite and shale (together 10%), and epidiorite or other, unidentified mafic lithologies (<1%). The second texturally distinguished phase occurs locally in parts of the inner part of the dike and is finer grained (<0.5 mm) and seemingly slightly darker than the other phase (noted in hand specimen). However, it must be emphasized that it has not been possible to identify contacts (distinct or gradational) between the two phases in the field.

The finer-grained phase is dominated by smaller clasts (see Figure 2b,e) compared with the first phase, but visible clast types are derived from the same main country rock varieties, and at similar proportions, as observed for the first type. These two Granophyre phases seemingly run parallel to each other, and parallel to the assumed contact between the dike and the host rock. Over its entire extension, the dike is not homogeneous with respect to amount, average size, and geometry of clasts, as well as flow patterns that are indicated by the alignment of matrix minerals and small clasts of granite and quartzite. Dike margins are generally rich in visible clasts, which are elongated and angular, up to 15 cm but mostly <5 cm in length, and often show elongation parallel to the dike margin. Most elongate clasts are aligned parallel to the strike of the dike. In contrast, the inner portions of the dike seem to be comparatively more clast-poor (Figure 2e). Here, fragments are more rounded and only up to 3 cm in size. Overall, in the dike, large clasts (10–30 cm in size) are considerably less abundant (<2%) than clasts <5 cm in size, which make up 10% estimated over the entire dike section mapped. Some elongated clasts of quartzite or granitoid have fluidal shapes, such as a quartzitic clast in Figure 2c, the shape of which is clearly the result of plasticity imparted when the clast was entrained in presumably superheated impact melt.

Large-scale impact melt generation requires that a very large volume of target rock is subjected to shock pressures of 60–100 GPa (e.g., Allen et al., 2022; French, 1998; Ivanov, 2005), as illustrated by the Sudbury Igneous Complex impact melt body (Lightfoot, 2016) and as also to be assumed in the case of the Vredefort impact, where remnants of impact melt rock are exposed still today over an area of 2000 km^2, the entire terrain of the Vredefort Dome (e.g., Reimold & Koeberl, 2014). The resulting post-shock temperatures are in the order of 1500–2500°C, clearly sufficient to melt quartzite (as obvious from the numerous completely annealed quartzite clasts in Granophyre). Such temperatures would also be sufficient to melt epidiorite or DGL country rock. As shock pressures/post-shock temperatures are not homogeneous

over large rock volumes, not even at microscopic scales, there is always a possibility to have relics of unshocked or moderately shocked target rock mixed with impact melt. This is irrespective of later (post-shock compression–decompression stage) mixing of unshocked or less strongly shocked material of the transient cavity with impact melt, or mixtures established between impact melt and comparatively cool material of the crater floor—during post-impact emplacement of melt. That Vredefort impact melt was still superheated when stoped into the central uplift rock to depths of up to 10 km must be assumed, too. Otherwise, the thermal effects (ranging from melting to partial annealing) on Witwatersrand quartzite clasts that are abundantly observed within Granophyre from the current exhumation level would not be so prevalent—in comparison with minor amounts of quartzite clasts entirely lacking shock metamorphic effects or only showing weak shock deformation.

Notably, it was observed in the field that clast-poor Granophyre frequently displays sizable mafic clasts (examples shown in Figure 2d,e); however, the clast-rich variety occasionally contains mafic clasts with sizes up to 5 cm as well—although at a much lower proportion in comparison to the clast-poor type.

Several sets of joints were observed along the dike with different orientations: vertical and parallel to the strike of the dike, horizontal and perpendicular to the dike walls (Figure 2d), and in two directions oblique to the walls of the dike and dipping in the direction of its strike. A few joints show displacement of up to 10 cm; some are filled with quartz. Individual clasts within the dike are often substantially fractured. Shear zones are entirely absent. Different joint orientations had also been recorded on Rensburgdrif by Reimold et al. (1990). No PTB veinlets were observed along this section of the Granophyre dike, whereas a single such vein had been reported from this property by those authors.

Petrography

Based on chemical composition, samples of the clast-rich phase identified in the field were classified as so-called "Felsic Granophyre"—chemically defined as impact melt rock with >66 wt% SiO_2 (see section Geochemistry). Samples of the clast-poor variety are classified as "Mafic Granophyre" with <66 wt% SiO_2 (see Reimold et al., 2017; Wannek, 2015). In the present section, optical and electron microscopic observations are reported for these Granophyre types, epidiorite, and DGL.

Felsic Granophyre

Felsic Granophyre from Rensburgdrif has a very fine-grained matrix of orthopyroxene, plagioclase, orthoclase, quartz, biotite, and opaque minerals (magnetite and ilmenite). Feldspar minerals and quartz abundantly form micropegmatitic clusters in the groundmass (e.g., Figure 4a). Lithic clasts are mainly derived from granite and quartzite, with minor contributions from shale, and—rarely—a medium-grained dioritic rock. The proportion of groundmass varies from 30 to 40 vol%. Some of the fine-grained minerals in the matrix may actually represent remnants of completely annealed microclasts.

The Felsic Granophyre displays a relatively homogeneous modal composition, but there are textural variations related to varied abundances of the main modal components. Felsic Granophyre samples have fine-grained matrix with short-prismatic (100–300 μm), zoned pyroxene crystals, and with plagioclase laths (800–1200 mm). Interstitial areas consist of granophyric intergrowth of quartz and mostly alkali feldspar. This kind of intergrowth often displays rosette and radial symplectite-like patterns (Figure 4a). Accessory apatite occurs in the form of fine needles, and accessory titanite as tiny, euhedral crystals. Many pyroxene crystals are partially altered to amphibole and biotite. Some portions of the groundmass are rich in annealed quartz—likely remnants of *part-melted* granitic or quartzitic microclasts. The term *part-melting* should not be confused with partial melting. In the former case, a part of a protolith is melted by the shock process, irrespective of the regular processes related to magmatic partial melting (dependent on temperature increase, pressure decrease, presence of fluids, in relation to the different melting temperatures of minerals).

Most of the lithic clasts are extensively recrystallized to finest-grained mosaics of felsic minerals. However, it is still frequently possible to determine the contact between clasts and matrix. Inclusions of metasedimentary rocks are fine- to medium-grained, angular, usually show a clastic texture, and are predominantly composed of quartz, with minor amounts of feldspar, and form sub-rounded inclusions in Granophyre groundmass. Granitoid clasts may still indicate igneous texture and are composed of rounded relic quartz grains and feldspar (more alkali feldspar than plagioclase) that may display local melting at grain boundaries. In remnant, not completely annealed quartz clasts it is sometimes possible to notice evidence of shock metamorphism, such as undulatory extinction and mosaicism. Remnant PDFs were not observed in this study. Both vermicular texture indicative of incipient melting of quartz crystals (Buchanan & Reimold, 2002) and checkerboard texture in plagioclase of granitoid clasts illustrate part melting. Some pyroxene crystals are chemically zoned, as illustrated in BSE images. A rare mafic clast with amphibole, biotite, and pyroxene around a mosaic of fine-grained quartz crystals with droplets of opaque phases is shown in Figure 4f. This assemblage clearly represents a mafic clast that was assimilated into the

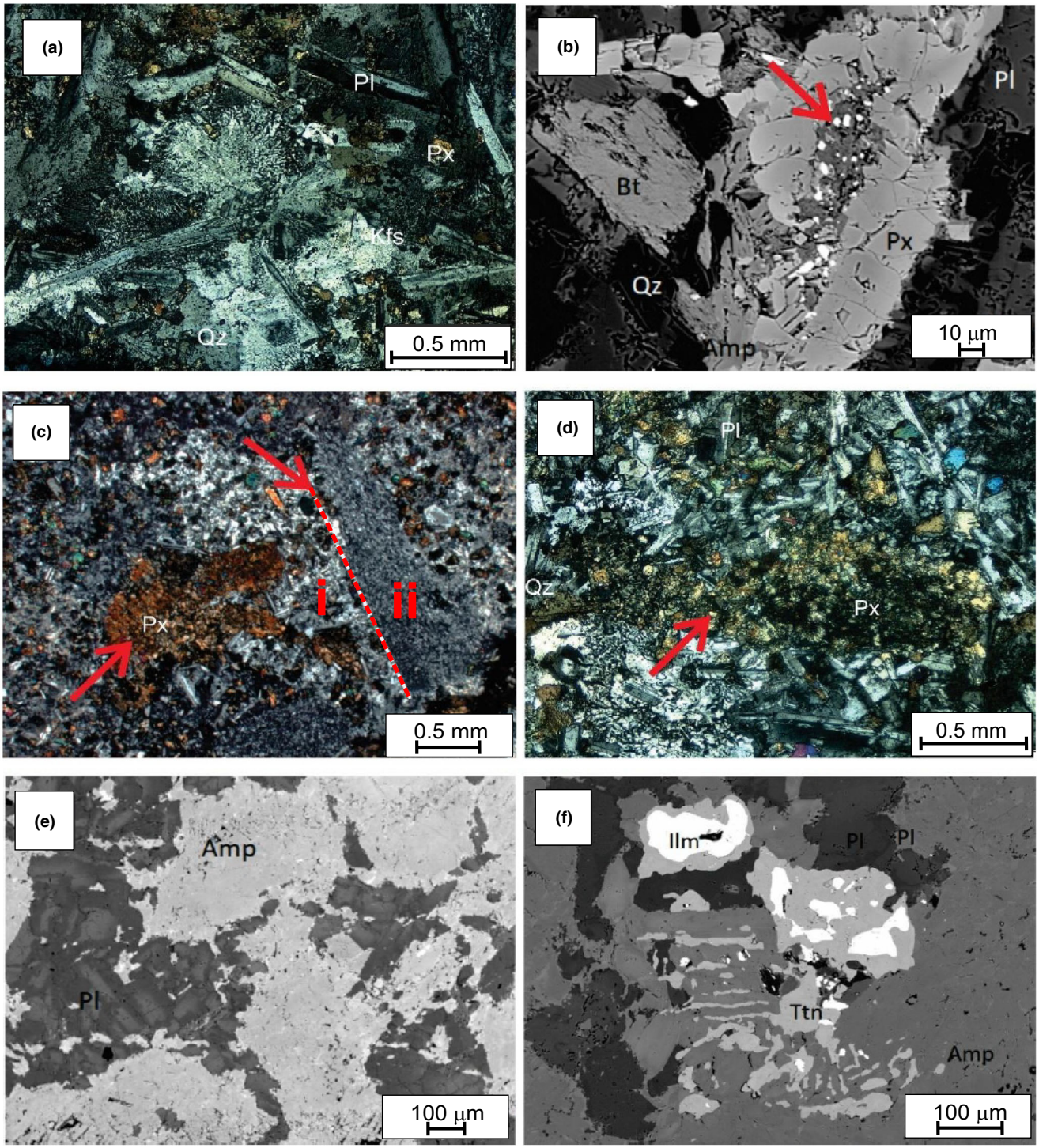

FIGURE 4. Selection of microphotographs and BSE images from samples of the main lithologies of this work. (a) Felsic Granophyre matrix of large plagioclase laths and short prismatic hypersthene crystals. Interstitial areas are composed of microgranophyric intergrowths of quartz and feldspar (both plagioclase and K-feldspar). (b) Pyroxene (Px), biotite (Bt), quartz (Qz), and amphibole (Amp) crystals in matrix of Felsic Granophyre. The red arrow emphasizes the numerous tiny droplets of opaque phases, indicating at least part-melting of this material. This assemblage is strongly suggestive of relic mafic clast material. (c) Mafic Granophyre with a polymineralic clast including a large pyroxene crystal (red arrow at left) and two felsic crystals that are entirely annealed to different textures in domains I and II (separated by the dashed red line). The matrix in the

environs of this clast is microcrystalline and contains tiny crystals of pyroxene (brownish) as well as feldspar and quartz. (d) Matrix in Mafic Granophyre with a mafic clast (marked by red arrow) that mostly consists of small crystals of pyroxene. The surrounding matrix consists mostly of small plagioclase laths and pyroxene crystals. In the lower left, a checkerboard feldspar clast is visible. (e) BSE image from an epidiorite sample, with amphibole crystals that display comparatively compact cores and outer porous zones that seemingly have experienced alteration. (f) Another BSE image from an epidiorite sample, with ilmenite (Ilm), titanite (Ttn), amphibole (Amp), and plagioclase (dark gray) with irregular crystal shapes. This assemblage may represent secondary products after alteration/metamorphic overprint of primary amphibole. The relatively larger amphibole crystal on the right not only contains amoeboid relics of titanite, but also tiny inclusions of feldspar (dark gray) and quartz (black). (Color figure can be viewed at wileyonlinelibrary.com)

Granophyre groundmass. There are also abundant micropegmatitic patches with relics of plagioclase or microperthitic K-feldspar that likely originate from quenched crystallized melt after granitic precursor material. These patches frequently contain roundish, fine-grained mosaic-textured, quartzitic-appearing patches that would represent a silica melt that was also recrystallized.

Mafic Granophyre

Mafic Granophyre samples possess the typical granophyre texture—but of the granular type with short-prismatic orthopyroxene crystals set into feldspar laths and micropegmatitic intergrowths. Mafic Granophyre (i.e., clast-poor Granophyre) has more plagioclase and orthopyroxene than the felsic type. Pyroxene crystals are zoned and somewhat larger (200–400 μm) than in Felsic Granophyre. Subhedral crystals of quartz and feldspar (400–800 μm) are prominent. Ophitic intergrowths of prismatic pyroxene and blade- or lath-shaped plagioclase crystals and micropegmatitic quartz and K-feldspar pockets in groundmass are typical for this Granophyre variety. The few biotite crystals observed are subhedral to euhedral, and they often include anhedral to euhedral magnetite and ilmenite crystals. Some pyroxene is replaced by biotite, amphibole, and chlorite. Mafic Granophyre contains the same clast types as the felsic phase. However, additionally, some lithic clasts composed of fine-grained aggregates of euhedral mafic crystals occur that have not been reported from Granophyre previously. These mafic clasts have sizes of up to 2 mm, are variably angular to rounded, and have irregular margins. Two examples of such clasts are shown in Figure 4c,d. BSE imaging shows that amphibole occurs as a secondary product of uralitization of pyroxene in Mafic Granophyre. In this melt rock type, pyroxene is much more altered than in Felsic Granophyre. This observation was also reported by Wannek (2015) for the Mafic Granophyre from Farm Kopjeskraal. Mafic Granophyre samples contain a significant number of mafic lithic clasts, many of them containing recrystallized amphibole. Textures with relatively large, bladed amphibole crystals resemble the amphibole in epidiorite. In addition, small amphibole clasts are also frequently noted in the groundmass. Sample ARp-38F contains a large, centimeter-sized, completely recrystallized quartz–feldspar clast that clearly is derived from a granitic protolith. In addition to the Mafic Granophyre described from the ARp profile across the dike and sample NWU-1 from close to the profile, a sample collected on Farm Rietkuil (sample AR-93—see Figure 3) was revealed by chemical analysis as belonging to the Mafic Granophyre type. This sample did not reveal amphibole-bearing mafic clasts though. A noteworthy clast of epidiorite-like texture was observed in a thin section of NWU-1. This clast does not exhibit any thermal alteration. In contrast, a second thin section from this same sample displays a mafic clast that is entirely recrystallized. We consider it likely that this clast is derived from epidiorite as well, but further detailed mineral analysis is required on such mafic clasts to confirm this.

Up to 5-mm-sized amygdales are common in samples of both Granophyre varieties. They are commonly distorted by flow, and partially to completely filled with mostly opaque phases, besides some phyllosilicate. Reaction aureoles with pyroxene of the matrix are often observed around the vesicles.

Epidiorite

The texture of epidiorite in the study area is a product of metamorphism that has effectively obliterated the original igneous texture of the protolith. Epidiorite is mainly composed of amphibole (up to 60%) and plagioclase (30%), with additional 10% of biotite, quartz, and oxides. The rock is mostly medium-grained with ± 3mm crystal size. Most amphibole crystals are euhedral to subhedral, but there are also many crystals that have irregular margins and show strong alteration. Amphibole is interpreted as a secondary product of uralitization of primary subhedral augite crystals (in accordance with Pybus, 1995). Plagioclase crystals are euhedral to subhedral, and locally sericitized. Chlorite and epidote are sometimes observed as alteration products after amphibole. Apatite occurs as small, needle-shaped inclusions in plagioclase. In BSE images, the porous texture in the outer parts of crystals (Figure 4e) is interpreted as a result of metamorphic overprint. An assemblage of ilmenite, titanite, amphibole, and plagioclase with irregular crystal shapes and complex grain margins represents the secondary products of alteration and/or metamorphic overprint (Figure 4f).

Epidiorite has rare, millimeter-sized pockets of recrystallized quartz that could represent Witwatersrand Supergroup material assimilated during emplacement of dioritic sills. On the other hand, there is a second quartz occurrence in the form of tiny, volumetrically <1 vol%, quartz aggregates that are intimately intergrown with plagioclase laths and clearly represent a magmatic component.

One of our samples is cut by sub-millimeter wide veinlets of pseudotachylitic breccia, along the margins of which plagioclase and quartz have reduced birefringence and are partially annealed. The groundmass of these veinlets is aphanitic. No diagnostic shock effects have been observed in our samples of epidiorite. However, all studied samples have experienced thermal alteration, as in some cores of amphibole crystals partially melted/decomposed oxides were noted, including some in droplet/spherule form.

Dominion Group Meta-Lava

In the southern part of the study area (Figure 3), a sample (AR-78) was taken from DGL. Here the DGL forms a very fine-grained, amphibole, quartz, and plagioclase dominated rock. It is ubiquitously transected by sub-millimeter wide (occasionally 1–2 mm wide), brownish-grayish micro-veinlets. The groundmass of this meta-igneous rock has a very fine-grained to fine-grained ophitic to poikilitic texture of oikocrysts of amphibole with quartz and plagioclase chadacrysts. Microscopic quartz occasionally forms clusters of micro-crystals or indicates a poorly defined ribbon structure. The clusters may, at least in part, represent recrystallized quartzitic microclasts that were entrained into the lava. However, the meta-lava around the Vredefort Dome is also characterized by the occurrence of amygdales (the rock was originally classified as a "basal amygdaloid"—Nel, 1927), many of which are microscopic in size. Amphibole and felsic minerals occur in roughly equal proportions of 48% each, with the remainder made up of accessories such as local occurrence of sphene, apatite, and secondary minerals such as chlorite or finest-grained opaques.

Comparatively larger quartz crystals are in part shocked and contain single sets of well-developed, crystal-penetrative PDFs. No other diagnostic shock evidence was observed. The micro-veinlets often occur in more or less parallel sets with abundant microfractures. The veinlet fills sometimes indicate distinct shear deformation. The fill is entirely derived from the host lithology. Our optical microscopic observations suggest that these fills are cataclasite that, where shearing is distinct, is ultracataclastic. Whether there are local occurrences of a melt phase in this generally aphanitic material could not be ascertained. Between micro-veinlets and fractures, especially where their density is enhanced, the felsic minerals of the host have a distinctly turbid appearance caused by strong fracturing, reduced birefringence, and likely local alteration of this comminuted material. Further details about the Dominion Group in this part of the Dome are given by Jackson (1994), who also refers to findings of Hall and Molengraaff (1925) and Nel (1927).

The Profile Across the Granophyre Dike at Rensburgdrif Homestead

The profile sampled across the dike comprises a sequence of samples denominated A-L (compare Figure 3b). Sample A at the northwestern end of the profile represents a normal-textured Felsic Granophyre with abundant micro-pegmatite domains. Sample B was recognized chemically as Mafic Granophyre; the thin section of this sample contains a sizable mafic clast. The following three samples (C, D, and E) are of Felsic Granophyre composition but exhibit a somewhat different texture in thin section. Here, the groundmass is formed of poikilitic orthopyroxene crystals that contain numerous inclusions of feldspar and pyroxene crystals. A few tiny mafic clasts were observed in these thin sections as well. This is followed by four samples of Mafic Granophyre (F–I) with significant proportions of orthopyroxene in normal, micropegmatite-bearing texture. However, these samples have less micropegmatite than normal Felsic Granophyre. Samples J–N from the southeastern side of the dike have normal Felsic Granophyre texture with comparatively more domains of micropegmatitic texture than observed in the Mafic Granophyre samples. Sample A from the northeastern end of the profile, and samples K and L from the opposite side contain significant amounts of clasts derived from granitic protolith (ample relics of K-feldspar and plagioclase). Sample N contains such clast material as well, especially in the form of rosettes and spherulites of feldspar attached to quartzitic micro-blobs.

Mineral Chemistry

Mineral chemical analyses by electron microprobe were obtained for one representative sample each of Felsic Granophyre (sample ARp-38M), Mafic Granophyre (ARp-38G), and epidiorite (AR-54). The compositions of pyroxene, feldspars, and amphibole were determined. Our data are compared in Figure 5a–c with analyses by Reimold et al. (1990), Therriault et al. (1996), and Wannek (2015).

The orthopyroxene (Figure 5a) in Felsic Granophyre is primarily hypersthene ($En_{46\text{-}73}Fs_{25\text{-}51}Wo_{02\text{-}04}$). There are also some occurrences of clinopyroxene along rims of orthopyroxene laths. Orthopyroxene is often partially

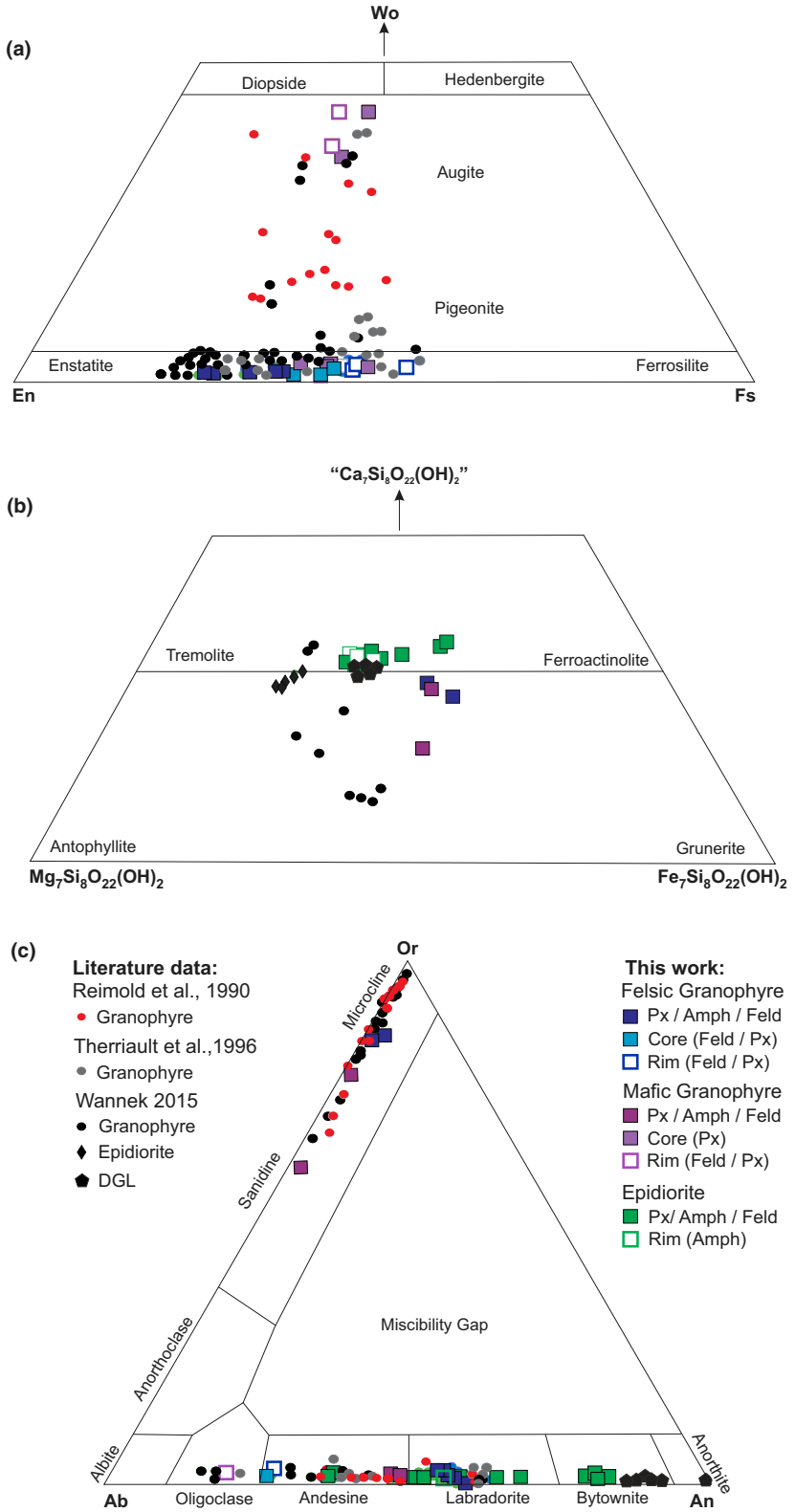

FIGURE 5. Mineral compositions obtained by field emission electron microprobe analysis for selected samples of Felsic and Mafic Granophyre, epidiorite, and Dominion Group meta-lava (DGL). For comparison, mineral compositions for Felsic Granophyre from Therriault et al. (1996), Reimold et al. (1990), and Wannek (2015), Mafic Granophyre from Wannek (2015), and for epidiorite and DGL from Wannek (2015) are plotted as well. (a) Pyroxene, (b) amphibole, and (c) feldspar compositions. (Color figure can be viewed at wileyonlinelibrary.com)

replaced by green pleochroic amphibole (ferri-actinolite to hornblende in composition). In Mafic Granophyre, hypersthene ($En_{51-59}Fs_{37-46}Wo_{04}$) as well as pigeonite and augite compositions ($En_{31-39}Fs_{23-27}Wo_{35-42}$) were identified, locally in fine exsolutions. There is clear evidence of Fe enrichment in the rim areas of pyroxene crystals, an effect that was also described by Wannek (2015) for Felsic Granophyre from Farm Kopjeskraal. Most of the amphibole analyses in epidiorite correspond to actinolitic hornblende compositions, with additional few magnesium-hornblende and actinolite analyses (Figure 5b).

Feldspar analyses are shown in Figure 5c. Alkali feldspar in the groundmass of both Granophyre types is generally K rich. In the Mafic Granophyre, the composition is $An_{0-3}Ab_{13-37}Or_{60-86}$, whereas in Felsic Granophyre generally K-enriched compositions ($An_{0.3–0.8}Ab_{13-14}Or_{84-86}$) are observed. Plagioclase compositions in Felsic Granophyre are $An_{25-59}Ab_{40-73}Or_{0.7–1.3}$, and in the Mafic Granophyre plagioclase is of $An_{19-57}Ab_{46-80}Or_{0-2}$ compositions. In the epidiorite sample, plagioclase compositions of $An_{36-82}Ab_{17-63}Or_{0.1–0.6}$ were determined, with some crystals being strongly normally zoned from cores of $An_{67.9–80.6}Ab_{19.2–31.5}Or_{0.1–0.6}$ to rims of $An_{55.4}Ab_{44.2}Or_{0.4}$—showing dominantly bytownite and labradorite compositions.

Geochemistry

In all, 27 samples were collected from the Granophyre dike on Rensburgdrif and adjacent farms, and from Rietkuil. The profile across the dike (samples ARp-38a-n, inset in Figure 3) includes samples of both Felsic and Mafic Granophyre. The other 13 samples comprise epidiorite (AR-54, NWU-2a), Felsic Granophyre (AR-3, 13, 18, 19, 53, 78, 83, 90; NWU-3), and Mafic Granophyre (AR-89 and -93, NWU-1), for which the sampling sites are also indicated in Figure 3. Chemical compositions for these samples are listed in Table 1. Published major and trace element contents for Granophyre samples and main target rock types were compiled for comparison with our data from Hall and Molengraaff (1925); Willemse (1937); Reimold et al. (1990); Jackson (1994); Pybus (1995); Therriault et al. (1997); Lieger and Riller (2012), Wannek (2015), and Huber et al. (2020).

In Figure 6a,b, the major and trace element characteristics of the profile samples from site 38 are illustrated. Distinct depletion in SiO_2 and complementary enrichments in Fe_2O_3 and MgO are noted for an inner part of the dike. In addition, profile sample ARp-38B from close to the western margin of the dike also has a more mafic character than the "normal" (in terms of the historical studies) Felsic Granophyre. Note that our epidiorite and granite sample locations for the analyses in these profiles of Figure 6 are from the closest occurrences of these lithologies next to the Granophyre dike, but this could be tens of meters and perhaps 1–2 m from dike margins, respectively. Trace elements (Figure 6b) mirror the appearance of this major element profile: for example, some samples from the dike interior and sample ARp-38B are relatively enriched in Cu and Zn, with concomitant depletion of, for example, Ba.

In a selection of Harker-type diagrams (Figure 7a,b), our major and trace element analyses of Granophyre samples, together with literature data, define a wide array of data for the felsic and mafic samples. The two types of impact melt rock can, however, be separated at 66 wt% silica. This separation agrees well with Wannek's (2015) distinction between Felsic and Mafic Granophyre compositions, and with the data of Huber et al. (2020, 2022). The major element data (Figure 7a) indicate negative trends for CaO, MgO, Fe_2O_3, and Al_2O_3 (slightly scattered) with SiO_2. Conversely, K_2O and Na_2O define positive trends against SiO_2. Huber et al. (2020 and 2022) refer to dacitic and andesitic Granophyre instead of Felsic and Mafic Granophyre types. In general, mafic samples are characterized by similar to higher Al_2O_3, K_2O, Fe_2O_3, and MgO contents, for a given SiO_2 content, than obtained for Felsic Granophyre. Both Granophyre types contain similar Na_2O contents, but mafic samples have distinctly lower K_2O concentrations than felsic ones. It is noteworthy that we analyzed one Granophyre sample with 65.9 wt% SiO_2—sample ARp-38C that has a composition right on the limit between Mafic and Felsic Granophyre compositions at < or >66 wt%. Petrographically, this sample is more akin to Felsic Granophyre based on apparent lack of mafic microclasts.

Our new epidiorite data are compared in Figure 7 with literature data (Pybus, 1995; Wannek, 2015). Epidiorite is characterized by higher CaO and MgO contents, similar to higher Al_2O_3 and Fe_2O_3 contents, and lower SiO_2, K_2O and Na_2O contents, compared to Mafic and Felsic Granophyre. On the other hand, the granite data plot on the opposite end of the compositional range. DGL data (after Jackson, 1994) plot together with epidiorite. Significant gaps separate the fields of Mafic Granophyre and the two mafic endmembers (epidiorite and DGL).

With respect to a selection of trace elements (Sr, Zr, Nb, and Ba), the scatter fields for DGL and epidiorite partially overlap (Figure 7b). Compared to Granophyre, concentrations of Sr and Zr are mostly higher in DGL than in epidiorite. Both DGL and epidiorite have lower Ba and somewhat lower Nb contents compared to Granophyre. Felsic and Mafic Granophyre form a swath of data, similar to the major elements, but again the two

types of impact melt rock cluster on both sides of the 66 wt% line.

The chondrite-normalized (McDonough & Sun, 1995) REE abundance patterns of 24 analyzed Granophyre samples (Figure 8a) are all rather similar. The patterns are characterized by enrichment of light REE (LREE) over heavy REE (HREE). In contrast, epidiorite displays an almost flat pattern. Granophyre patterns are somewhat comparable to patterns for granitoids of the core of the Vredefort Dome (not shown here), as, for example, indicated by the results published by Reimold et al. (1990). DGL REE abundance patterns are akin to the epidiorite patterns but characterized by higher REE abundances. Samples of VS metavolcanics have enriched REE patterns compared to epidiorite and display a moderate Tm anomaly (data from Gumsley et al., 2020).

Abundances for both the Felsic and Mafic Granophyre types are much alike and agree well with the abundances and abundance patterns determined by previous workers (Reimold et al., 1990; Wannek, 2015).

In Figure 8b, the obtained REE abundance patterns are shown at higher resolution, together with the patterns for average Felsic Granophyre and Mafic Granophyre. It is obvious that while the LREE averages are slightly enriched in Felsic Granophyre when compared with Mafic Granophyre, the HREE averages are slightly elevated in Mafic Granophyre samples above the abundances for Felsic Granophyre. Model REE patterns equivalent to mixtures of 80% Felsic Granophyre + 20% epidiorite and 60% Felsic Granophyre + 40% epidiorite are shown in the inset to Figure 8b.

The trace element spidergrams (Figure 9) show primitive-mantle normalized (Sun & McDonough, 1989) data for the REE, but also for a suite of other trace elements and potassium. Data for Felsic and Mafic Granophyre are contrasted with normalized abundance ranges compiled from the literature for epidiorite, regionally occurring VS metavolcanics, and for DGL. The abundance patterns for Felsic and Mafic Granophyre are very similar, and not only with respect to the REE—as already discussed in connection with Figure 8. In the case of all plotted elements, the concentrations of Felsic and Mafic Granophyre span a relatively narrow range. Granophyre patterns generally mimic the shape of the epidiorite range, which is also very similar to the VS range, albeit at lower concentrations. In contrast, the DGL range is distinct from all other pattern/range shapes by a strong negative Th anomaly, and a strong positive Zr anomaly (in keeping with the Zr trend already emphasized in Figure 7b). Especially the strong negative Th anomaly of DGL does not match the positive Th anomaly of the Granophyre. For many of these trace elements, a 20% addition of epidiorite or DGL to Felsic Granophyre matches the abundances in Mafic Granophyre.

Strontium–Neodymium Isotope Variations

All obtained isotope data are compiled in Tables 2 and 3, which also contain the relevant data from Reimold et al. (2017), for comparison. In the $^{87}Rb/^{86}Sr$ versus $^{87}Sr/^{86}Sr$ diagram (Figure 10a), all data fall along a regression line that represents a mixing line between a range of lithologies that are not coeval (granite/gneiss from the Archean Basement Complex of the core of the Dome [exemplified here by samples analyzed by Reimold et al., 2017], for which Lana et al. (2004) obtained a range of ages around 3.1–3.2 Ga; DGL of 3.07 Ga age [Armstrong et al., 1991]; epidiorite that if confirmed as an equivalent of the VS metavolcanics would be of 2.7 Ga age [Armstrong et al., 1991]; and 2.02 Ga old Granophyre [Kamo et al., 1996]). Thus, the age calculated for this mixing line is meaningless—although it indicates that the Sr isotopic systematics of the major contributor to the impact melt rock system, the Archean Basement Complex (Reimold et al., 1990), are still dominant within the impact melt rock. All Granophyre data cluster relatively close together in the same segment of the data swath as the epidiorite data. In contrast, the available DGL data are less radiogenic, with significantly lower isotopic ratios (Figure 10b).

The $^{87}Sr/^{86}Sr$ versus Sr mixing diagram (Figure 10b) shows a wide scatter of data for Archean granite. These granite samples stem from individual areas within the Archean core of the Vredefort Dome, such as the Rand Granite, Kudu, and Leeukop quarries (Reimold et al., 2017). In this diagram, too, the impact melt rock (Granophyre) data plot relatively close together with the data for epidiorite samples, whereas again the DGL data plot significantly off this main data cluster.

The measured isotopic ratios were recalculated to the impact age (t = 2020 Ma). The Felsic Granophyre samples are characterized by negative εNd_t values ranging from −11.18 (AR 53) to −12.65 (Arp 38K), and the Mafic Granophyre samples show similar negative εNd_t values between −11.45 (ARp-38F) and −12.61 (ARp-38B). The T_{DM} model ages are between 3.07 and 3.18 Ga for Felsic, and between 3.14 and 3.22 Ga, for Mafic Granophyre.

As in the case of the Sr isotope systematics, the Sm-Nd isotope data straddle an apparent mixing line (Figure 10c) without geological significance—corresponding to an Archean age but with a comparatively much higher error. The Sm-Nd isotope data for epidiorite samples are remarkably close to the Granophyre data. Neither in Sr nor Sm-Nd isotope systematics is it possible to observe a distinct trend between the data for Felsic and Mafic Granophyre, respectively. However, three samples of Felsic Granophyre plot further from the cluster of the other melt rock samples in the $^{147}Sm/^{144}Nd$ versus $^{143}Nd/^{144}Nd$ diagram (Figure 10c). Note that uncertainties on isotope data are smaller than sizes of plotted symbols.

TABLE 1. Major and trace element data for the different lithologies of this study.

Sample	AR-54	NWU-2a	AR-13	AR-19	AR-53	AR-83	AR-88	AR-92	ARp-38A	ARp-38C	ARp-38D	ARp-38E	ARp-38J	ARp-38K	ARp-38L
Lithology	Epidiorite	Epidiorite	FG	FG	FG	FG	FG	FG	FG	FG	FG	FG	FG	FG	FG
SiO_2	53.00	50.60	69.34	67.51	69.18	69.15	69.77	70.38	66.31	65.89	68.59	67.09	67.27	68.39	68.53
TiO_2	0.37	0.59	0.47	0.45	0.49	0.42	0.47	0.41	0.47	0.53	0.50	0.49	0.46	0.47	0.46
Al_2O_3	14.2	16.20	11.76	12.75	12.53	11.80	11.55	11.49	12.82	13.15	12.38	12.84	12.7	13.17	12.91
Fe_2O_3*	8.78	11.30	7.19	6.81	7.37	7.10	7.13	6.94	7.13	7.57	7.14	7.16	7.06	7.04	6.82
MnO	0.14	0.17	0.14	0.14	0.14	0.15	0.14	0.15	0.17	0.14	0.13	0.14	0.14	0.14	0.15
MgO	8.8	5.58	3.15	3.53	3.20	3.40	3.11	3.34	3.84	3.80	3.49	3.63	3.57	3.67	3.57
CaO	12.4	11.20	3.45	3.97	3.74	3.70	3.58	3.58	4.02	4.82	4.55	4.55	4.11	4.05	3.91
Na_2O	1.6	2.13	2.29	2.53	2.37	2.42	2.30	2.33	2.63	2.69	2.68	2.53	2.68	2.84	2.80
K_2O	0.15	0.29	1.98	2.25	2.06	2.16	2.02	2.04	2.39	2.02	1.88	2.06	2.2	2.31	2.28
P_2O_5	0.03	0.07	0.09	0.07	0.08	0.09	0.11	0.09	0.07	0.08	0.07	0.08	0.07	0.07	0.07
LOI	0.75	1.10	−0.20	0.21	0.07	0.02	0.28	0.04	0.15	0.12	0.18	0.25	0.15	0.23	0.13
Sum	100.2	99.23	99.66	100.24	101.36	100.41	100.46	100.79	100.05	100.85	101.62	100.85	100.41	102.42	101.67
Sc	36.3	39	nd	16.3	14.2	nd	nd	nd	14.4	17.9	17.5	17.1	15.2	15.6	14.4
Cr	742	10	nd	278	970	nd	nd	nd	330	217	192	217	282	272	274
Co	82	44	26	100	28	24	25	24	166	74	119	112	76	82	90
Ni	186	72	107	105	120	103	101	104	119	97	93	99	116	107	107
Cu	79	111	48	40	58	39	45	41	41	46	46	45	42	39	39
Zn	47	74	72	53	55	60	54	43	57	58	52	59	51	51	53
Rb	1.5	6	70	65.5	54.2	75.6	67.4	73.3	64.3	55.3	48.5	55.7	61.2	64.4	63.6
Sr	83	122	225	194	209	213	228	205	185	188	170	187	185	186	191
Y	11	16	13	14	14	12	13	13	14	15	14	14	13	14	13
Zr	30	48	144	135	132	138	140	138	133	127	120	124	129	131	132
Nb	1.17	2.0	6.27	7	5.78	6.56	5.9	6.6	6.67	6.11	5.68	6.02	6.5	6.61	6.58
Ba	39	96	474	409	452	416	460	412	405	387	358	391	389	393	401
La	3.5	4.5	22.6	31	31.2	20.8	22.5	21.1	29.7	28.7	26.9	29.2	29.5	31	30.5
Ce	7.3	8.8	45.1	57	57.6	40.6	43.5	41.8	55.1	53.9	49.5	52.8	54.5	56.4	55.7
Pr	0.97	1.04	4.6	6.05	6.18	4.41	4.66	4.34	5.95	5.77	5.41	5.84	5.95	5.99	6.0
Nd	4.1	4.9	17.4	20.7	22.1	16.0	17.1	16.1	20.5	20.2	19.5	20.8	20.5	21.6	21.4
Sm	1.21	1.3	3.2	3.81	3.89	2.7	3.1	2.9	3.55	3.69	3.45	3.78	3.72	3.55	3.5
Eu	0.48	0.56	0.74	0.93	0.97	0.64	0.77	0.68	0.91	0.96	0.86	0.98	0.97	0.92	0.91
Gd	1.4	1.9	2.59	2.94	3.12	2.43	2.78	2.46	2.9	3.29	3.15	3.2	3.1	3.18	2.98
Tb	0.28	0.36	0.38	0.43	0.47	0.37	0.41	0.38	0.45	0.45	0.46	0.45	0.42	0.47	0.45
Dy	1.87	2.48	2.36	2.6	2.66	2.12	2.37	2.14	2.51	2.87	2.73	2.76	2.59	2.73	2.61
Ho	0.43	0.52	0.44	0.51	0.54	0.43	0.47	0.4	0.5	0.55	0.54	0.54	0.52	0.53	0.54
Er	1.28	1.57	1.3	1.38	1.47	1.27	1.34	1.34	1.45	1.63	1.6	1.59	1.51	1.49	1.44
Tm	0.18	0.23	0.19	0.21	0.21	0.17	0.2	0.17	0.2	0.25	0.22	0.21	0.21	0.21	0.21
Yb	1.32	1.5	1.2	1.43	1.37	1.3	1.3	1.1	1.39	1.58	1.51	1.48	1.41	1.42	1.36
Lu	0.21	0.27	0.17	0.21	0.21	0.17	0.19	0.17	0.19	0.23	0.22	0.22	0.22	0.21	0.22
Hf	0.82	1.2	3.52	3.72	3.45	3.46	3.45	3.25	3.56	3.54	3.4	3.54	3.67	3.68	3.71
Ta	0.15	0.2	0.69	0.84	0.42	0.68	0.56	0.68	0.74	0.56	0.63	0.73	0.64	0.67	0.73
Pb	1.37	nd	nd	9.63	9.01	nd	nd	nd	10.4	8.7	8.63	8.88	9.63	10.5	10
Th	0.49	0.9	6.1	6.86	5.46	6.4	5.9	6.3	6.56	5.79	5.27	5.89	6.34	6.84	6.71
U	0.1	0.3	1.61	1.6	1.22	1.78	1.49	1.76	1.61	1.15	1.18	1.25	1.47	1.62	1.48

Note: Major element data are presented in wt%, and (*) total Fe as Fe_2O_3. Trace element data are presented in ppm.
Abbreviations: FG, Felsic Granophyre; LOI, loss on ignition; MG, Mafic Granophyre.

A diagram of $^{143}Nd/^{144}Nd$ versus Nd abundance is shown in Figure 10d. Granite data, as in the case of the complimentary Sr diagram (Figure 10b), form a wide swath, whereas Granophyre and epidiorite data fall into a tight data cluster. This clearly shows that the scatter of the three Felsic Granophyre data is related to the Sm/Nd isotope ratios. In this diagram, the DGL data again fall outside of the tight data cluster for the felsic and mafic impact melt rock samples and epidiorite.

Figure 10e,f shows the relationships between Sr and Nd isotopes, respectively, and SiO_2 contents of the Granophyre and epidiorite samples. As expected, the mafic and felsic impact melt rock data, respectively, can be separated by the 66 wt% SiO_2 line. However, it is obvious that the Felsic Granophyre samples have relatively more isotopic variation than the Mafic Granophyre samples. In terms of Nd isotopes, the data of Reimold et al. (2017) show wider scatter, whereas the Sr isotope data of both Reimold et al. (2017) and this study show a similar data spread.

We have attempted to model the Sr and Nd isotopic compositions of average Mafic Granophyre with admixture of percentages of average epidiorite or average DGL, respectively, to average Felsic Granophyre. The results of these mixing calculations are shown in Figure 10g (epidiorite) and h (DGL) representing the age-corrected data.

DISCUSSION

We have investigated the extension of a Granophyre (impact melt rock) dike in the northwestern sector of the Vredefort Dome toward the south of the Vaal River on and beyond Farm Rensburgdrif. The possibility that a mafic variety of Granophyre could occur in this section on Rensburgdrif (Lieger, 2011) was explored. In addition,

ARp-38M FG	ARp-38N FG	NWU-3 FG	AR-89 MG	AR-93 MG	ARp-38B MG	ARp-38F MG	ARp-38G MG	ARp-38H MG	ARp-38I MG	NWU-1 MG	Av.Epi	±2s	Av.FG	±2s	Av.MG	±2s
67.36	67.07	66.70	64.69	65.48	63.29	62.90	58.55	61.97	62.60	63.14	51.80	1.15	68.03	0.62	62.83	1.34
0.47	0.49	0.47	0.55	0.56	0.57	0.65	0.55	0.59	0.60	0.61	0.48	0.14	0.47	0.01	0.59	0.02
12.22	12.30	12.70	13.22	12.64	13.45	13.42	12.57	13.33	13.60	13.32	15.20	0.58	12.44	0.26	13.19	0.25
6.20	6.85	7.30	8.16	9.15	8.57	8.60	8.56	8.86	9.09	10.10	10.04	1.87	7.05	0.14	8.89	0.38
0.13	0.13	0.15	0.14	0.15	0.17	0.14	0.14	0.14	0.15	0.17	0.16	0.01	0.14	0.01	0.15	0.01
3.31	3.37	3.48	3.88	3.70	3.97	3.54	3.84	4.27	4.12	4.22	7.19	2.21	3.47	0.10	3.94	0.16
3.57	4.03	3.96	5.08	4.96	5.55	5.47	5.55	5.77	5.96	5.90	11.80	1.06	3.97	0.19	5.53	0.23
2.67	2.62	2.05	2.66	2.64	2.80	2.83	2.71	2.86	2.87	1.50	1.87	0.31	2.53	0.10	2.61	0.30
2.00	1.99	2.30	1.95	1.84	1.85	1.89	1.63	1.68	1.72	2.60	0.22	0.09	2.12	0.07	1.89	0.20
0.07	0.08	0.08	0.08	0.11	0.09	0.09	0.08	0.09	0.09	0.11	0.05	0.03	0.08	0.01	0.09	0.01
0.40	0.18	0.20	0.38	−0.11	0.18	0.29	0.21	0.27	0.17	−0.66	0.93	0.24	0.15	0.06	0.09	0.22
98.44	99.13	99.39	100.82	101.12	100.50	99.84	94.40	99.87	100.99	101.01	99.72	1.23	100.48	0.50	99.82	1.45
13.4	14.8	14	19.4	nd	20.2	21.4	22.2	20.4	23.2	nd	38	27	15	1	21	1
283	225	240	206	nd	221	157	176	200	185	nd	376	507	315	114	191	17
115	120	20	152	33	93	84	106	108	99	41.5	63	26	75	22	90	25
100	88	89	97	102	99	88	91	102	94	113	129	79.00	103	4.49	98.3	5.04
42	43	55	52	50	50	50	71	50	50	64	95	23	44	3	55	5
50	56	49	66	73	63	69	64	77	72	82	61	18	55	3	71	4
54.1	52.1	72	51.6	59.1	50	50.4	45.4	43.9	48.2	55.5	3.8	3.1	62.3	3.9	50.5	3.2
186	187	204	194	229	190	179	174	181	182	217	103	27	196	8	193	13
14	15	13	16	15	17	18	17	17	17	18	14	3	14	0	17	1
127	128	131	135	137	126	128	115	116	120	131	39	12	132	3	126	5
5.82	5.87	6.0	6.31	5.93	6.44	6.39	5.5	5.64	5.73	6	2	1	6	0	6	0
423	412	393	371	404	355	365	315	320	331	365	68	40	411	14	353	19
31.13	28.5	23	29.5	22.6	28	29.0	25.5	26.1	26.1	20.5	4.0	0.7	27.3	1.9	25.9	2.0
57.8	53.7	43.5	54.6	43.4	51.9	53.5	47.2	47.9	48.7	41.1	8.1	1.0	51.2	2.9	48.5	3.1
6.33	5.72	4.76	5.64	4.65	5.57	5.74	5.19	5.12	5.45	4.20	1.01	0.05	5.50	0.33	5.20	0.35
22.7	21.2	16.6	20.9	17.4	21.1	20.5	18.8	19.1	19.4	15.8	4.5	0.5	19.6	1.1	19.1	1.2
3.96	3.99	3.1	3.82	3.1	3.85	4.12	3.76	3.61	3.88	3.00	1.26	0.06	3.49	0.18	3.64	0.25
0.91	0.94	0.69	1.03	0.77	0.99	1.0	0.99	0.92	0.95	0.79	0.52	0.06	0.86	0.06	0.93	0.06
3.17	3.16	2.9	3.42	2.99	3.29	3.62	3.27	3.31	3.15	2.99	1.65	0.33	2.96	0.13	3.26	0.14
0.47	0.42	0.42	0.49	0.44	0.5	0.53	0.48	0.51	0.51	0.48	0.32	0.06	0.43	0.02	0.49	0.02
2.74	2.84	2.39	2.87	2.78	3.0	3.4	3.13	3.09	3.19	3.02	2.18	0.42	2.56	0.11	3.06	0.12
0.52	0.54	0.47	0.63	0.53	0.62	0.66	0.65	0.65	0.65	0.60	0.48	0.06	0.50	0.02	0.62	0.03
1.53	1.61	1.36	1.81	1.6	1.85	1.98	1.93	1.86	1.90	1.77	1.43	0.20	1.46	0.06	1.84	0.08
0.21	0.23	0.18	0.25	0.25	0.26	0.29	0.28	0.27	0.29	0.24	0.21	0.03	0.21	0.01	0.27	0.01
1.39	1.48	1.2	1.65	1.5	1.76	2.0	1.73	1.81	1.85	1.70	1.41	0.12	1.37	0.06	1.75	0.10
0.21	0.23	0.2	0.25	0.24	0.25	0.3	0.3	0.26	0.26	0.26	0.24	0.04	0.20	0.01	0.27	0.01
3.48	3.38	3.4	3.64	3.28	3.43	3.54	3.2	3.23	3.36	3.30	1.01	0.26	3.51	0.07	3.37	0.10
0.8	0.66	0.5	1	0.54	0.57	0.54	0.58	0.56	0.56	0.50	0.18	0.03	0.66	0.05	0.57	0.04
9.2	8.83	nd	9.55	nd	7.99	7.85	7.17	7.62	6.8	nd	1.37	0.00	9.40	0.39	7.83	0.69
5.89	5.77	6.3	5.74	5.6	5.21	5.47	4.76	4.83	4.93	5.20	0.70	0.28	6.15	0.23	5.22	0.24
1.43	1.24	1.8	1.09	1.29	1.1	1.06	0.92	1.02	0.99	1.20	0.20	0.14	1.48	0.10	1.08	0.08

two samples from a second Granophyre dike obtained on Rietkuil, to the southwest of Rensburgdrif (see Figure 3), were also analyzed.

Field Observations

Field study of the profile across the dike on Rensburgdrif (Figure 3b) showed that the Granophyre appears relatively uniform, but two distinct phases could be identified in hand specimen and thin sections: (1) a comparatively clast-poor phase was observed in the inner parts of the dike and (2) a clast-rich one along the dike margins. We could not identify contact relationships between these two phases. The contact between the Granophyre dike and epidiorite is not exposed on this property but it can be inferred to occur within about 80 m from the western dike margin (see Figure 3). In agreement with Therriault et al. (1996), granite, quartzite, very minor shale, and auxiliary mafic clasts of contrasting sizes and mineral compositions occur within Rensburgdrif Granophyre. There are some indications in the field of the local presence of mafic inclusions, generally smaller than 2 cm. Larger (up to 50 cm long) schlieren of comparatively slightly coarser-grained material occur especially near the Rensburgdrif homestead, but were not subject of the present investigation.

On Farm Rietkuil to the southwest of the main study area, only one type of Granophyre could be recognized in the field. However, our two samples represent both Felsic and Mafic Granophyre, and a Mafic Granophyre sample from the southern end of this dike had already been analyzed by Therriault et al. (1996). This finding, at that time, had not been discussed any further. This means, however, that Mafic Granophyre occurrence is now no longer restricted to the Kopjeskraal property only, but also confirmed on Rensburgdrif and at two further locations on the dike crossing Rietkuil. This result from

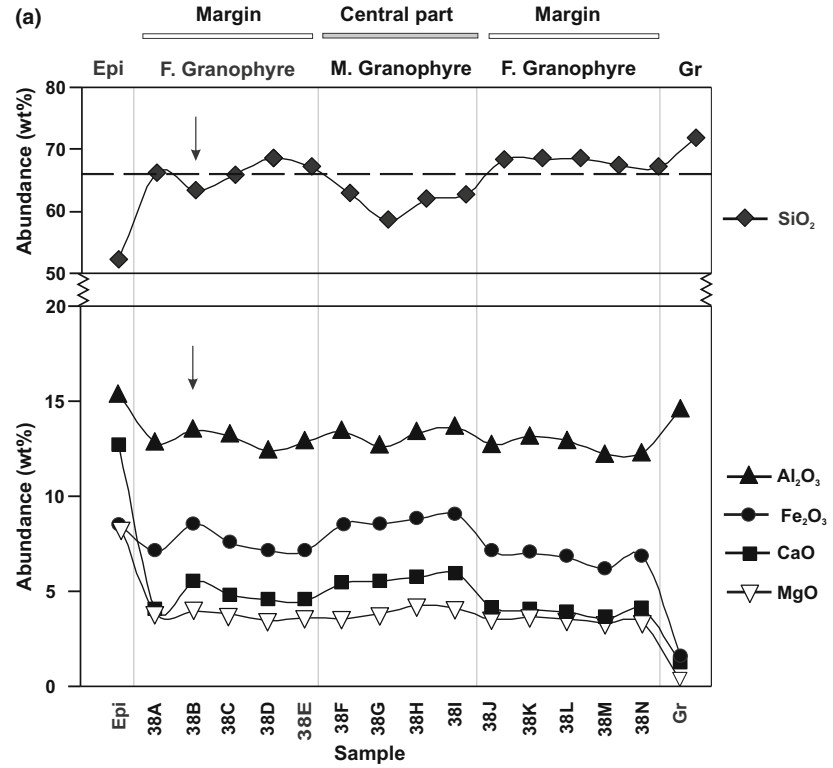
(a)
Margin
Central part
Margin
Epi
F. Granophyre
M. Granophyre
F. Granophyre
Gr
Abundance (wt%)
80
70
60
50
20
15
10
5
0
SiO2
Al2O3
Fe2O3
CaO
MgO
Epi
38A
38B
38C
38D
38E
38F
38G
38H
38I
38J
38K
38L
38M
38N
Gr
Sample

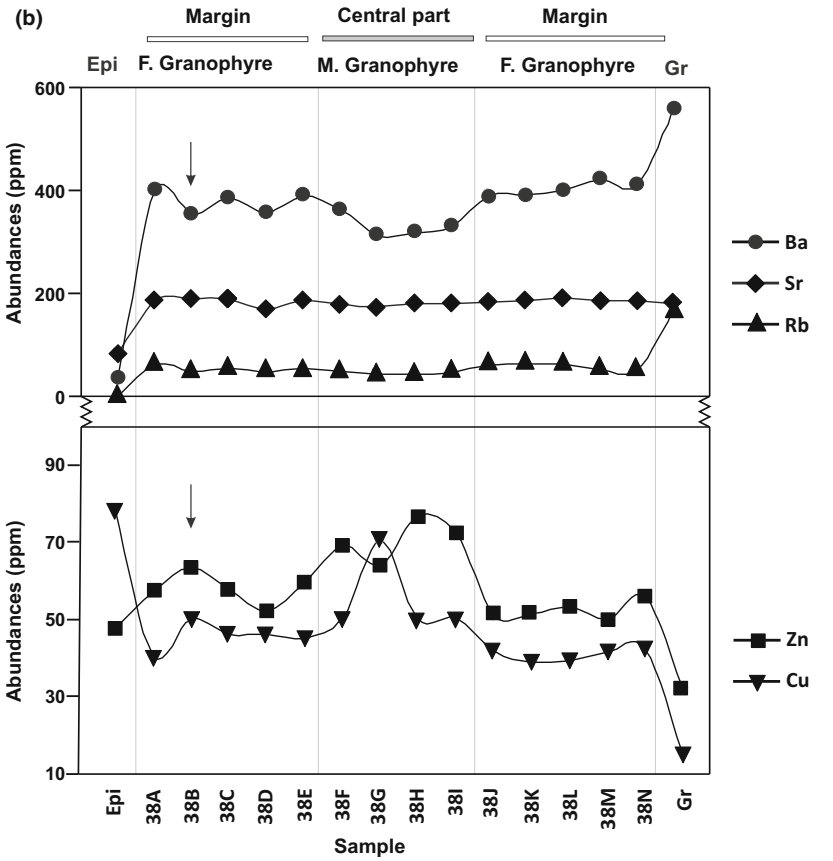
(b)
Margin
Central part
Margin
Epi
F. Granophyre
M. Granophyre
F. Granophyre
Gr
Abundances (ppm)
600
400
200
0
90
70
50
30
10
Ba
Sr
Rb
Zn
Cu
Epi
38A
38B
38C
38D
38E
38F
38G
38H
38I
38J
38K
38L
38M
38N
Gr
Sample

FIGURE 6. Major (a) and trace (b) element data for the samples from the profile across the dike (ARp-38A-N). Major element data in wt% and trace element data in ppm. The main Mafic Granophyre portion occurs in the interior of the dike. A second mafic occurrence is noted by the analysis of sample 38B from closer to the western edge of the dike (marked with a vertical arrow). The 66 wt% SiO_2 line schematically emphasizes which impact melt rock samples are the significantly more mafic ones. Note that the epidiorite (Epi) and granite (Gr) data at the limits of the profiles are indeed for samples from Rensburgdrif but not from the immediate vicinity of the profile across the dike; these data provide a general impression how these lithologies would plot in comparison to the Granophyre types.

Rietkuil clearly warrants continuing detailed analysis over the entire extent of this second impact melt rock dike.

Petrography Including Mineral Chemistry

In petrographic analysis, there are some observations that tentatively distinguish these two impact melt rock types. Clast-rich Granophyre (Felsic Granophyre) samples identified in the field have a fine-grained matrix with zoned pyroxene crystals and plagioclase laths. The clast-poor samples (Mafic Granophyre) have a mode with more pyroxene than the clast-rich phase (Felsic Granophyre). The matrix is found to be slightly coarser grained and in thin section is revealed as having a granular texture. Plagioclase laths are relatively smaller, and pyroxene crystals relatively larger than in the felsic phase. In both Granophyre types, amphibole is a product of uralitization of subhedral pyroxene crystals. Round fragments of equigranular, mosaic-textured quartz aggregates are relatively more abundant in the clast-rich phase. They likely result from recrystallization (annealing) of originally medium-grained quartz crystals of lithic clasts derived from quartzitic or granitic precursors.

Petrographically, the Mafic Granophyre observed on Farm Rensburgdrif is equivalent to the rare "mafic" Granophyre samples already observed from this dike in the northwest of the Vredefort Dome by earlier workers (Therriault et al., 1996; Willemse, 1937), later by Lieger (2011) and discussed by Lieger and Riller (2012), and most recently by Wannek (2015), Reimold et al. (2017, 2021), and Huber et al. (2020 [as well as 2022 where the same data are listed again]). Accordingly, the two varieties on farms Kopjeskraal and Rensburgdrif are similar with regard to the proportion of groundmass, modal compositions, and hypidiomorphic texture types in the two different phases. The medium- to coarse-grained granoblastic pyroxenitic clasts found in Mafic Granophyre samples from Rensburgdrif originally must have been derived from a mafic intrusive precursor lithology. Pyroxene of mafic clasts was revealed to often have irregular, embayed margins, which is likely indicative of corrosion by the superheated impact melt. In addition, pyroxene and amphibole seem to be more altered in the samples of Mafic Granophyre than in the Felsic Granophyre. A possible explanation for this could be that admixture of material from a mafic protolith that had already been affected by uralitization as a consequence of pre-impact metamorphism and alteration occurred. This component could have contributed a comparatively higher percentage of volatiles into the intruding felsic impact melt—in those melt volumes where such a mafic precursor was assimilated.

Our new electron microprobe analyses (Figure 5) show that pyroxenes from Felsic and Mafic Granophyre display very similar compositions. In general, our microprobe results are consistent with previously published data. Wannek (2015) reported comparatively wider compositional ranges for plagioclase ($An_{26-51}Ab_{48-72}Or_{1-2}$) and pyroxene ($En_{50-78}Fo_{20-47}Wo_{2-4}$) for Felsic Granophyre, and for plagioclase ($An_{16-61}Ab_{39-81}Or_{1-2}$) and pyroxene ($En_{36-60}Fo_{23-28}Wo_{9-36}$) in Mafic Granophyre than observed here. However, Wannek (2015) did not differentiate between core and rim analyses. For the epidiorite sample studied by this author, a range of plagioclase compositions of $An_{40-76}Ab_{24-59}Or_{0-1}$ was reported, which is narrower than the data spread reported here. For amphibole in epidiorite on Farm Kopjeskraal, Wannek (2015) determined hornblende compositions (see Figure 5b). She also presented microprobe analyses for feldspar and amphibole from DGL on Farm Kopjeskraal (compare Figure 5b,c). Plagioclase compositions in DGL were determined by Wannek to be even more An rich than found in our study.

Pyroxene and feldspar analyses by EMPA were also presented by Huber et al. (2020). Their fields for pyroxene analyses of Vredefort Granophyre are very similar to our results, but they have a few analyses that indicate somewhat higher ferrosilite contents. Most of their plagioclase compositions fall into the same field as our data. However, more oligoclase analyses are included in our work, whereas Huber et al. (2020) reported more data along the andesine/labradorite limit. Our alkali feldspar analyses extend from the orthoclase (Or) apex into the sanidine field, which encompasses but extends the alkali feldspar compositional field shown by Huber et al. (2020). Electron microprobe analyses for pyroxene and feldspars in selected Granophyre samples were also presented by Therriault et al. (1996); however, they did not provide sample numbers. Their figures 12 and 14 do indicate compositional ranges for these minerals that are similar to the spread of our data.

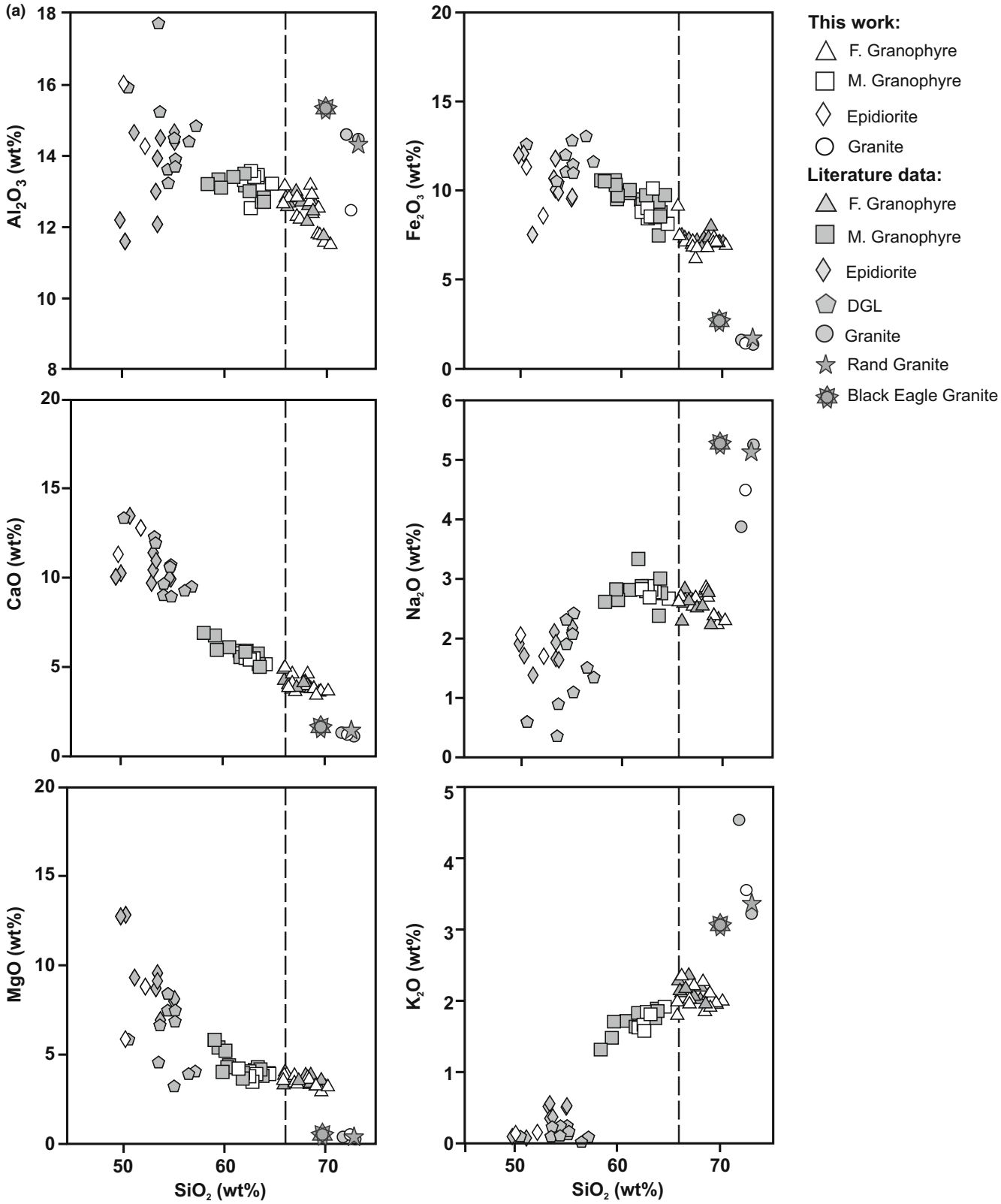
(a)
Al2O3 (wt%)
Fe2O3 (wt%)
CaO (wt%)
Na2O (wt%)
MgO (wt%)
K2O (wt%)
SiO2 (wt%)
SiO2 (wt%)
This work:
F. Granophyre
M. Granophyre
Epidiorite
Granite
Literature data:
F. Granophyre
M. Granophyre
Epidiorite
DGL
Granite
Rand Granite
Black Eagle Granite

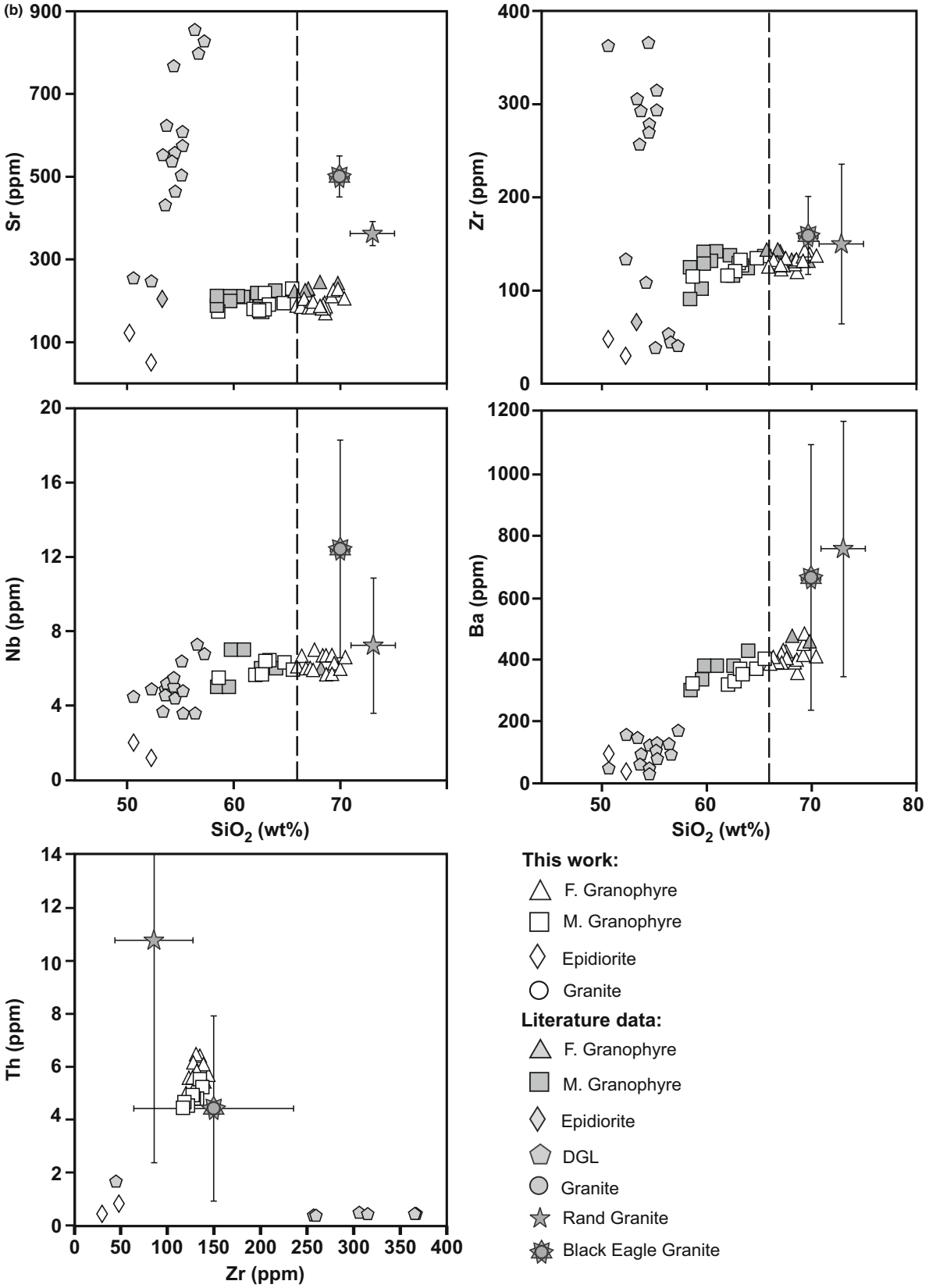
(b)
Sr (ppm)
Zr (ppm)
Nb (ppm)
Ba (ppm)
Th (ppm)
SiO2 (wt%)
SiO2 (wt%)
Zr (ppm)
This work:
F. Granophyre
M. Granophyre
Epidiorite
Granite
Literature data:
F. Granophyre
M. Granophyre
Epidiorite
DGL
Granite
Rand Granite
Black Eagle Granite

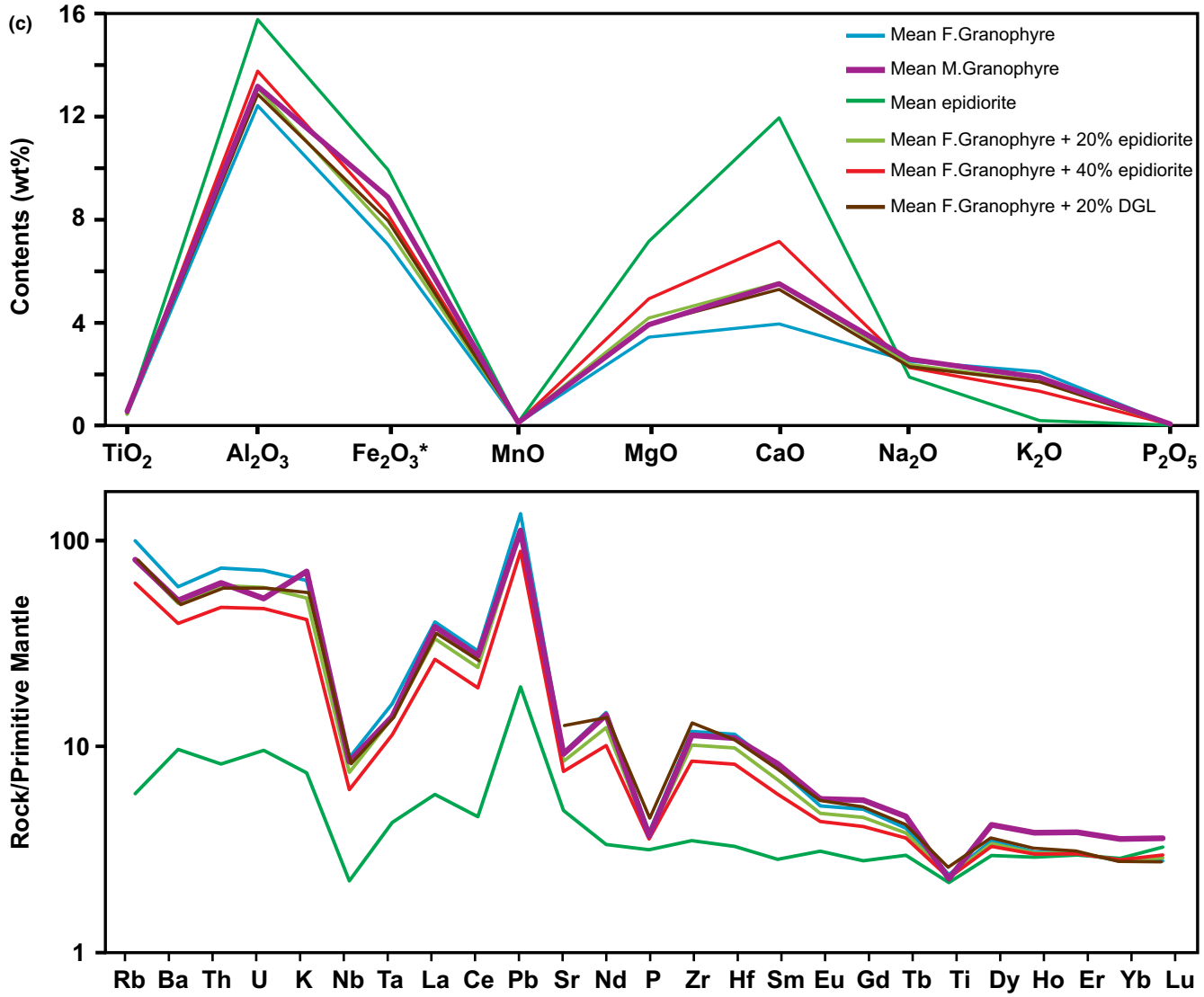

FIGURE 7. Harker type diagrams for selected major (a) and trace element (b) abundances in the Felsic and Mafic Granophyre lithologies, epidiorite, Dominion Group Lava (DGL), and granite. Major element data given in wt%, trace element data in ppm. The Felsic Granophyre samples have >66 wt% SiO_2, Mafic Granophyre >66 wt% (respective data fields reasonably well separated at this compositional limit, i.e., by the dashed, vertical line). Literature data were taken from Hall and Molengraaff (1925), Willemse (1937), Reimold et al. (1990), Jackson (1994), Pybus (1995), Therriault et al. (1997), Lieger and Riller (2012), Wannek (2015), and Huber et al. (2020). Epidiorite and Dominion Group meta-lava data plot similarly at a reduced SiO_2 content, compared to Granophyre data. The average (and standard deviations) compositions for two suites of Archean granite/granite gneiss from Rand Granite and Black Eagle Granite quarries (data from Otten, 1998) have been added to the diagrams. (c) Spidergrams with major and trace element abundances for Felsic and Mafic Granophyre, as well as epidiorite, and graphical solutions for mixtures of 80% and 60% Felsic Granophyre plus 20% and 40% epidiorite or 20% DGL, respectively. (Color figure can be viewed at wileyonlinelibrary.com)

Amphibole compositions from a DGL sample from Wannek (2015) and our amphibole compositions for epidiorite are comparable. Thus, it is not possible to distinguish these two mafic country rock lithologies—or remnants of these possible precursor components in Granophyre matrix—on the basis of currently available results from mineral analysis in Granophyre. The pyroxene crystals observed in the Mafic Granophyre are larger and sometimes have a higher Ca content than those in Felsic Granophyre. The latter observation is consistent with higher Ca abundances in bulk Mafic Granophyre samples.

Considering the generally wide range of feldspar compositions from Granophyre, it appears impossible to distinguish the mafic and felsic varieties of impact melt rock based on plagioclase or alkali feldspar compositions

either. It is not clear from the published results of electron microprobe work on Granophyre whether or not the limited differences in data spread may result from accumulations of analyses from matrix minerals and from clast material incorporated into the groundmass of Granophyre. A more dedicated mineral chemical analysis on clasts and matrix minerals for both Granophyre types, in comparison to these minerals in sections of selected precursor lithologies (especially epidiorite, DGL, granitic country rocks) remains warranted in order to better constrain which amphibole and feldspar analyses might denote authigenic Granophyre mineralization or be related to parental components.

Mafic clasts, at centimeter sizes observed in Granophyre in the field, and microscopically in Granophyre matrix—occur in Felsic and Mafic Granophyre alike—albeit at much higher abundance in Mafic Granophyre from Rensburgdrif. Earlier workers (e.g., French et al., 1989; French & Nielsen, 1990; Reimold et al., 1990; Reimold & Gibson, 2006; Therriault et al., 1996, 1997) discussed if it was possible to exclude that Felsic Granophyre might also contain a minor, or even a major (French & Nielsen, 1990) VS-derived basaltic component. Felsic Granophyre composition was modeled by Reimold et al. (1990) as a mixture of Archean basement granitoid, and Witwatersrand shale and quartzite, whereas French and Nielsen (1990) included in their modeling variable proportions of Ventersdorp basalt. Detailed mineralogical analysis of pyroxene and amphibole on such mafic micro-relics in groundmass and on larger mafic clasts, for comparison with compositions of these minerals in epidiorite and DGL, could further aid in constraining the nature and origin of these mafic clasts.

Geochemistry

The sample profile (ARp-38A-N, Figure 3b) across the dike on Rensburgdrif includes both Felsic (>66 wt% SiO_2) and Mafic Granophyre (<66 wt% SiO_2), which confirms the presence of Mafic Granophyre also to the south of the Vaal River on Rensburgdrif Farm. While this had previously been postulated by Lieger (2011) and Lieger and Riller (2012), these authors failed to confirm this occurrence, as their published chemical analysis, especially that of their sample 355, was incomplete. It is further demonstrated here that the Mafic Granophyre phase occurs in inner parts of the dike, whereas the felsic (clast rich) phase occurs along the dike margins. This is the same spatial arrangement of these two types of impact melt rock as reported by Wannek (2015) and Reimold et al. (2021) for the northern portion of this Granophyre dike on Kopjeskraal.

Our chemical analysis of two samples from the dike crossing the Rietkuil property yielded unambiguous evidence for the presence of both Felsic and Mafic Granophyre in this dike on Rietkuil as well. Thus, a further occurrence of Mafic Granophyre is confirmed from another dike, besides the one straddling Kopjeskraal and Rensburgdrif. That both dikes occur at the core-collar boundary in the northwestern to western sector of the Vredefort Dome (Figure 3) may be significant and indicate that only in this part of the central uplift structure generation of Mafic Granophyre occurred. However, reexamination of the other dikes is clearly warranted.

The composition of the so-called Mafic Granophyre is characterized by less than 66 wt% SiO_2 (range determined here for Rensburgdrif: 58.5–65 wt% SiO_2), whereas Felsic Granophyre has between 66 and 69.8 wt% SiO_2. Data from the literature and our study for Granophyre compositions show that major and trace element data form two groupings for the samples from Felsic and Mafic Granophyre, respectively (Figure 7). In general, samples of the mafic phase are characterized by similar to higher Al_2O_3 (a), and lower K_2O (b), Fe_2O_3 (d), and MgO (e) contents than obtained for Felsic Granophyre samples (Figure 7).

Our new epidiorite analyses fall right into the epidiorite field for literature analyses (e.g., Pybus, 1995)—see Figure 7. These data spreads for different major elements overlap with DGL compositional data. Considering the assimilation/admixture hypothesis for the generation of Mafic Granophyre, major element abundances (especially SiO_2, Al_2O_3, MgO, and CaO) indicate that the Mafic Granophyre composition could, in principle, have formed by admixture of either epidiorite or DGL to the Felsic Granophyre. This establishes a significant involvement of a mafic component in the formation of this Granophyre dike (Figure 7), but it does not allow to differentiate between the two optional mafic precursors. This is also the case when considering trace elements—both epidiorite and DGL remain possible mixing endmembers for the generation of Mafic Granophyre (Figure 7b). It must also be pointed out that the DGL data by Jackson (1994) allow us to distinguish two chemical groups, one more fractionated with higher SiO_2 and lower abundances for a number of trace elements, such as Ni, Co, and Cr, or higher abundances of, for example, Sr and Ba—in comparison to the other type. This is exemplified in the Zr versus SiO_2 diagram in Figure 7b. Thus, it is also difficult to define a single possible mixing component (see below).

When comparing average major and trace element abundances for Felsic and Mafic Granophyre, it is obvious that a sizable contribution of about 20%–40% of

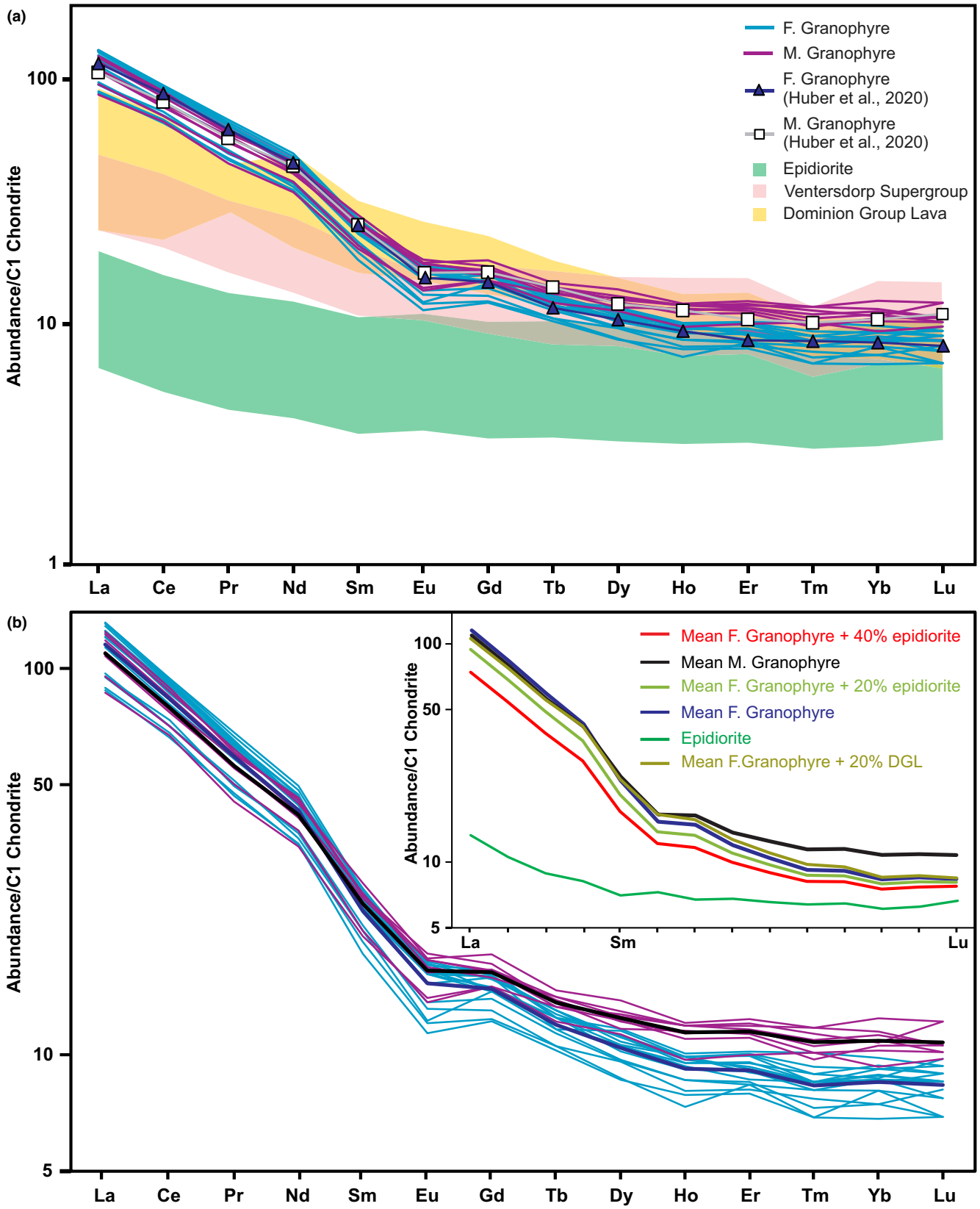
(a)
F. Granophyre
M. Granophyre
F. Granophyre (Huber et al., 2020)
M. Granophyre (Huber et al., 2020)
Epidiorite
Ventersdorp Supergroup
Dominion Group Lava
Abundance/C1 Chondrite
100
10
1
La Ce Pr Nd Sm Eu Gd Tb Dy Ho Er Tm Yb Lu
(b)
Mean F. Granophyre + 40% epidiorite
Mean M. Granophyre
Mean F. Granophyre + 20% epidiorite
Mean F. Granophyre
Epidiorite
Mean F.Granophyre + 20% DGL
Abundance/C1 Chondrite
100
50
10
5
La Ce Pr Nd Sm Eu Gd Tb Dy Ho Er Tm Yb Lu
La Sm Lu

FIGURE 8. (a) Chondrite-normalized (McDonough & Sun, 1995) rare-earth element patterns for Felsic and Mafic Granophyre (this work and literature data). These data are compared against DGL and epidiorite results. Granophyre literature data were compiled from Reimold et al. (1990), Wannek (2015), and Huber et al. (2020). Granophyre patterns are furthermore compared with the ranges of abundance patterns for epidiorite (Epi) after Wannek (2015), Dominion Group meta-lava (DGL) after Jackson (1994), and regionally occurring Ventersdorp Supergroup (VS) after Gumsley et al. (2020). (b) The REE patterns for Felsic and Mafic Granophyre samples are emphasized. In the main figure, blue patterns represent Felsic Granophyre (FG) and black patterns the Mafic Granophyre (MG), which is comparatively depleted in LREE and enriched in HREE. In the inset, the green pattern represents the mean REE composition of Mafic Granophyre, the blue pattern the mean REE composition of Felsic Granophyre. The inset shows how the average pattern for FG (blue) would change due to addition of 20% epidiorite (olive pattern), 40% epidiorite (red), or 20% DGL. (Color figure can be viewed at wileyonlinelibrary.com)

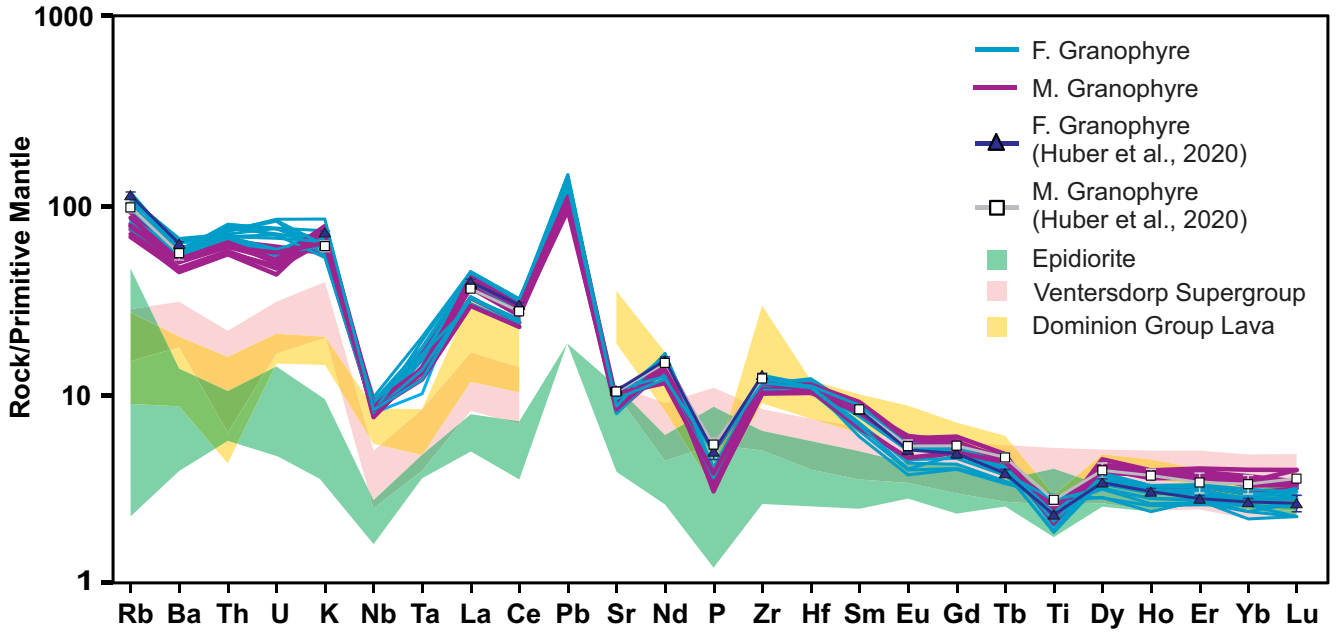

FIGURE 9. Spidergrams for primitive mantle normalized abundances of trace elements and potassium for our samples of Felsic Granophyre (FG, blue) and Mafic Granophyre (MG, purple), the averages for these lithologies after Huber et al. (2020), and the ranges of normalized abundances for epidiorite (data after Wannek, 2015), Dominion Group meta-lava (DGL; data after Jackson, 1992, 1994), and regionally occurring Ventersdorp Supergroup (VS, after Gumsley et al., 2020). Normalization factors after Sun and McDonough (1989). (Color figure can be viewed at wileyonlinelibrary.com)

epidiorite to Felsic Granophyre could approach the elemental abundances in Mafic Granophyre. This can be demonstrated for most major elements and for trace elements that have significant differences in their respective abundances in these two impact melt rock varieties, as shown in Figure 7c.

The REE systematics of Felsic and Mafic Granophyre, and of epidiorite, regionally sampled VS meta-volcanics, and DGL are investigated here as well (see Figure 8a). When considering the abundance patterns for average Felsic and Mafic Granophyre, they are rather similar but do have a slight discrepancy in that the HREE are comparatively slightly enriched. Both patterns lie within the variation for samples from the Archean Basement Complex, as, for example, shown by Reimold et al. (1990). These findings do not unequivocally pinpoint a contribution from a specific mafic precursor component to Mafic Granophyre. DGL patterns have abundance patterns that straddle the Granophyre field, with mostly depleted HREE in comparison with Granophyre. The epidiorite and VS pattern ranges (Figure 8a) are very similar, but the samples from the wider Witwatersrand region have comparatively significantly elevated REE abundances.

In Figure 8b (inset), the results of modeling an average REE pattern for Felsic Granophyre with the addition of 20% and 40% epidiorite component, respectively, are presented. This demonstrates that the average Mafic Granophyre abundance pattern is somewhat consistent with such mixtures and may explain the HREE relative enrichment. However, a perfect fit for

TABLE 2. Sr and Nd isotope data.

Sample	Laboratory[a]	Lithology type	Rb [μg g^{-1}]	Sr [μg g^{-1}]	$^{87}Rb/^{86}Sr$	$^{87}Sr/^{86}Sr_{[m]}$[b]	2se	$^{87}Sr/^{86}Sr_{(T)}$[c]	Sm [μg g^{-1}]	Nd [μg g^{-1}]	$^{147}Sm/^{144}Nd$	$^{143}Nd/^{144}Nd_{[m]}$[b]	2se	$\varepsilon Nd_{(0)}$	$^{143}Nd/^{144}Nd_{(T)}$[c]	$\varepsilon Nd_{(T)}$[c]	T_{DM}
AR-19	UnB	F. Granophyre	65.52	194.4	0.9753	0.74508	0.000010	0.71670	3.82	22.36	0.1041	0.510786	0.000008	−36.30	0.509401	−12.35	3.13
AR-53	UC	F. Granophyre	60.35	218.1	0.8028	0.73460	0.000060	0.71124									
AR-54	UC	Epidiorite	1.78	90.0	0.0572	0.70533	0.000080	0.70367									
AR-53	UnB	F. Granophyre							3.89	22.19	0.1069	0.510883	0.000018	−34.41	0.509461	−11.18	3.07
AR-54	UnB	Epidiorite							1.21	4.31	0.1707	0.512211	0.000018	−8.50	0.509941	−1.76	–
AR-89	UnB	M. Granophyre	51.56	194.0	0.7683	0.73583	0.000020	0.71347	3.87	21.45	0.1100	0.510879	0.00002	−34.49	0.509416	−12.07	3.17
ARp-38A	UnB	F. Granophyre	64.30	185.2	1.0039	0.74548	0.000009	0.71627	3.84	21.94	0.1065	0.510816	0.000020	−35.72	0.509400	−12.38	3.15
ARp-38B	UnB	M. Granophyre	49.69	190.3	0.7548	0.73514	0.000030	0.71318	3.91	21.46	0.1110	0.510864	0.000021	−34.78	0.509388	−12.61	3.22
ARp-38C	UnB	F. Granophyre	55.32	188.1	0.8505	0.73812	0.000030	0.71337	3.96	22.24	0.1084	0.511144	0.000007	−29.32	0.509702	−6.44	2.73
ARp-38D	UnB	F. Granophyre	48.51	169.6	0.8271	0.73780	0.000005	0.71373	3.69	20.52	0.1095	0.510896	0.000011	−34.16	0.509440	−11.59	3.13
ARp-38E	UnB	F. Granophyre	55.65	187.2	0.8598	0.73847	0.000030	0.71345	3.93	22.09	0.1083	0.510851	0.000009	−35.03	0.509410	−12.17	3.16
ARp-38F	UnB	M. Granophyre	50.37	179.2	0.8127	0.73601	0.000010	0.71236	4.17	22.73	0.1119	0.510935	0.000017	−33.40	0.509447	−11.45	3.14
ARp-38G	UC	M. Granophyre	45.39	173.5	0.7019				3.85	20.79	0.1129	0.510949	0.000005	−33.12	0.509448	−11.44	3.15
ARp-38I	UC	M. Granophyre	48.24	181.8	0.7669	0.73353	0.000020	0.71121	3.76	20.26	0.1130	0.510951	0.000008	−33.08	0.509448	−11.43	3.15
ARp-38 J	UnB	F. Granophyre	62.06	183.9	0.9765	0.74685	0.000012	0.71844	3.87	22.09	0.1068	0.510817	0.000013	−35.70	0.509396	−12.45	3.16
ARp-38 K	UnB	F. Granophyre	64.35	185.6	1.0031	0.74518	0.000020	0.71599	3.87	22.11	0.1067	0.510805	0.000015	−35.93	0.509386	−12.65	3.18
ARp-38 L	UC	F. Granophyre	63.64	190.5	0.9667	0.74503	0.000006	0.71690	3.93	21.95	0.1089	0.510812	0.000006	−35.79	0.509364	−13.09	3.24
ARp-38 M	UnB	F. Granophyre	54.07	185.9	0.8410	0.73863	0.000020	0.71416	4.19	24.08	0.1061	0.510833	0.000009	−35.38	0.509422	−11.95	3.12
ARp-38 N	UnB	F. Granophyre	52.09	187.2	0.8044	0.73691	0.000030	0.71350	5.01	22.07	0.1383	0.510859	0.000005	−34.88	0.509020	−19.83	4.51
NWU-1	UV	M. Granophyre	3.17	3.2	3.2200	2.73000	3.13000	3.16000	3.14	3.15	3.1500	3.160000	3.18	3.24	3.120000	4.51	3.20
NWU-2a	UV	Epidiorite	7.30	123.0	0.1700	0.70867	0.00000	0.70367	1.58	5.66	0.1700	0.512062	0.000008	−11.24	0.509818	−4.00	3.46
NWU-3	UV	F. Granophyre	70.50	204.0	1.0000	0.74433	0.00000	0.71513	3.56	20.25	0.1100	0.510828	0.000007	−35.21	0.509417	−11.86	3.18

[a] Laboratory where the respective analyses were done.

[b] [m]—measured.

[c] (T)—recalculated to 2.02 Ga impact age.

TABLE 3. Sr and Nd isotope data from Reimold et al. (2017).

Sample[a]	Lithology type	Rb [μg g^{-1}]	Sr [μg g^{-1}]	$^{87}Rb/^{86}Sr$	$^{87}Sr/^{86}Sr$ [m][b]	2se	$^{87}Sr/^{86}Sr$ (T)[c]	Sm [μg g^{-1}]	Nd [μg g^{-1}]	$^{147}Sm/^{144}Nd$	$^{143}Nd/^{144}Nd$ [m][b]	2se	εNd (0)	$^{143}Nd/^{144}Nd$ (T)[c]	εNd (T)[c]
VPU11	Contam. Granophyre	66.09	233.42	0.8185	0.73599	0.00001	0.71217	3.97	21.99	0.1099	0.510856	0.000004	−34.94	0.509395	−12.48
VPU5	Duplicate dissoln	63.00	227.30	0.8012	0.73591	0.00001	0.71260	3.68	21.15	0.1060	0.510798	0.000004	−36.07	0.509388	−12.60
VPU21	Epidiorite	63.37	234.11	0.7824	0.73461	0.00001	0.71184	4.01	21.98	0.1111	0.510898	0.000004	−34.12	0.509420	−11.98
WUR-VG	F. Granophyre	89.72	208.48	1.2466	0.75606	0.00001	0.71978	3.87	21.67	0.1089	0.510818	0.000004	−35.68	0.509370	−12.96
VPU5	F. Granophyre	62.92	227.33	0.8002	0.73589	0.00001	0.71261	3.68	21.12	0.1060	0.510796	0.000004	−36.11	0.509386	−12.65
VG2	F. Granophyre	75.19	214.19	1.0156	0.74406	0.00001	0.71451	3.57	20.39	0.1066	0.510795	0.000004	−36.13	0.509377	−12.82
VPU23	F. Granophyre	66.16	227.14	0.8421	0.73667	0.00001	0.71217	3.82	21.90	0.1062	0.510814	0.000004	−35.76	0.509402	−12.34
TMW144	Granite Leeukop	113.65	289.21	1.1374	0.74818	0.00001	0.71508	1.73	10.37	0.1015	0.510606	0.000004	−39.81	0.509256	−15.19
VPU20	Kudu granite	73.23	561.44	0.3764	0.71875	0.00001	0.70779	2.45	20.49	0.0728	0.510058	0.000004	−50.50	0.509090	−18.45
TMW19	Kudu-Amphi	26.71	337.00	0.2286	0.70957	0.00001	0.70292	2.57	11.99	0.1307	0.511325	0.000004	−25.79	0.509587	−8.71
P2TM3	Kudu-PTB	45.71	455.00	0.2898	0.71319	0.00001	0.70476	2.99	16.52	0.1102	0.510839	0.000004	−35.27	0.509374	−12.89
TMW38B	Leeukop-PTB	109.54	282.62	1.1221	0.75092	0.00001	0.71827	4.14	23.98	0.1052	0.510695	0.000004	−38.08	0.509295	−14.43
TMW39	Leuukop-Granite	141.57	241.17	1.7031	0.77241	0.00001	0.72285	2.03	11.00	0.1124	0.510827	0.000004	−35.50	0.509332	−13.71
Hybrid 24	M. Granophyre	56.77	214.41	0.7653	0.73416	0.00001	0.71190	3.34	18.28	0.1112	0.510929	0.000014	−33.51	0.509450	−11.40
Hybrid 33	M. Granophyre	56.91	218.67	0.7522	0.73382	0.00001	0.71193	3.76	20.44	0.1120	0.510930	0.000010	−33.49	0.509442	−11.56
DGL 26	Metabasalts	6.59	470.74	0.0403	0.70358	0.00001	0.70240	4.13	18.97	0.1328	0.511329	0.000021	−25.71	0.509563	−9.17
DGL 14	Metabasalts	2.12	415.31	0.0147	0.70453	0.00004	0.70410	3.21	13.46	0.1453	0.511544	0.000013	−21.51	0.509612	−8.23
TMU5	PTB Leeukop	123.51	254.54	1.4062	0.76108	0.00001	0.72016	4.72	28.69	0.1002	0.510630	0.000004	−39.34	0.509298	−14.38
RG-2+41	PTB Quarry	144.85	185.79	2.2688	0.80365	0.00001	0.73763	11.04	75.30	0.0893	0.510358	0.000004	−44.65	0.509171	−16.87
RG1	Rand Granite Quarry	197.04	167.28	3.4420	0.84659	0.00001	0.74643	6.62	48.02	0.0840	0.510233	0.000004	−47.09	0.509116	−17.94

[a] All data were obtained at Royal Holloway University, London.

[b] [m]—measured.

[c] (T)—recalculated to 2.02 Ga impact age.

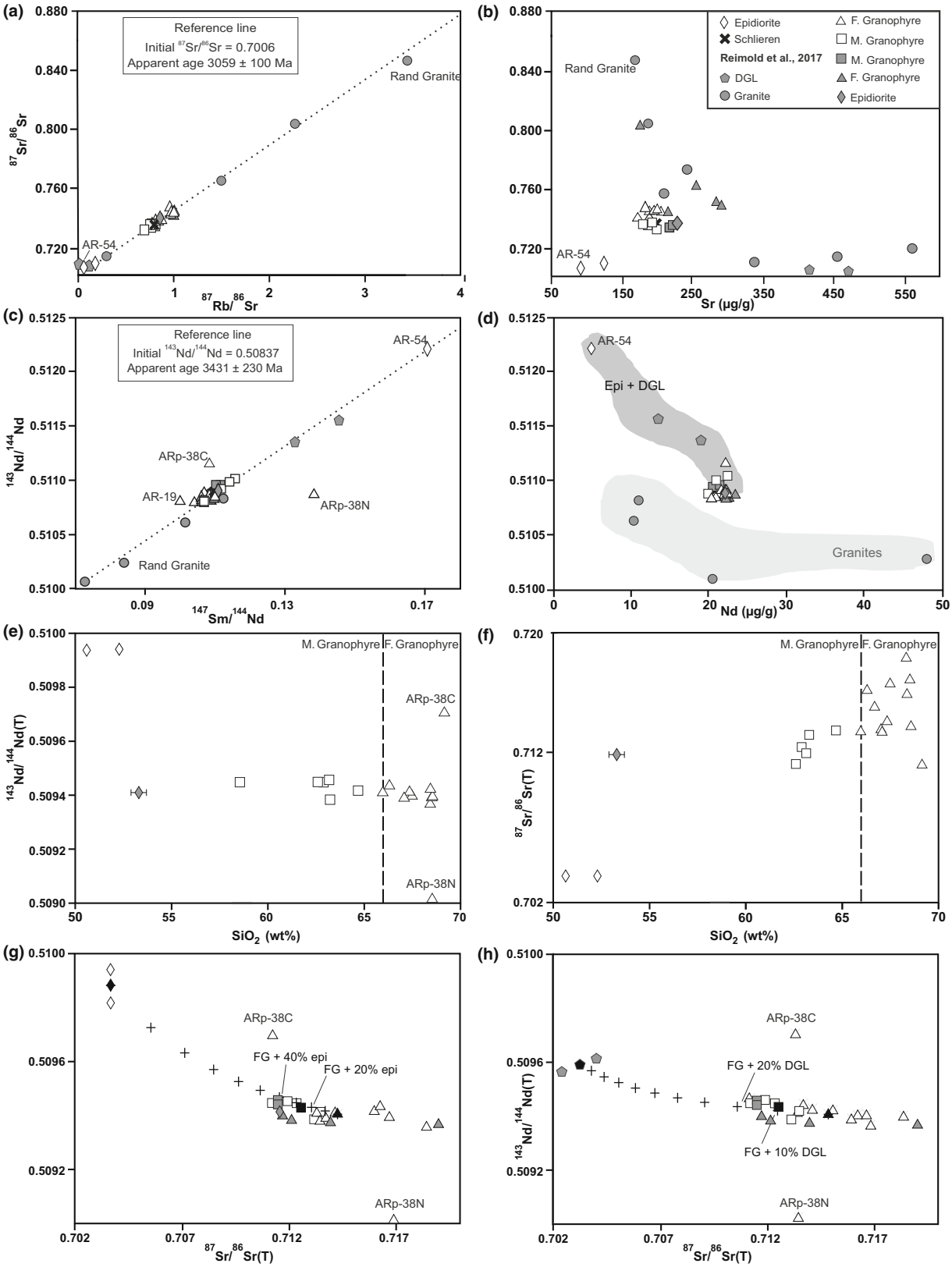
(a)
Reference line
Initial $^{87}Sr/^{86}Sr$ = 0.7006
Apparent age 3059 ± 100 Ma
Rand Granite
AR-54
$^{87}Sr/^{86}Sr$
$^{87}Rb/^{86}Sr$
(b)
Epidiorite
Schlieren
Reimold et al., 2017
DGL
Granite
F. Granophyre
M. Granophyre
M. Granophyre
F. Granophyre
Epidiorite
Rand Granite
AR-54
Sr (µg/g)
(c)
Reference line
Initial $^{143}Nd/^{144}Nd$ = 0.50837
Apparent age 3431 ± 230 Ma
AR-54
ARp-38C
AR-19
ARp-38N
Rand Granite
$^{143}Nd/^{144}Nd$
$^{147}Sm/^{144}Nd$
(d)
AR-54
Epi + DGL
Granites
Nd (µg/g)
(e)
M. Granophyre
F. Granophyre
ARp-38C
ARp-38N
$^{143}Nd/^{144}Nd(T)$
SiO_2 (wt%)
(f)
M. Granophyre
F. Granophyre
$^{87}Sr/^{86}Sr(T)$
SiO_2 (wt%)
(g)
ARp-38C
FG + 40% epi
FG + 20% epi
ARp-38N
$^{143}Nd/^{144}Nd(T)$
$^{87}Sr/^{86}Sr(T)$
(h)
ARp-38C
FG + 20% DGL
FG + 10% DGL
ARp-38N
$^{143}Nd/^{144}Nd(T)$
$^{87}Sr/^{86}Sr(T)$

FIGURE 10. Isotopic results for Mafic and Felsic Granophyre, and from the potential contributors to Mafic Granophyre—epidiorite and Dominion Group meta-lava (data from Reimold et al., 2017). Several data for Archean granite from Reimold et al. (2017) have also been plotted. Symbol sizes throughout are larger than the 2 sigma errors on these data. (a) $^{87}Rb/^{86}Sr$ versus $^{87}Sr/^{86}Sr$ and (b) Sr versus $^{87}Sr/^{86}Sr$ mixing diagram. (c) $^{147}Sm/^{144}Nd$ versus $^{143}Nd/^{144}Nd$. (d) Nd versus $^{143}Nd/^{144}Nd$, showing a stronger data scatter for the precursor lithologies than in the other diagrams. The epidiorite values from the present work are slightly depleted in Nd in comparison with the data from Reimold et al. (2017). (e, f) SiO_2 versus $^{143}Nd/^{144}Nd$ and $^{87}Sr/^{86}Sr$ diagrams, respectively, also indicating the cutoff at 66 wt% SiO_2 between felsic and mafic samples. The data from this study and from Reimold et al. (2017) are shown in these two panels. For sample VPU21 an individual SiO_2 value is not available so that we plotted this sample against the average epidiorite silica content as given in Table 3 of Reimold et al. (2021). (g, h) Mixing calculations with impact age-corrected Nd and Sr isotope data between average Felsic Granophyre (black triangle) and epidiorite (black diamond) or Dominion Group meta-lava (black pentagon), respectively. In both cases, 10%–40% addition of a mean component to Felsic Granophyre can account for the observed spread of Mafic Granophyre isotopic compositions (mean value represented by black square). Sample VPU21 (epidiorite) from Reimold et al. (2017) was not used to calculate a mean value for the epidiorite component in (g), because this sample has an outlier composition when compared to other epidiorite samples.

the whole suite of REE is not achieved, the mixing for 20% and 40% of epidiorite addition still falls below the actual pattern for average Mafic Granophyre. Similar epidiorite contributions were also proposed based on Re-Os and Se isotope data by Reimold et al. (2021). We have done similar modeling with the REE data for DGL, as well, but it must be pointed out that the positive Eu anomaly and adjacent Gd and Tb data do not agree, a priori, with the negative Eu anomaly and adjacent elemental trend of Mafic Granophyre.

Primitive crust-normalized trace element abundance ranges for epidiorite, DGL, and VS meta-volcanics are contrasted with the trace element patterns for Felsic and Mafic Granophyre in Figure 9. This illustration provides some support for an admixture of epidiorite to Felsic Granophyre in the generation of Mafic Granophyre rather than from DGL, as the abundances for Th, Sr, and Zr in DGL are not compatible with an admixture of this component to result in the abundances in Mafic Granophyre (e.g., Th elevated in DGL but depleted in MG).

We also compare the trace element systematics of epidiorite from the Vredefort area with data for samples from the VS (field in Figure 9) of the wider region (after Gumsley et al., 2020). Thus, our epidiorite data are, in terms of HREE, even more depleted than the most depleted Ventersdorp samples. The idea that Vredefort epidiorite could represent material from possible feeder dikes for the regional VS magmatism (e.g., Pybus, 1995; Reimold et al., 2000) may, thus, have to be reevaluated. Radiometric dating should be combined with isotopic studies for more in-depth comparison between Vredefort epidiorite and regional VS meta-volcanics.

Clues from Rb-Sr and Sm-Nd Isotope Systematics

New Rb-Sr and Sm-Nd isotopic ratios are compared here against the previous results of Reimold et al. (2017). From the main data clusters in Rb-Sr and Sm-Nd isotope space (Figure 10a,c), it is obvious that there is some scatter around the respective reference lines, with regard to both Granophyre and epidiorite data. In particular, in Figure 10c, three Felsic Granophyre data fall distinctly off the regression line. Another important observation is that the isotope data for DGL plot away from the Granophyre and epidiorite data cluster. In terms of Rb-Sr isotopes (Figure 10a), most of the data for Granophyre and epidiorite fall into an overlapping range, whereas the DGL data are comparatively depleted in radiogenic Sr. In the Sm-Nd isotope systematics (Figure 10c), the DGL data are strongly enriched in radiogenic Nd compared to the Granophyre samples that, again, form a tight cluster with the epidiorite data. Epidiorite sample AR-54 is highly radiogenic though, and this can currently not be explained on the basis of our petrographic or geochemical database. We interpret the reference lines in these diagrams as mixing lines, as various 3.1–3.2 Ga to 2.02 Ga lithologies are jointly regressed. The Sr isotope data (Figure 10a) for the Felsic and Mafic Granophyre samples plot relatively closely together with epidiorite samples.

In the $^{143}Nd/^{144}Nd$ versus Nd abundance diagram (Figure 10d), we note a trend involving a swath of granite data and an elongated field for epidiorite and DGL data that—combined—approximate the resemblance of a somewhat hyperbolic mixing trend. All impact melt rock plus some epidiorite data fall in between these two semi-trends.

In our assimilation model for the generation of Mafic Granophyre from admixture of a mafic component to Felsic Granophyre, the Archean Basement Complex constitutes the dominant component from which Felsic Granophyre was formed—in addition to Witwatersrand shale and quartzite (Reimold et al., 1990), but it is the Felsic Granophyre that constitutes one presumed endmember in the mixing process for Mafic Granophyre.

The currently available isotopic database does not favor DGL as a likely precursor component for the Mafic Granophyre phase, as was previously concluded by

Reimold et al. (2017, 2021) based on their Rb-Sr, Sm-Nd, Re-Os, and Se isotopic data. In all four systems, epidiorite is the favored mafic component in mixing toward formation of the Mafic Granophyre phase. However, it is clear that further isotope data need to be generated for these two mafic country rock types to confirm this tentative conclusion.

In Figure 10c, one Felsic Granophyre sample (ARp-38N) has similar radiogenic Nd isotope characteristics as the other FG samples, but has a higher Sm/Nd isotope ratio, whereas another FG sample (Arp-38C) has a more radiogenic Nd isotope composition. These samples do not plot along the reference line and could represent Felsic Granophyre compositions with additional epidiorite or DGL clasts that would produce such outlier values. However, there is no petrographic or geochemical evidence that currently would substantiate this possibility.

The εNd (t) values for Felsic Granophyre samples are between −11.18 (AR 53) and −12.65 (ARp-38K), and between −11.45 (ARp-38F) and −12.61(ARp-38B) for Mafic Granophyre. The T_{DM} model ages are between 3.18 and 3.07 Ga for Felsic and 3.22 and 3.14 Ga for Mafic Granophyre (Table 3). These results emphasize that both Granophyre types are based on Archean precursors, whereby the Archean granitoid component plays the major role. The average εNd(t) value for Felsic Granophyre is −12.37, in comparison with an average value for Mafic Granophyre of −11.80. Similarly, the T_{DM} ages for Felsic Granophyre are slightly older than the values for the Mafic Granophyre, with ranges of values of 3.23 and 3.17 Ga, respectively. Considering that the epidiorite has an εNd(t) value of −1.76 and should have a T_{DM} age (not determined in this study) of <3 Ga (if this lithology corresponds to the 2.7 Ga VS), this would corroborate a contribution from epidiorite to Felsic Granophyre to form Mafic Granophyre as well. Considering that sample VPU21 plots distinctly below the other epidiorite data in Figure 10e, it is obvious that Vredefort epidiorite chemically is quite diverse. Clearly, this may affect the outcome of mixing modeling.

Figure 10g,h offer solutions of mixing calculations with combined Sr and Nd isotope data. For the impact age-corrected data, Mafic Granophyre isotope compositions can be generated by mixing Felsic Granophyre with 20–40% of epidiorite, but admixture of relatively low percentages of average DGL can achieve the same result, as indicated along the mixture arrays.

Formation of the Mafic Granophyre

Previous work (e.g., Reimold & Gibson, 2006; Therriault et al., 1997, and references therein) indicated that the genesis of Granophyre can be explained by complete, impact-related melting of several different target rock types (Archean granitoid, Witwatersrand quartzite and shale—Reimold et al., 1990, possibly also Ventersdorp basalt—French & Nielsen, 1990). The mafic character of a few Granophyre samples was explained for a long time by local assimilation of mafic country rock, namely epidiorite.

The Mafic Granophyre phase was highlighted by Lieger (2011) and Lieger and Riller (2012), who suggested that the mafic melt had been emplaced first in the dikes, and the more felsic and fragment-rich melts followed during a second emplacement pulse from the overlying, differentiating impact melt sheet. Wannek (2015) opposed this and noted that the Mafic Granophyre occurs in the *central* part of the dike on Kopjeskraal. Based on chemical and isotope geochemical evidence, Wannek (2015) and Reimold et al. (2017, 2021) proposed that the Mafic Granophyre on Kopjeskraal Farm was formed by local admixture (assimilation) of an epidiorite-type component during dike emplacement. The isotope data of Reimold et al. (2016, 2017) favored an epidiorite over a DGL component.

According to, for example, Reimold & Gibson (2006), the distinctive clast population in the Vredefort impact melt rock, with strong metasedimentary and granitoid components, can only be explained by emplacement of the Granophyre from above, where the melt could assemble a clast population that involves all major supracrustal rock types (Transvaal Supergroup to Dominion Group), as well as Archean granitoid basement. Notably, the occurrence of Mafic Granophyre does not appear to be symptomatic for the 9 Granophyre dikes on the Vredefort Dome but limited to only two dikes in the NW-W sector (Kopjeskraal-Rensburgdrif and Rietkuil). Here, we report that Mafic Granophyre from Rensburgdrif contains an abundance of small, relict clasts of a mafic lithology. The compositional zoning in the dike could be explained by wall-rock assimilation (e.g., Therriault et al., 1996, 1997), as the marginal zones of the dike are more enriched in wall-rock material (granitoid) than the inner part of this dike. MgO and SiO_2 contents in fragment-poor Granophyre (3.9 wt% and 61.5 wt%, respectively) are intermediate between those of fragment-rich Granophyre (3.57 wt% MgO and 67 wt% SiO_2) and epidiorite country rock (8.8 wt% MgO and 52.3 wt% SiO_2). The analyzed profile across the Rensburgdrif dike contains two occurrences of a mafic phase in the interior of the dike, and the felsic phase is located predominantly along the margins. The chemical and isotopic results presented here for Granophyre, epidiorite, and DGL samples support that the Mafic Granophyre is the result of assimilation of a mafic component, possibly epidiorite (Reimold et al., 2017, 2021; this work), by the Felsic Granophyre.

One could consider that admixture of clasts from felsic (granitoid) host rock to the impact melt in the outer zones of the dikes could have changed an originally more mafic composition to a more felsic one. In this scenario, the more mafic phase would be the only stoped-in variety that would have been altered by added felsic country rock. This scenario—in principle a plausible one—does appear unrealistic, however, as all other dikes of Granophyre in the area of the Vredefort Dome lack the mafic phase, clearly do not exhibit this mafic-felsic impact melt rock duality of the dikes in the northwest of the dome, and a relative silica enrichment in their marginal parts.

Unfortunately, it was not possible to sample a profile across the Rensburgdrif dike exactly where it comes closest to the epidiorite in outcrop. However, the results of the two profile experiments reported by Reimold et al. (2021) for Kopjeskraal and here for Rensburgdrif, and the results of Wannek (2015) are consistent with respect to the occurrence of a Mafic Granophyre phase mainly in interior parts of the dike. The two Granophyre samples collected in the relative vicinity of epidiorite on Rensburgdrif (e.g., AR-13—150 m from the nearest exposure of epidiorite; AR-53—100 m from epidiorite) show felsic composition. Only further work can provide clarity as to the more regional distribution of, and the actual sizes of the possibly raft-like occurrences of the mafic impact melt rock along this Granophyre dike at the NW core-collar boundary.

There is a second group of Granophyre workers that has favored a different model for the formation of the Felsic and Mafic Granophyre phases. Lieger (2011), Lieger and Riller (2012), and, most recently, Huber et al. (2020, 2022) used major element data for these two Granophyre varieties to discuss that these two impact melt rock phases were generated in accordance with a model for the Offset Dikes at the Sudbury impact structure. These dikes are considered to comprise two different phases that were emplaced from the differentiating impact melt sheet (Sudbury Igneous Complex), where they originated from different depths. In particular, the more mafic phase had been derived from the mafic, basal layer of the Sudbury Igneous Complex. In analogy, the two Granophyre phases have also been considered to be derived from different levels of a differentiated Vredefort impact melt sheet that today has been entirely eroded. The base of the original impact melt sheet could have included assimilated mafic rock.

The identification of the Mafic Granophyre is essentially based on chemical analysis of random samples (e.g., by Therriault et al., 1997, from the dike on Rietkuil) and profile samples. With this lack of field observations related to possible contacts between the two Granophyre phases, it is not known what the real size of the occurrences of Mafic Granophyre is. Our group has referred to *rafts* in Felsic Granophyre (Reimold et al., 2017, 2021), but this expression does not contain any size constraints. The Mafic Granophyre portions sampled in our profile experiments indicate sizes of several meters (in the direction perpendicular to dike extension).

In continuation of their 2020 work, Huber et al. (2022) provided a quite sizable table of chemical analyses for Vredefort Granophyre, with many analyses duplicated from the earlier work. The geochemical discussion is also remarkably similar. Huber et al. (2022) claimed that Therriault et al. (1997) "noted that dikes in the collar appear to be more mafic and ascribed this observation to assimilation of the surrounding mafic metavolcanic rocks of the Dominion Supergroup" (Therriault et al., 1997, pp. 1–2). It should be noted that the Dominion is classified as the "Dominion Group." More importantly, Therriault et al. (1997) never made this claim and, instead, stated: "Chemical variations, although minor, are observed in the case of samples taken at localities where the Granophyre cross-cuts epidiorite intrusions . . . In these cases, the local composition of the Vredefort Granophyre has been slightly affected by the assimilation of epidiorite clasts" (Therriault et al., 1997, p. 118). This is in agreement with our conclusions regarding the formation of Mafic Granophyre (Reimold et al., 2017, 2021, this work).

Huber et al. (2022)—like Wannek (2015)—extended the occurrence of Mafic Granophyre into the Eldorado property southwest of Kopjeskraal. Thus, we can now summarize that Mafic Granophyre occurs widely along one specific dike of Vredefort Granophyre only—the dike that extends in the northwest of the Vredefort Dome from the Kopjeskraal, via the Eldorado and Kommandonek properties, to Rensburgdrif (dikes 7 and 8 of Therriault et al., 1996). In addition, two samples of Mafic Granophyre have now been analyzed from a second dike on Farm Rietkuil (this work and Therriault et al., 1996). Otherwise, until now, none of the many workers who have studied the Vredefort Granophyre since the earliest work by Hall and Molengraaff (1925) and Nel (1927) has identified such a mafic impact melt rock sample from any other Granophyre dike in the Vredefort Dome.

In conclusion, there are currently two hypotheses for the formation of the Mafic Granophyre: the Lieger (2011)–Huber et al. (2022) hypothesis of successive intrusions of felsic and more mafic impact melt gravitationally derived from a differentiated impact melt sheet, and the assimilation hypothesis by Wannek (2015) and Reimold et al. (2017, 2021), which is favored here as well. The former does not consider the fact that the Mafic Granophyre is observed only in the northwest of the Vredefort Dome. Furthermore, Lieger (2011) and Lieger and Riller (2012) erroneously reported the inverse of the Mafic/Felsic Granophyre configuration actually observed in the field (namely Felsic

Granophyre on the outside and Mafic Granophyre in the interior). They did not consider the clast petrography reported for all these dikes, whereby presence of clasts from a mafic country rock (epidiorite) exists only where an impact melt rock dike transects, or comes close to, epidiorite. Huber et al. (2022) discuss more felsic clasts in more mafic melt on Kopjeskraal and Eldorado and take this as support of an injection of more mafic impact melt into the fracture *after* injection of the more felsic variety. However, our geochemical analyses along profiles across the dike on Kopjeskraal (Reimold et al., 2016) and Rensburgdrif (this work), besides the detailed investigation by Wannek (2015) on Kopjeskraal, have demonstrated that the situation is inverse: Mafic Granophyre occurs in the interior of the dike with Felsic impact melt rock along the margins. The fact that there are rounded, up to decimeter-sized clasts of epidiorite in Felsic Granophyre on Kopjeskraal (Reimold et al., 2021) and that we found two distinct positions of Mafic Granophyre along the dike-cutting profile on Rensburgdrif can be taken as evidence that Mafic Granophyre (i.e., partially assimilated epidiorite) occurs in Felsic Granophyre, as epidiorite was incorporated into the dike in the form of rafts. We must also draw attention to the fact that no individual occurrences of Mafic Granophyre—separate from Felsic Granophyre—in dikes have been reported to date from the Vredefort Dome. This raises an interesting question: Why would a mafic differentiate off a stratified impact melt body only occur in discontinuous ("blobby") form in Felsic Granophyre dikes, exactly where these are coming very close to, or cut, at current erosion level epidiorite and DGL, only near the northwestern western core-collar contact?

Our new Rb-Sr and Sm-Nd isotope data for Rensburgdrif samples are in excellent agreement with previously reported isotopic results on Vredefort Granophyre (Reimold et al., 2017, 2021). These data support an admixture of a 20%–40% mafic component to Felsic Granophyre. This mafic protolith component is tentatively considered to be epidiorite—based on field observations of epidiorite inclusions in Granophyre (also Therriault et al., 1996) and some geochemical indications. However, it cannot yet be fully excluded that DGL could also have been involved.

The major and trace element geochemical data presented here and from our earlier work support the assimilation hypothesis. This study as well as our previous work has not provided any geochemical evidence in support of the multiple impact melt intrusion hypothesis.

Recommendations

Clearly, some progress has been made regarding the possible origin of the Mafic Granophyre. However, it has also been shown that a number of issues deserve further investigation. This includes further detailed study of the second Granophyre dike extending onto Rietkuil. The schlieren within the Granophyre dike on Rensburgdrif need to be analyzed. Field work must also be continued in search of evidence with respect to possible contact relationships between the Mafic and Felsic Granophyre phases. Further analysis of the pyroxene and amphibole in mafic microclasts in the Mafic Granophyre, in comparison to compositions of pyroxene and amphibole in epidiorite and DGL, is required. Additional chemical and isotopic analyses of samples of these mafic country rock types occurring along the western/northwestern core/collar boundary should be obtained to improve the still limited database for these lithologies on the Vredefort Dome. We have already begun to tackle these issues.

CONCLUSIONS

We have conducted a detailed multidisciplinary study of the Granophyre dike on Farm Rensburgdrif, south of the Vaal River, along the extension of the dike from farms Kopjeskraal and Eldorado, north of the Vaal River. In addition, a sample of Mafic Granophyre was identified from a second impact melt rock dike in the NW of the Vredefort Dome, on the Rietkuil property, confirming an early, so far neglected observation by Therriault et al. (1996). Petrographically and geochemically, this sample is similar to the Mafic Granophyre previously identified at Kopjeskraal and Rensburgdrif. Other main results of this study include:

- Analysis of the samples from a profile across the Granophyre dike on Rensburgdrif indicates that the Granophyre has a relatively homogeneous mineral composition, but also shows a significant variation in the abundance of the main modal components between the two types of Granophyre present.
- Two distinct impact melt rock types (felsic and more mafic) were recognized, whereby the mafic phase (clast poor) was observed in inner parts of the dike, as observed on Kopjeskraal to the north, and the felsic (clast rich) type occurs mainly along the dike margins.
- Two Mafic Granophyre occurrences are indicated in the interior of the dike on Rensburgdrif (inside of the northwestern margin and in the central part). This, together with the observation of mafic inclusions in Felsic Granophyre on Kopjeskraal (Reimold et al., 2021), may be evidence for the presence of mafic rafts in Granophyre dikes.
- The DGL isotope data plot far off the Granophyre and epidiorite data array in Sr-Nd isotope systematics (Figure 10), which supports that this lithology is not a likely precursor for the Mafic Granophyre.

- Our isotopic mixing trends strongly support formation of Mafic Granophyre as a mixture of Felsic Granophyre with 20%–40% epidiorite, in agreement with the Sr-Nd-Os-Se isotope work of Reimold et al. (2017, 2021). Our REE modeling with elevated proportions of epidiorite allows to resolve the apparent discrepancy between HREE abundances between Felsic and Mafic Granophyre. This indicates—like earlier isotope work by Reimold et al. (2021)—that a significant contribution (maybe as high as 40%) of epidiorite might generate the geochemical composition of Mafic Granophyre. However, in terms of Sr and Nd isotopes, we are showing that a comparatively lower admixture of maybe 20% DGL can also achieve a reasonable composition for Mafic Granophyre.
- Trace element systematics also indicate a 20%–40% admixture, and the mixing relationships between Felsic Granophyre and epidiorite in terms of Sr and Nd isotope data support this as well.
- It must be further investigated if the epidiorite intrusions into Witwatersrand Supergroup strata in the collar of the Vredefort Dome should be considered possible VS formations.

These new results for the Granophyre on Farm Rensburgdrif strongly mitigate against the hypothesis that Mafic Granophyre represents a differentiate from the original impact melt body in the—at Vredefort entirely eroded—impact crater. They favor the epidiorite assimilation/admixture hypothesis for the formation of Mafic Granophyre. That this phase has never been reported from impact melt rock dikes from elsewhere in the Vredefort Dome than in this NW/W sector at the core-collar boundary provides evidence for this assimilation to have occurred only locally. This is best explained as a result of stoping into mafic country rock by the downward advancing impact melt during its descent along extensional fractures opened during the collapse phase of the central uplift.

Acknowledgments—This work includes results from the MSc study of Ana Rita Pereira Maciel, at the University of Brasília. The authors thank the Geological Society of South Africa for their REI Fund grant to ARPM to support the field work and Christo Meyer of Kopjeskraal Lodge for access and permission to collect samples on his property, and for his hospitality. We thank the Institute of Geosciences of the University of Brasilia for the use of laboratory infrastructure, and Guilherme de Oliveira Gonçalves for essential support with LA-ICP-MS analysis. We are grateful to the technical staff of the geoscientific laboratories at the Vrije Universiteit Brussel (AMGC), the Naturhistorisches Museum Wien, the Department of Lithospheric Research of the University of Vienna, and the Institut für Geologie und Mineralogie of the Universität zu Köln, for expert petrographic, chemical, and isotopic support. This study was financed in part by the Coordenação de Aperfeiçoamento de Pessoal de Nível Superior—Brasil (CAPES)—Finance Code 001. SG and VD acknowledge the support from the FWO-FNRS EoS project "ET-HoME" and Belgian Science Policy (BELSPO) project "DESIRED." VD thanks the FRS-FNRS for support. The help from Cecilia Teller and Wendy Debouge at ULB was greatly appreciated. ALO acknowledges a post-doctoral research scholarship from FINATEC (UnB) (grant No. 695/2022). The research by WUR and NH was financed by the Conselho Nacional de Desenvolvimento Científico e Tecnológico (CNPq) through several research grants (projects 309878/2019-5 and 305761/2019-6, respectively). The constructive reviews and resulting recommendations by the Associate Editor, Meikel Poelchau, and the reviewers, John Spray and Lutz Hecht, are much appreciated.

Data Availability Statement—Most original data from this work are included in the manuscript. Other data used for comparison are properly referenced. The electron microprobe results can be obtained upon request from the Corresponding Author.

Editorial Handling—Dr. Michael H. Poelchau.

REFERENCES

Allen, N. H., Nakajima, M., Wünnemann, K., Helhoski, S., and Trail, D. 2022. A Revision of the Formation Conditions of the Vredefort Crater. *Journal of Geophysical Research: Planets* 127: e2022JE007186.

Armstrong R. A., Compston W., Retief E. A., Williams I. S., and Welke H. J. 1991. Zircon Ion Microprobe Studies Bearing on the Age and Evolution of the Witwatersrand Triad. *Precambrian Research* 53: 243–66. https://doi.org/10.1016/0301-9268(91)90074-K

Armstrong, R. A., Lana, C., Reimold, W. U., and Gibson, R. L. 2006. SHRIMP Zircon Age Constraint on Mesoarchean Crustal Development in the Vredefort Dome, Central Kaapvaal Craton, South Africa. In *Processes on the Early Earth*, edited by W. U. Reimold, and R. L. Gibson, Geological Society of America Special Papers 405, 233–53. Boulder, CO: Geological Society of America.

Beaton, K. J., Gibson, R. L., Bybee, G. M., Walker, S., Diener, J. F. A., and Baxter, E. F. 2022. Amphibolite Facies Metamorphism in Lower Witwatersrand Supergroup Rocks Exposed in the Vredefort Dome—A Ventersdorp LIP Connection. *South African Journal of Geology* 125: 191–210.

Bisschoff, A. A. 1972. The Dioritic Rocks of the Vredefort Dome. *Transactions of the Geological Society of South Africa* 76: 31–45.

Bisschoff, A. A. 1988. The History and Origin of the Vredefort Dome. *South African Journal of Science* 84: 413–7.

Bisschoff, A. A. 1999. *The Geology of the Vredefort Dome: Explanation of Geological Sheets 2627CA, CB, CC, CD, DA, DC, and 2727AA, AB, BA, as Well as the Map at 1:50,000 Scale*. Johannesburg: Council for Geoscience, Geological Survey of South Africa.

Buchanan, P. C., and Reimold, W. U. 2002. Planar Deformation Features and Impact Glass in Inclusions from the Vredefort Granophyre, South Africa. *Meteoritics & Planetary Science* 37: 807–22.

Coetzee, H., and Kruger, F. J. 1989. The Geochronology, Sr- and Pb-Isotope Geochemistry of the Losberg Complex, and the Southern Limit of Bushveld Complex Magmatism. *South African Journal of Geology* 92: 37–41.

De Paolo, D. J. 1981. Neodymium Isotopes in the Colorado Front Range and Crust-Mantle Evolution in the Proterozoic. *Nature* 291: 193–6.

Dietz, R. S. 1961. Vredefort Ring Structure: Meteorite Impact Scar? *Journal of Geology* 69: 496–505.

French, B. M. 1998. *Traces of Catastrophe: A Handbook of Shock-Metamorphic Effects in Terrestrial Meteorite Impact Structures*. LPI Contribution 954. Houston, TX: Lunar and Planetary Institute, 120.

French, B. M., and Koeberl, C. 2010. The Convincing Identification of Terrestrial Meteorite Impact Structures: What Works, What Doesn't, and Why. *Earth-Science Reviews* 98: 123–70.

French, B. M., and Nielsen, R. L. 1990. Vredefort Bronzite Granophyre: Chemical Evidence for Origin as a Meteorite Impact Melt. *Tectonophysics* 171: 119–38.

French, B. M., Orth, C. J., and Quintana, L. R. 1989. Iridium in the Vredefort Bronzite Granophyre: Impact Melting and Limits on a Possible Extraterrestrial Component. In *Proceedings of the 19th Lunar and Planetary Science Conference*, 733–44. Houston, TX, Cambridge, UK: Cambridge University Press.

Gibson, R. L. 2019. The Mesoarchaean Basement Complex of the Vredefort Dome, A Mid-Crustal Section through the Central Kaapvaal Craton Exposed by Impact. In *The Archaean Geology of the Kaapvaal Craton, Southern Africa*, edited by A. Kröner, and A. Hofmann, 109–32. Regional Geology Reviews, Springer Nature, London-New York-Berlin.

Gibson, R. L., Armstrong, R. A. and Reimold, W. U. 1997. The Age and Thermal Evolution of the Vredefort Impact Structure: A Single-Grain U-Pb Zircon Study. *Geochimica et Cosmochimica Acta* 61: 1531–40.

Gibson, R. L., and Reimold, W. U. 2005. Shock Pressure Distribution in the Vredefort Impact Structure, South Africa. In *Large Meteorite Impacts and Planetary Evolution III*, edited by T. Kenkmann, F. Hörz, and A. Deutsch, Geological Society of America Special Paper 384, 329–49. Boulder, CO: Geological Society of America.

Gibson, R. L., and Reimold, W. U. 2008. Geology of the Vredefort Impact Structure: A Guide to Sites of Interest. *Council for Geoscience, Pretoria, Memoir* 97: 181 pp.

Gioia, S., and Pimentel, M. 2000. The Sm-Nd Isotopic Method in the Geochronology Laboratory of the University of Brasília. *Anais da Academia Brasileira de Ciencias* 72: 219–45.

Gumsley, A., Stamsnijder, J., Larsson, E., Söderlund, U., Næraa, T., De Kock, M., Sałacińska, A., Gawęda, A., Humbert, F., and Ernst, R. 2020. Neoarchean Large Igneous Provinces on the Kaapvaal Craton in Southern Africa Re-Define the Formation of the Ventersdorp Supergroup and its Temporal Equivalents. *Geological Society of America Bulletin* 132: 1829–44.

Hall, A. L., and Molengraaff, G. A. F. 1925. The Vredefort Mountain Land in the Southern Transvaal and the Northern Orange Free State. *Verhandelingen, Koninklijke Akademie van Wetenschappen, Amsterdam* 24: 183.

Hart, R. J., Nicolaysen, L. O., and Gale, N. H. 1981. Radioelement Concentrations in the Deep Profile through Precambrian Basement of the Vredefort Structure. *Journal of Geophysical Research: Solid Earth* 86(B11): 10653–61.

Hecht, L., Wittek, A., Riller, U., Mohr, T., Schmitt, R. T., and Grieve, R. A. F. 2008. Differentiation and Emplacement of the Worthington Offset Dike of the Sudbury Impact Structure. *Meteoritics & Planetary Science* 43: 1659–79.

Henkel, H., and Reimold, W. U. 1998. Integrated Geophysical Modeling of a Giant, Complex Impact Structure: Anatomy of the Vredefort Structure, South Africa. *Tectonophysics* 287: 1–20.

Hoffmann, J. E., Münker, C., Næraa, T., Rosing, M. T., Herwartz, D., Garbe-Schönberg, C. D., and Svahnberg, H. 2011. Mechanisms of Archean Crust Formation Inferred from High-Precision HFSE Systematics in TTGs. *Geochimica et Cosmochimica Acta* 75: 4157–78.

Hopkins, R. G., and Spray, J. G. 2022. *Temperature-Facilitated Phase Transformations in Shock Melt Veins from the Manicouagan Impact Structure (Abstract)*. Rochechouart, France: ICF-CIRIR (International Congress-Festival). 2.

Huber, M. S., Kovaleva, E., Clark, M. D., Riller, U., and Fourie, F. D. 2022. Evidence from the Vredefort Granophyre Dikes Points to Crustal Relaxation Following Basin-Size Impact Cratering. *Icarus* 274: 114812.

Huber, M. S., Kovaleva, E., and Riller, U. 2020. Modeling the Geochemical Evolution of Impact Melts in Terrestrial Impact Basins: Vredefort Granophyre Dikes and Sudbury Offset Dikes. *Meteoritics & Planetary Science* 55: 2320–37.

Ivanov, B. A. 2005. Numerical Modeling of the Largest Terrestrial Meteorite Craters. *Solar System Research* 39: 381–409.

Jackson, M. C. 1992. A Review of the Late Archean Volcano-Sedimentary Dominion Group and Implications for the Tectonic Setting of the Witwatersrand Supergroup, South Africa. *Journal of African Earth Sciences* 15: 169–86.

Jackson, M. C. 1994. Geochemistry and Metamorphic Petrology of Dominion Group Metavolcanics in the Vredefort Area, South Africa. *South African Journal of Geology* 97: 62–77.

Johnson, M. R., Anhaeusser, C. R., and Thomas, R. J., editors. 2006. *The Geology of South Africa*. Johannesburg: Geological Society of South Africa and Council for Geoscience. 691.

Jochum, K. P., Weis, U., Schwager, B., Stoll, B., Wilson, S. A., Haug, G. H., Andreae, M. O., and Enzweiler, J. 2016. Reference Values Following ISO Guidelines for Frequently Requested Rock Reference Materials. *Geostandards and Geoanalytical Research* 40: 333–50.

Kamo, S. L., Reimold, W. U., Krogh, T. E., and Colliston, W. P. 1996. A 2.023 Ga Age for the Vredefort Impact Event and a First Report of Shock Metamorphosed Zircons in Pseudotachylitic Breccias and Granophyre. *Earth and Planetary Science Letters* 144: 369–88.

Koeberl, C. 2014. The Geochemistry and Cosmochemistry of Impacts. In *Treatise on Geochemistry*, edited by H. D. Holland, 2nd ed., 73–118. Amsterdam: Elsevier Publishers.

Lana, C., Gibson, R. L., Kisters, A. F. M., and Reimold, W. U. 2003. Archean Crustal Structure of the Kaapvaal Craton, South Africa—Evidence from the Vredefort Dome. *Earth and Planetary Science Letters* 206: 133–44.

Lana, C., Reimold, W. U., Gibson, R. L., Koeberl, C., and Siegesmund, S. 2004. Nature of the Archean Midcrust in the Core of the Vredefort Dome, Central Kaapvaal Craton, South Africa. *Geochimica et Cosmochimica Acta* 68: 623–42.

Lieger, D. 2011. *Structural and Geochemical Analyses of Fragment-Rich Pseudotachylite Bodies and the Vredefort Granophyre of the Vredefort Impact Structure, South Africa*. Ph.D. Thesis. Berlin, Germany: Department of Earth Sciences, Freie Universität Berlin. 212.

Lieger, D., and Riller, U. 2012. Emplacement History of Granophyre Dikes in the Vredefort Impact Structure, South Africa, Inferred from Geochemical Evidence. *Icarus* 219: 168–80.

Lightfoot, P. C. 2016. *Nickel-Sulfide Ores and Impact Melts—Origin of the Sudbury Igneous Complex*. Amsterdam: Elsevier. 662.

Mader, D., and Koeberl, C. 2009. Using Instrumental Neutron Activation Analysis for Geochemical Analyses of Terrestrial Impact Structures: Current Analytical Procedures at the University of Vienna Gamma Spectrometry Laboratory. *Applied Radiation and Isotopes* 67: 2100–3.

Marsh, J. S. 2006. The Dominion Group. In *The Geology of South Africa*, edited by M. R. Johnson, C. R. Anhaeusser, and R. J. Thomas, 149–54. Johannesburg: Geological Society of South Africa and Council for Geoscience.

McDonough, W. F., and Sun, S. S. 1995. The Composition of the Earth. *Chemical Geology* 120: 223–53.

Nagl, P., and Mader, D. 2019. X-Ray Fluorescence (XRF) and Instrumental Neutron Activation Analysis (INAA) for the Geochemical Analysis of Rocks, Presented on In-House Control Samples (Abstract). *Mitteilungen der Österreichischen Mineralogischen Gesellschaft* 165: 67.

Nebel, O., Mezger, K., Scherer, E. E., and Münker, C. 2005. High Precision Determinations of $^{87}Rb/^{85}Rb$ in Geologic Materials by MC-ICP-MS. *International Journal of Mass Spectrometry* 246: 10–8.

Nel, L. T. 1927. The Geology of the Country around Vredefort. *Special Publication of the Geological Survey of South Africa* 6: 134.

Otten, O. 1998. *Petrographische und Geochemische Untersuchungen am Outer Granite Gneiss im Vredefort Dome, Süd Afrika*. Diplomarbeit (unpubl.). Göttingen: Fakultät für Geowissenschaften und Geografie (IGDL), Universität Göttingen. 88.

Pin, C., and Zalduegui, J. F. S. 1997. Sequential Separation of Light Rare-Earth Elements, Thorium and Uranium by Miniaturized Extraction Chromatography: Application to Isotopic Analyses of Silicate Rocks. *Analytica Chimica Acta* 339: 79–89.

Pybus, G. Q. J. 1995. *Geological and Mineralogical Analysis of some Mafic Intrusives in the Vredefort Dome, Central Witwatersrand Basin*. M.Sc. Thesis. Johannesburg: University of the Witwatersrand. 376.

Reimold, W. U. 1998. Exogenic and Endogenic Breccias: A Discussion of Major Problematics. *Earth Science Reviews* 43: 25–47.

Reimold, W. U., and Gibson, R. L. 2006. The Melt Rocks of the Vredefort Impact Structure—Vredefort Granophyre and Pseudotachylitic Breccias: Implications for Impact Cratering and the Evolution of the Witwatersrand Basin. *Chemie der Erde—Geochemistry* 66: 1–35.

Reimold, W. U., Hauser, N., Hansen, B. T., Thirlwall, M., and Hoffmann, M. 2017. The Impact Pseudotachylitic Breccia Controversy: Insights from First Isotope Analysis of Vredefort Impact-Generated Melt Rocks. *Geochimica et Cosmochimica Acta* 214: 266–81.

Reimold, W. U., Hoffmann, M., Hauser, N., Schmitt, R.-T., Zaag, P., and Mohr-Westheide, T. 2016. A Geochemical Contribution to the Discussion about the Genesis of Impact-Related Pseudotachylitic Breccias: Studies of PTB in the Otavi and Kudu Quarries of the Vredefort Dome Support the "In Situ Formation" Hypothesis. *South African Journal of Geology* 119: 453–72.

Reimold, W. U., Horsch, H., and Durrheim, R. J. 1990. The "Bronzite"—Granophyre from the Vredefort Structure—A Detailed Analytical Study and Reflections on the Genesis of One of Vredefort's Enigmas. In *Proceedings of the 20th Lunar and Planetary Science Conference*, Houston, TX, USA, 433–50. Houston, TX: Lunar and Planetary Institute.

Reimold, W. U., and Koeberl, C. 2014. Impact Structures in Africa—A Review. *Journal of African Earth Sciences* 93: 57–175.

Reimold, W. U., Pybus, G., Kruger, F., Layer, P., and Koeberl, C. 2000. The Anna's Rust Sheet and Related Gabbroic Intrusions in the Vredefort Dome-Kibaran Magmatic Event on the Kaapvaal Craton and beyond? *Journal of African Earth Sciences* 31: 499–521.

Reimold, W. U., Schulz, T., König, S., Koeberl, C., Hauser, N., Wannek, D., and Schmitt, R.-T. 2021. Genesis of the Mafic Granophyre of the Vredefort Impact Structure (South Africa): Implications of New Geochemical and Se and Re-Os Isotope Data. In *Large Meteorite Impacts and Planetary Evolution VI*, edited by W. U. Reimold, and C. Koeberl, Geological Society of America Special Paper 550: 235–54.

Shand, S. J. 1916. The Pseudotachylyte of Parys (O.F.S.) and its Relation to 'Trap-Shotten Gneiss' and 'Flinty Crush-Rock'. *Quarterly Journal of the Geological Society of London* 72: 198–221.

Son, T. H., and Koeberl, C. 2005. Chemical Variation within Fragments of Australasian Tektites. *Meteoritics & Planetary Science* 40: 805–15.

Spray, J. G. S., and Biren, M. 2021. Distinguishing Friction-from Shock-Generated Melt Products in Hypervelocity Impact Structures. In *Large Meteorite Impacts and Planetary Evolution VI*, edited by W. U. Reimold, and C. Koeberl, Geological Society of America Special Paper 550: 147–70.

Spray J. G., Kelley S. P., and Reimold W. U. 1995. Laser probe argon-40/argon-39 dating of coesite- and stishovite-bearing pseudotachylytes and the age of the Vredefort impact event. *Meteoritics* 30:335–343.

Sun, S. S., and McDonough, W. F. 1989. Chemical and Isotopic Systematics of Oceanic Basalts; Implications for Mantle Composition and Processes. In *Magmatism in the Ocean Basins*. Geological Society of London Special Publication 42, edited by A. D. Saunders, and M. J. Norry, 313–45. London: The Geological Society of London.

Therriault, A. M., Reimold, W. U., and Reid, A. M. 1996. The Vredefort Granophyre—Part 1. Field Studies. *South African Journal of Geology* 99: 1–21.

Therriault, A. M., Reimold, W. U., and Reid, A. M. 1997. Geochemistry and Impact Origin of the Vredefort Granophyre. *South African Journal of Geology* 122: 100115.

Wannek, D. S. 2015. *Geologische Untersuchungen zur Genese des Vredefort Granophyrs im Nordwesten des Vredefort Doms*. M.Sc. Thesis (unpubl.). Berlin: Department of Earth Sciences, Freie Universität Berlin. 186.

Willemse, J. 1937. On the Old Granite of the Vredefort Region and Some of its Associated Rocks. *Transactions of the Geological Society of South Africa* 40: 195–206.

SUPPORTING INFORMATION

Additional supporting information may be found in the online version of this article.

Table S1. Major and trace element data from Wannek (2005). ICP-MS analyses at SGS GEOSOL laboratories, Vespasiano, Brazil.

The Meteoritical Society

Meteoritics & Planetary Science 54, Nr 10, 2286–2311 (2019)
doi: 10.1111/maps.13371

Linking shock textures revealed by BSE, CL, and EBSD with U-Pb data (LA-ICP-MS and SIMS) from zircon from the Araguainha impact structure, Brazil

Natalia HAUSER[1*], Wolf Uwe REIMOLD[1], Aaron J. CAVOSIE[2], Alvaro P. CRÓSTA[3], Winfried H. SCHWARZ[4], Mario TRIELOFF[4], Carolinna DA SILVA MAIA DE SOUZA[1], Luciana A. PEREIRA[1], Eduardo N. RODRIGUES[1], and Matthews BROWN[1]

[1]Laboratory of Geochronology, Geosciences Institute, Brasilia University, 70910 900 Brasília, DF, Brazil
[2]Space Science and Technology Centre, School of Earth and Planetary Sciences, Curtin University, Bentley, WA 6102, Australia
[3]Institute of Geosciences, University of Campinas, 13083-855, Campinas, SP, Brazil
[4]Institute of Earth Sciences, Klaus-Tschira-Labor für Kosmochemie, Heidelberg University, Im Neuenheimer Feld 234-236, 69120 Heidelberg, Germany
*Corresponding author. E-mail: nataliah@unb.br

(Received 16 July 2018; revision accepted 10 July 2019)

Abstract–A silicious impact melt rock from polymict impact breccia of the northern part of the alkali granite core of the Araguainha impact structure, central Brazil, has been investigated. The melt rock is thought to represent a large mass of impact-generated melt in suevite. In particular, a diverse population of zircon grains, with different impact-induced microstructures, has been analyzed for U-Pb isotopic systematics. Backscattered electron and cathodoluminescence images reveal heterogeneous intragrain domains with vesicular, granular, vesicular plus granular, and vesicular plus (presumably) baddeleyite textures, among others. The small likely baddeleyite inclusions are not only preferentially located along grain margins but also occur locally within grain interiors. LA-ICP-MS U-Pb data from different domains yield lower intercept ages of 220, 240, and 260 Ma, a result difficult to reconcile with the previous "best age" estimate for the impact event at 254.7 ± 2.7 Ma. SIMS U-Pb data, too, show a relatively large range of ages from 245 to 262 Ma. A subset of granular grains that yielded concordant SIMS ages were analyzed for crystallographic orientation by EBSD. Orientation mapping shows that this population consists of approximately micrometer-sized neoblasts that preserve systematic orientation evidence for the former presence of the high-pressure polymorph reidite. In one partially granular grain (#36), the neoblasts occur in linear arrays that likely represent former reidite lamellae. Such grains are referred to as FRIGN zircon. The best estimate for the age of the Araguainha impact event from our data set from a previously not analyzed type of impact melt rock is based on concordant SIMS data from FRIGN zircon grains. This age is 251.5 ± 2.9 Ma (2σ, MSWD = 0.45, p = 0.50, n = 4 analyses on three grains), indistinguishable from previous estimates based on zircon and monazite from other impact melt lithologies at Araguainha. Our work provides a new example of how FRIGN zircon can be combined with in situ U-Pb geochronology to extract an accurate age for an impact event.

INTRODUCTION

The 40 km diameter Araguainha impact structure (Araguainha Dome; Dietz and French 1973) in central Brazil is the largest known impact structure in South America (Crósta et al. 2019). The structure straddles the border between Goias and Mato Grosso states (Fig. 1a). The target rocks for this impact include Precambrian–Lower Paleozoic crystalline basement and sedimentary strata of the intracratonic Phanerozoic Paraná basin.

The structure exposes part of the Neoproterozoic–Cambrian/Ordovician basement, which is composed of phyllite and metasandstone of the Paraguay Belt, and

© The Meteoritical Society, 2019.

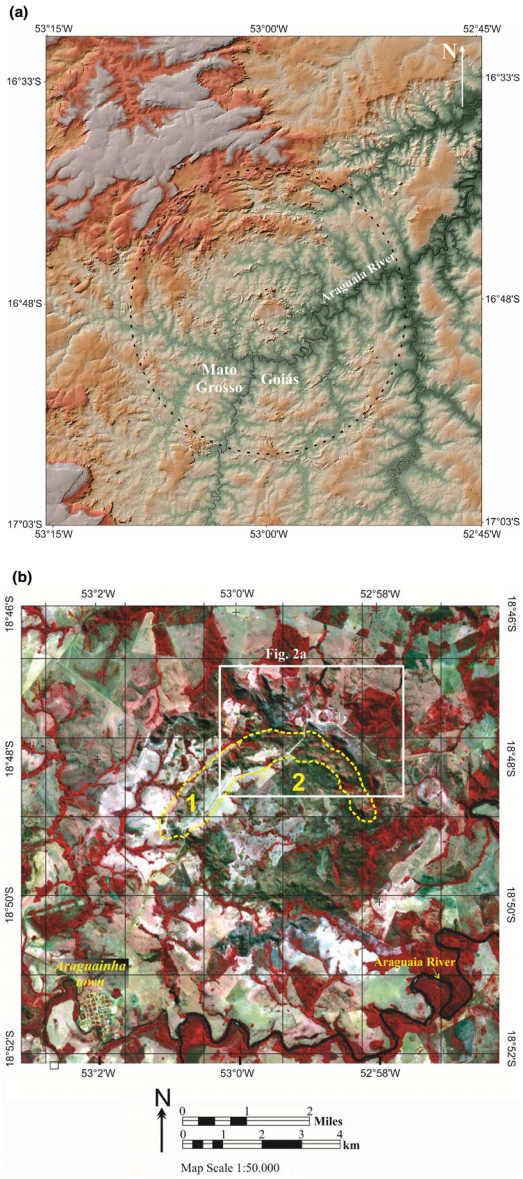

Fig. 1. a) TanDEM-X radar satellite image for the extent of the Araguainha impact structure at 52°45′–53°15′W and 16°30′–17°03′S (~53 × 61 km wide area). Color-coded, hill-shaded digital elevation model (illumination at elevation = 45°, azimuth = 315°). Note the meandering section of the Araguaia River around the southern part of the central uplift area. Courtesy of Manfred Gottwald, German Aerospace Center (DLR, Oberpfaffenhofen, Germany). b) A Landsat image of the central part of the Araguainha impact structure. The semiannular distribution of surface occurrences and widespread float of polymict impact breccias to the north of the innermost core of alkali granite has been emphasized with a dashed yellow line. The numbers make references to the main lithologies that outcrop in the area: 1) polymict breccia and 2) granite plus impact melt rock. The square indicates the location of Fig. 2a. (Color figure can be viewed at wileyonlinelibrary.com.)

post-tectonic alkali granite. The basement is overlain by supracrustal rocks related to the evolution of the Paraná basin. The ~8 km wide central uplift of the structure is composed of alkali granite shocked to 20–25 GPa (Martinez and Schärer 1994), rocks of the Ordovician Rio Ivaí Group, the folded sandstone of the Devonian Furnas Formation, and siltstone of the Devonian Ponta Grossa Formation (Crósta et al. [2019] and references therein).

The age of the Araguainha impact has been estimated by several studies that concur that the impact event occurred around the time of the Permian–Triassic boundary (e.g., Tohver et al. [2012, 2013] or Erickson et al. [2017a]). The first radiometric age dating of deformed granitic basement was provided by Crósta (1982), who obtained a K/Ar age for K-feldspar of 283.6 ± 17.2 Ma. He concluded that this age represents a mixed age between the original, pre-Devonian age of the granite and the impact event. Crósta (1982) pointed out that the shock level of the dated sample was probably not high enough for complete loss of inherited argon. A Rb-Sr isochron of 243 ± 19 Ma (whole rock and cordierite) on a sample of impact melt rock was obtained by Deutsch et al. (1992). Using the $^{40}Ar/^{39}Ar$ method, also on a sample of impact melt rock, Hammerschmidt and von Engelhardt (1995) obtained ages of 245.5 ± 3.5 Ma and 243.3 ± 3.0 Ma, later recalculated to 248 ± 4 Ma by Jourdan et al. (2009). Tohver et al. (2012) obtained a weighted mean U/Pb age of 254.7 ± 2.5 Ma on zircon from a typical Araguainha impact melt rock. Most recently, Erickson et al. (2017a) reported a slightly older (actually within error limits overlapping) U-Pb concordia age of 259 ± 5 Ma on neoblastic monazite from the same impact melt rock analyzed by Tohver et al. (2012).

The main objective of the present study is to apply in situ techniques (LA-ICP-MS and SIMS) for U-Pb dating of domains recognized in single zircon grains by backscattered electron (BSE) and cathodo-luminescence (CL) imaging. The sample studied here (sample Am-21b) is an impact melt rock of highly silicious composition, different from the impact melt rock of granitic composition used in previous investigations. The aim is to evaluate U-Pb isotope systematics, as measured by LA-ICP-MS and SIMS, for the various shock microstructures observed in zircon. Naturally, this will also provide an opportunity to further discuss the apparent close age relation between the Araguainha impact event and the timing of the Permian–Triassic boundary and associated mass extinction. Microstructures were characterized in individual zircon grains using scanning electron microscopy. Five zircon grains that broadly represent the microstructural variation observed in BSE/CL images were analyzed by electron backscatter diffraction (EBSD). The results are then

evaluated in view of recent age estimates for the Araguainha impact event.

GEOLOGICAL BACKGROUND

The central uplift of the Araguainha structure is 8 km wide and includes the central peak and the innermost part of the annular basin (Lana et al. 2006, 2007, 2008; Yokoyama et al. 2012). Within the central uplift, phyllites and metasandstones proposed by Yokoyama et al. (2012) to belong to the Neoproterozoic Cuiabá Group are the oldest rocks, followed by the 4–5 km wide innermost porphyritic alkali granite, which is locally known as the Araguainha granite. It was dated to 512 ± 11 Ma (Tohver et al. 2012) and may be related to other post-tectonic granites of the Brasilia and Paraguay orogenic belts (Pimentel et al. 1996).

The granite and Cuiabá Group strata are surrounded by occurrences of polymict impact breccia and rare occurrences of strata of the Ordovician Rio Ivaí Group. These rocks, in turn, are surrounded by a 1–2 km wide collar of highly deformed sandstone of the Devonian Furnas Formation. The annular basin, between the central peak and the outer rim, comprises folded strata of the Devonian Ponta Grossa Formation and the lower part of the Carboniferous Aquidauana Formation. The crater rim section involves the upper part of the Aquidauana Formation and the Iratí and Corumbataí formations of the Upper Permian Passa Dois Group (Lana et al. 2007; UnB-IG 2012).

Araguainha impactites are known only from the central uplift area. von Engelhardt et al. (1992) distinguished impact breccia with melt matrix (e.g., impact melt rock), red and gray dikes of melt rock, and polymict and monomict impact breccias. The red dikes were characterized as containing clasts of granite and schlieren of mobilized feldspar that are immersed in a fine-grained groundmass. These authors described a large occurrence of monomict breccia (cataclasites) in the southeastern sector of the dome, but subsequent researchers did not confirm this (e.g., Yokoyama et al. 2012; this work). von Engelhardt et al. (1992) also alleged that the impact melt rocks formed at least two large, allegedly continuous bodies, the main remnants of which were exposed on the top of hills in the southern and central parts of the central uplift. By field observation and petrographic studies, the impact melt rocks have been classified variably by different authors (von Engelhardt et al. 1992; Machado et al. 2009; Silva et al. 2011, 2016; Preuss 2012; Yokoyama et al. 2012; Fischer 2015). Yokoyama et al. (2012) and UnB-IG (2012) reported individual occurrences of impact melt rock within the larger areas mapped by earlier workers and demonstrated that these do not represent continuous bodies. Fischer (2015) carried out extensive fieldwork in the southern part of the central uplift, where hypothetically there should have been some of the large outcrops referred to by von Engelhardt et al. (1992). Fischer (2015) showed that there is no continuous outcrop and that there is no direct relationship between occurrences of impact melt rock and the tops of hills.

Several petrographic and geochemical studies have been carried out on the granite and impact melt rocks (von Engelhardt et al. 1992; Machado et al., 2009; Yokoyama et al. 2012; Preuss, 2012; Fischer 2015; Silva et al. 2016). They showed that the impact melt rocks and the granite are very similar in composition to each other. Some workers stated that—despite the observation that apparently no sedimentary rocks were involved in the production of melt (von Engelhardt et al. 1992; Machado et al. 2009)—there were subtle differences in their respective chemical compositions. Platinum group element analyses by Hippertt and Lana (1998), Machado et al. (2009), and N. Hauser (unpublished data) seemingly indicate that the Araguainha impact melt rock does not carry an identifiable meteoritic component.

Large outcrops of polymict impact breccia occur in the western, northern, and northeastern sectors (von Engelhardt et al. 1992; this work), and are more restricted in the southern part, of the central uplift (UnB-IG 2012; Yokoyama et al. 2012). The main components of the polymict breccia are sandstone and mudstone clasts of the supracrustal target rocks, besides a minor but locally important proportion of clasts derived from alkali granite and from the strata related to the Cuiabá Group. Preuss (2012) showed that there are distinct melt rock clasts in the polymict breccia from the northern sector—which therefore indicate that this rock should be classified as a suevite. Some of the melt clasts are of highly silicic composition. De Marchi et al. (2016) studied the polymict breccia in a thick sequence in the northwestern region. Their petrographic analysis showed that silicic melt rock also occurs in the form of abundant microscopic inclusions in the polymict breccia.

SAMPLE DESCRIPTION AND METHODS

Field and Hand Specimen Characteristics of the Analyzed Sample

The outcrop sampled for this study is located at 16°48′11.20″S and 52°58′27.50″W in the eastern inner part of the central uplift (Fig. 1b). The outcrop is an ~50 × 50 m wide plateau that is delimited to the north by megablocks (hundreds of meters to kilometer scale)

of folded Furnas Formation and to the south by alkali granite that contains crosscutting veins and pods of impact melt rock (Fig. 2a). Between these two outcrops, an extensive area of polymict breccia (Figs. 3a and 3b) occurs from which our sample Am-21b was derived. This sample represents a gray fluidal-structured "meta-sandstone" that is characterized in outcrop by folds with amplitudes of several centimeters and occurrence of quartz pebbles (Fig. 2b), denoting the sedimentary character of the protolith to the melt. In the map of von Engelhardt et al. (1992), the area where this sample is derived from was mapped as impact melt rock. In the field, it was observed that the outcrop is in contact with polymict impact breccia. The polymict breccia contains clasts of monomict conglomerate, deformed sandstone, as well as fused sandstone clasts similar to material at the Am-21b outcrop (Fig. 3a). Consequently, we interpret sample Am-21b to represent a portion of melt derived from polymict impact breccia, that is, from a suevite (Stöffler and Grieve 2007). Similar fused samples were described by von Engelhardt et al. (1992), also from outcrops of polymict breccias.

Macroscopically, sample Am-21b is a gray, fused, and recrystallized sandstone, which shows fluidal structure (Fig. 3c). It appears rather homogeneous, except for some local linear structures on the generally rough, dark weathered surface, that resemble sedimentary layering. Conspicuous yellow-brown spots up to 6 mm wide appear to represent altered clasts or possibly clay-filled vesicles; we tentatively interpret them either as pelitic inclusions in the precursor rock, or as amygdales (because of their mainly ovoid shapes). On fresh surfaces, two domains are visible: a mostly light blue-gray groundmass and relatively rare, up to several centimeter large, clasts of what seems to be white quartzite. Other pieces of the same material contain clasts of conglomerate-derived quartz pebbles, up to ~7 cm across.

The large quartzite clasts have highly variable shapes, ranging from irregular, angular, or rounded shapes to fluidal textured and elongated. The groundmass contains many small (1–2 mm sized) clasts and exhibits a folded structure (Fig. 3c). Fold structures of apparent schlieren range in amplitude from a few mm to 8 cm. We interpret these subparallel, millimeter-wide schlieren/bands to have been caused by deformation related to the macroscopic to mesoscopic folding of the sedimentary strata of the collar around the central uplift, rather than representing primary sedimentary features. With the exception of the yellow-brown weathered inclusions, the groundmass is well indurated.

Several blocks were cut for the preparation of thin sections. The blocks (Fig. 4a) display three different types of material (1) groundmass with irregularly shaped, rounded to strongly elongated quartzitic clasts, with local 2 cm-long schlieren of light-colored material (silica); (2) zones displaying well-banded, 2–3 mm-wide layering, locally disturbed; and (3) a few clasts that are smaller than 3 mm, but display rather sharply accentuated silica veins/bands that are partially subparallel to the layering described in (2).

Separation and Preparation Procedures

Zircon concentrates were extracted from ~10 kg of rock by panning at different sizes (100–400 μm) and by magnetic separation using a Frantz isodynamic separator; no chemical treatment was applied. Over 200 zircon grains were separated from sample Am-21b. The grains are generally turbid or opaque, and white in color (similar grains were referred to as "milky zircons" by Kamo et al. 1996). After separation, the grains were placed on a glass slide and the exterior surfaces were characterized by BSE and secondary electron (SE) imaging using a FEI QUANTA 450 scanning electron microscope (SEM) at the Laboratory of Geochronology of the University of Brasilia. The grains were then cast into an epoxy mount, polished to approximately half thickness, and the polished surfaces were characterized by BSE and CL imaging using the same instrument. Additional BSE and CL images were collected during EBSD analysis (see below).

U-Pb LA-MC-ICP-MS Analysis

Zircon epoxy mounts were cleaned with 3% nitric acid before U-Pb analysis. U-Pb isotopic analyses were obtained using a Thermo-Fisher Neptune HR-MC-ICP-MS coupled with a Nd:YAG UP213 New Wave laser ablation system, at the Laboratory of Geochronology of the University of Brasilia. The U-Pb analyses on zircon grains (Table S1a in supporting information) were carried out by the standard-sample bracketing method (Albarède et al. 2004) using the GJ-1 zircon standard (Jackson et al. 2004) in order to quantify the amount of ICP-MS instrumental fractionation. The tuned masses were ^{238}U, ^{204}Pb, ^{206}Pb, ^{207}Pb, and ^{202}Hg. Integration time was 1 second, and ablation time was 40 s for all isotopes. A 25 μm spot size was used and the laser setting was 10 Hz and 2–3 J cm^{-2}. Two to four unknown grains were analyzed between GJ-1 analyses. $^{206}Pb/^{207}Pb$ and $^{206}Pb/^{238}U$ ratios were time corrected. On smaller zircon grains (about 50 μm long), single-spot laser-induced fractionation of the $^{206}Pb/^{238}U$ ratio was corrected using the linear regression method (Koşler et al. 2002). Raw data were processed off-line in an Excel-based data reduction routine (Buhn et al. 2009). During analytical sessions, zircon standard 91500 (Wiedenbeck et al. 1995, 2004) was also analyzed as an unknown.

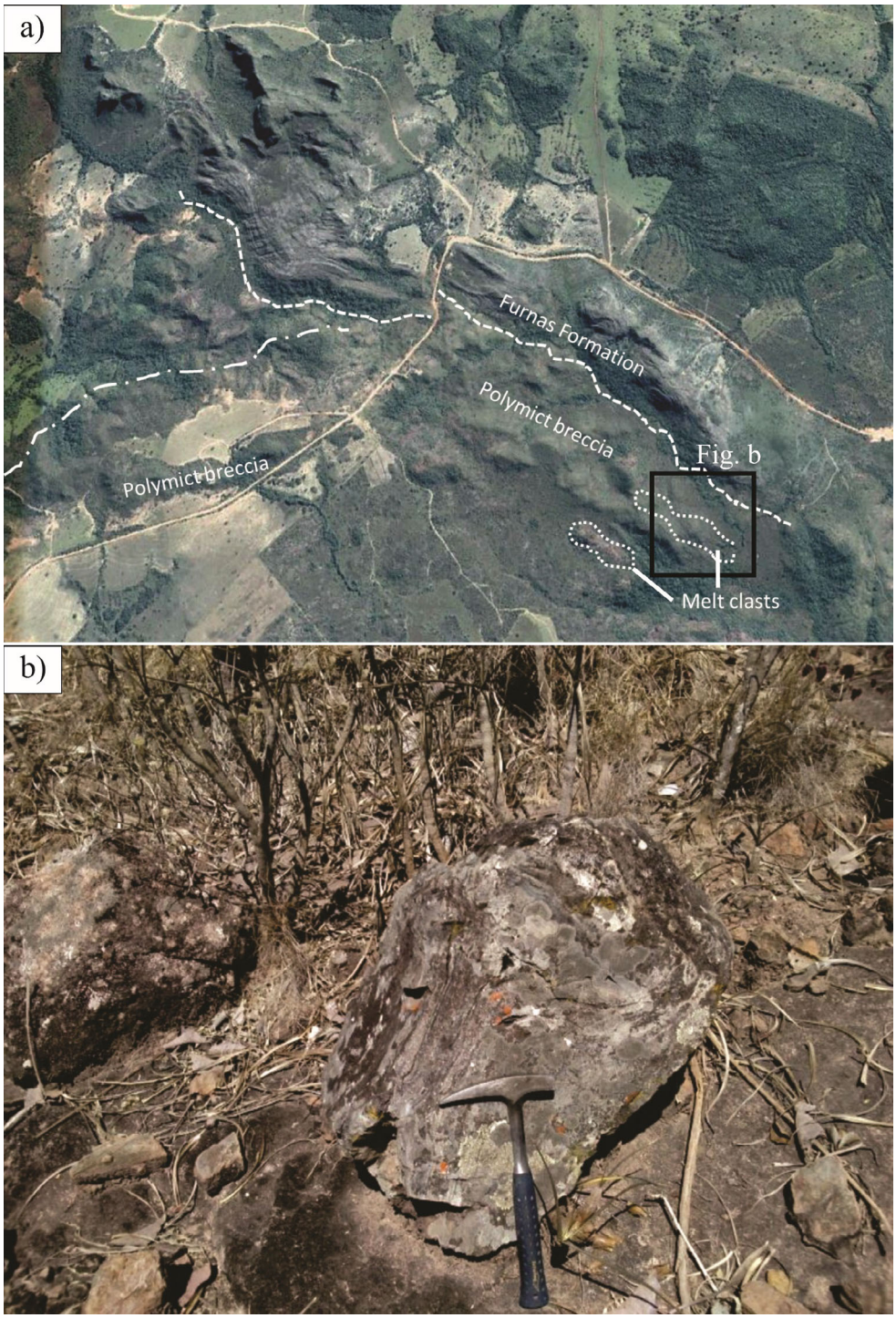

Fig. 2. a) Satellite image (from Google Earth) of the northern sector of the central uplift. The distribution of polymict breccia and Furnas Formation is indicated. b) A view of a typical outcrop at the sampling site for sample Am-21b, a partially melted sandstone interpreted as part of the suevite. (Color figure can be viewed at wileyonlinelibrary.com.)

Common ^{204}Pb was monitored using the ^{202}Hg and (^{204}Hg+^{204}Pb) masses. Common Pb corrections were not required though due to very low signals for ^{204}Pb (<30 cps) and high ^{206}Pb/^{204}Pb ratios. Reported errors are propagated by quadratic addition ($[2SD^2 + 2SE^2]^{1/2}$; SD = standard deviation; SE = standard error) of external reproducibility and within-run precision. External reproducibility is represented by the standard

Fig. 3. a) A section of a suevite outcrop a few meters to the north of the sample Am-21b location. Note the partially melted sandstone clast on the right. For scale, in the upper left part of the picture, highlighted by a white arrow, appears a geological compass, about 6 cm wide. b) Aspect of the suevite in a cut hand specimen from the same area. Clasts of different color are seen, some of which are clearly melted or partially melted (e.g., the black bands). c) Hand specimen showing the fluidal and banded structure of sample Am-21b. Coin, for scale, ~2 cm wide. (Color figure can be viewed at wileyonlinelibrary.com.)

deviation obtained from repeated analyses (n = 20, ~1.1% for $^{207}Pb/^{206}Pb$ and up to ~2% for $^{206}Pb/^{238}U$) of the GJ-1 zircon standard during the analytical sessions, and the within-run precision is the SE calculated for each analysis. Concordia diagrams (2σ error ellipses) and weighted average ages were calculated using the Isoplot-3/Ex software (Ludwig 2003). The geologic timescale applied follows that of Cohen et al. (2013).

U-Pb SIMS Analysis

U-Pb ages of zircon grains were also obtained with the Heidelberg ion probe (HIP) Cameca IMS 1280-HR at Heidelberg University, Institute of Earth Sciences. The data are shown in Table S1b in the supporting information. For U-Pb dating, a ~10 nA $^{16}O^-$ primary beam focused to a 10–15 μm spot was used to generate +10 kV secondary ions. The mass spectrometer was operated at a mass resolution (M/ΔM) of ~6000 to resolve molecular interferences. Oxygen flooding of the sample surface was used to increase Pb^+ yields. Presputtering time was set to 30 s to remove surficial Pb contamination. Secondary ion intensities were acquired in 10 magnet cycles through the species of interest. The reference zircons AS3 (Schmitz et al. 2003; t = 1099.1 ± 0.5 Ma) and 91500 (Wiedenbeck et al. 1995, 2004; t = 1065.4 ± 0.3 Ma) were used to determine relative sensitivities of the analyzed zircon grains. Data reduction (Table S1b) was performed using the software package ZIPS (v3.1; Chris Coath, University of Bristol). Common Pb correction was applied for the respective model age according to the Pb evolution model of Stacey and Kramers (1975). Concordia plots and age calculations were done using Isoplot/Ex 3.75 (Ludwig 2012) and the

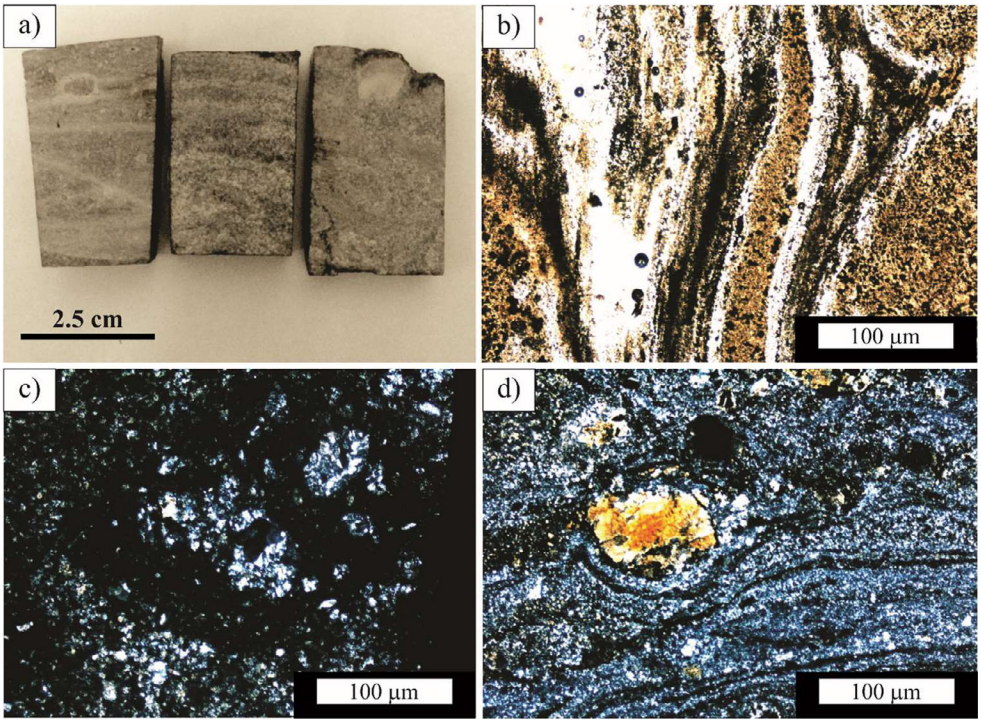

Fig. 4. Thin section cutoffs (a) and microphotographs (b–d) of sample Am-21b. a) Three cutoffs illustrating some of the mesoscopic characteristics of the sample as described in the text (clasts, schlieren texture, apparently crosscutting veinlets). b) The banded/schlieren structure of the glassy/cryptocrystalline groundmass. EDS analyses indicated that the white flow structures are highly silicious, whereas the brown to black layers are Fe-rich in comparison. These bands seem to be somewhat altered to phyllosilicate. These observations confirm that the precursor sandstone was not a pure silica rock. Plane-polarized light. c) In cross-polarized light, the opaque nature of much of the groundmass in Am-21b is evident. Clasts, in contrast, are generally annealed to cryptocrystalline to fine-grained silica aggregates. d) Fluidal-structured, largely finest-grained recrystallized melt flowing around one of the rare crystalline quartz clasts. In this case, the clasts do not display shock deformation, but some clasts with relics of single sets of planar deformation features have been observed. Cross-polarized light. (Color figure can be viewed at wileyonlinelibrary.com.)

decay constants and ratios recommended by Steiger and Jäger (1977). All uncertainties given for the U-Pb ages in this study are at 1σ level, unless noted differently.

Electron Backscatter Diffraction Analysis

Orientation analysis of selected zircon grains was accomplished by EBSD mapping using a Tescan Mira3 field emission SEM in the John de Laeter Centre at Curtin University, Australia. EBSD maps of grains were collected by automated indexing of EBSD patterns collected with an Oxford Symmetry CMOS camera and Oxford Instruments AZtec acquisition software (Table S2 in supporting information). EBSD analysis was conducted using a 20 kV accelerating voltage, 70° sample tilt, and 20 mm working distance, and a ~1.6 nA beam current. The maps were collected using step sizes ranging from 50 to 150 nm.

Maps and pole figures were created using the Tango and Mambo modules in the Oxford Instruments Channel 5 software (v. 5.12). The zircon match unit used is zircon5260 (Mincryst Database, card 5260, 1 atm; data from Hazen and Finger 1979); no other phases were indexed. The only noise reduction method applied was a "wild spike," to eliminate isolated errant pixels. Inverse pole figures are color coded to show orientation as a function of crystallography (Miller index) in the reference frame of the polished sample; pole figures are plotted as lower hemisphere, equal area plots in the same reference frame. Misorientation axis plots for adjacent pixels were calculated for high-angle misorientations (e.g., 75–95°), and are plotted in the same *x*-*y*-*z* reference frame as the pole figures.

RESULTS

Petrography of the Shocked Sandstone

The Am-21b sample (Fig. 4a) is here classified as a gray impact melt rock (Fig. 4b), composed nearly entirely of silica with different degrees of recrystallization. The main characteristics of this rock

are abundant relics of detrital quartz grains embedded in an aphanitic to microphaneritic recrystallized matrix (Figs. 4b and 4c). The groundmass is gray and aphanitic, varies in abundance from 20 to 80 vol%, and contains annealed and locally melted/recrystallized quartz and quartzitic microclasts until 500 μm in size (Fig. 4d). The matrix has fluidal texture in places and locally sweeps around quartzose clasts (Fig. 4d). Some microclasts do not appear to be completely annealed (Fig. 4d), but seem to have experienced partial melting. Local melts are readily recognized by small seams or patches with intersertal or needle-shaped silica crystals. Some clasts, up to 1 cm in size, are only weakly deformed and show undulose extinction. Many clasts of all sizes display a slightly toasted appearance due to the presence of small, opaque inclusions and decrepitated fluid inclusions. Many microclasts, some in the several millimeter size range, are rounded to ovoid and likely represent cross sections through conglomerate- or grit-derived quartz pebbles. Some clasts contain quartz grains that display remnants of planar deformation microstructures—including planar fractures (PF) and planar deformation features, and/or planar fluid inclusion trails. Some annealed quartzite clasts show a "myrmekitic," vermicular structure indicative of partial melting of the precursor, similar to features described from clasts in the Vredefort Granophyre (Buchanan and Reimold 2002).

Other evidence for melting includes acicular crystals of silica, probably after tridymite, that occur in networks in a quasi-intersertal texture at rims of, and in patches within, quartzitic-textured, annealed microclasts. Rare, strongly altered and nearly lath-shaped clasts may be indicative of a small feldspar component in the precursor material to this melt rock.

In cross-polarized light, the sample appears altered and full of oxides, and also contains small vesicles (compare Fig. 3b). This mass is essentially isotropic (Fig. 4c). Such material has been previously observed in the form of microscopic clasts in suevite from the northern collar of the Araguainha dome (De Marchi et al. 2016). It is likely melt that has been derived from a pelitic sandstone—whereby the phyllosilicate component melted first, together with a proportion of feldspathic and quartz precursor.

Locally, the matrix contains rounded to ovoid features that commonly display zonation with rhythmically alternating layers of mosaic crystals or radially oriented blade- to lath-shaped crystals of silica. These small bodies are often elongated into a preferred direction and aligned with a schlieren or banded texture. We interpret them as silica-filled vesicles within the melt matrix.

Trace amounts of fine-grained biotite aggregates occur locally in the matrix, or within vesicles. They are interpreted as a product of late-stage crystallization that took place during the cooling of the melt. Zircon crystals are rarely noted in thin section, despite the fact that this sample yielded many zircon grains. Very fine hairline cracks filled with silica cut across microclasts and vesicles, and parts of these components are displaced along fractures.

Overall, the textures described and illustrated above strongly suggest that sample Am-21b represents a volume of impact melt rock, with a highly heterogeneously distributed clast component derived from one (or more) sedimentary precursor(s). The source rock appears to have been pebbly, conglomeratic, and it must have had a pelitic sandstone component, as well as a strong proportion of white quartz/quartzite. At the moment, it is not possible to relate this melt rock to any particular stratigraphic unit—that is, the melted and partially recrystallized rock does not allow the determination of the sequence (e.g., Cuiabá Group or the overlying sedimentary rocks of the Paraná Basin), from which it was derived. The provenance of its sedimentary precursor is, therefore, unknown.

Zircon Characteristics (Optical, SE, BSE, CL)

The analyzed zircon grains are milky white in color, some of them are opaque, and all have a low luster. The majority are round to subrounded, with pointed terminations; some show an elongated habit, and a few are subprismatic. They are up to 300 μm long, but the common size range is from 70 to 200 μm (Fig. 5).

The most conspicuous feature on the exterior surface of zircon grains—when viewed in SE and BSE—is an apparent granular texture (Fig. 5). This texture has been reported previously in zircon from impact melt rock derived from granite at Araguainha (e.g., Tohver et al. 2012; Silva et al. 2016; Erickson et al. 2017a) and from shocked sandstone from the Furnas Formation, similar to the one studied here (Hippertt et al. 2014).

Neoblasts of different sizes occur in both random (Fig. 5a) and linear (Figs. 5b, 5c, and 5d) orientations. In the case of oriented neoblasts, some appear to be in orthogonal bands (Fig. 5b) with idiomorphic neoblasts up to 5 μm in size (G in Fig. 5b), apparently truncated by a set of smaller crystallites up to 1 μm in size (g in Fig. 5b). The neoblasts can also be aligned in multiple sets of parallel bands that form an angle of ~45° to each other. They appear to form narrow-spaced (~1–2 μm) planar microstructures that are continuous across the host grain (Figs. 5c and 5d). In Zircon#58 (Fig. 5e), neoblasts up to 5 μm in size grade into areas of vermicular texture of rounded crystallites (Fig. 5f). In some grains, the subplanar orthogonal lamellae appear bright in BSE images (Figs. 5e and 5f). The exteriors of some crystals are crosscut by nonplanar fractures (NPF)

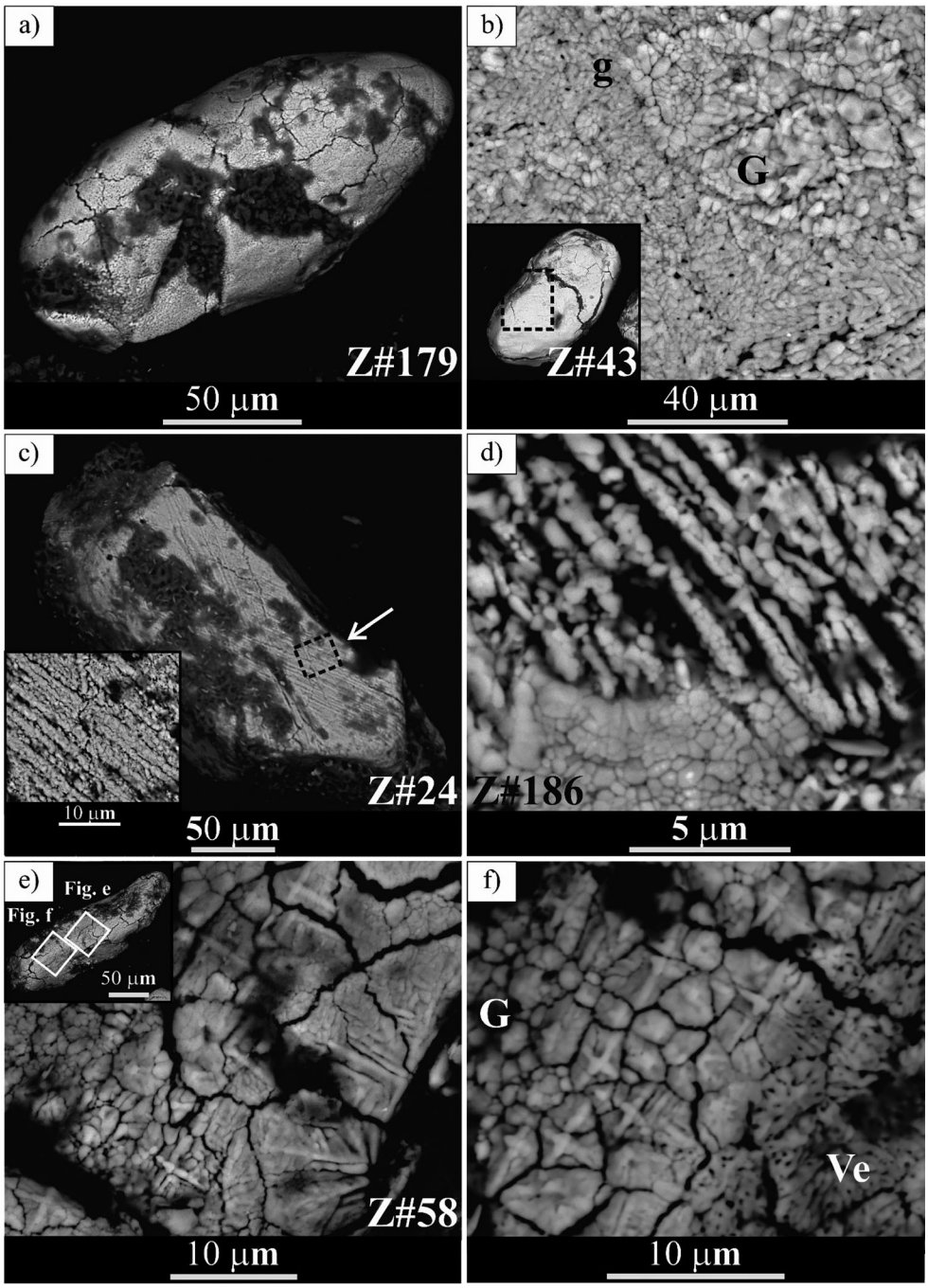

Fig. 5. Backscattered electron (BSE) images of typical zircon grains from the Am-21b fused sandstone. a) The more common feature observed on the surfaces of grains are the granular textures. Zircon #179 shows neoblasts of different sizes without any preferred orientation. Nonplanar fractures and a fault that dislocates the lower part of the grain are also observed. b) Sometimes the neoblasts are oriented and exhibit different sizes, as here in Zircon#43. Crystallites of relatively large (until 5 μm, G) size are oriented in orthogonal directions (indicated by lines), with respect to crystallites of smaller size (until 1 μm, g). In the intersection of these two directions, it is sometimes possible to observe the development of vermicular textures (not possible to see at the image scale). c) Zircon#24 shows two sets of planar microdeformations at 45° in combination with granular texture (see inset). d) Sometimes these neoblasts are concentrated in a specific region without any particular orientation directly in contact with strongly oriented neoblasts, as in Zircon#186. e) Stretched crystal Zircon#58 showing domains of granular texture and microdeformation. e) Neoblasts of about 5 μm size gradually pass into an area of vermicular texture (Ve). Note, in both these last figures, crosses of microdeformation of elevated electron density. Nonplanar fractures cut the neoblasts and cross-like features.

filled with what appears to be neoformed zircon. Some broken grains consist of finer grained granular core domains that are surrounded by coarser grained rims with granular texture.

The most common textures encountered on interior polished surfaces (Fig. 6) are small grains (neoblasts?) associated with variably pronounced vesicularity (porosity in the sense of Wittmann et al. 2006) that appears to be a manifestation of the apparent granular texture observed on exterior surfaces (e.g., Wittmann et al. 2006). The term vesicles is used here in a descriptive sense, and not in the sense of being related with any genetic processes associated with degassing. In many grains, the apparent granular texture is accompanied by variable amounts of vesicles passing gradually into vermicular texture and rounded crystallites (Fig. 6f). In some grains, the vesicular textures appear to be confined to specific magmatic growth zones, preferentially in the outer parts of crystals (Figs. 6e and 6f). In other grains, this texture is pervasive throughout the grain. Granular texture is intimately related to vesicular texture (as also noted by Wittmann et al. 2006). This is most visible in BSE images where zones of granularization occur directly adjacent to—or even grading into—zones of vesicularization.

Small (0.5–1 μm sized) inclusions are associated with many of the vesicular regions (Fig. 5f). EDS analysis shows that these tiny inclusions are characterized by increased Zr versus Si peaks, when compared with the typical Zr and Si peaks of analyses in zircon adjacent to the inclusions. Therefore, we interpret these electron-optically bright spots as baddeleyite (zirconia).

In summary, BSE images of zircon grains from sample Am-21b reveal variable amounts of vesicles/porosity, variable neoblast size domains (0.5–1.0 μm), and variable occurrences of sub-μm inclusions of zirconia. All of these features are consistent with the zircon grains preserving full to partial granular microstructures. Planar microstructures were observed (e.g., Zircon#24 analyzed by LA-ICP-MS—Figs. 5c and 6a), but in general are not common in the population of zircon grains surveyed.

Panchromatic CL imaging reveals that the grains yield colors ranging from brown-yellow and pink-orange in grain interiors, and violet-blue at the rims of grains (Figs. 6b and 6e). When the characteristics observed on surface of the grains are compared with their interior features, it is not so easy to identify the same type of shock deformation. For example, a zircon grain that appears to be fully granular on the surface may still show some magmatic zonation in its interior. In this regard, our CL study provided additional information with respect to intragrain deformation and recrystallization processes that affected the zircons of this fused Araguainha sandstone.

The partially granular zircon grains are characterized by brown–yellow, light pink to orange, concentric CL zoning in their inner parts (Fig. 6b). This zonation was not observed in BSE images. Violet to blue spotty CL, more frequently at the border of grains but also occurring in their inner parts (Zircon#43), is common for vesicular, vesicular plus baddeleyite, and vermicular domains. Some relics of planar microstructures can still be seen in the upper part of the image from Zircon#24 (Fig. 6a): they appear as violet luminescence lines under CL. Timms and Reddy (2009) noted that panchromatic CL intensity is controlled by structural defects and also by the modification of the CL-active REE systematics of deformed zircon. We observed that fully granular zircon grains lost their primary magmatic zonation completely, and the granular domains coincide with very low CL intensities. The vesicles and vermicular areas appear as bright blue, spotty luminescence domains (Zircon#58). Figure 7 summarizes the observed combinations of textural features observed in polished section and the relation of this with LA-ICP-MS and SIMS analyses.

U-Pb Analyses by LA-ICP-MS

Forty-eight U-Pb spot analyses were made by LA-ICP-MS in 31 grains (see Fig. 8; Table S1a). Most analyses are highly discordant. The least discordant data include seven spot analyses that are reversely discordant to discordant (84–114%, based on measured $^{206}Pb/^{238}U$ versus $^{207}Pb/^{235}U$ apparent ages). The majority of analyses were made in the rims of grains and the obtained concordant ages were 459 ± 15, 373 ± 5.2, 299 ± 4.5, 289 ± 12, 276 ± 6, 219 ± 11, and 195 ± 8.5 (1σ uncertainties).

Sixteen grains with granular texture were analyzed, 10 analyses of which correspond to rims and six to cores. The Th/U ratios vary between 0.21 and 2.31. Only one spot was concordant (Z72Core) showing a concordant age of 195 ± 8.5 Ma. Nine grains with concordance between 11% and 60% fall onto a well-defined trend that defines a lower intercept of 260 ± 12 Ma (Fig. S1 in supporting information). Thirteen analyses were made in domains with vesicular texture, with four yielding concordant to discordant (between 97% and 114%) ages of 298, 271, 256, and 219 Ma. The Th/U ratios for these analyses vary between 0.22 and 1.43. Two grains have concordant ages of 366 and 459 Ma, and two lower intercepts of 221 ± 22 Ma and 274 ± 14 Ma were obtained. Four analyzed granular plus vesicular domains, all corresponding to rim areas, yielded a lower intercept age of 365 ± 21 Ma. Four analyses on vesicular plus baddeleyite domains did not yield concordant data. The Th/U ratios are

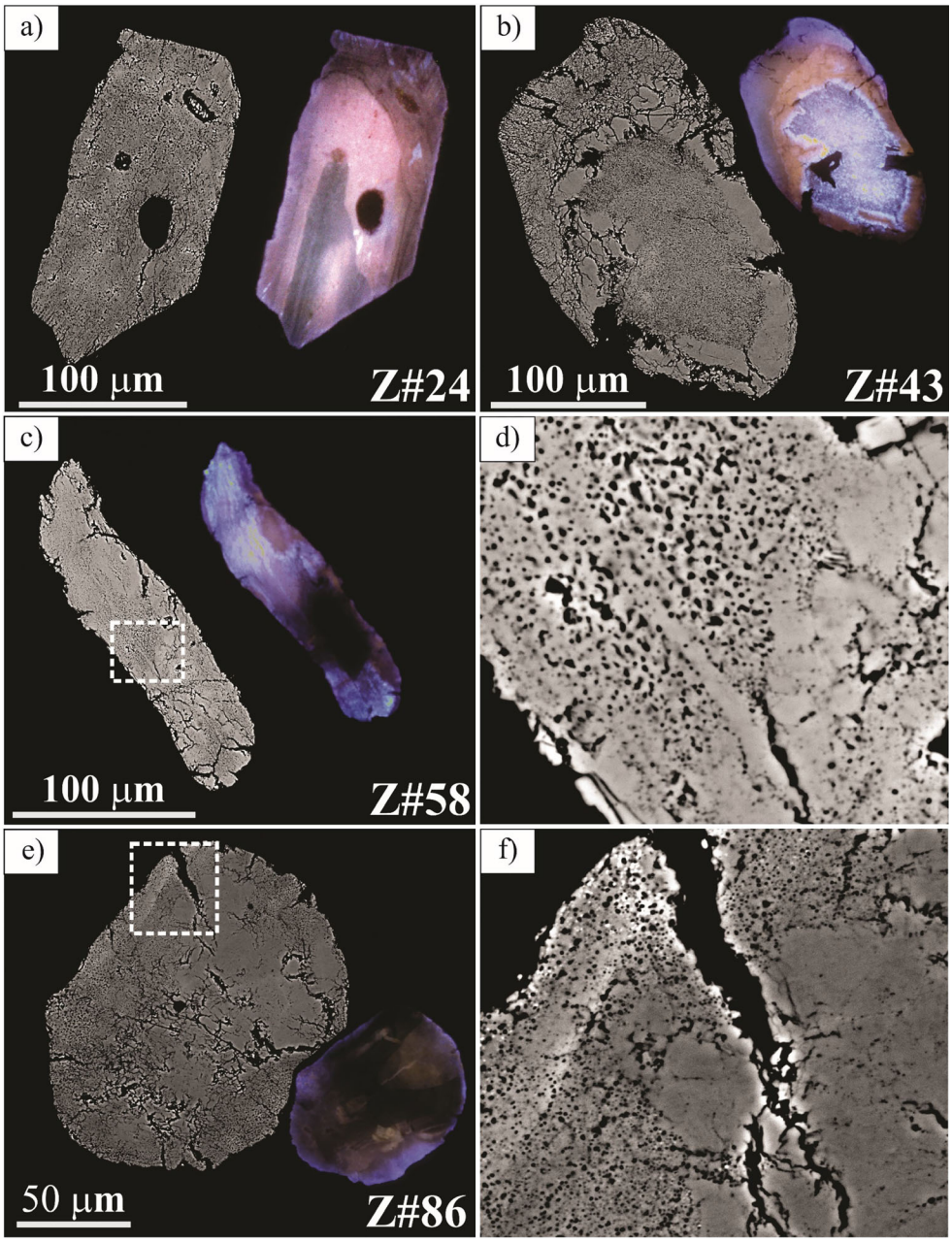

Fig. 6. Correlation between characteristics observed by BSE and CL imagery of zircon grains in polished section. a) Some grains, such as Zircon#24, with strongly oriented neoblasts observed on surface (Fig. 5c), preserve internal magmatic zonation (inset). Note that at the upper margin of the crystals in CL imaging, the planar microdeformation features are readily observed. b) Zircon#43 shows a core with microvesicles that gave a U-Pb (LA-ICP-MS) age of 219 ± 12 Ma. c) Zircon#58, characterized by areas with the orthogonal microdeformation on the surface (Figs. 5e and 5f), shows in the polished BSE image areas with vesicles that alternate with more homogeneous areas. In CL images, this grain shows a zone of poor CL intensity that cannot be related with some special features. d) A higly vesiculated area in between more coherent areas within the same grain. e) Zircon#86 shows sectorial zonation, possibly related to an old metamorphic overprint. The higly vesicular areas are always located at the edge of the crystal where—(f)—white spots, less that 1 μm in size and of high mean atomic number (baddeleyite?), are seemingly also concentrated. (Color figure can be viewed at wileyonlinelibrary.com.)

homogeneous per grain, and range between 0.22 and 0.98. A lower intercept age from analyses on zircon grains with this texture is 220 ± 8 Ma. The data for spots in the combination of vesicular texture plus planar microstructures gave a lower intercept age of 289 ± 24 Ma. The best lower intercept age of

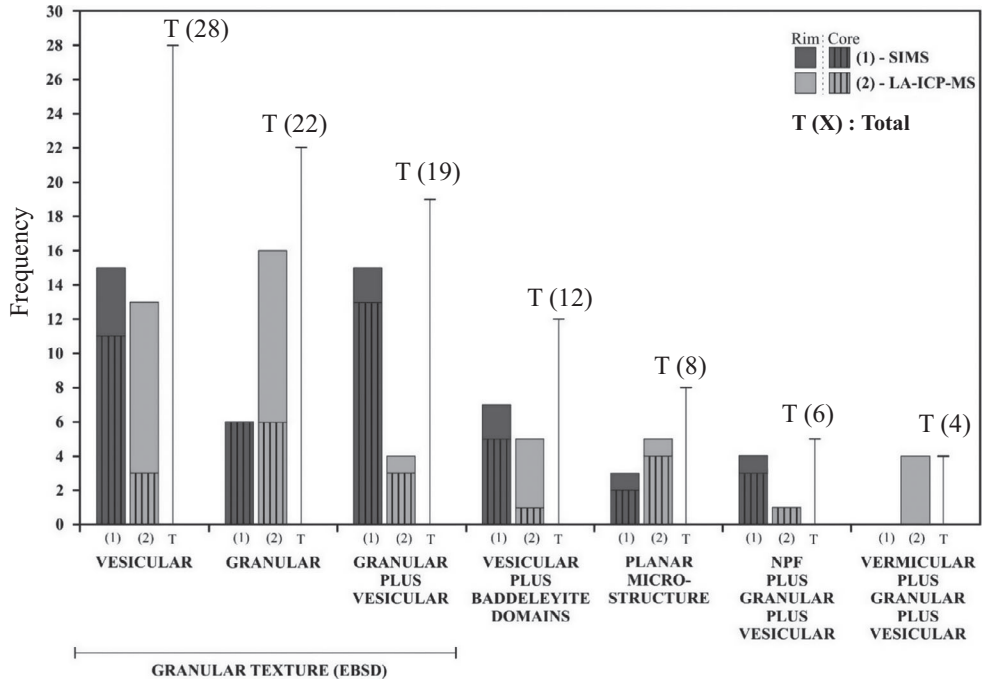

Fig. 7. Histogram showing the quantity of analyzed spots according to the seven textural categories of domains that could be recognized in the zircon population of Am-21b. Note that vesicular domains (28 spots) were analyzed most frequently, followed by granular domains (22 spots), and granular plus vesicular domains (19 spots). The EBSD analyses show that all of them (69 analyzed spots) can be classified as granular domains.

240 ± 4 Ma (Fig. 9a) was obtained when analyses from different textural domains are plotted together.

U-Pb Analyses by SIMS

Fifty U-Pb analyses were made by SIMS in 35 grains. Twenty-three concordant to discordant analyses (% concordance between 90% and 114% taking into account the $^{236}U/^{208}Pb$ versus $^{237}U/^{205}Pb$ apparent ages) show a polymodal zircon age distribution (Fig. 8; Table S1b). The main population ranges from 172.8 to 425.6 Ma, with a main peak at 254 Ma. Two older Neoproterozoic grains with ages of 675.7 ± 15 and 732.1 ± 17 Ma were identified (Fig. 10b). The majority of analyses were made in cores of grains; three spot analyses in rims gave concordant ages of 226, 245, and 425 Ma.

Two to three SIMS analyses were made in individual grains (Fig. S2 in supporting information) in order to evaluate the consistency of U-Pb ages in single grains. For example, on Zircon#9, two concordant ages of 172.8 ± 7 and 195.0 ± 5 Ma were obtained. The spots were analyzed close to the fractured core of the crystal. Zircon#24 (two spots) gave a concordant age of 280.0 ± 7 Ma, and vesicular Zircon#28 gave a concordant age of 252.7 ± 6 Ma. These results indicate that individual grains generally behaved as a closed system.

A group of six grains with concordant $^{206}Pb/^{238}U$ ages between 245.2 and 261.9 Ma allows us to obtain a concordia age of 252.8 ± 2.6 Ma (MSWD = 0.24). From these six data, four data with the smallest error gave our best age estimate of 251.5 ± 2.9 Ma (MSWD = 0.45, 2σ, $n = 4$ analyses on three grains) (Fig. 9b). In order to quantify the microstructural features in these and other grains, we selected a population of grains for orientation analysis by EBSD.

EBSD Analysis

Five zircon grains were analyzed by EBSD (grains 6, 26, 28, 36, and 37), of which grains 6, 26, and 28 had previously been analyzed by SIMS. The only phase detected (indexed) in each grain is zircon. The zirconia inclusions were too small to index, and reidite was not detected. Orientation analysis allowed all five grains to be confirmed as granular zircon, as all of the grains (6, 26, 28, and 37) are composed of ~0.5–1.0 μm neoblasts (Figs. 11a–e). In addition, grain 36 preserves a conspicuous irregular-shaped relic domain that forms a linear network across the grain (Fig. 11d).

Each of the five granular zircon grains consists of three dominant orientation clusters (Figs. 11a–e, panels C–E). The orientation clusters range from relatively

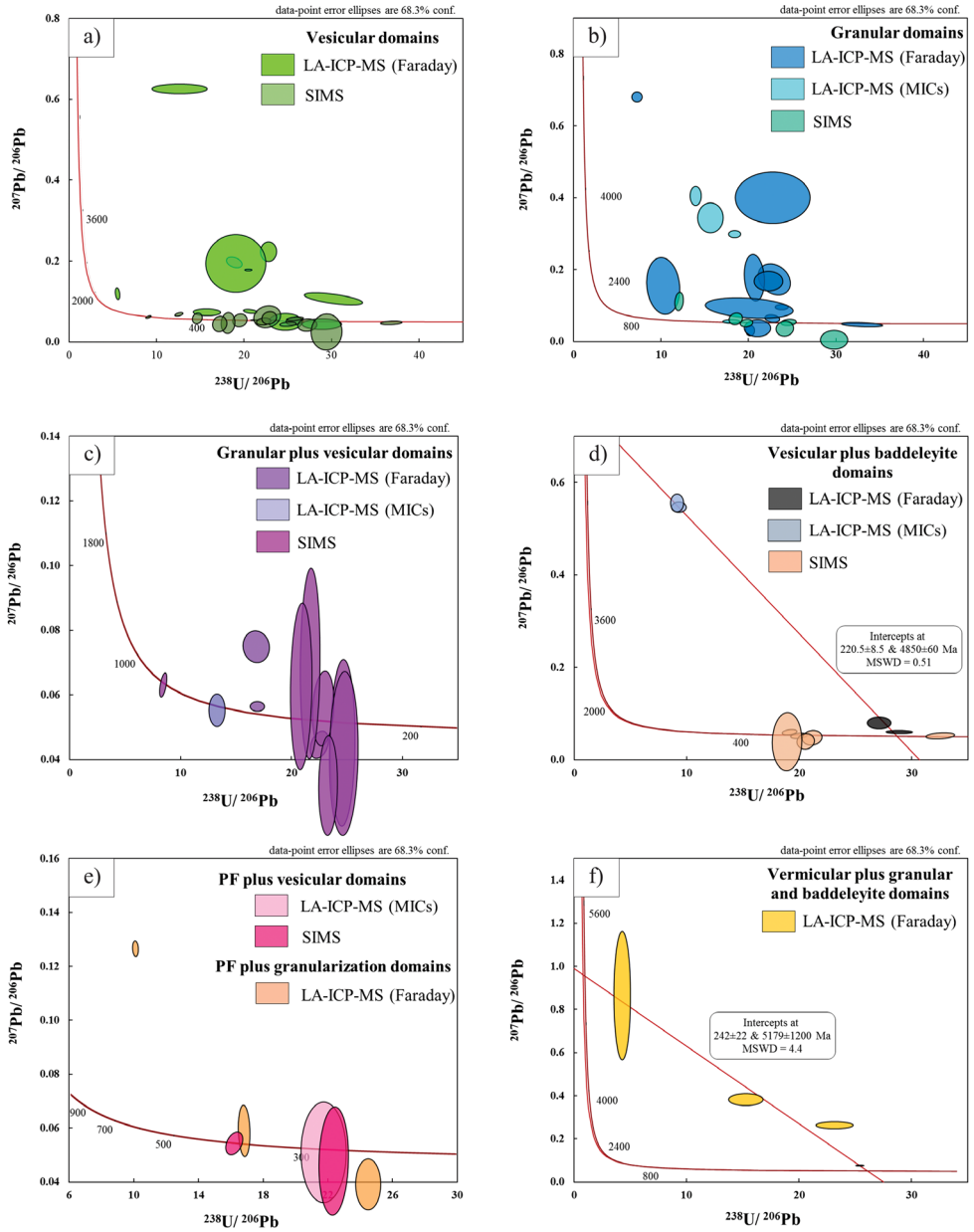

Fig. 8. Tera–Wasserburg plots showing the distribution of concordant and discordant data obtained by LA-ICP-MS and SIMS, respectively. The errors are given as 1σ (%) for ICP-MS data and as 1 sigma (absolute) for SIMS data. (Color figure can be viewed at wileyonlinelibrary.com.)

well-defined clusters (e.g., grains 6 and 36, Figs. 11a and 11d) to highly dispersed clusters (e.g., grain 28, Fig. 11c). In each case, when the orientation data are plotted on pole figures (Fig. 11, panel E), the centers of each cluster (found by contouring data density, e.g., grains 26 and 28) reveal a systematic orientation relation, whereby the clusters can be related by 90°/<110> of another cluster. In addition, a <110> direction is parallel to [001], and high-angle (75–95°) misorientation axes also coincide with <110>.

Zircon grains with these features have only been reported from confirmed impact structures and ejecta deposits, and form uniquely as a consequence of the formation of the high-pressure $ZrSiO_4$ polymorph reidite via 90°/<110> transformation (e.g., Cavosie et al. 2015; Erickson et al. 2017b; Cox et al. 2018), and its back-transformation to neoblastic zircon (Cavosie et al. 2016b; Timms et al. 2017a, 2017b; Cavosie et al. 2018a; Cavosie and Koeberl 2019). Reversion of reidite back to zircon occurs by the symmetrically equivalent transformation

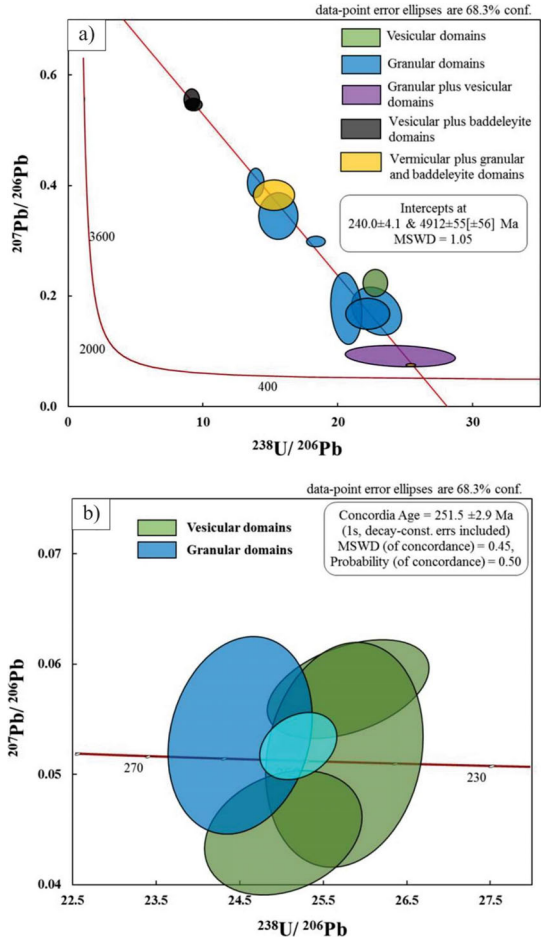

Fig. 9. a) The best LA-ICP-MS lower intercept ages obtained for different textural domains. Note that the granular domain is the more common texture for these domains that yielded lower intercept ages. b) The best SIMS concordant ages obtained for four spot analyses. Uncertainty ellipses are 1σ. (Color figure can be viewed at wileyonlinelibrary.com.)

that forms reidite, which produces up to three broadly orthogonal orientations, including the original zircon orientation plus two where (001) of the new zircon is aligned with [110] of the original orientation. This transformation results in a misorientation of ~90°/<110>. The EBSD analyses here proved that reversion of reidite back to zircon by the reverse orientation relationship or its symmetric equivalents had indeed taken place. Such grains have recently been referred as FRIGN zircon (Cavosie et al. 2018b). In this work, an enigmatic orthogonal relationship was further observed on the exterior surfaces of zircon, as shown in Figs. 5e and 5f for Zircon#58 (as indicated by the cross-like features), which is best explained by this back-transformation mechanism.

Reidite is not preserved in any of the grains analyzed in this study, and it has not previously been reported in FRIGN zircon grains described elsewhere. However, grain 36 (Fig. 11d) preserves a conspicuous relict part of the host domain that did not convert to granular neoblasts. The preserved domain consists of a mostly contiguous set of elongate regions of the host zircon, some 10–15 μm in width, exhibiting distinctly lamellar habit. Interspersed within the relict domain, between the lamellar forms, are similar-sized domains of neoblastic zircon (Figs. 11b and 11c, inset) that likely represent former discrete reidite lamellae that have reverted back to zircon. The orientation of both types of lamellar features (i.e., relict host and neoblasts) is in a strikingly similar orientation relationship as compared to reidite-bearing shocked zircons reported previously. Figure 11d-D shows a CL image of a reidite-bearing zircon from the Stac Fada impactite (Reddy et al. 2015), where the reidite lamellae appear as dark lines (nonluminescent features), and they are in a nearly identical orientation relative to the host zircon as that shown for the Araguinha zircon. Such grains lend support to the interpretation that the lamellar features in grain 36 (Fig. 11d) represent relict host domains interspersed with former reidite lamellae that transformed to neoblastic zircon in situ. This is the first example we are aware of where of a FRIGN zircon preserves discrete lamellae of former reidite, which lends support to the model proposed for the origin of FRIGN zircon (see Cavosie et al. 2018b).

DISCUSSION

We investigated a sample of silicious impact-generated melt rock with variably shock-deformed zircon grains from the polymict breccia-suevite belt around the core of the Araguainha impact structure. Our study reports the first SIMS and LA-ICP-MS U-Pb data for shocked zircon grains from this type of impact melt rock derived from a sandstone at the Araguainha structure, along with quantitative microstructural orientation analysis by EBSD for grains that yield concordant U-Pb ages.

The zircon grains have complex microstructures that include planar features and granular domains, all recording progressive shock deformation, formation of high-pressure polymorphs, recrystallization, and thermal disturbance to the crystal structure. Kamo et al. (1996) interpreted the vesicular texture as comprising degassing holes in between granular zircon. Bohor et al. (1993) and Krogh et al. (1993) described this texture as a result of incipient melting at extremely high temperatures, maybe as high as 1700 °C, which represents the upper limit of thermal dissociation of zircon. Kaiser et al. (2008) demonstrated that at high temperature (about 1700 °C), zircon dissociated to zirconia and silica. The challenge of determining an accurate impact age, thus, lies in

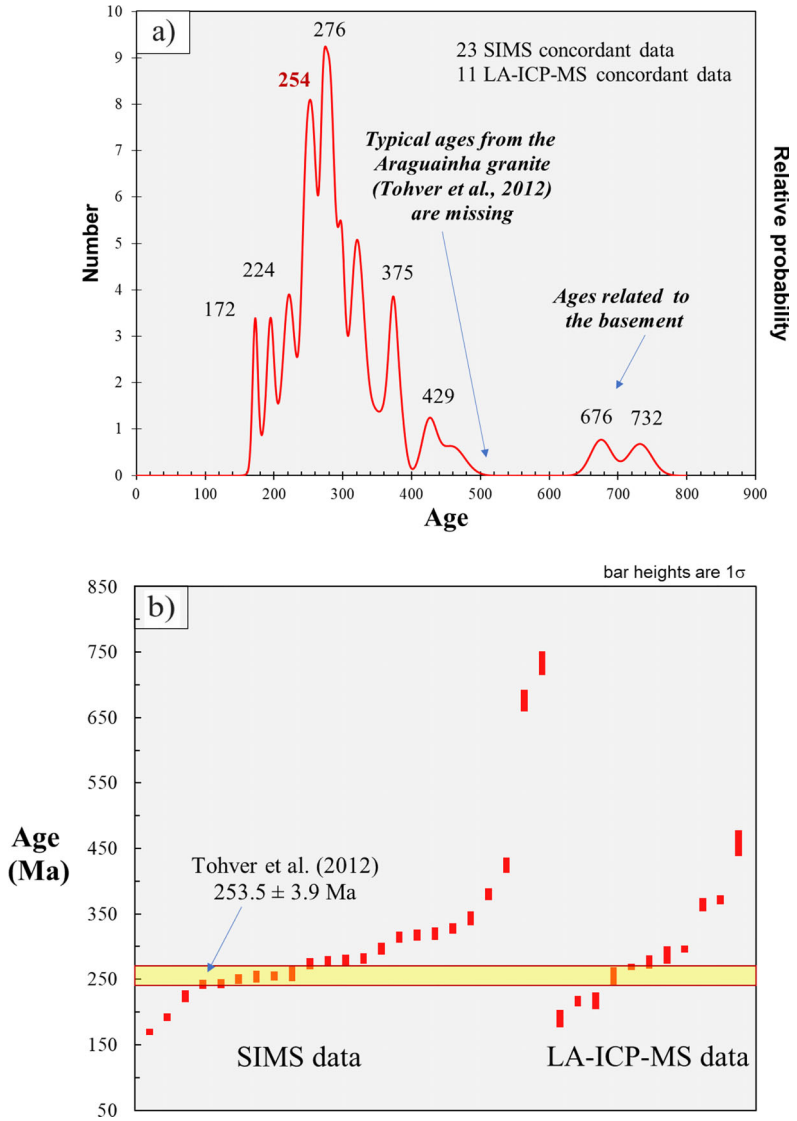

Fig. 10. a) All U-Pb concordant ages from this fused sandstone represented in a probability density plot. Note that no ages that could be related to that of the Araguainha granite (512 Ma; Tohver et al. 2012) were found in this sample. Uncertainty ellipses are 1σ. b) Distribution of the concordant $^{206}Pb/^{238}U$ ages among our SIMS results, in relation to the position of the so far accepted age for the Araguainha impact (Tohver et al. 2012). (Color figure can be viewed at wileyonlinelibrary.com.)

correlating age and microstructural data. The U-Pb isotopic systematics of such grains was here investigated. They are the result of various degrees of shock deformation; Pb loss; and, of course, the original (primary—i.e., prior to shock) isotopic systematics of each grain.

Comparison of LA-ICP-MS and SIMS U-Pb Data from Zircon: Relation with Textural Domains

Comparison of zircon U-Pb isotope data obtained by different techniques, including LA-ICP-MS and SIMS, is complicated if the grains have had complex and different histories, such as having different age domains or shock histories that result in strongly heterogeneous deformation at the microscale. Comparing data obtained by LA-ICP-MS and SIMS in similar textural domains (Fig. 8) shows that the data obtained by LA-ICP-MS are generally more discordant. In Fig. 10, data are plotted at the same uncertainty level for, on the one hand, SIMS (1σ absolute) and, on the other hand, LA-ICP-MS (1σ in %) data. The discordance observed in the LA-ICP-MS data may be attributed to the relatively large (~35 × 15 μm) volumes analyzed (about 400 ng), which could have incorporated heterogeneous domains not represented on the polished surface. Conspicuous heterogeneities observed in the

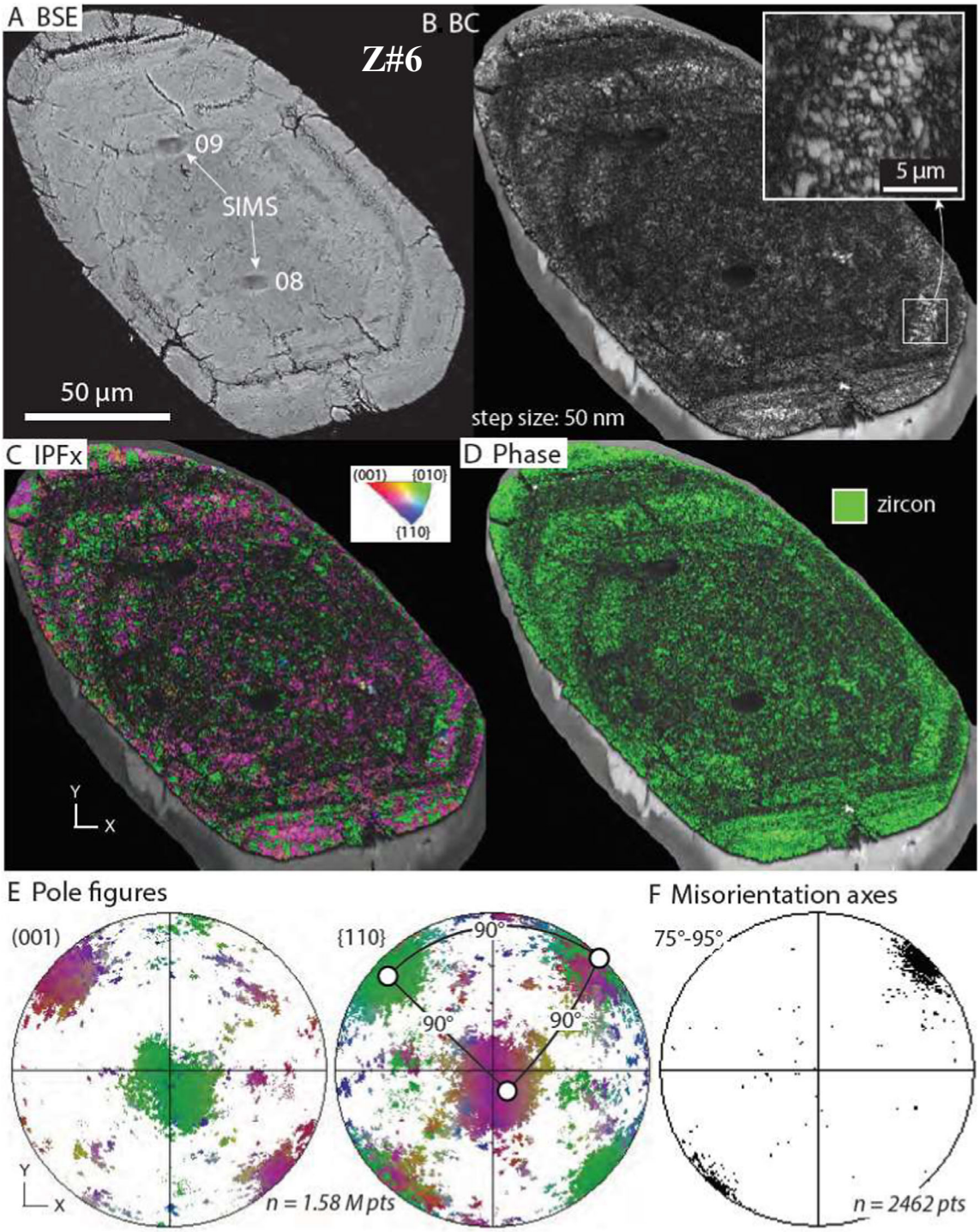

Fig. 11. a) Microstructural data for Zircon#6. A) BSE image, showing relict igneous growth zoning, and location of SIMS spots 08 and 09. B) EBSD band contrast image, showing mostly poor quality diffraction patterns; inset shows individual neoblasts. C) Phase map, showing that zircon was only indexed in some of the concentric zones. D) Orientation map colored with an inverse pole figure color scheme. E) Pole figures showing data from (D) Pole figures are lower hemisphere projections. The centers of data clusters were found by contouring. E) High-angle misorientation axis plot. (Color figure can be viewed at wileyonlinelibrary.com.)

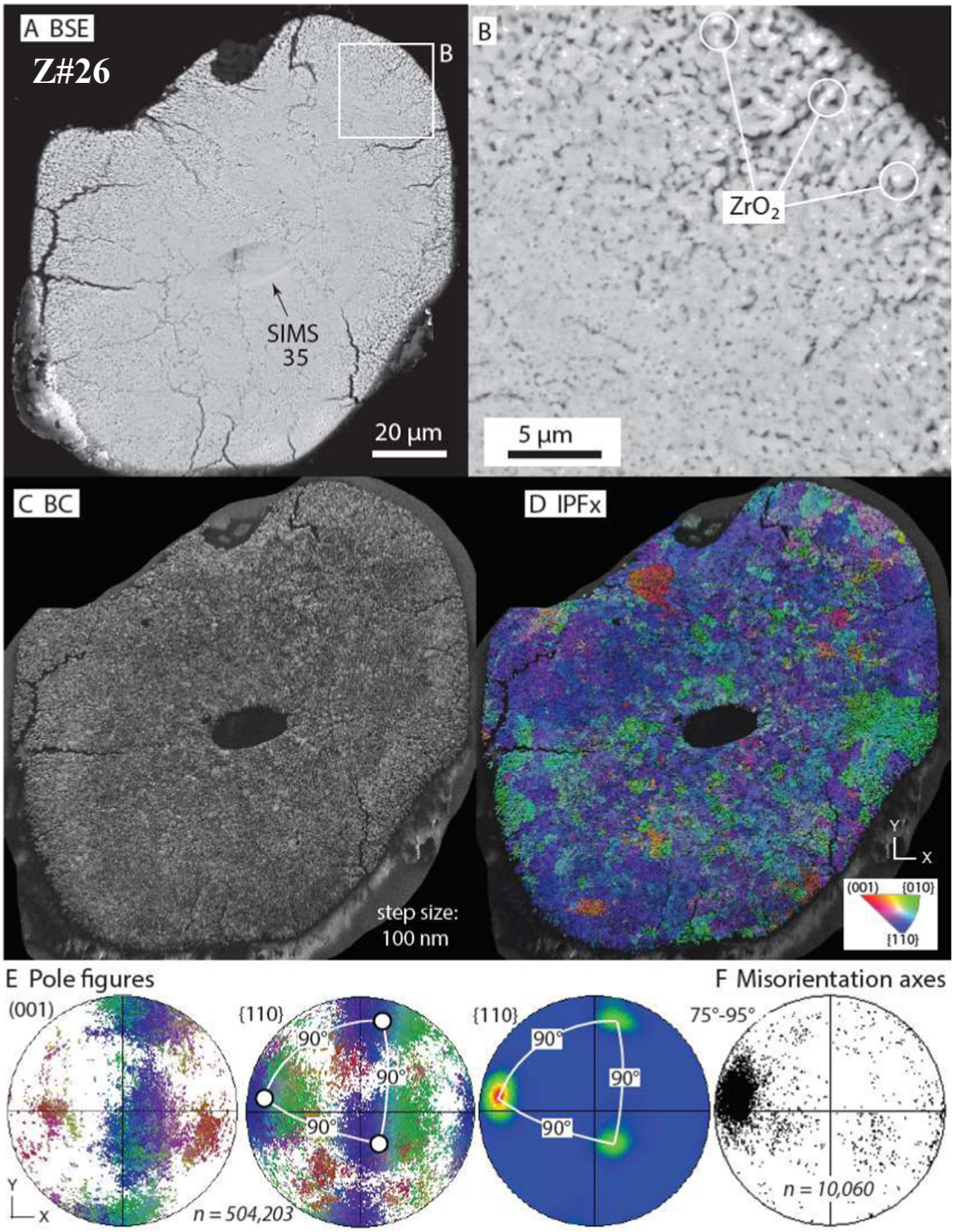

Fig. 11. b) Microstructural data for Zircon#26. A, B) BSE images, showing zirconia inclusions in a ˜10 lm-wide zone along the rim (inset). C) EBSD band contrast image, showing that the entire grain is granular. Variations in brightness along the grain margin are similar to that observed in zircon 4. D) Orientation map colored with an inverse pole figure color scheme. E) Pole figures showing data from (D). Pole figures are lower hemisphere projections. The centers of data clusters were found by contouring (see right image). E) High-angle misorientation axis plot. (Color figure can be viewed at wileyonlinelibrary.com.)

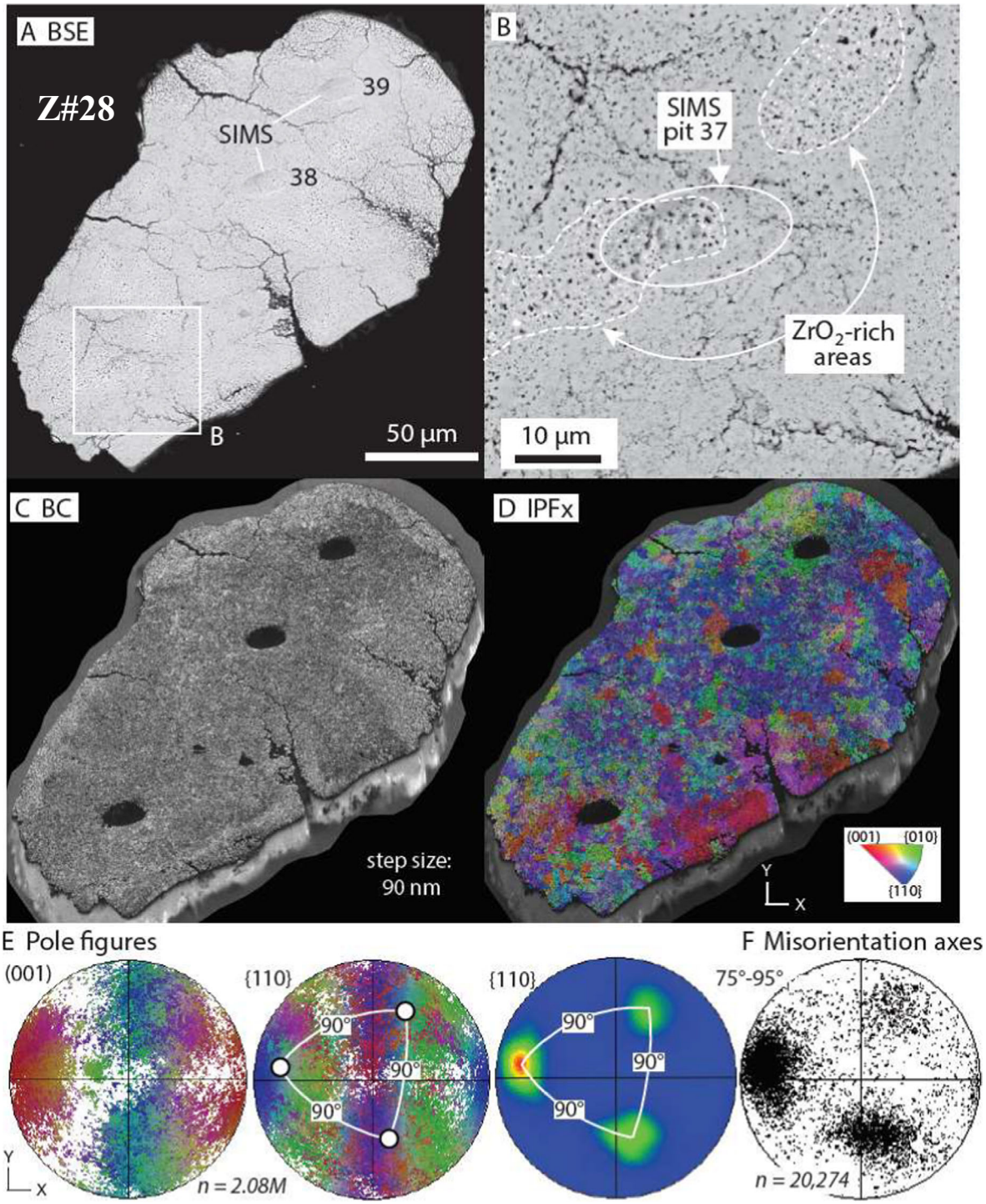

Fig. 11. c) Microstructural data for Zircon#28. A, B) BSE images, showing location of SIMS spots 37–39. The inset image shows how the distribution of zirconia inclusions is heterogeneous at small scales in this grain; SIMS spot 37 partially overlapped an inclusion-rich area, whereas spots 38–39 were made in inclusion-free areas. C) EBSD band contrast image, showing quality of diffraction patterns. The entire grain is granular; variations in brightness along the grain margin indicate higher quality diffraction patterns, perhaps due to thermal annealing in areas adjacent to melt. D) Orientation map colored with an inverse pole figure color scheme. E) Pole figures showing data from (D). Pole figures are lower hemisphere projections. The centers of data clusters were found by contouring (far right). F) High-angle misorientation axis plot. (Color figure can be viewed at wileyonlinelibrary.com.)

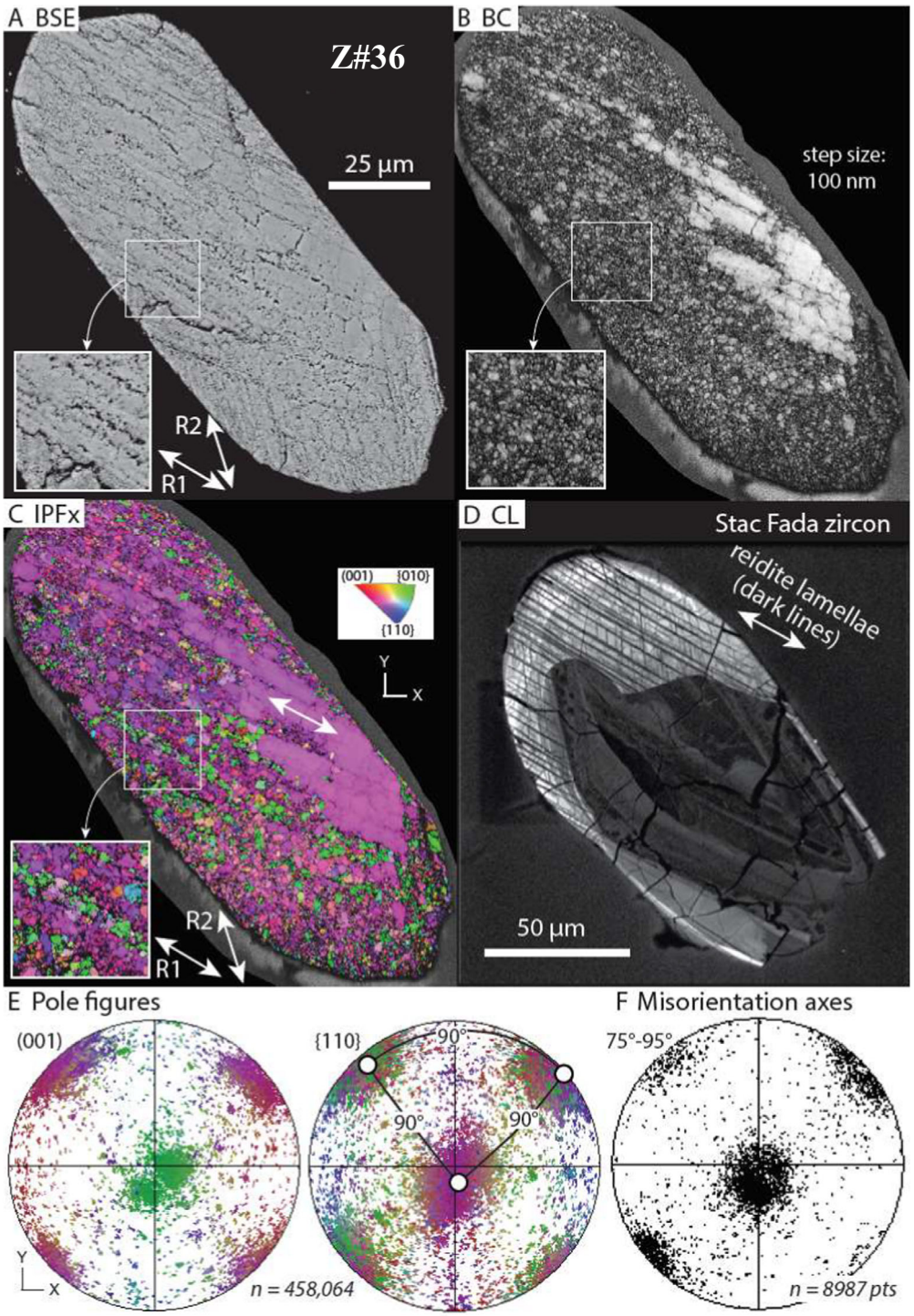

Fig. 11. d) Microstructural data for Zircon#36. A) BSE image, showing two sets of pervasive planar features (labeled R1, R2). B) EBSD band contrast image, showing that the grain is mainly composed of neoblasts (see inset), with the exception of an irregular-shaped linear domain of high-quality band contrast (bright area). C) Orientation map colored with an inverse pole figure color scheme. Arrows (labeled R1, R2) indicate the orientations of the two main sets of planar features. D) CL image of a reidite-bearing zircon from Stac Fada (after Reddy et al. 2015). The main set of reidite lamellae appear as dark lines in the image, and are in a similar orientation relative to the host as shown in (C). E) Pole figures showing data from (C). Pole figures are lower hemisphere projections. The centers of data clusters were found by contouring. F) High-angle misorientation axis plot. Note that the clusters coincide with [110]. (Color figure can be viewed at wileyonlinelibrary.com.)

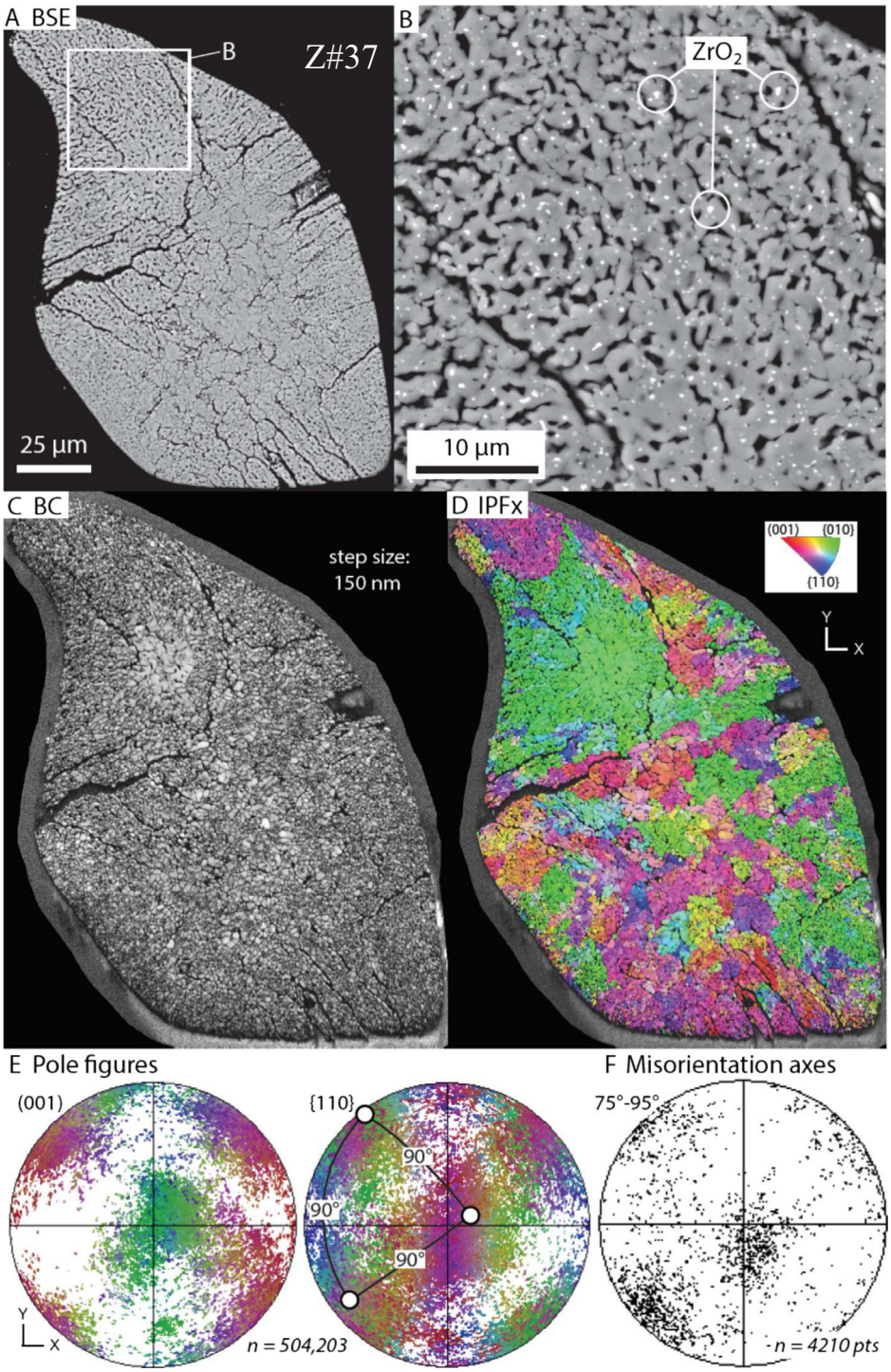

Fig. 11. e) Microstructural data for Zircon#37. A, B) BSE images, showing porous texture and fractures/partings. Zirconia inclusions are ubiquitous throughout the grain. C) EBSD band contrast image, showing quality of diffraction patterns; individual neoblasts are visible. D) Orientation map colored with an inverse pole figure color scheme. E) Pole figures showing data from (D). Pole figures are lower hemisphere projections. The centers of data clusters were found by contouring. F) Highangle misorientation axis plot. Note that the data clusters coincide with [110]. (Color figure can be viewed at wileyonlinelibrary.com.)

zircon population analyzed include growth zoning, domains that include zirconia inclusions, cracks, and other features.

The U-Pb data obtained by SIMS for Araguainha zircon grains are more concordant (Fig. 8). One reason may be that the SIMS analytical volume is smaller (~20 × 2 μm), which provides a better control of the analyzed texture. For this reason, the SIMS data are viewed as more reliable for estimating an age of impact (Tohver et al. 2012; Erickson et al. 2017a). Much of the U-Pb data obtained by SIMS in this study are concordant. However, analyses are spread out along the concordia curve (Fig. 8), making it difficult to extract an impact age from the entire data set.

For LA-ICP-MS, several lower intercept ages were obtained in different domains (see Fig. S1). The youngest lower intercept ages, between 220 ± 8 and 260 ± 12 Ma, were related to vesicular and vermicular plus granular and baddeleyite domains, whereas the oldest ones, between 289 ± 24 and 365 ± 21 Ma, were related to PF, NPF, and vesicular plus granular domains, respectively. The question is whether these lower intercept ages are geochronologically meaningful. The U-Pb SIMS data—related to textural domains—yielded two concordant ages of 249.0 ± 3.3 Ma (MSDW = 0.58, 1σ and n = three analyses) for vesicular domains, and a concordant age of 254.6 ± 4.7 Ma (MSDW = 0.90, 1σ and n = 3 analyses) for vesicular plus granular domains. In summary, the SIMS U-Pb data were more concordant than the LA-ICP-MS U-Pb data. The best age estimate, obtained from concordant SIMS analyses, is 251.5 ± 2.9 Ma (MSWD = 0.45, 2σ, n = 4 analyses on three grains, Fig. 9b).

History of the Shocked Sandstone

Martinez and Schärer (1994) analyzed shocked quartz and albite from highly brecciated granite in the center of the Araguainha impact structure to determine the peak shock pressure. They used the spindle-stage method (Medenbach 1985), because there is a strong correlation between refractive indices and shock pressure in minerals. For shocked quartz, they determined a peak shock pressure of 27 GPa, and for albite, they found that the maximum shock pressure was less than 32 GPa. Petrographic observations of features such as quartz of brown color and with planar structures or highly fractured plagioclase, often with very fine-grained polycrystalline, almost isotropic aggregates in the center of the grains, indicated that the peak shock pressure did not exceed 40 GPa (Stöffler 1974).

Zircon grains from the more common types of impact melt rocks from the Araguainha Dome are mostly granular (Tohver et al. 2012; Silva et al. 2016; Erickson et al. 2017a) and some exhibit planar microstructures. From sample Am-21b, the fused sandstone analyzed in this work, the zircon grains show granular texture sometimes superimposed onto planar microstructures in response to even greater shock pressure than that responsible for formation of planar microdeformations (Timms et al. 2017a).

In polished sections of our zircon sample, the vesicular, vesicular plus granular, and granular domains are the most frequently observed textures (Fig. 5). Granular zircon texture forms during or after shock decompression at high temperature where zircon is stable, and most likely preferentially forms in domains that contain defects (e.g., metamict domains, lamellae interfaces, etc.), where the energy barrier for nucleation is reduced (Cavosie et al. 2016; Timms et al. 2017a). In the case of FRIGN zircon, the neoblastic microstructure is developed after formation of reidite followed by its reversion back to zircon (Cavosie et al. 2018a, 2018b). FRIGN zircon, thus, is a >30 GPa microstructure.

Dissociation of zircon to baddeleyite (Fig. 11) is a high-T, low-P process that occurs via thermal processes (Kaiser et al. 2008; Timms et al. 2017b). It can occur after entrainment of shocked zircon into impact melt or as a result of decompression after passage of the shock wave. We conducted Raman analyses with the objective of searching for preserved reidite in grains from this study, but this turned out unsuccessful. In one grain, Zircon#58 (Figs. 5e and 5f), a particular orthogonal growth feature that was brighter in BSE contrast was observed, which may be an indirect indication of the former presence of reidite.

What Is the Age of the Araguainha Impact Event?

Thirty-four concordant analyses by LA-ICP-MS and SIMS for zircon grains from Am-21b yield a mainly Paleozoic/Triassic age population (Fig. 10a), with outlier analyses at 676 and 732 Ma. Within the main population, peaks were observed at 274 and 254 Ma, with smaller peaks at 375, 224, and 192 Ma. If the LA-ICP-MS data are considered, the best estimation of the impact age from this study is the lower intercept age of 240 ± 4 Ma (MSWD = 1.05, 2σ, n = 12) (Fig. 9a). In contrast, the best age obtained from concordant SIMS data is 251.5 ± 2.9 Ma (probability of concordance = 0.50, MSWD = 0.45, 2σ, n = 4; see Fig. 10b) for SIMS spots #11, 31, 38, and 39 (compare Tables S1a and S1b).

Geochronological data were previously obtained on samples of the most common impact melt rock type occurring within the alkali granite of the core of the dome (Crósta 1982; Hammerschmidt and von Engelhardt 1995; Tohver et al. 2012; Erickson et al. 2017a). Our new

results complement prior studies by providing a very similar isotopic age from a different type of impact melt rock, of highly siliceous composition. Our best age estimate of 251.5 ± 2.9 Ma overlaps with the age obtained by Tohver et al. (2012) on granular zircon grains (247.8 ± 3.8 Ma), and is within error of the best estimation for the impact event, the weighted mean age of 254.7 ± 2.5 Ma (95% confidence, MSWD = 0.039, p = 0.96) according to these authors.

We note that Tohver et al. (2012) did not use data obtained from zircon for the calculation of their "best age" estimate. They stated that, because their younger age of 247.8 ± 3.8 Ma was obtained on microgranular zircon aggregates, which they considered to be potentially affected by Pb-loss; this age represented only a minimum age for the impact event. It can be debated whether this assumption is justified or not in light of results from this present study, which included orientation analysis.

We cannot discard the possibility that our best estimate for the impact age may also represent a minimum age. Our age of 251.5 ± 2.9 Ma was obtained from four analyses with $^{206}Pb/^{238}U$ ages between 245 and 258 Ma, all derived from granular domains (Fig. 11b). Two zircon grains yielded the youngest ages around 245 and two others the slightly older ages of about 256 and 258 Ma. However, as these four ages overlap with the best age estimate of Tohver et al. (2012) within error, this age of 251.5 Ma may also represent a mixed age, between the true impact age and a Pb loss age (approximately 245 Ma).

Recently, Erickson et al. (2017a) obtained a U-Th-Pb concordia age of 259 ± 5 Ma on two neoblastic monazite grains (#10 and #11) from the same impact melt rock analyzed by Tohver et al. (2012). They further indicated that if they only considered analyses made in their grain #11 (lowest measured common Pb component, <5% $f^{206}Pb$), the age for the impact would be older than the previously proposed impact age of Tohver et al. (2012) and more precise at 262 ± 3 Ma (2σ, MSWD = 0.88, n = 5). Their SHRIMP analyses targeted neoblast interiors away from fractures in the partially recrystallized monazite grains, thus minimizing the effects of common Pb and Pb-loss.

In Fig. 12 we have plotted a summary of the U-Pb data on zircon obtained during this work by LA-ICP-

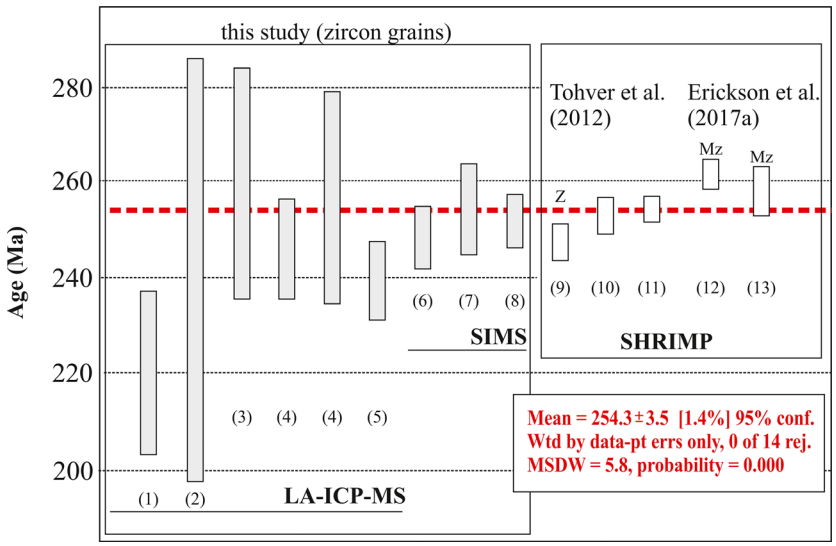

Fig. 12. Summary of the geochronological results obtained during this work and previously by other authors. Note that the errors are presented at 2 sigma levels. Note that the data and error bars presented here represent the respective authors' preferred ages and error values. Readers who may want to investigate further how these data are derived are referred to the original literature as listed below. Data by LA-ICP-MS of the fused sandstone, lower intercept ages (LI): (1) Vesicular plus baddeleyite domains—LI of 220.5 ± 22 Ma. (2) Vermicular plus granular plus baddeleyite domains—LI of 242 ± 44 Ma. (3) Granular domains—LI of 260 ± 24 Ma. (4) Individual grains with LI of 246 ± 10 Ma (Z#122) and 257 ± 22 Ma. (5) The best lower intercept age with U-Pb analysis done in different domains at 240 ± 8 Ma. Data by SIMS: (6) Vesicular domains with a concordant age at 249 ± 6 Ma. (7) Granular plus vesicular domains with a concordant age at 254 ± 9 Ma, and (8) best concordant age (Fig. 7c) at 252 ± 3 Ma. SHRIMP data by Tohver et al. (2012): (9) The best concordant age on granular zircon grains at 247.8 ± 3.8 Ma; (10) a concordant U-Th-Pb age from monazite at 253.5 ± 3.9 Ma, and (11) their best age estimate for the Araguainha impact. SHRIMP data in neoblastic monazite by Erickson et al. (2017a): (12) U-Th-Pb in their grain; (11) the age of 262 ± 3 Ma was considered by the authors as the best age for the impact; and (13) the calculated impact age on two grains of neoblastic monazite at 259 ± 5 Ma. (Color figure can be viewed at wileyonlinelibrary.com.)

MS and from Tohver et al. (2012). We also plotted the U-Th-Pb data for neoblastic monazite grains from Tohver et al. (2012) and Erickson et al. (2017a). All LA-ICP-MS ages correspond to lower intercept ages related with a specific domain within a specific grain. Except for the vesicular plus baddeleyite domains that show a youngest lower intercept age of 220 Ma, all the other data fall into the previously proposed impact age range. Note that the best lower intercept age obtained for different domains is 240 ± 8 Ma.

With respect to the often-referred apparent coincidence of the Araguainha impact and the Permian–Triassic extinction event (e.g., Tohver et al. 2012, 2013), identifying the true age of the Araguainha impact event is important. Understanding the significance of the internal structures of shocked zircon grains is vital to be able to discuss whether the ages record a primary igneous event; the impact age; or secondary, complete, or partial U-Pb disturbance. We doubt that it is valid to assume that the lower intercept ages obtained in this study by LA-ICP-MS for vesicular, granular, baddeleyite-bearing domains of 240 Ma really represent the minimum age for the impact event. We highlight that some of our zircon grains that yielded concordant SIMS U-Pb ages were likened to FRIGN zircon (Cavosie et al. 2018b) by EBSD analysis (Fig. 11). Recent SIMS U-Pb studies of granular zircon from the Lappajärvi impact structure (Finland) have demonstrated that in a population of heterogenous zircons from a sample of impact melt, the only grains that yielded accurate impact ages were those shown to be FRIGN zircon (Kenny et al. 2019). The study of Kenny et al. (2019) and the results obtained in this study strongly suggest that accurate impact ages can be determined from in situ U-Pb analysis of FRIGN zircon.

CONCLUSIONS

In this work, a silicious melt rock sample from the eastern lobe of the polymict impact breccia belt around the granitic core of the Araguainha central uplift structure has been thoroughly studied. We have presented evidence that supports the provenance of this sample from a large sandstone-derived melt inclusion in suevitic breccia.

The initial idea that discordant U-Pb data could be easily related with a specific metamorphic (or impact metamorphic) event is no longer tenable. We have compared LA-ICP-MS U-Pb isotope data on zircon with more precise SIMS data, in order to investigate the possibility that this enigmatic fused sandstone from Araguainha could help to further constrain the impact age. We also compared the obtained data with the textural variations in the analyzed domains, which we discuss in terms of shock metamorphism and postshock thermal overprint on zircon grains, and relate these effects to Pb loss processes. In this way, the obtained LA-ICP-MS data in different domains gave lower intercept ages of 220, 240, or 260 Ma—a result that is difficult to relate with the previous best age estimate for the impact event.

Even with the more concordant SIMS data, it may be difficult to find the impact age within an available range of concordant data. It is equally difficult in comparison with the interpretation of the LA-ICP-MS data to decide where the impact age would be in such a set of concordant data.

This new type of impact melt rock from Araguainha Dome was dated by U-Pb isotope analysis on zircon. The interpreted age of 251.5 ± 2.9 Ma for three zircon grains from granular domains and one from vesicular domains is in agreement with the previously obtained age for an impact melt rock derived from the granite. Nevertheless, it may sometimes be difficult to define the age of an impact event, because zircon grains may be derived from various target rocks of different ages, become shocked to variable degrees, and then subjected differently to remanent high temperature after the impact that can severely disturb the U-Pb system. Thus, it may be exceedingly difficult to interpret the obtained results and/or pinpoint the impact age—even if excellent, concordant SIMS data are available.

Some enigmatic characteristics of our zircon grains were already observed by BSE imaging, but only with EBSD analysis, their significance could be understood. We conclude that, in cases like the one reported here, it is important to have comprehensively investigated mineral grains, that is, to have complete sets of BSE, CL, and EBSD data, prior to isotopic analysis.

Acknowledgments—The LA-ICP-MS facility at the Universidade de Brasília (UnB) was funded by PETROBRAS and the Ministério de Minas e Energia do Brasil. The TanDEM-X radar satellite image in Fig. 1a was kindly provided by Dr. Manfred Gottwald of the German Aerospace Center, Oberpfaffenhofen, Germany. Natalia Hauser gratefully acknowledges the hospitality at the Museum für Naturkunde and the Geochemistry Group of Freie Universität Berlin during her sabbatical stay there from November 2017 to February 2018. Aaron J. Cavosie received support from the Space Sciences and Technology Centre, and the Microscopy and Microanalysis Facility of the John de Laeter Centre at Curtin University, Australia. Reviewers Nick Timms and Gavin Kenny, and Associate Editor Christian Koeberl are thanked for their input. Wolf Uwe Reimold and Natalia Hauser were supported by a Universal grant from CNPq (National Council for Scientific and Technological Development) of Brazil.

Eduardo Novais Rodrigues received a student grant from the CAPES Foundation.

Editorial Handling—Dr. Christian Koeberl

REFERENCES

Albarède F., Telouk S., Blichert-Toft J., Boyet M., Agranier A., and Nelson B. 2004. Precise and accurate isotopic measurements using multiple-collector ICPMS. *Geochimica et Cosmochimica Acta* 68:2725–2744.

Bohor B. F., Betterton W. J., and Krogh T. E. 1993. Impact-shocked zircons: discovery of shock-induced textures reflecting increasing degrees of shock metamorphism. *Earth and Planetary Science Letters* 119:419–424.

Buchanan P. C. and Reimold W. U. 2002. Planar deformation features and impact glass in inclusions from the Vredefort Granophyre, South Africa. *Meteoritics & Planetary Science* 37:807–822.

Buhn B., Pimentel M. M., Matteini M., and Dantas E. L. 2009. High spatial resolution analysis of Pb and U isotopes for geochronology by laser ablation multi-collector inductively coupled plasma mass spectrometry (LA-MC-ICPMS). *Annals of the Brazilian Academy of Sciences* 81:99–114.

Cavosie A. J. and Koeberl C. 2019. Overestimation of threat from 100 Mt-class airbursts? High-pressure evidence from zircon in Libyan Desert glass. *Geology* 47:609–612.

Cavosie A. J., Erickson T. M., and Timms N. E. 2015. Nanoscale records of ancient shock deformation: Reidite ($ZrSiO_4$) in sandstone at the Ordovician Rock Elm impact crater. *Geology* 43:315–318.

Cavosie A. J., Timms N. E., Erickson T. M., and Koeberl C. 2018a. New clues from Earth's most elusive impact crater: Evidence of reidite in Australasian tektites from Thailand. *Geology* 46:203–206.

Cavosie A. J., Timms N. E., Erickson T. M., Hagerty J. M., and Hörz F. 2016. Transformations to granular zircon revealed: Twinning, reidite, and ZrO_2 in shocked zircon from Meteor Crater. *Geology* 44:703–706.

Cavosie A. J., Timms N. E., Ferrière L., and Rochette P. 2018b. FRIGN zircon, the only terrestrial high-pressure and high-temperature mineral diagnostic of shock deformation. *Geology* 46:891–894.

Cohen K. M., Finney S. C., Gibbard P. L., and Fan J.-X. 2013. The ICS international chronostratigraphic chart. *Episodes* 36:199–204.

Cox M. A., Cavosie A. J., Bland P. A., Miljković K., and Wingate M. T. D. 2018. Crustal dynamics of central uplifts revealed: Reidite off-set by zircon twins at the Woodleigh impact structure, Australia. *Geology* 46:983–986.

Crósta A. P. 1982. Mapeamento geológico do Domo de Araguainha utilizando técnicas de sensoriamento remoto. M.Sc. Thesis, Instituto Nacional de Pesquisas Espaciais (INPE).

Crósta A. P., Reimold W. U., Vasconcelos M. A. R., Hauser N., Oliveira G. J. G., Maziviero M. V., and Góes A. M. 2019a. Impact cratering: The South American record—Part I. *Chemie der Erde-Geochemistry*, 79:1–61. https://doi.org/10.1016/j.chemer.2018.06.001.

De Marchi L., Hauser N., Reimold W. U., Crósta A. P., and Braz L. 2016. Geological and petrographical characterization of the polymict impact breccia of the Araguianha dome, Brazil (abstract #1120). 47th Lunar and Planetary Science Conference. CD-ROM.

Deutsch A., Buhl D., and Langenhorst F. 1992. On the significance of crater ages: New ages for Dellen (Sweden) and Araguainha (Brazil). *Tectonophysics* 216:205–218.

Dietz R. S. and French B. M. 1973. Two probable astroblemes in Brazil. *Nature* 244:561–562.

Engelhardt W. von, Matthäi S. K., and Walzebuck J. 1992. Araguainha impact crater, Brazil. 1. The interior part of the uplift. *Meteoritics* 27:442–457.

Erickson T. M., Timms N. E., Kirkland C. L., Tohver E., Cavosie A. J., Pearce M., and Reddy S. M. 2017a. Shocked monazite chronometry: Integrating microstructural and in situ isotopic age data for determining precise impact ages. *Contributions of Mineralogy and Petrology* 172:11. https://doi.org/10.1007/s00410-017-1328-2.

Erickson T. M., Pearce M. A., Reddy S. M., Timms N. E., Cavosie A. J., Bourdet J., Rickard W. D. A., and Nemchin A. A. 2017b. Microstructural constraints on the mechanisms of the transformation to reidite in naturally shocked zircon. *Contributions to Mineralogy and Petrology* 172:1–26. https://doi.org/10.1007/s00410-016-1322-0.

Fischer S. 2015. Ein Beitrag über die Impaktgesteine der Araguainha Impaktstruktur (Brasilien). M.Sc thesis. Freie Universität, Berlin.

Hammerschmidt K. and von Engelhardt W. 1995. Ar/Ar dating of the Araguainha impact structure, Mato Grosso, Brazil. *Meteoritics* 30:227–233.

Hauser N., Reimold W. U., Voll K, Chaves J. G. S., Alves de Mattos B., and Dantas E. L. 2017. Are the impact melt rocks from the Araguainha impact structure, Brazil, homogeneous? Evidence from geochemistry and Sr-nd isotopes. In 80th Annual Meeting of the Meteoritical Society. Santa Fe, USA (Abstract #6215).

Hazen R. M. and Finger L. W. 1979. Crystal structure and compressibility of zircon at high pressure. *American Mineralogist* 64:196–201.

Hippertt J. and Lana C. 1998. Aerial crystallization of hematite in impact bombs from the Araguainha astrobleme, Mato Grosso, central Brazil. *Meteoritics & Planetary Science* 33:1303–1309.

Hippertt J. P., Lana C., Weinberg F., Tohver E., Schmieder M., Scholz R., Gonçalves L., and Hippertt J. F. 2014. Hipper liquefaction of sedimentary rocks during impact crater development. *Earth and Planetary Science Letters* 408:285–295.

Jackson S. E., Pearson N. J., Griffin W. L., and Belousova E. A. 2004. The application of laser ablation-inductively coupled plasma-mass spectrometry to in situ U–Pb zircon geochronology. *Chemical Geology* 211:47–69.

Jourdan F., Renne P. R., and Reimold W. U. 2009. An appraisal of the ages of terrestrial impact structures. *Earth and Planetary Science Letters* 286:1–13.

Kaiser A., Lobert M., and Telle R. 2008. Thermal stability of zircon ($ZrSiO_4$). *Journal of the European Ceramic Society* 28:2199–211.

Kamo S. L., Reimold W. U., Krogh T. E., and Colliston W. P. 1996. A 2.023 Ga age for the Vredefort impact event and a first report of shock metamorphosed zircons in pseudotachylitic breccias and granophyre. *Earth and Planetary Science Letters* 144:369–388.

Kenny G. G., Schmieder M., Whitehouse M. J., Nemchin A. A., Morales L. F. G., Buchner E., Bellucci J. J., and

Snape J. F. 2019. A new U-Pb age for shock-recrystallised zircon from the Lappajärvi impact crater, Finland, and implications for the accurate dating of impact events. *Geochimica et Cosmochimica Acta* 245:479–494. https://doi.org/10.1016/j.gca.2018.11.021.

Koşler J., Fonneland H., Sylvester P., Tubrett M., and Pedersen R. B. 2002. U-Pb dating of detrital zircons for sediment provenance studies—a comparison of laser ablation ICPMS and SIMS techniques. *Chemical Geology* 182:605–618.

Krogh T. E., Kamo S. L., and Bohor B. F. 1993. Fingerprinting the K/T impact site and determining the time of impact by U-Pb dating of single shocked zircons from distal ejecta. *Earth and Planetary Science Letters* 119:425–429.

Lana C., Romano R., Reimold W. U., and Hippert J. P. 2006. Collapse of large complex impact structures: Implications from the Araguainha impact structure. *Geology* 34:9–12.

Lana C., Souza-Filho C. R., Marangoni Y. R., Yokoyama E., Trindade R. I. F., Tohver E., and Reimold W. U. 2007. Insights into the morphology, geometry, and post-impact erosion of the Araguainha peak-ring structure, central Brazil. *Geological Society of America Bulletin* 119:1135–1150.

Lana C., Souza-Filho C. R., Marangoni Y. R., Yokoyama E., Trindade R. I. F., Tohver E., and Reimold W. U. 2008. Structural evolution of the 40 km wide Araguainha impact structure, central Brazil. *Meteoritics & Planetary Science* 43:701–716.

Ludwig K. R. 2003. User's manual for isoplot 3.0: A geochronological toolkit for Microsoft Excel. *Berkeley Geochronology Center Special Publication* 4:1–71.

Ludwig K. R. 2012. User's manual for isoplot 3.75—A geochronological toolkit for Microsoft Excel. *Berkeley Geochronology Center Special Publication* 5:1–75.

Machado R., Lana C., Stevens G., Filho C. R. S., Reimold W. U., and McDonald I. 2009. Generation, mobilization and crystallization of impact-induced alkali-rich melts in granitic target rocks: Evidence from the Araguainha impact structure, central Brazil. *Geochimica et Cosmochimica Acta* 73:7183–7201.

Martinez I. and Schärer U. 1994. Determination of shock-wave peak pressure and Rb-Sr isotope systematics in a granite from the Araguainha impact crater (Brasil). Proceedings, 22nd Lunar and Planetary Science Conference. pp. 857–858.

Medenbach O. 1985. A new microrefractometer spindle-stage and its application. *Fortschritte der Mineralogie* 63:111–133.

Reddy S. M., Johnson T. E., Fischer S., Rickard W. D. A., and Taylor R. J. M. 2015. Precambrian reidite discovered in shocked zircon from the Stac Fada impactite, Scotland. *Geology* 43:899–902. https://doi.org/10.1130/g37066.1.

Pimentel M. M., Fuck R. A., and Alvarenga C. J. S. 1996. Post-Brasiliano (Pan-African) high-K granitic magmatism in central Brazil: Late Prccambrian/early Paleozoic extension. *Precambrían Research* 80:217–238.

Preuss J. 2012. Characterization of Impact-related melt breccias from the impact structure Araguainha (Brazil). M.Sc. Thesis, University of Potsdam, Berlin. 92 pp.

Schmitz M. D., Bowring S. A, and Ireland T. R. 2003. Evaluation of Duluth Complex anorthositic series (AS3) zircon as a U-Pb geochronological standard: new high-precision isotope dilution thermal ionization mass spectrometry results. *Geochimica et Cosmochimica Acta* 67:3665–3672.

Silva D., Lana C. C., Stevens G., and Souza-Filho C. R. 2011. Effects of shock-induced incongruent melting within Earth's crust: The case of biotite melting. *Terra Nova* 23:225–231.

Silva D., Lana C., and de Souza Filho C. R. 2016. Petrographic and geochemical characterization of the granitic rocks of the Araguainha impact crater, Brazil. *Meteoritics & Planetary Science* 51:1–25. https://doi.org/10.1111/maps.12601.

Stacey J. S. and Kramers J. D. 1975. Approximation of terrestrial lead isotope evolution by a two-stage model. *Earth and Planetary Science Letters* 26:207–221.

Steiger R. H. and Jäger E. 1977. Subcommission on geochronology: Convention on the use of decay constants in geo- and cosmochronology. *Earth and Planetary Science Letters* 36:359–362.

Stöffler D. 1974. Deformation and transformation of rock-forming minerals by natural and experimental shock processes. II. Physical properties of shocked minerals. *Fortschritte der Mineralogie* 51:256–289.

Stöffler D. and Grieve R. A. F. 2007. Impactites. In *Metamorphic rocks: A classification and glossary of terms*, edited by Fettes D. and Desmons J. *Recommendations of the International Union of Geological Sciences Subcommission on the Systematics of Metamorphic Rocks*. Cambridge, UK: Cambridge University Press. pp. 82–92, 111–125, and 126–142.

Timms N. E. and Reddy S. M. 2009. Response of cathodoluminescence to crystal-plastic deformation in zircon. *Chemical Geology* 261:11–23.

Timms N. E., Erickson T. M., Pearce M., Cavosie A. J., Schmieder M., Tohver E., Reddy S. M., Zanett R., Nemchin A. A., and Wittmann A. 2017a. A pressure-temperature phase diagram for zircon at extreme condition. *Earth-Science Reviews* 165:185–202.

Timms N. E., Erickson T. M., Zanetti M. R., Pearce M. A., Cayron C., Cavosie A. J., Reddy S. M., Wittmann A., and Carpenter P. K. 2017b. Cubic zirconia in >2370°C impact melt records Earth's hottest crust. *Earth and Planetary Science Letters* 477:52–58.

Tohver E., Cawood C., Fletcher I. R., Jourdan F., Sherlock S., Rasmussen B., Trindade R. I. F., Yokoyama E., Souza Filho C. R., and Marangoni Y. 2012. Geochronological constraints on the age of a Permo-Triassic impact event: U-Pb and $^{40}Ar/^{39}Ar$ results for the 40 km Araguainha structure of central Brazil. *Geochimica et Cosmochimica Acta* 86:214–227.

Tohver E., Cawood C., Riccomini C., Lana C., and Trindade R. I. F. 2013. Shaking a methane fizz: Seismicity from the Araguainha impact event and the Permian-Triassic global carbon isotope record. *Palaeogeography, Palaeoclimatology, Palaeoecology* 387:66–75.

UnB-IG. 2012. Final mapping project by the graduate class of 2012. Institute of Geosciences, University of Brasilia, Brasilia, Brasil, Unpubl. Report.

Wiedenbeck M. P., Allé P., Corfu F., Griffin W., Meier M., Oberli F., Von Quadt A., Roddick J., and Spiegel W. 1995. Three natural zircon standards for U-Th-Pb, Lu-Hf, trace element and REE analyses. *Geostandards Newsletter* 19:1–23.

Wiedenbeck M. P., Hanchar J. M., Peck W. H., Sylvester P., Valley J., Whitehouse M., Kronz A., Morishita Y., Nasdala L., Fiebig J., Franchi I., Girard J.-P., Greenwood R. C., Hinton R., Kita N., Mason P. R. D., Norman M.,

Ogasawara M., Piccoli P. M., Rhede D., Satoh H., Schulz-Dobrick B., Skår O., Spicuzza M. J., Terada K., Tindle A., Togashi S., Vennemann T., Xie Q., and Zheng Y.-F. 2004. Further characterisation of the 91500 zircon crystal. *Geostandards and Geoanalytical Research* 28:9–39.

Wittmann A., Kenkmann T., Schmitt R. T., and Stöffler D. 2006. Shock-metamorphosed zircon in terrestrial impact craters. *Meteoritics & Planetary Science* 41:433–454.

Yokoyama E., Trindade R. I. F., Lana C. R., Souza-Filho C. R., Baratoux D., Marangoni Y. R., and Tohver E. 2012. Magnetic fabric of Araguainha complex impact structure (Central Brazil): implications for deformation mechanisms and central uplift formation. *Earth and Planetary Science Letters* 86:331–332.

SUPPORTING INFORMATION

Additional supporting information may be found in the online version of this article.

Fig. S1. Tera–Wasserburg plots showing the distribution of concordant and discordant data obtained by LA-ICP-MS. The errors are given as 1σ (%).

Fig. S2. Wetherill plots showing the distribution of concordant and discordant data obtained by SIMS. The errors are given as 1σ (absolute).

Table S1a. Laser ablation ICP-MS U-Pb isotope data. The errors are given as 1σ (absolute).

Table S1b. SIMS U-Pb isotope data for zircon grains from the fused sandstone Am-21B of the Araguainha impact structure. All errors are given as 1σ (absolute). The gray highlighting indicates the data that were used for the calculation of the best lower intercept age, for LA-ICP-MS data, and for concordant data from SIMS analysis, respectively.

Table S2. EBSD analysis details.